THE UNIVERSITY *of* EDINBURGH

Downlink System Characterisation in LiFi Attocell Networks

Cheng Chen

A thesis submitted for the degree of Doctor of Philosophy.
The University of Edinburgh.
September 2016

Abstract

There is a trend to move the frequency band for wireless transmission to ever higher frequencies in the radio frequency (RF) spectrum to fulfil the exponentially increasing demand in wireless communication capacity. Research work has gone into improving the spectral efficiency of wireless communication system to use the scarce and expensive resources in the most efficient way. However, to make wireless communication future-proof, it is essential to explore ways to transmit wirelessly outside the traditional RF spectrum. The visible light (VL) spectrum bandwidth is 1000 times wider than the entire 300 GHz RF spectrum and is, therefore, a viable alternative. Visible light communication (VLC) enables existing lighting infrastructures to provide not only illumination but also wireless communication. In conjunction with the concept of cell densification, a networked VLC system, light fidelity attocell (LAC) network, has been proposed to offer wide coverage and high speed wireless data transmission. In this study, many issues related to the downlink system in LAC networks have been investigated.

When analysing the downlink performance of LAC networks, a large number of random channel samples are required for the empirical calculation of some system metrics, such as the signal-to-interference-plus-noise ratio (SINR). However, using state-of-the-art approaches to calculate the non-line-of-sight (NLoS) channel component leads to significant computational complexity and prolonged computation time. An analytical method has been presented in this thesis to efficiently calculate the NLoS channel impulse response (CIR) in VLC systems. The results show that the proposed method offers significant reduction in computation time compared to the state-of-the-art approaches.

A comprehensive performance evaluation of the downlink system of LAC networks is carried out in this thesis. Based on the research results in the literature in the field of optical wireless communication (OWC), a system level framework for the downlink system in LAC networks is developed. By using this framework, the downlink performance subject to a large number of parameters is evaluated. Additionally, the effect of varying network size, cell deployment and key system parameters are investigated. The calculation of downlink SINR statistics, cell data rate and outage probability are considered and analysed. The results show that the downlink performance of LAC networks is promising in terms of achievable data rate per unit area compared to other state-of-the-art RF small-cell networks.

It is found that co-channel interference (CCI) is a major source of signal impairment in the downlink of LAC network. In order to mitigate the influence of CCI on signal distortion in LAC networks, widely used interference mitigation techniques for RF cellular systems are borrowed and extensively investigated. In this study, fractional frequency reuse (FFR) is adapted to the downlink of LAC networks. The SINR statistics and the spectral efficiency in LAC downlink system with FFR schemes are evaluated. Results show that the FFR technique can greatly improve the performance of cell edge users and as well the overall spectral efficiency. Further performance improvements can be achieved by incorporating angular diversity transmitters (ADTs) with FFR and coordinated multi-point joint transmission (JT) techniques.

Lay summary

With the development of mobile communication technology and the emergence of smart devices, the number of mobile users and wireless service demand have increased significantly in the past two decades. The radio frequency (RF) resources for wireless communication is over-crowded nowadays, which motivates the development of the mobile communication using other unexplored frequency bands. Visible light communication (VLC) is one of such technologies, which enables daily lighting infrastructures to also transmit data, and maintains the lighting functionality at the same time. In order to adapt VLC to future mobile communication network, light fidelity (LiFi) system has been proposed to provide high speed and reliable wireless broadband services with full network functionality. Despite the advancement in VLC, a lot of questions regarding LiFi network research still remain open.

Efficient method to simulate wireless channels is important in many VLC and LiFi studies. Using conventional ray-tracing methods requires a large amount of time for computation. Thus, a novel efficient channel calculation method has been proposed in this thesis. The detailed analyses lead to a number of tractable expressions, which are straightforward to use in other research. In addition, the calculation accuracy and the computation time of the proposed method have been evaluated and compared with the state-of-the-art methods.

The current work focuses on the fundamental downlink characteristics of LiFi network. A number of system metrics related to the downlink performance of a LiFi network have been considered in this thesis, such as the connection quality and the download speed. In addition, the effects of varying several system parameters, such as the size of the area that a single access point (AP) covers, are studied. Furthermore, tractable expressions for calculating the downlink signal-to-interference-plus-noise ratio (SINR) statistics are derived, and an initial performance evaluation is conducted.

From the analysis and performance evaluation of LiFi networks, it has been found that the co-channel interference (CCI) between adjacent links poses a major limitation to the performance of a LiFi network. It is intuitive to adopt interference mitigation techniques used in RF mobile communications to LiFi networks to control CCI in a minimum level. In this thesis, two such techniques, fractional frequency reuse (FFR) and multi-point joint transmission (JT), are considered and studied in LiFi. In this work, the downlink performance of LiFi network with FFR and JT schemes are evaluated and studied. The results show that FFR and JT techniques can effectively improve the service quality experienced by cell edge users and the overall system spectral efficiency.

Declaration of originality

I hereby declare that the research recorded in this thesis and the thesis itself were composed and originated entirely by myself in the Department of Electronics and Electrical Engineering at The University of Edinburgh.

Cheng Chen
Edinburgh, Uk
September 2016

Acknowledgements

Firstly, I would like to offer my sincerest gratitude to my mother, Hongmei Jiang, and my father, Xiaoxing Chen, for their love and support. They have shaped me as who I am today. For the past 27 years, no matter what happened, they are always by my side to support and encourage me. Without them, I can never accomplish this thesis.

I would like to sincerely thank my supervisor Prof. Harald Haas, who has led me into the world of LiFi. With his guidance and support, I have gained so much knowledge in the cutting-edge technologies. I truly appreciate his patience and encouragement throughout my Ph.D. study.

Last but not least, I would like to thank my friends, who have helped and encouraged me during my academic experience in Edinburgh. The time shared with them is the most precious memory in my life.

Contents

List of figures

List of tables

Acronyms and abbreviations

1-D	one dimensional
2-D	two dimensional
3-D	three dimensional
4G	4^{th} generation
ACO-OFDM	asymmetrically clipped optical orthogonal frequency division multiplexing
ADT	angular diversity transmitter
AMC	adaptive modulation and coding
AP	access point
APD	avalanche photodiode
ASE	area spectral efficiency
AWGN	additive white Gaussian noise
BER	bit error rate
BS	base station
CCI	co-channel interference
CDF	cumulative distribution function
CDMA	code-division multiple access
CF	characteristic function
CIR	channel impulse response
CLT	central limit theorem
CP	cyclic-prefix
CSI	channel state information
DC	direct current
DCO-OFDM	direct-current-biased optical orthogonal frequency division multiplexing
DD	direct detection
eU-OFDM	enhanced unipolar-OFDM
FCR	floor-to-ceiling-to-receiver
FFR	fractional frequency reuse
FFT	fast Fourier transform
FoV	field of view

FSO	free-space optical
HCPP	hard-core point process
HEX	hexagonal
IEEE	Institute of Electrical and Electronics Engineers
IFFT	inverse fast Fourier transform
IM	intensity modulation
IrDA	Infrared data association
IR	infrared
ISI	inter-symbol interference
JT	joint transmission
LAC	LiFi attocell
LD	laser diode
LED	light-emitting diode
LiFi	light fidelity
LoS	line-of-sight
MIMO	multiple-input multiple-output
mmWave	millimetre-wave
MP	multi-path
NLoS	non-line-of-sight
NMSE	normalised mean square error
O-BS	optical base station
OFDMA	orthogonal frequency division multiple access
O-OFDM	Optical-orthogonal frequency division multiplexing
OOK	on-off keying
OWC	optical wireless communication
PAM-DMT	pulse-amplitude-modulated discrete multi-tone modulation
PAPR	peak-to-average power ratio
PD	photodiode
PDF	probability density function
PFS	proportional fairness scheduling
PIN	positive-intrinsic-negative
PLC	powerline communication
PMF	probability mass function

PoE	power-over-ethernet
PPM	pulse position modulation
PPP	Poisson point process
PSD	power spectral density
RF	radio frequency
SCNR	signal-to-clipping noise ratio
sFFR	strict fractional frequency reuse
SFR	soft frequency reuse
SINR	signal-to-interference-plus-noise ratio
SNR	signal-to-noise ratio
TDMA	time-division multiple access
TFCR	transmitter-to-floor-to-ceiling-to-receiver
TFWR	transmitter-to-floor-to-wall-to-receiver
TIA	transimpedance amplifier
TWC	transmitter-to-wall-to-ceiling
TWCR	transmitter-to-wall-to-ceiling-to-receiver
TWR	transmitter-to-wall-to-receiver
TWWR	transmitter-to-wall-to-wall-to-receiver
UE	user equipment
UFR	universal frequency reuse
VL	visible light
VLC	visible light communication
WDMA	wavelength-division multiple access
WiFi	wireless fidelity

Nomenclature

$[\cdot]^*$	complex conjugate operator
$[\cdot]^{\mathrm{T}}$	transpose operator
$[\cdot] \otimes [\cdot]$	convolution operator
$[\cdot] \cdot [\cdot]$	dot product operator
$\binom{\cdot}{\cdot}$	binomial operator
N_i	number of interfering O-BSs in a PPP network
$\mathbf{1}_{Д}(u)$	indicator function of u for a subset $Д$
a	maximum horizontal range for the interfering O-BSs
$\vec{a}_{\mathrm{b}}$	position vector of the point $(x, y, 0)$ on the reflector
$\vec{a}_{\mathrm{b,tfcr}}$	position vector of a point on the floor surface in the TFCR channel
$\vec{a}_{\mathrm{b,twcr}}$	position vector of the point $\vec{a}_{\mathrm{b,twcr}}$ on the ceiling plane in the TWCR channel
$\vec{a}_{\mathrm{r}}$	position vector of a receiving element
$\vec{a}_{\mathrm{r,tfcr}}$	position vector of the receiver in TFCR channel
$\vec{a}_{\mathrm{r,twcr}}$	position vector of the receiver in the TWCR channel
$\vec{a}_{\mathrm{r,twr}}$	position vector of the receiver in TWC channel
$\vec{a}_{\mathrm{s}}$	position vector of a source element
$\vec{a}_{\mathrm{s,tfcr}}$	position vector of the transmitter in TFCR channel
$\vec{a}_{\mathrm{s,twcr}}$	position vector of the transmitter in the TWCR channel
$\vec{a}_{\mathrm{s,twr}}$	position vector of the transmitter in TWC channel
A	area of a specified region
A_{r}	receiving element physical area
A_{cell}	coverage area of a cell
A_{e}	area of a reflection block in the deterministic NLoS simulation method
A_{pd}	PD physical area
A_{st}	total combined area of single point transmission regions in a finite LAC network with JT scheme
A_{sys}	entire coverage area of a finite LAC network with JT scheme
$\mathcal{A}_n$	coefficient for the n^{th} Laguerre polynomial
$\mathcal{B}(u_1, u_2)$	beta function

c	speed of light
$\vec{C}$	weighted spectral efficiency vector in the PFS Algorithm 2
D	euclidean distance between a source element and a receiving element
$D_{0,\mathrm{tfcr}}$	shortest propagation distance in the TFCR channel
$D_{0,\mathrm{twc}}$	shortest propagation distance in the TWC channel
$D_{0,\mathrm{twcr}}$	shortest propagation distance in the TWCR channel
D_1	euclidean distance between the source element and the point $(x, y, 0)$ on the reflector
D_2	euclidean distance between the point $(x, y, 0)$ on the reflector and the receiving element
D_{c2r}	propagation distance from the ceiling point $\vec{a}_{\mathrm{b,twcr}}$ to the receiver
D_i	euclidean distance between the i^{th} O-BS and the desired UE
D_n	euclidean distance between transmitter source $\mathcal{S}_{\mathrm{Tx}}$ and n^{th} block element in the deterministic NLoS simulation method
D_{r}	distance from the receiver to the wall plane
$D_{\mathrm{r},n}$	distance from the receiver to the n^{th} wall plane
D_{s}	distance from the transmitter to the wall plane
$D_{\mathrm{s},n}$	distance from the transmitter to the n^{th} wall plane
D_{tfcr}	shortest propagation distance via point $\vec{a}_{\mathrm{b,tfcr}}$ in the TFCR channel
$\hat{D}_{\mathrm{s}}$	modified distance from the transmitter to the wall plane in the TWC CIR approximation in the TWCR channel
e_{nmse}	normalised mean square error
$\mathbb{E}[\cdot]$	statistical expectation
$E_{\mathrm{r,bg}}$	the incident background light irradiance
E_{v}	illuminance or incident luminous flux per unit area
$\tilde{E}_{\mathrm{v}}$	target illuminance level
f	frequency variable
$f_{\mathcal{N}}(u)$	PDF of the standard normal distribution
$f_u(u)$	PDF function of random variable u
$f_{u\|\mathrm{K}}(u)$	PDF function of random variable u on condition that u is within the region of K
$\mathfrak{f}_1(t)$	a function of t
$\mathfrak{f}_2(r)$	a function of r

$\mathfrak{f}_\lambda$	a wavelength dependent metric
$\bar{\mathfrak{f}}_\lambda$	the average value of the metric $\mathfrak{f}_\lambda$ over the used spectrum range
F_{fe}	front-end elements frequency characteristic control factor
F_{s}	sampling frequency
$\mathcal{F}_{\mathrm{fcr}}$	scaling factor in the CFR CIR approximation in the TFCR channel
$\mathcal{F}_{\mathrm{twc}}$	scaling factor in the TWC CIR approximation in the TWCR channel
$\mathcal{F}_\gamma$	function defined for the SFR SINR calculation
g_{c}	optical concentrator gain
g_{f}	optical filter loss
$g_1(u)$	path loss function defined in the CCI power term in the simplified LAC downlink SINR expression with PPP cell deployment
G	path loss from the source element via the point $(x, y, 0)$ on the reflector to the receiving element
$h(t)$	time-domain CIR at time instant t
$h^{[2]}_{\mathrm{c2r}}(t)$	second part CIR in the TWCR channel from the point $\vec{a}_{\mathrm{b,twcr}}$ on the ceiling plane to the receiver
$h^{[2]}_{\mathrm{fcr},\tilde{r}=0}(t)$	FCR CIR on condition that $\tilde{r} = 0$ m
$h_{\mathrm{fe}}(t)$	CIR due to the effects of front-end elements
$h_{\mathrm{fs}}(t)$	CIR due to the free-space light propagation in the considered indoor environment
$h_{\mathrm{fs},i}(t)$	CIR due to free-space signal propagation from the i^{th} O-BS
$h_i(t)$	time-domain CIR at time instant t from the i^{th} O-BS
$h^{[2]}_{\mathrm{fcr}}(t)$	second part CIR in the TWCR channel from the point $\vec{a}_{\mathrm{b,tfcr}}$ on the floor plane via the ceiling to the receiver (CFR)
$h^{[2]}_{\mathrm{t2f}}(t)$	first part CIR in the TWCR channel from the transmitter to the point $\vec{a}_{\mathrm{b,tfcr}}$ on the floor plane
$h^{[2]}_{\mathrm{tfcr}}(t)$	CIR due to the second order reflection with TFCR category
$h^{[2]}_{\mathrm{twc}}(t)$	first part CIR in the TWCR channel from the transmitter via the wall plane to the point $\vec{a}_{\mathrm{b,twcr}}$ on the ceiling plane (TWC)
$h^{[2]}_{\mathrm{twc},y=0}(t)$	TWC CIR on condition that $y = 0$ m
$h^{[2]}_{\mathrm{twcr}}(t)$	CIR due to the second order reflection with TWCR category
$h^{[1]}_{\mathrm{twr}}(t)$	CIR due to the first order reflection with TWR category

$h^{[\mathfrak{i}]}(t, \mathcal{S}, \mathcal{R})$	CIR due to the free-space light propagation from source element $\mathcal{S}$ to receiving element $\mathcal{R}$ undergoing exactly $\mathfrak{i}$ reflections
$\hat{h}(t)$	CIR expression with approximation
$\mathfrak{h}$	the Plancks constant which has a value of 6.626×10^{-34} Js
$\hbar(t)$	CIR for the preliminary single reflection channel model
$H(f)$	frequency response at frequency f
H_{DC}	DC gain of a channel
$H_{\mathrm{DC},i,l}$	channel DC gain with LoS component only from the l^{th} LED chip in the ADT of the i^{th} O-BS to the desired UE
$H_{\mathrm{fe}}(f)$	frequency response due to the effects of front-end elements at frequency f
$H_{\mathrm{fe}}(k)$	frequency response due to the effects of front-end elements on subcarrier k
$H_{\mathrm{fs}}(f)$	frequency response due to the free-space light propagation at frequency f
$H_{\mathrm{fs},i}(k)$	frequency response due to free-space signal propagation from the i^{th} O-BS on subcarrier k
$H_{\mathrm{fs},r}$	free-space signal propagation channel gain with LoS component only and a horizontal separation of r
$H_i(k)$	channel frequency response on subcarrier k from the i^{th} O-BS
i	index of an O-BS
$\mathfrak{i}$	index of the order of reflection
I	input electrical current variable
$I(t)$	instantaneous input current at time instant t
$I_i(t)$	instantaneous input current at time instant t for the i^{th} O-BS
$I_{\max}$	maximum forward current after pre-distortion
$\hat{I}_{\max}$	original maximum forward current within the linear dynamic range
$I_{\min}$	minimum forward current after pre-distortion
$\hat{I}_{\max}$	original minimum forward current within the linear dynamic range
I_{photo}	photocurrent generated by PD
$\mathcal{I}$	the term corresponds to the power of CCI in the simplified LAC downlink SINR expression
$\mathcal{I}_{0^\circ}(r_0)$	a function of r_0 for the CCI power term in the simplified LAC downlink SINR expression with a 2-layer HEX network conditioning on a θ of 0°
$\mathcal{I}_{30^\circ}(r_0)$	a function of r_0 for the CCI power term in the simplified LAC downlink SINR expression with a 2-layer HEX network conditioning on a θ of 30°

$\mathcal{I}_{\mathrm{SFR}}$	the term corresponds to the power of CCI in the case with SFR scheme
$\hat{\mathcal{I}}$	a term with approximation corresponds to the power of CCI in the simplified LAC downlink SINR expression
j	the imaginary number $\sqrt{-1}$
k	index of subcarrier in O-OFDM system
K	total number of subcarriers
K_{c}	number of subcarriers assigned to the cell centre UEs in a FFR scheme
K_{e}	number of subcarriers assigned to the cell edge UEs in a FFR scheme
$K_{\mathrm{e/v}}$	luminous efficacy
K_{jt}	number of subcarriers used for JT in the LAC system with JT frequency plan 1
K_{jt1}	number of subcarriers in the JT sub-band 1 in the LAC system with JT frequency plan 2
K_{jt2}	number of subcarriers in the JT sub-band 2 in the LAC system with JT frequency plan 2
K_{n_1}	number of subcarriers in sub-band n_1 in the PFS Algorithm 2
K_{n_1,n_2}	number of subcarriers in sub-band n_1 for the n_2^{th} UE in the PFS Algorithm 2
K_{st}	number of subcarriers used for single point transmission in the LAC system with JT
$K_{\bar{\varepsilon}}$	number of subcarriers on which a specified average spectral efficiency of $\bar{\varepsilon}$ is achieved
$\hat{K}$	variable represents a number of subcarriers defined in the PFS Algorithm 2
$\tilde{K}$	number of symbols carry information bits in O-OFDM system
$\mathcal{K}_{\mathrm{B}}$	Boltzmann's constant with a value of 1.38×10^{-23} J/K
$\mathbf{K}$	matrix of the number of subcarriers within different sub-band for different UE
l	an integer
l_{x}	room length
l_{y}	room width
l_{z}	room height
L_0	minimum propagation distance in the single reflection channel model
L_{b}	horizontal separation between source element and receiving element in the single reflection channel model
$L_{\mathrm{b,twr}}$	distance between the projections of transmitter and receiver on the wall plane in the TWR channel

L_{r}	distance between receiving element and reflector plane in the single reflection channel model
L_{s}	distance between source element and reflector plane in the single reflection channel model
$\hat{L}_{\mathrm{b}}$	euclidean distance between source element and receiving element in the single reflection channel model
$\mathcal{L}_n^{\alpha}(v)$	n^{th} Laguerre polynomial
m	Lambertian emission mode number
$\hat{m}$	maximum configuration for m based on a specified σ_{P} in the case of interference limited system
$\tilde{m}$	minimum configuration for m in the case of noise limited system
M	the number of subcarriers in sub-band n_1 excluding those for the $n_{\max}^{\mathrm{th}}$ UE and the $n_{\min}^{\mathrm{th}}$ UE in the PFS Algorithm 2
n	an integer
n_1	an integer
n_2	an integer
$n_{\mathrm{clip}}(t)$	time-domain clipping noise sample at time instant t
$n_{\mathrm{clip},i}(t)$	time-domain clipping noise sample corresponding to the i^{th} O-BS
$n_{\max}$	the index of the user achieves the maximum weighted spectral efficiency using the specified subcarrier in the PFS Algorithm 2
$n_{\min}$	the index of the user achieves the minimum weighted spectral efficiency using the specified subcarrier in the PFS Algorithm 2
$n_{\mathrm{Rx}}(t)$	time-domain receiver noise samples at time instant t
$\hat{n}_1$	an integer
$\mathfrak{n}$	internal refractive index of the optical concentrator
N_0	PSD of the receiver noise
$N_{0,\mathrm{shot}}$	PSD of the shot noise
$N_{0,\mathrm{thermal}}$	PSD of the thermal noise
$N_{\mathrm{clip},i}(k)$	k^{th} sample of the frequency-domain clipping noise corresponding to the i^{th} O-BS
N_{iter}	maximum number of iterations
N_r	number of bins in the numerical calculation of the integral (3.25) respect to the variable r

$N_{\mathrm{Rx}}(k)$	k^{th} sample of the frequency-domain receiver noise
N_{u}	number of UEs in a LAC system
N_{W}	number of downlink sub-bands in a LAC network with FFR scheme
N_x	number of bins in the numerical calculation of the integral (3.37) respect to the variable x
N_y	number of bins in the numerical calculation of the integral (3.37) respect to the variable y
N_θ	number of bins in the numerical calculation of the integral (3.8) respect to the variable θ
$\mathfrak{N}$	maximum order of Laguerre polynomial included in the expansion in the SINR statistics calculation with PPP cell deployment
$\vec{o}_{\mathrm{b}}$	orientation vector of the point $(x, y, 0)$ on the reflector
$\vec{o}_{\mathrm{b,tfcr}}$	orientation vector of the point $\vec{a}_{\mathrm{b,tfcr}}$ on the floor plane in the TFCR channel
$\vec{o}_{\mathrm{b,twcr}}$	orientation vector of the point $\vec{a}_{\mathrm{b,twcr}}$ on the ceiling plane in the TWCR channel respect to the coordinates defined in Figure 3.8
$\vec{o}^{\star}_{\mathrm{b,twcr}}$	orientation vector of the point $\vec{a}_{\mathrm{b,twcr}}$ on the ceiling plane in the TWCR channel respect to the coordinates defined in Figure A.1
$\vec{o}_{\mathrm{r}}$	orientation vector of a receiving element
$\vec{o}_{\mathrm{r,tfcr}}$	orientation vector of the receiver in TFCR channel
$\vec{o}_{\mathrm{r,twcr}}$	orientation vector of the receiver in the TWCR channel
$\vec{o}_{\mathrm{r,twr}}$	orientation vector of the receiver in TWC channel
$\vec{o}_{\mathrm{s}}$	orientation vector of a source element
$\vec{o}_{\mathrm{s,tfcr}}$	orientation vector of the transmitter in TFCR channel
$\vec{o}_{\mathrm{s,twcr}}$	orientation vector of the transmitter in the TWCR channel respect to the coordinates defined in Figure 3.8
$\vec{o}^{\star}_{\mathrm{s,twcr}}$	orientation vector of the transmitter in the TWCR channel respect to the coordinates defined in Figure A.1
$\vec{o}_{\mathrm{s,twr}}$	orientation vector of the transmitter in TWC channel
p_0	0^{th} power control factor in the SFR SINR calculation
p_1	1^{th} power control factor in the SFR SINR calculation
p_2	2^{th} power control factor in the SFR SINR calculation
p_3	3^{th} power control factor in the SFR SINR calculation
P_{elec}	electrical signal power

$P_{\mathrm{elec},i}(k)$	received signal power from the i^{th} O-BS
$P_{\mathrm{elec},i}^{\mathrm{clip}}(k)$	received clipping noise power from the i^{th} O-BS
P_{opt}	output optical power from an optical source
$P_{\mathrm{opt,e}}$	optical power received by cell edge UE which is R away from the cell centre
$P_{\mathrm{opt,d}}$	optical power incident to the desired cell coverage area
$P_{\mathrm{opt},h}(t)$	vector recording the received optical power at time instant t
$P_{\mathrm{opt,led}}$	incident optical power to the PD detector from the optical source at the O-BSs
$P_{\mathrm{opt,max}}$	maximum output optical power from an optical source
$\hat{P}_{\mathrm{opt,max}}$	original maximum output optical power from an optical source within the linear dynamic range
$\hat{P}_{\mathrm{opt,min}}$	original minimum output optical power from an optical source within the linear dynamic range
$P_{\mathrm{opt,r}}$	optical power detected by PD
$P_{\mathrm{opt,Rx}}$	incident optical power to the PD detector at the UE receiver
$P_{\mathrm{opt},\Omega}$	emitted optical power within a solid angle Ω
$\bar{P}_{\mathrm{opt}}$	average output optical power from an optical source
$\hat{P}_{\mathrm{opt}}$	variable recording optical power loss in the ray-tracing process of the Monte Carlo NLoS calculation Algorithm 1
$\hat{P}_{\mathrm{opt},h}(t)$	power of the received optical signal with delay less than t in the ray-tracing process of the Monte Carlo NLoS calculation Algorithm 1
$\tilde{P}_{\mathrm{opt}}(\lambda)$	spectral radiant power density function of an optical source
$\mathcal{P}_0$	the probability that no UE in a specified area
$\mathcal{P}_{\mathrm{c}}$	the probability that all of the observed UEs fall into the cell centre area
$\mathcal{P}_{\mathrm{e}}$	the probability that all of the observed UEs fall into the cell edge area
$\mathcal{P}_{\mathrm{out}}$	LAC downlink system outage probability
$\mathbb{P}[\cdot]$	statistical probability
q	charge of an electron which has a value of 1.602×10^{-19} C
$\mathcal{Q}(u)$	tail probability of the standard normal distribution
r	radius variable in a polar coordinate system
r_i	horizontal separation between the i^{th} O-BS and the desired UE
$r_{\max}$	the maximum value of the horizontal separation between the desired O-BS and the UE r_0 within the region K

$r_{\min}$	the minimum value of the horizontal separation between the desired O-BS and the UE r_0 within the region K
$\tilde{r}$	distance between the projections of point $\vec{a}_{\mathrm{b,tfcr}}$ and the receiver on the floor plane in the TFCR channel
$\mathfrak{r}_\theta(t)$	the boundary value of r for the region $\mathcal{W}_0(t)$ with a specified t and θ
R	circular cell radius
R_{c}	radius of a cell central area in a LAC network with FFR scheme
R_{e}	equivalent circular cell radius corresponding to a HEX cell with a radius of $\tilde{R}$ in a LAC network with FFR scheme
R_{femto}	radius of a femtocell
R_i	horizontal separation between the i^{th} O-BS and the desired UE
R_{L}	load resistance in the receiver circuit
R_{sq}	square cell edge length
R_{thin}	thinning radius in a HCPP
$\tilde{R}$	HEX cell radius
$\mathcal{R}$	a receiving element
$\mathcal{R}_{\mathrm{Rx}}$	the PD detector of a receiver
$\mathfrak{R}(u)$	ramp function
s	average downlink cell data rate in a LAC network
s_{area}	average area data rate
$s_{\mathrm{n_2}}$	the data rate achieved by the n_2^{th} UE in the PFS Algorithm 2
$\mathfrak{s}$	vector including the achieved data rate by each user in the PFS Algorithm 2
$\bar{\mathfrak{s}}$	averaging user data rate vector in the PFS Algorithm 2
$\mathcal{S}$	a source element
$\mathcal{S}_{\mathrm{Tx}}$	the light source of a transmitter
t	time variable
$t_{\max}$	maximum time delay
T	a SINR threshold
T_{e}	the SINR threshold for the categorisation of cell edge sub-cell in the modified FFR scheme in a LAC system with ADTs
T_n	SINR threshold for the n^{th} level modulation and coding
T_{out}	SINR threshold for the outage probability
$\mathcal{T}$	absolute temperature

u	a variable of a function
u_1	a variable of a function
u_2	a variable of a function
$\mathcal{U}(u)$	unit step function
v	a variable
V	a random variable of a function
$V(\lambda)$	luminosity function against wavelength λ
$\mathcal{V}(u)$	signal clipping function
W	distance between projections of transmitter and receiver on the edge shared by the floor plane and the wall plane
W_n	distance between projections of transmitter and receiver on the edge shared by the floor plane and the n^{th} wall plane
W_{sc}	bandwidth of a subcarrier
$\hat{W}$	distance between projections of transmitter and receiver on the floor plane
$\mathcal{W}_0(t)$	region on the reflector plane leads to the received signal with delay less than t
$\mathcal{W}_{\mathrm{c}}$	entire area of the ceiling plane
$\mathcal{W}_{\mathrm{f}}$	entire area of the floor plane
x	One of the horizontal direction variable in a Cartesian coordinate system
x_{r}	x coordinate of a receiving element orientation vector
x_{s}	x coordinate of a source element orientation vector
x'	One of the horizontal direction variable in a rotated Cartesian coordinate system
$\hat{x}_{\mathrm{r}}$	x coordinate of a receiver position vector
$\hat{x}_{\mathrm{s}}$	x coordinate of a transmitter position vector
$\hat{x}$	modified distance from the point $\vec{a}_{\mathrm{b,twcr}}$ on the ceiling plane to the wall plane in the TWC CIR approximation in the TWCR channel
$x(t)$	transmitted time-domain OFDM symbol at time instant t
$X(k)$	k^{th} symbol of the transmitted O-OFDM frame
$X_i(k)$	k^{th} symbol of the transmitted O-OFDM frame from the i^{th} O-BS
$\hat{X}$	coded QAM symbols with unity average symbol energy
$\vec{X}$	transmitted O-OFDM frame QAM symbol vector with power scaling
$\mathcal{X}$	the term corresponds to the desired signal power in the simplified LAC downlink SINR expression

y	One of the horizontal direction variable in a Cartesian coordinate system
y_{r}	y coordinate of a receiving element orientation vector
y_{s}	y coordinate of a source element orientation vector
y'	One of the horizontal direction variable in a rotated Cartesian coordinate system
$\hat{y}_{\mathrm{r}}$	y coordinate of a receiver position vector
$\hat{y}_{\mathrm{s}}$	y coordinate of a transmitter position vector
$y(t)$	received time-domain OFDM symbol at time instant t
$Y(k)$	k^{th} symbol of the received O-OFDM frame
z	the vertical direction variable in a Cartesian coordinate system
z_{r}	z coordinate of a receiving element orientation vector
z_{s}	z coordinate of a source element orientation vector
$\hat{z}_{\mathrm{r}}$	z coordinate of a receiver position vector
$\hat{z}_{\mathrm{s}}$	z coordinate of a transmitter position vector
z'	the vertical direction variable in a rotated Cartesian coordinate system
z_{r}	distance from the receiver to the floor plane
z_{s}	distance from the transmitter to the floor plane
$\mathcal{Z}$	the term corresponds to the receiver noise power in the simplified LAC downlink SINR expression
α	the mean and variance of the Laguerre polynomial base function
α_{pfs}	user data rate forgetting factor in the PFS Algorithm 2
α_{twc}	ratio of $\hat{D}_{\mathrm{s}}$ to $D_{0,\mathrm{twc}}$
β	a scaling factor to ensure that the mean and the variance of the scaled random variable are the same
$\gamma(k)$	signal-to-interference-plus-noise ratio on subcarrier k
γ_{ADT}	downlink SINR in a LAC system with ADTs
γ^{c}	downlink SINR on a subcarrier in a common sub-band in a LAC network with sFFR scheme
γ_1^{c}	condition 1 SFR SINR achieved by cell centre UEs
γ_2^{c}	condition 2 SFR SINR achieved by cell centre UEs
γ_3^{c}	condition 3 SFR SINR achieved by cell centre UEs
γ^{e}	downlink SINR on a subcarrier in a protected sub-band in a LAC network with sFFR scheme

γ_1^{e}	condition 1 SFR SINR achieved by cell edge UEs
γ_2^{e}	condition 2 SFR SINR achieved by cell edge UEs
γ_{clip}	signal-to-clipping noise ratio
γ_{UFR}	downlink SINR on a subcarrier in a LAC network with UFR scheme
$\hat{\gamma}$	a value of downlink SINR
$\tilde{\gamma}$	a value of downlink SINR that is randomly selected from the cases with a number of conditions in the SFR average spectral efficiency calculation
$\Gamma(u_1, u_2)$	upper incomplete Gamma function
$\delta(u)$	Dirac delta function
$\Delta\epsilon$	effective signal amplitude range
Δt	time delay resolution
Δz	vertical separation between the transmitter of the O-BSs and the receiver
ϵ_{DC}	normalised DC-bias level
$\epsilon_{\max}$	normalised top clipping level
$\epsilon_{\min}$	normalised bottom clipping level
$\varepsilon(\gamma, \kappa_{\mathrm{rf}})$	spectral efficiency with a SINR of γ and a reuse factor of κ_{rf} calculated using Shannon Hartley formula
ε_n	spectral efficiency of the n^{th} level modulation and coding using an AMC scheme
ε_{n_1,n_2}	spectral efficiency achieved on a subcarrier in sub-band n_1 for the n_2^{th} UE in the PFS Algorithm 2
$\bar{\varepsilon}$	average spectral efficiency calculated using Shannon Hartley formula
$\bar{\varepsilon}^{\mathrm{c}}$	average spectral efficiency calculated using Shannon Hartley formula for the UEs in the cell centre area
$\bar{\varepsilon}^{\mathrm{e}}$	average spectral efficiency calculated using Shannon Hartley formula for the UEs in the cell edge area
$\bar{\varepsilon}_1^{\mathrm{c}}$	achievable average spectral efficiency corresponding to the SINR γ_1^{c} in a LAC system with SFR scheme
$\bar{\varepsilon}_1^{\mathrm{e}}$	achievable average spectral efficiency corresponding to the SINR γ_1^{e} in a LAC system with SFR scheme
$\bar{\varepsilon}_2^{\mathrm{c}}$	achievable average spectral efficiency corresponding to the SINR γ_2^{c} in a LAC system with SFR scheme

$\bar{\varepsilon}_2^{\mathrm{e}}$	achievable average spectral efficiency corresponding to the SINR γ_2^{e} in a LAC system with SFR scheme
$\bar{\varepsilon}_3^{\mathrm{c}}$	achievable average spectral efficiency corresponding to the SINR γ_3^{c} in a LAC system with SFR scheme
$\bar{\varepsilon}_{\mathrm{sFFR}}$	average spectral efficiency in a LAC network with sFFR scheme considering low user density issue
$\bar{\varepsilon}_{\mathrm{sFFR,nor}}$	average spectral efficiency in a LAC network with sFFR scheme in a normal condition
$\bar{\varepsilon}_{\mathrm{SFR}}$	average spectral efficiency in a LAC network with SFR scheme considering low user density issue
$\bar{\varepsilon}_{\mathrm{SFR}}^{\mathrm{e}}$	average spectral efficiency for the UEs in the cell edge area with SFR scheme
$\bar{\varepsilon}_{\mathrm{SFR,nor}}$	average spectral efficiency in a LAC network with SFR scheme in a normal condition
$\bar{\varepsilon}_{\mathrm{UFR}}$	average spectral efficiency in a LAC network with UFR scheme
$\bar{\varepsilon}_{\mathrm{UFR}}^{\mathrm{e}}$	average spectral efficiency for the UEs in the cell edge area with UFR scheme
ζ	averaging weight in the average spectral efficiency calculation in a LAC network with FFR schemes
ζ^{c}	averaging weight for the cell centre UEs that achieve an average spectral efficiency of $\bar{\varepsilon}^{\mathrm{c}}$ in a LAC network with sFFR scheme
ζ_1^{c}	SFR average spectral efficiency calculation averaging weight in the cell centre on condition 1
ζ_2^{c}	SFR average spectral efficiency calculation averaging weight in the cell centre on condition 2
ζ^{e}	averaging weight for the cell edge UEs that achieve an average spectral efficiency of $\bar{\varepsilon}^{\mathrm{e}}$ in a LAC network with sFFR scheme
ζ_1^{e}	SFR average spectral efficiency calculation averaging weight in the cell edge on condition 1
ζ_2^{e}	SFR average spectral efficiency calculation averaging weight in the cell edge on condition 2
ζ_3^{e}	SFR average spectral efficiency calculation averaging weight in the cell edge on condition 3
η_{clip}	clipping attenuation factor

η_{led}	conversion coefficient from the input current to the optical output power which includes the electrical signal amplification and the LED quantum efficiency
η_{pd}	PD responsivity
$\eta_{\mathrm{pd,qe}}$	quantum efficiency of a PD
θ	polar angle variable in a polar coordinate system
Θ_i	polar angle corresponds to the i^{th} O-BS
κ_n^V	n^{th} cumulant of random variable V
λ	wavelength variable
λ_{max}	maximum used wavelength
λ_{min}	minimum used wavelength
Λ	O-BS deployment density
Λ_0	initial PPP density in a HCPP
μ_n^V	n^{th} raw moment of random variable V
ξ	O-OFDM symbol power scaling factor
Ξ	the objective function of the PFS Algorithm 2
ρ	reflectance of a surface
ρ_{c}	reflectance of the ceiling
ρ_{f}	reflectance of the floor
ρ_{w}	reflectance of the walls
ϱ	ratio of the central area radius R_{c} to the equivalent circular cell radius R_{e} in a LAC system with a FFR scheme
σ^2_{clip}	variance of the clipping noise
σ_{P}	optical power drop for cell edge UE which is R away from the cell centre relative to the optical power received by cell centre UE which is right beneath the O-BS
σ^2_{Rx}	variance of the receiver noise
σ^2_{shot}	variance of the shot noise
$\sigma^2_{\mathrm{thermal}}$	variance of the thermal noise
σ_{x}	electrical signal amplification factor
ς	power control factor in SFR scheme
$\hat{\tau}$	variable recording transmission time
τ_{c}	LED response time constant
ϕ	radiant angle from an optical source

ϕ_1	radiant angle from the source element to the point $(x, y, 0)$ on the reflector
ϕ_2	radiant angle from the point $(x, y, 0)$ on the reflector to the receiving element
ϕ_n	radiant angle from transmitter source $\mathcal{S}_{\mathrm{Tx}}$ to n^{th} block element in the deterministic NLoS simulation method
Φ_{v}	luminous flux
$\Phi_{\mathrm{v},\Omega}$	emitted luminous flux within a solid angle Ω
$\varphi_V(\omega)$	the characteristic function of V
χ	user density in a specified area
ψ	incident angle to a receiving element
ψ_1	incident angle from the source element to the point $(x, y, 0)$ on the reflector
ψ_2	incident angle from the point $(x, y, 0)$ on the reflector to the receiving element
ψ_{FoV}	FoV of a receiver
ψ_n	incident angle from transmitter source $\mathcal{S}_{\mathrm{Tx}}$ to n^{th} block element in the deterministic NLoS simulation method
ω	variable of a characteristic function
ω_{c}	Cartesian coordinates rotation angle
Ω	solid angle variable
И	the set of indices of O-BSs causing CCI
$И_{\mathrm{A}}$	O-BS group A in a 2-layer HEX LAC network with FFR schemes
$И_{\mathrm{B}}$	O-BS group B in a 2-layer HEX LAC network with FFR schemes
$И_{\mathrm{C}}$	O-BS group C in a 2-layer HEX LAC network with FFR schemes
К	a valid region for a random variable
$Л_i$	a set including the indices of the LED chip of i^{th} O-BS that is transmitting using the considered transmission resources

Chapter 1
Introduction

1.1 Motivation

With the increasing popularity of 'smart devices', mobile data service become an important part of everyone's daily life [1]. It has been estimated that the global mobile data traffic would be 30.6 exabytes per month by 2020 [1]. In parallel, current radio frequency (RF) spectrum resource from 300 kHz to 30 GHz is becoming saturated. As a result of these conflicting trends, existing wireless communication systems based on RF spectrum are not able to fulfil the demands for mobile data traffic in the future. In order to deal with this looming spectrum shortage, mobile operators have been expanding the capability of their 4^{th}-generation (4G) networks and building more wireless fidelity (WiFi) - hotspots to offload wireless traffic [1]. In addition, researchers consider various innovative technologies to improve the spectral efficiency of existing RF wireless networks, such as multiple-input multiple-output (MIMO) techniques. However, on the account of the continuing increase of wireless traffic, it can be anticipated that the current RF spectrum resource will no longer fulfil the future wireless data traffic demand in spite of the efforts on further developments in RF wireless communication technology.

Therefore research has been focused on higher frequency spectrum resources. In particular, the millimetre-wave (mmWave) communication and optical wireless communication (OWC) [2] are two of the most popular research areas. In mmWave communication, the spectrum in the range from 30 GHz to 300 GHz has been considered for high speed broadband services [3]. A considerable amount of spectrum resources are expected to be released for wireless communication. In mmWave links, signal propagation experiences significant atmospheric loss due to the absorption by water vapour and oxygen [3]. Furthermore, according to the Friis transmission equation, the wireless transmission path loss increases proportionally to the square of the signal frequency. For these reasons, the mmWave systems rely on line-of-sight (LoS) channels in most of the cases, and have a relatively small coverage area. In order to compensate for the weak signal strength caused by high path loss, multiple steerable and directional antennas with beam-forming techniques are required in mmWave systems. This characteristic makes mmWave communication complex in system design and signal processing.

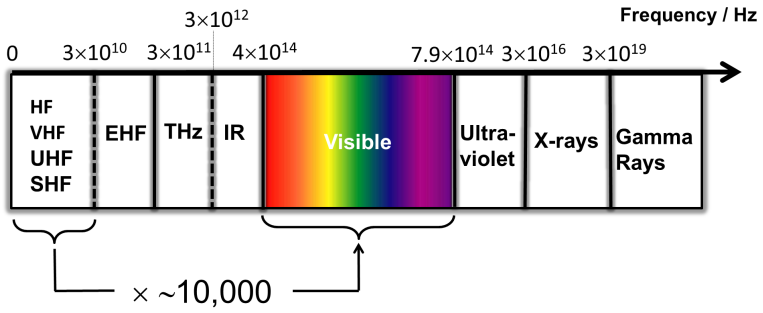

Figure 1.1: *The electromagnetic spectrum [6].*

The optical spectrum for OWC includes the infrared (IR) and visible light (VL) [4]. Figure 1.1 shows that the total frequency bandwidth of optical spectrum is several hundred THz, which is much wider than any RF spectrum [5, 6]. With further development in coherent transmission and detection techniques in OWC, the huge capacity with this wide spectrum bandwidth is possible to be achieved in the future. The main advantages of OWC over RF communication can be concluded as follows [4]: i) the optical signal does not interfere with any RF-based wireless systems; ii) OWC can be used in any radio radiation restricted area, such as intrinsically safe environments; iii) and the optical spectrum resource is unlicensed. In particular, OWC using VL, namely visible light communication (VLC), has the potential to be densely deployed using the existing lighting infrastructures, which is expected to be cost-effective. In addition, transmission directionality is obtained by beam-forming techniques with multiple antennas in RF-based communication systems, while VL sources and detectors provide directionality in nature with cost-effective optics. Therefore, VLC is a promising technology for future wireless communication systems.

In the development of RF wireless communication technology, various techniques have been explored to improve the data capacity of the wireless networks [7], such as developing advanced modulation schemes, coding schemes, equalisation techniques, MIMO techniques and 'cell densification' approaches. Among these techniques, the most effective approach is expected to be 'cell densification'. 'Cell densification' refers to deploying more access points (APs) in a certain area so that the spectrum resource can be shared among a fewer number of mobile users [8]. With 'cell densification', a significant gain in spectral efficiency per unit area is expected [9]. During the early stage of cellular wireless communication, macro cells covered

Cell type	Macro	Micro	Pico	Femto
Typical cell radius	> 1 km	250 m - 1 km	100 m - 300 m	10 m - 50 m

Table 1.1: *Typical cell radius of cellular networks [11].*

an area of several blocks in a city. In the latest cellular wireless communication systems, the smallest cells, femtocells [10], are designed and deployed covering one or more rooms in an indoor environment. Table 1.1 shows the typical cell radius of different cellular networks [11]. This trend of high spatial reuse is expected to continue in the design of mmWave and VLC systems, where a cell radius of a few metres are expected.

Combining the concept of small-cell network and VLC techniques, a fully networked VLC system can be established, and this is termed light-fidelity (LiFi) attocell (LAC) network [12]. In addition to the characteristics of a VLC system, a LAC network is able to achieve bi-direction transmission, serve multiple users with a single AP, and support mobility [12]. In other words, roaming and smooth handover functions are required. In a room of moderate size, multiple lighting infrastructures are typically available, which can be used as VLC APs. Additionally, due to the directionality of the light source, co-channel interference (CCI) is expected to be low compared with other RF cellular systems with the same spatial reuse strategy. Therefore, LAC networks have similar characteristics of a small-cell system based on mmWave communication, but the cell size is even smaller, which means LAC systems can achieve a much higher data capacity per unit area [6]. Deploying LAC networks as an extra layer in a future heterogeneous network is a very promising solution to offload the greatly increased mobile data traffic in the future wireless communication networks.

Since LAC network is a newly proposed concept, many questions related to this networked VLC system still remain open. In order to understand the characteristics of LAC networks, comprehensive theoretical studies are required. This thesis focuses on the analysis of LAC downlink performance, which is motivated by the following considerations. On the one hand, promising downlink performance could validate the effectiveness of applying LAC networks for off-loading wireless data traffic. On the other hand, there is a large body of research on physical layer techniques for point-to-point VLC transmission systems, which can be incorporated into the network downlink performance analyses of this work. Furthermore, a successful downlink analysis of LAC networks in physical layer could be used as a basis of future network layer or other higher layer studies on LAC networks.

In the downlink performance analysis, a system metric may be evaluated for a massive number of times with different random user positions. The difference in transmission geometry for each evaluation leads to different channel state information (CSI). If the effect of light propagation in indoor environment is taken into account, using the state-of-the-art methods to generate the CSI would lead to significantly long simulation time as these methods are primarily based on ray-tracing techniques. Therefore, an analytical approach is considered in this research to efficiently calculate the channel impulse response (CIR), which gives a straightforward indication of the CSI. A significant reduction in non-line-of-sight (NLoS) channel simulation time is expected by using the proposed method. In addition, the proposed method decomposes the CIR into multiple components with unique characteristics, which aids the analysis of VLC channel characteristics in future research.

Among a number of system metrics for the downlink performance of LAC systems, signal-to-interference-plus-noise ratio (SINR) offers a straightforward indication of the downlink quality in LAC systems. In addition, a number of other important metrics, such as cell data rate, can be estimated based on SINR. Furthermore, SINR can be used as a system metric to determine the impact of a number system factors, such as cell size, light source beamwidth, cell deployment. Knowing the effects of varying these system factors helps to find the optimal system configuration for LAC networks. For these reasons, a series of theoretical studies related to the downlink SINR in LAC networks are conducted in this research.

CCI poses a major limiting factor to the system performance in the LAC downlink. It is intuitive to adopt existing interference mitigation techniques used in RF cellular systems to achieve an improved downlink performance especially for cell edge users. Fractional frequency reuse (FFR) technique offers a reasonable balance between complexity and performance in interference mitigation. Additionally, the size of receiver photodiode (PD) detector is significantly large compared to the wavelength of the light signal, which introduces spatial diversity and prevents the effect of 'multi-path (MP) fading' in an intensity modulation (IM) / direct detection (DD) system [13]. For the same reason, it is unnecessary to consider the issue of destructive combination of multiple signals from different sources. This characteristic makes coordinated multi-point joint transmission (JT) a good candidate for the interference mitigation in LAC networks. Therefore, these two techniques have been considered and investigated in current research.

1.2 Contribution

This thesis focuses on investigating the characteristics of the LAC downlink systems. In a systematic approach I aim at addressing the following three research objectives:

- Establishing a system model for LAC downlink systems.
- Evaluating the downlink performance of LAC networks.
- Improving the downlink performance of LAC networks.

By following these objectives, several contributions have been established.

With regard to the first objective, suitable models have been found in the existing research publications for each component in the LAC downlink system except for the efficient model for NLoS channel. As the first contribution of this thesis, an analytical method for the calculation of VLC NLoS CIR is proposed. In this proposed channel calculation method, the overall NLoS channel is decomposed into multiple components according to the number of undergoing reflections and light propagation categories. The analytical expressions for the CIR with a number of categories that dominate the NLoS channel are developed. Each expression includes one or two 1-dimensional (1-D) integrals, which can be solved efficiently by using standard numerical methods. An expression for the overall NLoS CIR is obtained by combining the CIR results for each propagation category. The results of the proposed method are compared with those of the state-of-the-art method in terms of CIR, frequency response and computation time. The derivation of the proposed analytical CIR calculation method has led to the publication of [14] and the submitted paper [15].

Following the second research objective leads to the second contribution of this thesis: the comprehensive performance evaluation of the downlink in LAC networks for the first time. A major concern in the performance of a LAC system is whether the omission of NLoS channel causes significant error in the estimation of the downlink performance. This issue is investigated in a case study simulation. In addition, the effects of varying a number of factors, such as network size, cell deployment, reuse factor and other important system parameters, are considered. In the performance evaluation, SINR, cell data rate, outage probability, and area data rate are calculated. In particular, the analytical expression for the SINR statistics in the LAC networks with hexagonal (HEX) and Poisson point process (PPP) cell deployment are obtained. Furthermore,

the downlink performance of LAC networks are compared with other state-of-the-art small-cell systems in terms of area data rate. The work conducted on the downlink SINR calculation expression and the downlink performance analysis in LAC networks has led to the publication of [16–18].

Regarding the third objective, CCI is found to be a major issue in the LAC downlink with dense spatial reuse. Therefore, interference mitigation techniques used in RF systems are considered to be adopted in the LAC downlink. This leads to the third contribution of this thesis: adopting FFR and JT schemes into the LAC downlink. In the study of using FFR, unique characteristics in LAC downlink, such as low user density issue, are considered. Tractable analytical tools have been developed to efficiently calculate the downlink SINR statistics and spectral efficiency with FFR. In contrast to the case with universal frequency reuse (UFR), the LAC system with FFR offers cell edge users with improved signal quality and higher data rate. In contrast to the case with traditional resource partitioning considered in [19], the LAC system with FFR offers an improved overall spectral efficiency. To further improve the effectiveness of FFR, the combination of the FFR technique and angular diversity transmitters (ADTs) is investigated using computer simulations. The research conducted on the adaptation of FFR in LAC networks has led to the publication of [20, 21]. In the study of using JT in conjunction with ADTs, appropriate hardware configuration and frequency plans have been proposed. The performance improvement is evaluated by using computer simulations. The research conducted on the adaptation of JT in LAC networks has led to the publication of [22].

1.3 Thesis Layout

The remainder of this thesis is organised as follows. In Chapter 2, the concept of LAC system and the functionalities of LAC systems are briefly introduced. For the modelling of the downlink transmission of LAC network, the characteristics of several system components and a number of basic concepts are provided. In each individual section, the knowledge of LiFi or LAC network technology, the characteristics of the front-end elements, channel, sources of receiver noise, optical-orthogonal frequency division multiplexing (O-OFDM) transmission, cell deployment and spatial reuse, signal clipping and the downlink SINR in a LAC network are presented.

In Chapter 3, the issue of computational complexity in the NLoS channel calculation is intro-

duced. The description of the methodology of the proposed calculation approach is presented. Motivated by the result in [23], an extended analytical expression for the calculation of the CIR with a single diffuse reflection is derived. Based on this single reflection CIR model, the calculation of CIRs resulted from the 1^{st} and a fraction of the 2^{nd} order reflections are derived. By combining the derived CIR results, an expression to estimate the overall NLoS VLC CIR is obtained. The proposed method is compared with the state-of-the-art methods both in accuracy and computation time.

In Chapter 4, the downlink performance evaluation of LAC networks is considered. Firstly, the effects of NLoS signal propagation and the effects of varying network size are evaluated. Furthermore, the critical effects of varying cell radius and half-power semi-angle of the VL source are analysed. Next, the network performance with different cell deployments are assessed. Furthermore, the statistics of the downlink SINR of LAC networks are analysed. The cases with HEX / PPP cell deployments in an infinite network are considered in this analysis of SINR statistics. In addition, the cell data rate and the outage probability based on the SINR statistics are analysed and evaluated. Finally, The downlink performance of LAC networks are compared with those achieved by other state-of-the-art small-cell systems in terms of area data rate.

In Chapter 5, interference mitigation techniques for the downlink of LAC networks are considered. The basic concept of FFR and JT are introduced. For the study of using FFR in LAC networks, the downlink SINR statistics and spectral efficiency in a LAC network with FFR schemes are analysed. The numerical results are presented, and this exposed a low user density issue. The addition of a modified proportional fairness scheduling (PFS) method to the system is proposed to compensate for this issue. As an extension, an ADT is considered in combination with FFR scheme. For the study of using JT in LAC networks, The system setup for the deployment of JT algorithms is presented. The simulation results in terms of the SINR distribution, user throughput and cell throughout are considered. The results overwhelmingly demonstrate the achievable performance gain by using JT techniques in LAC systems.

Chapter 6 summarises key findings of this thesis. Additionally, the limitations of the research presented in this thesis and future research directions are also discussed.

1.4 Summary

The combination of VLC technology and the deployment of small cells is a promising solution to deal with the looming crisis in "spectrum shortage" in wireless communication. Despite the research efforts spent on many aspects in the field of VLC or OWC using analysis and experiments, very limited research has been conducted on the performance evaluation of a networked VLC system – a LiFi system or a LAC network. The research presented in this thesis provides a comprehensive downlink performance analysis of a LAC network in the physical layer. The motivation and the main contributions, together with the layout of the thesis are presented in this chapter.

Chapter 2
Background

2.1 Introduction

Optical communication is defined as any information transmission between two distant locations using electromagnetic radiation in optical spectrum. The earliest examples of optical communications can be traced back to the period before the century, when the fire beacons were used by ancient Greeks and Romans for signalling purposes [24]. In ancient China, the Great Wall was built to protect against the enemies from the north. A smoke signalling relay was used with a series of beacon towers to transmit the invasion messages efficiently. In 1880, the Scottish-born inventor Alexander Graham Bell invented a photophone [25], which can be considered as the first official record of using optical signals for wireless communication purpose. The voice signal was transmitted with a distance of about 200 m via sunlight. In the late 19^{th} century, the British Navy started to use signal lamps to communicate using light. These early methods have been significantly improved, and widely used today.

The high speed optical communications were achieved with the advance in optoelectronics, such as light-emitting diode (LED), laser diode (LD), and photodiode (PD), which can support efficient conversion between optical signal and electrical signal with sufficient wide modulation bandwidth [24]. For the applications of optical communications, free-space point-to-point long distance transmissions were first considered, which is known as free-space optical (FSO) communication [24]. A number of FSO links have been successfully demonstrated in 1960s and 1970s. FSO technologies have also been considered for military use because of its security characteristics. The optical wireless communication (OWC) technologies for short-range indoor applications are pioneered by the early work of Gfeller and Bapst, which demonstrated that a diffused infrared (IR) radiation communication system can achieve a data rate of around 100 kbps [26]. With the development of IR-based technology, the infrared data association (IrDA) founded in 1993 formulated a set of protocols for wireless IR communications between electronic devices [27]. With the emergence of energy-efficient white-LED, solid state lighting (SSL) is gaining popularity in the lighting industry [28]. It is expected that LED-based lighting

infrastructures will replace all conventional lighting infrastructures, such as fluorescent lamps, in the coming decades. This trend provides an opportunity to piggyback the wireless communication functionality on to the future lighting networks, which is known as visible light communication (VLC) [29]. With significant research efforts, links with multi-Gbps data rate have been experimentally demonstrated [30, 31]. In 2011, Institute of Electrical and Electronics Engineers (IEEE) published a set of standard for short-range VLC applications [32].

A cellular system is an infrastructure-based wireless network [7]. The coverage area of a cellular system is divided into many non-overlapping cells. A base station (BS) or access point (AP) is typically located in the centre of each cell, and serves mobile user equipments (UEs) in the cell where the BS is located. In addition, BSs are connected to the backhaul network, which allows the UEs connected to the wired network. Compared to a single AP wireless system, cellular system provides a much larger coverage area and allows multiple UEs to be connected simultaneously [33]. Additionally, the area spectral efficiency (ASE) of a cellular system is higher as the available transmission resources can be reused as long as the links are spatially separated. Compared to a wireless network without infrastructure (no backhaul connections) such as ad-hoc network, cellular systems are operated with a centralised control mechanism [7]. Thus, the implementation of adaptive resource allocation, power control, handover and many other system functions is possible with central control in a cellular system. Therefore, cellular systems achieve better communication performance and more flexibility than non-infrastructure-based systems. Because of these benefits, today's cellular systems are widely deployed in the world. Furthermore, research on improving the performance of cellular networks shows that network densification is one of the most effective methods to improve the capacity of cellular system [34]. With the development of various advanced wireless communication technologies, more APs are densely deployed to cater ever increasing wireless data traffic demands. This leads to modern heterogeneous networks and small-cell systems [35].

2.2 LiFi Attocell Networks

Although VLC systems offer a number of advantages over radio frequency (RF) wireless systems, a typical point-to-point VLC link has a very limited coverage range, which is undesired from mobility and flexibility perspective. An intuitive solution to this issue is to connect the multiple VLC infrastructures as a networked system, light fidelity (LiFi) attocell (LAC) network [6, 12]. Figure 2.1 illustrates the concept of a LAC network. Each VLC infrastructure

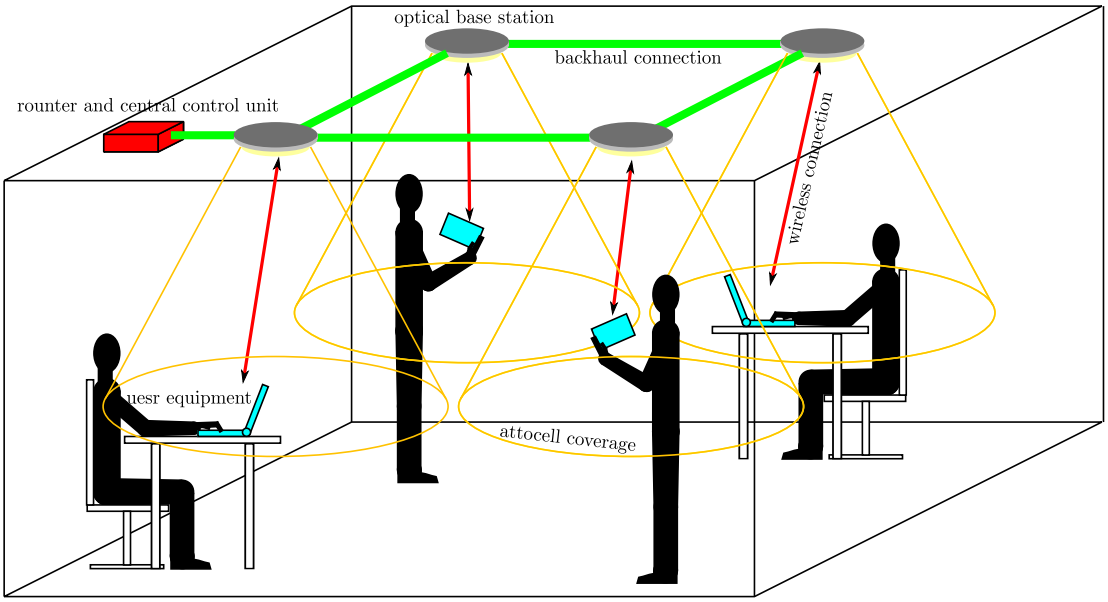

Figure 2.1: *Concept of LiFi attocell network.*

serves a number of UEs within its local coverage area, which operates as an optical base station (O-BS). The size of the combined coverage area is expected to be as large as that provided by any WiFi or femtocell systems, as lighting infrastructures are everywhere in modern indoor environments. This cellular design not only alleviates the coverage constraint, it also agrees with the trend of network densification. As a cellular network, VLC technology offers two more benefits. Unlike omnidirectional antennas radiating RF signal to all directions, a light source typically radiates optical power to a specified direction with a specified beam-width. Therefore, the radiation of the visible light (VL) signal can be confined within a limited region, typically the area underneath the light source. In contrast, RF small-cell network such as a millimetre-wave (mmWave) system requires complicated beam-forming techniques to achieve the same objective. Secondly, LAC networks can be implemented by modifying existing lighting networks. However, building a RF small-cell network with the same AP density, the cost for hardware is much higher. In addition, a LAC network could be designed as an extra layer of heterogeneous networks, and this new layer of access network causes and receives zero interference to and from existing RF access networks. This combination of using unlicensed spectrum and cell densification is desired from spectral efficiency perspective, which makes LAC network a promising future wireless access network design.

A LAC network is expected to have the full functionality of a cellular system [12]. Therefore,

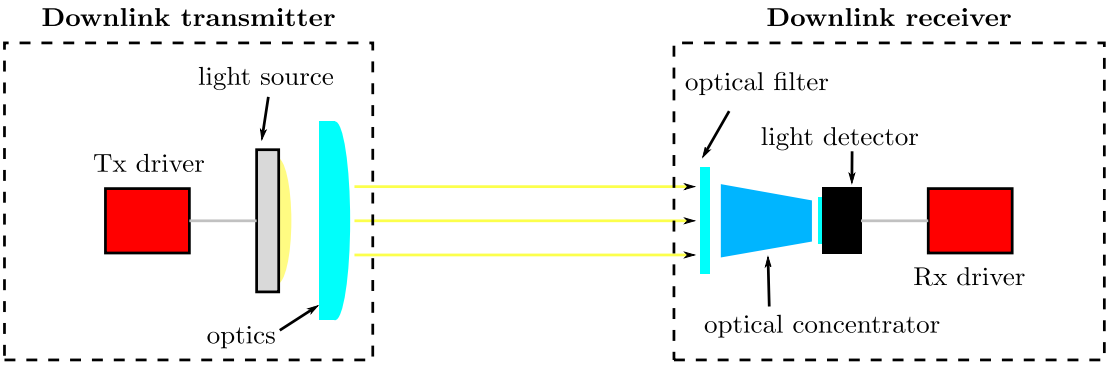

Figure 2.2: *Key components in a LAC downlink transmission system.*

many important research problems related to LAC network remain open for further studies, such as the issues pertaining to downlink / uplink transmission, interference mitigation techniques, multiple access techniques, mobility support, handover schemes and backhaul connection.

2.2.1 Downlink Transmission

In cellular systems, downlink connection is defined as the data transmission from a BS to a UE [7]. In LAC networks, it refers to a forward link from an O-BS to a LiFi UE. Intuitively, LAC system downlink is achieved by using a VLC connection. A basic setup for a LAC downlink system is shown in Figure 2.2. This study will focus on the downlink system of LAC networks in physical layer for the following reasons. Promising downlink performance is one of the most important motivations of using LAC networks in the future wireless communication system. In addition, the research of other higher layer issues like handover has to be conducted based on the physical layer characteristics. Furthermore, a lot of research resources in the field of single link VLC are available to support the LAC downlink study.

The downlink system in a LAC network is largely similar to that in a RF cellular network except for the front-end elements. In RF cellular systems, a modulated electrical signal is converted to a RF electromagnetic wave signal via a RF-chain. In a LAC downlink system, a modulated electrical signal is converted to a light signal by transmitter front-end elements, and the transmitted light signal is converted back to the modulated electrical signal via receiver front-end elements as shown in Figure 2.2 [36]. Most of the cost-effective incoherent LiFi front-ends determine that using intensity modulation (IM) with direct detection (DD) is appro-

priate in the downlink transmission. The use of IM/DD techniques partially determines the characteristics of downlink transmission channel. A number of candidate modulation schemes include on-off keying (OOK), pulse position modulation (PPM), pulse-amplitude-modulated discrete multi-tone modulation (PAM-DMT) and optical orthogonal frequency-division multiplexing (O-OFDM) [4, 37]. Since the downlink connection of LAC networks is expected to provide high data rate transmission, spectral efficient O-OFDM are considered in this study. In addition, different spatial cell deployments in a LAC system are considered in the downlink analysis.

2.2.2 Uplink Transmission

In a cellular system, uplink connection refers to a reverse link from an UE to one or more nearby BSs. In order to achieve a full-duplex communication system in a LAC network, an uplink is also essential. Wireless IR link is considered to be one of the options for uplink communication of LAC networks. Since IR signal has a different optical spectrum, it causes zero interference to the downlink transmission as long as appropriate optical filters are used at the receivers. The uplink signal output power should be kept to a low level due to the optical radiation safety constraint and limited power capacity of the UE. For this reason, energy-efficient modulation schemes, such as ACO-OFDM, are suitable for IR uplink transmission. In order to improve the spectral efficiency, an enhanced unipolar-OFDM (eU-OFDM) can be used [38]. A real-time full-duplex VLC system has been designed and manufactured by pureLiFi^{TM} limited [39]. Another viable uplink solution is using conventional RF transmission. In some applications, such as downloading large size files, the requirement for downlink capacity is typically much higher than that for the uplink. In this case, a small proportion of RF spectrum can be borrowed for a reliable uplink connection, while license-free VL spectrum is used to offload crowded downlink traffic. Studies show that a system with VLC downlink only can off-load a considerable wireless traffic from the existing RF networks [40].

2.2.3 Interference Mitigation

In cellular networks, dense spatial reuse is used for higher spectral efficiency. Consequently, the links using the same channel in adjacent cells interfere with each other, which is known as co-channel interference (CCI) [7]. The light radiation pattern of a VL source with strong directionality makes the majority of the radiated optical power confined within the coverage area

of the O-BS. Thus, as long as adjacent cells use different transmission resources, a LAC network would experience negligible CCI. However, in order to maximise the spectral efficiency in a LAC system, it is unavoidable to reuse the same channel in adjacent cells. Therefore, CCI poses major challenges to the downlink connections in LAC networks with dense spatial reuse.

To address this CCI issue, studies of interference mitigation techniques in networked OWC systems have been conducted. In [41], an interference coordination scheme based on busy-burst signalling has been proposed to be used in an OWC network in an aircraft cabin. Furthermore, angular diversity can be explored to achieve interference management [42]. In this thesis, fractional frequency reuse (FFR) and joint transmission (JT) in conjunction with angular diversity transmitter for LAC networks are analysed and evaluated.

2.2.4 Multiple Access

In a cellular network, multiple UEs are likely to be located at the same cell. In this case, the AP should be able to serve multiple UEs at the same time, which is known as multiple access. A number of multiple access techniques have been developed in cellular systems such as time-division multiple access (TDMA), code-division multiple access (CDMA) [7] and more advanced orthogonal frequency division multiple access (OFDMA) [43].

One of the solutions to the suitable multiple access scheme in a LAC network is to adopt the multiple access techniques used in RF cellular systems. A number of studies have been carried out to investigate the multiple access techniques in networked OWC systems [19, 44]. In TDMA, each UE is given a time slot for transmission. This scheme can be directly used in an IM/DD-based LAC system. In CDMA, the signal for each UE is assigned a unique orthogonal code, and the desired signal can be retrieved by using the assigned code. A number of designs of orthogonal code are available to accommodate CDMA in a LAC network, such as optical orthogonal code, unipolar m-sequences and Walsh-Hadamard codes. In O-OFDM-based LAC system, it is also viable to use OFDMA by distributing different groups of orthogonal subcarriers to multiple UEs. In addition, wavelength-division multiple access (WDMA) can also be considered, if the corresponding front-end elements support splitting signals with different colours [4].

The selection of multiple access scheme in LAC networks should take the unique characteristics of LAC system into account, such as the low pass effects of the front-end elements, indoor free-

space transmission channel and low user density per cell. For example, in the 4^{th} generation (4G) RF cellular system, OFDMA is widely used as it is able to explore the multi-user diversity gain. However, the multi-user diversity in a LAC system has not been studied. Therefore, whether OFDMA is worth using in a LAC system requires further investigation. In [44], it has been found that OFDMA outperforms CDMA in a multi-user VLC system, but OFDMA does not show any superiority compared to TDMA.

2.2.5 Handover

Handover is defined as the process of transferring the authority of an ongoing wireless transmission session from the current AP to another AP [33]. Handover is normally required in the case that a UE is moving out of the coverage area of an AP and is moving into the coverage area of an adjacent AP. In some cases, handover is also required as the transmission channel is severely degraded due to fading / interference or the current cell is fully loaded. Handover occurs in these two scenarios is usually classified as horizontal handover as it happens between APs in the same network [45]. There is another case happening in a heterogeneous network with multiple tiers. Different tiers means different types of access nodes in a heterogeneous network. For example, a heterogeneous network may include a high tier macro cell network and multiple low tier femtocell networks. If a UE is covered by a low tier AP when it is moving along the edge of the low tier AP coverage area, frequent handover may occur, which causes loss in throughput and low user service quality. Therefore, the UE should be transferred to a higher tier AP which has a larger coverage to avoid unnecessary handover. This handover between APs of different systems are categorised as vertical handover [45]. Generally, there are two types of handover schemes – hard handover and soft handover. In a hard handover process, the UE is disconnected from the current AP before it connects to the next AP, which is simpler to implement and has lower hardware requirement [33]. However, the service will be interrupted with hard handover scheme. In a soft handover process, the UE remains its connection to the current AP until successful connection to the next AP is established. Soft handover offers better user experience with more handover overhead. Furthermore, cooperation between APs and extra hardware are required.

With a decrease of cell size, handover frequency is expected to increase for moving UEs. Increased number of handover sessions causes losses in system throughput and degraded quality of service. In a LAC network, this handover issue is more critical as LAC can be considered as

the smallest cell compared to other types of small-cells. However, O-BSs are physically closed to each other, which implies that the backhaul constraints for centralised control and cooperation among O-BSs are easier to fulfil relative to the case in RF cellular systems. Since the handover frequency in LAC networks is high, soft handover should be preferred for better quality of service. The quality of service refers to the overall communication performance that the LAC users experienced. Novel handover decision algorithm for LAC networks is expected to be designed to decrease the number of handover session and to avoid the ping-pong effect [45]. Another solution to the issue of handover and mobility support is to operate a LAC network in conjunction with other RF wireless networks that has larger coverage. Static UEs are served by the LAC system to offload the wireless traffic as long as they are in the coverage of one of the O-BSs. On the other hand, moving UEs are assigned to RF wireless AP to reduce the number of handover process. In such heterogeneous system, not only the horizontal handover between a pair O-BSs should be considered, but also the vertical handover between an O-BS and a RF AP should be considered. A study of dynamic load-balancing schemes with handover in such hybrid system is presented in [46].

2.2.6 Backhaul Connection

Backhaul connection can be defined as the connection between cellular AP and radio controller [47]. Generally, backhaul connections are able to provide reliable high speed low latency transmission to accommodate the busy wireless traffic from the APs. If high speed access networks are densely deployed in the future, the requirement of backhaul capacity will increase significantly [48]. A straightforward solution to the backhaul issue is to increase the deployment of optical fibre, which offers excellent performance. Alternative backhaul solutions based on ethernet and powerline communication (PLC) have also been considered [49, 50].

As the smallest cellular system, a LAC network faces the backhaul issue to a larger extent. Furthermore, there are multiple APs in a single room, which makes the construction of backhaul connection more complicated. A LAC network is expected to be a cost-effective system. Thus, expensive and complex backhaul design should be avoided. Therefore, optical fibre and ethernet backhaul could be a promising solutions. With the advancement in optical fibre manufacturing techniques, the cost of the optical fibre has been significantly reduced. Ethernet infrastructure is easy to install and is convenient for maintenance, while the latest ethernet connection could provide a data rate of multiple Gbps [49]. In addition, it is possible to implement

power-over-ethernet (PoE) to supply the electrical power for lighting and communication to each O-BS. Moreover, cost-effective backhaul designs based on OWC are also under investigation [51].

2.3 Front-end Elements

Currently, a major limiting factor to the performance of a VLC system is the front-end elements. The key front-end element at the transmitter side is the light source that converts electrical signal to light signal. Additionally, optics are used to shape the radiation pattern of the light source. Light sensing device is the key front-end element at the receiver side. Furthermore, optical filter and concentrator are used to improve the connection quality. In this section, the characteristics of the key front-ends elements at the transmitter and receiver side in the LAC downlink system are briefly introduced.

2.3.1 Transmitter Front-end

At the transmitter side, commonly used front-end elements to convert electrical signal to optical signal include LED and LD. A typical LED is made of semiconductor with a p-n junction. Here the 'p' and 'n' refer to the p-type semiconductor and n-type semiconductor, which contain an excess of electron holes and electrons, respectively. When a LED is excited by electrons, incoherent photons are generated by spontaneous radiation [24]. Generally, a LED has a diffused radiation profile. A radiation profile defines the optical power output in a specified radiation direction. With decades of research and development, high efficiency VL LED has been developed, which has massively propelled the uptake of VL LEDs in the modern lighting industry. A LD is composed of an optical cavity which can bounce the photons back and forth to cause a stimulated radiation [24]. Compared to LEDs, LDs can operate under a higher level of driving current. Moreover, LDs have a higher electrical-to-optical conversion efficiency and a wider modulation bandwidth, which is very promising in terms of communication capability. However, LDs are currently more expensive than LEDs. In addition, LDs have a very focused radiation pattern, which is undesired in terms of eye-safety [52]. For indoor communication and lighting applications, appropriate optics are necessary to convert the LD output into a diffused radiation pattern. Some research shows that it is possible to convert LDs as communication and lighting sources for indoor application [53, 54]. However, further research and development are

required to reduce the cost of such source. LEDs are widely accepted as a suitable candidate for indoor VLC techniques and considered in most of related studies [55, 56]. Therefore, LEDs are considered as the default optical source in this thesis. Since a LED is a type of incoherent source, it is impossible to control the phase of the output electromagnetic wave. Therefore, IM in conjunction with DD is considered in this thesis. This means the signal amplitude is proportional to the power of the optical signal. A number of basic characteristics of LED will be briefly introduced in this subsections.

2.3.1.1 Lambertian Radiation Pattern

The light emission from a LED can be modelled by a radiation pattern defined by a generalised Lambertian law [26]. Relative to a given source location and orientation, the received optical power with a radiant angle of ϕ and a radiant solid angle Ω can be calculated as [26]:

$$P_{\mathrm{opt},\Omega} = \Omega P_{\mathrm{opt}} \frac{(m+1)}{2\pi} \cos^m \phi, \tag{2.1}$$

where P_{opt} is the total optical output of the LED source, and m denotes the Lambertian emission order, which is determined by the half-power semi-angle by $m = -1/\log 2(\cos \phi_{1/2})$. In the case of naked LED source, the half-power semi-angle is $\phi_{1/2} = 60°$. In other cases, appropriate optics can be applied to the LED source to shape the radiation pattern with narrower beamwidth ($\phi_{1/2} < 60°$) according to the application specifications. This characteristic is found to be very important to the CCI level in the downlink of LAC network. The two dimensional (2-D) and three dimensional (3-D) radiation patterns of three LED sources with $\phi_{1/2} = 60°, 40°, 20°$ are shown in Figure 2.3.

2.3.1.2 LED Optical Output

The output of the installed LED lamp should fulfil the indoor illumination standard and photobiological safety standard [52, 57]. In practice, many detailed metrics should be considered, such as colour appearance, unified glare rating, illuminance level, uniformity, retinal blue light hazard exposure limit, retinal thermal exposure limit and etc. The value of these metrics have to be kept within the permitted range. In this study, it is unnecessary to consider all of these metrics as they are not the major interest in a communication system. One of the most important metrics in a communication perspective is the optical output of the lamp as it determines

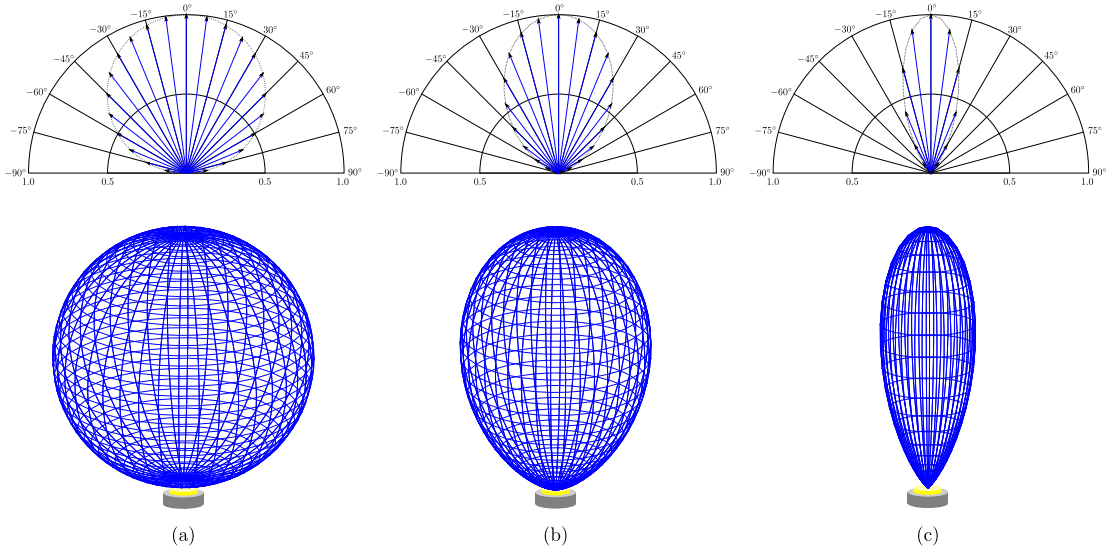

Figure 2.3: *2-D and 3-D views of LED source radiation patterns. (a)* $\phi_{1/2} = 60°$. *(b)* $\phi_{1/2} = 40°$. *(c)* $\phi_{1/2} = 20°$.

the maximum strength of the transmitted signal. Therefore, a simple method is used to estimate the light output that the lamp can provide.

According to [57], the required average illuminance in the task area[1] for working place, typically 0.75 m above the floor, should not be less than 500 lux. Illuminance is defined as the incident luminous flux per unit area [58], and is denoted as E_{v}. The illumination performance of a single lamp is evaluated. Equation (2.1) implies that the emitted optical power per steradian [2] reaches the maximum when $\phi = 0°$ as long as $m \geq 1$[3]. In a LAC system, this case corresponds to the location that is straight below the lamp. So it is assumed that the illuminance in the task area right below the lamp equals the minimum required value specified in [57]. Firstly, the luminous output flux of the source can be calculated by $\Phi_{\mathrm{v}} = P_{\mathrm{opt}} K_{\mathrm{e/v}}$, where $K_{\mathrm{e/v}}$ denotes the luminous efficacy which can be calculated as [58]:

$$K_{\mathrm{e/v}} = \frac{683 \int V(\lambda) \tilde{P}_{\mathrm{opt}}(\lambda) \mathrm{d}\lambda}{\int \tilde{P}_{\mathrm{opt}}(\lambda) \mathrm{d}\lambda}, \tag{2.2}$$

where $V(\lambda)$ is the luminosity function against wavelength λ; and $\tilde{P}_{\mathrm{opt}}(\lambda)$ is the spectral radiant power density function of the lamp. With a given luminous output flux Φ_{v}, the radiant luminous

[1] The area where illumination is required [57].
[2] unit of solid angle
[3] This configuration is preferred to reduce CCI, which will be introduced in Section 4.3.1 in Chapter 4.

flux to a solid angle of Ω can be calculated based on (2.1) as:

$$\Phi_{\mathrm{v},\Omega} = \Omega\Phi_{\mathrm{v}}\frac{(m+1)}{2\pi}\cos^{m}\phi. \tag{2.3}$$

Thus, the illuminance right below the luminary with a distance of z can be calculated as:

$$\tilde{E}_{\mathrm{v}} = \frac{A_{\mathrm{r}}}{z^2}\Phi_{\mathrm{v}}\frac{(m+1)}{2\pi A_{\mathrm{r}}}\left(\cos 0^{\circ}\right)^{m+1} = \frac{(m+1)\Phi_{\mathrm{v}}}{2\pi z^2}, \tag{2.4}$$

where z is the vertical separation between light source and the height of the task area, and A_{r} is the physical area of the receiving element. Therefore, the average optical radiant output power should be:

$$\bar{P}_{\mathrm{opt}} = \frac{\Phi_{\mathrm{v}}}{K_{\mathrm{e/v}}} = \frac{2\pi\tilde{E}_{\mathrm{v}}z^2}{(m+1)K_{\mathrm{e/v}}}. \tag{2.5}$$

With this configuration for the total optical power that the lamp outputs, the resulting average illuminance would be typically lower than the required value. So it is assumed that the area where illuminance level is not sufficient is complemented by other lamps which have no communication functionality. Considering a room height of 3 m, with a $\phi_{1/2}$ of 20° to 45°, the required luminous flux for a minimum illuminance of 500 lux is in the range of 1300 lumen to 5300 lumen. This amount of power agrees with the specification of commercially available LED downlighters and LED panels for lighting in offices and public areas [59, 60]. This high optical power output of the LED sources ensures sufficient signal strength for reliable communication. Note that the rated power of LED lamp for residential home is typically lower than this level (< 1000 lumen). In the case of low optical power output, a number of methods can be used to guarantee enough signal strength, such as using energy efficient modulation schemes.

A typical LED chip offers an optical power of about several mW, which is far lower than the value that is required for standard lighting function. In order to build a lamp with several thousands of lumens, multiple small LED chips should be integrated to form a LED array, which is equivalent to a single high power light source. Most of the high power LED products are implemented with this method [59, 60]. Therefore, it is assumed that the low output of a single LED chip does not limit the performance of the LAC downlink system.

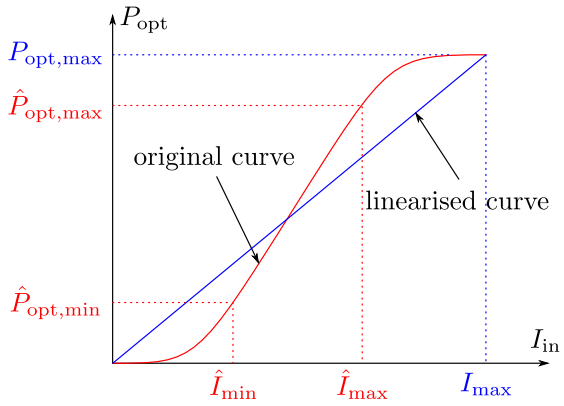

Figure 2.4: *A typical relationship between driving current and output optical power of a LED. The red curve shows a typical non-linear relationship between the driving current and the optical output power. The blue curve shows an ideal linearised conversion after pre-distortion.*

2.3.1.3 LED Non-linearity

In the process of IM with LED source, there is a non-linear relationship between the input signal and the output signal [61]. A number of sources could possibly lead to this non-linearity characteristic. Firstly, the LED device has a limited dynamic range. In addition, the conversion from forward voltage to forward current and the conversion from forward current to light power have a non-linear transfer relationship. Furthermore, the transition between digital signal and analogue signal has a quantisation effect, which also introduces non-linearity. Figure 2.4 shows the relationship between input current and output optical power of a typical LED device. When the input current is in the range of $[\hat{I}_{\text{min}}, \hat{I}_{\text{max}}]$, the LED linearly convert the forward current into the optical power within the range of $[\hat{P}_{\text{opt,min}}, \hat{P}_{\text{opt,max}}]$. In order to maximise the output electrical signal power per unit optical output, pre-distortion techniques can be used [61]. For the convenience of the following analysis in this thesis, it is assumed that by using pre-distortion technique, an idealised linear relationship between input current and optical output can be established as [24]:

$$P_{\text{opt}} = \begin{cases} \eta_{\text{led}} I & : 0 \leq I \leq I_{\text{max}} \\ P_{\text{opt,max}} & : I > I_{\text{max}} \end{cases}, \tag{2.6}$$

where I denotes the input current to the LED, and η_{led} denotes the conversion coefficient from the input current to the optical output power, which includes the electrical signal amplification and the LED quantum efficiency. An idealised linear relationship between input current and

output optical power is assumed on the condition that $I \leq I_{\max}$. The optical output power is saturated at a fixed level of $P_{\text{opt,max}}$ on the condition that $I > I_{\max}$. Therefore, in order to avoid signal being saturated, the input current has to fulfil $0 \leq I(t) \leq I_{\max}$, where $I(t)$ represents the instantaneous input current at time instant t. Thus, the relationship between the input current and the average optical output power can be given as:

$$\bar{P}_{\text{opt}} = \eta_{\text{led}} \mathbb{E}_t[I(t)]. \tag{2.7}$$

The electrical signal power conveyed in the light wave can be estimated based on the relationship in (2.7) with a specified dynamic range of LED and a specified clipping configuration for O-OFDM.

2.3.1.4 LED Modulation Bandwidth

The output frequency response of a LED typically shows a low-pass characteristic. This is because of the long carrier lifetime in the device active region and the large capacitance of the LED device [62]. In order to characterise the LED low pass frequency response, a number of expressions are used as approximations. For example, the normalised magnitude response is approximated by the following expression in several studies [63]:

$$|H(f)| = \frac{1}{\sqrt{1 + (2\pi f \tau_{\text{c}})^2}}, \tag{2.8}$$

where f represents the frequency, τ_{c} represents the response time constant, which is related to the diode capacitance of the LED device and the carrier lifetime in the device active region. The optical output waveform using LEDs transmitting a periodic square-wave signal with different response time constant is shown in Figure 2.5 (a). It implies that the raise and falling time of the output signal determines the modulation speed of the LED. Thus, The magnitude response results corresponding to Figure 2.5 (a) is shown in Figure 2.5 (b). These figures show that a LED with shorter response time constant has a shorter raise and fall time, thereby achieving wider modulation bandwidth. Commercially available LEDs can achieve a 3-dB bandwidth of 2 to 20 MHz. As a result of significant research efforts on developing high speed LEDs, a number of advanced LED sources emerge [56, 63, 64]. For instance, the micro-LED achieves a 3-dB bandwidth of 60 MHz [30].

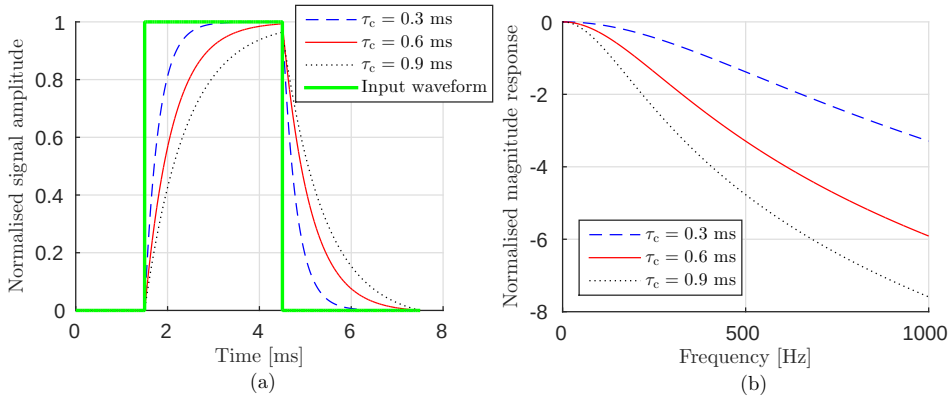

Figure 2.5: *(a) A typical LED low-pass response in time-domain. (b) A typical LED low-pass response in terms of normalised magnitude response.*

2.3.2 Receiver Front-end

In order to achieve high speed transmission in LAC systems, receiving front-end elements with high sensitivity and wide bandwidth are required. Currently, a PD is the most promising front-end element in the receiver to fulfil these requirements. A PD is a type of optoelectronic semiconductor that is able to produce a photocurrent that is proportional to the power of the detected optical electromagnetic wave [24], which is suitable for the DD scheme.

2.3.2.1 Photodiode Characteristics

In most of the indoor VLC applications, only a very small fraction of the emitted optical power can be detected by a PD. Therefore, a PD with high sensitivity to light signal is required to achieve desired performance. To quantify the light to current conversion efficiency, the amount of generated photocurrent per unit incident optical power is defined as PD responsivity, η_{pd}, which can be calculated as [24]:

$$\eta_{\mathrm{pd}} = \frac{\lambda q \eta_{\mathrm{pd,qe}}}{\mathfrak{h} c}, \tag{2.9}$$

where $q = 1.602 \times 10^{-19}$ C is the charge of an electron, $\eta_{\mathrm{pd,qe}}$ refers to the quantum efficiency of the PD, $\mathfrak{h} = 6.626 \times 10^{-34}$ Js denotes the Planck's constant, and c refers to the speed of light. Thus, the generated photocurrent can be calculated as: $I_{\mathrm{photo}} = \eta_{\mathrm{pd}} P_{\mathrm{opt,r}}$, where $P_{\mathrm{opt,r}}$ denotes the optical power that is collected by the PD detector.

The selection of semiconductor materials leads to different levels of responsivity at different

ranges of wavelengths. Similar to the characteristics of a LED, a PD is a capacitive electronic device. Hence, a receiver with PD detector also exhibits a low-pass characteristic. In the conversion from light to electrical signal via PD, the incident light excites free carriers. The transit time of these carriers also leads to the low-pass response of the PD [24]. High response speed of the PD is essential to accommodate high data rate transmission. Furthermore, the PD design should be robust to temperature variation and cause as little noise as possible.

The optical power collected by a PD detector from the incident light is proportional to the physical area of the PD. Therefore, in order to get a stronger electrical signal, a large PD is preferred. However, the capacitance of the PD is proportional to its physical area. Thus, in the communication speed perspective, the size of the PD should be as small as possible to ensure a sufficient wide modulation bandwidth. Consequently, a trade-off between the sensitivity of the PD and the modulation bandwidth has to be considered in the design of the PDs. A viable solution to this trade-off is to operate multiple PDs at the same time. In this way, the equivalent physical area is the combined area of each PD, while the response speed remains the same as that of an individual PD.

2.3.2.2 Types of Photodiodes

In general, there are two types of PDs. The first one is called positive-intrinsic-negative (PIN) PD. A PIN diode is constructed by p-type and n-type semiconductor materials [24]. Between these two parts, an intrinsic region with a light n-type dope inserted. For normal operation of PIN diode, a large reverse biased voltage is applied across the PD, which results in the depletion of free charges in the intrinsic region. The collected photons are concentrated on the intrinsic region. The energy of the incident photons excite electron-hole pairs. Under the electrical field caused by the voltage across the PD, the flow of the free electrons and holes leads to the generation of the photocurrent. In VL spectrum region, the achieved responsivity of a PIN PD is in the range of 0.2 to 0.4 A/W [24]. Responsivities of more than 0.6 A/W can be achieved in the IR spectrum range. The achievable 3-dB bandwdith of PIN PD ranges from several hundreds MHz to more than 100 GHz.

The other type of PD is called avalanche photodiode (APD) [24], which operates with a much higher reverse bias voltage than PIN PD. It triggers an impact ionisation effect, which offers a significant internal gain in the range of 50-300 [24]. Consequently, APD can have a much higher responsivity. However, this ‘avalanche’ effect also leads to excessive noise and extra

sensitivity to temperature change. Due to the internal current gain, the resulting responsivity is typically greater than unity.

2.3.2.3 Optical Concentrator and Optical Filter

In addition to the PD, an optical concentrator is normally included in the receiver. The concentrator can be used to trade field of view (FoV) for extra signal gain [13]. The concentrator gain is defined as:

$$g_{\mathrm{c}} = \frac{\mathfrak{n}^2}{\sin^2 \psi_{\mathrm{FoV}}} \mathbf{1}_{\psi \leq \psi_{\mathrm{FoV}}}(\psi) \tag{2.10}$$

where $\mathfrak{n}$ denotes the internal refractive index, ψ is the incident angle to the receiver, and ψ_{FoV} is the FoV of the receiver. The indicator function $\mathbf{1}_{Д}(u)$ is defined as:

$$\mathbf{1}_{Д}(u) = \begin{cases} 1 & : u \in Д \\ 0 & : u \notin Д \end{cases}. \tag{2.11}$$

Although the PD is able to detect the desired optical signal, it may also detect some unwanted signal such as the excessive background optical noise. If the spectrum of this unwanted signal is different from that of the desired signal, an optical filter made of glass or plastic can be used to remove the undesired signal [13]. This process causes an amount of power loss due to filter reflection or absorption. A filter loss factor g_{f} is defined to account for the power loss due to the addition of optical filter. Therefore, for an amount of optical power $P_{\mathrm{opt},\Omega}$ incident on the receiver, the optical power that is collected by the PD detector, $P_{\mathrm{opt,r}}$, can be calculated as follows:

$$P_{\mathrm{opt,r}} = P_{\mathrm{opt},\Omega} g_{\mathrm{f}} g_{\mathrm{c}}. \tag{2.12}$$

2.4 Channel

In the considered LAC downlink system in this study, O-OFDM is used for higher spectral efficiency. In order to maximise the achievable data rate, different numbers of bits are assigned to each subcarrier [30]. The maximum permitted number of bits depends on the channel gain at the frequency associated with the subcarrier. Therefore, it is essential to have the knowledge of the frequency response of the LAC downlink channel.

As mentioned in Section 2.3.1.4 and Section 2.3.2.1, the front-end elements, LED and PD, in-

troduce low-pass responses. In addition, due to the reflective indoor environment, the downlink receiver collects signal from multiple paths. The effect of downlink channel is equivalent to a number of filters connected in series, which include the filter corresponding to the effect of front-end elements, the effect of free-space propagation and other factors. Here the properties of this channel filter can be characterised by its impulse response as:

$$h(t) = h_{\text{fe}}(t) \otimes h_{\text{fs}}(t), \tag{2.13}$$

where $h_{\text{fs}}(t)$ denotes the channel impulse response (CIR) due to the free-space light propagation in the considered indoor environment, and $h_{\text{fe}}(t)$ denotes the CIR due to the effects of front-end elements. With the knowledge of CIR $h(t)$, the corresponding frequency response can be calculated by using Fourier transform as follows:

$$H(f) = \int_0^\infty h(t) \exp\left(-j2\pi ft\right) \mathrm{d}t = H_{\text{fe}}(f) H_{\text{fs}}(f). \tag{2.14}$$

2.4.1 Channel of Front-end Elements

The net-effects of multiple front-end elements at both the transmitter side and the receiver side lead to a channel with low-pass characteristics which is considered in this subsection. The front-end low-pass characteristics can be estimated from a number of experimental results [30, 56, 65, 66]. In the considered experimental results, a line-of-sight (LoS) point-to-point link was considered. Consequently, the free-space light propagation in these experiments causes a scalar attenuation to the received signal. Therefore, as long as the frequency response is normalised with respect to the gain at direct-current (DC), the effect of free-space propagation and other gain or attenuation effects can be removed. Figure 2.6 shows the normalised channel gains against frequency, f, in the aforementioned experimental results. The 3-dB bandwidth of these systems are in the range from 10 MHz to 60 MHz. Since the highest sampling frequency considered in this study is about 1 GHz, this low-pass effect will significantly decrease the signal strength when high modulation bandwidth are used. Therefore, the low-pass effect of the front-end elements is crucial to the downlink performance of a LAC system.

In this subsection, a simple function is adopted to approximate the normalised channel gain due to the effects of the front-end elements respect to frequency as [56]:

$$|H_{\text{fe}}(f)|^2 = \exp\left(-\frac{f}{F_{\text{fe}}}\right), \tag{2.15}$$

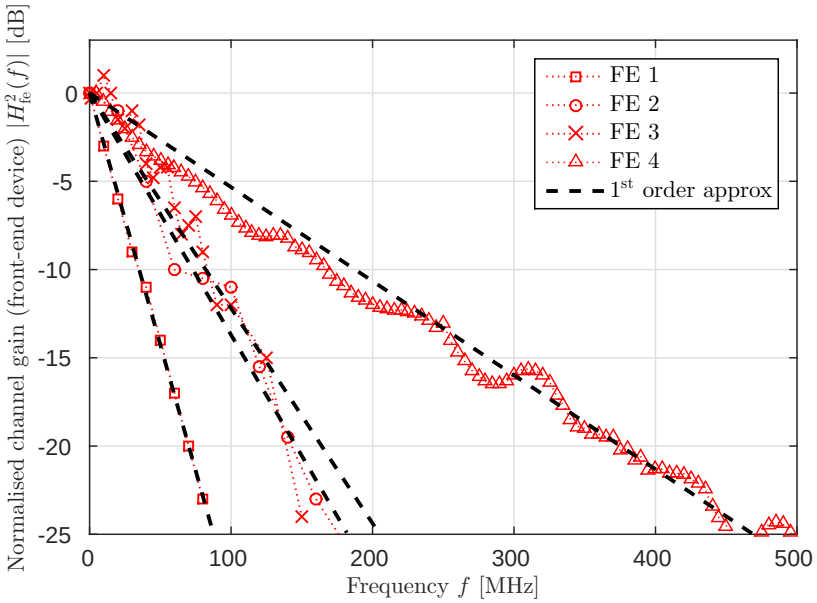

Figure 2.6: *Normalised channel gain caused by the effects of front-end elements. The channel gain information of 'FE 1','FE 2','FE 3' and 'FE 4' is extrapolated from [56], [66], [65] and [30], respectively.*

where F_{fe} controls the frequency characteristics of the front-end elements. The higher the value of F_{fe}, the wider the modulation bandwidth. As shown in Figure 2.6, the approximations offer a good estimation of the low-pass characteristics measured in the experiments. The property of each front-end element may vary with different specifications or even with different copies of the same specification. Therefore, it is trivial to characterise the exact property of the front-end elements.

2.4.2 Channel of Indoor Free-space Light Propagation

In this subsection, the major components of the free-space propagation channel are introduced. Primarily, if there is no obstruction between the transmitter and the receiver, a line-of-sight (LoS) channel exists. Secondly, there is a NLoS channel due to the reflections by room internal surfaces and other objects. For the convenience of characterising LoS and NLoS channels, the basic principle of the channel DC gain from a source element to a receiving element is introduced first [13].

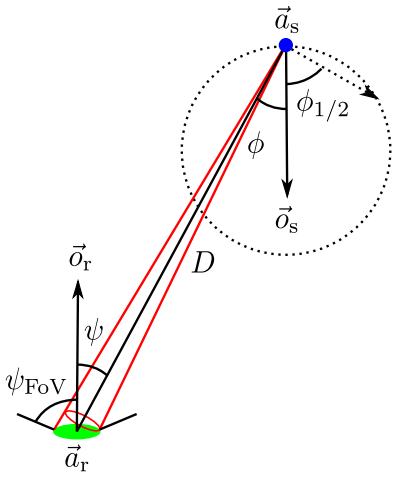

Figure 2.7: *Channel DC gain geometry.*

2.4.2.1 Channel DC Gain

As shown in Figure 2.7, an optical source, $\mathcal{S}$, with a location vector of $\vec{a}_{\rm s}$, a direction vector of $\vec{o}_{\rm s}$ and an emission mode number m is defined. In addition, a receiving element, $\mathcal{R}$, with a location vector of $\vec{a}_{\rm r}$, a direction vector of $\vec{o}_{\rm r}$, a FoV of $\psi_{\rm FoV}$ and a physical area of $A_{\rm r}$ is defined. Considering the source as origin, the emitted power within a certain solid angle will incident on to the receiving element. Since this solid angle is extremely small, it can be approximated as:

$$\Omega = \frac{A_{\rm r} \cos\psi}{D^2} \ [\text{sr}]. \tag{2.16}$$

where D denotes the euclidean distance between the $\mathcal{S}$ and $\mathcal{R}$. Since it is known that the emitted power with a solid angle of Ω and a radiant angle of ϕ at a source can be calculated by (2.1). Then the collected power by the receiving element, $\mathcal{R}$, can be calculated as:

$$H_{\rm DC} = \frac{(m+1)A_{\rm r}}{2\pi D^2} \cos^m\phi \cos\psi \mathbf{1}_{\psi \leq \psi_{\rm FoV}}(\psi)\,. \tag{2.17}$$

where the quantities D, ϕ and ψ can be calculated as [67]:

$$D = ||\vec{a}_{\rm s} - \vec{a}_{\rm r}||, \tag{2.18}$$

$$\cos\phi = \vec{a}_{\rm s} \cdot (\vec{a}_{\rm r} - \vec{a}_{\rm s})\,/D, \tag{2.19}$$

$$\cos\psi = \vec{a}_{\rm r} \cdot (\vec{a}_{\rm s} - \vec{a}_{\rm r})\,/D. \tag{2.20}$$

where the operator $\cdot$ represents the dot product operation.

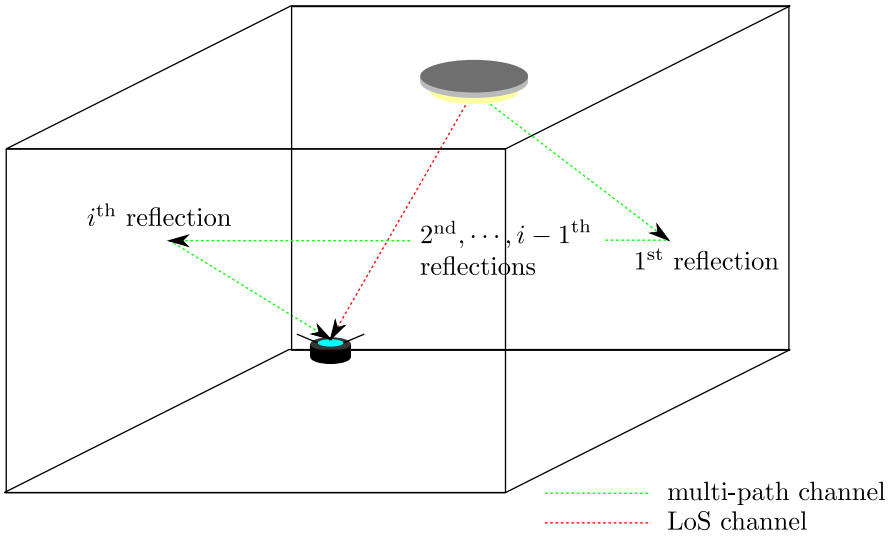

Figure 2.8: *Illustration of LoS propagation channel and NLoS propagation channel.*

2.4.2.2 Line-of-Sight Channel Impulse Response

The setup for LoS channel is illustrated in Figure 2.8. The LoS CIR can be directly calculated based on (2.12) and (2.17) with a specified transmitter $\mathcal{S}_{\text{Tx}}$ and receiver $\mathcal{R}_{\text{Rx}}$ as [67]:

$$h^{[0]}(t, \mathcal{S}_{\text{Tx}}, \mathcal{R}_{\text{Rx}}) = \frac{(m+1)}{2\pi D^2} A_{\text{pd}} g_{\text{f}} g_{\text{c}} \cos^m \phi \cos\psi \mathbf{1}_{\psi \leq \psi_{\text{FoV}}}(\psi)\, \delta\left(t - \frac{D}{c}\right), \tag{2.21}$$

where $\delta(u)$ represents the Dirac delta function and A_{pd} refers to the physical area of the PD. Note that the resulted CIR should be scaled by the optical filter loss g_{f} and optical concentrator gain g_{c} at the receiver side as introduced in Section 2.3.2.3.

2.4.2.3 Diffused Channel Impulse Response

A number of studies have been carried out to evaluate the NLoS channel due to the reflections by the indoor internal surfaces [23, 67–70]. Generally, a cuboid room is defined with a certain size and internal surfaces with fixed reflectance, as shown in Figure 2.8. Typical room internal surface such as plaster wall causes a diffused reflection. The specular reflections caused by mirror or windows are considered as rare and special cases. Therefore, the research in this study focuses on the channel caused by diffused reflections. The NLoS channel due to human body and other objects are difficult to predict and model. Developing more comprehensive channel models including these extra NLoS components requires further investigation. Thus, the effects of human body and other objects are not considered in this study. There are two

popular methods based on ray-tracing technique to calculate the NLoS CIR due to the internal surface reflections. The first approach uses a deterministic method to calculate the NLoS channel [67], while the other approach is based on a Monte Carlo method [68]. For the convenience of description, these two methods are termed as deterministic method and Monte Carlo method, respectively.

2.4.2.4 Deterministic NLoS CIR Calculation Method

In the deterministic method, the CIR is decomposed of multiple components due to different orders of reflections as [67]:

$$h_{\mathrm{fs}}\left(t, \mathcal{S}_{\mathrm{Tx}}, \mathcal{R}_{\mathrm{Rx}}\right) = \sum_{\mathfrak{i}=0}^{\infty} h^{[\mathfrak{i}]}\left(t, \mathcal{S}_{\mathrm{Tx}}, \mathcal{R}_{\mathrm{Rx}}\right), \tag{2.22}$$

where $h^{[\mathfrak{i}]}\left(t, \mathcal{S}, \mathcal{R}\right)$ is the CIR from $\mathcal{S}$ to receiving element $\mathcal{R}$ undergoing exactly $\mathfrak{i}$ reflections. In the case of $\mathfrak{i} = 0$, it refers to the LoS CIR. To accommodate the numerical evaluation of CIR, the entire internal surface is divide into N_{e} blocks. The location vector and orientation vector of each block are denoted as $\vec{a}_n$ and $\vec{o}_n$, respectively. These blocks operate in both transmitting mode and receiving mode in the considered NLoS channel. In the transmitting mode, the n^{th} block is treated as a source element, $\mathcal{S}_n$, with a radiation mode number of 1. In the receiving mode, the n^{th} block is treated as a receiving element, $\mathcal{R}_n$. The maximum incident angle can be as large as $\pi/2$ ($\psi_{\mathrm{FoV}} = \pi/2$), and the receiving block has a physical area of ΔA. In addition, the received power should be scaled by the reflectivity of the block ρ_n. The CIR component experiencing $\mathfrak{i}$ reflections can be calculated based on the CIR component experiencing $\mathfrak{i}-1$ reflections as [67]:

$$\begin{aligned} h^{[\mathfrak{i}]}\left(t, \mathcal{S}_{\mathrm{Tx}}, \mathcal{R}_{\mathrm{Rx}}\right) &= \sum_{n=1}^{N_{\mathrm{e}}} h^{[0]}\left(t, \mathcal{S}_{\mathrm{Tx}}, \mathcal{R}_n\right) \otimes h^{[\mathfrak{i}-1]}\left(t, \mathcal{S}_n, \mathcal{R}_{\mathrm{Rx}}\right) \\ &= \frac{m+1}{2\pi} \sum_{n=1}^{N_{\mathrm{e}}} \frac{\rho_n \cos^m \phi_n \cos \psi_n}{D_n^2} \mathbf{1}_{\psi_n \leq \pi/2}\left(\psi\right) h^{[\mathfrak{i}-1]}\left(t - \frac{D_n}{c}, \left\{\vec{a}_n, \vec{o}_n, 1\right\}, \mathcal{R}_{\mathrm{Rx}}\right) \Delta A, \end{aligned} \tag{2.23}$$

where D_n, ϕ_n and ψ_n refers to the quantities between $\mathcal{S}_{\mathrm{Tx}}$ and $\mathcal{R}_n$. The accuracy of this method increases as N_{e} increases or equivalently ΔA decreases. However, the calculation of an accurate CIR result requires a high computational complexity, thereby taking a very long time to generate a single CIR.

Algorithm 1 : CIR simulation with Monte Carlo method

1: Initialise $P_{\mathrm{opt},h}(t) = 0$ for all $t \in (0, t_{\max})$.
2: **for** $n_{\mathrm{iter}} = 1, 2, \cdots, N_{\mathrm{iter}}$ **do**
3: Start to trace a light ray with a unity power and a random direction, $\hat{\tau} = 0, \hat{P}_{\mathrm{opt}} = 1$
4: **while** $\hat{\tau} < t_{\max}$ **do**
5: Propagate the light ray until it reach any obstacle with a travelling distance of D, $\hat{\tau} = \hat{\tau} + \frac{D}{c}$.
6: Attenuate the power of the light ray with the reflectance of the surface, $\hat{P}_{\mathrm{opt}} = \rho \hat{P}_{\mathrm{opt}}$.
7: Calculate the CIR contribution to the receiver using (2.24).
8: Generate a new direction for the following propagation of the light ray.
9: **end while**
10: **end for**
11: Normalise the result CIR with N_{iter} as $h_{\mathrm{fs}}(t) = P_{\mathrm{opt},h}(t)/N_{\mathrm{iter}}$.

2.4.2.5 Monte Carlo NLoS CIR Calculation Method

In the Monte Carlo method, a random propagation path is traced in each Monte Carlo iteration [68]. By repeating the tracing process for a large number of times, a stable CIR result can be generated. The Monte Carlo method is summarised in Algorithm 1. In step 1 of Algorithm 1, an empty vector $P_{\mathrm{opt},h}(t)$ recording the received optical power at time instant t is initialised with a maximum delay of $t_{\max}$. In step 3, $\hat{P}_{\mathrm{opt}}$ is defined to record the optical power loss in the propagation, and it is initialised with a value of $\hat{P}_{\mathrm{opt}} = 1$. $\hat{\tau}$ is defined to record the time that the ray has experienced, and it is initialised with a value of zero. As long as the transmission time has not reached $t_{\max}$, the propagation continues. For each transmission from one point to another, the propagation distance D is calculated. Based on D, the experienced transmission time $\hat{\tau}$ can be updated. In addition, the output power for the next propagation will be attenuated by the reflectivity of the contacted surface ρ. Furthermore, the power contribution to the CIR optical power vector from the current point is updated using 2.24. For the next propagation, a new random direction should be generated. In step 3 and step 8 of Algorithm 1, the probability of each possible direction is proportional to the radiation intensity along that direction. With a large number of iterations of the same tracing process for N_{iter} times, the final CIR can be calculated by normalising $P_{\mathrm{opt},h}(t)$ with the number of iterations N_{iter}. The details of the Monte Carlo method are provided in [68]. As long as N_{iter} is large enough, an accurate CIR with low noise can be obtained. This method requires less computational complexity. However, due to the randomness in the calculation, minor simulation error is inevitable.

$$P_{\mathrm{opt},h}(\hat{\tau}) = P_{\mathrm{opt},h}(\hat{\tau}) + \frac{\hat{P}_{\mathrm{opt}} A_{\mathrm{pd}}}{\pi D^2} \mathbf{1}_{\psi \leq \pi/2}(\psi) \cos\phi \cos\psi. \tag{2.24}$$

2.4.3 Wavelength Dependency

In an OWC system, a number of quantities vary with wavelength λ, such as the LED electrical to optical conversion efficiency, η_{led}, PD responsivity, η_{pd}, receiver optical filter loss, g_{f}, and room internal surface reflectance, ρ. In wireless IR communication, the spectrum range used is typically narrow. Therefore, the variance of these parameters with wavelength is negligible. In some cases, VLC systems are also using narrow spectrum range. For example, the white LED-based VLC system using blue light component [71] and RGB LED-based VLC system [31] belong to this category. Since the used wavelength range is narrow, the assumptions used in IR system still hold. In another case, the VL signal includes a wider optical spectrum range. Consequently, the analysed result should be integrated over the used spectrum as [72]:

$$\bar{\mathfrak{f}_\lambda} = \int_{\lambda_{\min}}^{\lambda_{\max}} \mathfrak{f}_\lambda \left(\eta_{\mathrm{led}}(\lambda), \eta_{\mathrm{pd}}(\lambda), g_{\mathrm{f}}(\lambda), \rho(\lambda)\right) \mathrm{d}\lambda, \tag{2.25}$$

where $\mathfrak{f}_\lambda$ represents a metric that is a function of the listed parameters. Note that the limits $\lambda_{\max}$ and $\lambda_{\min}$ are typically determined by the passband of the optical filter. The dependency of the system parameters on wavelength is complex and not tractable. Including it in the analysis of a LAC system significantly increases the computational complexity. Therefore, an approximation is used in the remainder of this thesis for the system using wide optical spectrum as [72]:

$$\bar{\mathfrak{f}}_\lambda \approx \mathfrak{f}_\lambda \left(\bar{\eta}_{\mathrm{led}}, \bar{\eta}_{\mathrm{pd}}, \bar{g}_{\mathrm{f}}, \bar{\rho}\right), \tag{2.26}$$

which calculates the metric $\mathfrak{f}_\lambda$ using the averaged parameters over the spectrum range of interest. Here, $\bar{x}$ refers to the average value of parameter x over the considered spectrum range. In the remainder of this thesis, any parameter that vary with wavelength refers to the value that is averaged over the spectrum of interest.

2.5 Sources of Receiver Noise

In the point-to-point VLC link, noise at the receiver side causes impairment to the system performance. The effects of receiver noise also exist in LAC systems. In this subsection, different sources of receiver noise are introduced. Additionally, the calculation of receiver noise power spectral density (PSD) N_0 is considered. Thorough studies on the components and their characteristics were presented in the literature [24, 55]. However, current study focuses on the

effect of CCI. Thus, the major source of receiver noise with a simplified model is considered.

2.5.1 Shot Noise

One of the considered receiver noise is the so-called 'shot-noise'. Shot noise is resulted from the particle characteristic of photon [24]. For an incident light with constant power, the number of incoming photons per unit time fluctuates with a Poisson distribution. This randomness in number of arriving photons leads to the shot noise. If the number of photons that the PD detector received per unit time is large enough, the shot noise can be modelled as an additive white Gaussian noise (AWGN). The variance of the shot noise is proportional to the instantaneous optical power received by the PD detector. However, the received optical power is dominated by the constant background light and the DC component of the signal. Therefore, the varying of the shot noise variance is negligible, and the shot noise is assumed to follow a Gaussian distribution with zero mean and a variance of $\sigma^2_{\mathrm{shot}} = N_{0,\mathrm{shot}} F_{\mathrm{s}}$. The parameter F_{s} represents the modulation bandwidth. The term $N_{0,\mathrm{shot}}$ is the corresponding shot noise PSD which can be calculated as:

$$N_{0,\mathrm{shot}} = 2qP_{\mathrm{opt,Rx}}\eta_{\mathrm{pd}}, \tag{2.27}$$

where $P_{\mathrm{opt,Rx}}$ denotes the incident optical power to the PD detector at the receiver. The source of the incident light power $P_{\mathrm{opt,Rx}}$ includes the light from the transmitters and the light from the background, such as the skylight from the window. Therefore, the incident optical power can be estimated as:

$$P_{\mathrm{opt,Rx}} = P_{\mathrm{opt,led}} + E_{\mathrm{r,bg}} A_{\mathrm{pd}} \tag{2.28}$$

where $P_{\mathrm{opt,led}}$ accounts for the power from the transmitters, which can be calculated based on the method introduced in Section 2.4; $E_{\mathrm{r,bg}}$ represents the incident background light irradiance, which can be obtained from existing data or experimental measurement. Note that the effect of ambient light in practice will be smaller as only the light with the signal spectrum causes distortion as long as an appropriate optical filter is used. In addition, APD is more sensitive to the shot noise due to its Avalanche amplification effect.

2.5.2 Thermal Noise

Another receiver noise is termed as thermal noise. Thermal noise is mainly due to the temperature fluctuation caused by the resistive units in the receiver circuit [24]. In most of the

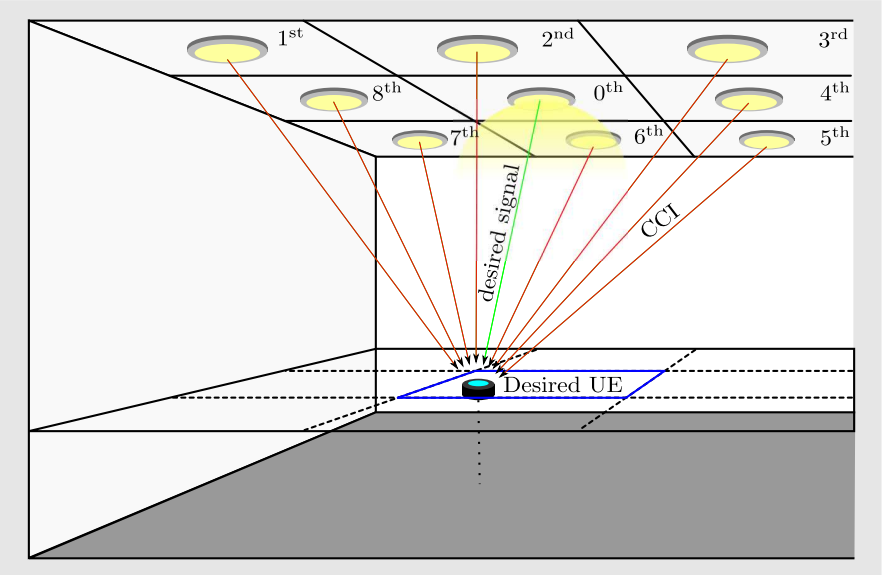

Figure 2.9: *LiFi attocell downlink system configuration.*

optical receiver, a transimpedance amplifier (TIA) is included to amplify the received signal. The resistance of the TIA is a major source of thermal noise. The thermal noise can also be modelled as an AWGN with a variance of $\sigma^2_{\text{thermal}} = N_{0,\text{thermal}} F_{\text{s}}$, where the thermal noise PSD $N_{0,\text{thermal}}$ can be calculated as [24]:

$$N_{0,\text{thermal}} = \frac{4\mathcal{K}_{\text{B}}\mathcal{T}}{R_{\text{L}}}, \tag{2.29}$$

where $\mathcal{K}_{\text{B}}$ denotes the Boltzmann's constant with a value of 1.38×10^{-23} J/K; $\mathcal{T}$ denotes the absolute temperature; and R_{L} denotes the load resistance in the receiver circuit. Finally, the total receiver noise PSD can be concluded as:

$$N_0 = 2q\left(P_{\text{opt,led}} + E_{\text{r,bg}} A_{\text{pd}}\right)\eta_{\text{pd}} + \frac{4\mathcal{K}_{\text{B}}\mathcal{T}}{R_{\text{L}}}. \tag{2.30}$$

2.6 O-OFDM-based Downlink Transmission

The downlink connection involves the transmitter of an O-BS and the receiver of an UE. In order to take the effect of downlink CCI into account, multiple O-BS transmitters are defined. In the vertical dimension, these transmitters are typically at the height of the ceiling. In addition, the downlink transmitters are directed to the floor. The desired receiver is defined with a specified

height, typically at the desktop level. In the horizontal space, the location of the receiver is randomly distributed in the room. In the downlink transmission, the desired receiver interacts with multiple O-BSs. To distinguish the signals from different transmitters, an index $i = 0, 1, 2, \cdots$ is added to mark different O-BS transmitters. Generally, the O-BS offering the strongest downlink is selected as the serving O-BS. The index of this 'tagged' O-BS is defined as $i = 0$. For the remaining O-BSs, if the i^{th} O-BS is transmitting using the resources that is used in the transmission for the desired receiver, the downlink signal from the i^{th} transmitter causes CCI to the desired receiver, which is indicated by $i \in И$. Here, $И$ denotes the set of the O-BSs using the same transmission resource. Otherwise, it causes zero interference to the desired UE. This downlink system is illustrated in Figure 2.9.

2.6.1 O-OFDM Transmission

As mention in Section 2.2.1, to ensure the high spectral efficiency in the LAC downlink, O-OFDM modulation is expected to be used. In this subsection, the downlink transmission with O-OFDM is analysed in link level. Figure 2.10 illustrates the key elements of an O-OFDM communication system. At the beginning of the transmission, the bit stream is coded and mapped to QAM symbols $\hat{X}$ with unity average symbol energy. Then, every $\tilde{K}$ QAM symbols are grouped and converted to a parallel sequence which forms an OFDM frame $\vec{X}$ as [73]:

$$\vec{X} = [X(0), X(1), \cdots, X(K-1)], \tag{2.31}$$

where $X(k)$ is the k^{th} QAM symbol in the OFDM frame $\vec{X}$. According to the introduction in Section 2.3.1, the limiting factor at the transmitter side is the output power and limited dynamic range of the light source. The electrical to optical conversion is carried out in time domain, and the time domain signal strength associated with a specified light source configuration is

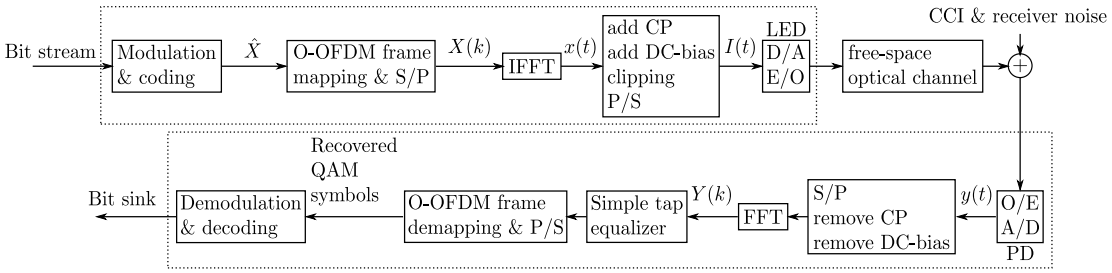

Figure 2.10: *O-OFDM transmission block diagram.*

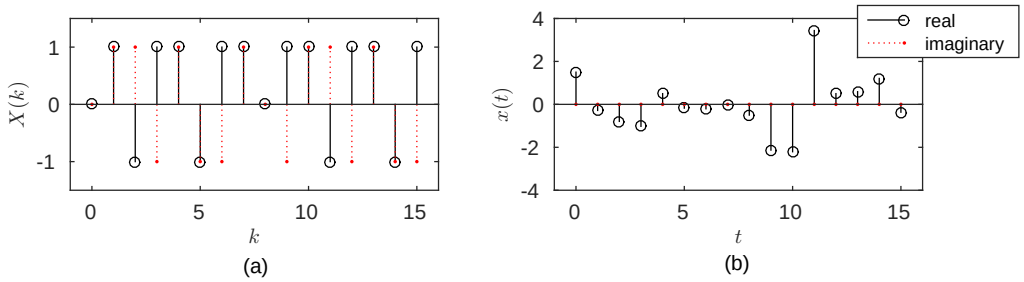

Figure 2.11: *An example of OFDM signal conversion from time domain to frequency domain with Hermitian symmetry. (a) Frequency-domain OFDM frame with QAM symbols before IFFT. (b) Time-domain OFDM signal after IFFT.*

important to the subsequent calculation. Therefore, the time-domain OFDM symbol should be normalised. In order to make the time-domain OFDM symbol have unity power after inverse fast Fourier transform (IFFT) operation, each QAM symbol is amplified by a factor of ξ as $X = \xi\hat{X}$ [74]. The value of the amplification coefficient ξ can be determined by the following relationship:

$$\frac{\xi^2}{K}\sum_{k=0}^{K-1}\hat{X}^2(k) = 1. \tag{2.32}$$

In an IM/DD-based O-OFDM system, the time-domain signal has to be a real and positive signal. Consequently, in the formation of the OFDM frame, Hermitian symmetry should be satisfied as: $X(0) = X(\frac{K}{2}) = 0$ and $X(K-k) = X^*(k)$ for $k = 1, 2, \cdots, \frac{K}{2} - 1$, where $[\cdot]^*$ denotes the complex conjugate operation. An example of OFDM signal conversion with Hermitian symmetry is illustrated in Figure 2.11. There are two types of basic O-OFDM schemes, namely direct-current-biased optical orthogonal frequency division multiplexing (DCO-OFDM) and asymmetrically clipped optical orthogonal frequency division multiplexing (ACO-OFDM) [73]. DCO-OFDM and ACO-OFDM use different frame structures and methods to avoid negative samples in time-domain. In DCO-OFDM frame, $\tilde{K} = \frac{K}{2} - 1$ symbols are mapped to $\vec{X}$ with $k = 1, 2, \cdots, \tilde{K}$. Thus, the scaling factor $\xi = \sqrt{K/(K-2)}$. In ACO-OFDM frame, $\tilde{K} = \frac{K}{4}$ symbols are mapped to $\vec{X}$ with odd subcarriers $\left(k = 1, 3, 5, \cdots, \tilde{K}\right)$. This leads to $\xi = \sqrt{2}$. All QAM symbols in the OFDM frame are associated with their unique subcarriers. The combination of the QAM symbols on carriers forms the discrete time-domain OFDM signal. This operation can be simply realised by a K-point IFFT operation as:

$$x(t) = \frac{1}{\sqrt{K}}\sum_{k=0}^{K-1} X(k)\exp\left(\frac{j2\pi kt}{K}\right). \tag{2.33}$$

Through this operation, the bi-polar discrete time-domain OFDM signal can be obtained. Next, a cyclic-prefix (CP) is added to the beginning of every K-samples of the discrete time-domain OFDM signal, which allows the impairment of dispersive channel to be removed by a single-tap equalisation at the receiver. Before the conversion from electrical signal to optical signal with IM, the bi-polar time-domain signal should be converted to a unipolar signal with limited amplitude range via clipping and biasing. This process can be described by the following equation:

$$I(t) = \sigma_{\mathrm{x}} \left(\mathcal{V} \left(x(t) \right) + \epsilon_{\mathrm{DC}} \right), \tag{2.34}$$

where ϵ_{DC} denotes a normalised DC-bias level, σ_{x} denotes a signal amplification factor that makes the forward current fit the dynamic range of the LED front-end element, and $\mathcal{V}(u)$ represents the signal clipping function which is defined as:

$$\mathcal{V}(u) = \begin{cases} \epsilon_{\max} & : u \geq \epsilon_{\max} \\ u & : \epsilon_{\max} > u > \epsilon_{\min} \\ \epsilon_{\min} & : u \leq \epsilon_{\min} \end{cases}, \tag{2.35}$$

where $\epsilon_{\max}$ and $\epsilon_{\min}$ are the normalised top and bottom clipping levels, respectively [74]. The realisation of unipolar signal is achieved differently in the two considered O-OFDM schemes. An example of the bi-polar discrete time-domain signal after the IFFT in DCO-OFDM is shown in Figure 2.12 (a). The basic concept of DCO-OFDM is adding a positive DC-bias to make the majority of the negative samples to be positive as shown in Figure 2.12 (b), and the remaining negative samples are clipped to zeros. Therefore, in DCO-OFDM, ϵ_{DC} is configured with a positive value. An example of the bi-polar discrete time-domain signal after the IFFT in

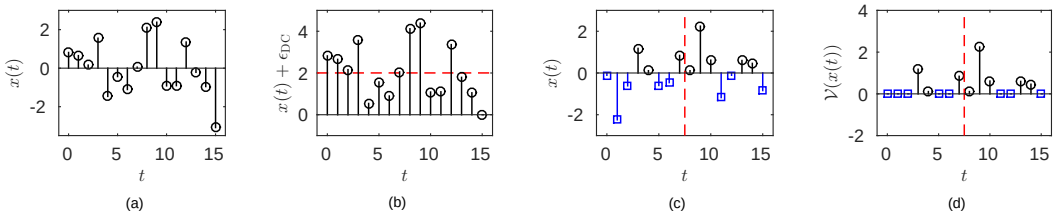

Figure 2.12: *Illustration of unipolar signal conversion in DCO-OFDM and ACO-OFDM. (a) Time-domain OFDM signal after IFFT operation in DCO-OFDM. (b) Time-domain OFDM signal with DC-bias in DCO-OFDM. (c) Time-domain OFDM signal after IFFT operation in ACO-OFDM. (d) Time-domain OFDM signal with negative samples clipped in ACO-OFDM.*

ACO-OFDM is shown in Figure 2.12 (c). It shows that the first half samples are the opposite numbers of the second half samples ($x(t + K/2) = -x(t)$). Therefore, after the clipping of all negative samples (Figure 2.12 (d)), the information of all samples can be recovered based on this relationship. With a linear dynamic range of $[0, I_{\max}]$, DC-bias is zero in ACO-OFDM ($\epsilon_{\mathrm{DC}} = 0$). Then the electrical signal with unity power is amplified by a factor of σ_{x} and converted to optical signal by the LED front-end element with IM. The output optical signal can be calculated as: $P_{\mathrm{opt}}(t) = \eta_{\mathrm{led}} I(t)$.

According to the Bussgang theorem, the non-linear clipped signal can be modelled as follows [74]:

$$\mathcal{V}(x(t)) = \eta_{\mathrm{clip}} x(t) + n_{\mathrm{clip}}(t), \tag{2.36}$$

where η_{clip} is a signal attenuation factor due to the clipping operation and $n_{\mathrm{clip}}(t)$ is the time-domain clipping noise sample which follows a Gaussian distribution with zero mean and a variance of σ^2_{clip} according to the Bussgang theorem.

2.6.2 Received Signal

A full buffer traffic model is assumed in the LAC downlink system. Thus, each O-BS is transmitting signal concurrently. Therefore, the desired UE receives the signals from the 0^{th} O-BS and the O-BSs with $i \in \mathit{И}$. The received signal sample at time instant t can be written as:

$$y(t) = \eta_{\mathrm{pd}} \left(\eta_{\mathrm{led}} I_0(t) \otimes h_0(t) + \sum_{i \in \mathit{И}} \eta_{\mathrm{led}} I_i(t) \otimes h_i(t) \right) + n_{\mathrm{Rx}}(t), \tag{2.37}$$

where $n_{\mathrm{Rx}}(t)$ represents the time-domain noise samples at the receiver. Based on the noise characteristics introduced in Section 2.5, this receiver noise can be modelled as an AWGN. In conjunction with the clipping process modelling in (2.36), the frequency domain received signal sample on sub-carrier k after the fast Fourier transform (FFT) operation can be written as:

$$\begin{aligned} Y(k) &= \frac{1}{\sqrt{K}} \sum_{t=0}^{K-1} y(t) \exp\left(-\frac{2\pi j k t}{K} \right) \\ &= \eta_{\mathrm{pd}} \eta_{\mathrm{led}} \sigma_{\mathrm{x}} \left(\eta_{\mathrm{clip}} X_0(k) + N_{\mathrm{clip},0}(k) \right) H_0(k) \\ &+ \eta_{\mathrm{pd}} \eta_{\mathrm{led}} \sigma_{\mathrm{x}} \sum_{i \in \mathit{И}} \left(\eta_{\mathrm{clip}} X_i(k) + N_{\mathrm{clip},i}(k) \right) H_i(k) + N_{\mathrm{Rx}}(k), \end{aligned} \tag{2.38}$$

where $H_i(k)$ is the frequency response of the VLC channel on the k^{th} subcarrier; $N_{\text{clip},i}(k)$ represents the FFT of $n_{\text{clip},i}(t)$. Thus, $N_{\text{clip},i}(k)$ follows a Gaussian distribution with zero mean and a variance of σ^2_{clip}, as well; and $N_{\text{Rx}}(k)$ represents the frequency domain receiver noise, which is modelled as an AWGN with zero mean and a variance of σ^2_{Rx}. The receiver noise PSD, N_0, can be estimated by (2.30) introduced in Section 2.5. With a sampling frequency (modulation bandwidth) of F_{s}, the receiver noise variance can be calculated as $\sigma^2_{\text{Rx}} = \frac{N_0 F_{\text{S}}}{\xi^2}$. Note that for the transmission of each OFDM frame, only $1/\xi^2$ of the total K subcarriers carries information symbols and the corresponding symbols for Hermitian symmetry. Consequently, the variance of the noise should be scaled by a factor of $1/\xi^2$. After a single-tap equalisation, the desired signal can be recovered to the original QAM symbols $X_0(k)$ with distortion, while the summation of CCI from different interfering O-BSs is assumed to be converted into a Gaussian noise. The Gaussian CCI assumption is based on the central limit theorem (CLT) and because of the fact that the interfering signal is not synchronised with the desired UE.

2.7 Signal Clipping

In O-OFDM transmission, the time-domain signal has been converted to an approximated Gaussian waveform, which has a very high peak-to-average power ratio (PAPR). However, the LED has a limited dynamic range as described in Section 2.3.1.3. Consequently, to reach a compromise between signal power and signal distortion, the samples with high amplitude are clipped to make sure the signal varies within the permitted range. This non-linear distortion is expected to cause minor impairment to the transmission as the probability of generating signal samples with high amplitude is typically low. A number of studies have been carried out to investigate the effects of this clipping process [37, 74].

In this study, the results in [74] are used to calculate the effects caused by the signal clipping process. It is assumed that the ideal OFDM follows a Gaussian distribution. As shown in Figure 2.13, a top clipping level $\epsilon_{\max}$, a bottom clipping level $\epsilon_{\min}$ and a DC-bias level ϵ_{DC} are defined. The configuration of these parameters should fulfil the following relationship:

$$\sigma_{\text{x}}(\epsilon_{\text{DC}} + \epsilon_{\max}) = I_{\max}, \tag{2.39}$$

$$\sigma_{\text{x}}(\epsilon_{\text{DC}} + \epsilon_{\min}) = I_{\min}, \tag{2.40}$$

where $I_{\max}$ and $I_{\min}$ denote the maximum and minimum forward current for the LED. The

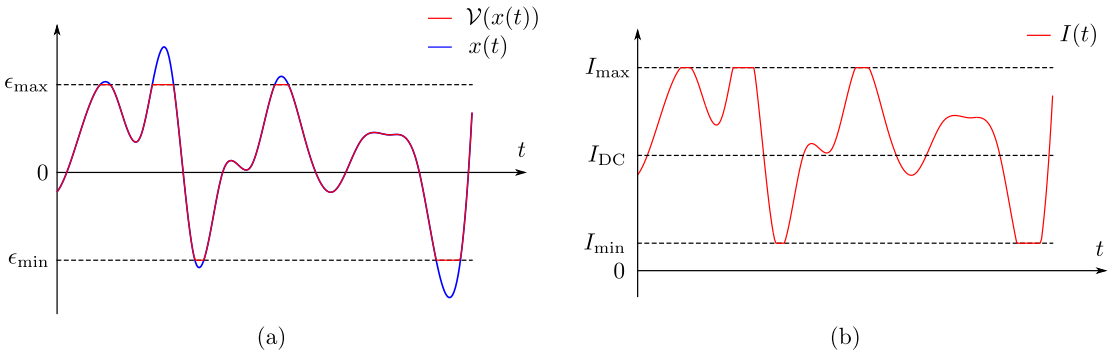

Figure 2.13: *(a) A clipped bi-polar signal with unity power. (b) A clipped signal after the addition of DC-bias and signal amplification to match the LED dynamic range.*

assumption made in Section 2.3.1.3 that $I_{\min} = 0$ leads to $\epsilon_{\min} = -\epsilon_{\mathrm{DC}}$ and $\epsilon_{\max} = \frac{I_{\max}}{\sigma_{\mathrm{x}}} - \epsilon_{\mathrm{DC}}$.

2.7.1 Optical Power Requirement

One of the important issues in the LAC downlink is how much optical output power is required to transmit a signal with certain strength and clipping distortion. According to (2.7) and (2.34), the output optical power can be calculated as:

$$\bar{P}_{\mathrm{opt}} = \eta_{\mathrm{led}} \mathbb{E}_t[\sigma_{\mathrm{x}} \left(\mathcal{V}\left(x(t)\right) + \epsilon_{\mathrm{DC}}\right)] = \eta_{\mathrm{led}} \sigma_{\mathrm{x}} \left(\mathbb{E}_t[\mathcal{V}\left(x(t)\right)] + \epsilon_{\mathrm{DC}}\right), \tag{2.41}$$

where $\mathbb{E}_t[\mathcal{V}\left(x(t)\right)]$ can be calculated based on the characteristics of truncated Gaussian distribution as [74]:

$$\begin{aligned} \mathbb{E}\left[\mathcal{V}(x(t))\right] &= \epsilon_{\max}\mathbb{P}[x > \epsilon_{\max}] + \epsilon_{\min}\mathbb{P}[x < \epsilon_{\min}] + \int_{\epsilon_{\min}}^{\epsilon_{\max}} x f_{\mathcal{N}}(x)\mathrm{d}x \\ &= \epsilon_{\min}\left(1 - \mathcal{Q}(\epsilon_{\min})\right) + \epsilon_{\max}\mathcal{Q}(\epsilon_{\max}) + f_{\mathcal{N}}(\epsilon_{\min}) - f_{\mathcal{N}}(\epsilon_{\max}) \end{aligned} \tag{2.42}$$

where $\mathcal{Q}(u) = \frac{1}{\sqrt{2\pi}} \int_u^{\infty} \exp\left(-\frac{v^2}{2}\right) \mathrm{d}v$ represents the Q-function; and $f_{\mathcal{N}}(u) = \frac{1}{\sqrt{2\pi}} \exp\left(-\frac{u^2}{2}\right)$ is the probability density function (PDF) of the standard normal distribution. Note that in the calculation of $\mathbb{E}\left[\mathcal{V}(x(t))\right]$ with ACO-OFDM, $\epsilon_{\min} = \epsilon_{\mathrm{DC}} = 0$. A parameter denoted as $\Delta\epsilon$ is defined to evaluate the effective signal amplitude range. In the case of DCO-OFDM, $\Delta\epsilon = \epsilon_{\max} - \epsilon_{\min}$. In the case of ACO-OFDM, despite the clipping of negative samples, the missing samples can be recovered at the receiver side. Therefore, the effective signal range

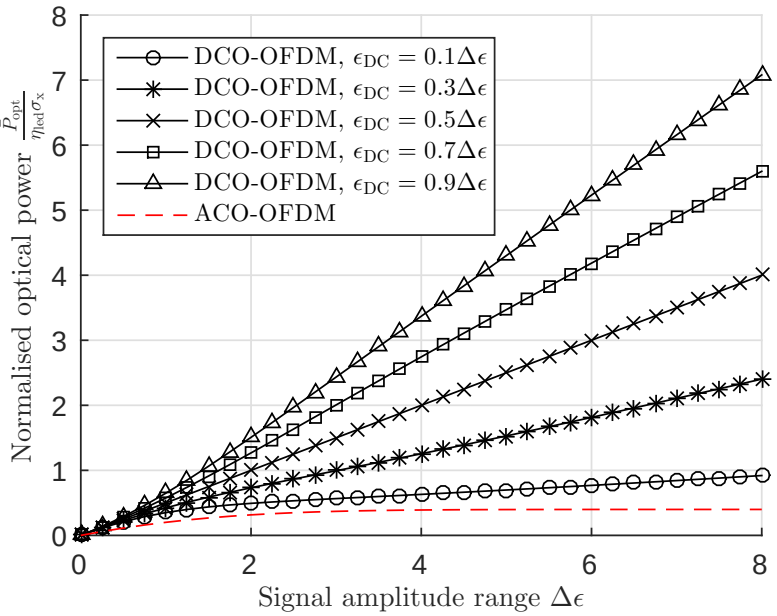

Figure 2.14: *Normalised optical output power varies with* $\Delta\epsilon$.

should be $\Delta\epsilon = 2\epsilon_{\max}$. Consider $\Delta\epsilon$ as given parameters, the required normalised optical output power $\frac{\bar{P}_{\mathrm{opt}}}{\eta_{\mathrm{led}}\sigma_{\mathrm{x}}}$ is calculated and the results are shown in Figure 2.14. It shows that with the increase of $\Delta\epsilon$, the required output optical power increases. For the same signal amplitude range, DCO-OFDM requires a much higher optical output power relative to the case of ACO-OFDM. Furthermore, with the increase of DC-bias level ϵ_{DC}, the required output optical power increases in DCO-OFDM system.

2.7.2 Clipping Distortion

As introduced in Section 2.6.1, the time-domain clipped signal can be modelled as (2.36). The attenuation factor can be derived as [37]:

$$\eta_{\mathrm{clip}} = \mathbb{E}[x(t)\mathcal{V}(x(t))] = \int_{-\infty}^{\infty} x(t)\mathcal{V}(x(t))f_{\mathcal{N}}(x(t))\mathrm{d}x(t) = \mathcal{Q}(\epsilon_{\min}) - \mathcal{Q}(\epsilon_{\max}). \quad (2.43)$$

The clipping noise variance in the frequency domain can be calculated as [37]:

$$\sigma^2_{\mathrm{clip}} = \mathbb{E}[n^2_{\mathrm{clip}}(t)] - \mathbb{E}^2[n_{\mathrm{clip}}(t)] \quad (2.44)$$

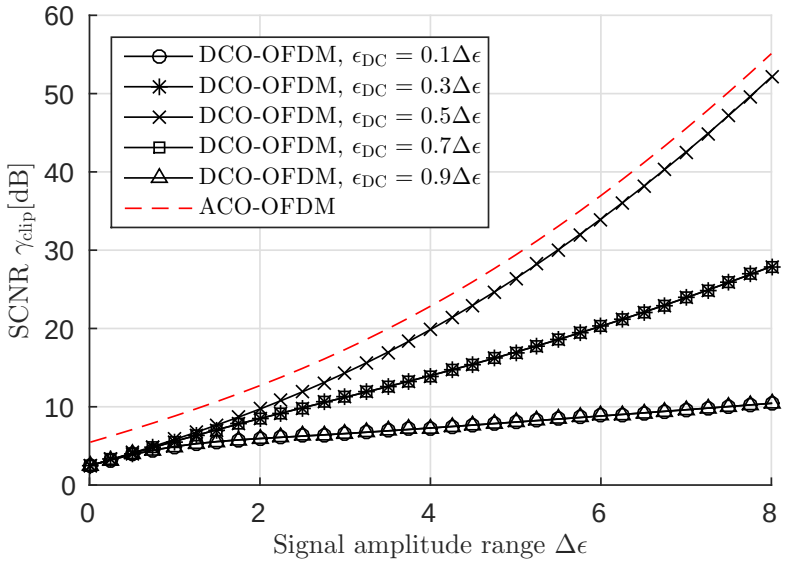

Figure 2.15: *Signal-to-clipping noise ratio varies with* $\Delta\epsilon$.

where $\mathbb{E}[n^2_{\mathrm{clip}}(t)] = \mathbb{E}[\mathcal{V}^2(x(t))] - \eta^2_{\mathrm{clip}}\mathbb{E}[x^2(t)]$ and $\mathbb{E}[n_{\mathrm{clip}}(t)] = \mathbb{E}[\mathcal{V}(x(t))]$. With further equation expansion, the clipping noise variance can be written as:

$$\sigma^2_{\mathrm{clip}} = \epsilon^2_{\mathrm{min}}\left(1 - \mathcal{Q}(\epsilon_{\mathrm{min}})\right) + \epsilon^2_{\mathrm{max}}\mathcal{Q}(\epsilon_{\mathrm{max}}) + \epsilon_{\mathrm{min}} f_{\mathcal{N}}(\epsilon_{\mathrm{min}}) - \epsilon_{\mathrm{max}} f_{\mathcal{N}}(\epsilon_{\mathrm{max}}) - \eta^2_{\mathrm{clip}}$$
$$+ \mathcal{Q}(\epsilon_{\mathrm{min}}) - \mathcal{Q}(\epsilon_{\mathrm{max}}) - \left(\epsilon_{\mathrm{min}}\left(1 - \mathcal{Q}(\epsilon_{\mathrm{min}})\right) + \epsilon_{\mathrm{max}}\mathcal{Q}(\epsilon_{\mathrm{max}}) + f_{\mathcal{N}}(\epsilon_{\mathrm{min}}) - f_{\mathcal{N}}(\epsilon_{\mathrm{max}})\right)^2. \tag{2.45}$$

In the calculation of η_{clip} and σ^2_{clip} with ACO-OFDM, the recovered signal at the receiver side is considered. Therefore, $\epsilon_{\mathrm{min}} = -\epsilon_{\mathrm{max}}$ is used in the calculation. In order to evaluate the clipping distortion with different clipping configurations, the signal-to-clipping noise ratio (SCNR) is defined as: $\gamma_{\mathrm{clip}} = \frac{\xi^2\eta^2_{\mathrm{clip}}}{\sigma^2_{\mathrm{clip}}}$. Figure 2.15 shows the results of SCNR varies with $\Delta\epsilon$. It shows that in order to avoid significant clipping distortion, $\Delta\epsilon$ has to be sufficiently large. It also shows that to achieve the same SCNR, ACO-OFDM requires less $\Delta\epsilon$ than the case of DCO-OFDM. In the cases of DCO-OFDM, with the same $\Delta\epsilon$, a DC-bias of $\epsilon_{\mathrm{DC}} = 0.5\Delta\epsilon$ offers the lowest clipping distortion.

The results shown in Figure 2.14 implies that with a limited amount of average optical output $\bar{P}_{\mathrm{opt}}$, the output signal strength gets weaker with the increase of $\Delta\epsilon$. On the other hand, the results shown in Figure 2.15 implies that less clipping distortion can be achieved with a higher value of $\Delta\epsilon$. Therefore, there is a trade-off between signal strength and clipping distortion with

the configuration of forward electrical signal.

2.8 Cell Deployments and Spatial Reuse

In Section 2.4.2, it is noted that the characteristics of indoor free-space channel depends on positions / orientations of the transmitters and the receivers. Therefore, the channel frequency response $H_i(k)$ and the performance of the LAC downlink system are strongly dependent on the spatial layout of the O-BSs. The significance of CCI is one of the most important factors to the downlink performance, and the significance of CCI is determined directly by the distance from the closest source of the CCI to the desired receiver. This distance is closely related to the cell deployment and the spatial reuse plan in the network which are introduced in the following subsections.

2.8.1 Different Cell Deployments

In RF cellular studies, a number of cellular models have been considered. Wyner model is an one-dimensional (1-D) model, which defines the BS on a linear array [75]. It offers good tractability for cellular study. However, the over-simplification causes considerable accuracy issue. Wyner model is suitable for studying the network that extends in one dimension, such as cellular systems along highway or railway. The most commonly used model in cellular study is the grid-based model [7]. In the grid-based model, BSs are placed on a 2-D hexagonal or square grid. Grid-based model offers ideal 2-D BS layout, and is widely used in system level cellular Monte-Carlo simulations. However, due to the nature of the model, the position of each BS is highly correlated and leads to intractability to the analysis based on this model. In practice, the placement of BSs has a number of extra constraints, such as geometric limitation, population density, and output power. Therefore, non-homogeneous layout of BSs has been proposed [76], and tools in stochastic geometry can be used in the analysis to get tractable result. Homogeneous Poisson Point Process (PPP) has been proposed in [77] to model the cell deployment as a pessimistic estimation. However, the case that two BSs are placed closely is not very likely in practice. To compensate the drawback of homogeneous PPP cell deployment, point processes offer better approximation to cellular network, such as hard-core point process (HCPP), have been considered [78].

In a LAC network, the cell deployments used in RF cellular system can be adopted. In this

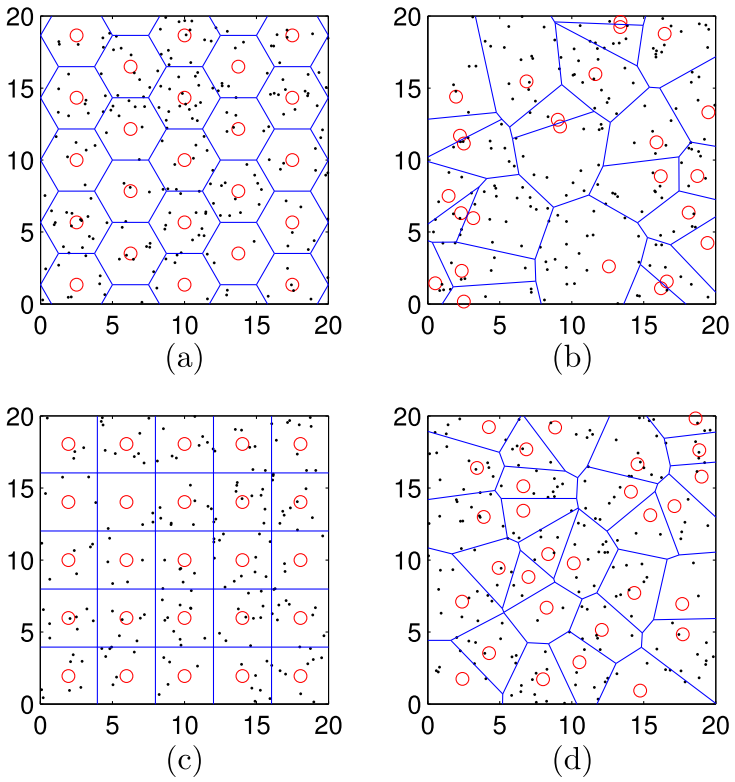

Figure 2.16: *Different cell deployments considered in LAC networks. (a) HEX cell deployment. (b) Homogeneous PPP cell deployment. (c) Square cell deployment. (d) HCPP cell deployment.*

study, two grid-based models and two point process-based models have been considered. The grid-based model includes the Hexagonal (HEX) and square cell deployments as shown in Figure 2.16 (a) and (c). Square cell deployment is the simplest layout, which is perfectly compatible to a cuboid room. It has been used in many OWC studies and practical lighting networks. HEX cell deployment is less common in lighting network, but it is a desired layout for LAC network as a hexagon shape offers a best approximation to a circle. An optimised performance is expected with a HEX cell deployment, but it may require extra engineering work to redesign the lighting infrastructure in a room. Grid-based network is expected to offer good modelling to a well-designed LAC network with dedicated O-BS layout.

The considered point process-based models include the homogeneous PPP cell deployment and the Matérn type II HCPP cell deployment as shown in Figure 2.16 (b) and (d). The spatial distribution of points in a homogeneous PPP is uniformly distributed, and the number of points

per unit area follows a Poisson distribution. A HCPP is similar to a PPP except an extra constraint that any pair of two points have a separation no less than a specified threshold. The irregular placement of luminaries is mainly motivated by the following considerations: firstly, the placement of a luminary may be limited by the wiring structure in the room. Secondly, in some cases, non-uniform illumination is required, which means that the lighting is enhanced in certain parts of the room, but not in other parts. Also, even for a uniform cell deployment, a user may be absent in some cells. In that case, the downlink transmission can be switched off, which results in a non-uniform cell deployment. Similar to the cases in RF cellular systems, the point process-based models are expected to offer pessimistic estimation. The case with PPP cell deployment is expected to offer the worst case performance, and in the case with HCPP cell deployment, the consideration that two lamps are less likely to be co-located is included. In the LAC network cell deployment modelling, it should be noted that LAC network is bounded by the room edges.

2.8.2 Spatial Reuse Plan

The other critical factor to the reuse distance is the spatial reuse plan of the transmission resources. In order to avoid CCI in a cellular network, a common method is to divide the entire network into multiple cell clusters [7]. Figure 2.17 shows a HEX cellular network as an example. In the cluster, κ_{rf} cells are deployed close together. The different colours of the cells in the cluster show that the UEs in each cell use different transmission resources. The network is formed by tessellation with the cell cluster. This resource allocation method leads to a decrease in the number of neighbouring cells using the same transmission resource as shown in Fig-

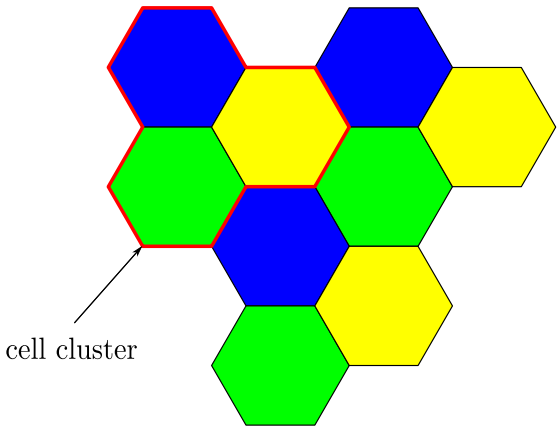

Figure 2.17: *An example of spatial reuse plan.*

ure 2.17. On the one hand, the CCI level is reduced. On the other hand, the spectral efficiency (available transmission resource per cell) is decreased. This method is also known as static resource partitioning. The number of cells in a cell cluster κ_{rf} is defined as the spatial reuse factor, which is a key parameter to the performance of a cellular network. Note that the case of $\kappa_{\mathrm{rf}} = 1$ is also known as universal frequency reuse (UFR). Since high spectral efficiency is considered as the main objective in this study, only the cases with $\kappa_{\mathrm{rf}} \leq 3$ are considered.

2.9 Downlink SINR in LiFi Attocell Networks

In order to evaluate the downlink performance in a LAC network, it is essential to determine the downlink signal-to-interference-plus-noise ratio (SINR). A number of other important downlink system metrics, such as cell data rate, SINR statistics, require the SINR calculation for a specified link setup as the basis. In a LAC downlink system, the SINR on subcarrier k can be defined as:

$$\gamma(k) = \frac{P_{\mathrm{elec},0}(k)}{\sum_{i \in \mathit{И}} P_{\mathrm{elec},i}(k) + P^{\mathrm{clip}}_{\mathrm{elec},0}(k) + \sigma^2_{\mathrm{Rx}}}, \tag{2.46}$$

where $P_{\mathrm{elec},0}(k)$ denotes the received desired signal power; $P_{\mathrm{elec},i}(k)$ denotes the received interfering signal power from the i^{th} O-BS; $P^{\mathrm{clip}}_{\mathrm{elec},0}(k)$ denotes the power of the received clipping noise. According to (2.38), $P_{\mathrm{elec},0}(k)$ can be calculated as:

$$P_{\mathrm{elec},0}(k) = \mathbb{E}\left[\left|\eta_{\mathrm{pd}}\eta_{\mathrm{led}}\sigma_{\mathrm{x}}\eta_{\mathrm{clip}}X_0(k)H_0(k)\right|^2\right] = \eta^2_{\mathrm{pd}}\eta^2_{\mathrm{led}}\sigma^2_{\mathrm{x}}\eta^2_{\mathrm{clip}}\xi^2\left|H_0(k)\right|^2. \tag{2.47}$$

Note that $\mathbb{E}\left[\left|X_0(k)\right|^2\right] = \xi^2$. Similarly, the received interfering signal power on subcarrier k from O-BS i can be calculated as:

$$\begin{aligned} P_{\mathrm{elec},i}(k) &= \mathbb{E}\left[\left|\eta_{\mathrm{pd}}\eta_{\mathrm{led}}\sigma_{\mathrm{x}}\left(\eta_{\mathrm{clip}}X_i(k) + N_{\mathrm{clip},i}(k)\right)H_i(k)\right|^2\right] \\ &= \eta^2_{\mathrm{pd}}\eta^2_{\mathrm{led}}\sigma^2_{\mathrm{x}}\left(\eta^2_{\mathrm{clip}} + \sigma^2_{\mathrm{clip}}\right)\left|H_i(k)\right|^2. \end{aligned} \tag{2.48}$$

In the calculation of (2.48), it is worth noting that $\mathbb{E}\left[\left|X_i(k)\right|^2\right] = 1$. This is because of the assumption that the CCI is converted to a complex Gaussian signal. The power of the received clipping noise components $P^{\mathrm{clip}}_{\mathrm{elec},0}(k)$ can be calculated as:

$$P^{\mathrm{clip}}_{\mathrm{elec},0}(k) = \mathbb{E}\left[\left|\eta_{\mathrm{pd}}\eta_{\mathrm{led}}\sigma_{\mathrm{x}}N_{\mathrm{clip},i}(k)H_0(k)\right|^2\right] = \eta^2_{\mathrm{pd}}\eta^2_{\mathrm{led}}\sigma^2_{\mathrm{x}}\sigma^2_{\mathrm{clip}}\left|H_0(k)\right|^2. \tag{2.49}$$

By inserting (2.47), (2.48) and (2.49) into (2.46), the SINR expression can be expanded as:

$$\gamma(k) = \frac{\eta_{\mathrm{pd}}^2 \eta_{\mathrm{led}}^2 \sigma_{\mathrm{x}}^2 \eta_{\mathrm{clip}}^2 \left|H_0(k)\right|^2 \xi^2}{\sigma_{\mathrm{Rx}}^2 + \eta_{\mathrm{pd}}^2 \eta_{\mathrm{led}}^2 \sigma_{\mathrm{x}}^2 \left|H_0(k)\right|^2 \sigma_{\mathrm{clip}}^2 + \eta_{\mathrm{pd}}^2 \eta_{\mathrm{led}}^2 \sigma_{\mathrm{x}}^2 \left(\eta_{\mathrm{clip}}^2 + \sigma_{\mathrm{clip}}^2\right) \sum_{i \in \mathcal{U}} \left|H_i(k)\right|^2}$$
$$= \left(\left(\frac{\eta_{\mathrm{clip}}^2 \xi^2 \left|H_0(k)\right|^2}{\left(\eta_{\mathrm{clip}}^2 + \sigma_{\mathrm{clip}}^2\right) \sum\limits_{i \in \mathcal{U}} \left|H_i(k)\right|^2 + \frac{\sigma_{\mathrm{Rx}}^2}{\eta_{\mathrm{pd}}^2 \eta_{\mathrm{led}}^2 \sigma_{\mathrm{x}}^2}} \right)^{-1} + \frac{\sigma_{\mathrm{clip}}^2}{\eta_{\mathrm{clip}}^2 \xi^2} \right)^{-1}, \tag{2.50}$$

where the term $\frac{\sigma_{\mathrm{clip}}^2}{\eta_{\mathrm{clip}}^2 \xi^2}$ is the reciprocal of SCNR. According to (2.14), the channel gain on subcarrier k can be written as:

$$\left|H(k)\right|^2 = \left|H_{\mathrm{fe}}(k)\right|^2 \left|H_{\mathrm{fs}}(k)\right|^2. \tag{2.51}$$

According to the approximation function (2.15), $\left|H_{\mathrm{fe}}(k)\right|^2$ can be calculated as:

$$\left|H_{\mathrm{fe}}(k)\right|^2 = \exp\left(-\frac{kF_{\mathrm{s}}}{KF_{\mathrm{fe}}}\right), \tag{2.52}$$

for $k = 1, 2, \cdots, \tilde{K}$. In addition, the noise variance can be written as $\sigma_{\mathrm{Rx}}^2 = \frac{N_0 F_{\mathrm{S}}}{\xi^2}$. Therefore, the SINR can be rewritten as:

$$\gamma(k) = \left(\left(\frac{\eta_{\mathrm{clip}}^2 \xi^2 \left|H_{\mathrm{fs},0}(k)\right|^2}{\left(\eta_{\mathrm{clip}}^2 + \sigma_{\mathrm{clip}}^2\right) \sum\limits_{i \in \mathcal{U}} \left|H_{\mathrm{fs},i}(k)\right|^2 + \frac{N_0 F_{\mathrm{s}} \exp\left(\frac{kF_{\mathrm{s}}}{KF_{\mathrm{fe}}}\right)}{\xi^2 \eta_{\mathrm{pd}}^2 \eta_{\mathrm{led}}^2 \sigma_{\mathrm{x}}^2}} \right)^{-1} + \frac{\sigma_{\mathrm{clip}}^2}{\eta_{\mathrm{clip}}^2 \xi^2} \right)^{-1}, \tag{2.53}$$

The configuration of $\eta_{\mathrm{led}}^2 \sigma_{\mathrm{x}}^2$ is related to the characteristics of the LED. If the limiting factor is the available average optical output power, the value of $\eta_{\mathrm{led}}^2 \sigma_{\mathrm{x}}^2$ can be calculated based on (2.41) as:

$$\eta_{\mathrm{led}}^2 \sigma_{\mathrm{x}}^2 = \frac{\bar{P}_{\mathrm{opt}}^2}{\left(\mathbb{E}_t[\mathcal{V}\left(x(t)\right)] + \epsilon_{\mathrm{DC}}\right)^2}. \tag{2.54}$$

If the limiting factor is the linear dynamic range with a maximum optical output power of $P_{\mathrm{opt,max}}$, the value of $\eta_{\mathrm{led}}^2 \sigma_{\mathrm{x}}^2$ can be calculated based on (2.6) and (2.39) as:

$$\eta_{\mathrm{led}}^2 \sigma_{\mathrm{x}}^2 = \frac{P_{\mathrm{opt,max}}^2}{\left(\epsilon_{\mathrm{DC}} + \epsilon_{\mathrm{max}}\right)^2}. \tag{2.55}$$

2.10 Summary

In this chapter, the basic concept of a LAC network system has been introduced. The essential technologies to establish a complete LAC network have been discussed. The characteristics of the front-end elements for the LAC network downlink have been introduced. The downlink channel components have been analysed, and the related channel simulation methods have been briefly introduced. The O-OFDM transmission scheme with the presence of CCI has been introduced. The major source of receiver noise has been presented. The effects of adding signal clipping have been introduced and evaluated. Finally, the downlink SINR expression in a LAC network has been derived.

Chapter 3
Analytical Calculation of Non-line-of-sight Channel Impulse Response in Visible Light Communication

3.1 Introduction

In order to accurately estimate the performance of a downlink connection in a light fidelity attocell (LAC) network, the characterisation of downlink channel is important. However, the light propagation in an indoor environment is a complex process, which leads to the difficulties in modelling of the visible light communication (VLC) channel. The primary component of a VLC channel is the line-of-sight (LoS) link which can be accurately characterised by a simple function [55]. In addition, the non-line-of-sight (NLoS) channel components caused by the indoor surface reflection leads to a major effects on the frequency response of the VLC channel. A number of methods have been developed to characterise this diffused channel [67–69]. However, most of these methods can only provides numerical results with a long computation time. It is difficult to achieve a reasonable compromise between tractability and modelling accuracy. Furthermore, reflection and blockage caused by other objects, such as human body, furnitures, are rarely considered in the literatures. Thus, their effects and significance remains unknown. Therefore, further research efforts are required for the development of VLC channel modelling.

In the LAC network downlink study, the LoS channel and the NLoS channel due to the indoor internal surface reflections are considered. Other factors to the free-space light propagation channel is not considered due to the lack of available models to include these factors. Wireless infrared (IR) communication and VLC are similar in many aspects. Firstly, low-cost light-emitting diodes (LEDs) and photodiodes (PDs) are used. Secondly, the signal propagation characteristics in wireless IR and VLC systems are similar as both systems use adjacent optical spectrum. Consequently, a number of methods developed for simulating wireless IR communication channel can be used for VLC studies [55, 79]. A widely used deterministic NLoS

channel impulse response (CIR) calculation method has been proposed in [67]. In this method, a cuboid room with internal surfaces causing diffusing reflections is considered. The internal surfaces are divided into large number of small reflecting elements. With a given locations and orientations of transmitter and receiver, accurate CIR result can be obtained by calculating the interaction between each pair of elements. The main drawback of this approach is its extremely high computational complexity. A significant time in the magnitude of days are required to calculate a CIR result of a small room considering up to 3^{rd} order reflections with a moderate time resolution. In order to reduce the computation time, improved methods based on DUSTIN algorithm [69] and Monte Carlo simulation [68] have been proposed. Both methods reduce the computation time significantly. Especially for Monte Carlo method, an accurate CIR result can be obtained within a period of several minutes. A physical model of the IR channel using a sphere model has been proposed in [70] to approximate the frequency response of NLoS channels. With respect to VLC channels, few studies have been conducted in the geometric channel modelling. It has been pointed out in [72] that since the visible light spectrum include a wide range of optical spectrum, the methods developed in wireless IR communications cannot be directly used in VLC channel calculation. The dependency on light wavelength is considered in the deterministic CIR calculation method for the CIR calculation in VLC [72]. A method calculating NLoS channels in frequency domain has been proposed in [80]. Despite the significantly computational complexity introduced by the inversion operation of an extremely large matrix, it has been shown that this complexity can be significantly reduced by using numerical methods. User mobility is taken into account in [81]. VLC channel characterisations based on a commercial optical design software Zemax® is considered in [82]. A number of the aforementioned studies of VLC channel modelling offer numerical results for a number of configurations, where generalisations are not straightforward.

In the analysis of a LAC network downlink, some important system metrics, such as SINR statistics, average cell data rate, need to be evaluated. However, the evaluation of these metrics requires large number of SINR samples, and each SINR sample requires the information of multiple free-space channels between each downlink transmitter and the considered downlink receiver. If the deterministic or Monte Carlo method is used to generate the channel with NLoS components, a considerable amount of time would be required. Similar issues also exist in many other VLC studies which require to calculate the major metric of the study that takes the effects of NLoS channel into account. For example, in a study that evaluate the performance of a multiple-input multiple-output (MIMO) VLC system at various positions in a room with

the consideration of NLoS channel [83], the calculation of a large number of channels based on wall reflections is required. Therefore, there is a demand of efficient method to calculate the NLoS VLC channel, which motivates the research presented in this chapter. An analytical closed-form expression of the LoS CIR with a ceiling-bounce model in a diffused IR link has been derived in [23]. Motivated by this approach, in this study, we extend the work in [23] and propose an analytical model to generate the NLoS CIR for VLC links. Firstly, we decompose the complicated NLoS channel into a number of components with less-complicated light propagation categories. These propagation categories are defined according to the number of reflections and the reflective surfaces that the light undergoes. Secondly, the analysis of the channel with each category is carried out, and the CIR analytical expressions are obtained for each category. Finally, the overall CIR is approximated as a superposition of these CIRs for each category. It is shown in this chapter that this method provides an efficient tight approximation for NLoS VLC CIRs considering up to 2^{nd} order reflections.

The remainder of this chapter is arranged as follows. The analysis methodology presented in this study is introduced in Section 3.2. A preliminary single reflection CIR calculation is introduced in Section 3.3. The detailed analysis of the component NLoS CIRs and the corresponding analytical results are presented in Section 3.4. The final approximated NLoS CIR calculation is presented in Section 3.5. In addition, the calculation accuracy and computation time is evaluated and compared with the state-of-the-art method in this section. This chapter is summarised in Section 3.6.

3.2 Non-line-of-sight Channel Analysis Methodology

In this section, the methodology of the proposed approach to analyse the NLoS channel in typical indoor environments such as cuboid rooms is presented. An indoor environment in this study is presented. Multi-path reflections caused by internal surfaces inflicts major NLoS channel components. It is assumed that the room internal surfaces cause diffused reflections with fixed reflectance. In addition, a transmitter and a receiver are defined with specified locations. The considered orientation of the light source in this study is towards the floor as this is the most common light deployment in practice. The considered orientation of the PD detector is towards the ceiling. The reason for this is two-fold. Firstly, the proposed method aims at providing efficient CIR calculation for other VLC research, and a PD detector orientation of directing upwards is used in many VLC studies. In addition, this configuration leads to CIR results with

reasonable complexity, which is one of the research objective of this study. In practice, the fixed direction of PD detector can be achieved by using a mechanical design or by installing multiple PD detectors with different orientations on the receiver.

For the convenience of analysis, the entire NLoS CIR can be decomposed into multiple components with respect to the number of reflections occurred as:

$$h_{\mathrm{NLoS}}(t) = \sum_{\mathfrak{i}=1}^{\infty} h^{[\mathfrak{i}]}(t), \tag{3.1}$$

where $h^{[\mathfrak{i}]}(t)$ represents the component CIR with light undergoing exactly $\mathfrak{i}$ reflections. Despite the decomposition according to the number of reflections, the complexity of each component is still too high for conducting a mathematically tractable analysis. In order to further decrease the analytical complexity, each component CIR $h^{[i]}(t)$ is further decomposed according to the light propagation category. A number of major light propagation categories are considered in this study.

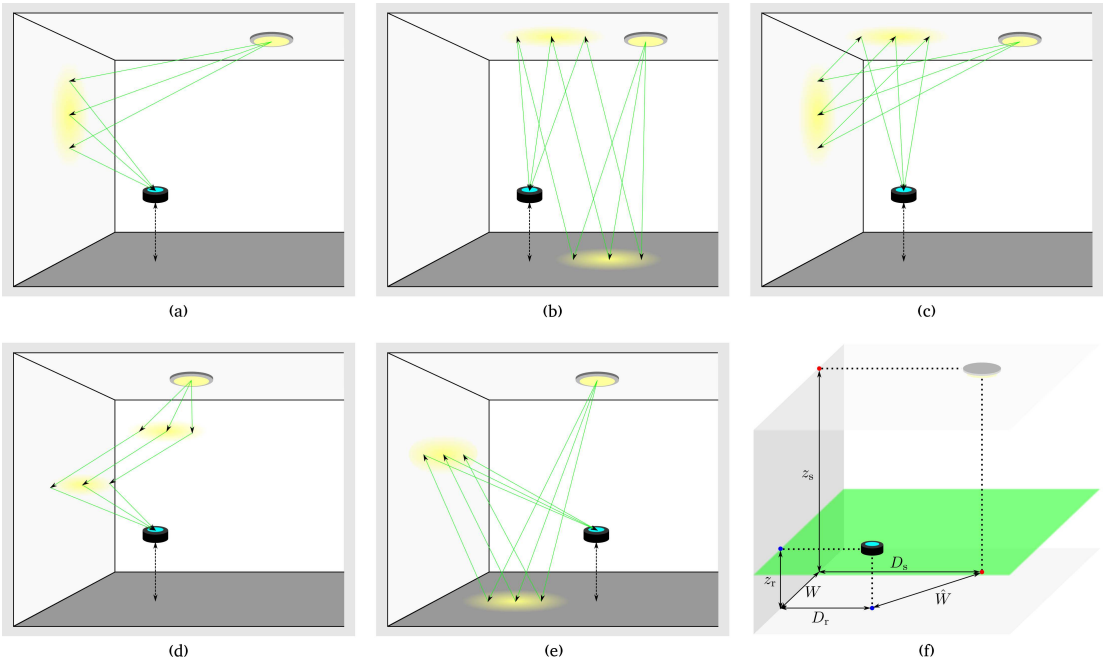

Figure 3.1: *(a) Light propagation in the case of transmitter-to-wall-to-receiver. (b) Light propagation in the case of transmitter-to-floor-to-ceiling-to-receiver. (c) Light propagation in the case of transmitter-to-wall-to-ceiling-to-receiver. (d) Light propagation in the case of transmitter-to-wall-to-wall-to-receiver. (e) Light propagation in the case of transmitter-to-floor-to-wall-to-receiver. (f) The notations of important geometric parameters*

In the case of $h^{[1]}(t)$, there is only one category that the light propagate from the transmitter, reflected by one of the four walls, and incident to the receiver, as shown in Figure 3.1 (a). This light propagation category is termed as transmitter-to-wall-to-receiver (TWR). For the channel of this category, the signal only interacts with a single surface. Consequently, the relationship between the geometric characteristics and the time delay characteristics of the channel is tractable for analysis as demonstrated in [23]. In the case of $h^{[2]}(t)$, light propagation between different surfaces exists. The different combinations of these propagations between different surfaces lead to four light propagation categories as shown in Figure 3.1 (b), (c), (d) and (e). For example, in one of the categories, the emitted light from the transmitter propagates via the floor and ceiling surfaces and incidents to the receiver. For short, this category is termed as transmitter-to-floor-to-ceiling-to-receiver (TFCR). Similarly, the other three categories are the transmitter-to-wall-to-ceiling-to-receiver (TWCR), the transmitter-to-wall-to-wall-to-receiver (TWWR) and the transmitter-to-floor-to-wall-to-receiver (TFWR) categories. The analytical complexity of these categories is higher than that of TWR as the CIR calculation of these categories requires two two-dimensional (2-D) integrations over two surfaces. However, it is demonstrated that via appropriate approximations and simplifications, analytical CIR expressions can be obtained for several dominant categories. Often these expressions have one or two one-dimensional (1-D) integrations with finite limits. The channel categories due to higher order reflections can also be defined in a similar manner, but omitted due to the exponential growth of analytical complexity as the order of reflections increases. Fortunately, it is shown in the final results that the omission of these higher order reflection CIR components causes acceptable loss in accuracy.

Ideally, the entire NLoS CIR should be the superposition of the CIR components considering all propagation categories. However, because of the unavailability of the expressions for the channel with some of the categories and the complexity constraint, the superposition of the CIRs with part of the categories that dominate the NLoS channel is used to approximate the overall NLoS CIR. In this chapter, the expressions for the CIR with TWR, TFCR and TWCR categories are derived and used to estimate the NLoS CIR. The channels with TFWR, TWWR categories and the categories corresponding to higher order reflections are omitted in this study. The reason is two-fold: the expressions for the CIR with these categories cannot be simplified and contains three or more unsolvable integrals. These unsolvable integrals would lead to a significant increase in numerical calculation complexity; in addition, the simulation results show that the omission of these CIRs causes minor error in the NLoS CIR estimation in the

cases with lower average room internal surface reflectivity or with room with medium / large size. The analysis of reflection and obstruction caused by other opaque objects, such as human bodies or furnitures, is complicated, and the generic model for these effects have not been developed yet. Therefore, it is assumed that the random objects in the room cause minor effects on the channel.

3.3 Preliminary

In the following CIR analysis, the same method is used in part of each CIR calculation with TWR, TFCR and TWCR. In this common method, a link from a light source element via a single diffused reflection by an infinite plane to a receiving element is considered. A closed-form expression for calculating the impulse response of this link in a special case is presented in [23]. However, the CIR result for the general case has not been presented in detail. For the convenience of presenting the NLoS CIR results with TWR, TFCR and TWCR, we extend the work in [23] and present the expression for the general case in the following subsection.

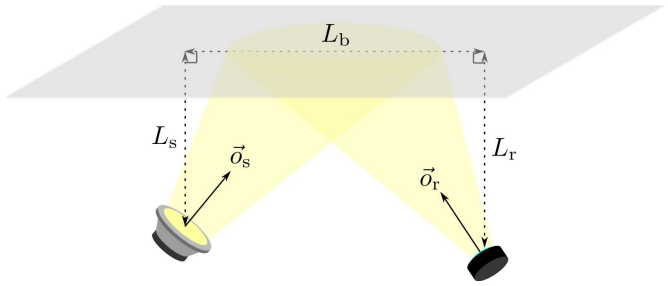

Figure 3.2: *The deployment of a single reflection light propagation channel.*

Figure 3.2 shows the setup for a single reflection channel. A light source with a Lambertian emission order of m and an orientation of $\vec{o}_{\mathrm{s}} = [x_{\mathrm{s}}\ y_{\mathrm{s}}\ z_{\mathrm{s}}]$ is L_{s} away from the plane. A receiving element with a physical area of A_{r} and an orientation of $\vec{o}_{\mathrm{r}} = [x_{\mathrm{r}}\ y_{\mathrm{r}}\ z_{\mathrm{r}}]$ is L_{r} away from the plane. Both the light source and the receiving element have the projection points on the plane. The distance between the two projection points is L_{b}. The effective reflectivity of the surface is ρ. The CIR for this single reflection link is concluded in the following proposition.

Proposition 1 *With specified values for m, A_{r}, ρ, L_{s}, L_{r}, L_{b}, $\vec{o}_{\mathrm{s}}$ and $\vec{o}_{\mathrm{r}}$, the impulse response*

for a single reflection channel can be calculated as:

$$\hbar_{\{m,A_\mathrm{r},\rho,L_\mathrm{s},L_\mathrm{r},L_\mathrm{b},\vec{o}_\mathrm{s},\vec{o}_\mathrm{r}\}}(t)=\frac{\rho(m+1)L_\mathrm{s}L_\mathrm{r}A_\mathrm{r}\mathcal{U}\left(t-\frac{L_0}{c}\right)}{2\pi^2}\int_0^{2\pi}\mathfrak{r}_\theta(t)\mathfrak{f}(\mathfrak{r}_\theta(t),\theta)\frac{\mathrm{d}\mathfrak{r}_\theta(t)}{\mathrm{d}t}\mathrm{d}\theta, \tag{3.2}$$

where

$$\mathfrak{f}(r,\theta)= \frac{\mathfrak{R}^m\left(r\left(x_\mathrm{s}\cos\theta+y_\mathrm{s}\sin\theta\right)+\frac{L_\mathrm{s}L_\mathrm{b}x_\mathrm{s}}{L_\mathrm{s}+L_\mathrm{r}}+L_\mathrm{s}z_\mathrm{s}\right)\mathfrak{R}\left(r\left(x_\mathrm{r}\cos\theta+y_\mathrm{r}\sin\theta\right)-\frac{L_\mathrm{r}L_\mathrm{b}x_\mathrm{r}}{L_\mathrm{s}+L_\mathrm{r}}+L_\mathrm{r}z_\mathrm{r}\right)}{\left(r^2+\frac{2L_\mathrm{s}L_\mathrm{b}r\cos\theta}{L_\mathrm{s}+L_\mathrm{r}}+L_\mathrm{s}^2+\frac{L_\mathrm{s}^2L_\mathrm{b}^2}{(L_\mathrm{s}+L_\mathrm{r})^2}\right)^{\frac{m+3}{2}}\left(r^2-\frac{2L_\mathrm{r}L_\mathrm{b}r\cos\theta}{L_\mathrm{s}+L_\mathrm{r}}+L_\mathrm{r}^2+\frac{L_\mathrm{r}^2L_\mathrm{b}^2}{(L_\mathrm{s}+L_\mathrm{r})^2}\right)^2}, \tag{3.3}$$

$$\mathfrak{r}_\theta(t)=\frac{ct\sqrt{\mathfrak{c}_\theta(t)}-\left(c^2t^2-L_0^2\right)\left(L_\mathrm{s}-L_\mathrm{r}\right)L_\mathrm{b}\cos\theta}{2\left(c^2t^2-L_\mathrm{b}^2\cos^2\theta\right)\left(L_\mathrm{s}+L_\mathrm{r}\right)}, \tag{3.4}$$

$$\begin{aligned}\frac{\mathrm{d}\mathfrak{r}_\theta(t)}{\mathrm{d}t}=&\frac{2c^2tL_\mathrm{b}\cos\theta\left(L_\mathrm{s}-L_\mathrm{r}\right)\left(L_\mathrm{b}^2\cos^2\theta-L_0^2\right)-c\left(c^2t^2+L_\mathrm{b}^2\cos^2\theta\right)\sqrt{\mathfrak{c}_\theta(t)}}{2(L_\mathrm{s}+L_\mathrm{r})\left(c^2t^2-L_\mathrm{b}^2\cos^2\theta\right)^2}\\&+\frac{c^3t^2\left(2L_\mathrm{s}L_\mathrm{r}\left(2c^2t^2-L_0^2-L_\mathrm{b}^2\cos^2\theta\right)+\left(L_\mathrm{s}-L_\mathrm{r}\right)^2\left(c^2t^2-L_0^2\right)\right)}{\left(L_\mathrm{s}+L_\mathrm{r}\right)\left(c^2t^2-L_\mathrm{b}^2\cos^2\theta\right)\sqrt{\mathfrak{c}_\theta(t)}},\end{aligned} \tag{3.5}$$

$$L_0=\sqrt{L_\mathrm{b}^2+\left(L_\mathrm{s}+L_\mathrm{r}\right)^2}, \tag{3.6}$$

$$\mathfrak{c}_\theta(t)=4L_\mathrm{s}L_\mathrm{r}\left(c^2t^2-L_\mathrm{b}^2\cos^2\theta\right)\left(c^2t^2-L_0^2\right)+\left(L_\mathrm{s}-L_\mathrm{r}\right)^2\left(c^2t^2-L_0^2\right)^2. \tag{3.7}$$

In Proposition 1, c represents the speed of light, $\mathcal{U}(u)$ is the the unit step function, and $\mathfrak{R}(u)$ is the the ramp function which is defined as: $\mathfrak{R}(u)=\frac{1}{2}(u+|u|)$. The expression of $\mathfrak{f}(r,\theta)$ is proportional to the power loss of the transmission through the path via the point (r,θ) on the plane. All of the photons reflected by the points at $(\mathfrak{r}_\theta(t),\theta)$ reach the receiving element with a delay of t. Formula $\frac{\mathrm{d}\mathfrak{r}_\theta(t)}{\mathrm{d}t}$ simply denotes the first derivative of $\mathfrak{r}_\theta(t)$ respect to t. The detailed proof of Proposition 1 is given in Appendix A. Note that the orientation vectors $\vec{o}_\mathrm{s}$ and $\vec{o}_\mathrm{r}$ are defined based on the Cartesian coordinate system shown in Figure A.1 in Appendix A. Figure 3.3 shows three example CIRs simulated using Monte Carlo method and that using (3.2). In the simulation of these CIR results, a receiving element physical area of $A_\mathrm{r}=1$ cm^2 and a effective reflectance of $\rho=0.74$ are defined. The configurations for different setups are listed in Table 3.1. The agreement between the curves generated using (3.2) and that simulated using Monte Carlo method proved the calculation accuracy of the proposed method with various link configurations. The impulse response in a continuous time system is considered in this study.

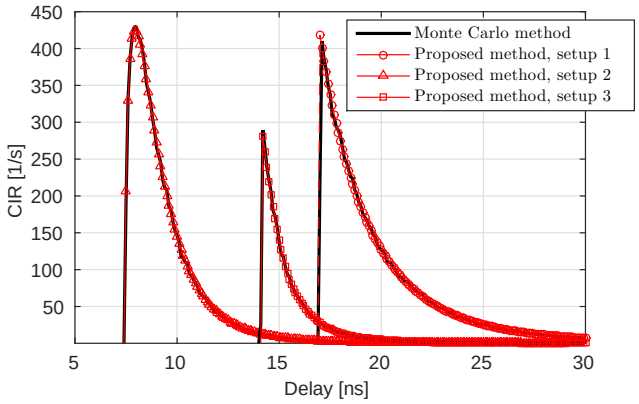

Figure 3.3: *Single reflection CIR simulation results calculated using* (3.2) *and the Monte Carlo method. A receiving element physical area of* $A_{\mathrm{r}} = 1$ *cm*^{2} *and a effective reflectance of* $\rho = 0.74$ *are defined. The configurations for different setups are listed in Table 3.1.*

Note that the unit of the impulse response is '1/s'. The output of a continuous time system can be written as $y(t) = h(t) \otimes x(t)$, where $x(t)$ refers to the input signal. In order to make sure the input signal and output signal have the same unit, the integral $\int h(t)\mathrm{d}t$ has to be dimensionless. Since the variable time is in the unit of 'second', the impulse response function should use the unit of '1/s'.

Parameter	$\phi_{1/2}$	L_{s}	L_{r}	L_{b}	$\vec{o}_{\mathrm{s}}$	$\vec{o}_{\mathrm{r}}$
Setup 1	60°	3 m	2 m	1 m	[0 0 1]	[0 0 1]
Setup 2	40°	1 m	1 m	1 m	[0 0 1]	[0 1 0]
Setup 3	60°	2 m	1 m	3 m	[1 0 0]	[-1 0 0]

Table 3.1: *Single reflection CIR simulation parameters*

3.4 Detailed Analysis of Component Non-line-of-sight Channel Impulse Response

In this section, the CIR analysis for the channel with TWR, TFCR and TWCR categories are presented. A cuboid room with a size of $l_{\mathrm{x}} \times l_{\mathrm{y}} \times l_{\mathrm{z}}$ is defined. For the convenience of description, a number of parameters related to the positions of the transmitter and the receiver are defined. As shown in Figure 3.1 (f), the ceiling, the floor and one of the walls are used as references. z_{s} denotes the distance from the transmitter (ceiling) to the floor plane; z_{r} denotes the distance from the receiver to the floor plane; D_{s} denotes the distance from the transmitter to

the wall plane; D_{r} denotes the distance from the receiver to the wall plane; the transmitter and the receiver have projections on the line where the floor plane and the wall plane intersect, and the distance between these two projection points is denoted as W; considering the projections of the transmitter and the receiver on the floor plane, the distance between these two projection points are denoted as $\hat{W}$. These parameters are also illustrated in Figure 3.1 (f).

3.4.1 Transmitter-to-Wall-to-Receiver Channel Impulse Response

The CIR of TWR can be readily calculated using (3.2) with a series of specified parameters. The configuration of these parameters in (3.2) for TWR category is closely related to the positions of the transmitter and receiver in the defined room. Figure 3.4 shows the TWR geometry associated with a Cartesian Coordinate system. From the geometry shown in this figure, the configuration to (3.2) in the TWR CIR calculation can be found as:

$$h_{\mathrm{twr}}^{[1]}(t) = \hbar_{\left\{m, A_{\mathrm{pd}}, \rho_{\mathrm{w}}, D_{\mathrm{s}}, D_{\mathrm{r}}, L_{\mathrm{b,twr}}, \vec{o}_{\mathrm{s,twr}}, \vec{o}_{\mathrm{r,twr}}\right\}}(t), \tag{3.8}$$

where

$$L_{\mathrm{b,twr}} = \sqrt{W^2 + (z_{\mathrm{s}} - z_{\mathrm{r}})^2}, \tag{3.9}$$

$$\vec{o}_{\mathrm{s,twr}} = \left(\frac{z_{\mathrm{s}} - z_{\mathrm{r}}}{L_{\mathrm{b,twr}}}, \frac{W}{L_{\mathrm{b,twr}}}, 0\right), \tag{3.10}$$

$$\vec{o}_{\mathrm{r,twr}} = \left(-\frac{z_{\mathrm{s}} - z_{\mathrm{r}}}{L_{\mathrm{b,twr}}}, -\frac{W}{L_{\mathrm{b,twr}}}, 0\right). \tag{3.11}$$

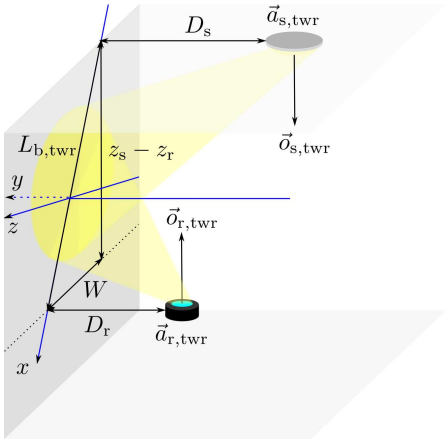

Figure 3.4: *Light propagation geometry in TWR category.*

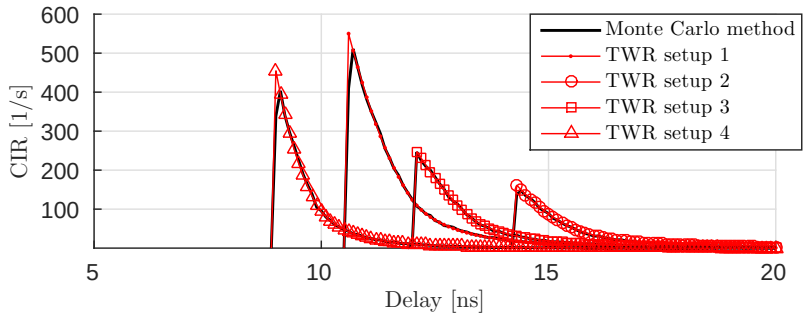

Figure 3.5: *NLoS CIR results with TWR category calculated using* (3.8) *and the Monte Carlo method. The configurations for different setups are listed in Table 3.2.*

Figure 3.5 shows a number of CIRs in TWR category with different setups calculated using (3.8). The corresponding CIR results generated using the Monte Carlo method are also presented in Figure 3.5. The configuration of these setups is listed in Table 3.2. The configuration of the remaining common parameters are listed in Table 3.3. The agreement between the CIR results generated by different methods validates the CIR calculation expression in TWR category (3.8).

Parameter	$\phi_{1/2}$	D_s	D_r	W	z_r
Setup 1	60°	1 m	1 m	1 m	0.75 m
Setup 2	60°	2 m	1.5 m	1 m	0.75 m
Setup 3	60°	1 m	1 m	2 m	0.75 m
Setup 4	40°	1 m	1 m	1 m	1.5 m

Table 3.2: *Setup configuration for the CIR with TWR category.*

Parameter	Symbol	Value
PD area / receiving area	A_pd / A_r	1 cm^2
Wall effective reflectance	ρ_w	0.74
Ceiling effective reflectance	ρ_c	0.38
Floor effective reflectance	ρ_f	0.61
Room height	z_s	3 m
Time delay step	Δt	0.1 ns

Table 3.3: *Default system parameters in the simulation of the NLoS CIR or part of the NLoS CIR.*

3.4.2 Transmitter-to-Floor-to-Ceiling-to-Receiver Channel Impulse Response

In the TFCR channel category, the light undergoes two reflections bounced by an infinite ceiling and an infinite floor, respectively. Therefore, the CIR calculation is decomposed into two parts.

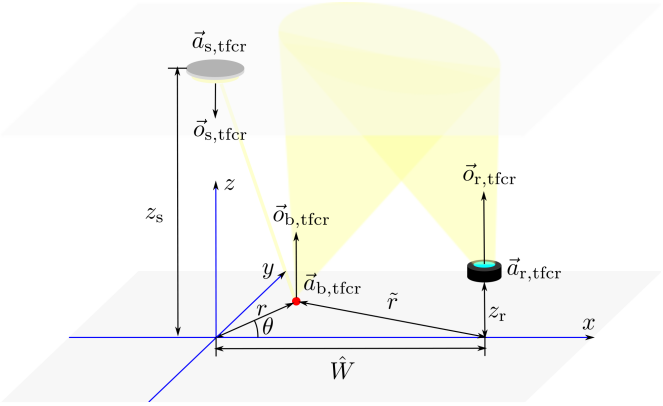

Figure 3.6: *Light propagation geometry in TFCR channel.*

The first part of the CIR is a line-of-sight (LoS) propagation from the transmitter to a point $\vec{a}_{\mathrm{b,tfcr}}$ on the floor as shown in Figure 3.6. The CIR of the first part of the channel is denoted as $h_{\mathrm{t2f}}^{[2]}(t)$. The second part of the channel can be treated as a single reflection link from the point $\vec{a}_{\mathrm{b,tfcr}}$ bounced by the ceiling to the receiver. The corresponding CIR is denoted as $h_{\mathrm{fcr}}^{[2]}(t)$, which can be calculated using the single reflection CIR model. The overall CIR with TFCR category can be obtained by integrating the convolution of $\rho_{\mathrm{f}}\mathrm{d}h_{\mathrm{t2f}}^{[2]}(t)$ and $h_{\mathrm{fcr}}^{[2]}(t)$ over the floor plane as:

$$h_{\mathrm{tfcr}}^{[2]}(t) = \iint_{\mathcal{W}_{\mathrm{f}}} \rho_{\mathrm{f}}\mathrm{d}h_{\mathrm{t2f}}^{[2]}(t) \otimes h_{\mathrm{fcr}}^{[2]}(t), \tag{3.12}$$

where $\otimes$ denotes the convolution operation, and $\mathcal{W}_{\mathrm{f}}$ denotes the area over an infinite floor. For the convenience of converting the 2-D integral into two 1-D integrals, the whole space is defined by a three-dimensional (3-D) Cartesian coordinate system x-y-z and a cylinder coordinate system r-θ-z. Both coordinate systems are shown in Figure 3.6. The origin is defined at the point right below the transmitter on the floor. Thus, in the Cartesian coordinate system, the coordinates of the point $\vec{a}_{\mathrm{b,tfcr}}$ can be defined as $(r\cos\theta, r\sin\theta, 0)$. In conjunction with the source position of $\vec{a}_{\mathrm{s,tfcr}} = (0, 0, z_{\mathrm{s}})$, the CIR calculus of the first part channel can be calculated as [26]:

$$\mathrm{d}h_{\mathrm{t2f}}^{[2]}(t) = \frac{(m+1)z_{\mathrm{s}}^{m+1} r\mathrm{d}r\mathrm{d}\theta}{2\pi\left(r^2+z_{\mathrm{s}}^2\right)^{\frac{m+3}{2}}} \delta\left(t - \frac{\sqrt{r^2+z_{\mathrm{s}}^2}}{c}\right), \tag{3.13}$$

where $\delta(u)$ represents the Dirac delta function. The CIR of the second part of channel can be calculated using (3.2) as:

$$h_{\mathrm{fcr}}^{[2]}(t) = h_{\left\{1, A_{\mathrm{pd}}, \rho_{\mathrm{c}}, z_{\mathrm{s}}, z_{\mathrm{s}}-z_{\mathrm{r}}, \tilde{r}, \vec{o}_{\mathrm{b,tfcr}}, \vec{o}_{\mathrm{r,tfcr}}\right\}}(t), \tag{3.14}$$

where the floor has a mode number $m = 1$; ρ_{c} denotes the reflectance of the ceiling; both the orientations of the floor and the receiver are upward towards the ceiling $\vec{o}_{\mathrm{b,tfcr}} = \vec{o}_{\mathrm{r,tfcr}} = (0, 0, 1)$; and $\tilde{r}$ can be calculated using the law of Cosine as:

$$\tilde{r} = \sqrt{r^2 + \hat{W}^2 - 2r\hat{W}\cos\theta}. \tag{3.15}$$

In order to reduce the computational complexity of the CIR calculation, the following approximation to $h^{[2]}_{\mathrm{fcr}}(t)$ is used to eliminate the unsolvable integral in (3.14).

$$h^{[2]}_{\mathrm{fcr}}(t) \approx \frac{2^7 A_{\mathrm{pd}} \rho_{\mathrm{c}} z_{\mathrm{s}}^2 \left(z_{\mathrm{s}} - z_{\mathrm{r}}\right)^2 \mathcal{F}_{\mathrm{fcr}} \mathcal{U}\left(t - \frac{\sqrt{(2z_{\mathrm{s}} - z_{\mathrm{r}})^2 + \tilde{r}^2}}{c}\right)}{\pi c^6 t^7 \left(1 - \frac{z_{\mathrm{r}}^2 (2z_{\mathrm{s}} - z_{\mathrm{r}})^2}{c^4 t^4}\right)^3}, \tag{3.16}$$

where the scaling function $\mathcal{F}_{\mathrm{fcr}}$ is defined as:

$$\mathcal{F}_{\mathrm{fcr}} = \left(\frac{0.107 z_{\mathrm{s}}}{z_{\mathrm{s}} - z_{\mathrm{r}}} + 0.02179\right) \frac{\tilde{r}^2}{z_{\mathrm{s}}^2} + 1. \tag{3.17}$$

The derivation of (3.16) and its accuracy are presented in Appendix B. Next, (3.13) and (3.16) can be inserted into (3.12), and the 2-D integral in (3.12) can be converted into two 1-D integrals as:

$$\begin{aligned} h^{[2]}_{\mathrm{tfcr}}(t) &= \int_{-\pi}^{\pi} \int_{0}^{\infty} h^{[2]}_{\mathrm{fcr}}\left(t - \frac{\sqrt{r^2 + z_{\mathrm{s}}^2}}{c}\right) \frac{\rho_{\mathrm{f}}(m+1) z_{\mathrm{s}}^{m+1} r \mathrm{d}r \mathrm{d}\theta}{2\pi \left(\sqrt{r^2 + z_{\mathrm{s}}^2}\right)^{m+3}} \\ &= \int_{0}^{\infty} \int_{-\pi}^{\pi} \frac{2^6 A_{\mathrm{pd}} c \rho_{\mathrm{f}} \rho_{\mathrm{c}} (m+1) z_{\mathrm{s}}^{m+3} \left(z_{\mathrm{s}} - z_{\mathrm{r}}\right)^2 r \mathcal{F}_{\mathrm{fcr}} \mathcal{U}\left(t - \frac{D_{\mathrm{tfcr}}}{c}\right)}{\pi^2 \left(\sqrt{r^2 + z_{\mathrm{s}}^2}\right)^{m+3} \left(ct - \sqrt{r^2 + z_{\mathrm{s}}^2}\right)^7 \left(1 - \frac{z_{\mathrm{r}}^2 (2z_{\mathrm{s}} - z_{\mathrm{r}})^2}{\left(ct - \sqrt{r^2 + z_{\mathrm{s}}^2}\right)^4}\right)^3} \mathrm{d}\theta \mathrm{d}r, \end{aligned} \tag{3.18}$$

where the term D_{tfcr} denotes the shortest propagation path via point $\vec{a}_{\mathrm{b,tfcr}}$ in the TFCR channel. Its value can be calculated as:

$$D_{\mathrm{tfcr}} = \sqrt{r^2 + z_{\mathrm{s}}^2} + \sqrt{\left(2z_{\mathrm{s}} - z_{\mathrm{r}}\right)^2 + r^2 + \hat{W}^2 - 2r\hat{W}\cos\theta}. \tag{3.19}$$

The term with unit step function in (3.18) indicates that a non-zero value of $h_{\text{tfcr}}^{[2]}(t)$ requires $ct \geq D_{\text{tfcr}}$, which can be expanded as:

$$\left(c^2t^2 - \hat{W}^2\cos^2\theta\right)r^2 - \left(c^2t^2 - \hat{W}^2 - (2z_\text{s} - z_\text{r})^2 + z_\text{s}^2\right)\hat{W}\cos\theta r + c^2t^2z_\text{s}^2 - \frac{1}{4}\left(c^2t^2 - \hat{W}^2 - (2z_\text{s} - z_\text{r})^2 + z_\text{s}^2\right)^2 \leq 0. \tag{3.20}$$

With the satisfaction of (3.20), the integration range in (3.18) should be changed to a limited region, and the unit step function in (3.18) can be modified to be $\mathcal{U}\left(t - D_{0,\text{tfcr}}/c\right)$, where $D_{0,\text{tfcr}} = \sqrt{(3z_\text{s} - z_\text{r})^2 + \hat{W}^2}$. Thus, (3.18) can be further modified as:

$$h_{\text{tfcr}}^{[2]}(t) = \int_{\mathfrak{r}_1}^{\mathfrak{r}_2}\int_0^{\vartheta} \frac{2^7 cA_\text{pd}\rho_\text{f}\rho_\text{c}(m+1)z_\text{s}^{m+3}\left(z_\text{s} - z_\text{r}\right)^2 r\mathcal{F}_\text{fcr}\mathcal{U}\left(t - \frac{D_{0,\text{tfcr}}}{c}\right)\mathrm{d}\theta\mathrm{d}r}{\pi^2\left(\sqrt{r^2+z_\text{s}^2}\right)^{m+3}\left(ct - \sqrt{r^2+z_\text{s}^2}\right)^7\left(1 - \frac{z_\text{r}^2(2z_\text{s}-z_\text{r})^2}{\left(ct-\sqrt{r^2+z_\text{s}^2}\right)^4}\right)^3}. \tag{3.21}$$

Note that in the modification (3.21), the expression is multiplied by a factor of 2, and the lower limit of the integral with θ is change to 0. This is because expression (3.18) is reflection symmetric respect to the x-axis. The integration limits $\mathfrak{r}_1$ and $\mathfrak{r}_2$ in (3.21) can be calculated by solving the inequality (3.20) with r as the unknown variable. The solution of $\mathfrak{r}_1$ and $\mathfrak{r}_2$ are found as:

$$\mathfrak{r}_2 = \frac{\hat{W}\left(c^2t^2 - \mathfrak{c}_{\text{tfcr},1}^2\right) + ct\mathfrak{c}_{\text{tfcr},2}}{2\left(c^2t^2 - \hat{W}^2\right)}, \tag{3.22}$$

$$\mathfrak{r}_1 = \Re\left(\frac{\hat{W}\left(c^2t^2 - \mathfrak{c}_{\text{tfcr},1}^2\right) - ct\mathfrak{c}_{\text{tfcr},2}}{2\left(c^2t^2 - \hat{W}^2\right)}\right), \tag{3.23}$$

where $\mathfrak{c}_{\text{tfcr},1}^2 = \hat{W}^2 + (2z_\text{s} - z_\text{r})^2 - z_\text{s}^2$ and $\mathfrak{c}_{\text{tfcr},2}^2 = \left(c^2t^2 - \mathfrak{c}_{\text{tfcr},1}^2\right)^2 - 4z_\text{s}^2\left(c^2t^2 - \hat{W}^2\right)$. To ensure the existence of real values of $\mathfrak{r}_1$ and $\mathfrak{r}_2$, the term $\mathfrak{c}_{\text{tfcr},2}^2$ have to be greater than zero, which leads to the solution of the limit ϑ as:

$$\vartheta = \begin{cases} \arccos\left(\frac{2ct\sqrt{r^2+z_\text{s}^2} - c^2t^2 + \mathfrak{c}_{\text{tfcr},1}^2}{2r\hat{W}}\right) & : r \geq \frac{ct\mathfrak{c}_{\text{tfcr},2} - \hat{W}\left(c^2t^2 - \mathfrak{c}_{\text{tfcr},1}^2\right)}{2\left(c^2t^2 - \hat{W}^2\right)} \\ \pi & : r < \frac{ct\mathfrak{c}_{\text{tfcr},2} - \hat{W}\left(c^2t^2 - \mathfrak{c}_{\text{tfcr},1}^2\right)}{2\left(c^2t^2 - \hat{W}^2\right)} \end{cases}, \tag{3.24}$$

A further simplification to (3.21) can be carried out by solving the integral respect to θ. Therefore, the final CIR expression for the TFCR category can be written in a form with a 1-D integral

as:

$$h_{\mathrm{tfcr}}^{[2]}(t)=\int_{\mathfrak{r}_1}^{\mathfrak{r}_2}\frac{\left(\left(\frac{0.107z_{\mathrm{s}}}{z_{\mathrm{s}}-z_{\mathrm{r}}}+0.02179\right)\left(r^2+\hat{W}^2-\frac{2r\hat{W}\sin\vartheta}{\vartheta}\right)+z_{\mathrm{s}}^2\right)\mathcal{U}\left(t-\frac{D_{0,\mathrm{tfcr}}}{c}\right)r\mathrm{d}r}{\frac{\pi^2\left(\sqrt{r^2+z_{\mathrm{s}}^2}\right)^{m+3}\left(ct-\sqrt{r^2+z_{\mathrm{s}}^2}\right)^7}{2^7cA_{\mathrm{pd}}\rho_{\mathrm{f}}\rho_{\mathrm{c}}(m+1)(z_{\mathrm{s}}-z_{\mathrm{r}})^2z_{\mathrm{s}}^{m+1}\vartheta}\left(1-\frac{z_{\mathrm{r}}^2(2z_{\mathrm{s}}-z_{\mathrm{r}})^2}{\left(ct-\sqrt{r^2+z_{\mathrm{s}}^2}\right)^4}\right)^3}. \tag{3.25}$$

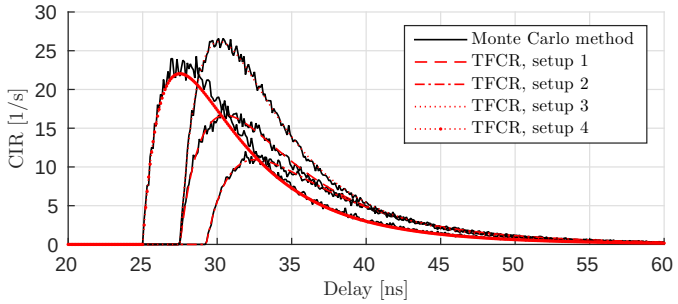

Figure 3.7: *NLoS CIR results with TFCR category calculated using* (3.25) *and the Monte Carlo method. The configurations for different setups are listed in Table 3.4.*

Figure 3.7 shows a number of CIRs in TFCR category with different setups calculated using (3.25). In addition, the corresponding CIR results generated using the Monte Carlo method are also presented in Figure 3.7. The configuration of these setups are listed in Table 3.4. The configuration of the remaining common parameters are listed in Table 3.3. The agreement between the CIR results generated by different methods validate the CIR calculation expression in TFCR category (3.25).

Parameter	$\phi_{1/2}$	$\hat{W}$	z_{r}
Setup 1	60°	0 m	0.75 m
Setup 2	60°	3 m	0.75 m
Setup 3	40°	0 m	0.75 m
Setup 4	60°	0 m	1.5 m

Table 3.4: *Setup configuration for the CIR with TFCR category.*

3.4.3 Transmitter-to-Wall-to-Ceiling-to-Receiver Channel Impulse Response

In the TWCR category, a half infinite ceiling and a half infinite wall are considered as shown in Figure 3.8. The bound of the ceiling and wall planes is the line of their intersection, and these two planes extend infinitely to any other directions. Similar to the case in TFCR category, the

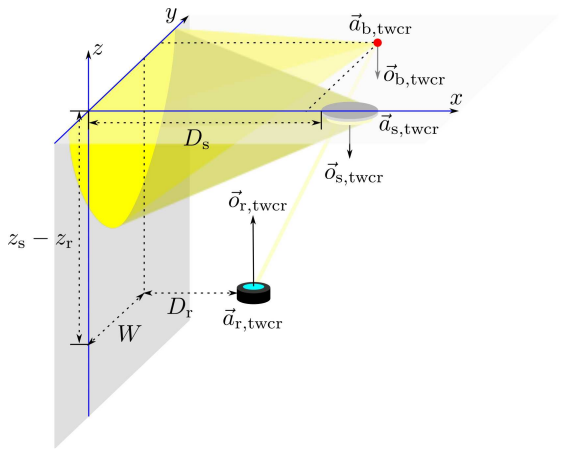

Figure 3.8: *Light propagation geometry in TWCR channel.*

TWCR channel is divided into two parts. The first part of the channel is from the transmitter reflected by the wall to a point $\vec{a}_{\mathrm{b,twcr}}$ on the ceiling. The corresponding CIR is denoted as $h^{[2]}_{\mathrm{twc}}(t)$, which can be calculated using the single reflection CIR expression (3.2). The second part of the channel is a LoS propagation from the ceiling point $\vec{a}_{\mathrm{b,twcr}}$ to the receiver which is denoted as $h^{[2]}_{\mathrm{c2r}}(t)$. The overall TWCR CIR can be obtained by integrating the convolution of $\rho_{\mathrm{c}}\mathrm{d}h^{[2]}_{\mathrm{twc}}(t)$ and $h^{[2]}_{\mathrm{c2r}}(t)$ over the ceiling plane as:

$$h^{[2]}_{\mathrm{twcr}}(t) = \iint_{\mathcal{W}_{\mathrm{c}}} \rho_{\mathrm{c}}\mathrm{d}h^{[2]}_{\mathrm{twc}}(t) \otimes h^{[2]}_{\mathrm{c2r}}(t), \tag{3.26}$$

where $\mathcal{W}_{\mathrm{c}}$ denotes the entire area of the ceiling plane. Similar to the case of TFCR category, a 3-D Cartesian coordinate system x-y-z used to define the space as shown in Figure 3.8. The origin is defined at the projection point of the transmitter on the wall plane. Thus, in the Cartesian coordinate system, the coordinates of the ceiling point $\vec{a}_{\mathrm{b,twcr}}$ can be written as $(x, y, 0)$. In conjunction with the source position of $\vec{a}_{\mathrm{s,twcr}} = (D_{\mathrm{s}}, 0, 0)$ and the wall plane $x = 0$, the CIR calculus of the first part channel can be calculated using (3.2) as:

$$\mathrm{d}h^{[2]}_{\mathrm{twc}}(t) = \hbar_{\left\{m,\mathrm{d}A,\rho_{\mathrm{w}},D_{\mathrm{s}},x,|y|,\vec{o}^{\star}_{\mathrm{s,twcr}},\vec{o}^{\star}_{\mathrm{b,twcr}}\right\}}(t)\,, \tag{3.27}$$

where ρ_{w} denotes the reflectance of the wall. Note that the orientation vectors $\vec{o}^{\star}_{\mathrm{s,twcr}} = \vec{o}^{\star}_{\mathrm{b,twcr}} = (0, 1, 0)$ are based on the Cartesian coordinate system defined in Appendix A. They are converted from $\vec{o}_{\mathrm{s,twcr}} = \vec{o}_{\mathrm{b,twcr}} = (0, 0, -1)$ which are based on the Cartesian coordinate system defined in Figure 3.8. Similar to the case in TFCR channel, an approximation to $\mathrm{d}h^{[2]}_{\mathrm{twc}}(t)$ is used to reduce the computational complexity. The approximated expression is given

as:

$$\mathrm{d}h_{\mathrm{twc}}^{[2]}(t) \approx \frac{\rho_{\mathrm{w}}(m+1)\hat{D}_{\mathrm{s}}\hat{x}\mathcal{B}\left(\frac{m+2}{2},\frac{m+2}{2}\right)2^{m}\mathfrak{r}_{\mathrm{twc}}^{2}(t)\mathcal{F}_{\mathrm{twc}}\mathcal{U}\left(t-\frac{D_{0,\mathrm{twc}}}{c}\right)\mathrm{d}A}{\pi^{2}t\left(1+\frac{\hat{D}_{\mathrm{s}}^{2}}{\mathfrak{r}_{\mathrm{twc}}^{2}(t)}\right)^{\frac{m-1}{2}}\left(\frac{c^{2}t^{2}}{4}-\frac{\left(\hat{D}_{\mathrm{s}}^{2}-\hat{x}^{2}\right)^{2}}{4c^{2}t^{2}}\right)^{3}}, \tag{3.28}$$

where $\mathcal{B}(u_1,u_2)$ is the β-function that is defined as: $\mathcal{B}(u_1,u_2)=\int_0^1 v^{u_1-1}(1-v)^{u_2-1}\mathrm{d}v$; $\hat{D}_{\mathrm{s}}$ denotes the modified distance from the transmitter to the wall surface; $\hat{x}$ denotes the modified distance from the $\vec{a}_{\mathrm{b,twcr}}$ to the wall surface; the shortest propagation distance from the transmitter via the wall plane to $\vec{a}_{\mathrm{b,twcr}}$ is denoted as $D_{0,\mathrm{twc}}=\sqrt{(D_{\mathrm{s}}+x)^2+y^2}$; and

$$\mathfrak{r}_{\mathrm{twc}}^{2}(t)=\frac{c^{2}t^{2}}{4}+\frac{\left(\hat{D}_{\mathrm{s}}^{2}-\hat{x}^{2}\right)^{2}}{4c^{2}t^{2}}-\frac{\hat{D}_{\mathrm{s}}^{2}+\hat{x}^{2}}{2}. \tag{3.29}$$

In (3.28) and (3.29), the modified distances $\hat{D}_{\mathrm{s}}$ and $\hat{x}$ can be calculated as:

$$\hat{D}_{\mathrm{s}}=\frac{D_{\mathrm{s}}D_{0,\mathrm{twc}}}{\sqrt{(D_{\mathrm{s}}+x)^2+4y^2\left(m^{0.045}-1\right)}}, \tag{3.30}$$

$$\hat{x}=D_{0,\mathrm{twc}}\left(1-\frac{D_{\mathrm{s}}}{\sqrt{(D_{\mathrm{s}}+x)^2+4y^2\left(m^{0.045}-1\right)}}\right). \tag{3.31}$$

In the approximated CIR (3.28), the scaling factor $\mathcal{F}_{\mathrm{twc}}$ can be calculated as:

$$\mathcal{F}_{\mathrm{twc}}=\frac{x+\beta_{\mathrm{twc}}D_{\mathrm{s}}}{\sqrt{(x+\beta_{\mathrm{twc}}D_{\mathrm{s}})^2+y^2+0.8125\frac{y^3|x-D_{\mathrm{s}}|^3}{(x+D_{\mathrm{s}})^4}}}, \tag{3.32}$$

where $\beta_{\mathrm{twc}}=0.8088\exp(-0.6878m)+0.5304\exp(-0.007006m)$. The derivation of (3.28) and the evaluation of its accuracy is presented in Appendix C. The second part of the TWCR CIR $h_{\mathrm{c2r}}^{[2]}(t)$ can be calculated as:

$$h_{\mathrm{c2r}}^{[2]}(t)=\frac{A_{\mathrm{pd}}\left(z_{\mathrm{s}}-z_{\mathrm{r}}\right)^{2}}{\pi D_{\mathrm{c2r}}^{4}}\delta\left(t-\frac{D_{\mathrm{c2r}}}{c}\right), \tag{3.33}$$

where the propagation distance from point $\vec{a}_{\mathrm{b,twcr}}$ to the receiver D_{c2r} is calculated as:

$$D_{\mathrm{c2r}}=\sqrt{(z_{\mathrm{s}}-z_{\mathrm{r}})^2+(x-D_{\mathrm{r}})^2+(y-W)^2}. \tag{3.34}$$

Thus, by inserting (3.28) and (3.33) into (3.26), the overall TWCR CIR can be calculated as:

$$\begin{aligned} h_{\mathrm{twcr}}^{[2]}(t) &= \int_{-\infty}^{\infty}\int_{0}^{\infty} \frac{\rho_{\mathrm{c}} A_{\mathrm{pd}} \left(z_{\mathrm{s}}-z_{\mathrm{r}}\right)^2}{\pi D_{\mathrm{c2r}}^4} \mathrm{d}h_{\mathrm{twc}}^{[2]}\left(t-\frac{D_{\mathrm{c2r}}}{c}\right) \\ &= \int_{-\infty}^{\infty}\int_{0}^{\infty} \frac{\rho_{\mathrm{w}}\rho_{\mathrm{c}} A_{\mathrm{pd}} \hat{D}_{\mathrm{s}} \hat{x} \mathcal{B}\left(\frac{m+2}{2}, \frac{m+2}{2}\right) \mathfrak{r}_{\mathrm{twc}}^2\left(t-\frac{D_{\mathrm{c2r}}}{c}\right) \mathcal{F}_{\mathrm{twc}} \mathcal{U}\left(t-\frac{D_{0,\mathrm{twc}}+D_{\mathrm{c2r}}}{c}\right) \mathrm{d}x\mathrm{d}y}{\frac{\pi^3 D_{\mathrm{c2r}}^4\left(t-\frac{D_{\mathrm{c2r}}}{c}\right)}{2^m(m+1)\left(z_{\mathrm{s}}-z_{\mathrm{r}}\right)^2}\left(1+\frac{\hat{D}_{\mathrm{s}}^2}{\mathfrak{r}_{\mathrm{twc}}^2\left(t-\frac{D_{\mathrm{c2r}}}{c}\right)}\right)^{\frac{m-1}{2}}\left(\frac{\left(ct-D_{\mathrm{c2r}}\right)^2}{4}-\frac{\left(\hat{D}_{\mathrm{s}}^2-\hat{x}^2\right)^2}{4\left(ct-D_{\mathrm{c2r}}\right)^2}\right)^3}, \end{aligned} \tag{3.35}$$

where the unit step function indicates that a non-zero value of $h_{\mathrm{twcr}}^{[2]}(t)$ requires $ct \geq D_{0,\mathrm{twc}} + D_{\mathrm{c2r}}$, which can be expanded as:

$$\begin{aligned} &\left(c^2t^2-W^2\right)y^2 - W\left(c^2t^2+2\left(D_{\mathrm{s}}+D_{\mathrm{r}}\right)x-\left(z_{\mathrm{s}}-z_{\mathrm{r}}\right)^2-W^2-D_{\mathrm{r}}^2+D_{\mathrm{s}}^2\right)y \\ &+c^2t^2\left(D_{\mathrm{s}}+x\right)^2-\frac{1}{4}\left(c^2t^2+2\left(D_{\mathrm{s}}+D_{\mathrm{r}}\right)x-\left(z_{\mathrm{s}}-z_{\mathrm{r}}\right)^2-W^2-D_{\mathrm{r}}^2+D_{\mathrm{s}}^2\right)^2 \geq 0. \end{aligned} \tag{3.36}$$

With the satisfaction of (3.36), the integration range in (3.35) should be changed to a limited region, and the term with unit step function in (3.35) can be modified as $\mathcal{U}\left(t-\frac{D_{0,\mathrm{twcr}}}{c}\right)$, where $D_{0,\mathrm{twcr}} = \sqrt{W^2+\left(D_{\mathrm{s}}+\sqrt{\left(z_{\mathrm{s}}-z_{\mathrm{r}}\right)^2+D_{\mathrm{r}}^2}\right)^2}$ denotes the shortest propagation path in the TWCR channel. Thus, (3.35) can be further modified as:

$$h_{\mathrm{twcr}}^{[2]}(t) = \int_{\mathfrak{y}_1}^{\mathfrak{y}_2}\int_{0}^{\mathfrak{x}} \frac{\rho_{\mathrm{w}}\rho_{\mathrm{c}} A_{\mathrm{pd}} \hat{D}_{\mathrm{s}} \hat{x} \mathcal{B}\left(\frac{m+2}{2}, \frac{m+2}{2}\right) \mathfrak{r}_{\mathrm{twc}}^2\left(t-\frac{D_{\mathrm{c2r}}}{c}\right) \mathcal{F}_{\mathrm{twc}} \mathcal{U}\left(t-\frac{D_{0,\mathrm{twcr}}}{c}\right) \mathrm{d}x\mathrm{d}y}{\frac{\pi^3 D_{\mathrm{c2r}}^4\left(t-\frac{D_{\mathrm{c2r}}}{c}\right)}{2^m(m+1)\left(z_{\mathrm{s}}-z_{\mathrm{r}}\right)^2}\left(1+\frac{\hat{D}_{\mathrm{s}}^2}{\mathfrak{r}_{\mathrm{twc}}^2\left(t-\frac{D_{\mathrm{c2r}}}{c}\right)}\right)^{\frac{m-1}{2}}\left(\frac{\left(ct-D_{\mathrm{c2r}}\right)^2}{4}-\frac{\left(\hat{D}_{\mathrm{s}}^2-\hat{x}^2\right)^2}{4\left(ct-D_{\mathrm{c2r}}\right)^2}\right)^3}. \tag{3.37}$$

The integration limits $\mathfrak{y}_1$ and $\mathfrak{y}_2$ in (3.37) can be calculated by solving the inequality (3.36) with y as the unknown variable. The solutions of $\mathfrak{y}_1$ and $\mathfrak{y}_2$ can be found as:

$$\mathfrak{y}_2 = \frac{W\left(c^2t^2-\mathfrak{c}_{\mathrm{twcr},1}^2+2\left(D_{\mathrm{s}}+D_{\mathrm{r}}\right)x\right)+ct\mathfrak{c}_{\mathrm{twcr},2}}{2\left(c^2t^2-W^2\right)}, \tag{3.38}$$

$$\mathfrak{y}_1 = \frac{W\left(c^2t^2-\mathfrak{c}_{\mathrm{twcr},1}^2+2\left(D_{\mathrm{s}}+D_{\mathrm{r}}\right)x\right)-ct\mathfrak{c}_{\mathrm{twcr},2}}{2\left(c^2t^2-W^2\right)}, \tag{3.39}$$

where $\mathfrak{c}_{\mathrm{twcr},1}^2 = \left(z_{\mathrm{s}}-z_{\mathrm{r}}\right)^2+W^2+D_{\mathrm{r}}^2-D_{\mathrm{s}}^2$ and $\mathfrak{c}_{\mathrm{twcr},2}^2 = \left(c^2t^2-\mathfrak{c}_{\mathrm{twcr},1}^2+2\left(D_{\mathrm{s}}+D_{\mathrm{r}}\right)x\right)^2 - 4\left(c^2t^2-W^2\right)\left(D_{\mathrm{s}}+x\right)^2$. To ensure the existence of the real-value solution to $\mathfrak{y}_1$ and $\mathfrak{y}_2$, the

term $\mathfrak{c}^2_{\mathrm{twcr},2}$ have to be greater than zero, which leads to the solution to the integration limit $\mathfrak{x}$:

$$\mathfrak{x} = \frac{\left(\sqrt{c^2t^2 - W^2} - D_{\mathrm{s}}\right)^2 - (z_{\mathrm{s}} - z_{\mathrm{r}})^2 - D_{\mathrm{r}}^2}{2\left(\sqrt{c^2t^2 - W^2} - D_{\mathrm{s}} - D_{\mathrm{r}}\right)}. \tag{3.40}$$

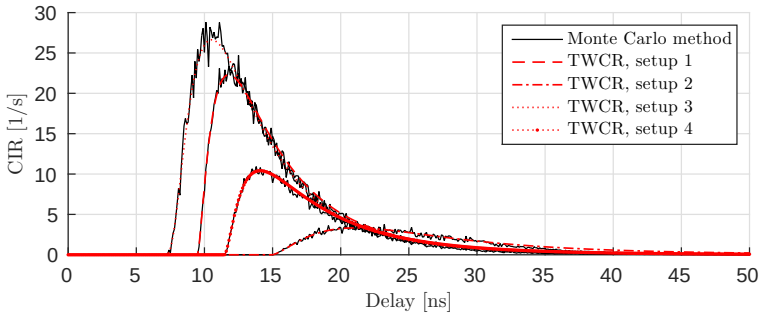

Figure 3.9: *NLoS CIR results with TWCR category calculated using* (3.37) *and the Monte Carlo method. The configurations for different setups are listed in Table 3.4..*

Figure 3.9 shows a number of CIRs in TFCR category with different setups calculated using (3.37). In addition, the corresponding CIR results generated using the Monte Carlo method are also presented in Figure 3.9. The configuration of these setups are listed in Table 3.5. The configuration of the remaining common parameters are listed in Table 3.3. The agreement between the CIR results generated by different methods validate the CIR calculation expression in TWCR category (3.37).

Parameter	$\phi_{1/2}$	D_{s}	D_{r}	W	z_{r}
Setup 1	60°	0.5 m	0.5 m	0.5 m	0.75 m
Setup 2	60°	2 m	1 m	0.5 m	0.75 m
Setup 3	40°	0.5 m	0.5 m	0.5 m	1.5 m
Setup 4	60°	0.5 m	0.5 m	2 m	0.75 m

Table 3.5: *Setup configuration for the CIR with TWCR category.*

3.5 Overall Non-line-of-sight Channel Impulse Response

In conjunction with analytical results for component CIRs in different light propagation categories, the overall CIR can be accurately approximated. Firstly, the geometric parameters with respect to each wall, such as D_{s}, D_{r}, W, $\hat{W}$, should be calculated as what follows. The defined cuboid room with a size of $l_{\mathrm{x}} \times l_{\mathrm{y}} \times l_{\mathrm{z}}$ is shown in Figure 3.10. The space in the room is defined

by a 3-D Cartesian coordinate system. The transmitter location is defined at $\vec{a}_{\mathrm{s}} = (\hat{x}_{\mathrm{s}}, \hat{y}_{\mathrm{s}}, \hat{z}_{\mathrm{s}})$ and the receiver location is defined at $\vec{a}_{\mathrm{r}} = (\hat{x}_{\mathrm{r}}, \hat{y}_{\mathrm{r}}, \hat{z}_{\mathrm{r}})$. Each wall is marked with a number $n = 1, 2, 3, 4$. The case with $n = 1$ and $n = 2$ correspond to the wall with $y = 0$ and $y = l_{\mathrm{y}}$, respectively. The case with $n = 3$ and $n = 4$ correspond to the wall with $x = 0$ and $x = l_{\mathrm{x}}$, respectively. Thus, the calculation of the geometric parameters can be found as the expressions listed in Table 3.6. Then, the overall NLoS CIR can be calculated as:

$$h_{\mathrm{NLoS}}(t) \approx \sum_{n=1}^{4} h_{\mathrm{twr}}^{[1],\{D_{\mathrm{s},n}, D_{\mathrm{r},n}, W_n\}}(t) + \sum_{n=1}^{4} h_{\mathrm{twcr}}^{[2],\{D_{\mathrm{s},n}, D_{\mathrm{r},n}, W_n\}}(t) + h_{\mathrm{tfcr}}^{[2],\{\hat{W}\}}(t), \tag{3.41}$$

where $h_{\mathrm{twr}}^{[1],\{D_{\mathrm{s},n}, D_{\mathrm{r},n}, W_n\}}(t)$, $h_{\mathrm{twcr}}^{[2],\{D_{\mathrm{s},n}, D_{\mathrm{r},n}, W_n\}}(t)$ and $h_{\mathrm{tfcr}}^{[2],\{\hat{W}\}}(t)$ can be calculated using (3.8), (3.25) and (3.37), respectively.

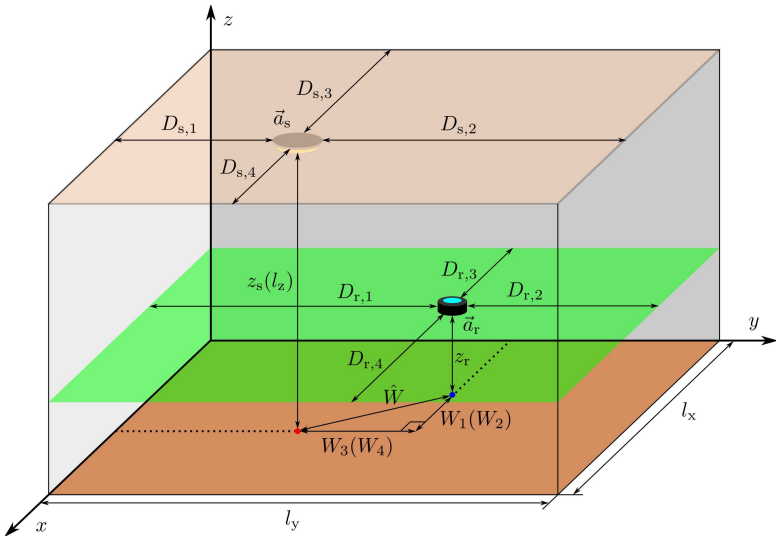

Figure 3.10: *A cuboid room of size $l_{\mathrm{x}} \times l_{\mathrm{y}} \times l_{\mathrm{z}}$ with transmitter and receiver location of $\vec{a}_{\mathrm{s}}$ and $\vec{a}_{\mathrm{r}}$, respectively.*

n	$D_{\mathrm{s},n}$	$D_{\mathrm{r},n}$	W_n	$\hat{W}$
1	$\hat{y}_{\mathrm{s}}$	$\hat{y}_{\mathrm{r}}$	$\lvert\hat{x}_{\mathrm{s}} - \hat{x}_{\mathrm{r}}\rvert$	$\sqrt{(\hat{x}_{\mathrm{s}} - \hat{x}_{\mathrm{r}})^2 + (\hat{y}_{\mathrm{s}} - \hat{y}_{\mathrm{r}})^2}$
2	$l_{\mathrm{y}} - \hat{y}_{\mathrm{s}}$	$l_{\mathrm{y}} - \hat{y}_{\mathrm{r}}$		
3	$\hat{x}_{\mathrm{s}}$	$\hat{x}_{\mathrm{r}}$	$\lvert\hat{y}_{\mathrm{s}} - \hat{y}_{\mathrm{r}}\rvert$	
4	$l_{\mathrm{x}} - \hat{x}_{\mathrm{s}}$	$l_{\mathrm{x}} - \hat{x}_{\mathrm{r}}$		

Table 3.6: *Expressions for the geometric parameters in the proposed NLoS CIR calculation method.*

3.5.1 Calculation Accuracy Evaluation

Figure 3.11 shows the NLoS CIR results based on (3.41) in comparison to the results of using Monte Carlo method. The setups of the analytical calculations and corresponding simulations are listed in Table 3.7. In Setup 1 and setup 2, a small square room and a longer rectangular

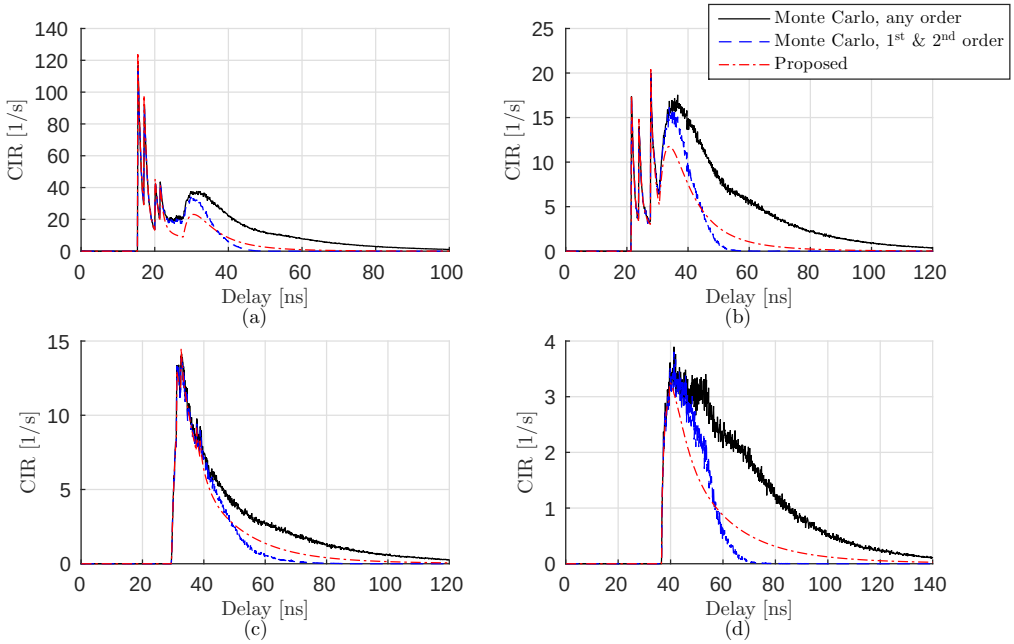

Figure 3.11: *NLoS CIR results with different configurations. The sub-plot (a), (b), (c) and (d) correspond to the link setup 1, 2, 3 and 4, respectively. In addition to the results generated using the proposed method, those generated using the Monte Carlo method considering all reflections and considering* 1^{st} *and* 2^{nd} *order reflections are also presented.*

room are considered, respectively. In setup 3 and setup 4, a much larger room is considered with various transmitter / receiver positions. In setup 1, the transmitter and the receiver are close to each other, and due to the small size of the room, the link is close to the walls. Consequently, the overall magnitude of the NLoS CIR is relatively higher, and the responses due to 1^{st} order reflections dominate the NLoS CIR, especially for the response with short delays. In setup 2, the increased indoor space and the increased transmitter receiver separation leads to a NLoS CIR with a decreased magnitude. In setup 3 and setup 4, the considered transmitter / receiver positions are further away from the walls. As expected, the magnitude of the CIRs due to 1^{st} order reflections decreases significantly. Compared to the case of setup 3, the distance between the transmitter and the receiver in setup 4 is longer, and the beam width of the transmitter is

narrower. Therefore, the resulting NLoS CIR has a very low response magnitude.

The accuracy of the approximation using the proposed method varies with the time delay. For the responses with short delays (roughly the first 10 ns), the proposed method offers excellent accuracy. For the responses with medium delay (roughly another 10 ns after the short delay), the proposed method underestimate the CIR due to the omission of the response caused by part of the 2^{nd} reflections with TWWR, TFWR categories and higher order reflections. For the responses with long delay, the proposed method over-estimate the CIR compared to the results generated using the Monte Carlo method considering the 1^{st} and 2^{nd} order reflections. This is because the proposed CIR calculation method with each propagation category omits the effects of the boundary of the surfaces, which introduces extra responses with long delay. However, this over-estimation is lower than the responses caused by higher order reflections. In another point of view, it slightly compensates the omission of the higher order reflections.

Parameters	Room size	Transmitter coordinate	Receiver coordinate	Half-power semi-angle
Setup 1	5 m $\times$ 5 m $\times$ 3 m	$(2.5, 2.5, 3)$	$(2\ 1.5\ 0.75)$	60°
Setup 2	5 m $\times$ 8 m $\times$ 3 m	$(2, 2, 3)$	$(2.5, 6, 0.75)$	60°
Setup 3	10 m $\times$ 10 m $\times$ 3 m	$(4, 4, 3)$	$(5, 7, 0.75)$	60°
Setup 4	10 m $\times$ 10 m $\times$ 3 m	$(2, 3, 3)$	$(8, 7, 0.75)$	40°

Table 3.7: *Link configurations correspond to the NLoS CIR results shown in Figure 3.11.*

Figure 3.12 shows the corresponding magnitude response of the NLoS channels. It can be observed that with the presence of LoS path between the transmitter and the receiver, the accuracy of the approximation using the proposed method varies with frequency. For the magnitude response with extremely low frequency (< 5 MHz), the proposed method underestimate the response relative to the case with the Monte Carlo method considering any order of reflections, but roughly the same as the case with the Monte Carlo method considering the 1^{st} and 2^{nd} order reflections. For the magnitude response with low frequency (5– 50 MHz), the trend of the three curves is similar with a slight mismatch. For the magnitude response with high frequency (> 50 MHz), the three curves are virtually identical.

3.5.2 Computational Time Evaluation

The calculation of (3.8), (3.25) and (3.37) requires solving only one or two 1-D numerical integrals. Therefore, the computational complexity of (3.41) is quite modest. In this section,

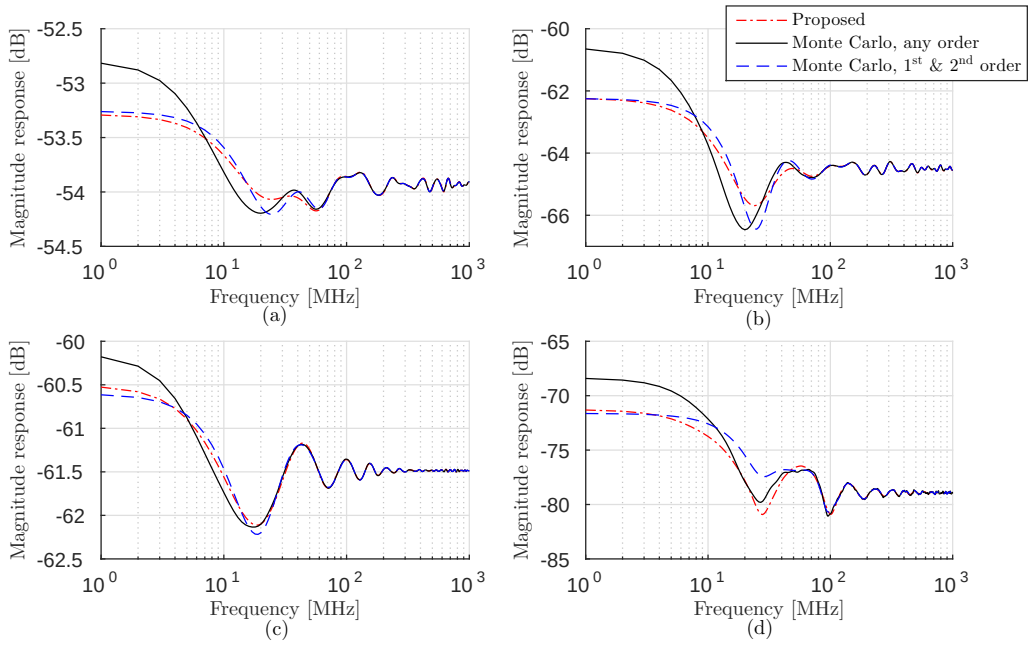

Figure 3.12: *NLoS magnitude response results correspond to the four setups shown in Figure 3.11.*

the computation time of the proposed method is evaluated compared with that of the state-of-the-art methods. In this study, the numerical integrations in (3.41) are implemented based on the Trapezoidal rule, and the interval for each definite integral is divided into N bins. The more number of the bins, the more accurate the calculated result. Since θ is the variable in the integral (3.8), the number of bins in the integral (3.8) is defined as N_θ. Similarly, the numbers of bins in the calculation of (3.25) and (3.37) are defined as N_r and N_x (N_y), respectively. It has been empirically identified that $N_\theta = 50$, $N_r = 50$ and $N_x = N_y = 30$ offer reasonably accurate NLoS CIR results with short computation time.

The impulse response of a channel is in a form of a continuous signal. In the actual CIR calculation, the result with a fixed time resolution is produced. By increasing the time resolution, a more clear view of the CIR can be obtained to characterise the channel with a wider frequency range. Two link setups are simulated to test the computation time of using different methods. The indoor environment configuration is listed in Table 3.8. The defined half-power semi-angle is $\phi_{1/2} = 60°$, and the remaining parameters are the same as those listed in Table 3.3. The first link considers a small room with closely located transmitter and receiver in the room centre. The second link considers a larger room with a distant separation between the transmitter and

the receiver. Figure 3.13 shows the required computation time in Matlab varies with the time resolution Δt.

Parameters	Room size	Transmitter coordinate	Receiver coordinate
Setup 1	5 m $\times$ 5 m $\times$ 3 m	$(2.5, 2.5, 3)$	$(2.5, 2.5, 0.75)$
Setup 2	10 m $\times$ 10 m $\times$ 3 m	$(2.5, 2.5, 3)$	$(7.5, 7.5, 0.75)$

Table 3.8: *Setup configurations in the computation time evaluation.*

The considered calculation methods include the deterministic method proposed in [67], the Monte Carlo method proposed in [68] and the proposed method in this study. To ensure the fairness of the comparison, up to 2^{nd} order reflections are considered in the deterministic method and the Monte Carlo method. In the case of deterministic method, the block size is configured based on the time resolution as $A_{\text{e}} = 2c^2\Delta t^2$ [69]. In the case of Monte Carlo method, the ray-tracing process is repeated until the normalised mean square error (NMSE) of the CIR result is less than 2.5×10^{-3}. Calculating low time resolution CIR ($\Delta t > 0.7$ ns), the deterministic and Monte Carlo methods are able to calculate the results with a computation time in the range from a few seconds to about 100 s. With the same time resolution, the proposed method is able to finish the calculation with a computation time of less than 0.1 s. With the decrease of Δt, the required computation time for all three methods increases. The required time for the deterministic method increases significantly. In the case of $\Delta t = 0.1$ ns, the computation time for the deterministic method is in the range from several hours to more than three days. This is because the increased time resolution leads to a significantly increased number of blocks with smaller size. Since the deterministic method considers all possible propagation paths between blocks and their combinations, the increased number of blocks significantly increases the computational complexity. In addition, increasing the room size requires more number of blocks to fill the larger internal surface area. Therefore, for the deterministic method, the computation time also increases significantly with the increase of the room size. In the case of the Monte Carlo method, the increase of computation time with the decrease of Δt is not as significant as that of the deterministic method. With $\Delta t = 0.1$ ns, several minutes are required for obtaining an accurate CIR result. This increase in computation time is because the time bin width gets narrower with higher time resolution. A narrower bin width requires more samples to average out the noise caused by the random process. In setup 2, the receiver is further away from the transmitter. Consequently, the traced ray has a lower probability to reach the region close to the receiver. Therefore, more computation time is required for the Monte Carlo method if the separation between the transmitter and receiver increases. In contrast, the computation time

for the proposed method increases slightly with the decrease of Δt. With a $\Delta t = 0.1$ ns, the computation time for the proposed method is still less than a second. Furthermore, the required computation time varies slightly for different link setups.

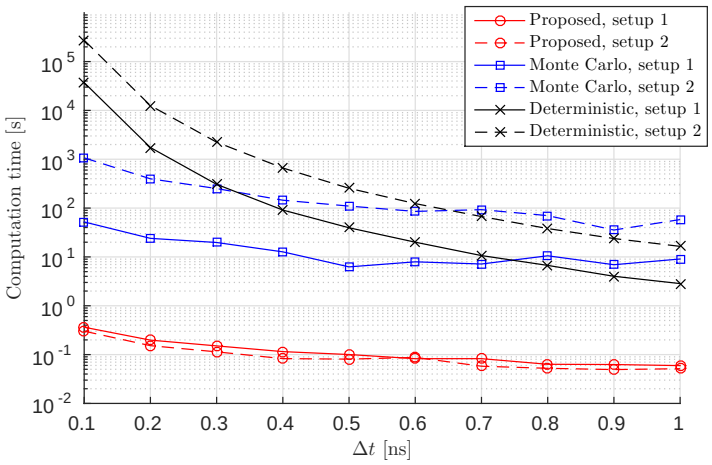

Figure 3.13: *NLoS CIR computation time with different calculation methods.*

3.6 Summary

In this chapter, a computationally efficient analytical method was proposed to calculate the NLoS CIR in typical indoor VLC deployments. In the proposed method, the NLoS channel are decomposed into multiple components with different categories. The categorisation is based on the terminals and surfaces that the light undergoes. Based on a single reflection CIR expression, the CIR calculations for TWR, TFCR and TWCR propagation categories are presented. In order to reduce the computational complexity, suitable approximation functions are used in the calculation. By combining the CIR calculation for different propagation categories, the final NLoS CIR calculation scheme is proposed. The CIR results calculated using the proposed method are compared with those generated by using the Monte Carlo method proposed in [68] and the deterministic ray-tracing method proposed in [67]. In comparison with the benchmark methods, the proposed method can provide accurate CIR results for NLoS channels with up to 2^{nd} order reflections. Furthermore, the required time for the proposed method is significantly shorter than the benchmarks (typically less than a second). Because of this computational efficiency, the proposed method will be used in Chapter 4 to evaluate the effects of the NLoS light propagation on the downlink performance of LAC networks.

Chapter 4
Downlink Performance of LiFi Attocell Networks

4.1 Introduction

With the recent great advancements in research of optical wireless communication (OWC) technologies and the demand of wide coverage OWC service, a few studies on the subject of networked OWC have been conducted by other researchers. The authors of [19] have proposed a cellular OWC scheme with traditional resource partitioning to mitigate co-channel interference (CCI) using a larger spatial reuse distance in an indoor infrared (IR) wireless communication system. In [84], the performance of optical wireless hotspots was compared to that achieved by a radio frequency (RF) system. That study also investigated the relationship between signal-to-noise ratio (SNR) and the horizontal distance of a user equipment (UE) from the cell centre. A visible light communication (VLC) system adopting cellular characteristics using a light shaping diffuser was proposed in [85]. As one of the networked OWC systems, a light fidelity (LiFi) attocell (LAC) network not only provides high data transmission and wide coverage, but also offers a number of more advanced features as introduced in Chapter 2. Since a LAC network is a newly proposed concept, many related research questions still remain open.

In this study, a number of fundamental issues related to the downlink performance of LAC networks are investigated using the downlink framework based on optical-orthogonal frequency division multiplexing (O-OFDM) introduced in Chapter 2. Firstly, a LAC network is deployed within a single room surrounded by walls, ceiling, floor and other objects. Thus, the effects of non-line-of-sight (NLoS) channel and network size are investigated by conducting simulations using the proposed method in Chapter 3. In addition, the effects of varying a number of key system parameters, such as cell radius and light source radiation pattern, are considered. This is particularly important when piggy-backing the LAC network on existing lighting infrastructures which leaves little possibilities to optimise the network for communication. Furthermore, the downlink performance with different cell deployments (regulated or randomly distributed) are evaluated. A series of downlink system metrics, such as signal-to-interference-plus-noise

ratio (SINR) statistics, cell data rate, are analysed and evaluated. Analytical expressions are derived to efficiently calculate the values of these metrics without using time consuming simulations. Finally, the performance of LAC networks are compared with that of other small-cell networks to demonstrate the potential of LAC networks.

The remainder of this chapter is arranged as what follows: the studies of the effects of NLoS channel and network size are presented in Section 4.2. In Section 4.3, the effects of varying key system parameters and their configurations are analysed and discussed. The downlink performance of the LAC networks with various cell deployments are evaluated in Section 4.4. The analysis of the SINR statistics with hexagonal (HEX) and Poisson point process (PPP) cell deployments are presented in Section 4.5. The analysis of the average cell data rate and outage probability with O-OFDM and bit-loading is presented in Section 4.6. The comparison between the downlink performance of LAC networks and that of the other small-cell systems is presented in Section 4.7. In the following LAC downlink simulation or calculation results in this chapter, the case with direct-current-biased optical orthogonal frequency division multiplexing (DCO-OFDM) scheme is used as an example, and the system parameters listed in Table 4.1 are used if they are not specified. The orientations of the transmitters and the receivers are directed downwards and directed upwards, respectively. The justification is the same as that introduced in Chapter 3 Section 3.2.

Parameters	Symbol	Values
Transmitter height	z_{s}	3 [m]
Receiver height	z_{r}	0.75 [m]
Receiver field of view	$\psi_{\max}$	90°
Modulation bandwidth	F_{s}	360 [MHz]
Front-end device bandwidth factor	F_{fe}	31.7 [MHz]
DC-bias level	ϵ_{DC}	$0.5\Delta\epsilon$
Signal amplitude range	$\Delta\epsilon$	6.4
PD responsivity	η_{pd}	0.4 [A/W]
PD physical area	A_{pd}	1 [cm^2]
Number of subcarriers	K	512
Cell centre illuminance from O-BS	$\tilde{E}_{\mathrm{v}}$	500 [lux]
Background illuminance	$E_{\mathrm{v,bg}}$	100 [lux]
Absolute temperature	T	300 [K]
Receiver load resistance	R_{L}	500 [Ω]

Table 4.1: *Default LAC downlink system parameters.*

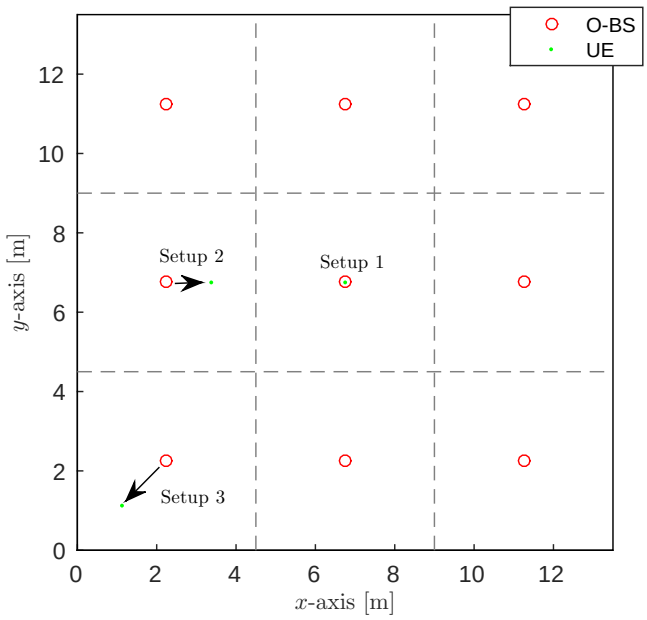

Figure 4.1: *Transmitter and receiver locations in a square room with* 3×3 *square cells.*

4.2 Effects of Non-line-of-sight Channel and Network Size

In Chapter 3, an analytical method to calculate the NLoS channel impulse response in VLC systems has been introduced. In this section, the downlink SINRs based on the free-space light propagation channel including the line-of-sight (LoS) and NLoS light propagations are evaluated in a case study. In addition, the corresponding downlink SINRs based on the channel with only LoS propagation are also presented for comparison. In addition, the performance of the LAC downlink system deployed in rooms with different number of cells is evaluated. In other words, the effects of varying the network size is considered.

4.2.1 Effects of Non-line-of-sight Channel

In this subsection, the effects of NLoS channel is investigated using a case study with simulations. A LAC network deployed in a square room is considered in this case study, and 3×3 square cells are deployed in the room as shown in Figure 4.1. An edge length of 4.5 m for a square cell and a half-power semi-angle of $\phi_{1/2} = 40^\circ$ for the downlink transmitter are assumed. The simulated UEs are located at $(6.75, 6.75)$, $(3.375, 6.75)$ and $(1.125, 1.125)$ in setup 1, 2 and 3, respectively. Each UE selects the closest optical-base station (O-BS) as its

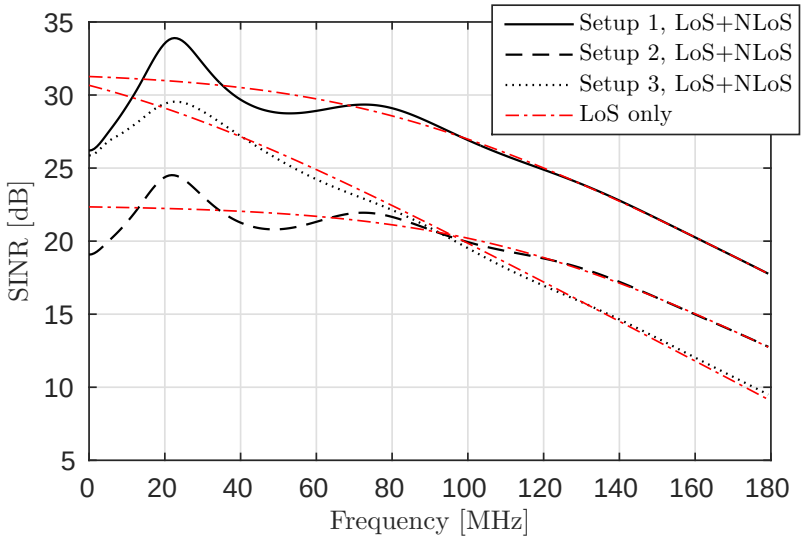

Figure 4.2: *SINR varies with frequency in setup 1, 2 and 3.*

serving access point (AP). The reflectance of wall, floor and ceiling are 0.74, 0.61 and 0.38, respectively [82]. The LAC downlink system parameters are listed in Table 4.1.

The vertical separation between transmitter and receiver is defined as $\Delta z = z_{\mathrm{s}} - z_{\mathrm{r}}$. According to the configuration listed in Table 4.1, the corresponding Δz is 2.25 m. The downlink SINR is calculated by using (2.53) in Section 2.9 of Chapter 2. Note that the method introduced in Chapter 3 is used to calculate the NLoS channel impulse response (CIR) of the link between each transmitter and the receiver. The CIR due to the LoS channel component is calculated using (2.17) in Section 2.4.2.1 of Chapter 2. The free-space CIR from the i^{th} O-BS to the receiver is denoted as $h_{\mathrm{fs},i}(t)$, and the free-space channel frequency response $H_{\mathrm{fs},i}(k)$ in (2.53) can be calculated as:

$$H_{\mathrm{fs},i}(k) = \int_0^{\infty} h_{\mathrm{fs},i}(t) \exp\left(\frac{-j2\pi k F_{\mathrm{s}} t}{K}\right) \mathrm{d}t. \tag{4.1}$$

The net-effect of the optical filter loss and optical concentrator gain at the receiver side is assumed to provide a unity gain for simplicity. The field of view (FoV) of the receiver is assumed to be 90°.

The results of the downlink SINR varying with frequency is shown in Figure 4.2. Due to the low pass characteristics of the front-end elements, the overall trend of the SINR decreases with the increase of the frequency. Setup 1 represents the performance of a UE in the cell centre

in the room centre, which offers the highest SINR results. Setup 2 and setup 3 represent the performance of UEs close to the room edge, which offers lower downlink SINR. Compared to setup 2, the UE in setup 3 is closer to the room corner, but further away from the interfering O-BSs. Consequently, the SINR at low frequency for setup 3 is higher than that achieved in setup 2. Comparing the case with LoS+NLoS and the case with LoS only, the SINRs with these two cases match each other at frequency higher than 100 MHz. With an increase of frequency in the low frequency range, the result with LoS+NLoS oscillates around the result with LoS only. The variance of the observed oscillation is up to a few dB. In addition, the SINR with LoS+NLoS is always lower than that with LoS only at DC.

Next, the achievable data rate is considered in this case study. Taking the advantage of O-OFDM system, adaptive modulation and coding (AMC) schemes [30] are used to assign different number of bits on each subcarrier according to the corresponding SINR level. In this study, the AMC schemes listed in Table 4.2 are considered, where T_n denotes the SINR threshold for the n^{th} level modulation and coding, and ε_n denotes the spectral efficiency (bits/symbol) of the n^{th} level modulation and coding.

	AMC scheme 1		AMC scheme 2	
n	T_n [dB]	ε_n [bits/symbol]	T_n [dB]	ε_n [bits/symbol]
0	-	0	-	0
1	9.8	2	-6	0.1523
2	13.4	3	-5	0.2344
3	16.5	4	-3	0.3770
4	19.6	5	-1	0.6016
5	22.5	6	1	0.8770
6	25.5	7	3	1.1758
7	28.4	8	5	1.4766
8	31.3	9	8	1.9141
9	34.3	10	9	2.4063
10	37.2	11	11	2.7305
11	-	-	12	3.3223
12	-	-	14	3.9023
13	-	-	16	4.5234
14	-	-	18	5.1151
15	-	-	20	5.5547

Table 4.2: *Adaptive Modulation and Coding*

The AMC scheme 1 is the uncoded quadrature amplitude modulation (QAM) [86] achieving a maximum bit error rate (BER) target of 1×10^{-3}. This scheme is reliable and simple to im-

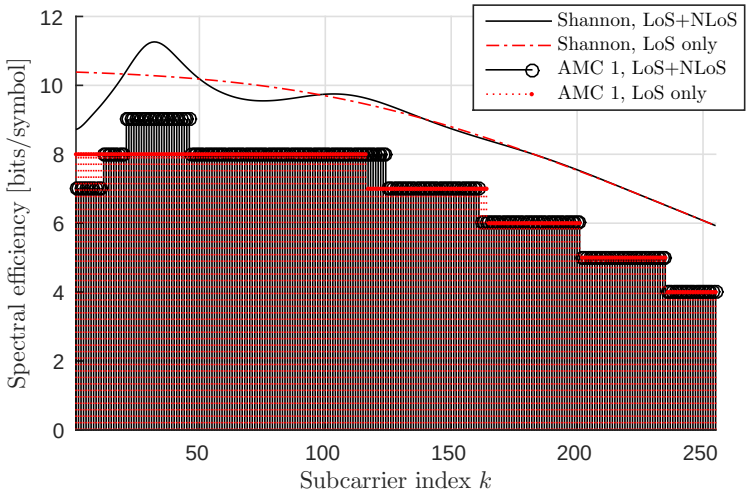

Figure 4.3: *Adaptive modulation and coding scheme in setup 1.*

plement, and has been used in several experimental studies [30, 65, 66]. However, this scheme achieves a relatively low spectral efficiency and the minimum required SINR is as high as 9.8 dB. The AMC scheme 2 is used in the Long Term Evolution (LTE) system [87], which is more spectrally efficient, and the lowest acceptable SINR is -6 dB. However, it is more complex to implement. Figure 4.3 shows an example for setup 1 with AMC scheme 1. The results with LoS+NLoS and the results with LoS only are presented. In addition, the corresponding results of using Shannon capacity are also provided for comparison.

The SINR with LoS+NLoS is higher than that with LoS only on some subcarriers, but lower on the other subcarriers. In other words, more number of bits are loaded in the case with LoS+NLoS on some carriers compared with the case with LoS only, but fewer on the remaining subcarriers. However, the accumulated sum rates including all subcarriers for both cases are very close. This is demonstrated in Figure 4.4, which shows the accumulated data rate in setup 1, 2 and 3 in the case with LoS+NLoS and the case with LoS only. The accumulated data rate results show little difference between the case with LoS+NLoS and the case with LoS only. Thus, it can be concluded that in the downlink analysis of LAC networks, the omission of NLoS channel components would not introduce significant error in the estimation of the accumulated data rate. Therefore, the case with channel considering only LoS light propagation is considered in the remaining analysis and simulations for lower simplicity and better tractability. However, this does not mean the effects of NLoS channel are negligible in LAC systems for all cases.

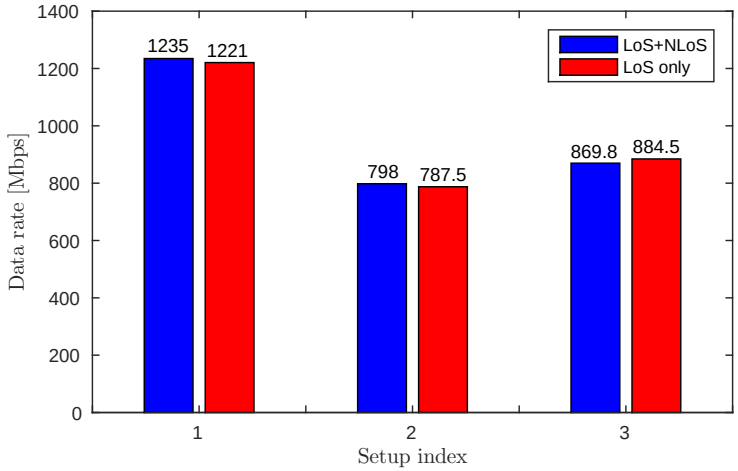

Figure 4.4: *Accumulated data rate in setups 1, 2 and 3.*

The importance of NLoS channel depends on the metric that is considered in the research. For example, if the exact bit-loading solution for highest data rate demonstrated in this section is the major concern, the effect of NLoS would be important and should not be omitted.

According to (2.17), the free-space light propagation channel gain with only LoS component in (2.53) can be calculated as:

$$H_{\mathrm{fs}} = \frac{A_{\mathrm{pd}}(m+1)}{2\pi D^2} \cos^m \phi \cos\psi \mathbf{1}_{\psi \leq \psi_{\mathrm{FoV}}}(\psi)\,. \tag{4.2}$$

Assume a horizontal offset r between the O-BS and the UE, which is related to the Euclidean distance between the O-BS and the UE as $r^2 + \Delta z^2 = D^2$. Therefore, the free-space signal propagation channel gain can be rewritten as a function of r:

$$H_{\mathrm{fs},r} = \frac{A_{\mathrm{pd}}(m+1)\Delta z^{m+1} \mathbf{1}_{\psi \leq \psi_{\mathrm{FoV}}}(\psi)}{2\pi \left(r^2 + \Delta z^2\right)^{\frac{m+3}{2}}}. \tag{4.3}$$

4.2.2 Effects of Network Size

In this subsection, the downlink performance of UEs with random user locations is evaluated. With large number of iterations in UE positions, the average achievable data rate per cell can be calculated for the considered LAC networks. Except the spatial location of UEs, the remaining configurations and parameters are the same as those considered in Section 4.2.1. Furthermore,

the LAC networks in a larger room with more cells are considered to determine the effect of varying network size.

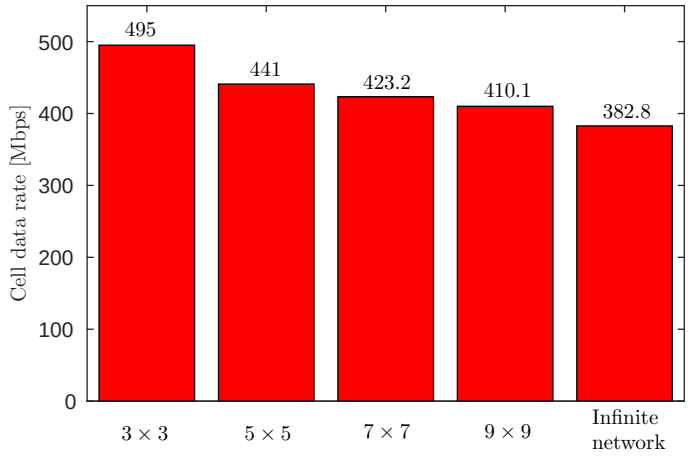

Figure 4.5: *Cell data rate varies with network size.*

Figure 4.5 shows the simulated downlink cell data rate of LAC networks with 3×3, 5×5, 7×7 and 9×9 square cells. It can be observed that with the increase of network size, the cell data rate decreases. This is because, there would be more interfering O-BSs around each cell if the network size increases, especially for cells away from the room edges. Consequently, the increase of the CCI level leads to a decrease of SINR and cell data rate. In an extreme case, the network extend infinitely in the horizontal space. The corresponding cell data rate result is also shown in Figure 4.5, which exhibits the minimal compared to the cases with smaller finite network size. This is because the number of surrounding interfering O-BSs is maximised for each cell in this worst case, thereby causing a maximised CCI level in each cell. Note that the simulation of 'infinite' network is achieved by considering a single cell surrounded by a large number of interfering O-BSs. Only the interfering O-BSs that is sufficiently far away from the considered cell (introduce negligible CCI) are not included in the simulation. This way of simulation uses the characteristic that the downlink setup (the number and spatial distribution of interfering O-BSs) respect to each cell is identical in an infinite network.

Therefore, in the following analysis in this thesis, LAC networks with infinite network size are considered. The reasons are two fold. Firstly, the LAC system with infinite network shows a worst case performance in terms of connection quality compared to the cases with smaller finite network. On the other hand, the performance characteristics in each cell is identical

in an infinite network. In other words, the analysis of a single cell is sufficient to reflect the performance in the whole network. This introduces significant reduction in analysis complexity, which leads to tractable theoretical results in the downlink performance analysis.

4.3 System Parameters Evaluation

The performance of a LAC network depends on many factors as implied by formula (2.53) in Chapter 2. Some of the parameters can be controlled by a predefined system configuration. In this section, two key parameters closely related to the network configuration are studied. One of the parameters is the cell radius R in a grid based LAC network or O-BS density Λ in a point process based LAC network. It determines the average number of UEs that an O-BS should serve and the number of cells in a room. The other parameter is the radiation pattern of the light source, which is controlled by the Lambertian emission order m. The radiation pattern defines the signal strength in any radiation direction from the light source. These two parameters determine spatial distribution of the received desired signal strength by a UE within each cell and the significance of CCI to other cells. Therefore, two configuration objectives are considered which include the maximisation of desired signal strength and the minimisation of introduced CCI in this section.

4.3.1 Co-Channel Interference Minimisation

Here a mathematical analysis is used to determine the appropriate setting for R and m with the objective of CCI minimisation. Considering an O-BS with an optical output of P_{opt} serving a circular cell underneath it, part of the radiated signal power received by the desired coverage area, while the remaining signal power is incident on other cells as CCI. Note that the received electrical signal power monotonically increases with the corresponding received optical power. Therefore, in this section, the received optical power is considered instead of the received electrical signal power for simplicity. Figure 4.6 shows the geometry of this setup.

The considered O-BS is Δz away from the cell centre. In order to minimise CCI, it is preferred to allow more radiated signal power from the O-BS to stay within the coverage area of that O-BS, and to let less signal power leak into other cells. If the optical power reaching the desired coverage area is defined as $P_{\mathrm{opt,d}}$, the objective becomes maximising $P_{\mathrm{opt,d}}$. Firstly, the calculation of $P_{\mathrm{opt,d}}$ should be determined. By considering the O-BS as the origin, the

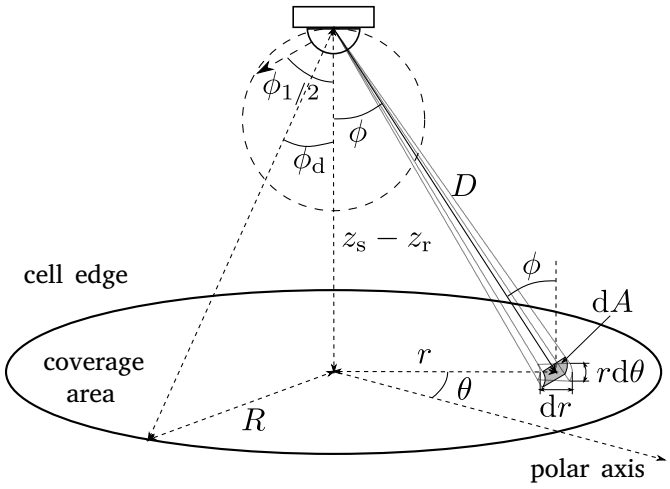

Figure 4.6: *Optical base station radiation geometry.*

circular coverage area of the cell corresponds to a certain solid angle. According to (2.1) in Chapter 2, the desired signal power $P_{\mathrm{opt,d}}$ for a certain solid angle can be calculated as:

$$P_{\mathrm{opt,d}} = \iint_{\mathcal{W}_{\mathrm{cell}}} P_{\mathrm{opt}} \frac{m+1}{2\pi} \cos^m \phi \mathrm{d}\Omega, \tag{4.4}$$

The differential of this solid angle in (4.4) $\mathrm{d}\Omega$ can be derived according to the geometry shown in Figure 4.6 as:

$$\mathrm{d}\Omega = \frac{\mathrm{d}A}{D^2} = \frac{r\mathrm{d}\theta\mathrm{d}r\cos\phi}{\Delta z^2 \sec^2\phi} = \mathrm{d}\theta\mathrm{d}\phi\sin\phi. \tag{4.5}$$

By inserting (4.5) into (4.4), the 2-dimensional (2-D) integration can be decomposed into two 1-dimensional (1-D) integration as:

$$\begin{aligned} P_{\mathrm{opt,d}} &= P_{\mathrm{opt}} \frac{m+1}{2\pi} \int_0^{2\pi} \int_0^{\phi_{\mathrm{d}}} \cos^m \phi \sin\phi \mathrm{d}\phi\mathrm{d}\theta \\ &= P_{\mathrm{opt}} \left(1 - \left(\frac{\Delta z}{\sqrt{\Delta z^2 + R^2}}\right)^{m+1}\right), \end{aligned} \tag{4.6}$$

where ϕ_{d} can be calculated by $\phi_{\mathrm{d}} = \arctan(R/\Delta z)$ as shown in Figure 4.6. The partial derivatives of ϕ_{d} with respect to R and m are calculated as:

$$\frac{\partial P_{\mathrm{opt,d}}}{\partial R} = \frac{P_{\mathrm{opt}} R(m+1)\Delta z^{m+1}}{(\Delta z^2 + R^2)^{\frac{m+3}{2}}} > 0, \tag{4.7}$$

$$\frac{\partial P_{\mathrm{opt,d}}}{\partial m} = P_{\mathrm{opt}} \ln\left(\frac{\sqrt{\Delta z^2 + R^2}}{\Delta z}\right) \left(\frac{\Delta z}{\sqrt{\Delta z^2 + R^2}}\right)^{m+1} > 0, \tag{4.8}$$

which implies that $P_{\mathrm{opt,d}}$ is a monotonically increasing function of R and m. This means that less CCI can be achieved by using a larger cell size as a larger cell size will increase the distance between each neighbouring interfering O-BS and the desired UE. In addition, using a source with a narrower beam width would also decrease the level of CCI as smaller half-power semi-angle leads to a more collimated beam pointing to the desired coverage area.

4.3.2 Desired Signal Strength Maximisation

Since the Lambertian radiation pattern is used to model the light emission from the source, the further the UE is away from the cell centre, the weaker the desired signal received. Consequently, the UE at the cell edge receives the weakest signal from the O-BS. In other words, as long as the signal strength of the cell edge UE is high enough, all of the UEs in the cell coverage area should have sufficient signal power. Therefore, the objective can be converted to maximising the signal power received by the cell edge UE which is R away from the cell centre. According to the analysis in Section 2.4.2.1 of Chapter 2, the received optical power by a cell edge UE $P_{\mathrm{opt,e}}$ can be determined as:

$$P_{\mathrm{opt,e}} = P_{\mathrm{opt}} H_{\mathrm{fs},r=R} = \frac{P_{\mathrm{opt}} A_{\mathrm{pd}} (m+1) \Delta z^{m+1}}{2\pi \left(R^2 + \Delta z^2\right)^{\frac{m+3}{2}}}. \tag{4.9}$$

Similar to the case of minimising CCI, the partial derivatives of $P_{\mathrm{opt,e}}$ respect to R and m are calculated as:

$$\frac{\partial P_{\mathrm{opt,e}}}{\partial R} = -\frac{P_{\mathrm{opt}} A_{\mathrm{pd}} (m+1)(m+3) R \Delta z^{m+1}}{2\pi \left(R^2 + \Delta z^2\right)^{\frac{m+5}{2}}} < 0, \tag{4.10}$$

$$\frac{\partial P_{\mathrm{opt,e}}}{\partial m} = \frac{P_{\mathrm{opt}} A_{\mathrm{pd}} \Delta z^{m+3} \left(1 + \ln\left(\frac{\Delta z^{m+1}}{\left(R^2+\Delta z^2\right)^{\frac{m+1}{2}}}\right)\right)}{2\pi \Delta z^2 \left(R^2 + \Delta z^2\right)^{\frac{m+3}{2}}}. \tag{4.11}$$

which implies that $P_{\mathrm{opt,e}}$ is a monotonically decreasing function of R. Therefore, for a source with a specified radiation pattern, a smaller cell offers higher received signal power for the cell edge UEs. This is because a smaller cell size reduces the distance from the cell edge UE to the cell centre. On the other hand, $P_{\mathrm{opt,e}}$ is a concave function of m, which means there is an optimal value for m to maximise the cell edge UE signal strength. By letting $\frac{\partial P_{\mathrm{opt,e}}}{\partial m} = 0$, the

optimal radiation pattern can be calculated as:

$$\tilde{m} = 1 \Big/ \ln\left(\sqrt{R^2 + \Delta z^2} \Big/ \Delta z\right) - 1 \ . \tag{4.12}$$

For the case of using a source with narrower beam width ($m > \tilde{m}$), the beam is over concentrated, which causes significant signal strength variance between cell centre UEs and cell edge UEs, and the signal strength for the cell edge UE would be too weak for reliable communication. For the case of using a source with wider beam width ($m < \tilde{m}$), the beam is over diffused, which causes too much power leakage to other cells and the overall signal strength in the desired cell is not sufficient.

4.3.3 Parameter Configurations

From the analysis in Section 4.3.1 and Section 4.3.2, it can be found that appropriate settings for R and m also depend on the value of each other. Therefore, the configurations of cell size and source beam width should be interconnected. Apart from the requirement of communication, there are many other constraints on the configuration of cell size. For example, if the cell size is too large, the illumination performance will be undesired. An extremely small cell size leads to too many required O-BSs in the room, which increases the installation complexity and increases the load of the handover process. In contrast, beam width of the source is more flexible, which can be simply achieved by appropriate optical diffuser design. Therefore, the configuration of R is considered as a given parameter, and the suitable setting of m is analysed.

According to (4.8) and (4.12), if m is smaller than $\tilde{m}$, both CCI increases and cell edge signal strength decreases. If m equals or greater than $\tilde{m}$, there is a trade-off between the two objectives. Therefore, $\tilde{m}$ can be considered as a lower bound for m. In a noise limited system, a m closer to $\tilde{m}$ is preferred. In the case of a CCI limited system, equation (4.8) shows that m should be maximised to minimise the CCI level. However, an upper bound should be set to allow the cell edge UE signal strength to be high enough to achieve the minimum acceptable SNR. In order to find this upper bound, a simple metric is defined: the ratio between the SNR of the cell centre UE ($r = 0$) to that of the cell edge UE ($r = R$), which is denoted as σ_{P}. From the analysis in Section 2.9 of Chapter 2, it can be deduced that σ_{P} is proportional to the square of the ratio of received optical power by the cell centre UE to that received by the cell

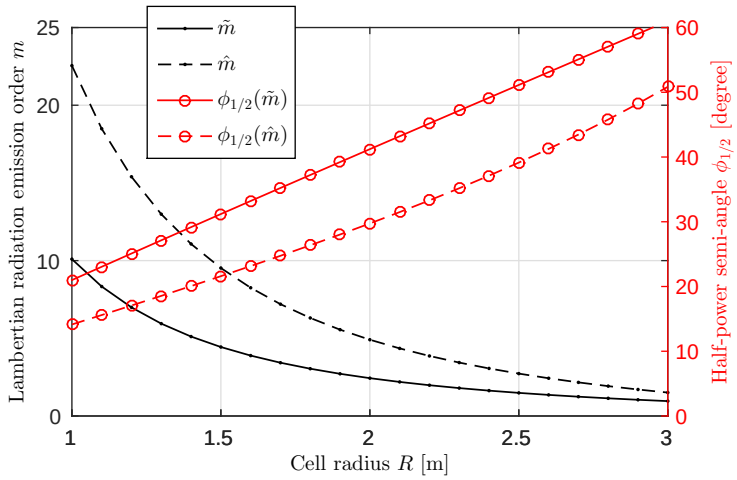

Figure 4.7: *The configuration of half-power semi-angle $\phi_{1/2}$ and the corresponding Lambertian emission order m against the cell radius R.*

edge UE as:

$$\sigma_{\mathrm{P}} = \left(\frac{P_{\mathrm{opt}} H_{\mathrm{fs},r=0}}{P_{\mathrm{opt}} H_{\mathrm{fs},r=R}}\right)^2 = \frac{\Delta z^{-2(m+3)}}{(R^2+\Delta z^2)^{-m-3}}. \tag{4.13}$$

For a fixed σ_{P}, the required lower bound for m can be calculated as:

$$\hat{m} = \frac{\ln \sigma_{\mathrm{P}}}{\ln\left(1+\frac{R^2}{\Delta z^2}\right)} - 3. \tag{4.14}$$

According to [30] and [66], the achievable cell centre SNR is around 30 dB. For uncoded 4 QAM, the minimum required SNR is approximately 10 dB. Therefore, $\sigma_{\mathrm{P}} = 20$ dB is chosen in this study. The result of $\tilde{m}$, $\hat{m}$ and the corresponding $\phi_{1/2}$ against R based on (4.12) and (4.14) are plotted in Figure 4.7. It can be seen that the area between the two curves is the appropriate configuration region, which is the preferred settings for $\phi_{1/2}$. In the case that CCI is the main limiting factor, m can be set to a value that is close or equal to $\hat{m}$, which is calculated using (4.14). In the case that receiver noise is the limiting factor, m can be configured to a value that is close or equal to $\tilde{m}$, which is calculated using (4.12). Note that the cell shape in different cell deployments varies from hexagon to irregular polygon, which is different from the desired circular cell considered in this section. However, it has been found that the general characteristics identified in the case of circular cell are also valid in the case with other cell shapes using simulation studies. Furthermore, configuring LAC networks with different cell deployments using (4.12) and (4.14) generally leads to desired performance.

4.4 Cell Deployment

In Chapter 2 Section 2.8.1, a number of cell deployments considered in this study are introduced, which include the HEX, PPP, square and hard-core point process (HCPP) cell deployment. In this section, the downlink SINR statistics of the LAC systems with these cell deployments are evaluated and compared. Infinite networks are assumed for the cases with all cell deployments. In order to achieve a fair comparison between the cases with different cell deployments, the cell size used with each cell deployment should be the same. In the cases of HEX and square cell deployments, the coverage area for each cell is identical. Despite the difference in cell shape, the same cell size can be achieved by letting the area of different cell shape to be the same. Assume a circular cell radius of R. In a HEX cell, the distance from the centre to one of the vertex is defined as $\tilde{R}$. In a square cell, the edge length of the cell is defined as R_{sq}. To ensure the same cell size, the following relationships should be fulfilled:

$$\tilde{R} = \sqrt{\frac{2\pi}{3\sqrt{3}}} R, \tag{4.15}$$

$$R_{\mathrm{sq}} = \sqrt{\pi} R. \tag{4.16}$$

In the cases of PPP and HCPP cell deployments, the cell size is a random variable, and the size of each cell is different in the same network. A fixed O-BS density Λ is defined to determine the average number of O-BS per unit area. Since it is impossible to ensure the cell size constraint for every cell in the cases with PPP and HCPP cell deployments, an alternative method is to let the average cell size to be the same as the coverage area of the equivalent circular cell as $\Lambda = \frac{1}{\pi R^2}$. In the simulation of HCPP cell deployment, a PPP with a density of Λ_0 is applied first. Then each point is tagged with a random number, and a dependent thinning process is carried out for each marked node as follows: retain the marked node if there is no other node within the circle centred at the marked node with a radius of R_{thin}. After the thinning, the HCPP nodes density would be reduced. Therefore, to generate a set of O-BS locations with HCPP of density Λ, the initial PPP density Λ_0 has to be [88]:

$$\Lambda_0 = \frac{-\ln(1 - \Lambda\pi R_{\mathrm{thin}}^2)}{\pi R_{\mathrm{thin}}^2}. \tag{4.17}$$

In Figure 4.8, the statistics of the SINR in terms of cumulative distribution function (CDF) of the systems with different cell deployments are shown and compared. The SINR statistics

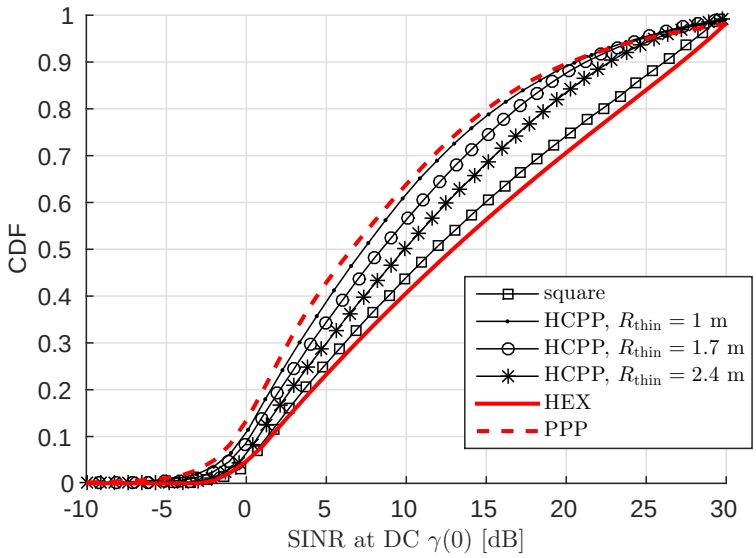

Figure 4.8: *Compare the SINR statistics in terms of CDF at DC of systems with different cell deployments. An equivalent circular cell radius of $R = 3$ m and a half-power semi-angle of $\phi_{1/2} = 40°$ are used. For the results of the HCPP networks, $R_{\text{thin}} = 1, 1.7, 2.4$ m. Other parameters are the same as those listed in Table 4.1.*

on different subcarriers have a similar trend. Here only the SINR on the DC subcarrier is demonstrated as an example. An equivalent circular cell radius of $R = 3$ m and a half-power semi-angle of $\phi_{1/2} = 40°$ are used. The remaining system parameters are listed in Table 4.1. Figure 4.8 shows that the SINR distributions of the square network and HCPP network are bounded by the curves for the cases of the PPP network and the HEX network within the SINR region of interest. Similar to the conclusion drawn in [76], the SINR distribution of a PPP (HEX) network can be considered as a lower (upper) bound for the SINR statistics of the LAC systems with other cell deployments. Therefore, it is important to analyse the LAC system downlink performance with HEX and PPP cell deployments, which are the two extreme cases among all cell deployments.

4.5 Downlink SINR Statistics Analysis

When a UE has access to a network, the UE will have a random level of service quality because of the random location of the UE. The probability of receiving a certain service quality level can be determined by calculating the statistics of the achievable downlink SINR. This metric is

important as it directly determines the performance of a LAC network, such as achievable data rate and outage probability. The SINR statistics vary with large number of parameters, and it also varies with different cell deployments. In this study, the SINR statistics with HEX and PPP cell deployments are studied as they are the two extreme cases as introduced in Section 4.4.

4.5.1 System Model Simplification

In order to simplify the following analysis and make the evaluation tractable, the SINR expression (2.53) in Section 2.9 of Chapter 2 has to be modified. Firstly, the NLoS channel components are omitted as it is shown in Section 4.2.1 that this omission introduces little variance in the downlink system performance. In addition, the function $\mathbf{1}_{\psi\leq\psi_{\mathrm{FoV}}}(\psi)$ in (4.3) makes the SINR expression a piecewise function, which causes extra mathematical complexity in the analysis. Therefore, the worst case with a full FoV of $\psi_{\mathrm{FoV}} = 90^{\circ}$ is assumed, thereby making $\mathbf{1}_{\psi\leq\psi_{\mathrm{FoV}}}(\psi)$ always equal to 1 in the region of interest. Thus, by inserting (4.3) into (2.53), the simplified SINR expression can be written as:

$$\gamma(k) = \left(\frac{\left(\eta_{\mathrm{clip}}^2 + \sigma_{\mathrm{clip}}^2\right)\mathcal{I} + \mathcal{Z}(k)}{\eta_{\mathrm{clip}}^2 \mathcal{X}} + \frac{\sigma_{\mathrm{clip}}^2}{\xi^2 \eta_{\mathrm{clip}}^2} \right)^{-1}, \tag{4.18}$$

where

$$\mathcal{X} = \xi^2 \left(r_0^2 + \Delta z^2\right)^{-m-3}, \tag{4.19}$$

$$\mathcal{I} = \sum_{i \in \mathcal{U}} \left(r_i^2 + \Delta z^2\right)^{-m-3}, \tag{4.20}$$

$$\mathcal{Z}(k) = \frac{4\pi^2 N_0 F_{\mathrm{s}} \exp\left(\frac{kF_{\mathrm{s}}}{KF_{\mathrm{fe}}}\right)}{\xi^2 \eta_{\mathrm{pd}}^2 \eta_{\mathrm{led}}^2 \sigma_{\mathrm{x}}^2 A_{\mathrm{pd}}^2 (m+1)^2 \Delta z^{2m+2}}. \tag{4.21}$$

4.5.2 Hexagonal Cell Deployment SINR Statistics

An infinite HEX network is considered in this analysis as the performance of a LAC system with an infinite network exhibits a worst case performance compared to the system with smaller finite network size. However, it is unnecessary to consider interfering O-BSs that are too far away from the considered cell as they introduce negligible CCI, and considering these O-BSs leads to significant increase of analysis complexity. Instead, a 2-layer HEX cell deployment is considered to approximate the infinite network as shown in Figure 4.9, and the user performance

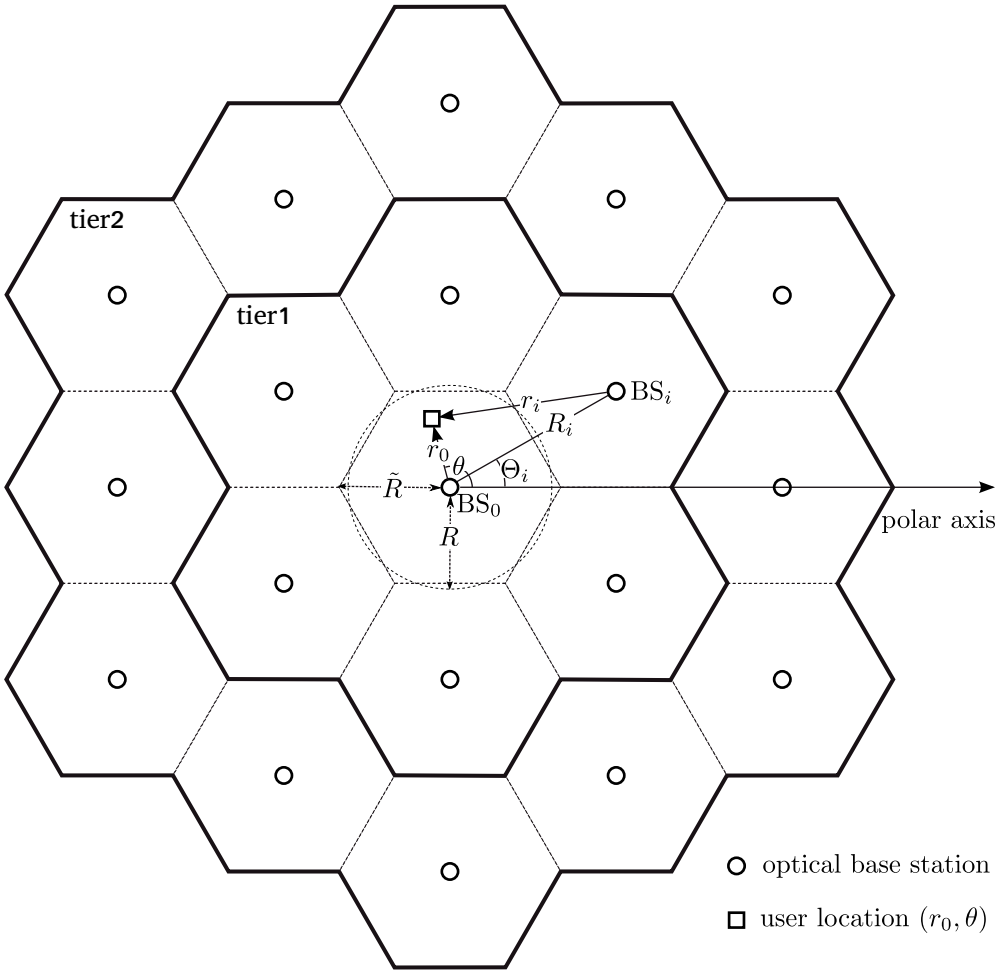

Figure 4.9: 2*-layer HEX network model with polar coordinates.*

in the central cell is analysed. In this study, all networks are assumed to be heavily loaded. In addition, the cases with $\kappa_{\mathrm{rf}} = 1$ and $\kappa_{\mathrm{rf}} = 3$ are considered, since these cases are more likely to achieve a spectral efficient system. In this model, a polar coordinate system is used to represent the location of the UE and O-BSs. Each 2-D location has a specified distance to the origin and a polar angle. A UE is r_0 away from the origin and has a polar angle of θ, as shown in Figure 4.9. Similarly, the i^{th} O-BS is located at (R_i, Θ_i). Then the horizontal offset between the i^{th} O-BS and the UE at (r_0, θ) can be calculated as:

$$r_i(r_0, \theta) = \sqrt{r_0^2 + R_i^2 - 2R_i r_0 \cos(\theta - \Theta_i)}. \tag{4.22}$$

The UE at (r_0, θ) in the central cell is served by the 0^{th} O-BS. The remaining O-BSs using the same transmission resource ($i \in \mathit{И}$) causes CCI to the desired UE. Since the coordinates of all O-BSs are known, by inserting (4.22) into (4.18), the SINR $\gamma(k)$ can be calculated as a function of the UE location. Thus, the statistics of the SINR can be converted from the random distribution of UE location (r_0, θ). Since the UEs are uniformly distributed in the cell, the probability density function (PDF) of r_0 and θ should follow: $f_{r_0}(r_0) = \frac{2r_0}{R^2}$ and $f_\theta(\theta) = \frac{1}{2\pi}$. The objective is defined as $\mathbb{P}[\gamma(k) < T]$, which calculates the probability that the downlink SINR is less than a threshold T. In conjunction with (4.18) and letting the probability conditioning on r_0, the following probability calculation can be obtained:

$$\mathbb{P}[\gamma(k) < T | r_0] = \mathbb{P}\left[\mathcal{I} > \frac{\eta_{\text{clip}}^2 \mathcal{X}\left(\frac{1}{T} - \frac{\sigma_{\text{clip}}^2}{\eta_{\text{clip}}^2 \xi^2}\right) - \mathcal{Z}(k)}{\eta_{\text{clip}}^2 + \sigma_{\text{clip}}^2} \middle| r_0 \right]. \tag{4.23}$$

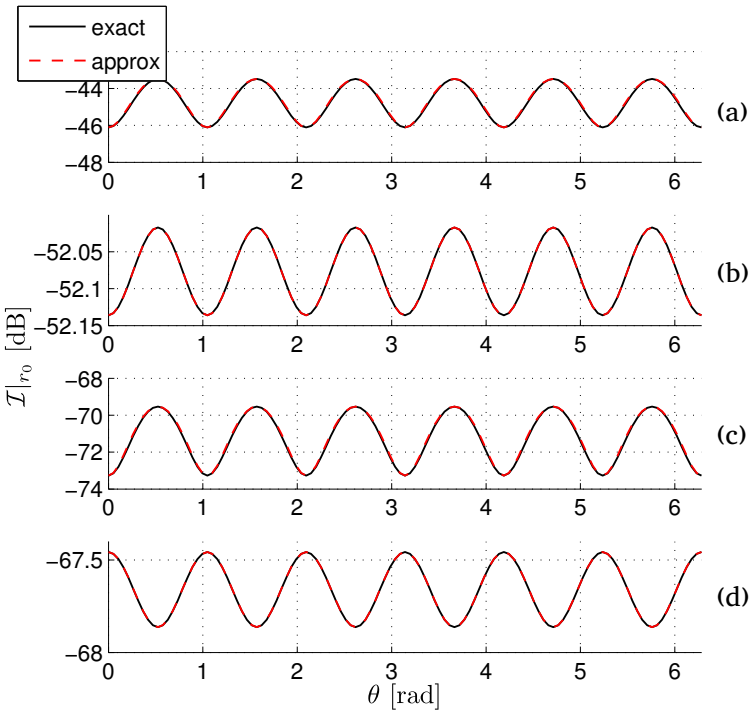

Figure 4.10: *Approximation to the CCI term in the case of HEX cell deployment. In configuration (a) $R = 3$ m, $\kappa_{\text{rf}} = 1$ and $r = R$ m. m is calculated using* (4.14)*. Relative to configuration (a), configuration (b) changes r to $R/2$, configuration (c) changes R to 2 m, and configuration (d) changes κ_{rf} to 3.*

The combination of (4.22) and (4.18) makes $\mathcal{I}$ an extremely complex function of θ for carrying out a PDF transformation. Therefore, this relationship between $\mathcal{I}$ and θ should be simplified in order to make the calculation tractable. Figure 4.10 shows the CCI term $\mathcal{I}$ in a HEX network against θ with a given r_0. It can be observed that with an increase of θ, $\mathcal{I}(\theta|r_0)$ oscillates between two extreme values with a period of 60°. This is because of the central symmetric deployment of the interfering O-BSs. Therefore, an approach that is similar to the 'flower' model introduced in [89] is used to simplify the relationship between $\mathcal{I}$ and θ. The concept is to use a cosine function to approximate the oscillation of the function $\mathcal{I}(\theta|r_0)$. Firstly, $\mathcal{I}_{0^\circ}(r_0)$ and $\mathcal{I}_{30^\circ}(r_0)$ are calculated, which are the function $\mathcal{I}$ of r_0 assuming a θ of 0° and of 30°, respectively. Both values constitute the oscillation bounds of the function $\mathcal{I}(\theta|r_0)$. The expressions for $\mathcal{I}_{0^\circ}(r_0)$ and $\mathcal{I}_{30^\circ}(r_0)$ can be calculated as:

$$\begin{aligned}\mathcal{I}_{0^\circ}(r_0) = \mathbf{1}_{\{\kappa_{\mathrm{rf}}=1\}}(\kappa_{\mathrm{rf}})\Bigg(&2\mathfrak{q}\left(-\frac{3\tilde{R}}{2}, \frac{3\tilde{R}^2}{4}+\Delta z^2\right) + 2\mathfrak{q}\left(\frac{3\tilde{R}}{2}, \frac{3\tilde{R}^2}{4}+\Delta z^2\right)\\ &+ 2\mathfrak{q}\left(0, 3\tilde{R}^2+\Delta z^2\right) + 2\mathfrak{q}\left(-3\tilde{R}, 3\tilde{R}^2+\Delta z^2\right) + 2\mathfrak{q}\left(3\tilde{R}, 3\tilde{R}^2+\Delta z^2\right)\\ &+ 2\mathfrak{q}\left(0, 12\tilde{R}^2+\Delta z^2\right)\Bigg) + \mathfrak{q}\left(-3\tilde{R}, \Delta z^2\right) + \mathfrak{q}\left(3\tilde{R}, \Delta z^2\right) + 2\mathfrak{q}\left(-\frac{3\tilde{R}}{2}, \frac{27\tilde{R}^2}{4}+\Delta z^2\right)\\ &+ 2\mathfrak{q}\left(\frac{3\tilde{R}}{2}, \frac{27\tilde{R}^2}{4}+\Delta z^2\right),\end{aligned} \tag{4.24}$$

$$\begin{aligned}\mathcal{I}_{30^\circ}(r_0) = \mathbf{1}_{\{\kappa_{\mathrm{rf}}=1\}}(\kappa_{\mathrm{rf}})\Bigg(&\mathfrak{q}\left(-\sqrt{3}\tilde{R}, \Delta z^2\right) + 2\mathfrak{q}\left(-\frac{\sqrt{3}\tilde{R}}{2}, \frac{9\tilde{R}^2}{4}+\Delta z^2\right) + \mathfrak{q}\left(\sqrt{3}\tilde{R}, \Delta z^2\right)\\ &+ 2\mathfrak{q}\left(\frac{\sqrt{3}\tilde{R}}{2}, \frac{9\tilde{R}^2}{4}+\Delta z^2\right) + \mathfrak{q}\left(-2\sqrt{3}\tilde{R}, \Delta z^2\right) + \mathfrak{q}\left(2\sqrt{3}\tilde{R}, \Delta z^2\right)\\ &+ 2\mathfrak{q}\left(-\sqrt{3}\tilde{R}, 9\tilde{R}^2+\Delta z^2\right) + 2\mathfrak{q}\left(\sqrt{3}\tilde{R}, 9\tilde{R}^2+\Delta z^2\right)\Bigg) + 2\mathfrak{q}\left(-\frac{3\sqrt{3}\tilde{R}}{2}, \frac{9\tilde{R}^2}{4}+\Delta z^2\right)\\ &+ 2\mathfrak{q}\left(\frac{3\sqrt{3}\tilde{R}}{2}, \frac{9\tilde{R}^2}{4}+\Delta z^2\right) + 2\mathfrak{q}\left(0, 9\tilde{R}^2+\Delta z^2\right),\end{aligned} \tag{4.25}$$

where the function $\mathfrak{q}(x, y)$ is defined as:

$$\mathfrak{q}(x, y) = \left((r_0+x)^2+y\right)^{-m-3}. \tag{4.26}$$

Then, the approximated CCI term can be calculated using the following expression:

$$\hat{\mathcal{I}} = \frac{\mathcal{I}_{30^\circ}(r_0)+\mathcal{I}_{0^\circ}(r_0)}{2} + \frac{|\mathcal{I}_{30^\circ}(r_0)-\mathcal{I}_{0^\circ}(r_0)|}{2}\cos(6\theta). \tag{4.27}$$

Figure 4.10 compares the exact conditional CCI term $\mathcal{I}(\theta|r_0)$ to the approximated one $\hat{\mathcal{I}}(\theta|r_0)$ with different system configurations. In the system with each of the configurations, the approximated model $\hat{\mathcal{I}}(\theta|r_0)$ matches well with the exact model $\mathcal{I}(\theta|r_0)$. The difference between the two curves is minimal as shown in each plot of Figure 4.10. Thus, it is reasonable to replace $\mathcal{I}$ with $\hat{\mathcal{I}}$. By replacing $\mathcal{I}$ in (4.23) with (4.27), the conditional probability $\mathbb{P}[\gamma(k) < T|r_0]$ can be written as:

$$\mathbb{P}[\gamma(k) < T|r_0] = \mathbb{P}\left[\cos(6\theta) > \frac{2\eta_{\text{clip}}^2\mathcal{X}\left(\frac{1}{T} - \frac{\sigma_{\text{clip}}^2}{\eta_{\text{clip}}^2\xi^2}\right) - 2\mathcal{Z}(k)}{\left(\eta_{\text{clip}}^2 + \sigma_{\text{clip}}^2\right)|\mathcal{I}_{30^\circ} - \mathcal{I}_{0^\circ}|} - \frac{\mathcal{I}_{30^\circ} + \mathcal{I}_{0^\circ}}{|\mathcal{I}_{30^\circ} - \mathcal{I}_{0^\circ}|}\middle| r_0\right]$$
$$= \frac{1}{2} - \frac{1}{\pi}\arcsin^\dagger\left(\frac{2\eta_{\text{clip}}^2\mathcal{X}\left(\frac{1}{T} - \frac{\sigma_{\text{clip}}^2}{\eta_{\text{clip}}^2\xi^2}\right) - 2\mathcal{Z}(k)}{\left(\eta_{\text{clip}}^2 + \sigma_{\text{clip}}^2\right)|\mathcal{I}_{30^\circ} - \mathcal{I}_{0^\circ}|} - \frac{\mathcal{I}_{30^\circ} + \mathcal{I}_{0^\circ}}{|\mathcal{I}_{30^\circ} - \mathcal{I}_{0^\circ}|}\right), \quad (4.28)$$

where

$$\arcsin^\dagger(x) = \begin{cases} 1 & : x > 1 \\ \arcsin(x) & : |x| \leq 1 \\ -1 & : x < -1 \end{cases}. \quad (4.29)$$

The final CDF of SINR can be calculated by averaging (4.28) over r_0 as:

$$\mathbb{P}[\gamma(k) < T] = \int_0^R f_{r_0}(r_0)\mathbb{P}[\gamma(k) < T|r_0]\mathrm{d}r_0$$
$$= \int_0^R \frac{r_0}{R^2} - \frac{2r_0}{\pi R^2}\arcsin^\dagger\left(\frac{2\eta_{\text{clip}}^2\mathcal{X}\left(\frac{1}{T} - \frac{\sigma_{\text{clip}}^2}{\eta_{\text{clip}}^2\xi^2}\right) - 2\mathcal{Z}(k)}{\left(\eta_{\text{clip}}^2 + \sigma_{\text{clip}}^2\right)|\mathcal{I}_{30^\circ} - \mathcal{I}_{0^\circ}|} - \frac{\mathcal{I}_{30^\circ} + \mathcal{I}_{0^\circ}}{|\mathcal{I}_{30^\circ} - \mathcal{I}_{0^\circ}|}\right)\mathrm{d}r_0, \quad (4.30)$$

which can be solved efficiently by using numerical methods. In this integration, the range of r_0 is from 0 to R, which corresponds to the integration over the equivalent circular cell. This approximation is made for simplicity.

4.5.3 Poisson Point Process Cell Deployment SINR Statistics

Similar to the HEX network, an infinite extending network is considered. However, the origin of the coordinates is placed at a random UE [76] in the PPP case. The horizontal positioning of the nearby optical O-BSs follows a 2-D homogeneous PPP with a density of Λ, as shown in Figure 4.11. In the PPP case, a similar method is used to retrieve the SINR statistics by

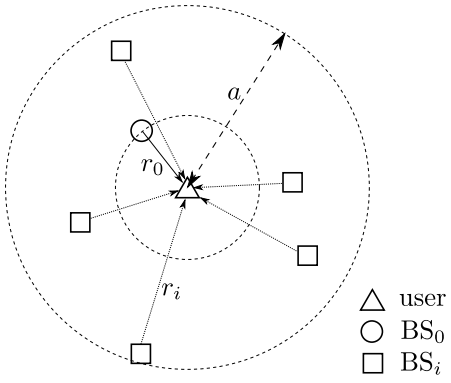

Figure 4.11: *Poisson point process network geometry.*

calculating $\mathbb{P}[\gamma(k) < T|r_0]$ using (4.23). Similar to the case of HEX network, the distribution of $\mathcal{I}$ is necessary. The exact distribution of $\mathcal{I}$ is complicated to solve. However, the method presented in [90] can be used to calculate the characteristic function (CF) of $\mathcal{I}$ conditioned on r_0.

Since there is no dependency between the location of O-BSs, the only significant variable in this model is the Euclidean distance between an O-BS and the desired UE D_i. The CCI power term $\mathcal{I}$ in (4.18) can be rewritten as: $\mathcal{I} = \sum g_1(D_i)$, where function $g_1(x) = x^{-2(m+3)}$. It is assumed that the furthest O-BS is a away from the UE and the interfering O-BS is not closer than the desired O-BS which is r_0 away from the UE. As shown in Figure 4.11, r_i is within the range of $[r_0, a]$. Since the interfering O-BSs are uniformly distributed, then the PDF of r_i can be found as:

$$f_{r_i}(r_i) = \frac{2r_i}{a^2 - r_0^2}, \;\; r_0 \leq r_i \leq a. \tag{4.31}$$

Then the PDF of D_i can be calculated using the PDF transformation rule from (4.31) as:

$$f_{D_i}(D_i) = \frac{2D_i}{a^2 - r_0^2}, \;\; \sqrt{r_0^2 + \Delta z^2} \leq D_i \leq \sqrt{a^2 + \Delta z^2}. \tag{4.32}$$

The conditional CF of $\mathcal{I}$ is defined as $\varphi_{\mathcal{I}_a}(\omega|r_0) = \mathbb{E}\left[\mathrm{e}^{j\omega\mathcal{I}_a}\right]$. Since the number of interfering O-BSs N_i is a non-negative integer random variable, $\varphi_{\mathcal{I}_a}(\omega|r_0)$ can be extended as:

$$\varphi_{\mathcal{I}_a}(\omega|r_0) = \mathbb{E}_{N_i}\left[\mathbb{E}\left[\mathrm{e}^{j\omega\mathcal{I}_a}|N_i = n\right]\right]. \tag{4.33}$$

Since each D_i in $\mathcal{I}$ is independent of each other, $\varphi_{\mathcal{I}_a}(\omega)$ conditioned on N_i can be factorised

as follows:

$$\mathbb{E}\left[\mathrm{e}^{j\omega\mathcal{I}_a}|N_i=n\right]=\prod_{i=1}^{n}\mathbb{E}\left[\mathrm{e}^{j\omega g_1(D_i)}\right]=\left(\int_{\sqrt{r_0^2+\Delta z^2}}^{\sqrt{a^2+\Delta z^2}}\frac{2D\mathrm{e}^{j\omega g_1(D)}}{a^2-r_0^2}\mathrm{d}D\right)^n. \tag{4.34}$$

Because N_i follows a Poisson distribution with a mean of $\frac{\Lambda}{\kappa_{\mathrm{rf}}}$, the corresponding probability mass function of N_i can be written as follows:

$$\mathbb{P}[N_i=n]=\frac{\mathrm{e}^{-\frac{\Lambda\pi}{\kappa_{\mathrm{rf}}}\left(a^2-r_0^2\right)}\left(\frac{\Lambda\pi}{\kappa_{\mathrm{rf}}}\left(a^2-r_0^2\right)\right)^n}{n!}. \tag{4.35}$$

Next, equation (4.33) can be extended as:

$$\begin{aligned}\varphi_{\mathcal{I}_a}(\omega|r_0)&=\sum_{n=0}^{\infty}\mathbb{P}[N_i=n]\mathbb{E}\left[\mathrm{e}^{j\omega\mathcal{I}_a}|N_i=n\right]\\&=\mathrm{e}^{-\frac{\Lambda\pi}{\kappa_{\mathrm{rf}}}\left(a^2-r_0^2\right)}\sum_{n=0}^{\infty}\frac{1}{n!}\left(\frac{\Lambda\pi}{\kappa_{\mathrm{rf}}}\int_{\sqrt{r_0^2+\Delta z^2}}^{\sqrt{a^2+\Delta z^2}}2D\mathrm{e}^{j\omega g_1(D)}\mathrm{d}D\right)^n\\&\overset{(a)}{=}\mathrm{e}^{-\frac{\Lambda\pi}{\kappa_{\mathrm{rf}}}\left(a^2-r_0^2-\int_{\sqrt{r_0^2+\Delta z^2}}^{\sqrt{a^2+\Delta z^2}}2D\mathrm{e}^{j\omega g_1(D)}\mathrm{d}D\right)},\end{aligned} \tag{4.36}$$

where (a) uses the Taylor series for e^x. By limiting $a\to\infty$, the CF can be calculated as follows:

$$\varphi_{\mathcal{I}}(\omega|r_0)=\exp\left(\sum_{n=1}^{\infty}\frac{(j\omega)^n}{n!}\cdot\frac{\Lambda\pi\left(r_0^2+\Delta z^2\right)^{1-n(m+3)}}{\kappa_{\mathrm{rf}}(n(m+3)-1)}\right). \tag{4.37}$$

The proof for (4.37) is provided in Appendix D. Theoretically, (4.37) can be converted to the corresponding PDF. However, this operation is intractable. Therefore, an alternative approximation approach is used to obtain the PDF of the CCI. The cumulant generating function respect to $\mathcal{I}$ can be written as:

$$\ln\left(\varphi_{\mathcal{I}}(\omega)\right)=\sum_{n=1}^{\infty}\kappa_n^{\mathcal{I}}\frac{(j\omega)^n}{n!}. \tag{4.38}$$

By comparing (4.38) and (4.37), the n^{th} cumulant of $\mathcal{I}$ conditioning on r_0 can be found as:

$$\kappa_n^{\mathcal{I}}=\frac{\Lambda\pi\left(r_0^2+\Delta z^2\right)^{1-n(m+3)}}{\kappa_{\mathrm{rf}}(n(m+3)-1)}. \tag{4.39}$$

With all cumulants known, the corresponding n^{th} raw moment can be calculated recursively by

the following set of equations:

$$\mu_n = \begin{cases} 1 & : n = 0 \\ \kappa_1 & : n = 1 \\ \kappa_n + \sum\limits_{l=1}^{n-1} \begin{pmatrix} n-1 \\ l-1 \end{pmatrix} \kappa_l \mu_{n-l} & : n \geq 2 \end{cases}. \tag{4.40}$$

With all moments of the CCI power distribution known, an expansion of the PDF as a sum of Gamma densities proposed in [91] can be used. This expansion is based on the Gram-Charlier series and Laguerre polynomials. The Gamma density used in this expansion is $f_V(v) = \frac{v^{\alpha-1}\mathrm{e}^{-v}}{\Gamma(\alpha)}$ for a random variable V. The expansion of the PDF is given as [91]:

$$f_V(v) = \frac{v^{\alpha-1}\mathrm{e}^{-v}}{\Gamma(\alpha)} \sum_{n=0}^{\infty} \mathcal{A}_n \mathcal{L}_n^{\alpha}(v), \tag{4.41}$$

where the Laguerre polynomial $\mathcal{L}_n^{\alpha}(v)$ can be calculated as:

$$\begin{aligned} \mathcal{L}_n^{\alpha}(v) &= (-1)^n v^{1-\alpha} \mathrm{e}^{v} \frac{\mathrm{d}^n}{\mathrm{d}v^n} \left(v^{n+\alpha-1} \mathrm{e}^{-v} \right) \\ &= \sum_{l=0}^{n} \begin{pmatrix} n \\ l \end{pmatrix} (-1)^{n-l} v^l S_l^n, \end{aligned} \tag{4.42}$$

where l is a non-negative integer, and

$$S_l^n = \begin{cases} 1 & : l > n-1 \\ \prod_{\iota=l}^{n-1} (\alpha + \iota) & : l \leq n-1 \end{cases}. \tag{4.43}$$

The coefficients $\mathcal{A}_n$ in (4.41) can be calculated using the following expression:

$$\begin{aligned} \mathcal{A}_n &= \frac{\Gamma(\alpha)}{n!\Gamma(\alpha+n)} \int_0^{\infty} f_V(v) \mathcal{L}_n^{\alpha}(v) \mathrm{d}v \\ &= \frac{(-1)^n \Gamma(\alpha)}{n!\Gamma(\alpha+n)} \sum_{l=0}^{n} \begin{pmatrix} n \\ l \end{pmatrix} (-1)^l S_l^n \int_0^{\infty} v^l f_V(v) \mathrm{d}v \\ &= \frac{(-1)^n \Gamma(\alpha)}{n!\Gamma(\alpha+n)} \sum_{l=0}^{n} \begin{pmatrix} n \\ l \end{pmatrix} (-1)^l S_l^n \mu_l^V. \end{aligned} \tag{4.44}$$

The expansion (4.41) requires the random variable V to have its mean and variance equal to α

as:

$$\mathbb{E}[V] = \sigma_V^2 = \alpha. \tag{4.45}$$

Therefore, the CCI random variable $\mathcal{I}$ has to be scaled to satisfy the condition in (4.45). So $V = \beta\mathcal{I}$ is defined, where β is the scaling factor. Then the cumulants and moments of V should follow:

$$\kappa_n^V = \beta^n \kappa_n^{\mathcal{I}}, \tag{4.46}$$

$$\mu_n^V = \beta^n \mu_n^{\mathcal{I}}. \tag{4.47}$$

Note that $\kappa_1^{\mathcal{I}}$ and $\kappa_2^{\mathcal{I}}$ equal to the mean and variance of $\mathcal{I}$, respectively. Then the mean and variance of V should be $\beta\kappa_1^{\mathcal{I}}$ and $\beta^2\kappa_2^{\mathcal{I}}$, respectively. The value of α and β can be calculated in conjunction with (4.39) and (4.45) as:

$$\beta = \frac{(2m+5)\left(r_0^2 + \Delta z^2\right)^{m+3}}{m+2}, \tag{4.48}$$

$$\alpha = \beta\kappa_1^{\mathcal{I}} = \beta^2\kappa_2^{\mathcal{I}} = \frac{\Lambda\pi(2m+5)\left(r_0^2 + \Delta z^2\right)}{\kappa_{\mathrm{rf}}(m+2)^2}. \tag{4.49}$$

By substituting $\beta\mathcal{I}$ for V in (4.41) and rearrangement, the conditional PDF $f_{\mathcal{I}}(\mathcal{I}|r_0)$ can be determined as follows:

$$f_{\mathcal{I}}(\mathcal{I}|r_0) = \sum_{n=0}^{\infty}\left(\sum_{l_1=0}^{n}\frac{\beta^\alpha C_{l_1}^n \mu_{l_1}^{\mathcal{I}}}{n!\Gamma(\alpha+n)}\right)\left(\sum_{l_2=0}^{n}\frac{C_{l_2}^n \mathcal{I}^{l_2+\alpha-1}}{\mathrm{e}^{\beta\mathcal{I}}}\right), \tag{4.50}$$

where

$$C_l^n = \begin{pmatrix} n \\ l \end{pmatrix}(-1)^{n-l}\beta^l S_l^n. \tag{4.51}$$

Next, the probability

$$\begin{aligned}\mathbb{P}\left[\mathcal{I} > \tilde{\mathcal{I}}|r_0\right] &= \int_{\tilde{\mathcal{I}}}^{\infty} f_{\mathcal{I}}(\mathcal{I}|r_0)\mathrm{d}\mathcal{I} \\ &= \sum_{n=0}^{\infty}\left(\sum_{l_1=0}^{n}\frac{\beta^\alpha C_{l_1}^n \mu_{l_1}^{\mathcal{I}}}{n!\Gamma(\alpha+n)}\right)\left(\sum_{l_2=0}^{n}\frac{C_{l_2}^n}{\beta^{l_2+\alpha}}\Gamma\left(l_2+\alpha, \beta\tilde{\mathcal{I}}\right)\right),\end{aligned} \tag{4.52}$$

where $\Gamma(u_1, u_2) = \int_{u_2}^{\infty} \mathrm{e}^{-v} v^{u_1-1} \mathrm{d}v$ is the upper incomplete Gamma function; and

$$\tilde{\mathcal{I}} = \frac{\rho^2 \mathcal{X}\left(\frac{1}{T} - \frac{\sigma_{\text{clip}}^2}{\rho^2 \xi^2}\right) - \mathcal{Z}(k)}{\rho^2 + \sigma_{\text{clip}}^2}. \tag{4.53}$$

Because r_0 equals to the distance between the UE (origin) and the serving O-BS (closest node to origin), the PDF of r_0 with node density of Λ should be $f_{r_0}(r_0, \Lambda) = 2\pi\Lambda r_0 \mathrm{e}^{-\Lambda\pi r_0^2}$ in a PPP [92]. Then, the final SINR CDF can be calculated by combining (4.52) with (4.23) and averaging $\mathbb{P}[\gamma(k) < T | r_0]$ over r_0 as:

$$\begin{aligned}\mathbb{P}[\gamma(k) < T] &= \int_0^{\infty} f_{r_0}(r_0, \Lambda) \mathbb{P}[\gamma(k) < T | r_0] \mathrm{d}r_0 \\ &= \int_0^{\infty} \frac{2\pi\Lambda r_0}{\mathrm{e}^{\pi\Lambda r_0^2}} \sum_{n=0}^{\infty} \left(\sum_{l_1=0}^{n} \frac{\beta^{\alpha} C_{l_1}^n \mu_{l_1}^{\mathcal{I}}}{n! \Gamma(\alpha + n)} \right) \left(\sum_{l_2=0}^{n} \frac{C_{l_2}^n \Gamma\left(l_2 + \alpha, \beta\tilde{\mathcal{I}}\right)}{\beta^{l_2+\alpha}} \right) \mathrm{d}r_0. \end{aligned} \tag{4.54}$$

Note that there is a summation with an upper bound of infinity in (4.54) which makes the calculation intractable. Therefore, the infinity upper bound of the summation is replaced by a finite integer number $\mathfrak{N}$. With the increase of $\mathfrak{N}$, equation (4.54) quickly converges to the case of $\mathfrak{N} = \infty$. When calculating the results, $\mathfrak{N} = 10$ is found to be sufficient to provide accurate analytical results. With this approach, (4.54) can be solved using standard numerical methods.

4.5.4 SINR Statistics Results and Discussions

Figure 4.12 shows the SINRs statistics in terms of CDF achieved by different system setups considering HEX and PPP cell deployments. The SINR at DC is shown as an example, and the SINR at other frequencies decreases with an increase of frequency due to the low-pass effect of the front-end elements. The values shown in Table 4.1 are used if the system parameter is not specified for each setup, where the configuration of F_{s} and F_{fe} are in accordance with the setup in [66]. It can be found that the numerical results calculated using (4.30) and (4.54) agree with the corresponding Monte Carlo simulation in the region of interests.

In setup 1, $R = 2.5$ m, $\phi_{1/2} = 40^{\circ}$ and $\kappa_{\text{rf}} = 1$. The results for both the HEX and the PPP networks are shown. It can be observed that with the same system configuration, a PPP network performs worse than a HEX network. In addition, the considered background light level is 100 lux in illuminance. Therefore, the O-BSs operate with their full power to provide enough illumination. The highest SINR of above 30 dB shows that the noise at the receiver side

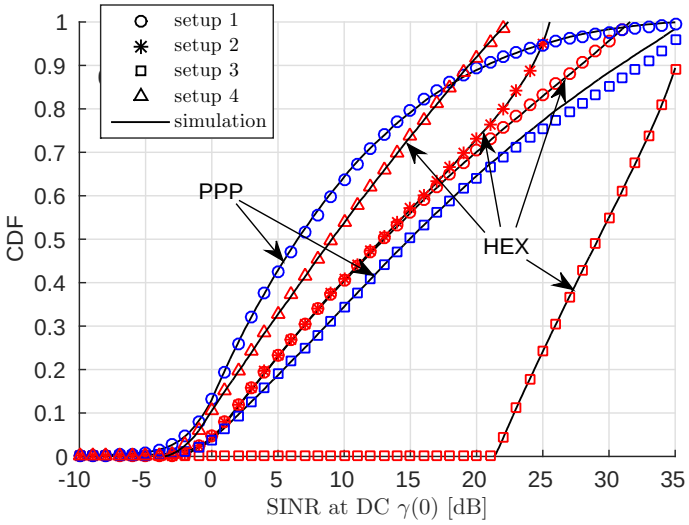

Figure 4.12: *The CDF of the SINR at DC. Setup 1:* $R = 2.5$ *m,* $\phi_{1/2} = 40°$, $\kappa_{\text{rf}} = 1$, 100% *output. Setup 2: same as setup 1 except* $\Delta\epsilon = 5$. *Setup 3:* $R = 3$ *m,* $\phi_{1/2} = 50°$, $\kappa_{\text{rf}} = 3$, 100% *output. Setup 4: same as setup 1 except* 15% *output and* 1000 *lux ambient light illuminance. Other parameters are listed in Table 4.1 if they are not specified.*

causes little effect to the system performance. In setup 2, the signal amplitude range is modified to 5. This results in a more serious signal clipping distortion. Consequently, the highest SINR in this system is limited by the clipping noise. In setup 3, $R = 3$ m, $\phi_{1/2} = 50°$, $\kappa_{\text{rf}} = 3$. Other parameters are the same as setup 1. The high reuse factor leads to a lower level of CCI and the overall SINR level improved significantly compared with that of setup 1. Therefore, the corresponding SINR is improved compared to the case of setup 1 for both HEX and PPP networks. Setup 4 considers a special case with sufficient illumination from ambient light with an illuminance of 1000 lux. Thus, the O-BS works in a dimmed mode with only 15% of its normal output. Due to the reduced signal power and increased noise level, the overall SNR level is decreased to a range of -3 dB to 22 dB. This demonstrates that the system will work in strong background light conditions, and even in dimmed mode.

4.6 Downlink Cell Data Rate and Outage Probability

In this section, the average cell data rate and outage probability are calculated and analysed. Since the information about the per subcarrier SINR and its statistics is known, different modu-

lation and coding schemes can be assigned to each subcarrier adaptively according to the value of $\gamma(k)$. The average achievable data rate in a LAC can be calculated using:

$$\begin{aligned} s &= \frac{1}{\kappa_{\mathrm{rf}}} \sum_{k=1}^{\tilde{K}} \sum_{n=1}^{N} W_{\mathrm{sc}} \varepsilon_n \mathbb{P}\left[T_n < \gamma\left(\tilde{k}\right) < T_{n+1}\right] \\ &= \frac{F_{\mathrm{s}}}{\kappa_{\mathrm{rf}} K} \sum_{k=1}^{\tilde{K}} \sum_{n=1}^{N} \varepsilon_n \left(\mathbb{P}\left[\gamma\left(\tilde{k}\right) < T_{n+1}\right] - \mathbb{P}\left[\gamma\left(\tilde{k}\right) < T_n\right]\right), \end{aligned} \tag{4.55}$$

where W_{sc} is the bandwidth on each subcarrier. In the case of DCO-OFDM, $\tilde{K} = \frac{K}{2} - 1$ and $\tilde{k} = k$. In the case of asymmetrically clipped optical orthogonal frequency division multiplexing (ACO-OFDM), $\tilde{K} = \frac{K}{4}$ and $\tilde{k} = 2k - 1$. The two AMC schemes listed in Table 4.2 are used here.

Outage probability is defined as the probability that the received signal SINRs on all subcarriers are below the lowest SINR requirement for an AMC scheme. Since we know that the value of $\gamma(1)$ is the highest compared with the SINR on the remaining subcarriers, the outage probability can be calculated as:

$$\mathcal{P}_{\mathrm{out}} = \mathbb{P}[\gamma(1) < T_{\mathrm{out}}]. \tag{4.56}$$

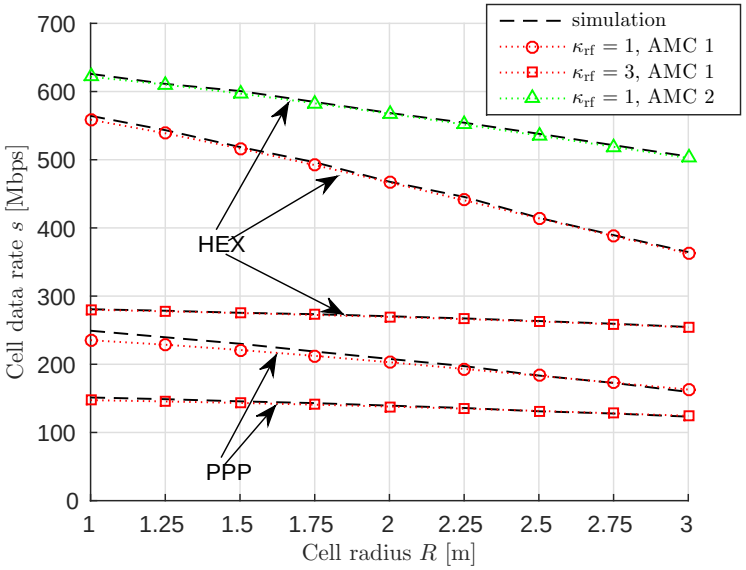

Figure 4.13: *Achievable cell data rate against cell radius R. The emission order m is configured based on* (4.14)*. Other system parameters are listed in Table 4.1 if not specified.*

Next, the accuracy of the cell data rate calculation is evaluated, and the cell data rate / outage probability performance of a LAC network is analysed. The results with DCO-OFDM are presented as examples as this modulation scheme offers higher spectral efficiency. The results include the systems with the HEX / PPP network model and the system with reuse factor of $\kappa_{\mathrm{rf}} = 1$ and $\kappa_{\mathrm{rf}} = 3$. The cell radius R and the modulation bandwidth F_{s} are considered as the variables for study. Figure 4.13 shows the cell data rate against the cell radius R. As shown in Section 4.5.4, a network operating with full transmission power from O-BSs will not be limited by noise. Therefore, according to the analysis in Section 4.3.3, the emission order m is configured based on (4.14) to achieve a better performance. A cell edge UE optical power drop factor $\sigma_{\mathrm{P}} = 20$ dB is used, which has been justified in Section 4.3.3. Other system parameters are the same as those listed in Table 4.1 if they are not specified. For all of the systems, the Monte Carlo simulation results show close agreement with the analytical calculations, which prove the accuracy of (4.55). As expected, a HEX network system performs better than a PPP network system with the same remaining system configuration. The cell data rate generally decreases with the increase of R. This is because a system with a smaller cell has a higher value of m according to (4.14), which introduces less CCI to nearby O-BSs. Firstly, the system using AMC scheme 1 is considered. With the same cell deployment, the system with $\kappa_{\mathrm{rf}} = 1$ always achieves a higher data rate than the system with $\kappa_{\mathrm{rf}} = 3$. In the case of HEX cell deployment,

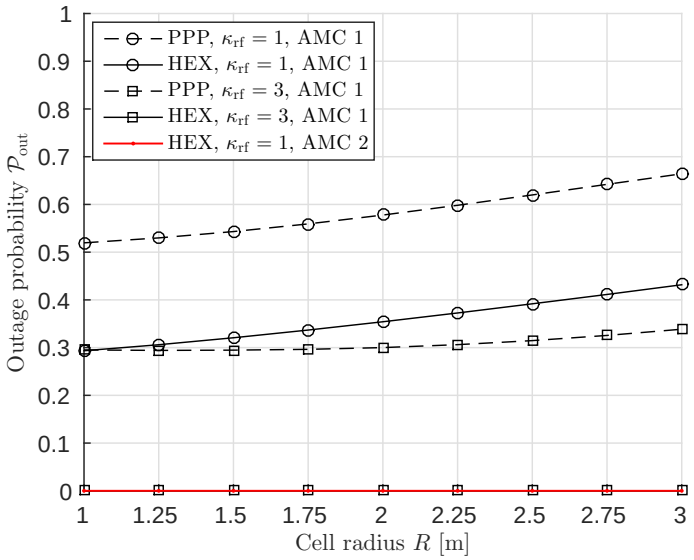

Figure 4.14: *Outage probability against cell radius R. The emission order m is configured based on* (4.14)*. Other system parameters are listed in Table 4.1 if not specified.*

the $\kappa_{\mathrm{rf}} = 1$ system achieves 40% to 100% more data rate than the $\kappa_{\mathrm{rf}} = 3$ system. However, the $\kappa_{\mathrm{rf}} = 1$ system always has a much higher outage probability than the $\kappa_{\mathrm{rf}} = 3$ system as shown in Figure 4.14. For example, in the case of the HEX cell deployment, the $\kappa_{\mathrm{rf}} = 1$ system has an outage probability of about 30% – 45%. In contrast, the $\kappa_{\mathrm{rf}} = 3$ system has an outage probability of zero. In Section 4.5, it has been demonstrated that a $\kappa_{\mathrm{rf}} = 1$ system with an appropriate configuration, the minimum SINR can be kept above -5 dB. Therefore, using AMC scheme 2 in a HEX network, the zero outage probability can be achieved even with $\kappa_{\mathrm{rf}} = 1$. In addition, the cell data rate is further improved by 60 to 140 Mbps.

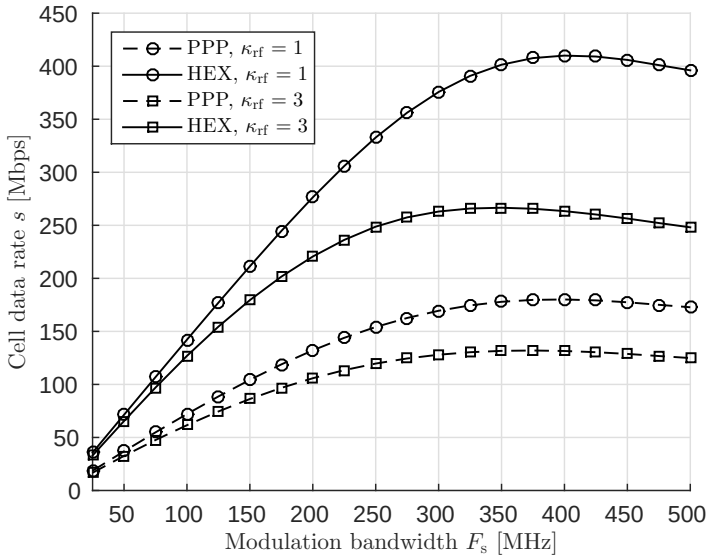

Figure 4.15: *Achievable cell data rate against modulation bandwidth F_{s} with $R = 2.5$ m, $\phi_{1/2} = 40^{\circ}$ and AMC scheme 1. Other parameters are listed in Table 4.1 if they are not specified.*

The relationship between cell data rate / outage probability and the modulation bandwidth is examined, as shown in Figure 4.15 and Figure 4.16. A cell radius of $R = 2.5$ m, a half-power semi-angle of $\phi_{1/2} = 40^{\circ}$ and AMC scheme 1 are used in this system. Other system parameters are the same as those listed in Table 4.1 if they are not specified. With an increase of the modulation bandwidth F_{s}, the cell data rate increases when modulation bandwidth is low. This is because the more bandwidth that the system uses, the higher the data rate that the system can achieve. However, when the modulation bandwidth increases further, the channel quality on the high frequency subcarriers becomes worse. Meanwhile, the total transmission power is spread to a wider frequency band. Thus the signal power on each subcarrier decreases.

Consequently, the increasing speed of the cell data rate with modulation bandwidth becomes slower. In addition, with a further increase of modulation bandwidth, the SINR of the cell edge UE becomes below the threshold for reliable transmission. Consequently, the outage probability also increases with the bandwidth increase, as shown in Figure 4.16. When the modulation bandwidth is far beyond the 3-dB bandwidth, too much signal power is wasted on the subcarriers that are subject to unfavourable channel conditions with the degradation of the signal quality on the subcarriers which exhibit good channel conditions. Consequently, the cell data rate starts to decrease.

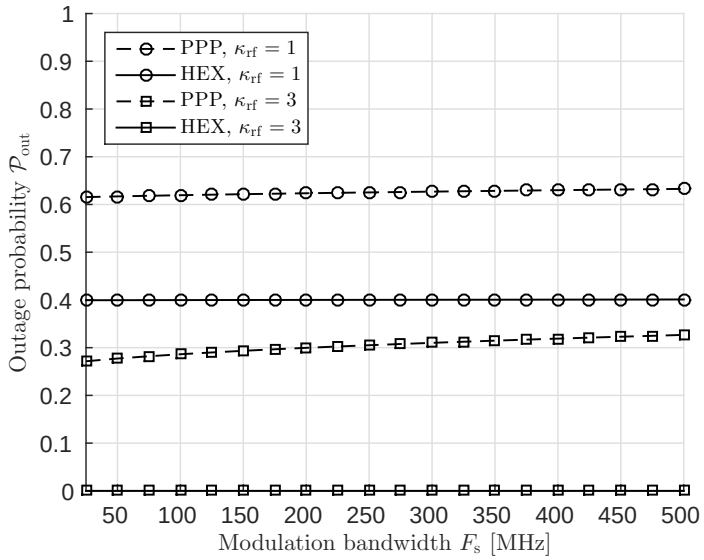

Figure 4.16: *Outage probability against modulation bandwidth $F_{\rm s}$ with $R = 2.5$ m, $\phi_{1/2} = 40^\circ$ and AMC scheme 1. Other parameters are listed in Table 4.1 if they are not specified.*

4.7 LiFi Attocell Network versus Other Small-cell Networks

In this subsection, the performance of LAC networks are compared to those achieved by RF femtocell networks and millimetre wave (mmWave) indoor networks. A LAC network achieves a high communication performance due to its extremely dense spatial reuse ($R \in [1, 3]$ m). Compared with RF femtocell systems, LAC networks have a relatively large license-free modulation bandwidth (100 MHz to $>$ 1 GHz) availability. In contrast, a femtocell has a relatively larger cell size ($R_{\rm femto} \in [10, 40]$ m) and a limited downlink bandwidth of about 10 MHz [93].

The modulation bandwidth of an indoor mmWave system, such as 60 GHz wireless personal area network (WPAN), is generally in the range of 500 MHz to > 2 GHz, which is typically wider than that used by LAC networks. Therefore, a data rate of up to 7 Gbps achieved by a mmWave system for a single link has been validated by simulations [94], while the maximum data rate that has been achieved by a single LED source is about 3 Gbps [30], which can be further improved with the development of high-speed front-end elements. One of the motivations of using mmWave spectrum for indoor wireless communication is using walls between adjacent rooms to attenuate the mmWave signal, thereby avoiding significant CCI. In other words, installing multiple mmWave APs in the same room for dense spatial reuse is unlikely due to CCI issue. Consequently, the coverage area of each mmWave AP is equal to the room area. In contrast, multiple O-BSs (luminaries) can be installed in a single room. This means the coverage area of each LiFi AP is a fraction of the room area. Due to the differences in downlink capability per AP and in coverage area per AP, a normalised metric termed area data rate is used for comparing the performance of LAC, mmWave and femtocell networks. Area data rate is defined as:

$$s_{\text{area}} = \frac{s}{A_{\text{cell}}}, \tag{4.57}$$

which determines the ratio of downlink data rate per cell to the coverage area per cell. Since different type of small-cell networks have different amount of available modulation bandwidth, the area data rate is estimated with various modulation bandwidth F_{s}.

Figure 4.17 shows the area data rate performance of different systems. The results of the femtocell systems and mmWave systems are extrapolated from [93, 95–97] and [94, 98, 99], respectively. In these publications, many networks with different performances have been presented. Some of the networks are optimised with dense spatial reuse and various interference mitigation / resource allocation techniques, while others with worst case performance are used as comparison benchmarks. Among these available data, the information of the best case performance and of the worst case performance is collected for comparison as these extreme values can indicate the range of the performance that different small-cell networks can achieved. However, the information of area data rate is not directly available in the literature, but can be estimated based on other provided data. In order to calculate the area data rate with any possible modulation bandwidth, area spectral efficiency (ASE) of the system should be estimated. In some publications, the information about the average spectral efficiency and the cell radius is available. Thus, the ASE can be estimated by the ratio of average spectral efficiency to the cell coverage

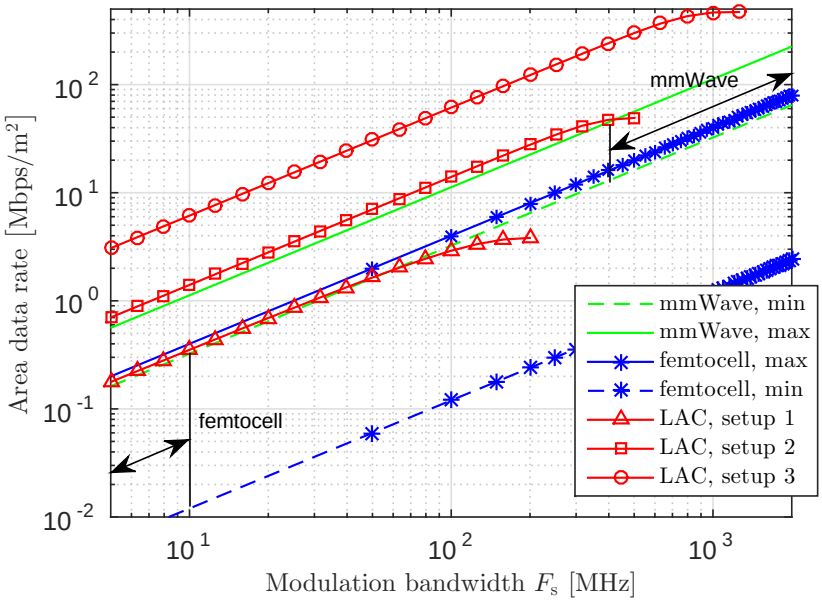

Figure 4.17: *Area data rate comparison among LAC networks, RF femtocell networks and mmWave networks. The configuration of the LAC downlink systems are listed in Table 4.3. The remaining parameters are specified in Table 4.1.*

area. In some other publications, spectral efficiency is not provided, but the cell data rate and the used bandwidth is given, which can also be used to estimate the spectral efficiency. However, the information about the coverage area is not provided in some mmWave publications. In this case, a room of size $10\ \mathrm{m} \times 10\ \mathrm{m}$ (coverage area per cell) is assumed. A coverage area smaller than this size is not considered as it is unlikely to have a massive number of users in a small room. High data density will be pointless if the network is lightly loaded.

As shown in Figure 4.17, the ASE achieved by the femtocell network is generally in the range from 0.03 to 0.0012 bps/Hz/m^2. With a bandwidth of 10 MHz, the area data rate achieved by femtocell networks is in the range from 0.012 to 0.3 Mbps/m^2. The spectral efficiency achieved by the mmWave system is generally in the range from 3.24 to 11.25 bps/Hz. Considering a room of size $10\ \mathrm{m} \times 10\ \mathrm{m}$, with a bandwidth in the range of 400 MHz to 2 GHz, the achievable area data rate is in the range of 13 to 225 Mbps/m^2.

The downlink area data rate of three LAC systems are also presented in Figure 4.17. The corresponding configurations are listed in Table 4.3. The remaining parameters are configured according to Table 4.1. In setup 1, a low performance LAC system with unregulated cell plan-

Parameter	Cell deployment	F_{fe}	$\phi_{1/2}$	R	κ_{rf}	AMC scheme
Setup 1	PPP	15.2 MHz	40°	2.5 m	3	1
Setup 2	HEX	31.7 MHz	30°	2 m	1	2
Setup 3	HEX	81.5 MHz	15°	1 m	1	2

Table 4.3: *Configuration of LAC downlink systems in the comparison with other small-cell networks.*

ning is considered. The low speed front-end element parameter $F_{\text{fe}} = 15.2$ MHz corresponds to the results presented in [56]. Figure 4.17 shows that the performance of the LAC system with setup 1 is within the femtocell performance range. It is worth noting that the maximum achievable data rate of 3.82 Mbps/m^2 with a bandwidth of 200 MHz in LAC system setup 1 is much higher than those achieved by the femtocells with a bandwidth of 10 MHz. Also note that the performances of the systems using different bandwidth are compared. This is because of the difference in the costs and availability of the two types of frequency bands. For the VLC system, the intensity modulation frequency band is totally unlicensed and does not cause any interference to a system in an adjacent frequency band. Therefore, there is no requirement for spectrum masks or leakages into neighbouring bands used by other systems. In contrast, the RF spectral resources are scarce and hence expensive. In setup 2 and setup 3, two LAC systems with moderate and high performance are demonstrated. The front-end configuration $F_{\text{fe}} = 31.7$ MHz corresponds to the results presented in [66], and the high performance front-end elements $F_{\text{fe}} = 81.5$ MHz corresponds to an experimental measurement of the same system presented in [30] which uses a 50-μm gallium nitride LED. As shown in Figure 4.17, both LAC systems perform better than the femtocell systems. For the LAC system with setup 2, a maximum achievable area data rate of 49 Mbps/m^2 with a modulation bandwidth of 501 MHz can be achieved, which is in the range that a mmWave system can achieve. In particular, a maximum area data rate of 469 Mbps/m^2 is achieved by the system with setup 3 with a modulation bandwidth of 1.26 GHz. This is about 2 times higher than the high performance mmWave system with a spectral efficiency of 11.25 bps/Hz and a bandwidth of 2 GHz. This result highlights the huge potential of LAC networks in terms of downlink data density, which is extremely useful when the user density is very high and the network is heavily loaded.

4.8 Summary

In this chapter, the downlink performance of LAC networks was evaluated. In order to optimally design a LAC system, it is important to understand how key network parameters such as cell size and network deployments affect the system performance. An analysis of the SINR distribution and the corresponding data rate assuming different cell deployments was performed. The analysis in this chapter offers an accurate estimation of the downlink performance of a LAC system that is subject to a large number of parameters. This study provides detailed guidelines for appropriate configurations of these parameters. Because of the potential benefits of combining LAC networks with existing lighting infrastructures and due to other practical constraints, optimised regular HEX cell deployments may not be always achievable. Therefore, in this study, several other network topologies such as square and random cell deployments were also considered. In particular, a LAC network with PPP cell deployment was considered to closely model a random scenario where there are no underlying network planning considerations. The extensive simulation study confirms that the HEX and PPP cell deployments represent the best and the worst case performance of practical LAC deployments, respectively. The simulation results also demonstrate that the LAC networks deployed in a finite room offer better performance than the networks which are horizontally infinite because the CCI in the room edges is very low. In addition, the simulation results also imply that in the downlink analysis of a LAC network, the omission of NLoS channel components causes little error in the evaluation of the system performance. Because LACs can be deployed densely in a room, the LAC networks can typically achieve very high data rate density. In order to demonstrate this advantage, the downlink performance of LAC systems is compared with that achieved by RF femtocell networks and indoor mmWave systems in terms of area data rate. The result shows that the LAC networks generally outperform the femtocell network. In particular, a high performance LAC network can achieve an area data rate of 469 Mbps/m^2 which is twice as that achieved by a high performance mmWave system. The high performance mmWave system uses a spectral efficiency of 11.25 bps/Hz and a bandwidth of 2 GHz in a room of size $10\ \mathrm{m} \times 10\ \mathrm{m}$.

Chapter 5
Interference Mitigation Techniques in LiFi Attocell Networks

5.1 Introduction

In order to maximise the spectral efficiency of the downlink system in a light fidelity attocell (LAC) network, a short reuse distance is preferred. Because of this short reuse distance, the downlink connections in adjacent cells using the same transmission resources interfere with each other. This is known as co-channel interference (CCI). Consequently, it causes high outage probability and low data rate, especially for cell edge user equipments (UEs). Comparing to the CCI level in the RF cellular systems, the CCI introduced in LAC networks is lower, which is implied in the results presented in Chapter 4. However, in the case of using dense spatial reuse, CCI still poses a major impairment to the downlink performance of LAC networks relative to the impairment caused by other factors.

Therefore, interference mitigation techniques are required to alleviate the effects of CCI in the downlink of LAC systems. Many researchers have studied interference mitigation techniques in optical wireless communication (OWC) systems. In [19], the use of static resource partitioning was proposed to avoid CCI in a cellular optical wireless system. This technique assigns different sub-bands to neighbouring cells to avoid CCI. In [100], an optical femtocell system was proposed, which uses transmission with different wavelengths in adjacent cells to avoid CCI. The methods used in these two studies effectively mitigate the impairment of CCI. However, this technique significantly reduces the available bandwidth in each cell and restricts the achievable peak data rates of the downlink system [101]. In [41], a self-organising interference coordination based on the busy-burst signalling technique was proposed to be used in an optical wireless cellular system in an aircraft cabin environment. This method offers improvements both in cell edge user performance and in average spectral efficiency, but it requires a considerable overhead for the transmission of channel state information (CSI).

Another interference mitigation method, termed fractional frequency reuse (FFR), strikes a reasonable trade-off among the overall spectral efficiency, the cell-edge user performance and the

system complexity [102]. Over the past few years, the FFR technique has been studied for applications in RF cellular networks. The FFR scheme does not require precise instantaneous CSI and is of low computational complexity. There are two typical FFR schemes: i) strict fractional frequency reuse (sFFR) and ii) soft frequency reuse (SFR) [103]. sFFR divides the whole frequency band into multiple protected sub-bands and one common sub-band. Cell centre UEs in each cell experience minor interference from nearby base stations (BSs), so the common sub-band is assigned to them. Since cell edge UEs receive higher interference power, protected sub-bands are assigned to the cell edge UEs, and the sub-bands are arranged such that there is a minimum spatial reuse distance between them. The SFR applies an even shorter reuse distance compared to the sFFR scheme. In addition to the use of a different sub-band for cell edge UEs in each adjacent cell, the SFR scheme allows the centre UEs to take the sub-bands that are assigned to cell edge UEs in adjacent cells. To protect the cell edge UEs, the transmission power for cell edge UEs is typically higher than that for the transmission for cell centre UEs. In [104], an optical access point (AP) using two LED sources with different beam-width is considered. A VLC cellular system using a SFR scheme based on such an AP is proposed. The corresponding bit error rate (BER) performance and the effect of changing LED beam-width is evaluated. In this chapter, a first analytical framework for the evaluation of FFR in a LAC network is presented. In the analysis, the effect of user density is considered. In addition, angular diversity transmitter (ADT) is considered in conjunction with FFR to further improve the downlink performance in a LAC network.

In addition to the FFR techniques, the concept of coordinated multi-point joint transmission (JT) technique [105] can also be adapted to LAC networks to mitigate CCI. In a JT system, a UE can be served by multiple nearby BSs, thereby improving the acquired signal quality. Since this approach substitutes interference signals with desired signals, the received signal-to-interference-plus-noise ratio (SINR) can be significantly improved, especially for the cell-edge UEs. However, many challenges such as backhaul constraints, accurate synchronisation and multi-path fading effects limit the performance of JT systems. In a LAC system, due to the special features of intensity modulation and direct detection (IM/DD) [13], it is possible to overcome these difficulties. The authors in [106] demonstrate that it is possible to achieve a multi-point cooperative transmission scheme in a single user VLC system in a small indoor environment with improved optical power gain and reduced BER. In this study, JT is adapted to the downlink transmission in a LAC network in order to mitigate CCI and improve the cell-edge user performance in terms of received SINR and system throughput.

The remainder of this chapter is organised as follows: The application of FFR in the downlink of LAC systems is presented Section 5.2. It includes the introduction of the considered FFR schemes, the analysis of SINR statistics and spectral efficiency, and the combination of FFR and ADT. The application of JT in conjunction with ADT is presented in Section 5.3, which includes the characteristics of JT scheme in a LAC network, and the corresponding simulation results. Finally, the key points in this chapter are summarised in Section 5.4.

5.2 Fractional Frequency Reuse

In a LAC system with FFR, the serving optical base station (O-BS) needs to know whether the UE is in the cell centre or is in the cell edge. This can be simply realised by determining the average signal strength of the downlink pilot signal. If the pilot signal power is higher than a threshold, it is categorised as a cell centre UE. Otherwise, it is categorised as a cell edge UE. The movement of UEs within the period between two adjacent pilot signal transmissions is assumed to be negligible. In addition, a FFR scheme is based on a specified multiple access scheme. According to the analysis in Section 2.2.4, the potential multiple access scheme for LAC networks could be time-division multiple access (TDMA) or orthogonal frequency division multiple access (OFDMA) if optical-orthogonal frequency division multiplexing (O-OFDM) is used. FFR can be used in both multiple access schemes. If TDMA is used, the sub-band is divided in time. If OFDMA is used, the sub-band is divided by grouping part of the available subcarriers. In this study, FFR based on OFDMA is considered as an example.

5.2.1 Fractional Frequency Reuse Schemes

The first considered FFR is the sFFR scheme, which divides the whole frequency band to three protected sub-bands and an individual common sub-band as shown in Figure 5.1 (a). The number of subcarriers of each sub-band is set to be proportional to the area of the central or edge regions, which offers good fairness and optimal performance [103]. The common sub-band is reused by the centre UEs in each cell. As shown in Figure 5.1 (a), one of the three protected sub-bands is assigned to the edge UEs of each cell. This assignment also ensures that the same protected sub-band is not reused in adjacent cells. Therefore, the number of subcarriers assigned to the cell centre UEs K_{c} and the number of subcarriers assigned to the cell edge UEs K_{e} are given as:

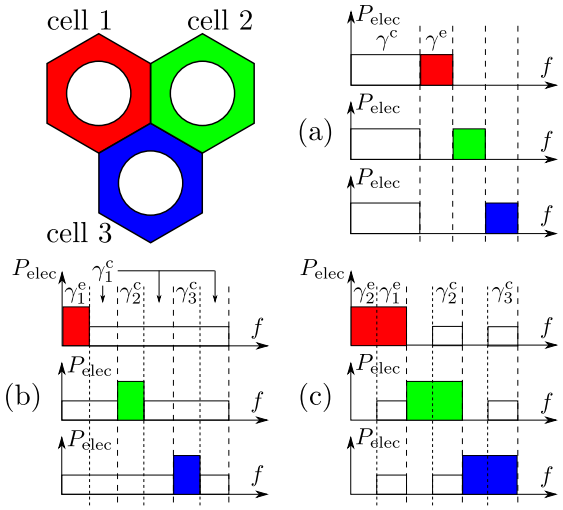

Figure 5.1: *(a) Strict fractional frequency reuse (b) Soft frequency reuse with $\varrho^2 > \frac{2}{3}$ (c) Soft frequency reuse with $\varrho^2 < \frac{2}{3}$*

$$K_{\text{c}} = \left\lceil \tilde{K}\varrho^2 \right\rceil, \tag{5.1}$$

$$K_{\text{e}} = \left\lfloor (\tilde{K} - K_{\text{c}})/3 \right\rfloor, \tag{5.2}$$

where ϱ denotes a parameter determines the size of cell central and edge area, and $\tilde{K}$ is the number of subcarriers carrying information. With a total number of K subcarriers in the O-OFDM system, the number of information carriers can be calculated as $\tilde{K} = \frac{K}{2\xi^2}$. ξ denotes a power scaling factor in the OFDM frame, which is introduced in Section 2.6.1 in Chapter 2. In the frequency plan, subcarriers in each sub-band are equally distributed to the UEs in the corresponding coverage region for simplicity and user fairness.

In the SFR scheme, the protected sub-bands for cell edge UEs are also reused in adjacent cells. In order to guarantee the performance of the cell edge UEs, the transmission power for the cell edge UE is increased with a gain of ς. In addition, the different groups of subcarriers are assigned to edge UEs in adjacent cells. Similar to the sFFR scheme, for fairness, the number of subcarriers assigned to different user groups is proportional to the area of the corresponding coverage region. Therefore, the following frequency plan is used:

$$K_{\text{c}} = \left\lceil \tilde{K}\varrho^2 \right\rceil, \tag{5.3}$$

$$K_{\text{e}} = \min\left(\left\lceil \tilde{K}/3 \right\rceil, \tilde{K} - K_{\text{c}} \right), \tag{5.4}$$

which is shown in Figure 5.1 (b) and (c). Note that the maximum available bandwidth for edge

UEs is $\tilde{K}/3$ to ensure the orthogonality of the protected sub-bands.

5.2.2 Signal-to-Interference-Plus-Noise Ratio Statistics and Spectral Efficiency

In this subsection, the downlink SINR statistics and the system spectral efficiency in the LAC systems with FFR are considered. Since interference mitigation techniques are considered in this chapter, the impairment of CCI should be the primary issue of concern, and the effects of other form of distortions can be simplified or omitted as long as it is reasonable to do so.

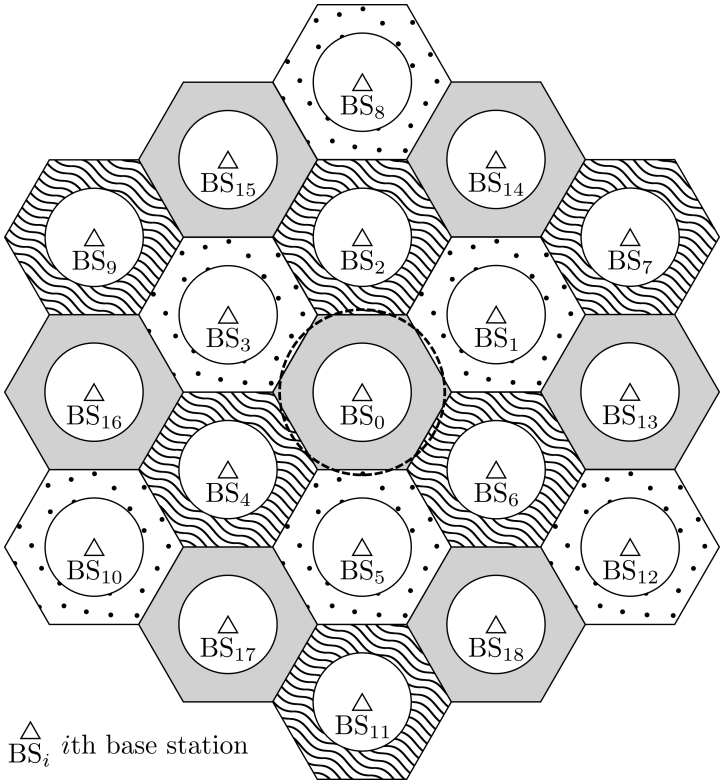

Figure 5.2: *2-layer LAC network model with 19 cells and FFR schemes. The patterns in the edge regions of every cell demonstrate the frequency reuse pattern for the FFR schemes, and the corresponding reuse factor is 3.*

5.2.2.1 System Models

Firstly, the effects of non-line-of-sight (NLoS) channel components are omitted in this chapter. This is because the omission of NLoS channel causes negligible error in the evaluation of downlink data rate, which has been demonstrated in Section 4.2.1 of Chapter 4. Secondly, a LAC system with an optimised hexagonal (HEX) cell deployment is considered in this study.

The analysis based on point process based cell deployments are also possible [102], and it will be the subject of future research. In addition, the analysis is based on a network extending infinitely in the horizontal directions as it offers the worst case performance and leads to reduction in analysis complexity. This has been demonstrated in Section 4.2.2 of Chapter 4.

Similar to the case in Section 4.5.2 of Chapter 4, a 2-layer HEX network is considered in this study, and the performance of the UEs in the central cell is evaluated. Higher layer O-BSs are omitted as they causes little CCI with a very long signal propagation distance to the central cell. In the 2-layer network model, the coverage area of each cell is divided into a cell central area and a cell edge area as shown in Figure 5.2. In order to further simplify the analysis, a circular cell approximation is applied to the considered central cell as shown in Figure 5.3. The radius of the HEX cell is defined as $\tilde{R}$. The approximated circular cell has the same coverage area as the original HEX cell. Therefore, the equivalent radius of the circular cell is defined as $R_{\mathrm{e}} \approx 0.91\tilde{R}$. In the system using FFR, the radius of the central area is defined as R_{c}. The parameter ϱ is defined as $\varrho = \frac{R_{\mathrm{c}}}{R_{\mathrm{e}}}$. For the convenience of the following analysis in this section, the indices of the 18 nearby O-BSs are grouped into three sets based on the reuse pattern shown in Figure 5.2. They include $\mathit{И}_{\mathrm{A}} = \{13, 14, 15, 16, 17, 18\}$, $\mathit{И}_{\mathrm{B}} = \{2, 4, 6, 7, 9, 11\}$ and $\mathit{И}_{\mathrm{C}} = \{1, 3, 5, 8, 10, 12\}$. Note that the edge UEs in the 0^{th} cell reuse the same spectral resources as those in $\mathit{И}_{\mathrm{A}}$ in the FFR systems.

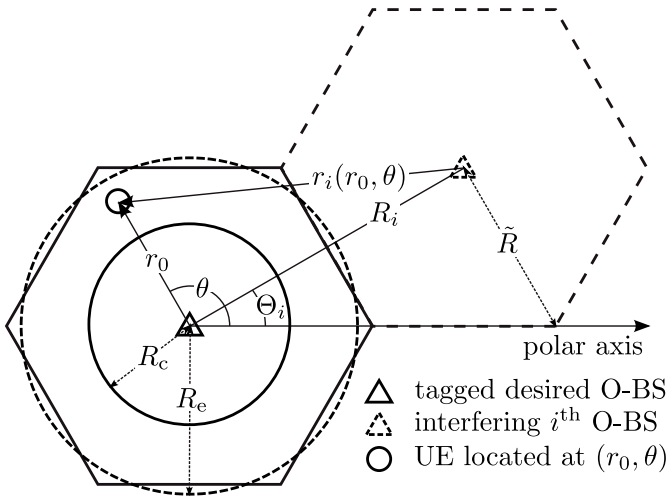

Figure 5.3: *Geometric model with polar coordinates in a LAC network with FFR schemes.*

The location of a UE and interfering O-BSs are defined using a two dimensional (2-D) polar coordinate system, which is similar to the case in Section 4.5.2 of Chapter 4. The origin of the coordinates is placed at the location of the centre of the central cell. The orientation of

the polar axis is shown in Figure 5.3. The location of a UE in the central cell is defined by (r_0, θ), where r_0 is the horizontal separation between the UE and the origin which has a range of $r_0 \in [0, R_{\mathrm{e}}]$, and θ is the polar angle corresponding to the location of the UE which has a range of $\theta \in [0, 2\pi)$. The location of the i^{th} O-BS is defined in a similar way as (R_i, Θ_i), where R_i is the horizontal separation between the i^{th} O-BS and the origin, and Θ_i is the polar angle of i^{th} O-BS. Since the network deployment and the cell radius $\tilde{R}$ are given, the values of (R_i, Θ_i) are fixed and can be readily calculated. In order to estimate the signal power from i^{th} O-BS to the observed UE, the horizontal separation between i^{th} O-BS and the UE at (r_0, θ) is essential, which is defined as $r_i(r_0, \theta)$. Since the positions of the origin, the observed UE and the i^{th} O-BS form a regular triangle in the case of $i \neq 0$, $r_i(r_0, \theta)$ can be calculated using the rule of cosine as:

$$r_i(r_0, \theta) = \sqrt{r_0^2 + R_i^2 - 2R_i r_0 \cos(\theta - \Theta_i)}. \tag{5.5}$$

The simplified SINR expression and the corresponding assumptions in Section 4.5.1 of Chapter 4 are used here. According to the analysis in Chapter 2 Section 2.7, the effects of clipping distortion can be omitted as long as the used signal amplitude range $\Delta\epsilon$ is wide enough. Thus, a clipping attenuation of $\eta_{\mathrm{clip}} = 1$ and a clipping noise variance of $\sigma^2_{\mathrm{clip}} = 0$ are assumed. The low-pass channel characteristics caused by front-end elements make the subcarriers with higher frequency offers lower channel gains. This variance of channel gain with frequency causes extra complexity in the division of sub-band in FFR schemes. Therefore, it is assumed that the front-end elements offers a relatively wide 3-dB bandwidth and the modulation bandwidth is relatively narrow. This assumption leads to $\frac{F_{\mathrm{s}}}{F_{\mathrm{fe}}} \to 0$, and the exponential term in $\mathcal{Z}(k)$ can be considered to have a value of one. In other words, a flat frequency response is assumed over the entire modulation frequency range. With the fore-mentioned simplification, the SINR expression (4.18) presented in Section 4.5.1 of Chapter 4 can be rewritten as a function of 2-D location (r_0, θ) as:

$$\gamma(r_0, \theta) = \frac{\xi^2 \left(r_0^2 + \Delta z^2\right)^{-m-3}}{\sum\limits_{i \in \text{И}} \left(r_i^2 + \Delta z^2\right)^{-m-3} + \mathcal{Z}}, \tag{5.6}$$

$$\mathcal{Z} = \frac{4\pi^2 N_0 F_{\mathrm{s}}}{\xi^2 \eta_{\mathrm{pd}}^2 \eta_{\mathrm{led}}^2 \sigma_{\mathrm{x}}^2 A_{\mathrm{pd}}^2 (m+1)^2 \Delta z^{2m+2}}. \tag{5.7}$$

Note that the SINR on each subcarrier is identical if an equal power allocation is applied. Therefore, the variable k in the function (4.18) is removed in the simplified expression.

5.2.2.2 Universal Frequency Reuse

The most straightforward spectral efficient frequency plan is universal frequency reuse (UFR), which reuses the whole frequency band in each cell. With UFR scheme, a reuse factor of $\kappa_{\mathrm{rf}} = 1$ is used. In this study, the LAC downlink system with UFR is used as the benchmark. Since all of the neighbouring O-BSs introduces CCI to the desired UE, expression (5.6) is readily available for the calculation of the downlink SINR with UFR, which is denoted as γ_{UFR}. In the UFR case, the set of interfering O-BSs can be defined as $И = И_{\mathrm{A}} \cup И_{\mathrm{B}} \cup И_{\mathrm{C}}$.

In this study, a semi-analytical method is used to calculate the downlink SINR statistics $\mathbb{P}[\gamma_{\mathrm{UFR}} < T]$, where T is a threshold value. Assuming a specified polar angle of θ, the function of the SINR on a subcarrier is monotonically decreasing with respect to r_0 in the region of interest. Therefore, the conditional probability density function (PDF) of SINR can be calculated by using the PDF transformation rule as:

$$f_{\gamma|\theta}(\hat{\gamma}, f_{r_0|r_0\in\mathrm{K}}(r_0)) = \left.\frac{f_{r_0|r_0\in\mathrm{K}}(r_0)}{\left|\frac{\partial}{\partial r_0}\gamma(r_0,\theta)\right|}\right|_{r_0=\gamma^{-1}(\hat{\gamma}|\theta)}, \tag{5.8}$$

where $f_{r_0|r_0\in\mathrm{K}}(r_0)$ is the PDF of r_0 with a range of r_0 of K; $f_{r_0|r_0\in\mathrm{K}}(r_0)$ is determined by the locations of the considered UEs (cell edge / centre UEs); $\gamma^{-1}(\hat{\gamma}|\theta)$ is the inverse function of the SINR function with respect to r_0 for a given θ, in which $\gamma(r_{\max},\theta) \le \hat{\gamma} \le \gamma(r_{\min},\theta)$. Here, $r_{\max}$ ($r_{\min}$) is the maximum (minimum) of r_0 in its feasible region K. A closed-form solution to $\gamma^{-1}(\hat{\gamma}|\theta)$ is unavailable. Thus, numerical methods are used to compute the function. Then the cumulative density function (CDF) of SINR can then be calculated as follows:

$$\mathbb{P}[\gamma < T] = \int_0^{2\pi}\int_0^{T} f_{\gamma|\theta}(\hat{\gamma}, f_{r_0|r_0\in\mathrm{K}}(r_0))\mathrm{d}\hat{\gamma} f_{\theta}(\theta)\mathrm{d}\theta. \tag{5.9}$$

It is assumed that the spatial location of the UEs in each cell follows a homogeneous Poisson point process (PPP). Therefore, the PDF of θ should follow: $f_{\theta}(\theta) = \frac{1}{2\pi}$.

In the case of the UFR scheme, the statistics in the whole cell is calculated, which leads to a K of $[0, R_{\mathrm{e}}]$. Therefore, the PDF of r_0 is given as:

$$f_{r_0|0\le r_0\le R_{\mathrm{e}}}(r_0) = \frac{2r_0}{R_{\mathrm{e}}^2}. \tag{5.10}$$

In the case of FFR systems, statistics in part of the cell is required. In the calculation of

$\mathbb{P}[\gamma < T | r_0 < R_\mathrm{c}]$ and $\mathbb{P}[\gamma < T | r_0 \geq R_\mathrm{c}]$, the conditional PDF of r_0 should be calculated as:

$$f_{r_0|r_0<R_\mathrm{c}}(r_0) = \frac{f_{r_0|0\leq r_0\leq R_\mathrm{e}}(r_0)}{\mathbb{P}[r_0 < R_\mathrm{c}]}, r_0 \in [0, R_\mathrm{c}], \tag{5.11}$$

$$f_{r_0|r_0\geq R_\mathrm{c}}(r_0) = \frac{f_{r_0|0\leq r_0\leq R_\mathrm{e}}(r_0)}{\mathbb{P}[r_0 \geq R_\mathrm{c}]}, r_0 \in [R_\mathrm{c}, R_\mathrm{e}], \tag{5.12}$$

where $\mathbb{P}[r_0 < R_\mathrm{c}]$ ($\mathbb{P}[r_0 \geq R_\mathrm{c}]$) is the probability that the UE is in the cell central (edge) area. It is shown in [107] that:

$$\mathbb{P}[r_0 < R_\mathrm{c}] = \varrho^2, \tag{5.13}$$

$$\mathbb{P}[r_0 \geq R_\mathrm{c}] = 1 - \varrho^2. \tag{5.14}$$

In this chapter, the Shannon Hartley formula is used to estimate the wireless capacity of the system. This method slightly overestimate the actual achievable spectral efficiency compared with the adaptive bit-loading used in Section 4.2.1 of Chapter 4. However, the relative improvement by using FFR is of concern, which should not vary with the method of spectral efficiency calculation. Therefore, Shannon Hartley formula is selected as it has a lower calculation complexity. In an O-OFDM system, the spectral efficiency of a UE at (r_0, θ) can be calculated by a function of $\gamma(r_0, \theta)$ and κ_rf as:

$$\varepsilon\left(\gamma(r_0, \theta), \kappa_\mathrm{rf}\right) = \frac{1}{2\xi^2\kappa_\mathrm{rf}} \log_2\left(1 + \gamma(r_0, \theta)\right). \tag{5.15}$$

The average spectral efficiency for the UEs in the whole cell can be calculated as:

$$\bar{\varepsilon} = \mathbb{E}[\varepsilon(\gamma(r_0, \theta), \kappa_\mathrm{rf})] = \int_0^{2\pi}\int_0^{R_\mathrm{e}} \varepsilon(\gamma(r_0, \theta), \kappa_\mathrm{rf}) f_{r_0|0\leq r_0\leq R_\mathrm{e}}(r_0)\mathrm{d}r_0 f_\theta(\theta)\mathrm{d}\theta. \tag{5.16}$$

In addition, the average spectral efficiency for the UEs in the cell centre area can be calculated as:

$$\begin{aligned}\bar{\varepsilon}^\mathrm{c} &= \mathbb{E}[\varepsilon(\gamma(r_0, \theta), \kappa_\mathrm{rf}) | r_0 < R_\mathrm{c}], \\ &= \int_0^{2\pi}\int_0^{R_\mathrm{c}} \varepsilon(\gamma(r_0, \theta), \kappa_\mathrm{rf}) f_{r_0|r_0<R_\mathrm{c}}(r_0)\mathrm{d}r_0 f_\theta(\theta)\mathrm{d}\theta.\end{aligned} \tag{5.17}$$

Similarly, in the case of UEs in the cell edge area,

$$\begin{aligned}\bar{\varepsilon}^{\mathrm{e}} &= \mathbb{E}[\varepsilon(\gamma(r_0,\theta),\kappa_{\mathrm{rf}})|r_0 \geq R_{\mathrm{c}}],\\ &= \int_0^{2\pi}\int_{R_{\mathrm{c}}}^{R_{\mathrm{e}}} \varepsilon(\gamma(r_0,\theta),\kappa_{\mathrm{rf}}) f_{r_0|r_0\geq R_{\mathrm{c}}}(r_0)\mathrm{d}r_0 f_\theta(\theta)\mathrm{d}\theta. \end{aligned} \tag{5.18}$$

In the case of UFR scheme, we have $\kappa_{\mathrm{rf}} = 1$. By using (5.16), the corresponding average spectral efficiency can be calculated as:

$$\bar{\varepsilon}_{\mathrm{UFR}} = \mathbb{E}[\varepsilon(\gamma_{\mathrm{UFR}}(r_0,\theta),1)]. \tag{5.19}$$

For comparison purpose, the cell edge UE spectral efficiency in the case of UFR scheme can be calculated as:

$$\bar{\varepsilon}^{\mathrm{e}}_{\mathrm{UFR}} = \mathbb{E}[\varepsilon(\gamma_{\mathrm{UFR}}(r_0,\theta),1)|r_0 \geq R_{\mathrm{c}}]. \tag{5.20}$$

5.2.2.3 Strict Fractional Frequency Reuse

In a sFFR system, the SINR at (r_0,θ) on a subcarrier in the common sub-band can be written as:

$$\gamma^{\mathrm{c}}(r_0,\theta) = \frac{\xi^2\left(r_0^2+\Delta z^2\right)^{-m-3}}{\sum\limits_{i\in \mathit{И}}\left(r_i^2(r_0,\theta)+\Delta z^2\right)^{-m-3} + \frac{1+2\varrho^2}{3}\mathcal{Z}}. \tag{5.21}$$

According to the frequency plan defined in Section 5.2.1, the SINR on a subcarrier in protected sub-bands $\gamma^{\mathrm{e}}(r_0,\theta)$ can also be calculated using (5.21) except for substituting $\mathit{И}_{\mathrm{A}}$ for $\mathit{И}$. The factor $\frac{1+2\varrho^2}{3}$ of $\mathcal{Z}$ is due to the change of the number of used subcarriers in sFFR compared to the case of the UFR system. Since a fixed amount of available electrical power and an equal power distribution on each subcarrier are assumed, varying the number of used subcarriers causes change in the available power for the transmission on each subcarrier.

When determining the distribution of SINR for a sFFR system, both cases of a UE in the cell central area and a UE in the cell edge area need to be considered. The overall CDF of the SINR can be calculated as:

$$\begin{aligned}\mathbb{P}[\gamma_{\mathrm{sFFR}} < T] &= \mathbb{P}[r_0 < R_{\mathrm{c}}]\mathbb{P}[\gamma^{\mathrm{c}} < T | r_0 < R_{\mathrm{c}}]\\ &\quad + \mathbb{P}[r_0 \geq R_{\mathrm{c}}]\mathbb{P}[\gamma^{\mathrm{e}} < T | r_0 \geq R_{\mathrm{c}}],\end{aligned} \tag{5.22}$$

where $\mathbb{P}[\gamma^{\mathrm{c}} < T | r_0 < R_{\mathrm{c}}]$ and $\mathbb{P}[\gamma^{\mathrm{e}} < T | r_0 \geq R_{\mathrm{c}}]$ are the CDF of the SINR with the conditions that the user is in the cell centre using common sub-band and is in the cell edge using protected sub-band, respectively. They can be calculated using the same method as that described in Section 5.2.2.2.

Since the average spectral efficiency varies in different sub-bands, the overall average spectral efficiency should be the average over the whole frequency band. When there are users in both the cell central area and the cell edge area, the overall average spectral efficiency can be calculated as [107]:

$$\bar{\varepsilon}_{\mathrm{sFFR,nor}} = \zeta^{\mathrm{c}} \bar{\varepsilon}^{\mathrm{c}} + \zeta^{\mathrm{e}} \bar{\varepsilon}^{\mathrm{e}}, \tag{5.23}$$

where $\bar{\varepsilon}^{\mathrm{c}}$ ($\bar{\varepsilon}^{\mathrm{e}}$) is the average spectral efficiency for the users taking the common (protected) sub-band for transmission; ζ^{c} and ζ^{e} are the averaging weights for $\bar{\varepsilon}^{\mathrm{c}}$ and $\bar{\varepsilon}^{\mathrm{e}}$, respectively. The averaging weight ζ of an average spectral efficiency $\bar{\varepsilon}$ is calculated as:

$$\zeta = \frac{\kappa_{\mathrm{rf}} K_{\bar{\varepsilon}}}{\tilde{K}}, \tag{5.24}$$

where $K_{\bar{\varepsilon}}$ refers to the number of subcarriers on which achieve an average spectral efficiency of $\bar{\varepsilon}$. All ζ for FFR can be simply derived according to the FFR frequency reuse schemes described in Section 5.2.1. Since all of the averaging weights ζ follow the same rule as (5.24), and the derivations of each ζ is long but very simple, it would be unnecessary to list all of the derivations of ζs. Instead, only the final results are listed. In the case of sFFR here, ζ^{c} and ζ^{e} can be found as $\zeta^{\mathrm{c}} \cong \varrho^2$ and $\zeta^{\mathrm{e}} \cong 1 - \varrho^2$, respectively [107].

The cell centre UEs use the common sub-band with $\kappa_{\mathrm{rf}} = 1$, while the cell edge UEs use the protected sub-band with $\kappa_{\mathrm{rf}} = 3$. Therefore, in conjunction with (5.17) and (5.18), $\bar{\varepsilon}^{\mathrm{c}}$ and $\bar{\varepsilon}^{\mathrm{e}}$ in sFFR case can be calculated as:

$$\bar{\varepsilon}^{\mathrm{c}} = \mathbb{E}[\varepsilon(\gamma^{\mathrm{c}}(r_0, \theta), 1) | r_0 < R_{\mathrm{c}}], \tag{5.25}$$

$$\bar{\varepsilon}^{\mathrm{e}} = \mathbb{E}[\varepsilon(\gamma^{\mathrm{e}}(r_0, \theta), 3) | r_0 \geq R_{\mathrm{c}}]. \tag{5.26}$$

A LAC network is a small-cell cellular network in which each O-BS serves several UEs and these UEs are fewer than those in a normal RF cell. Consequently, the problem of an uneven load in different cells is more critical in a LAC network. In some extreme cases, there may be no UE in a cell when the user density is very low. The use of the FFR technique makes this

issue even worse. Since the cell coverage area is divided into centre and edge areas, which are smaller compared with the total cell coverage area, the chance that no active user is present in a specified region (a cell centre or a cell edge area) will be much higher. Consequently, in the case of no UE present in a specified area, the corresponding assigned sub-band remains idle, which is a waste of transmission resources. Therefore, the case of no UE present in the cell central or edge area needs to be considered. Since the common sub-band is restricted to the cell edge users, for the case that there is no UE in the central area, the common sub-band is wasted and $\zeta^{\mathrm{c}} = 0$. Therefore, the corresponding average spectral efficiency is only $\zeta^{\mathrm{e}}\bar{\varepsilon}^{\mathrm{e}}$. For the same reason, when there is no UE present in the cell edge area, the average spectral efficiency is only $\zeta^{\mathrm{c}}\bar{\varepsilon}^{\mathrm{c}}$. Thus, the final average spectral efficiency achieved by a sFFR system can be calculated as:

$$\bar{\varepsilon}_{\mathrm{sFFR}} = \mathcal{P}_{\mathrm{c}}\zeta^{\mathrm{c}}\bar{\varepsilon}^{\mathrm{c}} + \mathcal{P}_{\mathrm{e}}\zeta^{\mathrm{e}}\bar{\varepsilon}^{\mathrm{e}} + (1 - \mathcal{P}_{\mathrm{c}} - \mathcal{P}_{\mathrm{e}})\bar{\varepsilon}_{\mathrm{sFFR,nor}}, \tag{5.27}$$

where $\mathcal{P}_{\mathrm{c}}$ ($\mathcal{P}_{\mathrm{e}}$) denotes the probability that all of the observed UEs fall into the cell centre (edge) area. It is assumed that the UE spatial distribution follows a PPP with a user density of χ. By limiting the UEs in a specified area of A, the average number of UEs within this area is $A\chi$. According to the probability mass function (PMF) of the Poisson distribution, the probability that no UE in this area is given as:

$$\mathcal{P}_0 = \mathrm{e}^{-A\chi}. \tag{5.28}$$

The area of a cell can be found as $A_{\mathrm{cell}} = \pi R_{\mathrm{e}}^2$ according to the geometry shown in Figure 5.3. Then, the cell central area and the cell edge area are $A_{\mathrm{cell}}\varrho^2$ and $A_{\mathrm{cell}}\left(1 - \varrho^2\right)$, respectively. Therefore, $\mathcal{P}_{\mathrm{c}}$ and $\mathcal{P}_{\mathrm{e}}$ can be calculated as:

$$\mathcal{P}_{\mathrm{c}} = \mathrm{e}^{-A_{\mathrm{cell}}\left(1-\varrho^2\right)\chi}, \tag{5.29}$$

$$\mathcal{P}_{\mathrm{e}} = \mathrm{e}^{-A_{\mathrm{cell}}\varrho^2\chi}. \tag{5.30}$$

Since the cell edge UEs only use the protected sub-band for transmission, the cell edge spectral efficiency for sFFR can be calculated using (5.26).

5.2.2.4 Soft Frequency Reuse

In a SFR system, due to the more complex SFR frequency reuse scheme, there are five conditions in the SFR system SINR calculation. In order to efficiently present these SINR expres-

sions, a function is defined as follows:

$$\mathcal{F}_{\gamma}(p_0,p_1,p_2,p_3,r_0,\theta)=\frac{p_0\xi^2\left(r_0^2+\Delta z^2\right)^{-m-3}}{\mathcal{I}_{\mathrm{SFR}}(p_1,p_2,p_3,r_0,\theta)+\left(\varsigma\left(1-\max\left(\varrho^2,\frac{2}{3}\right)\right)+\varrho^2\right)\mathcal{Z}}, \quad (5.31)$$

where p_0, p_1, p_2, p_2 are the power control factors which equals ς or 1 or 0, and

$$\begin{aligned}\mathcal{I}_{\mathrm{SFR}}(p_1,p_2,p_2,r_0,\theta)=&\,p_1\sum_{i\in И_{\mathrm{A}}}\left(r_i^2(r_0,\theta)+\Delta z^2\right)^{-m-3}\\&+p_2\sum_{i\in И_{\mathrm{B}}}\left(r_i^2(r_0,\theta)+\Delta z^2\right)^{-m-3}+p_3\sum_{i\in И_{\mathrm{C}}}\left(r_i^2(r_0,\theta)+\Delta z^2\right)^{-m-3}. \quad (5.32)\end{aligned}$$

According to the five cases shown in Figure 5.1 (b) and (c), the corresponding SINR in each cases can be calculated as follows: $\gamma_1^{\mathrm{e}}(r_0,\theta)=\mathcal{F}_{\gamma}(\varsigma,\varsigma,1,1,r_0,\theta)$, $\gamma_2^{\mathrm{e}}(r_0,\theta)=\mathcal{F}_{\gamma}(\varsigma,\varsigma,0,0,r_0,\theta)$, $\gamma_1^{\mathrm{c}}(r_0,\theta)=\mathcal{F}_{\gamma}(1,1,1,1,r_0,\theta)$, $\gamma_2^{\mathrm{c}}(r_0,\theta)=\mathcal{F}_{\gamma}(1,1,\varsigma,1,r_0,\theta)$ and $\gamma_3^{\mathrm{c}}(r_0,\theta)=\mathcal{F}_{\gamma}(1,1,1,\varsigma,r_0,\theta)$. According to the frequency plan described in Section 5.2.2.4 and (5.24), the corresponding averaging weights for average spectral efficiency with each case are calculated as:

$$\zeta_1^{\mathrm{e}}=\zeta_2^{\mathrm{c}}=\zeta_3^{\mathrm{c}}\cong\frac{2}{3}-\max\left(\varrho^2,\frac{2}{3}\right)+\frac{1}{2}\min\left(\varrho^2,\frac{2}{3}\right), \quad (5.33)$$

$$\zeta_2^{\mathrm{e}}\cong 1-\frac{3}{2}\min\left(\varrho^2,\frac{2}{3}\right)\text{ and }\zeta_1^{\mathrm{c}}\cong 3\max\left(\varrho^2,\frac{2}{3}\right)-2. \quad (5.34)$$

Similar to the case of sFFR, $\mathcal{Z}$ is multiplied by a scaling factor to compensate for the change in transmission power on each subcarrier.

The SINR CDF of a SFR system can be calculated by:

$$\begin{aligned}\mathbb{P}[\gamma_{\mathrm{SFR}}<T]=&\mathbb{P}[r_0<R_{\mathrm{c}}]\mathbb{P}[\gamma_{\mathrm{SFR}}<T|r_0<R_{\mathrm{c}}]\\&+\mathbb{P}[r_0\geq R_{\mathrm{c}}]\mathbb{P}[\gamma_{\mathrm{SFR}}<T|r_0\geq R_{\mathrm{c}}]. \quad (5.35)\end{aligned}$$

According to the resource plan described in Section 5.2.1, it is noted that a UE in a SFR system receives the signal on multiple subcarriers with different SINR. To simplify the calculation, the SINR experienced by a UE in a SFR system is defined as follows: the UE randomly selects one of the available subcarriers for transmission, and the SINR experienced on the selected subcarrier is $\tilde{\gamma}$. In (5.35), the cell edge UE SINR distribution $\mathbb{P}[\gamma_{\mathrm{SFR}}<T|r_0\geq R_{\mathrm{c}}]$ can be

calculated as:

$$\mathbb{P}[\gamma_{\mathrm{SFR}} < T | r \geq R_{\mathrm{c}}] = \mathbb{P}[\tilde{\gamma} = \gamma_1^{\mathrm{e}}]\mathbb{P}[\gamma_1^{\mathrm{e}} < T | r \geq R_{\mathrm{c}}] + \mathbb{P}[\tilde{\gamma} = \gamma_2^{\mathrm{e}}]\mathbb{P}[\gamma_2^{\mathrm{e}} < T | r \geq R_{\mathrm{c}}], \tag{5.36}$$

where $\mathbb{P}[\tilde{\gamma} = \gamma]$ refers to the probability that the subcarrier with a SINR of γ is selected. $\mathbb{P}[\tilde{\gamma} = \gamma_1^{\mathrm{e}}]$ and $\mathbb{P}[\tilde{\gamma} = \gamma_2^{\mathrm{e}}]$ can be calculated as:

$$\mathbb{P}[\tilde{\gamma} = \gamma_1^{\mathrm{e}}] = \frac{\zeta_1^{\mathrm{e}}}{\zeta_1^{\mathrm{e}} + \zeta_2^{\mathrm{e}}/3} = \frac{3}{2}\min\left(\varrho^2, \frac{2}{3}\right), \tag{5.37}$$

$$\mathbb{P}[\tilde{\gamma} = \gamma_2^{\mathrm{e}}] = 1 - \mathbb{P}[\tilde{\gamma} = \gamma_1^{\mathrm{e}}] = 1 - \frac{3}{2}\min\left(\varrho^2, \frac{2}{3}\right). \tag{5.38}$$

Similarly, the centre UE SINR CDF $\mathbb{P}[\gamma_{\mathrm{SFR}} < T | r < R_{\mathrm{c}}]$ can be calculated as:

$$\mathbb{P}[\gamma_{\mathrm{SFR}} < T | r < R_{\mathrm{c}}] = \mathbb{P}[\tilde{\gamma} = \gamma_1^{\mathrm{c}}]\mathbb{P}[\gamma_1^{\mathrm{c}} < T | r < R_{\mathrm{c}}] + \mathbb{P}[\tilde{\gamma} = \gamma_2^{\mathrm{c}}]\mathbb{P}[\gamma_2^{\mathrm{c}} < T | r < R_{\mathrm{c}}] + \mathbb{P}[\tilde{\gamma} = \gamma_3^{\mathrm{c}}]\mathbb{P}[\gamma_3^{\mathrm{c}} < T | r < R_{\mathrm{c}}], \tag{5.39}$$

where

$$\mathbb{P}[\tilde{\gamma} = \gamma_1^{\mathrm{c}}] = \frac{\zeta_1^{\mathrm{c}}}{\zeta_1^{\mathrm{c}} + \zeta_2^{\mathrm{c}} + \zeta_3^{\mathrm{c}}} = 3 - \frac{2}{\max\left(\varrho^2, \frac{2}{3}\right)}, \tag{5.40}$$

$$\mathbb{P}[\tilde{\gamma} = \gamma_2^{\mathrm{c}}] = \mathbb{P}[\tilde{\gamma} = \gamma_3^{\mathrm{c}}] = \frac{\zeta_2^{\mathrm{c}}}{\zeta_1^{\mathrm{c}} + \zeta_2^{\mathrm{c}} + \zeta_3^{\mathrm{c}}} = \frac{1}{\max\left(\varrho^2, \frac{2}{3}\right)} - 1. \tag{5.41}$$

All the conditional CDF of the SINR in each case can be calculated using the method described in Section 5.2.2.2.

When there are UEs in both the cell central and the cell edge areas, the overall average spectral efficiency of a SFR system can be determined as follows:

$$\bar{\varepsilon}_{\mathrm{SFR,nor}} = \zeta_1^{\mathrm{e}}\bar{\varepsilon}_1^{\mathrm{e}} + \zeta_2^{\mathrm{e}}\bar{\varepsilon}_2^{\mathrm{e}} + \zeta_1^{\mathrm{c}}\bar{\varepsilon}_1^{\mathrm{c}} + \zeta_2^{\mathrm{c}}\bar{\varepsilon}_2^{\mathrm{c}} + \zeta_3^{\mathrm{c}}\bar{\varepsilon}_3^{\mathrm{c}}, \tag{5.42}$$

where $\bar{\varepsilon}_1^{\mathrm{e}}$, $\bar{\varepsilon}_2^{\mathrm{e}}$, $\bar{\varepsilon}_1^{\mathrm{c}}$, $\bar{\varepsilon}_2^{\mathrm{c}}$ and $\bar{\varepsilon}_3^{\mathrm{c}}$ denote the achievable average spectral efficiency corresponding to

γ_1^{e}, γ_2^{e}, γ_1^{c}, γ_2^{c} and γ_3^{c}, respectively. They can be calculated using (5.17) and (5.18) as:

$$\bar{\varepsilon}_1^{\mathrm{e}} = \mathbb{E}[\varepsilon(\gamma_1^{\mathrm{e}}(r_0,\theta),1)|r_0 \geq R_{\mathrm{c}}], \tag{5.43}$$

$$\bar{\varepsilon}_2^{\mathrm{e}} = \mathbb{E}[\varepsilon(\gamma_2^{\mathrm{e}}(r_0,\theta),3)|r_0 \geq R_{\mathrm{c}}], \tag{5.44}$$

$$\bar{\varepsilon}_1^{\mathrm{c}} = \mathbb{E}[\varepsilon(\gamma_1^{\mathrm{c}}(r_0,\theta),1)|r_0 < R_{\mathrm{c}}], \tag{5.45}$$

$$\bar{\varepsilon}_2^{\mathrm{c}} = \mathbb{E}[\varepsilon(\gamma_2^{\mathrm{c}}(r_0,\theta),1)|r_0 < R_{\mathrm{c}}], \tag{5.46}$$

$$\bar{\varepsilon}_3^{\mathrm{c}} = \mathbb{E}[\varepsilon(\gamma_3^{\mathrm{c}}(r_0,\theta),1)|r_0 < R_{\mathrm{c}}]. \tag{5.47}$$

Similar to the sFFR case, the problem of no UE in a specified area needs to be considered. Accounting for no UE in the cell edge and also the cell central area, the final average spectral efficiency of a SFR system can be found as:

$$\begin{aligned}\bar{\varepsilon}_{\mathrm{SFR}} = {} & \mathcal{P}_{\mathrm{c}}(\zeta_1^{\mathrm{c}}\bar{\varepsilon}_1^{\mathrm{c}} + \zeta_2^{\mathrm{c}}\bar{\varepsilon}_2^{\mathrm{c}} + \zeta_3^{\mathrm{c}}\bar{\varepsilon}_3^{\mathrm{c}}) + \mathcal{P}_{\mathrm{e}}(\zeta_1^{\mathrm{e}}\bar{\varepsilon}_1^{\mathrm{e}} + \zeta_2^{\mathrm{e}}\bar{\varepsilon}_2^{\mathrm{e}}) \\ & + (1 - \mathcal{P}_{\mathrm{c}} - \mathcal{P}_{\mathrm{e}})\bar{\varepsilon}_{\mathrm{SFR,nor}}.\end{aligned} \tag{5.48}$$

The cell edge spectral efficiency in a SFR system can be calculated as:

$$\bar{\varepsilon}_{\mathrm{SFR}}^{\mathrm{e}} = \frac{K_{\bar{\varepsilon}_1^{\mathrm{e}}}}{K_{\mathrm{e}}}\bar{\varepsilon}_1^{\mathrm{e}} + \frac{3K_{\bar{\varepsilon}_2^{\mathrm{e}}}}{K_{\mathrm{e}}}\bar{\varepsilon}_2^{\mathrm{e}} = \frac{\zeta_1^{\mathrm{e}}\bar{\varepsilon}_1^{\mathrm{e}} + \zeta_2^{\mathrm{e}}\bar{\varepsilon}_2^{\mathrm{e}}}{1-\varrho^2}. \tag{5.49}$$

Parameters	Symbol	Values
Transmitter height	z_{s}	3 [m]
Transmitter half-power semi-angle	$\phi_{1/2}$	60°
Receiver height	z_{r}	0.85 [m]
Modulation bandwidth	F_{s}	40 [MHz]
DC-bias level	ϵ_{DC}	$0.5\Delta\epsilon$
Signal amplitude range	$\Delta\epsilon$	6
PD responsivity	η_{pd}	0.1 [A/W]
PD physical area	A_{pd}	1 [cm^2]
Number of subcarriers	K	512
Cell centre illuminance from O-BS	$\bar{E}_{\mathrm{v}}$	500 [lux]
Noise power spectral density	N_0	1×10^{-21} [A^2/Hz]

Table 5.1: *LAC system parameters with FFR schemes*

5.2.2.5 Results and Discussions

In the remainder of this section, the downlink performance results of LAC networks with direct-current-biased optical orthogonal frequency division multiplexing (DCO-OFDM) and FFR schemes in terms of SINR statistics, average spectral efficiency and cell edge spectral efficiency are presented. The system parameters of the evaluated systems are listed in Table 5.1. These values are the default settings in the results presented in this section if the parameters are not otherwise specified. A $\phi_{1/2}$ of 60° is reasonable for lighting performance. A photodiode (PD) physical area A_{pd} of 1 cm^2 is the generally acceptable in VLC systems [55, 108]. The 40 MHz modulation bandwidth agrees with the 20 MHz flat bandwidth that is provided by a phosphorescent white light LED with equalisation [71]. A PD responsivity R_{pd} of 0.1 is suitable when the receiver only accepts the blue component of light [108]. According to the analysis in Section 2.7 of Chapter 2, a ϵ_{DC} of $0.5\Delta\epsilon$ and a $\Delta\epsilon$ of 6 leads to a signal-to-clipping noise ratio (SCNR) of 34 dB. This signal clipping configuration is sufficient for the omission of clipping distortion as the achieved SINR in the following results is in the range from -5 dB to 25 dB. A receiver noise PSD of $N_0 = 1 \times 10^{-21}$ A^2/Hz is based on the results presented in [79]. The optical output of the O-BSs are configured based on an illuminance requirement of 500 lux using the method introduced in Section 2.3.1.2 of Chapter 2

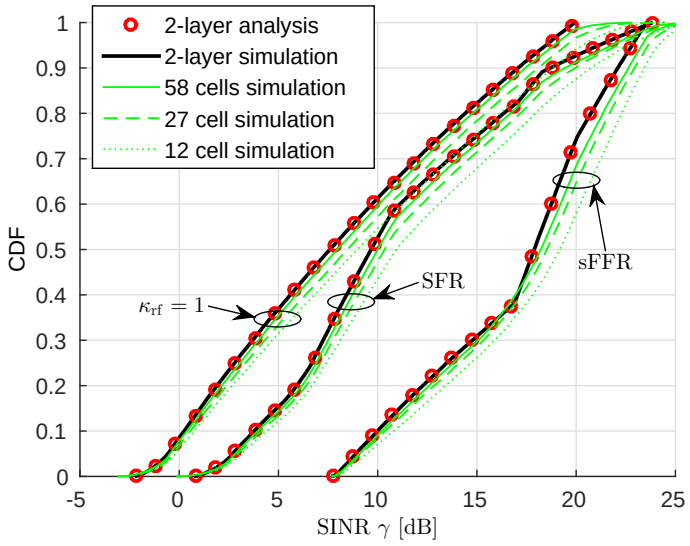

Figure 5.4: *SINR statistics for different reuse schemes. System parameters:* $\tilde{R} = 2.5$ *m,* $\varrho = 0.7$ *and* $\varsigma = 2$*.*

Figure 5.4 shows the results of the SINR statistics based on the 2-layer HEX network with a HEX cell radius of $\tilde{R} = 2.5$ m. In the FFR systems, $\varrho = 0.7$ and $\varsigma = 2$. These results include

the calculation using (5.9), (5.22) and (5.35) using the numerical method, and the corresponding empirical statistics obtained by Monte Carlo simulation. The agreements between the two results validate the mathematics in the analysis. In addition, the simulation results of the systems with networks deployed in a room with finite number of cells are presented to validate the accuracy of the estimation by using a 2-layer network model. As expected, there is an acceptable difference, less than 2 dB, between the results of 2-layer network model and those of the network deployed in a 10.8 m$\times$12.5 m room with 12 cells. However, with an increase of the number of cells, the difference between the curves of the finite networks and that for the 2-layer network diminishes, which agrees with the results of varying network size presented in Section 4.2.2 of Chapter 4. In the case of 58 cells (room size 26 m$\times$30 m), the SINR CDF differences decrease to be in a range between 0.3 dB to 0.7 dB. Note that another source of mismatch is the circular cell approximation of the 0^{th} cell in the 2-layer network model. This mismatch is considered reasonable in many cellular system analysis [107]. Therefore, the performance of the 2-layer network model is a reasonable estimation to the practical LAC system.

As shown in Figure 5.4, the UFR system offers the worst SINR as expected. In contrast, FFR schemes offer the LAC network an improved SINR. The sFFR system and the SFR system show improvements of 9.74 dB and 3.54 dB in terms of minimum SINR (at 10^{th} percentile), respectively. In addition, they also show improvements of 10.3 dB and 2.07 dB in terms of medium SINR, respectively. Note that the bends in the FFR curves are the results of combining different SINR statistics in multiple regions in a cell and in different sub-bands.

Figure 5.5 shows the average spectral efficiency and the cell edge spectral efficiency results with different HEX cell radius $\tilde{R}$. In these results, $\varrho = 0.7$ and $\chi = 1$ UE/m^2. Both the analytical calculation and the simulation are presented. The analytical average spectral efficiencies are calculated using (5.19), (5.27) and (5.48). The analytical cell edge spectral efficiencies are calculated using (5.20), (5.26) and (5.49). The close agreement between analytical calculation and simulation validates the related analysis. With a fixed $\phi_{1/2}$, the increase of cell radius results in a decrease in the interference between UEs in adjacent cells [16]. In other words, a larger cell provides better overall signal quality. In addition, a smaller cell leads to a higher value of $\mathcal{P}_{\text{c}}$ and $\mathcal{P}_{\text{e}}$, which results in loss in average spectral efficiency in FFR systems. Therefore, both the average spectral efficiency and the cell edge spectral efficiency for any reuse scheme is an increasing function of $\tilde{R}$.

Figure 5.6 shows the average spectral efficiency against ϱ. In the results, $\tilde{R} = 2.5$ m, $\chi =$

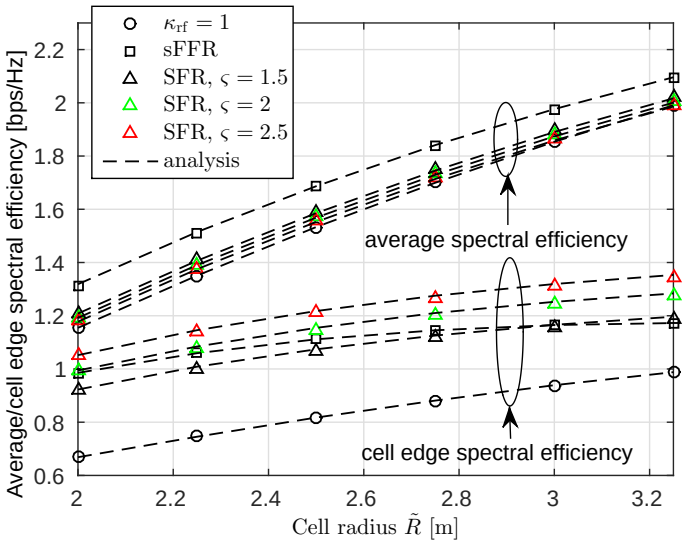

Figure 5.5: *Average spectral efficiency and cell edge spectral efficiency against cell radius $\tilde{R}$. System parameters: $\varrho = 0.7$ and $\chi = 1$ UE/m^2.*

1 UE/m^2 and $\varsigma = 2$ in SFR systems. According to the FFR scheme introduced in Section 5.2.1, the channel assignment is proportional to the corresponding coverage area for FFR systems. When ϱ is too small, the majority of the UEs are cell edge UEs which are assigned a reuse factor of 3, which considerably decreases the spectral efficiency of the system. When ϱ is too large, fewer UEs can be covered by the cell edge area. Consequently, average spectral efficiency decreases significantly due to the increased interference received by the cell centre UEs which are close to the edge of the cell central area ($r_0 \to R_{\rm c}$). In addition, when ϱ is close to 0 or 1, either $\mathcal{P}_{\rm c}$ or $\mathcal{P}_{\rm e}$ is significant, which also causes a decrease in spectral efficiency.

Figure 5.6 also shows the cases with different noise levels. Intuitively, the higher the noise level, the lower the average spectral efficiency for systems with any reuse schemes. In addition, the higher the noise level, the less improvement that can be obtained from the FFR schemes. For example, when considering the improvement of the sFFR scheme with optimal ϱ, the improvement in terms of average spectral efficiency is 15% if there is no receiver noise. However, this improvement decreases to 8% if the noise level is increased to $N_0 = 2 \times 10^{-21}$ A^2/Hz. Furthermore, it is noted that the noise level may affect the optimal configuration of ϱ. When noise is zero, the optimal ϱ for sFFR is around 0.7 and this is in line with [107]. In the case of SFR, the optimal ϱ is around 0.55. However, with the increase in the noise level, optimal ϱs for FFR systems increase to a slightly higher level.

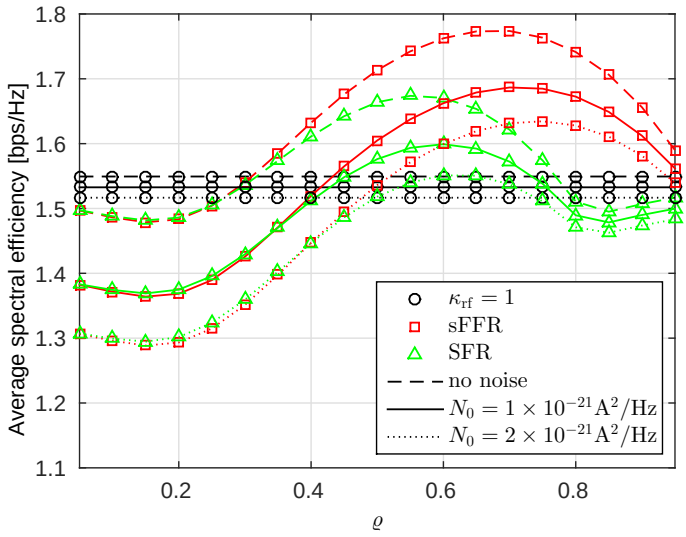

Figure 5.6: *Average spectral efficiency against ϱ. System parameters: $\tilde{R} = 2.5$ m, $\chi = 1$ UE/m^2 and $\varsigma = 2$.*

5.2.2.6 Effects of Active User Density and Proportional Fairness Scheduling

As implied in (5.29) and (5.30), the user density χ is crucial to the value of $\mathcal{P}_{\mathrm{c}}$ and $\mathcal{P}_{\mathrm{e}}$, which may cause a significant effect on the system spectral efficiency. Figure 5.7 shows the effect of user density on the average spectral efficiency of different systems. In the results, $\varrho = 0.7$, $\tilde{R} = 2.5$ m and $\varsigma = 2$ in SFR systems. Both FFR systems show a similar trend with respect to the variations in the χ. Generally, if χ is too small, the average spectral efficiency of FFR systems decreases significantly. For example, in the case of $\chi = 0.1$ UE/m^2, the FFR system exhibits an average spectral efficiency lower than 1 bps/Hz, which is much lower than the benchmark.

In order to solve the issue caused by low user density, proportional fairness scheduling (PFS) [109] is considered in conjunction with the FFR techniques. With a given frequency reuse scheme, there are N_{W} different sub-bands for transmission. The sub-band n_1 has K_{n_1} subcarriers, where $n_1 = 1, 2, \cdots, N_{\mathrm{W}}$. Assuming there are N_{u} UEs, K_{n_1,n_2} subcarriers in sub-band n_1 are assigned to the n_2^{th} UE. Thus $\sum_{n_2=1}^{N_{\mathrm{u}}} K_{n_1,n_2} = K_{n_1}$. Therefore, the data rate achieved by the n_2^{th} UE can be calculated as follows:

$$s_{n_2}\left(K_{1,n_2}, \cdots, K_{N_{\mathrm{W}},n_2}\right) = \sum_{n_1=1}^{N_{\mathrm{W}}} K_{n_1,n_2}\varepsilon_{n_1,n_2}, \tag{5.50}$$

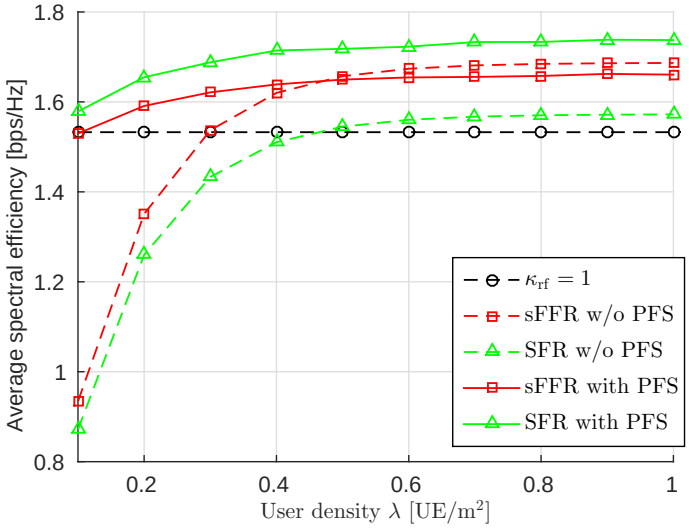

Figure 5.7: *Average spectral efficiency against user density* χ*. System parameters:* $\varrho = 0.7$*,* $\tilde{R} = 2.5$ *m and* $\varsigma = 2$*.*

where ε_{n_1,n_2} is the achievable data rate by UE n_2 on a subcarrier in sub-band n_1. With a given system realisation, UE locations are determined. Therefore, all ε_{n_1,n_2} are fixed for that realisation. In this study, PFS aims at maximising the following objective function:

$$\Xi = \sum_{n_2=1}^{N_\mathrm{u}} \ln\left(s_{n_2}\left(K_{1,n_2}, \cdots, K_{N_\mathrm{W},n_2}\right)\right). \tag{5.51}$$

Conventional per subcarrier PFS requires channel frequency selectivity to converge to a robust solution. However, the assumptions used in this study make the channel gain flat within each sub-band. This causes problems in the convergence of the scheduling solution by using the per subcarrier based PFS. Therefore, an alternative algorithm is used to achieve the same PFS function. The details of this modified PFS is introduced as follows. A scheduling plan matrix is defined as:

$$\mathbf{K} = \begin{bmatrix} K_{1,1} & \cdots & K_{N_\mathrm{W},1} \\ \vdots & \ddots & \vdots \\ K_{1,N_\mathrm{u}} & \cdots & K_{N_\mathrm{W},N_\mathrm{u}} \end{bmatrix},$$

which lists the K_{n_1,n_2} for all UEs in every sub-bands. Based on a specified $\mathbf{K}$, the correspond-

Algorithm 2 : Proportional fairness scheduling

for $n_1 = 1, 2, \cdots, N_{\mathrm{W}}$ **do**
  $K_{n_1,1} = K_{n_1,2} = \cdots = K_{n_1,N_{\mathrm{u}}} = K_{n_1}/N_{\mathrm{u}}$
end for
$\bar{\mathfrak{s}} = \mathfrak{s}\{\mathbf{K}\}$
for $n_1 = 1, 2, \cdots, N_{\mathrm{W}}$ **do**
  $\vec{C} = \left[\frac{\varepsilon_{n_1,1}}{\bar{\mathfrak{s}}_1}, \frac{\varepsilon_{n_1,2}}{\bar{\mathfrak{s}}_2}, \cdots, \frac{\varepsilon_{n_1,N_{\mathrm{u}}}}{\bar{\mathfrak{s}}_{N_{\mathrm{u}}}}\right]$ and $\vec{C}_{n_2} = \frac{\varepsilon_{n_1,n_2}}{\bar{\mathfrak{s}}_{n_2}}$.
  $n_{\max} = \arg\max_{n_2} \vec{C}_{n_2}$ and $n_{\min} = \arg\min_{n_2} \vec{C}_{n_2}$.
  if $K_{n_1,n_{\max}} = K_{n_1}$ **then**
    Exclude $\vec{C}_{n_{\max}}$ from $\vec{C}$ and go back to step 7.
  else
    if $K_{n_1,n_{\min}} = 0$ **then**
      Exclude $\vec{C}_{n_{\min}}$ from $\vec{C}$ and go back to step 7.
    else
      $K_{n_1,n_{\max}} = K_{n_1,n_{\max}} + 1$, $K_{n_1,n_{\min}} = K_{n_1,n_{\min}} - 1$
    end if
  end if
end for
$\bar{\mathfrak{s}} = (1 - \alpha_{\mathrm{pfs}})\bar{\mathfrak{s}} + \alpha_{\mathrm{pfs}}\bar{\mathfrak{s}}\{\mathbf{K}\}$
Iterate from step 6 to step 18 until $\mathbf{K}$ converge.

ing set of user data rates can be calculated as follows:

$$\mathfrak{s}\{\mathbf{K}\} = \begin{bmatrix} s_1(K_{1,1}, \cdots, K_{N_{\mathrm{W}},1}) \\ \vdots \\ s_{N_{\mathrm{u}}}(K_{1,N_{\mathrm{u}}}, \cdots, K_{N_{\mathrm{W}},N_{\mathrm{u}}}) \end{bmatrix}^{\mathrm{T}}.$$

The modified PFS algorithm is listed in Algorithm 2. The α_{pfs} in Algorithm 2 is a forgetting factor for the calculation of average user data rate $\bar{\mathfrak{s}}$. The proof of Algorithm 2 maximising (5.51) is shown in Appendix E.

PFS can achieve a good balance between spectral efficiency and user fairness. More importantly, it can dynamically distribute spectral resources depending on the current load condition. With this benefit of PFS, the sub-band availability constraint can be adjusted as follows: the whole sub-band assigned to a cell is available to any active UE in that cell. In the case of no UE in the edge (centre) area of the cell, PFS will assign the resources preserved for edge (centre) UEs to centre (edge) UEs. Note that although cell edge UEs achieve low SINR by using the sub-band prepared for centre UEs, through appropriate modulation and coding adjustment, transmission with low spectral efficiency can be established [87], which is better than

the sub-band being unused. This is the reason for the PFS approach improving the FFR system performance when user density is low. Under conditions where UEs are present in both areas, PFS avoids assigning subcarriers in sub-bands for centre UE to edge UEs, because these resources are extremely inefficient for cell edge UEs. Consequently, the majority of the transmission resources are assigned to the cell centre UEs. Since PFS has the ability to keep the fairness between centre and edge UE, it will prevent the centre UEs accessing 'good' resources in the protected sub-band. Therefore, PFS also avoids assigning subcarriers in sub-bands for cell edge UEs to centre UEs. This is the reason why the sub-band availability constraint can be lessened when PFS is used in FFR systems. Additionally, due to the small number of UEs in a LAC, the computational complexity of the PFS will be much lower than the PFS in conventional RF cellular systems.

In Figure 5.7, the average spectral efficiency of the FFR systems with PFS are also demonstrated. It can be observed that PFS effectively alleviates the spectral efficiency decrease for FFR systems under the condition of low χ. In addition, it is noted that the performance of sFFR with PFS and $\chi = 1$ UE/m^2 is slightly worse compared with that without PFS. This is because the data rate difference between centre UEs and edge UEs is significant. Therefore, the PFS trades some spectral efficiency for better fairness. In the case of SFR with $\chi = 1$ UE/m^2, PFS further increases the average spectral efficiency. This is because the data rate gap between centre UEs and edge UEs is small. Therefore, the PFS can gain additional spectral efficiency with a low loss of fairness.

5.2.3 Fractional Frequency Reuse with Angular Diversity Transmitter

High directionality of light source with appropriate optics makes it possible to further mitigate CCI by exploring spatial diversity with low complexity. Motivated by this idea, an ADT is considered to be used in O-BSs in a LAC networks in conjunction with the FFR scheme. Further improvement in cell edge UE signal quality and overall spectral efficiency are expected by using this approach. In this subsection, the combination of FFR scheme with ADT transmitter in the application of LAC networks is investigated using simulations.

5.2.3.1 Angular Diversity Transmitter Configuration

In this study, an ADT with 19 narrow beam-width ($\phi_{1/2} = 10°$) LED chips is assumed. Each LED chip has a different beam direction, which covers a small region of the HEX cell coverage area. The configuration of the ADT is illustrated in Figure 5.8. Thus, each small region of the cell can be defined as a sub-cell. The spatial alignment of all the beams of the LED chips establishes the total cell coverage.

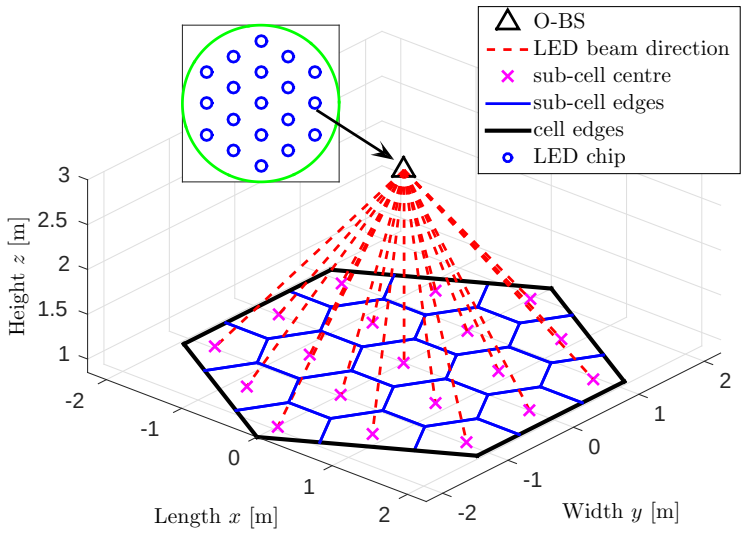

Figure 5.8: *The inlay figure at the top left corner illustrates the arrangement of the ADT. The main figure illustrates the coverage arrangement in a cell. Each LED chip in the ADT covers a different region of a cell.*

Due to the addition of ADT, each O-BS has multiple light sources. In conjunction with the assumptions stated in Section 5.2.2.1, the downlink SINR expression can be modified based on (2.53) in Chapter 2 as:

$$\gamma_{\mathrm{ADT}} = \frac{\xi^2 \left(\sum_{l \in \mathrm{JI}_0} H_{\mathrm{DC},0,l}\right)^2}{\sum\limits_{i \in \mathit{И}} \left(\sum_{l \in \mathrm{JI}_i} H_{\mathrm{DC},i,l}\right)^2 + \frac{N_0 F_{\mathrm{s}}}{\xi^2 \eta_{\mathrm{pd}}^2 \eta_{\mathrm{led}}^2 \sigma_{\mathrm{x}}^2}}, \tag{5.52}$$

where $H_{\mathrm{DC},i,l}$ denotes the line-of-sight (LoS) DC gain of the free-space propagation channel from the l^{th} LED chip in i^{th} O-BS to the desired UE, and JI_i denotes the set including the indices of the LED chip of i^{th} O-BS that is transmitting using the considered transmission resources.

5.2.3.2 Fractional Frequency Reuse Scheme Modification

Taking the advantages of ADT and the further division of sub-cells, a modified FFR scheme based on SFR scheme is considered. The entire modulation band is partitioned into three sub-bands. The links for the cell centre UEs are assigned a reuse factor of 1 as they experience better signal quality and less CCI. The links for the cell edge UEs are assigned a reuse factor of 3 and an amplification of signal power with a factor of ς. In addition to these SFR characteristics, each sub-cell is categorised as a cell centre sub-cell or a cell edge sub-cells. The categorisation is as what follows: Considering a UE in the l^{th} sub-cell in the 0^{th} cell, the desired signal is transmitted by the l^{th} LED chip of the 0^{th} O-BS only. In addition, all LED chips of all remaining O-BS are transmitting at the same frequency. If the considered UE experiences a SINR that is lower than a threshold value T_{e} in any location in the sub-cell, this sub-cell is categorised as a cell edge sub-cell. Otherwise, it is categorised as a cell centre sub-cell. Figure 5.9 illustrates the reuse scheme and the categorisation of the sub-cells. This categorisation of sub-cells can be pre-configured, thereby causing no extra system complexity. Furthermore, the LED chips covering the cell centre (edge) sub-cells are grouped and marked as cell centre (edge) sources. The UEs in cell centre (edge) sub-cells are covered by the cell centre (edge) sources only. Note that this configuration could effectively confine CCI in a minimum region, thereby significantly improve the overall downlink SINR experienced by each UE.

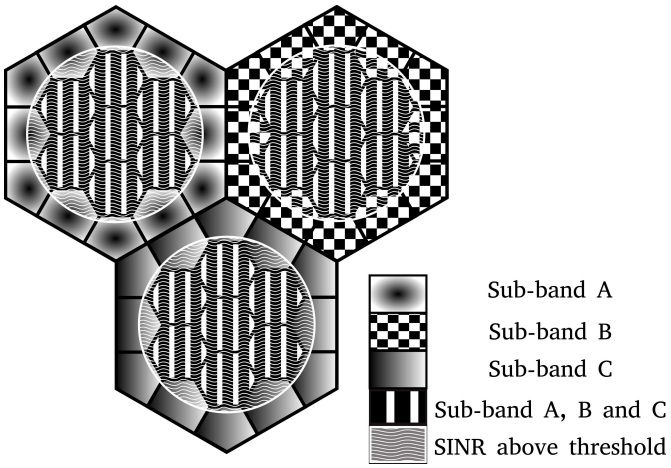

Figure 5.9: *The modified FFR scheme in a LAC downlink system with ADT.*

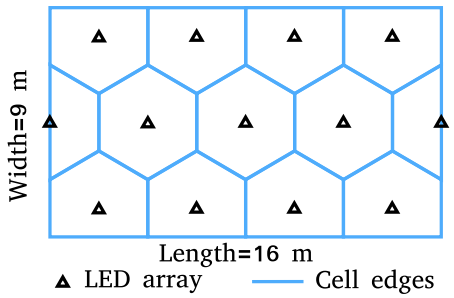

Figure 5.10: *The cellular network arrangement in the simulated room.*

5.2.3.3 Results and Discussions

Next, the performance of LAC systems with ADT is evaluated using simulations. A cellular network is assumed in a 16 m $\times$ 9 m $\times$ 3 m large office. The coverage area in the room is divided into 13 HEX cells and served by 13 O-BSs with ADT, as shown in Figure 5.10. DCO-OFDM with OFDMA is used in the simulation. The remaining system parameters are listed in Table 5.2.

Parameters	Symbol	Values
Transmitter height	z_{s}	3 [m]
LED-chip half-power semi-angle	$\phi_{1/2}$	10°
Receiver height	z_{r}	0.85 [m]
Receiver field of view	$\psi_{\max}$	70°
Modulation bandwidth	F_{s}	40 [MHz]
DC-bias level	ϵ_{DC}	$0.5\Delta\epsilon$
Signal amplitude range	$\Delta\epsilon$	6
PD responsivity	η_{pd}	0.28 [A/W]
PD physical area	A_{pd}	1.5 [cm^2]
Number of subcarriers	K	512
Cell centre illuminance from O-BS	$\tilde{E}_{\mathrm{v}}$	500 [lux]
Noise power spectral density	N_0	1×10^{-21} [A^2/Hz]
edge region SINR threshold	T_{e}	10 dB

Table 5.2: *LAC system parameters with FFR schemes and ADT.*

The downlink SINR spatial distributions in the room with UFR and FFR are illustrated in Figure 5.11 and Figure 5.12, respectively. As previously mentioned, the bandwidth is equally partitioned into sub-band A, B and C for interference coordination in the edge region of the cell in the FFR technique. The first three SINR spatial distributions depicted in Figure 5.12 correspond to the distributions of SINR on the sub-carriers in sub-bands A, B and C, respectively.

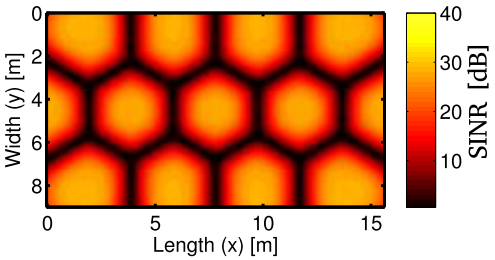

Figure 5.11: *The spatial distributions of the received SINR on the whole frequency band in the room for the system applying UFR.*

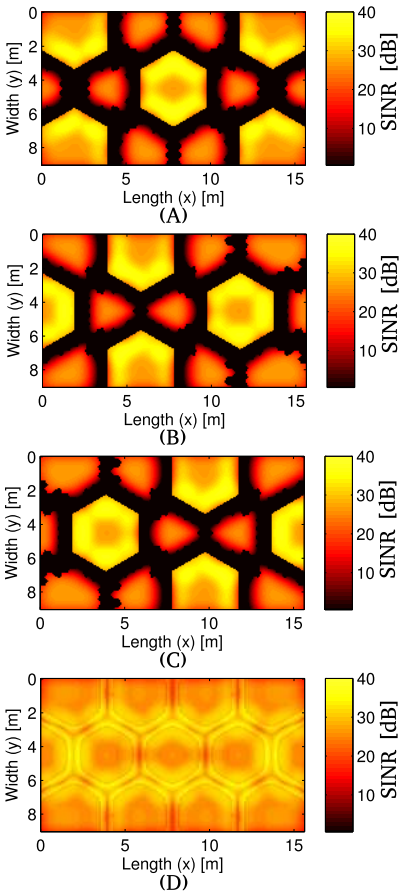

Figure 5.12: *Plot (A), (B) and (C) correspond to the spatial distributions of the received SINR on the sub-band A, B and C for the system using FFR, respectively. The value of ς is 16. The black region indicates the sub-band is unavailable to the users in that region. Plot D corresponds to the average SINR distribution over all three sub-bands*

The last distribution shown in Figure 5.12 (D) is the average SINR distribution over all three sub-bands. In the UFR system, the cell-edge UE SINR falls in the range of -2.6 dB to 9 dB. In contrast, in the FFR system, since interference is mitigated for the exterior sub-cells by applying traditional resource partitioning, there is an increase in the SINR. Consequently, the SINR for the exterior region of the cell is within the range of 26 dB to 36 dB. On the one hand, in the UFR system, the cell-centre SINR is within the range of 10 dB to 29 dB. On the other hand, in the FFR system, the interference mitigation also improves the cell-centre average SINR to the range of 24 dB to 32 dB, as shown in Figure 5.12 (D). Therefore, significant improvement in terms of overall SINR is achieved by using FFR relative to the UFR system.

Interference mitigation technique technique	ASE [bps/Hz/m^2]	Guaranteed user throughput [Mbps]
$\kappa_{\mathrm{rf}} = 1$	0.2607	0.6
$\kappa_{\mathrm{rf}} = 3$	0.1776	4.1
FFR, $\varsigma = 4$	0.3389	4.3
FFR, $\varsigma = 16$	0.3211	5.2
FFR, $\varsigma = 64$	0.2937	5.6

Table 5.3: *Area spectral efficiency and guaranteed user throughput.*

It is assumed that 40 UEs are uniformly distributed in the network. The PFS introduced in Algorithm 2 is used to allocate the sub-carriers to multiple UEs in each cell to solve the issue of low user density. Table 5.3 shows the area spectral efficiency (ASE) of the LAC networks and the guaranteed user throughput (measured at the first percentile of the user throughput) achieved by the systems with different techniques and parameters. Figure 5.13 shows the CDF of the

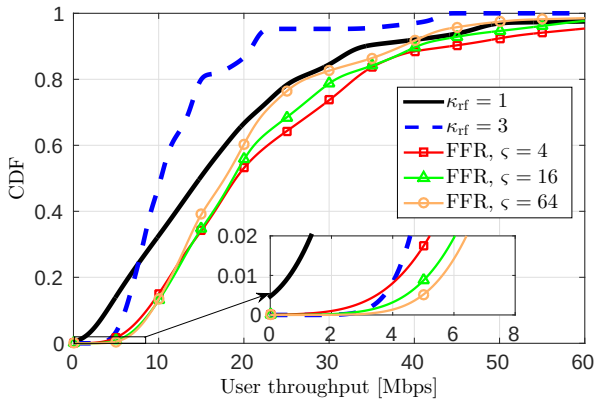

Figure 5.13: *The CDF of user downlink throughput in a LAC network with ADT.*

downlink user throughput.Figure 5.14 shows the CDF of the downlink cell throughput. In the

systems with FFR, the cases with ς values of 4, 16 and 64 are considered. For the cell edge UEs in the system applying FFR, a power gain of ς increases the signal quality further. This results in a better performance for the cell edge UEs in the FFR system relative to a system applying only traditional resource partitioning. The improvement in terms of guaranteed user throughput is in the range of 5% to 37%. All three sub-bands are available for transmission for the cell centre UEs in the system applying FFR. In addition, due to the interference mitigation, the average SINR in the FFR system is higher than the SINR in the UFR system. This improves the performance of the FFR system relative to the two benchmark systems in terms of both the user throughput and cell throughput, as shown in Figure 5.13 and Figure 5.14. The improvement relative to the UFR system in terms of ASE is in the range of 13% to 30%.

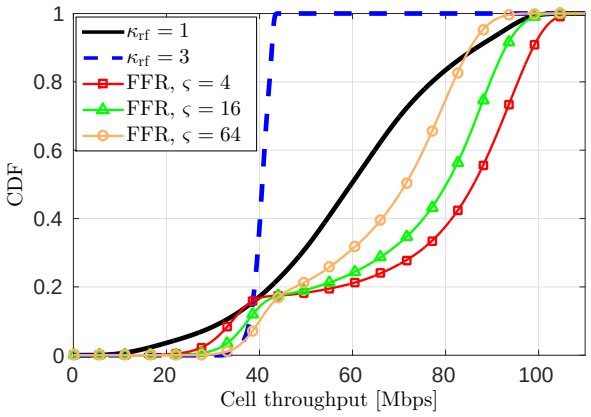

Figure 5.14: *The CDF of cell downlink throughput in a LAC network with ADT.*

On the one hand, when $\varsigma = 64$, the cell-edge user throughput is enhanced at the cost of cell-centre user throughput. In this case, a guaranteed user throughput of 5.6 Mbps is achieved. However, the ASE is only 0.2937 bps/Hz/m^2. On the other hand, when ς is decreased to 4, the SINR of the cell-centre users is improved. This results in a higher ASE of 0.3389 bps/Hz/m^2 and a lower guaranteed user throughput of 4.3 Mbps. In Figure 5.14, it is shown that there is a small proportion of the cells which have a relatively lower system throughput of about 35 Mbps. This occurs when all UEs in these cells are in the cell edge region, which is reasonable due to the low user density in each cell. In this case, the sub-band for cell centre users remains idle which wastes transmission resources and results in a lower cell throughput.

5.3 Coordinated Multi-point Joint Transmission Based on Angular Diversity Transmitter

In a LAC network, many system specific properties support the implementation of JT: i) a very high-speed low-latency backhaul connection between O-BSs is easy to realise due to the short physical distance between O-BSs; ii) an IM/DD system is not impaired by small-scale fading effect due to constructive combination of intensity modulated signals; Therefore, extra coding and strict synchronisation requirement are unnecessary; iii) since the LoS signal component is significant, the time differences between the arrival of signal components from different O-BSs are small relative to a symbol period; iv) the inter-symbol interference (ISI) introduced by the slight difference in time delay of each signal component can be inherently removed by O-OFDM system. Applying JT not only improves the communication quality at cell-edges, but also makes the connection more reliable. Since multiple LoS transmission paths exist simultaneously as a result of the proposed cellular structure, data connection can still be guaranteed for the case that one or two LoS paths are blocked. In this section, the application of JT in LAC networks with ADTs is investigated using simulations.

5.3.1 Joint Transmission Configurations and Frequency Plans

For the convenience of analysis, the same assumptions made in Section 5.2.1 are also used here. The basic configuration of the considered JT in LAC networks is illustrated in Figure 5.15. The network deployment is similar to that assumed in Section 5.2.3, where multiple O-BSs cover a numbers of HEX cells in the considered LAC system. Each O-BS is equipped with a 7-LED chip ADT. Among the 7 LED-chips in an ADT, the central LED chip is directed to the cell centre and covering the cell centre UEs. Each of the remaining 6 exterior LED chip faces one of the 6 vertices of the HEX cell. Since every three adjacent cells have a common vertex, three exterior LED chips of different adjacent O-BSs cover a cell corner region. This region is defined as a JT region which is centred at a vertex of a cell. If the UE is in the centre of a cell, the system works in a single point transmission mode, and the UE receives signal from the central LED chip. In the case that the UE is far away from any O-BS receiving weak downlink signal, the system works in a multi-point JT mode, and the UE is served by three closest O-BSs. Each O-BS transmit the signal using one of the exterior LED chips as shown in Figure 5.15. Similar to the case in Section 5.2.3.1, a narrow half-power semi-angle of 20° is assumed for each LED chip to avoid the wide spread of CCI.

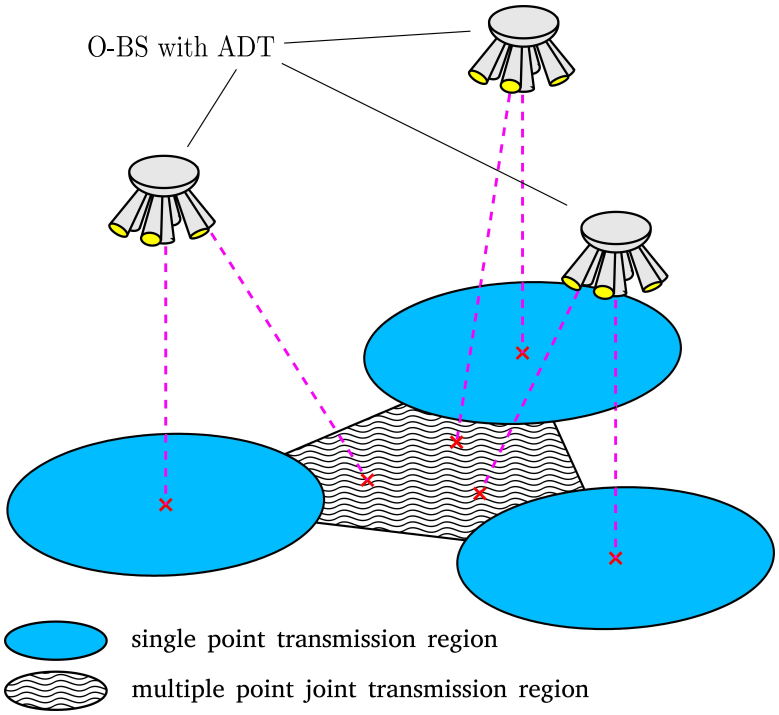

Figure 5.15: *Illustration of coordinated multi-point joint transmission in LAC downlink system.*

The working mechanisms of the system are described as follows: 1) the central LED chip of each O-BS transmits a pilot signal to all UEs with a unique sequence to identify the corresponding O-BS; 2) each UE selects the BS providing the strongest signal as a primary AP and selects the O-BSs providing the second and the third strongest signals as the secondary APs; 3) a UE estimates the received SINR by considering the signal from the primary AP as a desired signal and the other signals as interference; 4) if the SINR is above a pre-determined threshold T_{jt} which determines the maximum BER for reliable data transmission, the UE replies to the O-BSs through uplink channel requesting single point transmission from the primary BS; 5) otherwise, the UE replies to the O-BSs requesting JT from the primary and the secondary APs. Then, the BSs use a predetermined look up table to select the appropriate LED chips for transmission. With a given O-BS cooperation set, the look up table provides the information of LED chips that are used to serve the UE using JT.

Since the magnitude response of the channel is assumed to be flat, scheduling algorithm is simplified. We assume that the subcarriers are evenly distributed among the user population in the coverage area. Figure 5.16 illustrates the frequency reuse pattern. For the first plan shown in Figure 5.16 (A), the frequency band is divided into two sub-bands. The first sub-band is reused

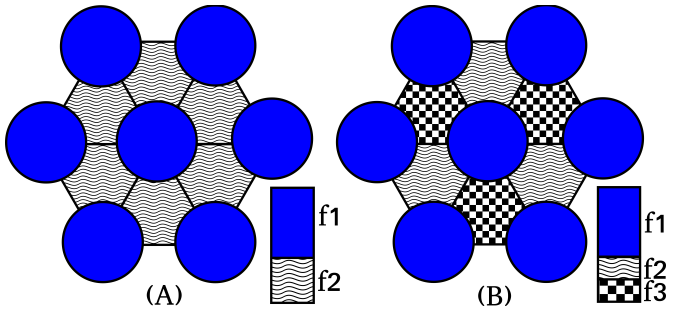

Figure 5.16: *Frequency plans considered in the LAC downlink system with JT. (A) plan 1 (B) plan 2*

in each single point transmission region, while the second sub-band is reused in each multi-point JT region. Considering a total of $\tilde{K}$ subcarriers carrying information bits, the number of subcarriers in single point transmission sub-band K_{st} is set as follows:

$$K_{\mathrm{st}} = \left\lceil \frac{A_{\mathrm{st}}\tilde{K}}{A_{\mathrm{sys}}} \right\rceil, \tag{5.53}$$

where A_{st} denotes the total combined area of single point transmission regions, and A_{sys} denotes the entire coverage area of the LAC system. The number of subcarriers in the JT sub-band, K_{jt}, is calculated as:

$$K_{\mathrm{jt}} = \tilde{K} - K_{\mathrm{st}}. \tag{5.54}$$

This frequency allocation plan ensures spatially uniform availability of frequency resources, which supports the assumptions of a uniform UE distribution as well as equal target data rate of all UEs in the network. However, there is no interference mitigation between adjacent JT regions. Therefore, low SINRs are achieved at the boundaries of two adjacent JT regions. For the second plan shown in Figure 5.16 (B), the sub-band for JT regions is divided into two partitions as follows:

$$K_{\mathrm{jt1}} = K_{\mathrm{jt2}} = \left\lfloor \left(\tilde{K} - K_{\mathrm{st}}\right) \Big/ 2 \right\rfloor. \tag{5.55}$$

The two JT sub-bands are reused in a pattern such that adjacent JT regions always use different sub-bands in order to mitigate CCI. The sub-band for single point transmission remains the same. This frequency plan offers improved receiver SINR performance, but fewer number of subcarriers are available in the JT regions. For the convenience of presentation, the JT systems with frequency plan 1 and 2 are defined as JT 1 system and JT 2 system, respectively.

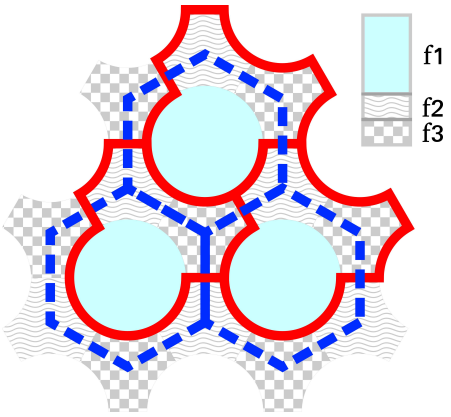

Figure 5.17: *The area of the region specified by the blue dashed lines (cell coverage area) equals the area of the region specified by the red solid curves. This implies that the JT 2 system has the same reuse factor as that of a UFR system.*

In a UFR system, the whole frequency band is permitted to be used in each cell. Within a cell coverage area (hexagon indicated by blue dashed line boundaries in Figure 5.17), subcarriers are not reused. In a JT 2 system, the entire set of subcarriers are prevented from being reused within the region bounded by red solid curves in Figure 5.17. The area of this region is exactly equal to the coverage area of a HEX cell. Therefore, the reuse factor of a JT 2 system is equivalent to the one in a UFR system.

Parameters	Symbol	Values
Transmitter height	z_{s}	3 [m]
LED-chip half-power semi-angle	$\phi_{1/2}$	20°
Receiver height	z_{r}	0.85 [m]
Receiver field of view	$\psi_{\max}$	70°
Modulation bandwidth	F_{s}	40 [MHz]
DC-bias level	ϵ_{DC}	$0.5\Delta\epsilon$
Signal amplitude range	$\Delta\epsilon$	6
PD responsivity	η_{pd}	0.28 [A/W]
PD physical area	A_{pd}	1.5 [cm^2]
Number of subcarriers	K	512
Cell centre illuminance from O-BS	$\tilde{E}_{\mathrm{v}}$	500 [lux]
Noise power spectral density	N_0	1×10^{-21} [A^2/Hz]
JT SINR threshold	T_{jt}	10 dB
Number of users	N_{u}	40

Table 5.4: *LAC system parameters with JT schemes and ADT.*

5.3.2 Simulation Results and Discussions

The simulated LAC network is assumed to be deployed in a room of size 16 m $\times$ 9 m $\times$ 3 m. The coverage area in the room is divided into 13 HEX cells and served by 13 O-BSs with ADT, as shown in Figure 5.10. DCO-OFDM with OFDMA is used in the simulation. For simplicity, no power control is applied and all LEDs have the same average optical transmit power. The remaining system parameters are listed in Table 5.4.

The simulation of the SINR spatial distribution and throughput statistics are based on the modified SINR expression (5.52). The JT systems are compared against two benchmark systems. One of the benchmark systems uses UFR with a reuse factor of one. The other system uses traditional static resource partitioning with a reuse factor of 3 [19]. The simulation parameters for them are the same as those for the JT systems in order to guarantee a fair comparison.

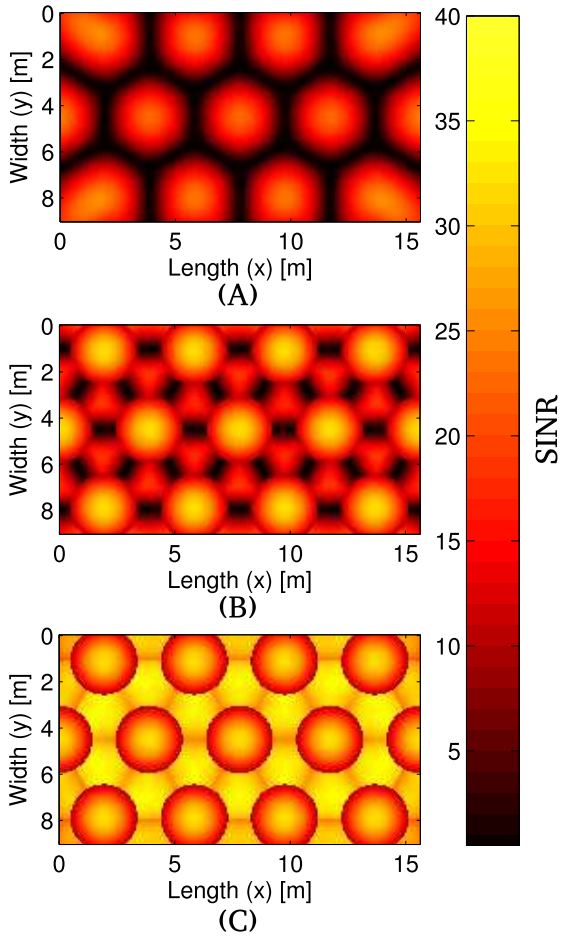

Figure 5.18: *SINR spatial distribution of the LAC system using (A) UFR (B) JT 1 (C) JT 2.*

Figure 5.18 shows the SINR spatial distribution for the different systems. The benchmark UFR system achieves the worst SINRs. For the JT 1 system, the cell-edge SINRs are improved compared to the UFR system, especially for the UEs near the centre of JT regions. However, due to the lack of interference mitigation between adjacent JT regions, the UEs at the boundaries between adjacent JT regions achieve low SINR. In contrast, in the JT 2 system, the same frequency band is not reused in adjacent JT regions. Therefore, the cell-edge UE SINR is further improved (above 30 dB) compared to the JT 1 system at the cost of less available spectrum resource per JT region.

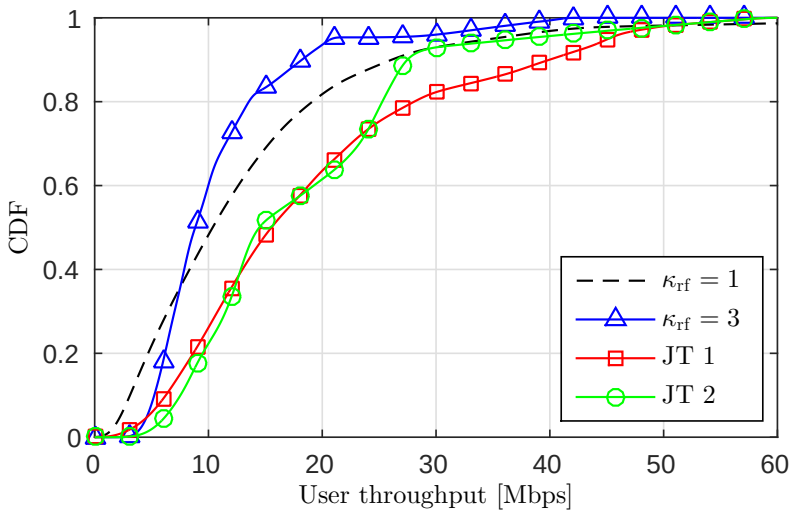

Figure 5.19: *The CDF of user downlink throughput in a LAC network with ADT.*

Figure 5.19 and Figure 5.20 show the CDF of the downlink cell throughput and the user throughput in different systems. The cell throughput is defined as the aggregate data rate in a cell, while the user throughput is defined as the transmission data rate achieved by a single UE. With the largest reuse factor, the resource partitioning system achieves the lowest median cell throughput of 34.9 Mbps. In contrast, a UFR system with a reuse factor of one achieves a higher median system throughput of 42.3 Mbps. The JT 2 system has the same reuse factor as the UFR system. In addition, the JT 2 system exhibits strong robustness to CCI. Therefore, the JT 2 technique achieves a median system throughput of 56.3 Mbps, which is significantly higher than both benchmark systems. However, the maximum number of subcarriers that a UE could use is determined by its location and is limited by the size of the respective sub-band. Therefore, the peak user throughput for the JT 2 system is lower than the JT 1 system. Since the JT 1 system enforces a more aggressive frequency reuse, it achieves the highest median

system throughput of 58.5 Mbps. The JT 1 and the JT 2 systems show a 67.6% and a 61.3% improvement compared to the resource partitioning system, respectively. The JT scheme also shows improvement in terms of the guaranteed user throughput, defined as the minimum data rate with 90% confidence, compared to the benchmarks. The JT 1 and the JT 2 systems achieve a 6.3 Mbps and a 7.5 Mbps guaranteed user throughput, respectively. These numbers are 100% to 140% higher than the guaranteed user throughput achieved by a UFR system.

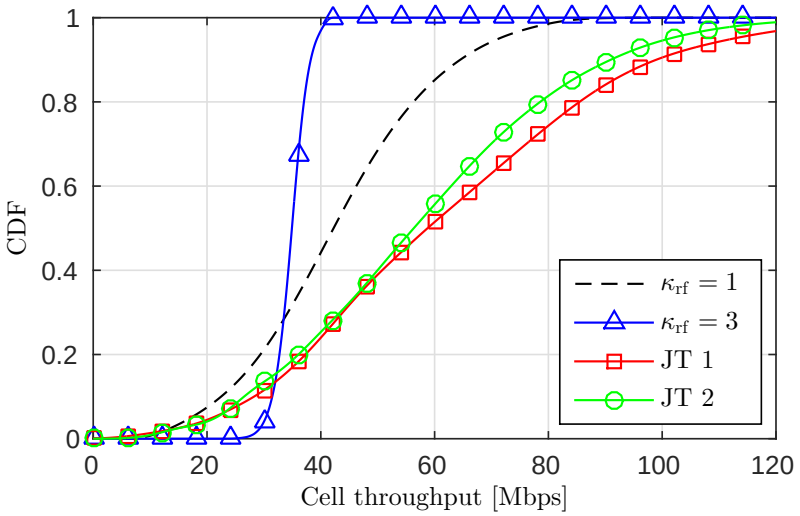

Figure 5.20: *The CDF of cell downlink throughput in a LAC network with ADT.*

5.4 Summary

In this chapter, two interference mitigation techniques for LAC networks have been introduced. The first technique is FFR. An analytical framework of the FFR application in a LAC network was proposed. Both the sFFR and SFR schemes were considered. A method of calculating the statistics of the achievable SINR and the average spectral efficiency in a 2-layer HEX cell network was presented. The numerical results show a close agreement with the results of the Monte Carlo simulations. The performance of the LAC network with FFR was evaluated and compared with a benchmark system with UFR. The results showed that FFR schemes can effectively improve the downlink SINR in a LAC network. In addition, FFR schemes offer significant improvements in the cell edge spectral efficiency. Furthermore, the average spectral efficiency is slightly improved. Also, the effects of the key parameters were studied, such as

cell radius, cell centre / radius ratio and active use density. It was identified that the optimal value for cell centre / radius ratio is 0.7 for sFFR and 0.55 for SFR in a typical setup considered in this study. With an increase in the noise level, these optimal values become greater and the gain from FFR schemes decreases. In addition, a low user density significantly decreases the achievable average spectral efficiency. However, PFS can be used to effectively alleviate this problem. Furthermore, the combination of ADT and FFR is considered for further improvement in interference mitigation and system performance. The results showed that the combination of FFR and ADT significantly improves the downlink performance of the considered LAC system in terms of overall SINR level, user throughput and cell throughput, especially for the cell-edge UEs. The second considered interference mitigation technique is known as coordinated multi-point JT. Its application in a LAC network is achieved by using ADT in the O-BSs. The results showed that JT schemes can also effectively improve the performance of the cell edge UE in LAC systems. In addition, a joint transmission system also achieved 67.6% improvement in terms of median system throughput compared to a static resource partitioning system.

Chapter 6

Conclusions, Limitations and Future Research

6.1 Summary and Conclusions

In this thesis, a series of fundamental studies related to the downlink performance of light fidelity (LiFi) attocell (LAC) networks at the physical layer have been presented. To the best of the author's knowledge, this is the first comprehensive study of a LAC downlink. The study includes an analysis and evaluation of the downlink performance of LAC networks based on signal-to-interference-plus-noise ratio (SINR). In addition, an efficient analytical method for the calculation of the non-line-of-sight (NLoS) channel impulse response (CIR) in a visible light communication (VLC) system was proposed, which has been used to estimate the free-space propagation channel in LAC downlink systems. Finally, two interference mitigation techniques, namely fractional frequency reuse (FFR) and multi-point joint transmission (JT) were introduced at the downlink of LAC networks in order to mitigate the detrimental effects of co-channel interference (CCI).

In Chapter 2, the relevant background related to the LAC network downlink has been presented. Firstly, a brief history of optical wireless communication (OWC) has been provided. Furthermore, the essential subsystems to establish a complete LAC network have been introduced and discussed. Then the focus is put on the basic concepts underpinning the LAC network downlink, which include the VLC front-ends, channel, receiver noise, optical-orthogonal frequency division multiplexing (O-OFDM) transmission, signal clipping effects in O-OFDM, and cellular system. Based on the introduced basic concepts, a new expression for a key system metric, downlink SINR, has been proposed. In contrast to the existing SINR models, the new SINR expression is based on O-OFDM transmission. Therefore, the effects of signal clipping, signal power adjustment and the frequency characteristics of the front-end elements have been taken into account in the new expression. The proposed SINR expression forms the foundation for the studies in the subsequent chapters. It could also be potentially used in future research. For

example, the SINR expression could be used as the metric / object function of simulations / optimisation in future LAC network studies.

In Chapter 3, an efficient novel method was proposed to calculate the NLoS CIR in VLC systems. This method is an analytical approach to calculate the CIR for VLC NLoS channel. In particular, the proposed method provides tractable expressions for the CIR calculation. Using these expressions calculating the CIR is straightforward and requires extremely short time to compute (< 1 s). In many VLC studies, it is required to consider NLoS CIRs for the accuracy of the research results, but it takes too much time to calculate the NLoS CIR using state-of-the-art ray-tracing simulations. In addition, in the proposed CIR calculation method, the CIR is decomposed into multiple components corresponding to the signals that interact with different room surfaces. Therefore, researchers working on VLC channel characterisation could use the expressions and results proposed in this thesis in order to analyse the effects of different surfaces on the NLoS channel in different cases.

In Chapter 4, based on the downlink SINR expression in Chapter 2 and the proposed analytical CIR calculation method in Chapter 3, a comprehensive downlink performance analysis and an evaluation of LAC networks has been presented. Firstly, a simulation including the effects of NLoS channel has been conducted. The results show that the SINR decreases with signal frequency due to the low pass characteristics of the front-end elements. At the same time, the NLoS channel has minor effect on the SINR. Therefore, when modulation bandwidth is beyond the 3-dB bandwidth of the front-end elements, it is essential to take the effect of the front-end elements into account. However, the lack of NLoS channel analysis leads to minor variance in the downlink performance analysis of LAC networks as long as there exists a relatively reliable line-of-sight (LoS) path for the communication signal. In addition, the study on the size of the network shows that the larger the network size, the worse the downlink performance. The downlink performance with different cell deployments was evaluated and compared. Among the considered cell deployments, hexagonal (HEX) cell deployment and Poisson point process (PPP) cell deployment were found to offer the best and worst case in terms of SINR statistics, respectively. Tractable expressions for the SINR statistics of the system with these two cell deployments have been derived. These expressions could be used by researchers to quickly estimate the potential downlink performance of a LAC network with a certain system specification. It has been found that the effects of varying cell radius and the light beamwidth (half-power semi-angle) are vital to the downlink performance of LAC networks, and the con-

figuration of these two variables should be interconnected. A desired configuration to the source beamwidth for a specified cell radius has been proposed. Furthermore, the cell data rate of the LAC downlink has been evaluated. It has been found that with a smaller cell size, a smaller half-power semi-angle should be used, which leads to a decreased CCI level and an improvement in the cell data rate. Additionally, there is always an optimal value for the modulation bandwidth to allow the LAC network to achieve a maximum downlink data rate. These results help to select suitable parameters for a LAC network in both computation simulation and actual system implementation. Finally, the downlink performance of LAC networks has been compared with the performance achieved by the state-of-the-art small-cell systems. The result shows that the LAC networks generally outperform femtocell networks. In particular, a high performance LAC network can achieve an area data rate of 469 Mb/(s·m^2) which is twice the area data rate achieved by a high performance millimetre wave (mm-Wave) system. The mmWave system assumes a spectral efficiency of 11.25 b/(s·Hz) and uses a bandwidth of 2 GHz in a room of size $10\ \mathrm{m} \times 10\ \mathrm{m}$. This study demonstrates that LAC networks are capable to off-load a significant amount of downlink traffic from the existing radio frequency (RF) network. The study can also support future studies on LAC networks at the data-link and network layers, where the focus could be on handover algorithms or network load balancing.

In Chapter 5, interference mitigation techniques for LAC downlink have been considered. Firstly, a FFR technique is considered, and it achieves a reasonable compromise between complexity and interference mitigation performance. Two types of FFR schemes, strict FFR (sFFR) and soft frequency reuse (SFR), were introduced. A series of analytical tools have been developed to calculate the SINR statistics and spectral efficiency of the LAC downlink using FFR. The presented results show that FFR provides an improvement of 2 dB to 10 dB in downlink SINR and a 20% to 50% improvement in cell edge spectral efficiency in a LAC network compared with the case using universal frequency reuse (UFR). These results justify that it is effective to use a FFR scheme to mitigate CCI in a LAC downlink. It is also found that sFFR offers better gain in almost every aspect when compared to SFR. In addition, it is found that using FFR leads to a low active user density issue. Given a user density lower than 0.2 user/m^2, the average spectral efficient of the system using FFR schemes decrease significantly. This result implies that a FFR is not suitable to be used in a lightly loaded LAC system. A modified proportional fairness scheduling (PFS) scheme has been introduced to alleviate the low user density issue. To further improve the effectiveness of the FFR, an angular diversity transmitter (ADT) was introduced at the transmitter side. Consequently, an improvement of 20 dB in

the cell edge user SINR and an improvement of up to 30% in terms of area spectral efficiency (ASE) have been observed in the simulation results. Secondly, the multi-point JT technique with ADTs is considered. It converts harmful CCI into useful desired signal at the cell edge. Similar to the case of using FFR and ADTs, an improvement of 30 dB at the cell edge SINR and an improvement of 60% to 70% in medium user throughput relative to the case of UFR can be observed in the simulation results. The results of the systems using ADTs shows that exploring spatial diversity can significantly improve the system performance in LAC networks. The presented study offers two solutions to the interference issues in future LAC networks with dense spatial reuse, and proves their effectiveness. Furthermore, the research results of this study could be used as benchmarks for future research on interference mitigation techniques in LAC networks.

6.2 Limitations and Future Research

In the analysis presented in this thesis, a large number of factors have been taken into account to give insights into the actual downlink performance of LAC systems in practice. However, a number of assumptions have been made to reduce the analytical complexity. In some cases, the related analytical tool is unavailable in the literature. Consequently, idealised assumption has to be made so that the analysis can be tractable. In addition, the studies in this thesis are purely based on analysis or simulations. Therefore, more experimental research is needed to validate the presented results. Furthermore, a number of the research findings and limitations inspire potential future research directions, which is important for the further development of LiFi technology.

In the development of the analytical method for the NLoS CIR calculation, cost-effective modelling of the channel components undergoing three or more number of reflections with low complexity was not available. With the omission of these channel components, a noticeable underestimation of the NLoS CIR components with long time delay can be observed. Simplified geometric models may be considered to approximate the characteristics of the channel components with higher order reflections. In addition, the proposed method considers light source with Lambertian radiation pattern, diffused reflection only, a vertical receiver orientation and a full receiver field of view (FoV). More general modelling considering other light source, specular reflection, receiver rotation and limited FoV can be the subjects in the future work.

Currently, most of the study on indoor NLoS VLC channel modelling or simulation considers the effects of room internal surfaces only. In order to simulate a more accurate NLoS channel, the effects of other random objects, such as human bodies, furnitures, should be thoroughly studied. Despite a number of related evaluation studies considering several specified environments [110], the generic characteristics of the influences of these objects still remains unknown. A significant challenge for characterising the effects of random objects is the difficulty of defining the generic model for the random objects. On the one hand, there are too many uncertainties about the random objects (type of objects, reflectivity of the objects). On the other hand, the geometry of the random objects are not as simple as a flat plane. Consequently, it is much more difficult to capture its effects on the channel compared to the case considering internal surfaces only.

In addition, the majority of the state-of-the-art channel simulation / modelling methods considers a static setup, where the geometry of transmitter, receiver and the environment does not vary with time. Comprehensive Evaluation of the time-varying characteristics of the VLC channel can also be the future research topic. The related research result, such as coherence time, will be useful to the design of channel estimation algorithm, handover algorithm, etc..

Another important issue in the VLC channel modelling is the effects of the user equipment (UE) orientation and position. However, very few study has worked on the statistics of the distance from the floor to the UE and of the latitude angle of the UE. These statistics strongly depends on the height of the user, poses / habits of using the UE. A comprehensive study on these statistics using experiments can be carried out in the future research.

In the analysis of the downlink performance of LAC networks, perfect reliable backhaul and uplink connections with infinite capacity are assumed. A full buffer traffic model has been assumed for all UEs in the LAC networks. In addition, the effects of handover and mobility are omitted. Limited backhaul, uplink capacities, different traffic model or handover / mobility issues can be added to the analysis in the future research in the downlink perspective. It is unlikely to jointly consider all these issues with a detailed model as it will lead to significant increase in analysis complexity. Therefore, detailed analysis / performance evaluation of each algorithms / subsystem with a number of case studies is more practical in the future research.

In conventional RF cellular network, several dozens or even hundreds of UEs are connected to a single base station (BS). In contrast, the number of active UEs within a LAC is much

smaller because of the smaller cell size. This issue can potentially affect the LAC system performance. For example, in an extreme case that the number of users is much fewer than the number of optical-base stations (O-BSs), the O-BS serving no UE is not transmitting which leads to a reduced CCI level. Therefore, evaluating the effect of active UE density is worth considering in the future research. In chapter 4, an infinite network in an indoor environment is considered. In order to accurately reflect the performance of LAC network in practice, a number of typical indoor application scenes can be defined, which may have different room dimension, UE density or number of available light source. The performance evaluation regarding each specified scene can be carried out independently.

In addition, the LAC downlink system configuration considered in Chapter 4 is adjusted in order to achieve an improved wireless communication performance. The only constraint considering the lighting performance is the illuminance level right underneath the O-BS. Each O-BS has a circular 'foot-print' on the serving plane. In the communication perspective, the overlapping between adjacent 'foot-prints' should be avoided to prevent significant CCI. On the other hand, in the lighting perspective, the cell edge has a reduced illuminance level. The overlapping between adjacent 'foot-prints' is preferred to superpose the light from multiple sources to enhance the illumination and the illuminance uniformity. Therefore, new design which can accommodate both communication and lighting functionalities should be considered in future research.

In the analysis of interference mitigation techniques, perfect channel state information (CSI) at the O-BS and perfect centralised control unit are assumed. In addition, idealised channel with flat frequency response is assumed. The detailed analytical framework developed in Chapter 4 can be used in the study of the interference mitigation techniques in LAC systems to provide more accurate performance estimation. Furthermore, only the cases with infinite HEX network are considered. The cases with other point process based cell deployments can be investigated in future research. In the study of using JT, multiple signals from different O-BSs via LoS paths arrive the receiver with different time delays. This may introduce frequency selectivity to the JT channel. Therefore, studying the JT channel characteristics can also be a future research topic.

In Chapter 5, the analysis shows that using the static low complexity, such as FFR technique, in LAC network may leads to the waste of spectrum resources due to the low active user density issue. In order to avoid such waste, the centralised / distributed dynamic resource allocation

schemes developed for RF cellular network can be considered in LAC networks. In a LAC network, all O-BSs are physically close to each other and the number of UEs per cell is smaller relative to RF cellular systems. These facts imply that the backhaul communication latency issue and the computation complexity issue of the resource allocation solution will not restrict the implementation of these dynamic schemes in LAC networks.

In RF wireless system, the random small-scale fading leads to different frequency selectivity for each user, which is known as multi-user diversity. In most of the dynamic resource allocation schemes, multi-user diversity is explored to significantly improve the system performance. However, the small-scale fading introduces little frequency selectivity in VLC transmission due to the large size of photodiode (PD) detector relative to the wavelength of the light and the use of incoherent intensity modulation (IM) and direct detection (DD). Therefore, when using resource allocation schemes in VLC systems, the unique characteristics of VLC system in frequency domain should be taken into account.

In the field of VLC research, the majority of the experimental studies are considering a point-to-point single link. However, there is little work has been carried out on the networked VLC system. In the future experimental studies on LAC networks, the following issues should be considered in particular: 1. validation of the CCI characteristics. 2. light source coverage validation. Regarding the first issue, the effects of a certain level of CCI can be experimentally evaluated. For example, the bit error rate (BER) performance with a specified level of CCI and modulation scheme can be measured and compared with the corresponding BER distorted by the same level of additive white Gaussian noise (AWGN). In addition, the CCI spatial distribution can be experimentally measured within the coverage area of interest. Regarding the second issue, the effective coverage area of the light source can be experimentally validated. In a single link VLC experiment, the light beam is typically focused on the receiver detector using appropriate optics to increase the collected optical power as much as possible. However, in a networked VLC system based on non-directed configuration, the system design should take the case with low signal-to-noise ratio (SNR) into account. This means that a high power, diffused optical source should be used in a networked VLC experiment. Thus, it is valid to measure the effective coverage radius respect to different vertical separations between the light source and the UE.

Appendix A

Derivation of the Single Reflection Channel Impulse Response

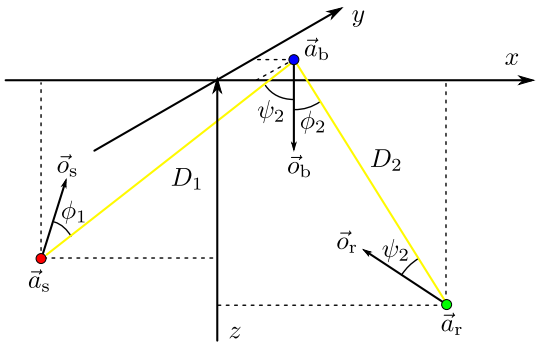

Figure A.1: *Single reflection channel in Cartesian coordinates.*

Firstly, the setup shown in Figure 3.2 is placed in a Cartesian coordinate system. As shown in Figure A.1, the locations of the source element and the receiving element are defined in the coordinates as $\vec{a}_{\mathrm{s}} = \left(-\frac{L_{\mathrm{s}}L_{\mathrm{b}}}{L_{\mathrm{s}}+L_{\mathrm{r}}}, 0, -L_{\mathrm{s}}\right)$ and $\vec{a}_{\mathrm{r}} = \left(\frac{L_{\mathrm{r}}L_{\mathrm{b}}}{L_{\mathrm{s}}+L_{\mathrm{r}}}, 0, -L_{\mathrm{r}}\right)$, respectively. The orientations of the source element and the receiving element are defined as $\vec{o}_{\mathrm{s}} = (x_{\mathrm{s}}, y_{\mathrm{s}}, z_{\mathrm{s}})$ and $\vec{o}_{\mathrm{r}} = (x_{\mathrm{r}}, y_{\mathrm{r}}, z_{\mathrm{r}})$. All orientation vectors have a unity modulus. Considering an amount of light power incident to a point on the reflector at $\vec{a}_{\mathrm{b}} = (x, y, 0)$, the Euclidean distance between the source and this point is D_1 and the Euclidean distance between the receiver and this point is D_2. Intuitively, the orientation of the reflector $\vec{o}_{\mathrm{b}}$ is opposite to the direction of z-axis. According to [26], the calculus of the path loss via $\vec{a}_{\mathrm{b}}$ can be calculated as:

$$\mathrm{d}G = \frac{\rho(m+1)A_{\mathrm{r}}\mathrm{d}A}{2\pi^2 D_1^2 D_2^2}\cos^m\phi_1\cos\psi_1\cos\phi_2\cos\psi_2, \tag{A.1}$$

where ϕ_1 and ψ_1 denote the radiant angle and incident angle from the light source and to the point at $\vec{a}_{\mathrm{b}}$ on the reflector, respectively; ϕ_2 and ψ_2 denote the radiant angle and incident angle from the the point at $\vec{a}_{\mathrm{b}}$ on the reflector to the receiving element, respectively; and $\mathrm{d}A$ denotes the calculus of the physical area of the reflecting point. The relevant terms in (A.1) can be

calculated as [67]:

$$D_1 = \sqrt{\left(x + \frac{L_\mathrm{s} L_\mathrm{b}}{L_\mathrm{s} + L_\mathrm{r}}\right)^2 + y^2 + L_\mathrm{s}^2}, \tag{A.2}$$

$$D_2 = \sqrt{\left(x - \frac{L_\mathrm{r} L_\mathrm{b}}{L_\mathrm{s} + L_\mathrm{r}}\right)^2 + y^2 + L_\mathrm{r}^2}, \tag{A.3}$$

$$\cos\phi_1 = \frac{\vec{o}_\mathrm{s}\left(\vec{a}_\mathrm{b} - \vec{a}_\mathrm{s}\right)^\mathrm{T}}{D_1} = \frac{x_\mathrm{s}\left(x + \frac{L_\mathrm{s} L_\mathrm{b}}{L_\mathrm{s}+L_\mathrm{r}}\right) + y_\mathrm{s} y + z_\mathrm{s} L_\mathrm{s}}{D_1}, \tag{A.4}$$

$$\cos\psi_1 = \frac{\vec{o}_\mathrm{b}\left(\vec{a}_\mathrm{s} - \vec{a}_\mathrm{b}\right)^\mathrm{T}}{D_1} = \frac{L_\mathrm{s}}{D_1}, \tag{A.5}$$

$$\cos\phi_2 = \frac{\vec{o}_\mathrm{b}\left(\vec{a}_\mathrm{r} - \vec{a}_\mathrm{b}\right)^\mathrm{T}}{D_2} = \frac{L_\mathrm{r}}{D_2}, \tag{A.6}$$

$$\cos\psi_2 = \frac{\vec{o}_\mathrm{r}\left(\vec{a}_\mathrm{b} - \vec{a}_\mathrm{r}\right)^\mathrm{T}}{D_2} = \frac{x_\mathrm{r}\left(x - \frac{L_\mathrm{r} L_\mathrm{b}}{L_\mathrm{s}+L_\mathrm{r}}\right) + y_\mathrm{r} y + z_\mathrm{r} L_\mathrm{r}}{D_2}. \tag{A.7}$$

Thus, equation (A.1) can be rewritten as:

$$\mathrm{d}G(x,y) = \frac{\rho(m+1)A_\mathrm{r} L_\mathrm{s} L_\mathrm{r}}{2\pi^2}\mathfrak{f}(x,y)\mathrm{d}x\mathrm{d}y \tag{A.8}$$

$$\mathfrak{f}(x,y) = \frac{\mathfrak{R}^m\left(x_\mathrm{s}\left(x + \frac{L_\mathrm{s} L_\mathrm{b}}{L_\mathrm{s}+L_\mathrm{r}}\right) + y_\mathrm{s} y + L_\mathrm{s} z_\mathrm{s}\right)\mathfrak{R}\left(x_\mathrm{r}\left(x - \frac{L_\mathrm{r} L_\mathrm{b}}{L_\mathrm{s}+L_\mathrm{r}}\right) + y_\mathrm{r} y + L_\mathrm{r} z_\mathrm{r}\right)}{\left(\left(x + \frac{L_\mathrm{s} L_\mathrm{b}}{L_\mathrm{s}+L_\mathrm{r}}\right)^2 + y^2 + L_\mathrm{s}^2\right)^{\frac{m+3}{2}}\left(\left(x - \frac{L_\mathrm{r} L_\mathrm{b}}{L_\mathrm{s}+L_\mathrm{r}}\right)^2 + y^2 + L_\mathrm{r}^2\right)^2},$$

where the ramp function $\mathfrak{R}(x)$ is used to prevent the negative value of $\cos\phi_1$ and $\cos\psi_2$ in the case of $\phi_1 > \frac{\pi}{2}$ and $\psi_2 > \frac{\pi}{2}$. The total received signal power can be calculated by integrating (A.8) over the entire reflector.

However, channel impulse response is a quantity closely related to delay t. In order to make the received signal power involve the time delay, we firstly consider calculating the power of the received signal experienced a delay of less than t. This amount of power is denoted as $\hat{P}_{\mathrm{opt},h}(t)$. The time delay is in conjunction with the length of the transmission path. With a given positions of light source element and receiving element, all of the single reflection paths with a delay less than t are within an ellipsoid with the foci at the positions of light source and the receiving element as shown in Figure A.2. The ellipsoid is central symmetric respect to the line via the light source and the receiving element positions. For the convenience of defining this ellipsoid, another Cartesian coordinate system x'-y'-z' is defined. In x'-y'-z' system, the centre of the ellipsoid is placed at the origin of the coordinates, and the two foci are placed on

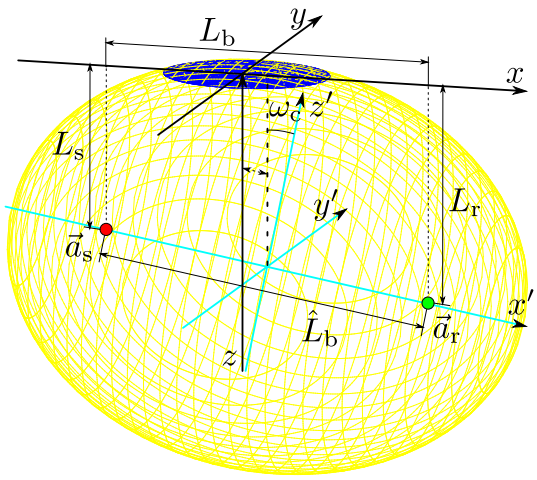

Figure A.2: *Single reflection transmission geometry with considering the paths experiencing a delay less than a certain value t.*

the x' axis with the coordinates of $\left(-\frac{\hat{L}_\mathrm{b}}{2},0,0\right)$ and $\left(\frac{\hat{L}_\mathrm{b}}{2},0,0\right)$, where $\hat{L}_\mathrm{b}^2 = L_\mathrm{b}^2 + (L_\mathrm{s}-L_\mathrm{r})^2$. The equation for the ellipsoid can be written as:

$$\frac{x'^2}{(ct/2)^2} + \frac{y'^2}{(ct/2)^2 - \left(\hat{L}_\mathrm{b}/2\right)^2} + \frac{z'^2}{(ct/2)^2 - \left(\hat{L}_\mathrm{b}/2\right)^2} \leq 1, \tag{A.9}$$

With a given coordinate in x-y-z, the corresponding coordinate in x'-y'-z' can be obtained by carrying out a coordinate transformation as follows:

$$\begin{bmatrix} x' \\ y' \\ z' \end{bmatrix} = \begin{bmatrix} \cos\omega_\mathrm{c} & 0 & \sin\omega_\mathrm{c} \\ 0 & 1 & 0 \\ -\sin\omega_\mathrm{c} & 0 & \cos\omega_\mathrm{c} \end{bmatrix} \begin{bmatrix} x \\ y \\ z \end{bmatrix} + \begin{bmatrix} \frac{2L_\mathrm{s}L_\mathrm{r}}{L_\mathrm{s}+L_\mathrm{r}}\sin\omega_\mathrm{c} + \frac{\hat{L}_\mathrm{b}(L_\mathrm{s}-L_\mathrm{r})}{2(L_\mathrm{s}+L_\mathrm{r})} \\ 0 \\ \frac{2L_\mathrm{s}L_\mathrm{r}}{L_\mathrm{s}+L_\mathrm{r}}\cos\omega_\mathrm{c} \end{bmatrix}, \tag{A.10}$$

where ω_c is the rotation angle of the coordinates, and $\omega_\mathrm{c} = \arctan\left(\frac{L_\mathrm{s}-L_\mathrm{r}}{L_\mathrm{b}}\right)$. In conjunction with (A.10), the ellipsoid equation in the x-y-z system can be written as:

$$\frac{\left(x\cos\omega_\mathrm{c} + z\sin\omega_\mathrm{c} + \frac{2L_\mathrm{s}L_\mathrm{r}}{L_\mathrm{s}+L_\mathrm{r}}\sin\omega_\mathrm{c} + \frac{\hat{L}_\mathrm{b}(L_\mathrm{s}-L_\mathrm{r})}{2(L_\mathrm{s}+L_\mathrm{r})}\right)^2}{(ct/2)^2} + \frac{y^2}{(ct/2)^2 - \left(\hat{L}_\mathrm{b}/2\right)^2}$$
$$+ \frac{\left(z\cos\omega_\mathrm{c} - x\sin\omega_\mathrm{c} + \frac{2L_\mathrm{s}L_\mathrm{r}}{L_\mathrm{s}+L_\mathrm{r}}\cos\omega_\mathrm{c}\right)^2}{(ct/2)^2 - \left(\hat{L}_\mathrm{b}/2\right)^2} \leq 1. \tag{A.11}$$

In the case that the signal is reflected by a single diffusing surface, all reflected point have to

fulfil the condition $z = 0$, which leads to an area on the x-y plane as:

$$\mathcal{W}_0(t): \left(1 - \frac{L_{\mathrm{b}}^2}{c^2t^2}\right) x^2 + y^2 + \left(\frac{L_{\mathrm{b}}\left(L_{\mathrm{s}} - L_{\mathrm{r}}\right)\left(c^2t^2 - L_0^2\right)}{c^2t^2\left(L_{\mathrm{s}} + L_{\mathrm{r}}\right)}\right) x - \left(\frac{\left(c^2t^2 - L_0^2\right)^2\left(L_{\mathrm{s}} - L_{\mathrm{r}}\right)^2}{4c^2t^2\left(L_{\mathrm{s}} + L_{\mathrm{r}}\right)^2} + \frac{\left(c^2t^2 - L_0^2\right)L_{\mathrm{s}}L_{\mathrm{r}}}{\left(L_{\mathrm{s}} + L_{\mathrm{r}}\right)^2}\right) \leq 0. \tag{A.12}$$

This ellipse defines the integration limits for x and y when calculating $\hat{P}_{\mathrm{opt},h}(t)$. Therefore, $\hat{P}_{\mathrm{opt},h}(t)$ can be calculated as:

$$\hat{P}_{\mathrm{opt},h}(t) = \frac{\rho(m+1)A_{\mathrm{r}}L_{\mathrm{s}}L_{\mathrm{r}}}{2\pi^2} \iint_{\mathcal{W}_0(t)} \mathfrak{f}(x,y)\mathrm{d}x\mathrm{d}y. \tag{A.13}$$

Thus, the channel impulse response can be calculated as $\hbar(t) = \frac{\mathrm{d}\hat{P}_{\mathrm{opt},h}(t)}{\mathrm{d}t}$. For the convenience of calculating $\hbar(t)$, a polar coordinate system with a radius r and a polar angle θ is used. The polar coordinates can be calculated based on the following relationships:

$$x = r\cos\theta, \tag{A.14}$$

$$y = r\sin\theta. \tag{A.15}$$

By inserting (A.14) and (A.15) into (A.8), it gives:

$$\mathrm{d}G(r,\theta) = \frac{\rho(m+1)A_{\mathrm{r}}L_{\mathrm{s}}L_{\mathrm{r}}}{2\pi^2}\mathfrak{f}(r,\theta)r\mathrm{d}r\mathrm{d}\theta, \tag{A.16}$$

where $\mathfrak{f}(r,\theta)$ can be found in (3.3). By inserting (A.14) and (A.15) into (A.12), it gives:

$$\mathcal{W}_0(t): \left(1 - \frac{L_{\mathrm{b}}^2\cos^2\theta}{c^2t^2}\right) r^2 + \left(\frac{L_{\mathrm{b}}\left(L_{\mathrm{s}} - L_{\mathrm{r}}\right)\left(c^2t^2 - L_0^2\right)\cos\theta}{c^2t^2\left(L_{\mathrm{s}} + L_{\mathrm{r}}\right)}\right) r - \left(\frac{\left(c^2t^2 - L_0^2\right)^2\left(L_{\mathrm{s}} - L_{\mathrm{r}}\right)^2}{4c^2t^2\left(L_{\mathrm{s}} + L_{\mathrm{r}}\right)^2} + \frac{\left(c^2t^2 - L_0^2\right)L_{\mathrm{s}}L_{\mathrm{r}}}{\left(L_{\mathrm{s}} + L_{\mathrm{r}}\right)^2}\right) \leq 0. \tag{A.17}$$

Thus, the channel impulse response can be decomposed into two one-dimensional integrations as:

$$\hbar(t) = \frac{\mathrm{d}}{\mathrm{d}t}\left(\frac{\rho(m+1)A_{\mathrm{r}}L_{\mathrm{s}}L_{\mathrm{r}}}{2\pi^2}\int_0^{2\pi}\int_0^{\mathfrak{r}_\theta(t)}\mathfrak{f}(r,\theta)r\mathrm{d}r\mathrm{d}\theta\right), \tag{A.18}$$

where the value of the limit $\mathfrak{r}$ can be calculated by evaluating the bound value of r in $\mathcal{W}_0(t)$. It

is determined by making the inequality $\mathcal{W}_0(t)$ into an equality, and solving this equation with considering r as the unknown. Thus, this solution to r is $\mathfrak{r}_\theta(t)$ which can be concluded as (3.4). According the Chain rule $\frac{\mathrm{d}}{\mathrm{d}t}\int_0^{\mathfrak{f}_1(t)}\mathfrak{f}_2(r)\mathrm{d}r = \mathfrak{f}_2(\mathfrak{f}_1(t))\frac{\mathrm{d}\mathfrak{f}_1(t)}{\mathrm{d}t}$, the CIR can be further simplified as (3.2).

Appendix B

Floor-to-Ceiling-to-Receiver Channel Impulse Response Approximation

In this approximation, a special case floor-to-ceiling-to-receiver (FCR) channel impulse response (CIR) result in closed-form is used as a base function. The FCR CIR expression with $\tilde{r} = 0$ m can be calculated as:

$$\begin{aligned} h^{[2]}_{\mathrm{fcr},\tilde{r}=0}(t) &= \hbar_{\left\{1, A_{\mathrm{pd}}, \rho_{\mathrm{c}}, z_{\mathrm{s}}, z_{\mathrm{s}}-z_{\mathrm{r}}, 0, \vec{a}_{\mathrm{b,tfcr}}, \vec{a}_{\mathrm{r,tfcr}}\right\}}(t), \\ &= \frac{2^7 A_{\mathrm{pd}} \rho_{\mathrm{c}} z_{\mathrm{s}}^2 \left(z_{\mathrm{s}} - z_{\mathrm{r}}\right)^2 \mathcal{U}\left(t - \frac{2z_{\mathrm{s}} - z_{\mathrm{r}}}{c}\right)}{\pi c^6 t^7 \left(1 - \frac{z_{\mathrm{r}}^2 (2z_{\mathrm{s}} - z_{\mathrm{r}})^2}{c^4 t^4}\right)^3}, \end{aligned} \tag{B.1}$$

which is a modification to the result derived in [23]. In order to find the suitable approximation to the case with any $\tilde{r} \geq 0$, three CIR examples with $\tilde{r} = 0, 3, 6$ m are shown in Figure. B.1. In these examples, $z_{\mathrm{r}} = 0.75$ m and the configuration of the remaining parameters are the same as those listed in Table 3.3. It shows that the shapes of the curves with different $\tilde{r}$ are similar. With the increase of $\tilde{r}$ the delay of the beginning of the response is larger. In addition, the magnitude of the CIR is slightly increased compared to the case with $\tilde{r} = 0$ m. Therefore, the CIR with $\tilde{r} \neq 0$ m is approximated as:

$$h^{[2]}_{\mathrm{fcr}}(t) \approx \hat{h}^{[2]}_{\mathrm{fcr}}(t) = \mathcal{F}_{\mathrm{fcr}} \mathcal{U}\left(t - \frac{D_{0,\mathrm{FCR}}}{c}\right) h^{[2]}_{\mathrm{fcr},\tilde{r}=0}(t), \tag{B.2}$$

where $\mathcal{U}\left(t - D_{0,\mathrm{FCR}}/c\right)$ correct the minimum delay of the CIR, and $\mathcal{F}_{\mathrm{fcr}}$ is a scaling factor to linearly amplify the overall magnitude of $\mathcal{U}\left(t - D_{0,\mathrm{FCR}}/c\right) h^{[2]}_{\mathrm{fcr},\tilde{r}=0}(t)$ to match $h^{[2]}_{\mathrm{fcr}}(t)$. The shortest path in the FCR link is $D_{0,\mathrm{FCR}} = \sqrt{\left(2z_{\mathrm{s}} - z_{\mathrm{r}}\right)^2 + \tilde{r}^2}$. A number of suitable function of $\mathcal{F}_{\mathrm{fcr}}$ causing little error has been found by using curve fitting tools. The following function is selected as it achieves a good balance between accuracy and complexity:

$$\mathcal{F}_{\mathrm{fcr}}(u, v) = \left(\frac{0.107}{u} + 0.02179\right) v^2 + 1, \tag{B.3}$$

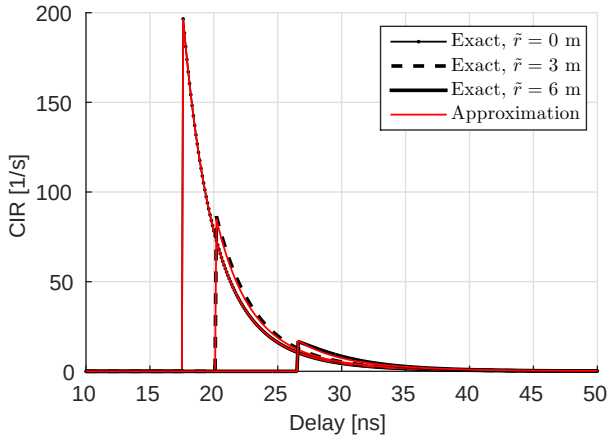

Figure B.1: *CIRs with FCR category $h_{\text{fcr}}^{[2]}(t)$ with $\tilde{r} = 0$ m, $\tilde{r} = 3$ m and $\tilde{r} = 6$ m. The results of the approximated calculation are also shown in this figure.*

where $u = \frac{z_{\text{s}} - z_{\text{r}}}{z_{\text{s}}}$ and $v = \frac{\tilde{r}}{z_{\text{s}}}$. Therefore, the final approximated expression can be found as (3.16). In Figure. B.1, the approximated CIR results are presented in addition to their corresponding exact CIR results. It can be observed that the approximated curve offers an accurate estimation to the exact expression of the FCR CIR. In order to further evaluate the accuracy of the approximation with various configurations. The normalised mean square error (NMSE) of the CIR approximation is calculated, which is defined as:

$$e_{\text{nmse}} = \frac{\mathbb{E}_t\left[\left(\hat{h}(t) - h(t)\right)^2\right]}{\mathbb{E}_t\left[h^2(t)\right]}, \tag{B.4}$$

where $\hat{h}(t)$ denotes the approximated CIR result. Figure B.2 shows results of NMSE varies with $\tilde{r}/z_{\text{s}}$ and with $z_{\text{r}}/z_{\text{s}}$. It shows that with most of the configurations, the NMSE is negligi-

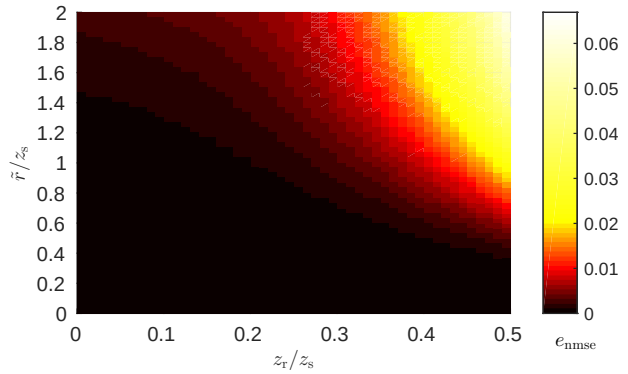

Figure B.2: *NMSE of the FCR CIR approximation.*

ble. When both $\tilde{r}/z_{\mathrm{s}}$ and $z_{\mathrm{r}}/z_{\mathrm{s}}$ are significantly large, the NMSE start to increase. However, compared with other significant channel component in the following calculation, the magnitude of the FCR CIR is extremely small in this case. Therefore, this approximation error will not significantly affect the accuracy of the final result of the CIR calculation with the transmitter-to-floor-to-ceiling-to-receiver (TFCR) category.

Appendix C
Transmitter-to-Wall-to-Ceiling Channel Impulse Response Approximation

In this approximation, a special case transmitter-to-wall-to-ceiling (TWC) channel impulse response (CIR) result in closed-form is used as a base function. The TWC CIR expression with $y = 0$ m can be calculated as:

$$\begin{aligned} h^{[2]}_{\mathrm{twc},y=0}(t) &= \hbar_{\left\{m,\mathrm{d}A,\rho_\mathrm{w},D_\mathrm{s},x,0,\vec{a}^{*}_{\mathrm{s,twcr}},\vec{a}^{*}_{\mathrm{b,twcr}}\right\}}(t) \\ &= \frac{\rho_\mathrm{w}(m+1)D_\mathrm{s}x\mathcal{B}\left(\frac{m+2}{2},\frac{m+2}{2}\right)2^m\mathfrak{r}^2_\mathrm{twc}(t)A_\mathrm{r}\mathcal{U}\left(t-\frac{D_\mathrm{s}+x}{c}\right)}{\pi^2 t\left(1+\frac{D_\mathrm{s}^2}{\mathfrak{r}^2_\mathrm{twc}(t)}\right)^{\frac{m-1}{2}}\left(\frac{c^2t^2}{4}-\frac{(D_\mathrm{s}^2-x^2)^2}{4c^2t^2}\right)^3}, \end{aligned} \tag{C.1}$$

where $\mathcal{B}(u,v)$ is the beta function, and

$$\mathfrak{r}^2_\mathrm{twc}(t) = \frac{c^2t^2}{4} + \frac{\left(D_\mathrm{s}^2-x^2\right)^2}{4c^2t^2} - \frac{D_\mathrm{s}^2+x^2}{2}. \tag{C.2}$$

Considering a TWC channel with $y \neq 0$, the overview of the channel geometry is shown in Figure C.1 (a). The shortest propagation path can be calculated as $D_{0,\mathrm{twc}} = \sqrt{(D_\mathrm{s}+x)^2+y^2}$. The base function (C.1) with the modified separation between the wall and transmitter (receiver)

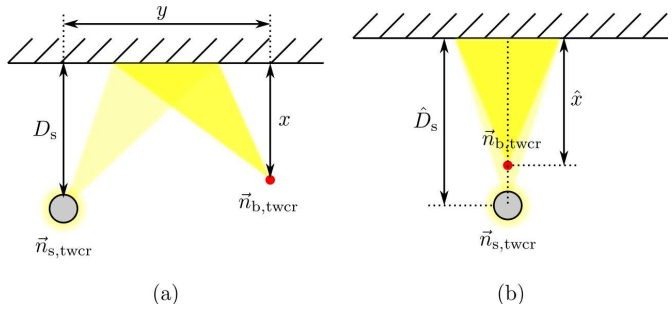

Figure C.1: *(a) Top view of the TWC channel geometry with $y \neq 0$ m. (b) Top view of the approximated TWC channel geometry with $y = 0$ m; Note that the distance from the transmitter / ceiling point $\vec{a}_{\mathrm{b,twcr}}$ to the wall surface is modified as $\hat{D}_\mathrm{s}$ / $\hat{x}$.*

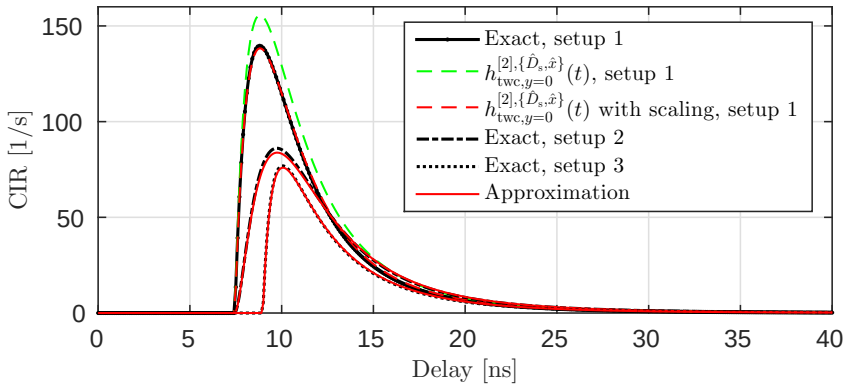

Figure C.2: *CIR results of the first part of the Channel in TWCR case* $h_{\text{twc}}^{[2]}(t)$. *Setup 1:* $D_{\text{s}} = 1$ *m,* $x = 1$ *m,* $y = 1$ *m,* $\phi_{1/2} = 60°$. *Setup 2:* $D_{\text{s}} = 1$ *m,* $x = 1$ *m,* $y = 1$ *m,* $\phi_{1/2} = 40°$. *Setup 3:* $D_{\text{s}} = 2$ *m,* $x = 0.5$ *m,* $y = 1$ *m,* $\phi_{1/2} = 60°$. *The results of the approximated curves are also shown in this figure. Setup 1 is used to demonstrate the approximation method.*

of $\hat{D}_{\text{s}}$ ($\hat{x}$) is used to approximate the exact TWC channel as shown in Figure C.1 (b). To ensure that the approximated CIR and the exact CIR have the same minimum delay, the corresponding shortest propagation distances in the exact and approximated TWC channel should be the same: $D_{0,\text{twc}} = \hat{D}_{\text{s}} + \hat{x}$. Due to the difference in the incident (radiant) angles to (from) the wall in the exact and approximated channel, a scaling factor $\mathcal{F}_{\text{twc}}$ is required to adjust the power level of the approximated CIR. Therefore, the proposed method to approximate the TWC CIR is defined as:

$$h_{\text{twc}}^{[2],\{D_{\text{s}},x,y\}}(t) \approx \mathcal{F}_{\text{twc}} h_{\text{twc},y=0}^{[2],\{\hat{D}_{\text{s}},\hat{x}\}}(t). \tag{C.3}$$

Next, an example setup is considered to demonstrate this approximation. A TWC channel with $D_{\text{s}} = 1$ m, $x = 1$ m, $y = 1$ m and $\phi_{1/2} = 60°$ is assumed. The remaining channel parameters are the same as those listed in Table 3.3. The CIR result calculated using (3.27) is shown in Figure C.2. In addition, the CIR result calculated using the base function (C.1) with $\hat{D}_{\text{s}} = 1.118$ m and $\hat{x} = 1.118$ m is presented, which shows a similar response to that calculated using (3.27) with a greater magnitude as shown in Figure C.2. By scaling the CIR result calculated using the base function with a factor of 0.8882, the approximated CIR curve shows a reasonable approximation to the exact CIR curve. This example shows the effectiveness of the TWC CIR approximation method of using (C.3). Appropriate functions for the calculation of $\hat{D}_{\text{s}}$, $\hat{x}$ and $\mathcal{F}_{\text{twc}}$ are important to the accuracy of the approximation. In this study, curve fitting tool is used to develop these functions. With the relationship $D_{0,\text{twc}} = \hat{D}_{\text{s}} + \hat{x}$, the values of $\hat{D}_{\text{s}}$ and $\hat{x}$ can

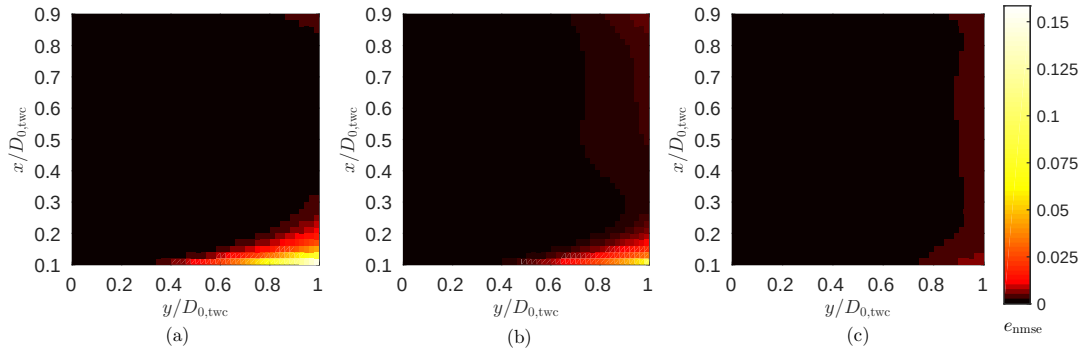

Figure C.3: *NMSE of the TWC CIR approximation. (a)* $\phi_{1/2} = 20°$. *(b)* $\phi_{1/2} = 40°$. *(c)* $\phi_{1/2} = 60°$.

be calculated as:

$$\hat{D}_{\mathrm{s}} = \alpha_{\mathrm{twc}} D_{0,\mathrm{twc}}, \tag{C.4}$$

$$\hat{x} = (1 - \alpha_{\mathrm{twc}})\, D_{0,\mathrm{twc}}, \tag{C.5}$$

where the factor α_{twc} is defined as the ratio of $\hat{D}_{\mathrm{s}}$ to $D_{0,\mathrm{twc}}$. a suitable expression for α_{twc} is found as:

$$\alpha_{\mathrm{twc}} = \frac{D_{\mathrm{s}}}{\sqrt{(D_{\mathrm{s}} + x)^2 + 4y^2\,(m^{0.045} - 1)}}. \tag{C.6}$$

Based on (C.6), a suitable function for $\mathcal{F}_{\mathrm{twc}}$ is found as:

$$\mathcal{F}_{\mathrm{twc}} = \frac{x + \beta_{\mathrm{twc}} D_{\mathrm{s}}}{\sqrt{(x + \beta_{\mathrm{twc}} D_{\mathrm{s}})^2 + y^2 + 0.8125 \frac{y^3 |x - D_{\mathrm{s}}|^3}{(x + D_{\mathrm{s}})^4}}}, \tag{C.7}$$

where $\beta_{\mathrm{twc}} = 0.8088 \exp(-0.6878m) + 0.5304 \exp(-0.007006m)$. In Figure C.2, the CIRs of another two setups calculated using (C.3) in conjunction with (C.4), (C.5), (C.6) and (C.7) are demonstrated. Both results agree with the exact result calculated using (3.27). In order to proof that the functions (C.6) and (C.7) offer reasonable approximation with the configurations of interest, the normalised mean square error (NMSE) of the approximation is evaluated, which is defined by (B.4) in Appendix B. The results of NMSE varies with $y/D_{0,\mathrm{twc}}$ and $x/D_{0,\mathrm{twc}}$ in the case of $\phi_{1/2} = 20°, 40°, 60°$ are shown in Figure C.3. It shows that with majority of the configurations, the NMSE level is negligible. It is noted that in the case of $y/D_{0,\mathrm{twc}}$ is

significant and $x/D_{0,\mathrm{twc}}$ is very close to zero, the NMSE start to increase, especially when $\phi_{1/2}$ is small. However, in the calculation of transmitter-to-wall-to-ceiling-to-receiver (TWCR) CIR, the power contribution from the TWC channel with this configuration is very little. Therefore, this approximation error will not significantly affect the accuracy of the final result of the CIR calculation with the TWCR category.

Appendix D
Derivation of the Characteristic Function of the Interference Term

The derivations start from the term with bracket in the exponent of (4.36). with $a \to \infty$ as:

$$\begin{aligned}
&\lim_{a\to\infty}\left(a^2 - r_0^2 - \int_{\sqrt{r_0^2+\Delta z^2}}^{\sqrt{a^2+\Delta z^2}} 2D\mathrm{e}^{j\omega g_1(D)}\mathrm{d}D\right) \overset{\text{(a)}}{=} \lim_{a\to\infty}\Bigg(\left(r_0^2+\Delta z^2\right)\mathrm{e}^{j\omega g\left(\sqrt{r_0^2+\Delta z^2}\right)} \\
&+ a^2 - r_0^2 - \left(a^2+\Delta z^2\right)\mathrm{e}^{j\omega g\left(\sqrt{a^2+\Delta z^2}\right)} - \int_{g\left(\sqrt{a^2+\Delta z^2}\right)}^{g\left(\sqrt{r_0^2+\Delta z^2}\right)} \left(g^{-1}(x)\right)^2 j\omega\mathrm{e}^{j\omega x}\mathrm{d}x\Bigg) \\
&= \lim_{a\to\infty}\left(a^2\left(1-\mathrm{e}^{j\omega g\left(\sqrt{a^2+\Delta z^2}\right)}\right)\right) + r_0^2\left(\mathrm{e}^{j\omega g\left(\sqrt{r_0^2+\Delta z^2}\right)}-1\right) + \Delta z^2\mathrm{e}^{j\omega g\left(\sqrt{r_0^2+\Delta z^2}\right)} \\
&- \lim_{a\to\infty}\left(\Delta z^2\mathrm{e}^{j\omega g\left(\sqrt{a^2+\Delta z^2}\right)}\right) - \lim_{a\to\infty}\left(\int_{g\left(\sqrt{a^2+\Delta z^2}\right)}^{g\left(\sqrt{r_0^2+\Delta z^2}\right)} \left(g^{-1}(x)\right)^2 j\omega\mathrm{e}^{j\omega x}\mathrm{d}x\right) \\
&= \left(r_0^2+\Delta z^2\right)\left(\mathrm{e}^{j\omega\left(r_0^2+\Delta z^2\right)^{-m-3}}-1\right) - \int_0^{\left(r_0^2+\Delta z^2\right)^{-m-3}} x^{-\frac{1}{m+3}} j\omega\mathrm{e}^{j\omega x}\mathrm{d}x, \qquad \text{(D.1)}
\end{aligned}$$

where in (a), integration by substitution is used. By using (D.1), the characteristic function of the CCI can be found as:

$$\begin{aligned}
\varphi_{\mathcal{I}}(\omega|r_0) &= \mathrm{e}^{\frac{\Lambda\pi}{\kappa_{\mathrm{rf}}}\left(\left(r_0^2+\Delta z^2\right)\left(1-\mathrm{e}^{j\omega\left(r_0^2+\Delta z^2\right)^{-m-3}}\right)+j\omega\int_0^{\left(r_0^2+\Delta z^2\right)^{-m-3}} x^{-\frac{1}{m+3}}\mathrm{e}^{j\omega x}\mathrm{d}x\right)} \\
&\overset{\text{(a)}}{=} \exp\Bigg(\frac{\Lambda\pi}{\kappa_{\mathrm{rf}}}\Bigg(\left(r_0^2+\Delta z^2\right)\left(1-\sum_{n_1=0}^{\infty}\frac{(j\omega)^{n_1}\left(r_0^2+\Delta z^2\right)^{-n_1(m+3)}}{n_1!}\right) \\
&+ j\omega\int_0^{\left(r_0^2+\Delta z^2\right)^{-m-3}} x^{-\frac{1}{m+3}}\sum_{n_2=0}^{\infty}\frac{(j\omega x)^{n_2}}{n_2!}\mathrm{d}x\Bigg)\Bigg) \\
&\overset{\text{(b)}}{=} \exp\Bigg(-\frac{\Lambda\pi}{\kappa_{\mathrm{rf}}}\Bigg(\sum_{n_1=1}^{\infty}\frac{(j\omega)^{n_1}\left(r_0^2+\Delta z^2\right)^{1-n_1(m+3)}}{n_1!} \\
&- \sum_{n_3=1}^{\infty}\frac{(j\omega)^{n_3}}{n_3!}\cdot\frac{n_3(m+3)\left(r_0^2+\Delta z^2\right)^{1-n_3(m+3)}}{n_3(m+3)-1}\Bigg)\Bigg) \\
&= \exp\left(\sum_{n=1}^{\infty}\frac{(j\omega)^n}{n!}\cdot\frac{\Lambda\pi\left(r_0^2+\Delta z^2\right)^{1-n(m+3)}}{\kappa_{\mathrm{rf}}(n(m+3)-1)}\right), \qquad \text{(D.2)}
\end{aligned}$$

where in (a), the Taylor series for e^x is used, and in (b), the two summations can be combined.

Appendix E
Proof of the Modified Proportional Fairness Scheduling

In step 12 of Algorithm 2, $K_{n_1,n_{\max}}$ and $K_{n_1,n_{\min}}$ are adjusted while other elements in $\mathbf{K}$ remain the same. In this proof, we only consider varying one of the N_{W} sub-bands $\hat{n}_1$. The resource allocation plan for other sub-bands remains the same. Since $\sum_{n_2} K_{\hat{n}_1,n_2} = K_{\hat{n}_1}$, $K_{\hat{n}_1,n_{\min}}$ varies if $K_{\hat{n}_1,n_{\max}}$ changes its value. Their relationship is shown as follows:

$$K_{\hat{n}_1,n_{\min}} = M - K_{\hat{n}_1,n_{\max}}, \tag{E.1}$$

$$M = K_{\hat{n}_1} - \sum_{n_2 \neq n_{\min},n_{\max}} K_{\hat{n}_1,n_2}. \tag{E.2}$$

A variable $\hat{K}$ is defined to replace $K_{\hat{n}_1,n_{\max}}$. Then Ξ can be considered to be a function of $\hat{K}$. Thus, we can write Ξ as:

$$\begin{aligned}\Xi\left(\hat{K}\right) &= \ln\left(s_{n_{\max}}\left(\hat{K}\right)\right) + \ln\left(s_{n_{\min}}\left(\hat{K}\right)\right) + \sum_{n_2 \neq n_{\min},n_{\max}} \ln\left(s_{n_2}\right) \\ &= \ln\left(\hat{K}\varepsilon_{\hat{n}_1,n_{\max}} + \sum_{n_1 \neq \hat{n}_1} K_{n_1,n_{\max}}\varepsilon_{n_1,n_{\max}}\right) + \sum_{n_2 \neq n_{\min},n_{\max}} \ln\left(s_{n_2}\right) \\ &+ \ln\left(\left(M - \hat{K}\right)\varepsilon_{\hat{n}_1,n_{\min}} + \sum_{n_1 \neq \hat{n}_1} K_{n_1,n_{\min}}\varepsilon_{n_1,n_{\min}}\right).\end{aligned} \tag{E.3}$$

Then it can be found that:

$$\frac{\mathrm{d}\Xi\left(\hat{K}\right)}{\mathrm{d}\hat{K}} = \frac{\varepsilon_{\hat{n}_1,n_{\max}}}{s_{n_{\max}}\left(\hat{K}\right)} - \frac{\varepsilon_{\hat{n}_1,n_{\min}}}{s_{n_{\min}}\left(\hat{K}\right)}. \tag{E.4}$$

If we let $\hat{K} = K_{\hat{n}_1,n_{\max}}$, according to step 7 of Algorithm 2, we have that $\frac{\mathrm{d}\Xi\left(\hat{K}\right)}{\mathrm{d}\hat{K}} \geq 0$. This means that $\Xi\left(\hat{K}\right)$ is an increasing function at $K_{\hat{n}_1,n_{\max}}$. Therefore, if we slightly increase $\hat{K}$, the probability that $\Xi\left(\hat{K}\right)$ will increase is high. To guarantee the convergence of Algorithm 2,

the increment of $\hat{K}$ is minimised to one, since the number of subcarriers has to be an integer. With the updating of $\mathbf{K}$ in Algorithm 2, the values of elements in $\vec{C}$ in step 6 of Algorithm 2 will converge to a same value. When $\vec{C}$ converge for all sub-bands, Ξ is maximised.

Appendix F
List of Publications

This chapter contains a list of published papers.

F.1 Journal Papers

C. Chen, D. A. Basnayaka, and H. Haas, "Downlink Performance of Optical Attocell Networks," J. Lightw. Technol., vol. 34, pp. 137–156, Jan., 2016.

C. Chen, S. Videv, D. Tsonev, and H. Haas, "Fractional Frequency Reuse in DCO-OFDM-Based Optical Attocell Networks," J. Lightw. Technol., vol. 33, pp. 3986–4000, Oct., 2015.

F.2 Conference Papers

C. Chen, D. Basnayaka and H. Haas, "Non-line-of-sight channel impulse response characterisation in visible light communications," IEEE Int. Conf. on Commun., (Kuala Lumpur, Malaysia) pp. 1-6, May., 22–27 2016.

C. Chen, I. Muhammad, D. Tsonev, and H. Haas, "Analysis of Downlink Transmission in DCO-OFDM-Based Optical Attocell Networks," in Proc. of IEEE Global Commun. Conf., (Austin, TX), Dec., 8–12 2014.

C. Chen, D. Basnayaka, and H. Haas, "Downlink SINR Statistics in OFDM-Based Optical Attocell Networks with a Poisson Point Process Network Model," in Proc. of IEEE Global Commun. Conf., (San Diego, CA), pp. 1–6, Dec., 6–10 2015.

C. Chen, N. Serafimovski, and H. Haas, "Fractional Frequency Reuse in Optical Wireless Cellular Networks," in Proc. of the Int. Symp. on Personal, Indoor and Mobile Radio Commun., (London, United Kingdom), pp. 35943598, Sept., 8–11 2013.

C. Chen, D. Tsonev, and H. Haas, "Joint Transmission in Indoor Visible Light Communication

Downlink Cellular Networks," in IEEE Globecom Workshops, (Atlanta, GA), pp. 11271132, Dec., 9–13 2013.

Appendix G
Selected Publications

This chapter contains all published work.

JOURNAL OF LIGHTWAVE TECHNOLOGY, VOL. 34, NO. 1, JANUARY 1, 2016 137

Downlink Performance of Optical Attocell Networks

Cheng Chen, *Student Member, IEEE*, Dushyantha A. Basnayaka, *Member, IEEE*, and Harald Haas, *Member, IEEE*

(Tutorial Review)

***Abstract*—An optical attocell network is proposed as an indoor small-cell cellular network based on visible light communication. In this paper, the downlink performance of optical attocell networks is comprehensively analyzed. In particular, signal-to-interference-plus-noise ratio, outage probability, and the resulting achievable cell data rates of optical attocell networks with optical orthogonal frequency division multiplexing are analyzed. With different lighting network designs, the cell deployments of optical attocell networks may vary considerably. Hence, attocell networks with different cell deployments are considered and compared. The results show that the hexagonal and Poisson point process random cell deployments represents the best- and the worst-case performance of practical optical attocell deployments, respectively. In addition, the performance of optical attocell networks is compared with that achieved by other radio frequency small-cell networks. The results show that a well-designed optical attocell network can perform better than the state-of-the-art femtocell network or millimeter-wave system in terms of indoor area data rate (data rate per unit area).**

***Index Terms*—Cellular network, optical attocell network, orthogonal frequency division multiplexing (OFDM), Poisson point process (PPP), visible light communication (VLC).**

I. Introduction

With the introduction of mobile communication technologies, the number of wireless data services and users have increased significantly. This has resulted in a considerable increase in wireless data traffic [1]. If this trend continues, the limited available radio frequency (RF) spectrum would no longer fulfill the future wireless data traffic demand. One of the solutions to this challenge is to explore the visible light region of the electromagnetic spectrum for wireless data communication. This is generally referred to as visible light communication (VLC) [2]. It has been recognized that wireless data mostly originates in indoor environments (70%) [3]. Therefore, using indoor luminaries for wireless data transmission offers a promising solution to alleviate the exponentially increasing traffic of existing RF wireless systems. In addition, VLC has advantages such as license-free bandwidth and secure data transmission. In addition, the visible light spectrum is 1000 times larger than the entire 300 GHz RF spectrum, and it use does not generate interference to existing RF systems [4].

Key techniques to enhance spectral efficiency of wireless communication systems include advanced transmission schemes that harness the spatial dimension, channel aggregation, improved resource allocation, and cell densification. Among these techniques, cell densification has been shown to be the most effective approach, which can potentially achieve over 1000-fold area spectral efficiency (ASE) gains [3]. Therefore, the small-cell concept as part of heterogeneous wireless networks is a key enabling element. A femtocell network is one such indoor small-cell system. Research has shown that the femtocell system can significantly increase the ASE of a cellular system [5]. VLC enables a step-change improvement of the small-cell concept while completely avoiding interference to incumbent wireless networks [6]. Each light fixture in a room is used as an optical base station (BS) to serve multiple users. This VLC cellular network is termed an optical light fidelity (LiFi) attocell network. Similar to a femtocell network, an optical attocell exhibits full functionality offered by a cellular system (full duplexing, multiple access and handover). However, its cell size is smaller, and it uses the license-free visible light spectrum. With the development of solid state lighting technology, a light emitting diode (LED) is now commonly used by the lighting industry due to its high energy efficiency and long lifetime. Therefore, an LED is considered to be used as the main element of the transmitter side. Since an LED is a non-coherent light source, intensity modulation (IM) is the most appropriate method to encode digital information [7]. A photo-diode (PD) is used as the main element at the receiver side, which directly converts the received optical intensity into an electrical current signal. This mechanism is referred to as direct detection (DD).

One of the main factors that limits the maximum achievable data rate of an LED/PD based VLC system is the available modulation bandwidth, which is mainly limited by the response time of the front-end devices, primarily the LED device. Thus, research has been carried out to expand the bandwidth of the LED. In [8], a commercially available phosphor-based LED is considered. By filtering out the phosphor component of the optical output, a 3-dB bandwidth of 20 MHz can be achieved with only the blue component of the optical output. In [9], a single 50-μm gallium nitride LED is used in an experimental VLC link. The measured channel 3 dB bandwidth is about 60 MHz. Modulation techniques that ensure non-negativity of the signal while achieving close to optimum practical data rates are developed [10]. In [11], two types of optical-orthogonal frequency division multiplexing (O-OFDM) are introduced, namely, DC (direct current)-biased optical (DCO)-OFDM and asymmetrically clipped optical (ACO)-OFDM. In [10], [12], enhanced unipolar OFDM (eU-OFDM) is proposed. eU-OFDM combines the advantages of DCO-OFDM and ACO-OFDM in a unique way. This results in both excellent spectral and also energy efficiency. In an attempt to study the achievable data rate of a single link VLC, an

Manuscript received June 29, 2015; revised November 15, 2015; accepted December 15, 2015. Date of publication December 21, 2015; date of current version January 24, 2016. The work of Professor H. Haas was supported by EPSRC under Established Career Fellowship Grant EP/K008757/1.

The authors are with the University of Edinburgh, Li-Fi Research and Development Centre, Edinburgh EH9 3JL U.K. (e-mail: cheng.chen@ed.ac.uk; d.basnayaka@ed.ac.uk; h.haas@ed.ac.uk).

Color versions of one or more of the figures in this paper are available online at http://ieeexplore.ieee.org.

Digital Object Identifier 10.1109/JLT.2015.2511015

adaptive DCO-OFDM/discrete multitone (DMT) transmission scheme is used in [9], [13], [14]. In particular, in [9], adaptive DCO-OFDM is combined with a large bandwidth μLED, and this system achieves a data rate of 3 Gb/s. One of the limiting factors for the performance of an optical attocell network is co-channel interference (CCI) caused by using the same transmission resources in adjacent cells. Therefore, several methods have been studied to mitigate CCI in optical attocell networks. In [15] and [16], the concept of fractional frequency reuse and joint transmission is introduced in an optical attocell network, respectively. The results show an improvement in terms of both signal quality and spectral efficiency. In addition, a busy-burst signaling approach is applied in an optical wireless system deployed in an aircraft cabin environment [17]. Spatial diversity is explored in an optical attocell system: in [18] and [19], an angular diversity receiver and spatial division multiple access are considered in an optical attocell network, respectively. Multiple-input multiple-output techniques are considered in VLC systems in [20]–[22]. In addition, the application of orbital angular momentum technique to optical wireless communication is studied in [23].

An optical attocell network is a newly proposed concept which has great potential. There is very little research on the performance of such systems. In [24], an analytical framework for the downlink of an optical attocell network with hexagonal (HEX) cell deployment is proposed. A semi-analytical approach was presented to calculate the statistics of the signal-to-interference-plus-noise ratio (SINR) and spectral efficiency. This work extends [24] by providing an in-depth analysis of the downlink performance of an optical attocell network.

A. Main Contributions

The main contributions of this study are summarized as follows:

1) A system level downlink framework based on DCO-OFDM is introduced. This framework considers several important issues related to the calculation of the SINR. These issues include the available output signal power, the channel characteristics and signal clipping.
2) The effects of varying key network system parameters on the performance are studied. These parameters include the cell radius and Lambertian emission order of the LED light source. This study also provides guidelines for appropriate configurations of these aforementioned parameters.
3) Analytical expressions for the SINR statistics with HEX/Poisson point process (PPP) random networks are derived. HEX cell deployment is considered to be the idealized cellular structure. In contrast, the PPP network model represents the worst case cellular deployment. The analysis of the system performance of both cell deployments provides useful insights in the performance of practical optical attocell networks.
4) The performance of optical attocell networks in terms of data rate and coverage probability is evaluated and compared to the performance achieved by other RF small-cell systems.

The remainder of this paper is organized as follows: the downlink transmission framework is introduced in Section II. The effects of key parameters are presented in Section III. The statistics of SINR with different cell deployment is presented in Section IV. The cell data rate and the outage probability of an optical attocell system are analyzed in Section V. The simulation results with infinite network model is compared to those with a finite network deployed in a room in Section VI. The multi-path (MP) effect due to room surface reflections is taken into account. The performance of the optical attocell systems with different cell deployments is compared in Section VII, and the significance of each cell deployment is discussed. The performance of optical attocell networks are compared to those achieved by other small-cell networks in Section VIII. Finally, the conclusions are given in Section IX.

The following notations are used in this paper: $(\cdot)^*$ is the complex conjugate operation; $\otimes$ is the convolution operator; $\mathbb{E}[\cdot]$ is the statistical expectation; $\mathbb{P}[\cdot]$ is the statistical probability.

II. Downlink Framework

This study focuses on evaluating the downlink capacity of an optical attocell network. Generally, most of the system metrics are based on the achievable SINR. Therefore, this paper develops a framework to analyse the SINR in the system. Handover is important in optical attocell systems. However, mobile users in indoor environments are generally static or moving slowly. Therefore, handover is outside the scope of this study. The cost-effective back-haul network can be realized by using power line communication or ethernet—in particular, power-over-ethernet where the same connection powers the light and provides gigabit connectivity. Alternatively, a high throughput back-haul network can be realized by optical fiber connection with passive optical networking or point-to-point wireless millimeter-wave (mmWave) connection [25]. It is assumed these back-haul connections can provide enough data capacity and would not limit the performance of the optical attocell network. Since this study focuses on the performance of the access network, the effect of the back-haul network is outside the scope of this study. The uplink connection is typically achieved by using wavelength division duplexing with wireless infrared or RF transmission [26], [27]. An in-depth analysis of the uplink performance of a LiFi attocell network is subject to future studies. It has been shown that using VLC in the downlink can off-load a large portion of traffic from RF communication systems [26]. Since the spectrum used for the uplink (infrared or RF) is sufficiently distant from the visible light spectrum, there is negligible interference between the uplink and the downlink.

A. O-OFDM Transmission

In this study, O-OFDM systems are considered. Since the main objective is to achieve high data rates, a spectrum efficient DCO-OFDM system is analyzed as a candidate system. However, the analysis also applies to other types of O-OFDM systems in a similar manner. The block diagram of the downlink system is shown in Fig. 1. For each OFDM frame, K quadrature amplitude modulation (QAM) symbols are fed into the modulator. Since the 0th and $K/2$th samples require no energy, this amount of energy is equally distributed to the remaining samples to ensure that the time-domain signal is normalized. Therefore, the

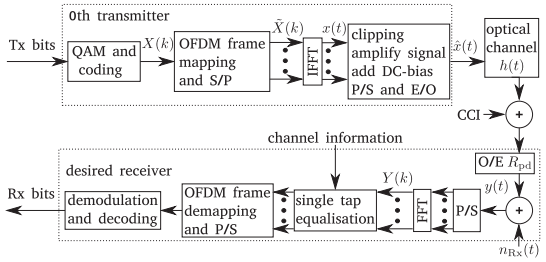

Fig. 1. An optical attocell network DCO-OFDM downlink system.

OFDM frame is normalized by a factor of $\xi = \sqrt{K/(K-2)}$. After the inverse fast Fourier transform (IFFT) operation, the real time domain signal $x(t)$ follows a Gaussian distribution with zero mean and a unity variance. Next, a cyclic-prefix (CP) with a length based on the length of the maximum delay of the channel is added to the frame. Furthermore, the time domain signal $x(t)$ is clipped, amplified by a factor of $\sigma_{\rm x}$ and biased by a DC component $I_{\rm DC}$ in order to modulate the signal by the intensity of the light. The optical signal sample at time slot t can be written as:

$$\hat{x}(t) = \eta_{\rm led}\left(\sigma_{\rm x} U(x(t)) + I_{\rm DC}\right), \tag{1}$$

where $\eta_{\rm led}$ denotes the electrical to optical conversion coefficient. Note that the output optical power is proportional to the input signal current; $\sigma_{\rm x}$ is equivalent to the standard deviation of the electrical signal; and the clipping function $U(v)$ is defined as:

$$U(v) = \begin{cases} \lambda_{\rm t} & : v > \lambda_{\rm t} \\ v & : \lambda_{\rm t} \geq v \geq \lambda_{\rm b} \\ \lambda_{\rm b} & : v < \lambda_{\rm b} \end{cases}, \tag{2}$$

where $\lambda_{\rm t}$ and $\lambda_{\rm b}$ are the normalized top and bottom clipping levels, respectively [28]. According to the Bussgang theorem, the non-linear clipped signal can be modeled as follows:

$$U(x(t)) = \rho x(t) + n_{\rm clip}(t), \tag{3}$$

where ρ is an attenuation factor and $n_{\rm clip}(t)$ is the time domain clipping noise sample.

In this study, multiple optical BSs are considered. Among these BSs, the one offering the highest signal power is assigned to serve the desired user, and the BSs that use the same transmission resources within the remaining BSs causes CCI to the desired user. To distinguish the signals from different BSs, a subscript $i = 0, 1, 2, \ldots$ is added. The case of $i = 0$ corresponds to the case of the desired BS, while $i \in \mathit{И}$ corresponds to the case of the interfering BSs, in which $\mathit{И}$ denotes the set of the BSs using the same transmission resources. Subsequently, the signals pass through the free-space optical channels and are received by the receiver of the desired user. The received signal sample at time slot t can be written as:

$$y(t) = \eta_{\rm pd}\left(\hat{x}_0(t) \otimes h_0(t) + \sum_{i \in \mathit{И}} \hat{x}_i(t) \otimes h_i(t)\right) + n_{\rm Rx}(t), \tag{4}$$

where $\eta_{\rm pd}$ is the PD responsivity of the receiver; $h_i(t)$ denotes the channel impulse response of the VLC system from the ith BS to the desired user; $n_{\rm Rx}(t)$ represents the time domain noise samples at the receiver. In conjunction with the clipping process modeling in (3), the frequency domain received signal sample on subcarrier k after the fast Fourier transform (FFT) operation can be written as:

$$\begin{aligned} Y(k) = {} & \eta_{\rm pd}\eta_{\rm led}\sigma_{\rm x}\left(\rho X_0(k) + N_{{\rm clip},0}(k)\right) H_0(k) + N_{\rm Rx}(k) \\ & + \eta_{\rm pd}\eta_{\rm led}\sigma_{\rm x} \sum_{i \in \mathit{И}} \left(\rho X_i(k) + N_{{\rm clip},i}(k)\right) H_i(k), \end{aligned} \tag{5}$$

where $H_i(k)$ is the frequency response of the VLC channel on the kth subcarrier; $N_{\rm Rx}(k)$ corresponds to the frequency domain receiver noise which follows a Gaussian distribution with zero mean and variance of $\sigma^2_{\rm Rx}$. Here a noise power spectral density (PSD) of N_0 is defined. With a sampling frequency (modulation bandwidth) of $F_{\rm s}$, the receiver noise variance $\sigma^2_{\rm Rx} = \frac{N_0 F_{\rm s}}{\xi^2}$; and $N_{{\rm clip},i}(k)$ represents the FFT of $n_{{\rm clip},i}(t)$. According to the central limit theorem, $N_{{\rm clip},i}(k)$ follows a Gaussian distribution with zero mean and a variance of $\sigma^2_{\rm clip}$. After the single-tap equalization, the desired signal can be recovered to the original QAM symbols $X_0(k)$, while the CCI is converted to Gaussian noise $X_i(k)$ since the interfering signal is not synchronized with the desired user.

SINR is an important metric to evaluate the communication link quality and the transmission capacity in a cellular system. Based on (5), an expression for the SINR on subcarrier k can be written as:

$$\begin{aligned} \gamma(k) = {} & \left(\eta^2_{\rm pd}\eta^2_{\rm led}\sigma^2_{\rm x}\rho^2\xi^2 \left|H_0(k)\right|^2\right) \Big/ \Big(\eta^2_{\rm pd}\eta^2_{\rm led}\sigma^2_{\rm x}\sigma^2_{\rm clip}\left|H_0(k)\right|^2 \\ & + \sum_{i \in \mathit{И}} \eta^2_{\rm pd}\eta^2_{\rm led}\sigma^2_{\rm x}\left(\rho^2 + \sigma^2_{\rm clip}\right)\left|H_i(k)\right|^2 + \sigma^2_{\rm Rx}\Big) \\ = {} & \left(\left(\frac{\rho^2\xi^2\left|H_0(k)\right|^2}{\left(\rho^2 + \sigma^2_{\rm clip}\right)\sum_{i \in \mathit{И}}\left|H_i(k)\right|^2 + \frac{N_0 F_{\rm s}}{\xi^2\eta^2_{\rm pd}\eta^2_{\rm led}\sigma^2_{\rm x}}}\right)^{-1} + \frac{\sigma^2_{\rm clip}}{\rho^2\xi^2}\right)^{-1}, \end{aligned} \tag{6}$$

where the channel gain $|H(k)|^2$, the electrical signal variance $\sigma^2_{\rm x}$, the clipping related parameters $\rho, \sigma^2_{\rm clip}$ and the receiver noise PSD N_0 are analyzed in the following sections. The general ways of calculating these terms are concluded.

B. Channel Model

As implied by formula (6), the VLC channel gain $|H(k)|^2$ has an important role in the value of the SINR. The characteristics of $|H(k)|^2$ is influenced by the response of the front-end devices (LED, PD) and of the free-space transmission. Therefore, $|H(k)|^2$ can be modeled as:

$$|H(k)|^2 = |H_{\rm fe}(k)|^2 |H_{\rm fs}(k)|^2, \tag{7}$$

where $H_{\rm fe}(k)$ is the frequency response due to the filtering of the front-end device; and $H_{\rm fs}(k)$ represents the frequency response accounting for the free-space transmission in an indoor environment.

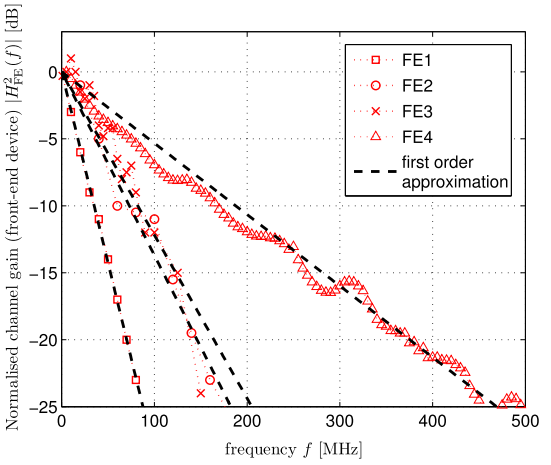

Fig. 2. Normalized channel gain due to the front-end device filtering. The channel gains of the FE1, FE2 and FE3 are presented in [8], [14], [13], respectively. Commercially available white LEDs are used in these systems. The channel gain of FE4 is an experimental measurement of the same system presented in [9] which uses a 50-μm gallium nitride LED.

1) Front-End Device Filtering: The general effect of the front-end device filtering shows low-pass characteristics. The corresponding bandwidth is typically limited by the response speeds of the LED and the PD. Four normalized channel gains due to the front-end device filtering in [8], [14], [13] and [9] are demonstrated in Fig. 2. The 3-dB bandwidth of these systems are in the range from 10 to 60 MHz. Since the highest sampling frequency is about 1 GHz, this low-pass effect will significantly decrease the signal strength when using a high sampling rate. Therefore, the low-pass effect of the front-end device filtering is crucial to the performance of an optical attocell system.

However, it is trivial to characterize the exact front-end device property. The device property may vary with different specifications or even with different copies of the same specification. Therefore, a first order function is adopted to approximate the normalized channel gain of the front-end device filtering in this study as [8]:

$$|H_{\rm fe}(f)|^2 = \exp\left(-\frac{f}{F_{\rm fe}}\right), \tag{8}$$

where $F_{\rm fe}$ controls the frequency characteristics of the front-end device. The higher the value of $F_{\rm fe}$, the wider the modulation bandwidth. As shown in Fig. 2, the approximations offer a good estimation of the low-pass characteristics. Converting (8) to the normalized channel gain on subcarrier k gives:

$$|H_{\rm fe}(k)|^2 = \exp\left(-\frac{kF_{\rm s}}{KF_{\rm fe}}\right), \tag{9}$$

for $k = 1, 2, \ldots, K/2 - 1$. In the remainder of this paper, systems with different front-end device are considered. For the convenience of description, the front-end device used in [8] is denoted as FE1 with a corresponding $F_{\rm fe}$ of 15.2 MHz. Similarly, the front-end devices used in [14], [13] and [9] are denoted as FE2, FE3 and FE4 with corresponding $F_{\rm fe}$ of 35.6, 31.7 and 81.5 MHz, respectively.

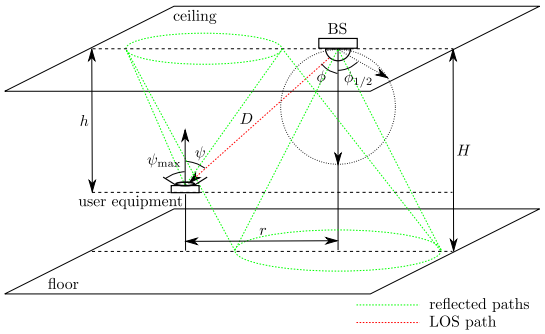

Fig. 3. Transmission geometry in an optical attocell system.

2) Free-Space Transmission: In this study, a geometric ray-tracing method is used to analyze the channel characteristics. The wireless transmission geometry is given in Fig. 3. The optical BS, oriented to the floor, is installed on the ceiling of the room. At the user side, the user receiver is placed at a certain height with the PD detector facing upward. This results in a vertical separation between user and the BS of h. The fixed direction of the PD detector can be achieved by using a mechanical design or by installing multiple PD detectors on the receiver. This is possible given the small size of PD detectors. Due to the limited space here, the effect of receiver rotation variance of vertical separation will be the subject of future research.

As shown in Fig. 3, the line-of-sight (LOS) path transmission between a pair of BS and user is considered here. This LOS path free-space transmission channel can be calculated using the DC channel gain $H_{\rm los}$ between the BS and the desired user as [29]:

$$H_{\rm los} = \frac{A_{\rm pd}(m+1)}{2\pi D^2}\cos^m(\phi)\cos(\psi)\mathbf{1}_{Д_{\rm l}}(\psi), \tag{10}$$

$$H_{\rm los}(r) = \frac{A_{\rm pd}(m+1)h^{m+1}\mathbf{1}_{Д_{\rm l}}(\psi)}{2\pi\left(r^2+h^2\right)^{\frac{m+3}{2}}}, \tag{11}$$

where m denotes the Lambertian emission order which is given by $m = -\ln(2)/\ln(\cos(\phi_{1/2}))$ in which $\phi_{1/2}$ is the half-power semi-angle of the LED. This quantity determines the beam width of the light source; $A_{\rm pd}$ is the physical area of the receiver PD; D is the Euclidean distance between the BS and the user; ϕ is the corresponding light radiance angle; ψ is the corresponding light incidence angle; and the function $\mathbf{1}_{Д}(x)$ is defined as:

$$\mathbf{1}_{Д}(x) = \begin{cases} 1 & : x \in Д \\ 0 & : x \notin Д. \end{cases} \tag{12}$$

In (10), $Д_{\rm l} = [0, \psi_{\max}]$, where $\psi_{\max}$ is the field of view (FOV) of the receiver. According to the geometry shown in Fig. 3, $H_{\rm los}$ can be rewritten as a function of the horizontal offset r between the BS and the user, as implied by (11).

As shown in Fig. 3, another source of the received signal is from the reflected paths, which mainly result from reflections

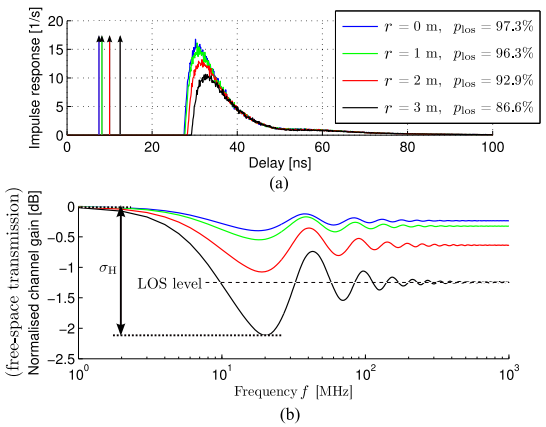

Fig. 4. (a) Channel impulse response in time domain. (b) Normalized channel gain in frequency domain.

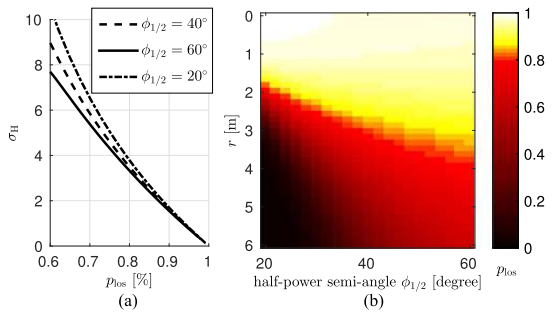

Fig. 5. (a) Maximum channel gain variance $\sigma_{\rm H}$ against power proportion of LOS component $p_{\rm los}$. (b) $p_{\rm los}$ against transmission horizontal offset r_0 and half-power semi-angle $\phi_{1/2}$.

by the room internal surfaces (walls, ceiling and floor). Diffuse reflections are considered in this study as typically these internal surfaces have a rough surface campared to the considered wavelengths. A large room with edge length of 5 m to 50 m is considered to accommodate the multi-cell VLC system. In this case, most of the users and BSs are away from the room edges. Consequently, in most cases (in the cells not near walls) the signal contribution from the first order reflection would be negligible. Therefore, the MP effect is mainly caused by the second order reflections bounced by the floor and ceiling.

In order to evaluate the effect of the reflected signals on the channel, computer simulations based on [30] are carried out. To simplify the problem, an extreme case is simulated with the floor and ceiling extending infinitely in all directions. A pair of serving BS and user is considered with a horizontal offset of r. The transmission geometry is given in Fig. 3. The simulation time bin width is 0.1 ns and the number of iterations is 5×10^5. The results of four example channels with $r = 0, 1, 2, 3$ m are shown in Fig. 4 in the form of the time domain impulse response and the frequency domain normalized channel gain. A dispersive source with $\phi_{1/2}$ of $60°$ is simulated. The reflectivity of the ceiling is 0.7 and the reflectivity of the floor is 0.3. The height of the room is 3 m and the measured plane is 0.75 m above the floor.

In Fig. 4(a), the impulse response results show that the first received signal is a strong LOS component, followed by a period of no signals until the first reflected signal reaches the receiver. Then, it is followed by a stream of closely spaced reflected signals. This is because the signal propagation delay of the LOS path is much shorter than the delay incurred by the reflected paths. To show the strength of the LOS component, a parameter $p_{\rm los}$ is defined. $p_{\rm los}$ represents the ratio of the received optical power of the LOS signal component to the total received optical power. These channels result in normalized channel gains $\left|\frac{H_{\rm fs}(f)}{H_{\rm fs}(0)}\right|^2$ as shown in Fig. 4(b). The maximum channel gain always appears at DC. With an increase of frequency, the channel gain decreases and reaches a minimum value at about 20 MHz. With a further increase of the frequency, the channel gain oscillates at a constant level and the magnitude of this oscillation diminishes. The constant level corresponds to the channel gain considering the LOS component only. It can be observed that the maximum variance in the channel gain $\sigma_{\rm H}$ is less than 2.5 dB. This means that the variation of the channel gain due to the reflected signal is minor compared to the effect due to the limitation of the front-end device filtering.

It is known that the flatness of the channel gain is strongly related to the strength of the LOS component [31]. Therefore, the relationship between the maximum channel gain variance $\sigma_{\rm H}$ and the proportion of the LOS power $p_{\rm los}$ is evaluated using simulation with different transmitter half-power semi-angles $\phi_{1/2}$. It can be observed that $\sigma_{\rm H}$ is a decreasing function of $p_{\rm los}$, as shown in Fig. 5(a). As long as $p_{\rm los}$ is above 80%, $\sigma_{\rm H}$ can be kept below 4 dB. Instead of evaluating the channel gain directly, $p_{\rm los}$ can be evaluated to estimate the flatness of the channel gain. In addition to the case shown in Fig. 4, the performance with all of the configurations of interest needs to be considered. Specifically, $p_{\rm los}$ is evaluated using different r and $\phi_{1/2}$. In conjunction with the analysis in Section III, it is shown that in this study, $p_{\rm los}$ is always high in the region of interest as shown in Fig. 5(b). This is due to the longer traveling distance ℓ in combination with the high electrical path loss in IM/DD systems, $L \propto (\ell)^4$, and the high absorption by the floor and ceiling.

The results shown in Figs. 4 and 5 do not cover the performance of users near the edge of the room. Therefore, $p_{\rm los}$ considering reflections from all surfaces of a room is calculated in an example room, in order to validate the assumption that the first order reflection is negligible in most cases. In this example, 23 HEX cells in a room of size of 26 m $\times$ 26 m $\times$ 3 m are considered. A half-power semi-angle $\phi_{1/2}$ of $60°$, and cell radius R of 3 m are used. The result is shown in Fig. 6(a). Users in the cells not close to the room edges have $p_{\rm los}$ above 85%. In addition, users in the center of the room edge cells also have high $p_{\rm los}$. The remaining users in the cells close to the walls have a lower value of $p_{\rm los}$, but generally above 50%. The results given in Fig. 6(a) are also presented in the form of the cumulative distribution function (CDF), shown as the setup 1 curve in Fig. 6(b). Fig. 6(b) shows that nearly 80% of the users experience $p_{\rm los}$ above 80%. Although the indoor signal propagation causes

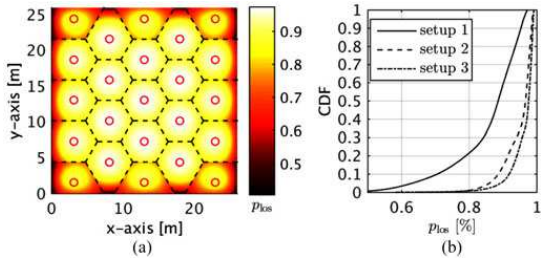

Fig. 6. (a) Spatial distribution of $p_{\rm los}$ in setup 1: $\phi_{1/2} = 60^\circ$, $R = 3$ m, $L_{\rm room} = 26$ m. (b) $p_{\rm los}$ distribution in the form of CDF. Setup 2: $\phi_{1/2} = 20^\circ$, $R = 1$ m, $L_{\rm room} = 8.5$ m. Setup 3: $\phi_{1/2} = 20^\circ$, $R = 1$ m, $L_{\rm room} = 14.5$ m.

some considerable frequency selectivity in the channel for the remaining 20% of the low $p_{\rm los}$ users, the inter-symbol interference can be easily removed by the use of OFDM in conjunction with a well-designed CP. In addition, the $p_{\rm los}$ distribution with smaller $\phi_{1/2}$ of 20° and $R = 1$ m is demonstrated. When the number of cells is the same as the $\phi_{1/2} = 60^\circ$ case (setup 2), the room size is decreased to $8.5\ {\rm m} \times 8.5\ {\rm m} \times 3\ {\rm m}$. The resulting $p_{\rm los}$ CDF shows that about 99% of the users have $p_{\rm los}$ above 80%. If the room size is increased to $14.5\ {\rm m} \times 14.5\ {\rm m} \times 3\ {\rm m}$ with 67 cells (setup 3), $p_{\rm los}$ is further improved. Therefore, it can be concluded that the reflected signal causes negligible MP effect on the channel for the majority of the users as long as the user experiences a dominant LOS signal component. Thus, $|H_{\rm fs}(k)| \approx H_{\rm los}$ for any k.

Occasionally, the LOS path may be shadowed or completely blocked. In these cases, a user may need an alternative serving BS or a diffused link.

C. Light Source Output Power

The relationship between the electrical signal standard deviation $\sigma_{\rm x}$ and the output optical power $P_{\rm opt}$ from the light source can be written as [28]:

$$P_{\rm opt} = \mathbb{E}\left[\hat{x}(t)\right] = \eta_{\rm led}\left(\sigma_{\rm x}\mathbb{E}\left[U(x(t))\right] + I_{\rm DC}\right). \tag{13}$$

Generally, a fixed ratio of DC-bias level to the electrical signal standard deviation is defined as $\zeta = \frac{I_{\rm DC}}{\sigma_{\rm x}}$. By combining (13) with ζ, it can be found that:

$$\sigma_{\rm x}^2 = \frac{P_{\rm opt}^2}{\eta_{\rm led}^2\left(\zeta + \mathbb{E}\left[U(x(t))\right]\right)^2}, \tag{14}$$

which represents the maximum possible $\sigma_{\rm x}^2$ with a given $P_{\rm opt}$. To get more electrical signal power, more optical power is needed assuming that the denominator in (14) is constant. However, optical power is finite and is typically constrained by the illumination requirement. This requirement is specified by the indoor lighting regulation [32], which requires a maintained illuminance of 500 lux in a typical working indoor environment for writing and reading purposes. To accommodate this requirement, the illuminance in the area below the luminary (cell center) should be at least 500 lux. According to the analysis in Section II-B2, the illuminance at the cell center can be calculated as:

$$E_{\rm v} = \Phi_{\rm v}\frac{H_{\rm los}(0)}{A_{\rm pd}} = \frac{(m+1)\Phi_{\rm v}}{2\pi h^2}, \tag{15}$$

where $\Phi_{\rm v}$ is the output luminous flux of the luminary. It is the output power measure in photometry which corresponds to the optical power in radiometry [33]. The conversion between luminous flux and radiant optical power can be given as:

$$\frac{\Phi_{\rm v}}{P_{\rm opt}} = K_{\rm e/v} = \frac{683\int V(\lambda)\Phi_{\rm e}(\lambda){\rm d}\lambda}{\int \Phi_{\rm e}(\lambda){\rm d}\lambda}, \tag{16}$$

where $K_{\rm e/v}$ is called luminous efficacy; $V(\lambda)$ is the luminosity function against wavelength λ; and $\Phi_{\rm e}(\lambda)$ is the spectral radiant power density function. The value of $K_{\rm e/v}$ is determined by the characteristic of the specific LED chip in the system. Therefore, the configuration of $P_{\rm opt}$ can be calculated as:

$$P_{\rm opt} = \frac{\Phi_{\rm v}}{K_{\rm e/v}} = \frac{2\pi E_{\rm v} h^2}{(m+1)K_{\rm e/v}}. \tag{17}$$

Considering a room height of 3 m, with a $\phi_{1/2}$ of 20° to 45°, the required luminous flux for a minimum illuminance of 500 lux is in the range of 1300 to 5300 lumen. This amount of power agrees with the specification of commercially available LED downlighters and LED panels for lighting in offices and public areas [34], [35]. Note that the LED lamp output level for residential home is typically lower than this level (< 1000 lumen). However, this does not necessarily affect the communication performance as only a fraction of the optical output power, modelled by ζ, is used for the communication link. Moreover, by closer inspection of (3) and (14) it can be found that the performance also depends on the signal clipping, i.e., the linearity of the LED transfer characteristic. An optimization of these parameters is beyond the scope of this work, and the interested reader is referred to [7].

D. Signal Clipping

In this study, the results in [28] are used to calculate the effects caused by the signal clipping process in (1). First, clipping affects the transfer relationship between BS output optical power and electrical signal power as shown in (14). The expectation of the clipped signal $\mathbb{E}\left[U(x(t))\right]$ in (14) can be calculated by [28]:

$$\mathbb{E}\left[U(x(t))\right] = \left(f_{\mathcal{N}}(\lambda_{\rm b}) - f_{\mathcal{N}}(\lambda_{\rm t}) + \lambda_{\rm t}\mathcal{Q}(\lambda_{\rm t}) + \lambda_{\rm b}(1-\mathcal{Q}(\lambda_{\rm b}))\right) \tag{18}$$

where $\mathcal{Q}(u) = \frac{1}{\sqrt{2\pi}}\int_u^\infty \exp\left(-\frac{v^2}{2}\right){\rm d}v$ is the Q-function; and $f_{\mathcal{N}}(u) = \frac{1}{\sqrt{2\pi}}\exp\left(-\frac{u^2}{2}\right)$ is the probability density function (PDF) of the unit normal distribution. In addition, the transmitted signal is attenuated by a factor of ρ which can be calculated as $\rho = \mathcal{Q}(\lambda_{\rm b}) - \mathcal{Q}(\lambda_{\rm t})$. Finally, the clipping noise variance $\sigma_{\rm clip}^2$ can calculated as:

$$\begin{aligned}\sigma_{\rm clip}^2 = {} & \mathcal{Q}(\lambda_{\rm b}) - \mathcal{Q}(\lambda_{\rm t}) + f_{\mathcal{N}}(\lambda_{\rm b})\lambda_{\rm b} - f_{\mathcal{N}}(\lambda_{\rm t})\lambda_{\rm t} \\ & + (1-\mathcal{Q}(\lambda_{\rm b}))\lambda_{\rm b}^2 + \mathcal{Q}(\lambda_{\rm t})\lambda_{\rm t}^2 - \rho^2 \\ & - \left(f_{\mathcal{N}}(\lambda_{\rm b}) - f_{\mathcal{N}}(\lambda_{\rm t}) + (1-\mathcal{Q}(\lambda_{\rm b}))\lambda_{\rm b} + \mathcal{Q}(\lambda_{\rm t})\lambda_{\rm t}\right)^2.\end{aligned} \tag{19}$$

E. Noise at Receiver

Three noise sources at the receiver side is considered in this study. The considered noise PSD N_0 can be calculated as:

$$N_0 = N_{0,\mathrm{s}} + N_{0,\mathrm{ab}} + N_{0,\mathrm{th}}, \tag{20}$$

where $N_{0,\mathrm{s}}$ corresponds to the shot noise caused by the received optical signal from the BS; $N_{0,\mathrm{ab}}$ corresponds to the shot noise caused by the received ambient light (mainly daylight); and $N_{0,\mathrm{th}}$ corresponds to the thermal noise in the receiver circuit. The PSD of the shot noise caused by the signal can be calculated as [29]:

$$N_{0,\mathrm{s}} = 2qP_{\mathrm{opt,Rx}}\eta_{\mathrm{pd}}, \tag{21}$$

where q is the charge of an electron, 1.6×10^{-19} C; $P_{\mathrm{opt,Rx}}$ denotes the incident optical power to the PD detector at the receiver from the optical BS. Intuitively, the main contributor of this amount of optical power is from the desired BS. To avoid unnecessary calculation complexity, the incident optical power from the remaining BSs is omitted. Thus, $P_{\mathrm{opt,Rx}} = P_{\mathrm{opt}} H_{\mathrm{los}}(r_0)$, where r_0 denotes the horizontal offset between the desired BS and the considered user. The PSD of the shot noise caused by the ambient light can be calculated as [29]:

$$N_{0,\mathrm{ab}} = 2qE_{\mathrm{r,ab}}A_{\mathrm{pd}}\eta_{\mathrm{pd}}, \tag{22}$$

where $E_{\mathrm{r,ab}}$ denotes the incident irradiance in the indoor environment. Note that the actual effect of ambient light will be smaller as only the light with the signal spectrum causes distortion as long as an appropriate optical filter is used. Finally, the PSD of the thermal noise can be calculated as [17]:

$$N_{0,\mathrm{th}} = \frac{4\mathcal{K}_{\mathrm{B}}T}{R_{\mathrm{L}}}, \tag{23}$$

where $\mathcal{K}_{\mathrm{B}}$ denotes the Boltzmann's constant with a value of 1.38×10^{-23} J/K; T denotes the absolute temperature; and R_{L} denotes the load resistance in the receiver circuit.

$$\gamma(k) = \left(\left(\frac{\rho^2 \xi^2 \left(r_0^2 + h^2\right)^{-m-3} \mathbf{1}_{Д_2}(r_0)}{\left(\rho^2 + \sigma_{\mathrm{clip}}^2\right) \sum\limits_{i \in И} \left(r_i^2 + h^2\right)^{-m-3} \mathbf{1}_{Д_2}(r_i) + \mathcal{Z}(k)} \right)^{-1} + \frac{\sigma_{\mathrm{clip}}^2}{\rho^2 \xi^2} \right)^{-1} \tag{24}$$

By inserting (7), (9), (11), (14) and (17) into the SINR expression (6), (6) can be modified as (24), where $Д_2 = \left[0, h\sqrt{\sec^2(\psi_{\max}) - 1}\right]$ and:

$$\mathcal{Z}(k) = \frac{K_{\mathrm{e/v}}^2 N_0(r_0) F_{\mathrm{s}} \exp\left(\frac{kF_s}{KF_{\mathrm{fe}}}\right) \left(\zeta + \mathbb{E}\left[U(x(t))\right]\right)^2}{\left(\xi E_{\mathrm{v}} A_{\mathrm{pd}} \eta_{\mathrm{pd}} h^{m+3}\right)^2}. \tag{25}$$

Note that N_0 is a function of r_0 as the shot noise varies with user locations with different received signal strength.

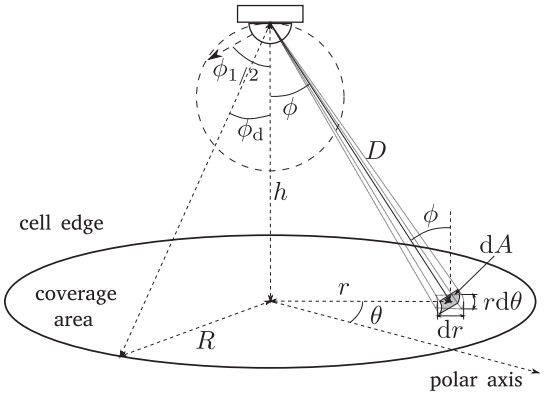

Fig. 7. Optical BS radiation geometry.

F. Multiple-Access and Spatial Reuse Schemes

Since it is recognized that the channel magnitude response is mainly affected by the front-end device, the magnitude response excluding the path loss changes little with the location of the user. In other words, there is little multi-user diversity and therefore time-division is assumed to be used to separate the multiple users within a cell. In addition, in the system with reuse factor Δ larger than 1, the resources are also divided in the frequency domain.

III. System Parameters Evaluation

The performance of an optical attocell network depends on many factors as implied by (24). Some of the parameters can be controlled by a predefined system configuration. In this section, two key parameters closely related to the network configuration are studied. One of the parameters is the cell radius R or BS density Λ of a network. These determine the number of users per cell and the number of cells in a room. The other parameter is the radiation pattern of the source, which is controlled by the Lambertian emission order, m. The pattern determines the signal strength distribution within each cell and the level of CCI to other cells. Appropriate configuration of these two parameters offers higher probability of achieving the desired system performance. Two configuration objectives are considered which include the maximization of desired signal strength and the minimization of introduced CCI.

A. CCI Minimization

In this section, a mathematical analysis is used to determine the appropriate setting for R and m with the objective of CCI minimization. Considering an optical BS with an optical output of P_{opt} serving a cell underneath it, part of the radiated signal power falls within the desired coverage area, while the remaining signal power is incident on other cells as CCI. Fig. 7 shows the geometry of this setup. The considered BS is h away from the cell center. In order to minimize CCI, it is preferred to

allow more radiated signal power from the BS to stay within the coverage area of that BS, and to let less signal power leak into other cells. If the optical power reaching the desired coverage area is defined as $P_{\mathrm{opt,d}}$, the objective becomes maximizing $P_{\mathrm{opt,d}}$. First, the calculation of $P_{\mathrm{opt,d}}$ should be determined. By considering the BS as the origin, the circular coverage area of the cell corresponds to a certain solid angle. Then, the desired signal power $P_{\mathrm{opt,d}}$ for a certain solid angle can be calculated as [36]:

$$P_{\mathrm{opt,d}} = \int_{\mathrm{cell}} P_{\mathrm{opt}} \frac{m+1}{2\pi} \cos^m(\phi) \mathrm{d}\Omega, \tag{26}$$

where Ω represents the solid angle of the radiation. The differential of this solid angle $\mathrm{d}\Omega$ can be derived as (27) according to the geometry shown in Fig. 7.

$$\mathrm{d}\Omega = \frac{\mathrm{d}A}{D^2} = \frac{r\mathrm{d}\theta\mathrm{d}r\cos(\phi)}{h^2\sec^2(\phi))} = \mathrm{d}\theta\mathrm{d}\phi\sin(\phi). \tag{27}$$

By inserting (27) into (26), the two-dimensional (2-D) integration can be decomposed into two one-dimensional integration as:

$$\begin{aligned} P_{\mathrm{opt,d}} &= P_{\mathrm{opt}} \frac{m+1}{2\pi} \int_0^{2\pi} \int_0^{\phi_{\mathrm{d}}} \cos^m(\phi)\sin(\phi)\mathrm{d}\phi\mathrm{d}\theta \\ &= P_{\mathrm{opt}} \left(1 - \left(\frac{h}{\sqrt{h^2+R^2}}\right)^{m+1}\right) \end{aligned} \tag{28}$$

where ϕ_{d} can be calculated by $\phi_{\mathrm{d}} = \arctan(R/h)$ as shown in Fig. 7. The partial derivatives of ϕ_{d} with respect to R and m are calculated as:

$$\frac{\partial P_{\mathrm{opt,d}}}{\partial R} = \frac{P_{\mathrm{opt}} R(m+1)h^{m+1}}{\left(h^2+R^2\right)^{\frac{m+3}{2}}} > 0, \tag{29}$$

$$\frac{\partial P_{\mathrm{opt,d}}}{\partial m} = P_{\mathrm{opt}} \ln\left(\frac{\sqrt{h^2+R^2}}{h}\right)\left(\frac{h}{\sqrt{h^2+R^2}}\right)^{m+1} > 0, \tag{30}$$

which implies that $P_{\mathrm{opt,d}}$ is a monotonically increasing function of R and m. This means that less CCI can be achieved by using a larger cell size as a larger cell size will increase the distance between each neighboring interfering BS and the desired user. In addition, using a source with a narrower beam width would also decrease the level of CCI as smaller half-power semi-angle leads to a more collimated beam pointing to the desired coverage area.

B. Desired Signal Strength Maximization

Since the Lambertian radiation pattern is used to model the light emission from the source, the further the user is away from the cell center, the weaker the received desired signal. Consequently, the user at the cell edge receives the weakest signal from the BS. In other words, as long as the signal strength of the cell edge user is high enough, all of the users in the cell coverage area should have sufficient signal power. Therefore, the objective can be converted to maximizing the signal power received by the cell edge user who is R away from the cell center. According to the analysis in Section II-B2, $P_{\mathrm{opt,e}}$ can be determined as:

$$P_{\mathrm{opt,e}} = P_{\mathrm{opt}} H_{\mathrm{los}}(R) = \frac{P_{\mathrm{opt}} A_{\mathrm{pd}}(m+1)h^{m+1}}{2\pi\left(R^2+h^2\right)^{\frac{m+3}{2}}}. \tag{31}$$

Similarly, the partial derivatives of $P_{\mathrm{opt,e}}$ respect to R and m are calculated as:

$$\frac{\partial P_{\mathrm{opt,e}}}{\partial R} = -\frac{P_{\mathrm{opt}} A_{\mathrm{pd}}(m+1)(m+3)Rh^{m+1}}{2\pi\left(R^2+h^2\right)^{\frac{m+5}{2}}} < 0, \tag{32}$$

$$\frac{\partial P_{\mathrm{opt,e}}}{\partial m} = \frac{P_{\mathrm{opt}} A_{\mathrm{pd}} h^{m+3}\left(1+\ln\left(\frac{h^{m+1}}{\left(R^2+h^2\right)^{\frac{m+1}{2}}}\right)\right)}{2\pi h^2\left(R^2+h^2\right)^{\frac{m+3}{2}}}. \tag{33}$$

which implies that $P_{\mathrm{opt,e}}$ is a monotonically decreasing function of R. Therefore, for a source with a specified radiation pattern, a smaller cell offers higher received signal power for the cell edge users. This is because a smaller cell size reduces the distance from the cell edge user to the cell center. On the other hand, $P_{\mathrm{opt,e}}$ is a concave function of m, which means there is an optimal value for m to maximize the cell edge user signal strength. By letting $\frac{\partial P_{\mathrm{opt,e}}}{\partial m} = 0$, the optimal radiation pattern can be calculated as:

$$\tilde{m} = 1/\ln\left(\sqrt{R^2+h^2}/h\right) - 1. \tag{34}$$

For the case of using a source with narrower beam width ($m > \tilde{m}$), the beam is over concentrated, which causes significant signal strength variance between cell center users and cell edge users, and the signal strength for the cell edge user would be too weak for reliable communication. For the case of using a source with wider beam width ($m < \tilde{m}$), the beam is over-diffused, which causes too much power leakage to other cells and the overall signal strength in the desired cell is not sufficient.

C. Parameter Configurations

From the analysis in Sections III-A and B, it can be found that appropriate settings for R and m also is mutually dependant. Therefore, the configurations of cell size and source beam width should be interconnected. Apart from the requirement of communication, there are many other constraints on the configuration of cell size. For example, if the cell size is too large, the illumination performance will be undesired. An extremely small cell size leads to too many required BSs in the room, which increases the installation complexity and increases the load of the handover process. In contrast, beam width of the source is more flexible, which can be simply achieved by appropriate optical diffuser design. Therefore, the configuration of R is considered as a given parameter, and the suitable setting of m is analyzed.

According to (30) and (34), if m is smaller than $\tilde{m}$, CCI increases and cell edge signal strength decreases. If m is equal or greater than $\tilde{m}$, there is a trade-off between the two objectives. Therefore, $\tilde{m}$ can be considered as a lower bound for m. In a noise limited system, a m closer to $\tilde{m}$ is preferred. In the case of a CCI limited system, (30) shows that m should be maximized to minimize CCI. However, an upper bound should be set to allow the cell edge user signal strength to be high enough to

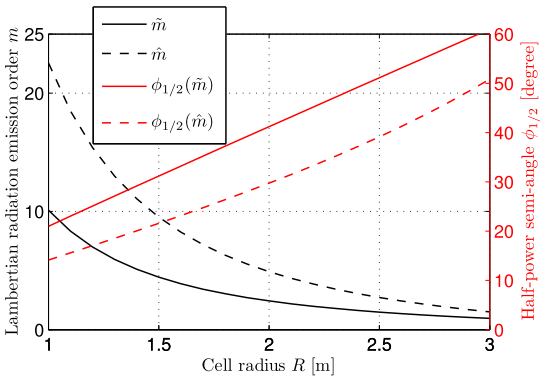

Fig. 8. The configuration of half-power semi-angle $\phi_{1/2}$ and the corresponding Lambertian emission order m against the cell radius R.

achieve the minimum acceptable signal-to-noise ratio (SNR). In order to find this upper bound, a simple metric is defined: the ratio between the SNR of the cell center user $(r = 0)$ to that of the cell edge user $(r = R)$, which is denoted as σ_{P}. From the analysis in Section II, it can be deduced that σ_{P} is proportional to the square of the ratio of received optical power by the cell center user to that received by the cell edge user as:

$$\sigma_{\mathrm{P}} = \left(\frac{P_{\mathrm{opt}} H_{\mathrm{los}}(0)}{P_{\mathrm{opt}} H_{\mathrm{los}}(R)}\right)^2 = \frac{h^{-2(m+3)}}{(R^2+h^2)^{-m-3}}. \tag{35}$$

For a fixed σ_{P}, the required lower bound for m can be calculated as:

$$\hat{m} = \frac{\ln \sigma_{\mathrm{P}}}{\ln\left(1+\frac{R^2}{h^2}\right)} - 3. \tag{36}$$

According to [9] and [13], the achievable cell center SNR is around 30 dB. For uncoded 4 QAM, the minimum required SNR is approximately 10 dB. Therefore, $\sigma_{\mathrm{P}} = 20$ dB is chosen in this study. The result of $\tilde{m}$, $\hat{m}$ and the corresponding $\phi_{1/2}$ against R based on (34) and (36) are plotted in Fig. 8. It can be seen that the area between the two curves is the appropriate configuration region, which is the preferred settings for $\phi_{1/2}$. In the case that CCI is the main limiting factor, m can be set to a value that is close or equal to $\hat{m}$, which is calculated using (36). In the case that receiver noise is the limiting factor, m can be configured to a value that is close or equal to $\tilde{m}$, which is calculated using (34).

IV. SINR Statistics Evaluations

The probability of receiving a certain service quality level can be determined by calculating the statistics of the achievable SINR. This metric is important as it directly determines the performance of an optical attocell network, such as achievable data rate and outage probability. The SINR statistics vary with large number of parameters, as noted in Sections II and III. In addition, it also varies with different cell deployment (BS placement topology). In order to provide a comprehensive characterization of the SINR statistics, two extreme cases are studied. For one of the cases, the placement of BSs is optimized with a HEX deployment. Such cell deployment most likely may require extra engineering work to redesign the lighting infrastructure in a room, which may be more difficult to implement, but offers the best performance. For the other case, the placement of BSs is completely random. The 2-D spatial distribution of BSs follows a homogeneous PPP. The irregular placement of luminaries is mainly motivated by the following considerations: first, the placement of a luminary may be limited by the wiring structure in the room. Second, in some cases, non-uniform illumination is required, which means that the lighting is enhanced in certain parts of the room, but not in other parts. Also, even for a uniform cell deployment, some cells may not have users. In that case, the downlink transmission can be switched off, which results in a non-uniform active cell deployment. Due to practical issues, the cell deployments of these two extreme cases (HEX and PPP) would be very rare in practice. Therefore, similar to [37], we expect that the downlink SINR achieved by the system with PPP (HEX) cell deployment works as a lower (upper) bound for the cases with other potential cell deployments that may be used in practice. In different cell deployments, the shape of the cell varies. In order to guarantee a fair comparison, the average cell size of the systems with each cell deployment is scaled to be the same as a circular cell with a radius of R.

A. System Model Simplification

In order to simplify the following analysis and to make the analysis tractable, the SINR expression (24) has to be modified. First, it is assumed that the non-linear characteristic of the relationship between the input current to the output optical power is minimized by using pre-distortion techniques [38], [39]. Therefore, a linear dynamic range from 0 to $2I_{\mathrm{DC}}$ is considered. This leads to a clipping level of $\lambda_{\mathrm{t}} = -\lambda_{\mathrm{b}} = \zeta$ and $\mathbb{E}\left[U(x(t))\right] = 0$. In addition, the $\mathbf{1}_{Д_2}(x)$ function makes (24) a piecewise function, which causes extra mathematical complexity in the analysis. Therefore, the worst case with a full FOV of $\psi_{\max} = 90^\circ$ is assumed, thereby making $\mathbf{1}_{Д_2}(x)$ always equal to 1 in the region of interest. Then, the simplified SINR expression can be written as:

$$\gamma(k) = \left(\frac{\left(\rho^2 + \sigma_{\mathrm{clip}}^2\right)\mathcal{I} + \mathcal{Z}(k)}{\rho^2 \mathcal{X}} + \frac{\sigma_{\mathrm{clip}}^2}{\xi^2 \rho^2}\right)^{-1}, \tag{37}$$

where $\mathcal{X} = \xi^2 \left(r_0^2 + h^2\right)^{-m-3}$ and $\mathcal{I} = \sum_{i \in И} \left(r_i^2 + h^2\right)^{-m-3}$.

B. HEX Cell Deployment

Instead of considering a specified network in a room, an infinite extending HEX network is considered in this analysis. There are two reasons for considering this deployment. First, since the main concern in this study is CCI from neighboring BSs, the number of neighboring BSs causing CCI is maximized in an infinite network. Consequently, an infinite network should

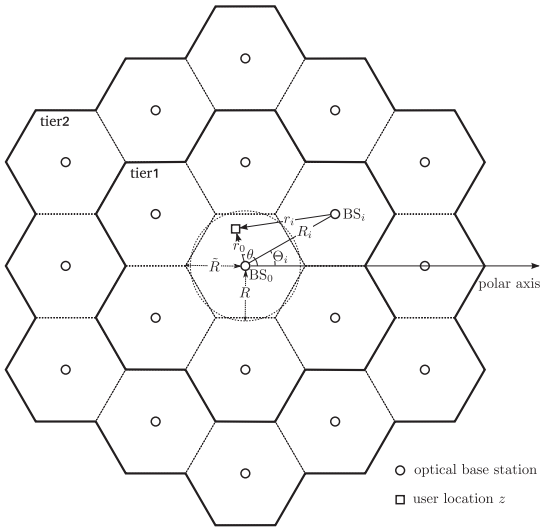

Fig. 9. Two-layer HEX network model with polar coordinates.

exhibit a worst case system performance. Second, removing the boundary effect of the network significantly reduces the complexity of the analysis. However, it is unnecessary to consider neighboring BSs that are too far away from the considered cell as they cause negligible CCI to the considered users and cause greater analysis complexity. Instead, a two-layer HEX cellular cell deployment is considered to approximate the infinite network as shown in Fig. 9 and the user performance in the central cell is analyzed. In this study, all networks are assumed to be heavily loaded. In addition, the cases with $\Delta = 1$ and $\Delta = 3$ are considered, since these cases are more likely to be used in practice. In this model, a polar coordinate system is used to represent the location of the user and BSs. Each 2-D location has a specified distance to the origin and a polar angle. A user at z is r_0 away from the origin and has a polar angle of θ, as shown in Fig. 9. Similarly, the ith BS is located at (R_i, Θ_i). In order to make the area of the HEX cell equal to that of the equivalent circular cell, the HEX cell radius satisfies $\tilde{R} \approx 1.1R$, as shown in Fig. 9. Then the horizontal offset between the ith BS and the user at z can be calculated as:

$$r_i(z) = \sqrt{r_0^2 + R_i^2 - 2R_i r_0 \cos(\theta - \Theta_i)}. \tag{38}$$

The user at $z = (r_0, \theta)$ in the central cell is served by the 0th BS. The remaining BSs using the same transmission resource ($i \in \mathcal{U}$) causes CCI to the desired user at z. Since the coordinates of all BSs are known, by inserting (38) into (37), the SINR $\gamma(k)$ can be calculated as a function of the user location z. Thus, the statistics of the SINR can be converted from the random distribution of user location z. Since the users are uniformly distributed in the cell, the PDFs of r_0 and θ follow: $f_{r_0}(r_0) = \frac{2r_0}{\tilde{R}^2}$ and $f_\theta(\theta) = \frac{1}{2\pi}$, respectively. The objective is defined as $\mathbb{P}[\gamma(k) < T]$, which calculates the probability that the downlink SINR is less than a threshold T. Using (37) and conditioning on

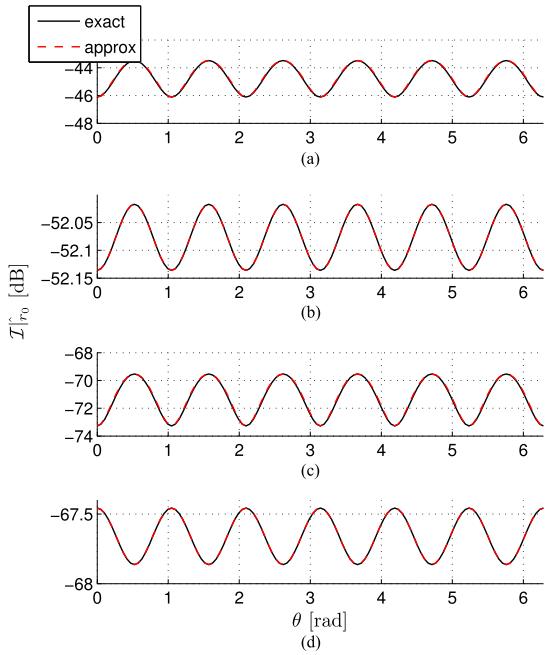

Fig. 10. CCI term approximation. In configuration (a) $R = 3$ m, $\Delta = 1$ and $r = R$ m. m is calculated using (36). Relative to configuration (a), configuration (b) changes r to $R/2$, configuration (c) changes R to 2 m, and configuration (d) changes Δ to 3.

r_0, this yields:

$$\mathbb{P}[\gamma(k) < T | r_0] = \mathbb{P}\left[\mathcal{I} > \frac{\rho^2 \mathcal{X}\left(\frac{1}{T} - \frac{\sigma_{\text{clip}}^2}{\rho^2 \xi^2}\right) - \mathcal{Z}(k)}{\rho^2 + \sigma_{\text{clip}}^2} \middle| r_0\right]. \tag{39}$$

The combination of (38) and (37) makes $\mathcal{I}$ an extremely complex function of θ for carrying out a PDF transformation. Therefore, this relationship between $\mathcal{I}$ and θ should be simplified in order to make the calculation tractable. Fig. 10 shows the CCI term $\mathcal{I}$ in a HEX network against θ with a given r_0. It can be observed that with the increase of θ, $\mathcal{I}(\theta|r_0)$ oscillates between two extreme values with a period of 60°. This is because of the central symmetric deployment of the interfering BSs. Therefore, an approach that is similar to the "flower" model introduced in [40] is used to simplify the relationship between $\mathcal{I}$ and θ. The concept is to use a cosine function to approximate the oscillation of the function $\mathcal{I}(\theta|r_0)$. First, $\mathcal{I}_{0^\circ}(r_0)$ and $\mathcal{I}_{30^\circ}(r_0)$ are calculated, which are the function $\mathcal{I}$ of r_0 assuming a θ of 0° and of 30°, respectively. Both values constitute the oscillation bounds of the function $\mathcal{I}(\theta|r_0)$. The expressions for $\mathcal{I}_{0^\circ}(r_0)$ and $\mathcal{I}_{30^\circ}(r_0)$ can be calculated in a closed form, as shown in Appendix A. Then, the approximated CCI term can be calculated using the following expression:

$$\hat{\mathcal{I}} = \frac{\mathcal{I}_{30^\circ}(r_0) + \mathcal{I}_{0^\circ}(r_0)}{2} + \frac{|\mathcal{I}_{30^\circ}(r_0) - \mathcal{I}_{0^\circ}(r_0)|}{2} \cos(6\theta). \tag{40}$$

Fig. 10 compares the exact conditional CCI term $\mathcal{I}(\theta|r_0)$ to the approximated one $\hat{\mathcal{I}}(\theta|r_0)$ with different system configurations. In the system with each of the configurations, the approximated model $\hat{\mathcal{I}}(\theta|r_0)$ matches well with the exact model $\mathcal{I}(\theta|r_0)$. The difference between the two curves is minimal as shown in each plot of Fig. 10. Thus, it is reasonable to replace $\mathcal{I}$ with $\hat{\mathcal{I}}$. By replacing $\mathcal{I}$ in (39) with (40), the conditional probability $\mathbb{P}[\gamma(k) < T|r_0]$ can be written as:

$$\mathbb{P}[\gamma(k) < T|r_0] =$$

$$\mathbb{P}\left[\cos(6\theta) > \frac{2\rho^2\mathcal{X}\left(\frac{1}{T}-\frac{\sigma^2_{\text{clip}}}{\rho^2\xi^2}\right)-2\mathcal{Z}(k)}{\left(\rho^2+\sigma^2_{\text{clip}}\right)|\mathcal{I}_{30^\circ}-\mathcal{I}_{0^\circ}|}-\frac{\mathcal{I}_{30^\circ}+\mathcal{I}_{0^\circ}}{|\mathcal{I}_{30^\circ}-\mathcal{I}_{0^\circ}|}\middle| r_0\right]$$

$$=\frac{1}{2}-\frac{1}{\pi}\arcsin^\dagger\left(\frac{2\rho^2\mathcal{X}\left(\frac{1}{T}-\frac{\sigma^2_{\text{clip}}}{\rho^2\xi^2}\right)-2\mathcal{Z}(k)}{\left(\rho^2+\sigma^2_{\text{clip}}\right)|\mathcal{I}_{30^\circ}-\mathcal{I}_{0^\circ}|}-\frac{\mathcal{I}_{30^\circ}+\mathcal{I}_{0^\circ}}{|\mathcal{I}_{30^\circ}-\mathcal{I}_{0^\circ}|}\right), \tag{41}$$

where

$$\arcsin^\dagger(x) = \begin{cases} 1 & : x > 1 \\ \arcsin(x) & : |x| \le 1 \\ -1 & : x < -1 \end{cases}. \tag{42}$$

The final CDF of SINR can be calculated by averaging (41) over r_0 as described in (43), which can be solved efficiently by using numerical methods. In this integration, the range of r_0 is from 0 to R, which corresponds to the integration over the equivalent circular cell. This approximation is made for simplicity.

$$\begin{aligned}\mathbb{P}[\gamma(k) < T] &= \int_0^R f_{r_0}(r_0)\mathbb{P}[\gamma(k) < T|r_0]\mathrm{d}r_0 \\ &= \int_0^R \frac{r_0}{R^2}-\frac{2r_0}{\pi R^2}\arcsin^\dagger \\ &\quad\times\left(\frac{2\rho^2\mathcal{X}\left(\frac{1}{T}-\frac{\sigma^2_{\text{clip}}}{\rho^2\xi^2}\right)-2\mathcal{Z}(k)}{\left(\rho^2+\sigma^2_{\text{clip}}\right)|\mathcal{I}_{30^\circ}-\mathcal{I}_{0^\circ}|}\right. \\ &\quad\left.-\frac{\mathcal{I}_{30^\circ}+\mathcal{I}_{0^\circ}}{|\mathcal{I}_{30^\circ}-\mathcal{I}_{0^\circ}|}\right)\mathrm{d}r_0. \end{aligned} \tag{43}$$

C. PPP Cell Deployment

Similar to the HEX network, an infinite extending network is considered. However, the origin of the coordinates is placed at a random user [37]. The horizontal positioning of the nearby optical BSs follows a 2-D homogeneous PPP with a density of Λ, as shown in Fig. 11. In the PPP case, a similar method is used to retrieve the SINR statistics by calculating $\mathbb{P}[\gamma(k) < T|r_0]$ using (39). Similar to the case of HEX network, the distribution of $\mathcal{I}$ is necessary. The exact distribution of $\mathcal{I}$ is complicated to solve. However, the method presented in [41] can be used to calculate the characteristic function (CF) of $\mathcal{I}$ conditioned on r_0. The details are as follows.

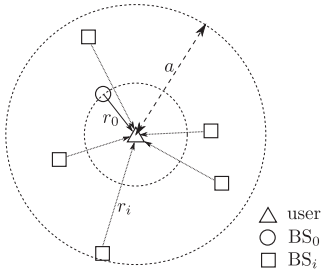

Fig. 11. PPP network geometry.

Since there is no dependency between BSs, the only significant variable in this model is the Euclidean distance between a BS and the user D_i. According to the geometry shown in Fig. 3, the CCI term $\mathcal{I}$ in (37) can be rewritten as: $\mathcal{I} = \sum g(D_i)$, where $g(x) = x^{-2(m+3)}$. It is assumed that the furthest BS is a away from the user and the interfering BS is not closer than the desired BS which is r_0 away from the user. As shown in Fig. 11, r_i is within the range of $[r_0, a]$. Since the interfering BSs are uniformly distributed, then the PDF of r_i can be found as:

$$f_{r_i}(r_i) = \frac{2r_i}{a^2-r_0^2},\ r_0 \le r_i \le a. \tag{44}$$

Then the PDF of D_i can be calculated using the PDF transformation rule from (44) as:

$$f_{D_i}(D_i) = \frac{2D_i}{a^2-r_0^2},\ \sqrt{r_0^2+h^2} \le D_i \le \sqrt{a^2+h^2}. \tag{45}$$

The conditional CF of $\mathcal{I}$ is defined as $\varphi_{\mathcal{I}_a}(\omega|r_0) = \mathbb{E}\left[\mathrm{e}^{j\omega\mathcal{I}_a}\right]$. Since the number of interfering BSs I is a non-negative integer random variable, $\varphi_{\mathcal{I}_a}(\omega)$ can be extended as:

$$\varphi_{\mathcal{I}_a}(\omega|r_0) = \mathbb{E}_I\left[\mathbb{E}\left[\mathrm{e}^{j\omega\mathcal{I}_a}|I=n\right]\right]. \tag{46}$$

Since each D_i in $\mathcal{I}$ is independent of each other, $\varphi_{\mathcal{I}_a}(\omega)$ conditioned on I can be factorized as follows:

$$\begin{aligned}\mathbb{E}\left[\mathrm{e}^{j\omega\mathcal{I}_a}|I=n\right] &= \prod_{i=1}^n \mathbb{E}\left[\mathrm{e}^{j\omega g(D_i)}\right] \\ &= \left(\int_{\sqrt{r_0^2+h^2}}^{\sqrt{a^2+h^2}} \frac{2D\mathrm{e}^{j\omega g(D)}}{a^2-r_0^2}\mathrm{d}D\right)^n. \end{aligned} \tag{47}$$

Because I follows a Poisson distribution with a mean of $\frac{\Lambda}{\Delta}$, the corresponding probability mass function of I can be written as follows:

$$\mathbb{P}[I=n] = \frac{\mathrm{e}^{-\frac{\Lambda\pi}{\Delta}\left(a^2-r_0^2\right)}\left(\frac{\Lambda\pi}{\Delta}\left(a^2-r_0^2\right)\right)^n}{n!}. \tag{48}$$

Next, (46) can be extended as:

$$\begin{aligned}\varphi_{\mathcal{I}_a}(\omega|r_0) &= \sum_{n=0}^{\infty}\mathbb{P}[I=n]\mathbb{E}\left[\mathrm{e}^{j\omega\mathcal{I}_a}|I=n\right]\\ &= \mathrm{e}^{-\frac{\Lambda\pi}{\Delta}\left(a^2-r_0^2\right)}\sum_{n=0}^{\infty}\frac{1}{n!}\\ &\quad\left(\frac{\Lambda\pi}{\Delta}\int_{\sqrt{r_0^2+h^2}}^{\sqrt{a^2+h^2}}2D\mathrm{e}^{j\omega g(D)}\mathrm{d}D\right)^n\\ &\overset{(a)}{=} \mathrm{e}^{-\frac{\Lambda\pi}{\Delta}\left(a^2-r_0^2-\int_{\sqrt{r_0^2+h^2}}^{\sqrt{a^2+h^2}}2D\mathrm{e}^{j\omega g(D)}\mathrm{d}D\right)},\end{aligned}\tag{49}$$

where (a) uses the Taylor series for e^x. By limiting $a\to\infty$, the CF can be calculated as follows:

$$\varphi_{\mathcal{I}}(\omega|r_0)=\exp\left(\sum_{n=1}^{\infty}\frac{(j\omega)^n}{n!}\frac{\Lambda\pi\left(r_0^2+h^2\right)^{1-n(m+3)}}{\Delta(n(m+3)-1)}\right).\tag{50}$$

The proof for (50) is provided in Appendix IX-B. Theoretically, (50) can be converted to the corresponding PDF. However, this operation is intractable. Therefore, an alternative approximation approach is used to obtain the PDF of CCI. Since the cumulant generating function can be written as:

$$\ln\left(\varphi_{\mathcal{I}}(\omega)\right)=\sum_{n=1}^{\infty}\kappa_n(\mathcal{I})\frac{(j\omega)^n}{n!}.\tag{51}$$

By comparing (51) and (50), the nth cumulant of $\mathcal{I}$ conditioning on r_0 can be found as:

$$\kappa_n^{\mathcal{I}}=\frac{\Lambda\pi\left(r_0^2+h^2\right)^{1-n(m+3)}}{\Delta(n(m+3)-1)}.\tag{52}$$

With all cumulants known, the corresponding nth raw moment can be calculated recursively by the following set of equations:

$$\mu_n=\begin{cases}1 & :n=0\\ \kappa_1 & :n=1\\ \kappa_n+\sum_{l=1}^{n-1}\binom{n-1}{l-1}\kappa_l\mu_{n-l} & :n\geq 2\end{cases}.\tag{53}$$

With all moments of the CCI distribution known, an expansion of the PDF as a sum of Gamma densities proposed in [42] can be used. This expansion is based on the Gram-Charlier series and Laguerre polynomials. The Gamma density used in this expansion is $f_V(v)=\frac{v^{\alpha-1}\mathrm{e}^{-v}}{\Gamma(\alpha)}$ for a random variable V. The expansion of the PDF is given as [42]:

$$f_V(v)=\frac{v^{\alpha-1}\mathrm{e}^{v}}{\Gamma(\alpha)}\sum_{n=0}^{\infty}\mathcal{A}_n\mathcal{L}_n^{\alpha}(v),\tag{54}$$

where the Laguerre polynomial $\mathcal{L}_n^{\alpha}(v)$ can be calculated as:

$$\begin{aligned}\mathcal{L}_n^{\alpha}(v)&=(-1)^n v^{1-\alpha}\mathrm{e}^{v}\frac{\mathrm{d}^n}{\mathrm{d}v^n}\left(v^{n+\alpha-1}\mathrm{e}^{-v}\right)\\ &=\sum_{l=0}^{n}\binom{n}{l}(-1)^{n-l}v^l S_l^n,\end{aligned}\tag{55}$$

where l is a non-negative integer, and

$$S_l^n=\begin{cases}1 & :l>n-1\\ \prod_{\iota=l}^{n-1}(\alpha+\iota) & :l\leq n-1\end{cases}.\tag{56}$$

The coefficients $\mathcal{A}_n$ in (54) can be calculated using the following expression:

$$\begin{aligned}\mathcal{A}_n&=\frac{\Gamma(\alpha)}{n!\Gamma(\alpha+n)}\int_0^{\infty}f_V(v)\mathcal{L}_n^{\alpha}(v)\mathrm{d}v\\ &=\frac{(-1)^n\Gamma(\alpha)}{n!\Gamma(\alpha+n)}\sum_{l=0}^{n}\binom{n}{l}(-1)^l S_l^n\int_0^{\infty}v^l f_V(v)\mathrm{d}v\\ &=\frac{(-1)^n\Gamma(\alpha)}{n!\Gamma(\alpha+n)}\sum_{l=0}^{n}\binom{n}{l}(-1)^l S_l^n\mu_l^V.\end{aligned}\tag{57}$$

The expansion (54) requires the random variable V to have its mean and variance equal to α:

$$\mathbb{E}[V]=\sigma_V^2=\alpha.\tag{58}$$

Therefore, the CCI random variable $\mathcal{I}$ has to be scaled to satisfy the condition in (58). So $V=\beta\mathcal{I}$ is defined, where β is the scaling factor. Then the cumulants and moments of V should follow:

$$\kappa_n^V=\beta^n\kappa_n^{\mathcal{I}},\tag{59}$$

$$\mu_n^V=\beta^n\mu_n^{\mathcal{I}}.\tag{60}$$

Note that $\kappa_1^{\mathcal{I}}$ and $\kappa_2^{\mathcal{I}}$ are equal to the mean and variance of $\mathcal{I}$, respectively. Then the mean and variance of V should be $\beta\kappa_1^{\mathcal{I}}$ and $\beta^2\kappa_2^{\mathcal{I}}$, respectively. The value of α and β can be calculated in conjunction with (52) and (58) as:

$$\beta=\frac{(2m+5)\left(r_0^2+h^2\right)^{m+3}}{m+2},\tag{61}$$

$$\alpha=\beta\kappa_1^{\mathcal{I}}=\beta^2\kappa_2^{\mathcal{I}}=\frac{\Lambda\pi(2m+5)\left(r_0^2+h^2\right)}{\Delta(m+2)^2}.\tag{62}$$

By substituting $\beta\mathcal{I}$ for V in (54) and after rearranging, the conditional PDF $f_{\mathcal{I}}(\mathcal{I}|r_0)$ can be determined as follows:

$$f_{\mathcal{I}}(\mathcal{I}|r_0)=\sum_{n=0}^{\infty}\left(\sum_{l_1=0}^{n}\frac{\beta^{\alpha}C_{l_1}^n\mu_{l_1}^{\mathcal{I}}}{n!\Gamma(\alpha+n)}\right)\left(\sum_{l_2=0}^{n}\frac{C_{l_2}^n\mathcal{I}^{l_2+\alpha-1}}{\mathrm{e}^{\beta\mathcal{I}}}\right),\tag{63}$$

where

$$C_l^n=\binom{n}{l}(-1)^{n-l}\beta^l S_l^n.\tag{64}$$

Next, the probability

$$\begin{aligned}\mathbb{P}\left[\mathcal{I}>\tilde{\mathcal{I}}|r_0\right]&=\int_{\tilde{\mathcal{I}}}^{\infty}f_{\mathcal{I}}(\mathcal{I}|r_0)\mathrm{d}\mathcal{I}\\ &=\sum_{n=0}^{\infty}\left(\sum_{l_1=0}^{n}\frac{\beta^{\alpha}C_{l_1}^n\mu_{l_1}^{\mathcal{I}}}{n!\Gamma(\alpha+n)}\right)\\ &\quad\times\left(\sum_{l_2=0}^{n}\frac{C_{l_2}^n}{\beta^{l_2+\alpha}}\Gamma\left(l_2+\alpha,\beta\tilde{\mathcal{I}}\right)\right),\end{aligned}\tag{65}$$

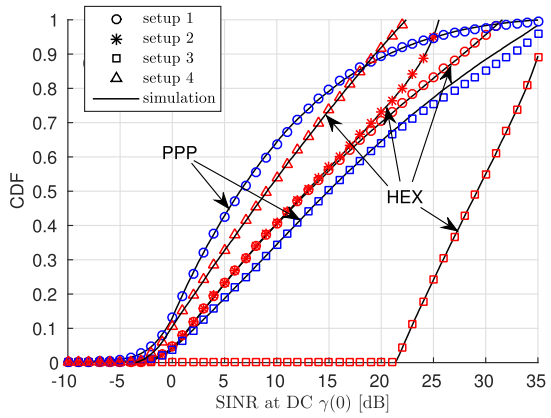

Fig. 12. The CDF of the SINR at DC. Setup 1: $R = 2.5$ m, $\phi_{1/2} = 40°$, $\Delta = 1$, 100% output. Setup 2: same as setup 1 except $\zeta = 2.5$. Setup 3: $R = 3$ m, $\phi_{1/2} = 50°$, $\Delta = 3$, 100% output. Setup 4: same as setup 1 except 15% output and 1000 lux ambient light illuminance. Other parameters are listed in Table I if they are not specified.

where $\Gamma(\nu, \epsilon) = \int_{\epsilon}^{\infty} \mathrm{e}^{-x} x^{\nu-1} \mathrm{d}x$ is the upper incomplete Gamma function; and

$$\tilde{\mathcal{I}} = \frac{\rho^2 \mathcal{X}\left(\frac{1}{T} - \frac{\sigma_{\mathrm{clip}}^2}{\rho^2 \xi^2}\right) - \mathcal{Z}(k)}{\rho^2 + \sigma_{\mathrm{clip}}^2}. \tag{66}$$

Because r_0 equals the distance between the user (origin) and the serving BS (closest node to origin), the PDF of r_0 with node density of Λ should be $f_{r_0}(r_0, \Lambda) = 2\pi\Lambda r_0 \mathrm{e}^{-\Lambda\pi r_0^2}$ in a PPP [43]. The final SINR CDF can be calculated by combining (65) with (39) and averaging $\mathbb{P}[\gamma(k) < T | r_0]$ over r_0 as (67).

$$\begin{aligned}\mathbb{P}[\gamma(k) < T] &= \int_0^{\infty} f_{r_0}(r_0, \Lambda) \mathbb{P}[\gamma(k) < T | r_0] \mathrm{d}r_0 \\ &= \int_0^{\infty} \frac{2\pi\Lambda r_0}{\mathrm{e}^{\pi\Lambda r_0^2}} \sum_{n=0}^{\infty} \left(\sum_{l_1=0}^{n} \frac{\beta^{\alpha} C_{l_1}^n \mu_{l_1}^{\mathcal{I}}}{n! \Gamma(\alpha + n)} \right) \\ &\quad \times \left(\sum_{l_2=0}^{n} \frac{C_{l_2}^n \Gamma\left(l_2 + \alpha, \beta\tilde{\mathcal{I}}\right)}{\beta^{l_2+\alpha}} \right) \mathrm{d}r_0. \end{aligned} \tag{67}$$

Note that there is a summation with infinite upper bound in (67) which makes the calculation intractable. Therefore, the infinity upper bound of the summation is replaced by a finite integer number N. With the increase of N, (67) quickly converges to the case of $N = \infty$. When calculating the results, $N = 10$ is found to be sufficient to provide accurate analytical results. With this approach, (67) can be solved using numerical methods.

D. SINR Statistics Results and Discussions

Fig. 12 shows the CDF of the SINRs at dc achieved by different system setups considering HEX and PPP cell deployments. The SINR at DC is shown as an example. The SINR at other frequencies decreases with an increase of frequency due to the low-pass effect of the front-end devices. The values shown in Table I are used if the system parameter is not specified for each setup, where the configuration of F_{s} and F_{fe} are in accordance with the setup in [13]. The configuration of σ_{P} is justified in Section III-C. It can be found that the numerical results calculated using (43) and (67) agree with the corresponding Monte Carlo simulation in the region of interests.

TABLE I

Parameters	Symbol	Values
Vertical Separation	h	2.25 [m]
Receiver FOV	ψ_{max}	90°
Sampling frequency	F_{s}	360 [MHz]
Front-end device bandwidth factor	F_{fe}	31.7 [MHz]
DC-bias level	ζ	3.2
PD responsivity	η_{pd}	0.4 [A/W]
PD physical area	A_{pd}	1 [cm^2]
Number of subcarriers	K	512
Power decrease factor	σ_{P}	20 [dB]
Cell center illuminance from BS	E_{v}	500 [lux]
illuminance from ambient light	$E_{\mathrm{v,ab}}$	100 [lux]
Absolute temperature	T	300 [K]
Receiver load resistance	R_{L}	500 [Ω]

In setup 1, $R = 2.5$ m, $\phi_{1/2} = 40°$ and $\Delta = 1$. The results for both the HEX and the PPP networks are shown. It can be observed that with the same system configuration, a PPP network performs worse than a HEX network. In addition, the considered ambient light level is 100 lux in illuminance. Therefore, the BSs works with their full power to provide enough illumination. The highest SINR of above 30 dB shows that the noise at the receiver side causes little effect to the system performance. In setup 2, the DC-bias level is modified to 2.5. This results in a higher signal clipping level. Consequently, the highest SINR in this system is limited by the clipping noise. In setup 3, $R = 3$ m, $\phi_{1/2} = 50°$, $\Delta = 3$. Other parameters are the same as setup 1. The high reuse factor leads to a lower level of CCI and the overall SINR level improved significantly compared with that of setup 1. Therefore, the corresponding SINR is improved compared to the case of setup 1 for both HEX and PPP networks. Setup 4 considers a special case with sufficient illumination from ambient light with a illuminance of 1000 lux. Thus, the BS works in a dimmed mode with only 15% of its normal output. Due to the reduced signal power and increased noise level, the overall SNR level is decreased (−3 dB – 22 dB). This demonstrates that the system will work in strong ambient light conditions, and even in dimmed mode. Furthermore, energy-efficient modulation techniques such as eU-OFDM [12] may be used to further improve performance when the lights are dimmed.

V. Cell Data Rate and Outage Probability

In this section, the average cell data rate and outage probability are calculated and analyzed. Since the information about the per subcarrier SINR and its statistics is known, different modulation and coding schemes can be assigned to each subcarrier adaptively according to the value of $\gamma(k)$. The average

TABLE II
ADAPTIVE MODULATION AND CODING

	AMC1		AMC2	
n	T_n [dB]	ε_n [bits/symbol]	T_n [dB]	ε_n [bits/symbol]
0	–	0	–	0
1	9.8	2	−6	0.1523
2	13.4	3	−5	0.2344
3	16.5	4	−3	0.3770
4	19.6	5	−1	0.6016
5	22.5	6	1	0.8770
6	25.5	7	3	1.1758
7	28.4	8	5	1.4766
8	–	–	8	1.9141
9	–	–	9	2.4063
10	–	–	11	2.7305
11	–	–	12	3.3223
12	–	–	14	3.9023
13	–	–	16	4.5234
14	–	–	18	5.1151
15	–	–	20	5.5547

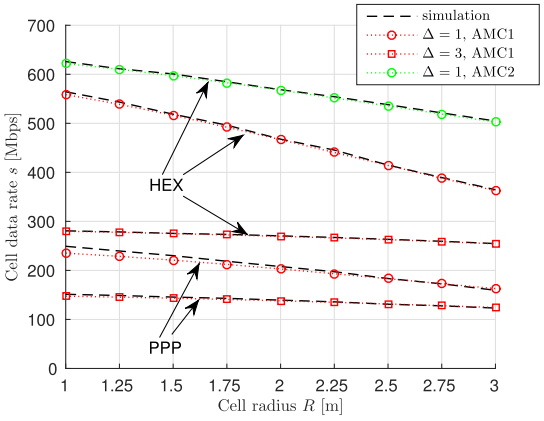

Fig. 13. Achievable cell data rate against cell radius R. The emission order m is configured based on (36). Other system parameters are listed in Table I if not specified.

achievable data rate in an optical attocell can be calculated using:

$$s = \frac{1}{\Delta}\sum_{k=1}^{K/2-1}\sum_{n=1}^{N} W_{\rm sc}\varepsilon_n \mathbb{P}[T_n < \gamma(k) < T_{n+1}]$$

$$= \frac{F_{\rm s}}{\Delta K}\sum_{k=1}^{\frac{K}{2}-1}\sum_{n=1}^{N} \varepsilon_n \left(\mathbb{P}[\gamma(k) < T_{n+1}] - \mathbb{P}[\gamma(k) < T_n]\right), \quad (68)$$

where $W_{\rm sc}$ is the bandwidth on each subcarrier; ε_n is the spectral efficiency (bits/symbol) of the nth adaptive modulation and coding (AMC) level; and T_n is the corresponding minimum required SINR to achieve ε_n. In this study, two AMC schemes are considered, which are listed in Table II. The AMC scheme 1 is the uncoded QAM modulation [44] achieving a maximum bit error rate target of 1×10^{-3}. This scheme is reliable and simple to implement, and has been used in several experimental studies [9], [13], [14]. However, this scheme achieves a relatively low spectral efficiency and the minimum required SINR is as high as 9.8 dB. The AMC scheme 2 is used in the long term evolution (LTE) system [45], which is more spectrally efficient, and the lowest acceptable SINR is -6 dB. However, it is more complex to implement.

Outage probability is defined as the probability that the received signal SINRs on all subcarriers are below the lowest SINR requirement for an AMC scheme. Since we know that the value of $\gamma(1)$ is the highest among the SINR on the all the subcarriers, the outage probability can be calculated as:

$$\mathcal{P}_{\rm out} = \mathbb{P}[\gamma(1) < T_1]. \quad (69)$$

Next, the accuracy of the cell data rate calculation is evaluated and the cell data rate/outage probability performance of an optical attocell is analyzed. The results include the systems with the HEX/PPP network model and the system with reuse factor of $\Delta = 1$ and $\Delta = 3$. The cell radius R and the sampling frequency (modulation bandwidth) $F_{\rm s}$ are considered as the variables for study. Fig. 13 shows the cell data rate against the cell radius R. As shown in Section IV-D, a network operating with full BS power will not be limited by noise. Therefore, according to the analysis in Section III-C, the emission order m is configured based on (36) to achieve a better performance. Other system parameters are the same as those listed in Table I if they are not specified. For all of the systems, the Monte Carlo simulation results show close agreement with the analytical calculations, which prove the accuracy of (68). As expected, a HEX network system performs better than a PPP network system with the same remaining system configuration. The cell data rate generally decreases with the increase of R. This is because a system with a smaller cell has a higher value of m according to (36), which introduces less CCI to nearby BSs. First, the system using AMC1 is considered. With the same cell deployment, the system with $\Delta = 1$ always achieves a higher data rate than the system with $\Delta = 3$. In the case of the HEX cell deployment, the $\Delta = 1$ system achieves 40% to 100% higher data rate than the $\Delta = 3$ system. However, the $\Delta = 1$ system always has a much higher outage probability than the $\Delta = 3$ system as shown in Fig. 14. For example, in the case of the HEX cell deployment, the $\Delta = 1$ system has an outage probability of about 30% – 45%. In contrast, the $\Delta = 3$ system has an outage probability of zero. In Section IV, it has been demonstrated that a $\Delta = 1$ system with an appropriate configuration, the minimum SINR can be kept above -5 dB. Therefore, using AMC2 in a HEX network, the zero outage probability can be achieved even with $\Delta = 1$. In addition, the cell data rate is further improved by 60 Mb/s to 140 Mb/s.

The relationship between cell data rate/outage probability and the sampling frequency (modulation bandwidth) is examined, as shown in Figs. 15 and 16. A cell radius of $R = 2.5$ m, a half-power semi-angle of $\phi_{1/2} = 40^\circ$ and AMC1 are used in this system. Other system parameters are the same as those listed in Table I if they are not specified. With an increase of the sampling frequency $F_{\rm s}$, the cell data rate increases when sampling frequency is low. This is because the more bandwidth

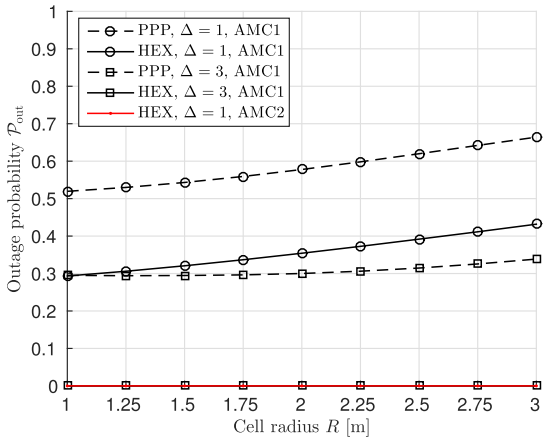

Fig. 14. Outage probability against cell radius R. The emission order m is configured based on (36). Other system parameters are listed in Table I if not specified.

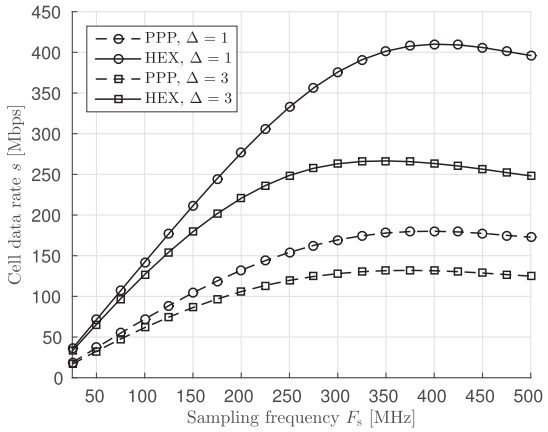

Fig. 15. Achievable cell data rate against sampling frequency F_{s} with $R = 2.5$ m, $\phi_{1/2} = 40^\circ$ and AMC1. Other parameters are listed in Table I if they are not specified.

that the system uses, the higher the data rate that the system can achieve. However, when the sampling frequency increases further, the channel quality on the high frequency subcarriers becomes worse. Meanwhile, the total transmission power is spread to a wider frequency band. Thus the signal power on each subcarrier decreases. Consequently, the increasing speed of the cell data rate with sampling frequency becomes slower. In addition, with a further increase of sampling frequency, the SINR of the cell edge user becomes below the threshold for transmission. Consequently, the outage probability also increases with the bandwidth increase, as shown in Fig. 16. When the sampling frequency is far beyond the 3-dB bandwidth, too much signal power is wasted on the subcarriers that are subject to unfavorable channel conditions with the degradation of the signal quality on

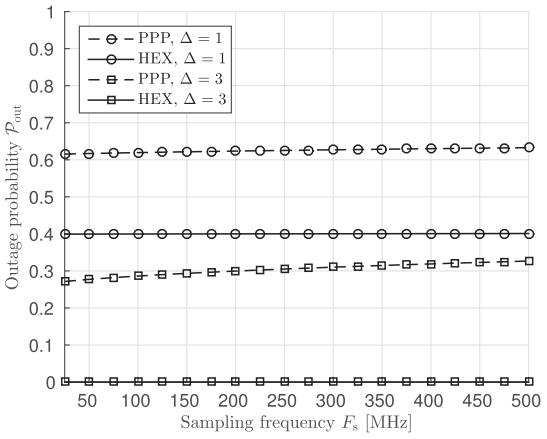

Fig. 16. Outage probability against sampling frequency F_{s} with $R = 2.5$ m, $\phi_{1/2} = 40^\circ$ and AMC1. Other parameters are listed in Table I if they are not specified.

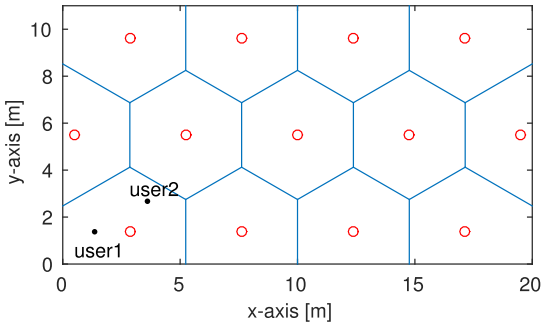

Fig. 17. Cell deployment of the finite HEX network in a room of size 20 m × 11 m × 3 m.

the subcarriers which exhibit good channel conditions. Consequently, the cell data rate starts to decrease.

VI. Performance of Finite Networks and MP Effect

In previous sections, infinite networks are analyzed to approximate the performance of the practical system. In this section, the performance of a finite network deployed in a room is compared with the corresponding infinite network with the same system configurations. The MP effects due to room internal surface reflections are considered here.

The considered finite network is deployed in a room of size 20 m × 11 m × 3 m with HEX model as shown in Fig. 17. The reflectivity of the ceiling and walls is 0.7, and the reflectivity of the floor is 0.3. A cell radius of $R = 2.5$ m, a half-power semi-angle of $\phi_{1/2} = 40^\circ$ and AMC2 are used in this system. The remaining parameters are as given in Table I if they are not specified. First, two typical users in a room edge cell in this finite HEX network are considered, as shown in Fig. 17. Both of the two users are 1.5 m away from the cell center and they are close to one of the edges of the hexagon cell boundary. A

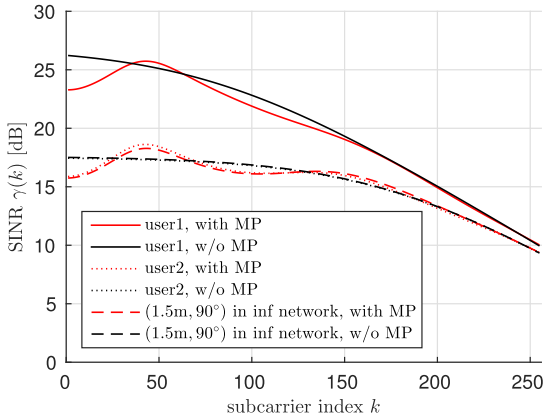

Fig. 18. SINR on subcarrier k. User 1 and user 2 are located at the bottom left cell in the considered finite network as shown in Fig. 17.

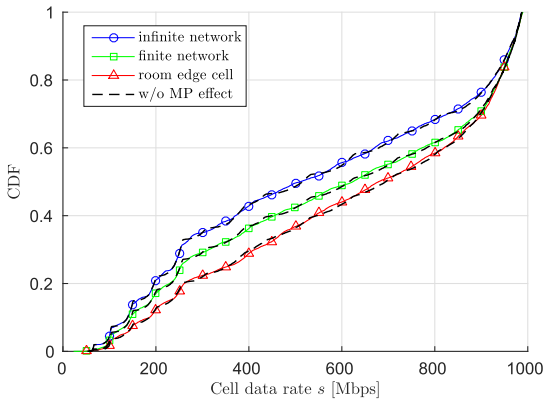

Fig. 19. Cell data rate statistics. AMC2 is used in these systems. The considered finite network corresponds to the system shown in Fig 17. The considered room edge cell corresponds to the cell in the bottom left cell shown in Fig 17.

third user at $(1.5, 40°)$ in an infinity HEX network, denoted as user 3, corresponding to the positions of user 1 and user 2 is also considered for comparison. Fig. 18 shows the achieved SINR on each subcarrier with and without the MP effect. Due to the low-pass effect of the front-end device filtering, the achieved SINR decreases with the increase of subcarrier index. It can be observed that the SINRs calculated without MP effect offers a very close estimation to those calculated with MP effect for each user. Compared with user 2, user 1 is closer to the room edge and further away from the interfering BSs. Consequently, the overall SINR achieved by user 1 is much higher than that achieved by user 2. However, due to the stronger MP effect, the SINR calculated without MP effect slightly over-estimates the one with MP effect. In contrast, user 2 is closer to the room center, which is similar to the case in an infinite network. Therefore, the performances of user 2 and user 3 are very similar.

Next, the performance of this finite network in terms of data rate is considered. Fig. 19 shows the simulated statistics of the

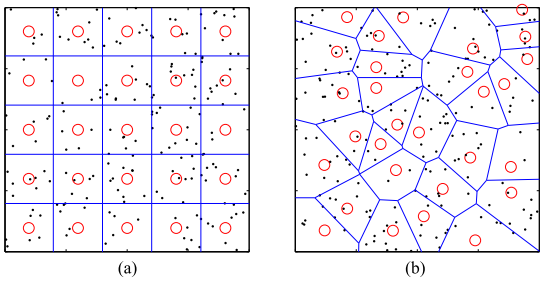

Fig. 20. Cell deployment for comparison. (a) Square network. (b) HCPP network.

cell data rate. Both the results with and without MP effect are simulated, and as shown, the MP effect does not cause any significant variance in the cell data rate performance of the systems. It can be observed that the infinite network offers the worst cell data rate. In contrast, the finite network achieves a slightly improved cell data rate. Furthermore, the cell data rate achieved in the room edge cell offers the highest cell data rate because of the lower CCI level. Therefore, it can be concluded that MP effect does not limit the performance of an optical attocell system. In addition, a worst case performance can be obtained by evaluating an infinite network.

VII. System Performance Comparison With Different Cell Deployment

On the one hand, in a practical network arrangement where the existing lighting infrastructure is used, a BS layout with regular HEX lattice is possible but unlikely. On the other hand, a PPP network is also not entirely practical, because having light fixtures deployed in a completely random manner is not standard. In order to demonstrate the significance of the analyzed HEX/PPP network, the following two cell deployments are considered in addition in order to model typical optical attocell systems with potential cell deployments in practice.

A. Square Network

The first potential practical network model considered is the square lattice cellular model, in which BSs are placed on a square lattice, as shown in Fig. 20(a). This arrangement is common in indoor lighting network deployment for several reasons including design simplicity, good illumination uniformity and compliance with rectangular-shaped rooms. In the square network, the cell size is controlled by a parameter R_{sq} which is defined as the distance between the two closest BSs. In order to have a fair comparison, R_{sq} needs to be consistent with the circular cell radius R. This requires: $R_{\mathrm{sq}} = \sqrt{A_{\mathrm{cell}}} = \sqrt{\pi R^2} \approx 1.77R$.

B. Hard-Core Point Process (HCPP) Network

In a PPP network, two BSs can be extremely close to each other, which is unlikely in practice. This is the main drawback of the PPP network model. Therefore, the Matérn type I HCPP is considered to approximate the network model, as shown in

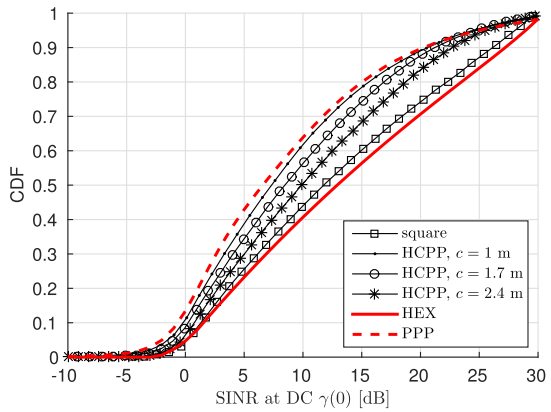

Fig. 21. Compare the SINR statistics at dc of systems with different cell deployments. An equivalent circular cell radius of $R = 3$ m and a half-power semi-angle of $\phi_{1/2} = 40^\circ$ are used. For the results of the HCPP networks, $c = 1, 1.7, 2.4$ m. Other parameters are listed in Table I.

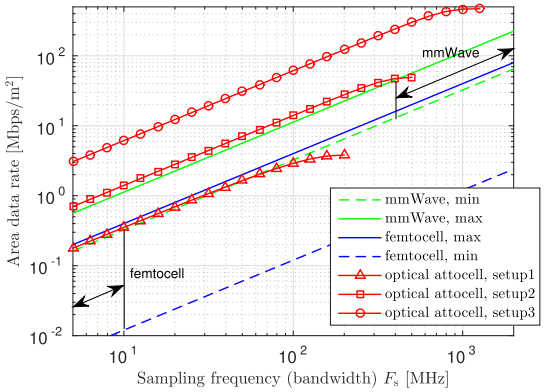

Fig. 22. Area data rate comparison among optical attocell networks, RF femtocell networks and mmWave networks. Optical attocell network setup 1: FE1 with $F_{\text{fe}} = 15.2$ MHz, PPP network, $\Delta = 3$, AMC1, $R = 2.5$ m and $\phi_{1/2} = 40^\circ$. Setup 2: FE3 with $F_{\text{fe}} = 31.7$ MHz, HEX network, $\Delta = 1$, AMC2, $R = 2$ m and $\phi_{1/2} = 30^\circ$. Setup 3: FE4 with $F_{\text{fe}} = 81.5$ MHz, HEX network, $\Delta = 1$, AMC2, $R = 1$ m and $\phi_{1/2} = 15^\circ$.

Fig. 20(b). The HCPP is based on a PPP with the condition that the shortest distance between any two nodes is greater than a specified threshold, c. To generate a set of nodes according to a HCPP, a PPP with a density of Λ_0 is applied. Then each point is tagged with a random number, and a dependent thinning process is carried out for each marked node as follows: retain the marked node if there is no other node within the circle centered at the marked node with a radius of c. After the thinning, the HCPP nodes density would be reduced. Therefore, to generate a HCPP with density of Λ, the initial PPP density Λ_0 has to be [46]: $\Lambda_0 = -\ln(1 - \Lambda\pi c^2)/\pi c^2$. In order to have a fair comparison, the configuration of Λ_0 also has to make sure that the average cell area is the same as the equivalent circular cell area with the radius of R. Therefore, $\Lambda_0 = -\ln(1 - c^2/R^2)/\pi c^2$.

C. Performance Comparison

In Fig. 21, the CDF of the SINR at DC level of the systems with difference cell deployments are given and compared. An equivalent circular cell radius of $R = 3$ m and a half-power semi-angle of $\phi_{1/2} = 40^\circ$ are used. The remaining system parameters are listed in Table I. Fig. 21 shows that the SINR distributions of the square network and HCPP network are bounded by the curves for the cases of the PPP network and the HEX network within the SINR region of interest. Similar to the conclusion drawn in [37], the SINR performance of a PPP (HEX) network can be considered as a lower (upper) bound for the case of practical optical attocell systems.

VIII. Optical Attocell Network versus Other Small-cell Network

In this section, the performance of the optical attocell networks are compared to those achieved by RF femtocell networks and mmWave indoor networks. An optical attocell network achieves a high communication performance due to its extremely dense spatial reuse ($R_{\text{atto}} \in [1, 3]$ m). Compared with RF femtocell systems, optical attocell networks have a relatively large license-free modulation bandwidth (100 MHz to > 1 GHz) availability. In contrast, a femtocell has a relatively larger cell size ($R_{\text{femto}} \in [10, 40]$ m) and a limited downlink bandwidth of about 10 MHz [3]. The modulation bandwidth of an indoor mmWave system, such as 60 GHz wireless personal area network, is generally in the range of 500 MHz to > 2 GHz, which is typically wider than that used by optical attocell networks. Therefore, a data rate of up to 7 Gb/s can be achieved by a mmWave system for a single link [47], while the maximum data rate that can be achieved by a single LED source is about 3 Gb/s [9]. However, due to hardware limitation and CCI issues, typically only one mmWave access point is available for each room. In contrast, multiple optical BSs can be installed in a room. This makes an optical attocell network advantageous in terms of data density. The benefits of high data density are obvious when a large number of devices in a room need high speed wireless service. To demonstrate the high data density achieved by an optical attocell system, a metric termed area data rate is defined as follows:

$$s_{\text{area}} = \frac{s}{A_{\text{cell}}}. \tag{70}$$

Fig. 22 shows the area data rate performance of different systems. The results of the femtocell are extrapolated from [3], [5], [48], [49]. As shown, the indoor ASE achieved by the femtocell network is generally in the range from 0.03 to 0.0012 b/(s·Hz·m^2). With a bandwidth of 10 MHz, the area data rate achieved by femtocell networks is in the range from 0.012 to 0.3 Mb/(s·m^2). The results of the mmWave systems are extrapolated from [47], [50], [51]. The spectral efficiency achieved by the mmWave system is generally in the range from 3.24 to 11.25 b/(s·Hz). Considering a room of size 10 m $\times$ 10 m, with a bandwidth in the range of 400 MHz to 2 GHz, the achievable area data rate is in the range of 13 to 225 Mb/(s·m^2). The

estimated minimum and maximum values for these two systems are used as the benchmarks.

First, a low performance optical attocell system with setup 1 is considered, which uses the FE1 with $F_{\text{fe}} = 15.2$ MHz and a PPP cell deployment with $R = 2.5$ m, $\phi_{1/2} = 40^\circ$ and $\Delta = 3$. The modulation and coding scheme is AMC1. Fig. 22 shows that the performance of this system is within the femtocell performance range. Note that the maximum achievable area data rate of 3.82 Mb/(s·m^2) with a bandwidth of 200 MHz is much higher than those achieved by the femtocells with a bandwidth of 10 MHz. Note that the performance of the systems using different bandwidth is compared. This is because of the difference in the costs and availability of the two type of frequency bands. For the VLC system, the frequency band is totally unlicensed and does not cause any interference to a system in an adjacent frequency band. Therefore, there is no requirement for spectrum masks or leakages into neighboring bands used by other systems. In contrast, the RF resources are scarce and hence require tight spectrum masks. Next, two optical attocell systems with moderate (setup 2) and high (setup 3) performance are demonstrated. In setup 2, a HEX cell deployment with $R = 2$ m, $\phi_{1/2} = 30^\circ$, $\Delta = 1$ and AMC2 is used. In setup 3, a HEX cell deployment with $R = 1$ m, $\Delta = 1$, $\phi_{1/2} = 15^\circ$ and AMC2 is used. As shown in Fig. 22, both optical attocell systems perform better than the femtocell systems. For the attocell system with setup 2, the maximum achievable area data rate of 49 Mb/(s·m^2) at a sampling frequency of 500 MHz is in a similar range of what the mmWave system can achieve. In particular, a maximum area data rate of 469 Mb/(s·m^2) is achieved by the system with setup 3 with a sampling frequency of 1.26 GHz. This is about two times higher than the high performance mmWave system with a spectral efficiency of 11.25 b/(s·Hz) and a bandwidth of 2 GHz. This result highlights the huge potential of optical attocell networks.

IX. Conclusion

In this paper, the downlink performance of an optical attocell network was evaluated. In order to be able to optimally design an optical attocell system, it is important to understand how key network parameters such as cell size and network deployments affect the system performance. This is particularly important when piggy-backing the optical attocell network on existing lighting infrastructures which leaves little possibilities to optimise the network for communication. To this end, an analysis of the SINR distribution and the corresponding data rate assuming different cell deployments was performed. The analysis in this paper offers an accurate estimation of the downlink performance of an optical attocell system that is subject to a large number of parameters. This study provides detailed guidelines for appropriate configurations of these parameters. Because of the potential benefits of combining optical attocell networks with existing lighting infrastructures and due to other practical constraints, optimized regular HEX cell deployments may not always be achievable. Therefore, in this study, several other network topologies such as square and random cell deployments were also considered. In particular, an optical attocell network with PPP cell deployment was considered to closely model a random real-world scenario where there are no underlying network planning considerations. The extensive simulation study confirms that the HEX and PPP cell deployments represent the best and the worst case performance of practical attocell deployments, respectively. The simulation results also demonstrate that the attocell networks deployed in a finite room offer better performance than the networks which are horizontally infinite because the CCI in the room edges is very low. In addition, the simulation results also imply that the MP effect due to the room internal surface reflections is minor relative to the effect of CCI. Because optical attocells can be deployed densely in a room, the optical attocell networks can typically achieve very high data rate density. In order to demonstrate this advantage, the downlink performance of optical attocell systems is compared with that achieved by RF femtocell networks and indoor mmWave systems in terms of area data rate (achievable data rate per unit area). The result showed that the optical attocell networks generally outperform the femtocell network. In particular, a high performance optical attocell network can achieve an area data rate of 469 Mb/(s·m^2) which is twice that achieved by a high performance mmWave system. The mmWave system assumes a spectral efficiency of 11.25 b/(s·Hz) and uses a bandwidth of 2 GHz in a room of size $10\ \text{m} \times 10\ \text{m}$. The system improvement by a reduction in cell size is more pronounced in regular HEX network deployments than in random PPP network deployments. Future research will continue with the studies on the effect of handover and system uplink performance.

Appendix

A. HEX Network Interference Approximation

The closed form expressions of $\mathcal{I}_{0^\circ}(r_0)$ and $\mathcal{I}_{30^\circ}(r_0)$ are calculated as (A.2) and (A.3), where

$$q(x,y) = \left((r_0+x)^2 + y\right)^{-m-3}. \tag{A.1}$$

B. Derivation of (50)

The derivations start from the term with bracket in the exponent of (49). By limiting $a \to \infty$, this term can be calculated as (A.4), where in (a), integration by substitution is used. By using (A.4), the CF of the CCI can be found as (A.5), where in (a), the Taylor series for e^x is used.

$$\begin{aligned}\mathcal{I}_{30^\circ}(r_0) = \mathbf{1}_{\{1\}}(\Delta)\Bigg(& q\left(-\sqrt{3}\tilde{R}, h^2\right) + q\left(\sqrt{3}\tilde{R}, h^2\right) + 2q \\ & \times \left(-\frac{\sqrt{3}\tilde{R}}{2}, \frac{9\tilde{R}^2}{4} + h^2\right) + 2q\left(\frac{\sqrt{3}\tilde{R}}{2}, \frac{9\tilde{R}^2}{4} + h^2\right) \\ & + q\left(-2\sqrt{3}\tilde{R}, h^2\right) + q\left(2\sqrt{3}\tilde{R}, h^2\right) \\ & + 2q\left(-\sqrt{3}\tilde{R}, 9\tilde{R}^2 + h^2\right) + 2q\left(\sqrt{3}\tilde{R}, 9\tilde{R}^2 + h^2\right)\Bigg) \\ & + 2q\left(-\frac{3\sqrt{3}\tilde{R}}{2}, \frac{9\tilde{R}^2}{4} + h^2\right) + 2q\left(\frac{3\sqrt{3}\tilde{R}}{2}, \frac{9\tilde{R}^2}{4} + h^2\right) \\ & + 2q\left(0, 9\tilde{R}^2 + h^2\right),\end{aligned} \tag{A.2}$$

$$\begin{aligned}\mathcal{I}_{0^\circ}(r_0)=&\mathbf{1}_{\{1\}}(\Delta)\left(2q\left(-\frac{3\tilde{R}}{2},\frac{3\tilde{R}^2}{4}+h^2\right)+2q\left(\frac{3\tilde{R}}{2},\frac{3\tilde{R}^2}{4}+h^2\right)\right.\\&+2q\left(0,3\tilde{R}^2+h^2\right)+2q\left(-3\tilde{R},3\tilde{R}^2+h^2\right)+2q\\&\times\left(3\tilde{R},3\tilde{R}^2+h^2\right)+2q\left(0,12\tilde{R}^2+h^2\right)\Big)+q\left(-3\tilde{R},h^2\right)\\&+q\left(3\tilde{R},h^2\right)+2q\left(-\frac{3\tilde{R}}{2},\frac{27\tilde{R}^2}{4}+h^2\right)\\&+2q\left(\frac{3\tilde{R}}{2},\frac{27\tilde{R}^2}{4}+h^2\right).\end{aligned}\tag{A.3}$$

$$\begin{aligned}&\lim_{a\to\infty}\left(a^2-r_0^2-\int_{\sqrt{r_0^2+h^2}}^{\sqrt{a^2+h^2}}2D\mathrm{e}^{j\omega g(D)}\mathrm{d}D\right)\\&\overset{(a)}{=}\lim_{a\to\infty}\left(a^2-r_0^2-\left(\left(a^2+h^2\right)\mathrm{e}^{j\omega g\left(\sqrt{a^2+h^2}\right)}\right.\right.\\&\quad-\left(r_0^2+h^2\right)\mathrm{e}^{j\omega g\left(\sqrt{r_0^2+h^2}\right)}\\&\quad\left.\left.+\int_{g\left(\sqrt{a^2+h^2}\right)}^{g\left(\sqrt{r_0^2+h^2}\right)}\left(g^{-1}(x)\right)^2j\omega\mathrm{e}^{j\omega x}\mathrm{d}x\right)\right)\\&=\lim_{a\to\infty}\left(a^2\left(1-\mathrm{e}^{j\omega g\left(\sqrt{a^2+h^2}\right)}\right)\right)+r_0^2\left(\mathrm{e}^{j\omega g\left(\sqrt{r_0^2+h^2}\right)}-1\right)\\&\quad-\lim_{a\to\infty}\left(h^2\mathrm{e}^{j\omega g\left(\sqrt{a^2+h^2}\right)}\right)+h^2\mathrm{e}^{j\omega g\left(\sqrt{r_0^2+h^2}\right)}-\lim_{a\to\infty}\\&\quad\times\left(\int_{g\left(\sqrt{a^2+h^2}\right)}^{g\left(\sqrt{r_0^2+h^2}\right)}\left(g^{-1}(x)\right)^2j\omega\mathrm{e}^{j\omega x}\mathrm{d}x\right)\\&=\left(r_0^2+h^2\right)\left(\mathrm{e}^{j\omega\left(r_0^2+h^2\right)^{-m-3}}-1\right)\\&\quad-\int_0^{\left(r_0^2+h^2\right)^{-m-3}}x^{-\frac{1}{m+3}}j\omega\mathrm{e}^{j\omega x}\mathrm{d}x\end{aligned}\tag{A.4}$$

$$\begin{aligned}\varphi_{\mathcal{I}}(\omega|r_0)&=\exp\left(\frac{\Lambda\pi}{\Delta}\left(\left(r_0^2+h^2\right)\left(1-\mathrm{e}^{j\omega\left(r_0^2+h^2\right)^{-m-3}}\right)\right.\right.\\&\quad\left.\left.+j\omega\int_0^{\left(r_0^2+h^2\right)^{-m-3}}x^{-\frac{1}{m+3}}\mathrm{e}^{j\omega x}\mathrm{d}x\right)\right)\\&\overset{(a)}{=}\exp\left(\frac{\Lambda\pi}{\Delta}\left(\left(r_0^2+h^2\right)\left(1-\sum_{n_1=0}^{\infty}\right.\right.\right.\\&\quad\left.\left.\frac{(j\omega)^{n_1}\left(r_0^2+h^2\right)^{-n_1(m+3)}}{n_1!}\right)+j\omega\int_0^{\left(r_0^2+h^2\right)^{-m-3}}\\&\quad\left.x^{-\frac{1}{m+3}}\sum_{n_2=0}^{\infty}\frac{(j\omega x)^{n_2}}{n_2!}\mathrm{d}x\right)\right)\\&\overset{(b)}{=}\exp\left(-\frac{\Lambda\pi}{\Delta}\left(\sum_{n_1=1}^{\infty}\frac{(j\omega)^{n_1}\left(r_0^2+h^2\right)^{1-n_1(m+3)}}{n_1!}\right.\right.\\&\quad\left.\left.+\sum_{n_3=1}^{\infty}\frac{(j\omega)^{n_3}}{n_3!}\cdot\frac{n_3(m+3)\left(r_0^2+h^2\right)^{1-n_3(m+3)}}{n_3(m+3)-1}\right)\right)\\&=\exp\left(\sum_{n=1}^{\infty}\frac{(j\omega)^n}{n!}\cdot\frac{\Lambda\pi\left(r_0^2+h^2\right)^{1-n(m+3)}}{\Delta(n(m+3)-1)}\right)\end{aligned}\tag{A.5}$$

REFERENCES

[1] Cisco Visual Networking Index, "Global Mobile Data Traffic Forecast Update, 2014-2019," CISCO, White Paper, Feb. 2015.

[2] GBI Research, "Visible light communication (VLC)—A potential solution to the global wireless spectrum shortage," Tech. Rep. GBISC017MR, 2011.

[3] V. Chandrasekhar, J. Andrews, and A. Gatherer, "Femtocell Networks: A survey," *IEEE Commun. Mag.*, vol. 46, no. 9, pp. 59–67, Sep. 2008.

[4] H. Elgala, R. Mesleh, and H. Haas, "Indoor Optical Wireless Communication: Potential and State-of-the-Art," *IEEE Commun. Mag.*, vol. 49, no. 9, pp. 56–62, Sep. 2011.

[5] P. Chandhar and S. Das, "Area spectral efficiency of Co-Channel deployed OFDMA femtocell networks," *IEEE Trans. Wireless Commun.*, vol. 13, no. 7, pp. 3524–3538, Jul. 2014.

[6] H. Haas, "High-speed wireless networking using visible light," SPIE Newsroom, 2013.

[7] S. Dimitrov and H. Haas, *Principles of LED Light Communications: Towards Networked Li-Fi*. Cambridge, U.K.: Cambridge Univ., 2015.

[8] H. L. Minh, D. O'Brien, G. Faulkner, L. Zeng, K. Lee, D. Jung, Y. Oh, and E. T. Won, "100-Mb/s NRZ visible light communications using a postequalized white LED," *IEEE Photon. Technol. Lett.*, vol. 21, no. 15, pp. 1063–1065, Aug. 2009.

[9] D. Tsonev, H. Chun, S. Rajbhandari, J. J. D. McKendry, S. Videv, E. Gu, M. Haji, S. Watson, A. E. Kelly, G. Faulkner, M. D. Dawson, H. Haas, and D. O'Brien, "A 3-Gb/s single-LED OFDM-based wireless VLC link using a gallium nitride μLED," *IEEE Photon. Technol. Lett.*, vol. 26, no. 7, pp. 637–640, Apr. 2014.

[10] D. Tsonev, S. Videv, and H. Haas, "Unlocking spectral efficiency in intensity modulation and direct detection systems," *IEEE J. Sel. Areas Commun.*, vol. 33, no. 9, pp. 1758–1770, Sept 2015.

[11] J. Armstrong, "OFDM for optical communications," *J. Lightw. Technol.*, vol. 27, no. 3, pp. 189–204, Feb. 2009.

[12] D. Tsonev and H. Haas, "Avoiding spectral efficiency loss in unipolar OFDM for optical wireless communication," in *Proc. IEEE Int. Conf. Commun.*, Sydney, Australia, Jun., 2014, pp. 3336–3341.

[13] A. M. Khalid, G. Cossu, R. Corsini, P. Choudhury, and E. Ciaramella, "1-Gb/s transmission over a phosphorescent white LED by using rate-adaptive discrete multitone modulation," *IEEE Photon. J.*, vol. 4, no. 5, pp. 1465–1473, Oct. 2012.

[14] J. Vucic, C. Kottke, S. Nerreter, K. D. Langer, and J. W. Walewski, "513 Mbit/s visible light communications link based on DMT-modulation of a white LED," *J. Lightw. Technol.*, vol. 28, no. 24, pp. 3512–3518, Dec. 2010.

[15] C. Chen, N. Serafimovski, and H. Haas, "Fractional frequency reuse in optical wireless cellular networks," in *Proc. Int. Symp. Personal, Indoor Mobile Radio Commun.*, London, U.K., Sep. 2013, pp. 3594–3598.

[16] C. Chen, D. Tsonev, and H. Haas, "Joint transmission in indoor visible light communication downlink cellular networks," in *Proc. IEEE Globecom Workshops*, Atlanta, GA, USA, Dec. 2013, pp. 1127–1132.

[17] B. Ghimire and H. Haas, "Self-organising interference coordination in optical wireless networks," *EURASIP J. Wireless Commun. Netw.*, vol. 1, no. 131, pp. 1–15, Apr. 2012.

[18] Z. Chen, N. Serafimovski, and H. Haas, "Angle diversity for an indoor cellular visible light communication system," in *Proc. IEEE Veh. Technol. Conf.*, Seoul, South Korea, May 2014, pp. 1–5.

[19] Z. Chen and H. Haas, "Space division multiple access in visible light communications," in *Proc. IEEE Int. Conf. Commun.*, London, U.K., Jun. 2015, pp. 5115–5119.

[20] L. Zeng, D. O'Brien, H. Minh, G. Faulkner, K. Lee, D. Jung, Y. Oh, and E. T. Won, "High data rate multiple input multiple output optical wireless communications using white LED lighting," *IEEE J. Sel. Areas Commun.*, vol. 27, no. 9, pp. 1654–1662, Dec. 2009.

[21] R. Mesleh, H. Elgala, and H. Haas, "Optical spatial modulation," *IEEE/OSA J. Opt. Commun. Netw.*, vol. 3, no. 3, pp. 234–244, Mar. 2011.

[22] A. Azhar, T. Tran, and D. O'Brien, "A gigabit/s idoor wireless transmission using MIMO-OFDM visible-light communications," *IEEE Photon. Technol. Lett.*, vol. 25, no. 2, pp. 171–174, Jan. 15, 2013.

[23] G. Xie, Y. Ren, H. Huang, Y. Yan, C. Bao, N. Ahmed, M. Willner, M. Lavery, M. Padgett, and A. Willner, "Analysis of aperture size for partially receiving and de-multiplexing 100-Gbit/s optical orbital

angular momentum channels over free-space link," in *Proc. IEEE Globecom Workshops*, Dec. 2013, pp. 1116–1120.
[24] C. Chen, I. Muhammad, D. Tsonev, and H. Haas, "Analysis of downlink transmission in DCO-OFDM-based optical attocell networks," in *Proc. IEEE Global Commun. Conf.*, Austin, TX, USA, Dec. 2014, pp. 2072–2077.
[25] K. Chandra, R. Venkatesha Prasad, and I. Niemegeers, "An architectural framework for 5G indoor communications," in *Proc. Int. Wireless Commun. Mobile Comput. Conf.*, Dubrovnik, Croatia, Aug. 2015, pp. 1144–1149.
[26] M. B. Rahaim, A. M. Vegni, and T. D. C. Little, "A hybrid radio frequency and broadcast visible light communication system," in *Proc. IEEE GLOBECOM Workshops*, Dec. 2011, pp. 792–796.
[27] (2015). Purelifi product: Li-flame. [Online]. Available: http://purelifi.com/lifi-products/li-flame/
[28] S. Dimitrov, S. Sinanovic, and H. Haas, "Clipping noise in OFDM-based optical wireless communication systems," *IEEE Trans. Commun.*, vol. 60, no. 4, pp. 1072–1081, Apr. 2012.
[29] J. M. Kahn and J. R. Barry, "Wireless infrared communications," *Proc. IEEE*, vol. 85, no. 2, pp. 265–298, Feb. 1997.
[30] F. J. Lopez-Hernandez, R. Perez-Jimenez, and A. Santamara, "Ray-tracing algorithms for fast calculation of the channel impulse response on diffuse IR wireless indoor channels," *Opt. Eng.*, vol. 39, no. 10, pp. 2775–2780, 2000.
[31] V. Jungnickel, V. Pohl, S. Nonnig, and C. von Helmolt, "A physical model of the wireless infrared communication channel," *IEEE J. Sel. Areas Commun.*, vol. 20, no. 3, pp. 631–640, Apr. 2002.
[32] *Lighting of Indoor Work Places*, European Standard EN 12464-1, Jan. 2009.
[33] J. R. Meyer-Arendt, "Radiometry and Photometry: Units and conversion factors," *Appl. Opt.*, vol. 7, no. 10, pp. 2081–2084, Oct. 1968.
[34] (2015, Dec.) VESTA 165 mm Recessed LED Downlighter. [Online]. Available: http://www.istl.com/vesta.php
[35] (2014, Aug.). 64 W LED panel. [Online]. Available: http://wellmaxled.com/portfolio/64-w-led-panel-light/
[36] F. R. Gfeller and U. Bapst, "Wireless in-house data communication via diffuse infrared radiation," *Proc. IEEE*, vol. 67, no. 11, pp. 1474–1486, Nov. 1979.
[37] J. Andrews, F. Baccelli, and R. Ganti, "A tractable approach to coverage and rate in cellular networks," *IEEE Trans. Commun.*, vol. 59, no. 11, pp. 3122–3134, Nov. 2011.
[38] H. Elgala, R. Mesleh, and H. Haas, "Non-linearity effects and predistortion in optical OFDM wireless transmission using LEDs," *Inderscience Int. J. Ultra Wideband Commun. Syst.*, vol. 1, no. 2, pp. 143–150, 2009.
[39] D. Tsonev, S. Sinanovic, and H. Haas, "Complete modeling of nonlinear distortion in OFDM-based optical wireless communication," *J. Lightw. Technol.*, vol. 31, no. 18, pp. 3064–3076, Sep. 15, 2013.
[40] B. Almeroth, A. Fehske, G. Fettweis, and E. Zimmermann, "Analytical interference models for the downlink of a cellular mobile network," in *Proc. IEEE Globcom Workshops*, Houston, TS, USA, Dec. 5–9, 2011, pp. 739–743.
[41] E. Sousa and J. Silvester, "Optimum transmission ranges in a direct-sequence spread-spectrum multihop packet radio network," *IEEE J. Sel. Areas Commun.*, vol. 8, no. 5, pp. 762–771, Jun. 1990.
[42] J. Bowers and L. Newton, "Expansion of probability density functions as a sum of gamma densities with applications in risk theory," *Trans. Soc. Actuaries*, vol. 18, no. 52, pp. 125–147, 1966.
[43] M. Haenggi, "On distances in uniformly random networks," *IEEE Trans. Inf. Theory*, vol. 51, no. 10, pp. 3584–3586, Oct. 2005.
[44] F. Xiong, *Digital Modulation Techniques*, 2nd ed. Norwood, MA, USA: Artech House, 2006.
[45] H. Burchardt, S. Sinanović, Z. Bharucha, and H. Haas, "Distributed and autonomous resource and power allocation for wireless networks," *IEEE Trans. Commun.*, vol. 61, no. 7, pp. 2758–2771, Aug. 2013.
[46] D. Stoyan, W. S. Kendall, and J. Mecke, *Stochastic Geometry and Its Applications*, 2nd ed. Hoboken, NJ, USA: Wiley, 1995.
[47] C. Hansen, "WiGiG: Multi-Gigabit wireless communications in the 60 GHz Band," *IEEE Wireless Commun.*, vol. 18, no. 6, pp. 6–7, Dec. 2011.
[48] H.-S. Jo, P. Xia, and J. Andrews, "Downlink femtocell networks: Open or closed?" in *Proc. IEEE Int. Conf. Commun.*, Kyoto, Japan, Jun., 2011, pp. 1–5.
[49] W. C. Cheung, T. Quek, and M. Kountouris, "Throughput optimization, spectrum allocation, and access control in two-tier femtocell networks," *IEEE J. Sel. Areas Commun.*, vol. 30, no. 3, pp. 561–574, Apr. 2012.
[50] D. Muirhead, M. A. Imran, and K. Arshad, "Insights and approaches for low-complexity 5G small-cell base-station design for indoor dense networks," *IEEE Access*, vol. 3, pp. 1562–1572, 2015.
[51] C. Yiu and S. Singh, "Empirical capacity of mmWave WLANS," *IEEE J. Sel. Areas Commun.*, vol. 27, no. 8, pp. 1479–1487, Oct. 2009.

Cheng Chen (S'14) received the B.Eng. degree in electronic and electrical engineering (first class hons.) from the University of Strathclyde, Glasgow, U.K., in 2011, and the M.Sc. degree in communications and signal processing from the Imperial College, London, U.K., in 2012. He is currently working toward the Ph.D. degree in electrical engineering from the University of Edinburgh, Edinburgh, U.K.. His research focus include the visible light communication networking and interference mitigation.

Dushyantha A. Basnayaka (S'11–M'12) received the B.Sc. Eng. degree (first class hons.) from the University of Peradeniya, Peradeniya, Sri Lanka, in 2006, and the Ph.D. degree in electrical engineering from the University of Canterbury, Christchurch, New Zealand, in 2012. From 2006 to 2009, he was with MillenniumIT (a member company of the London Stock Exchange Group). From 2009 to 2012, he was with the Communication Research Group, the University of Canterbury. He is currently with the Institute for Digital Communications, the University of Edinburgh, Edinburgh, U.K. He is a holder of one U.S. patent. His current research interests include massive multiple-input multiple-output, spatial modulation, interference mitigation techniques for cellular wireless systems, coordinated multipoint systems, and visible light communication systems. He received the University of Canterbury International Doctoral Scholarship for his Doctoral Studies and the Best Paper Award at the Spring 2015 IEEE Vehicular Technology Conference (IEEE VTC-Spring 2015).

Harald Haas (S'98–AM'00–M'03) received the Ph.D. degree from the University of Edinburgh, Edinburgh, U.K., in 2001. He is currently the Chair of Mobile Communications at the University of Edinburgh, and is the Cofounder and Chief Scientific Officer of pureLiFi Ltd. and the Director of the LiFi Research and Development Center at the University of Edinburgh. His main research interests include optical wireless communications, hybrid optical wireless and RF communications, spatial modulation, and interference coordination in wireless networks. He first introduced and coined spatial modulation and LiFi. LiFi was listed among the 50 best inventions in TIME Magazine 2011. He was an Invited Speaker at TED Global 2011, and his talk: "Wireless Data from Every Light Bulb" has been watched online more than 2.2 million times. He gave the second TED Global lecture in 2015 on the use of solar cells as LiFi data detectors and energy harvesters which was viewed online more than 1 million times. He holds 31 patents and has more than 30 pending patent applications. He has published 300 conference and journal papers including a paper in Science. He coauthors a book entitled: "Principles of LED Light Communications Towards Networked Li-Fi" (Cambridge, U.K.: Cambridge Univ. Press, 2015). He was a corecipient of recent Best Paper Awards at the IEEE Vehicular Technology Conference (VTC-Fall) in Las Vegas in 2013, and VTC-Spring in Glasgow in 2015. He was a corecipient of the EURASIP Best Paper Award for the *Journal on Wireless Communications and Networking* in 2015, and a corecipient of the Jack Neubauer Memorial Award of the IEEE Vehicular Technology Society. In 2012, he received the prestigious Established Career Fellowship from the Engineering and Physical Sciences Research Council (EPSRC) within Information and Communications Technology in the U.K. He received the Tam Dalyell Prize 2013 awarded by the University of Edinburgh for excellence in engaging the public with science. In 2014, he was selected by EPSRC as one of ten Recognizing Inspirational Scientists and Engineers Leaders in the U.K.

3986 JOURNAL OF LIGHTWAVE TECHNOLOGY, VOL. 33, NO. 19, OCTOBER 1, 2015

Fractional Frequency Reuse in DCO-OFDM-Based Optical Attocell Networks

Cheng Chen, *Student Member, IEEE*, Stefan Videv, Dobroslav Tsonev, *Member, IEEE*, and Harald Haas, *Member, IEEE*

***Abstract*—In this paper a fractional frequency reuse (FFR) technique is considered in a direct-current optical orthogonal frequency-division multiplexing-based optical attocell network. An optical attocell network is proposed as a special type of visible light communication system that has the complete function of a cellular network. The cellular network is composed of many cells of extremely small size—the optical attocells. Two FFR schemes, strict fractional frequency reuse and soft frequency reuse, are considered. The signal-to-interference-plus-noise ratio (SINR) statistics and the spectral efficiency of the optical cellular system with FFR are analyzed. The performance of the systems with full frequency reuse and FFR is evaluated and compared. The results show that the FFR scheme can effectively achieve interference mitigation in an optical attocell network. The cell edge user SINR and spectral efficiency are significantly improved. Additionally, FFR provides improvements in average spectral efficiency. The effects of important parameters such as cell radius are also studied.**

***Index Terms*—Cellular network, fractional frequency reuse, orthogonal frequency division multiplexing, visible light communications.**

I. Introduction

The level of data traffic in wireless communication networks has increased exponentially in the past two decades. If this trend continues in the future, the limited radio frequency (RF) spectrum will no longer meet the wireless data transmission demand [1]. One of the emerging solutions to this spectrum crisis is the migration of wireless communication techniques into the visible light spectrum due to its many promising advantages [2]. For example, visible light communication (VLC) can be embedded in the existing lighting infrastructure.

In a typical VLC system, a low-cost commercially available light emitting diode (LED) and photodiode (PD) can be used as the front-end devices [2]. Since an LED is an incoherent optical source, information is encoded using intensity modulation (IM). At the receiver side, the light intensity is converted to an electrical signal by a PD using direct detection (DD). A limiting factor of such an IM/DD system is the bandwidth of the LED and PD devices. Various techniques have been considered to boost the transmission speed of VLC systems. Some researchers have explored the spatial diversity gain by using multiple-input multiple-output techniques [3], [4]. Advanced spectral efficient modulation techniques have also been considered [5], [6]. Another approach to improve the spectral efficiency of a wireless communication system is to increase the spatial reuse of the spectrum resources [7]. In many large indoor environments, multiple light fixtures are installed, and this provides the opportunity to set up a VLC system with dense spatial reuse of the limited modulation bandwidth. An optical attocell network uses each of the luminaries as a small base station (BS) or access point (AP) serving multiple wireless users within the illuminated area [8]. Such a cellular system would have an uplink connection to achieve full-duplexing and provide handovers to allow users to roam within the room or an entire building. This is similar to a RF femtocell network, but an optical attocell network uses smaller cell sizes.

Direct-current optical orthogonal frequency division multiplexing (DCO-OFDM) has been considered for optical attocell networks because of its advantages: i) it can eliminate the effect of the time dispersive channel with low complexity equalisation [5]; ii) adaptive power and bit loading can be used in an OFDM system, thus the available spectral resources can be used with their full potential [9]; iii) a multiple access scheme can be easily achieved in an optical attocell network by dividing time and frequency resources among multiple users, which in RF is known as orthogonal frequency division multiple access (OFDMA) [10].

Similar to other cellular systems, co-channel interference (CCI) is an important issue that affects the user performance in an optical attocell network. Interference mitigation techniques have been extensively researched for optical wireless systems. In [11], the use of static resource partitioning was proposed to avoid CCI in a cellular optical wireless system. In [12], an optical femtocell system was proposed, which uses different wavelengths in adjacent cells to avoid CCI. The methods used in these two studies effectively mitigate CCI. However, the loss in spectral efficiency is also significant. In [13], a self-organising interference coordination technique based on the busy-burst signalling was proposed for an optical wireless cellular system in an aircraft cabin environment. This method offers improvements both in cell edge user performance and in average spectral efficiency, but it requires additional overhead for the busy burst time slot.

The fractional frequency reuse (FFR) technique is a cost-effective approach to achieve interference mitigation in a cellular system. It maintains the balance between the average spectral

Manuscript received January 12, 2015; revised May 15, 2015 and July 1, 2015; accepted July 5, 2015. Date of publication July 19, 2015; date of current version August 17, 2015. This publication was made possible by NPRP grant no. [5-980-2-411] from the Qatar National Research Fund (a member of Qatar Foundation). The statements made herein are solely the responsibility of the authors.

The authors are with the Li-Fi R&D Centre, University of Edinburgh, Edinburgh EH9 3JL, U.K. (e-mail: cheng.chen@ed.ac.uk; s.videv@ed.ac.uk; d.tsonev@ed.ac.uk; h.haas@ed.ac.uk).

Color versions of one or more of the figures in this paper are available online at http://ieeexplore.ieee.org.

Digital Object Identifier 10.1109/JLT.2015.2458325

efficiency and cell edge user performance with low system complexity [14]. Over the past few years, the FFR technique has been studied for applications in RF cellular networks. The FFR scheme does not require precise instantaneous channel state information (CSI) and is of low computational complexity. There are two typical FFR schemes: ii) strict fractional frequency reuse (sFFR) and ii) soft frequency reuse (SFR) [15]. sFFR divides the whole frequency band into multiple protected sub-bands and one common sub-band. Cell centre users in each cell experience minor interference from nearby BS, so the common sub-band is assigned to them. Since cell edge users receive higher interference power, protected sub-bands are assigned to the cell edge users, and the sub-bands are arranged such that there is a minimum spatial reuse distance between them. The SFR applies an even shorter reuse distance compared to the sFFR scheme. In addition to the use of a different sub-band for cell edge users in each adjacent cell, the SFR scheme allows the centre users to take the sub-bands that are assigned to cell edge users in adjacent cells. To protect the cell edge users, the transmission power for cell edge users is typically higher than that for the cell centre users.

In [16], an optical AP using two LED sources with different beam-width is considered. A VLC cellular system using a SFR scheme based on such an AP is proposed. The corresponding bit error rate performance and the effect of changing LED beamwidth is evaluated. In a previous study [17], an FFR scheme is considered in a VLC cellular system using adaptive LED arrays with specified LED orientations as APs. The simulation results show that the FFR scheme achieves effective interference mitigation and improves the spectral efficiency. However, the improvements reported in these studies result partly from the spatial diversity. In order to evaluate the benefit solely from FFR schemes, a more general case is presented in this paper. A VLC system with APs that only transmit using a LED luminary with Lambertian radiation pattern is considered. This paper presents a first analytical framework for the evaluation of FFR in a DCO-OFDM-based optical attocell network.

The remainder of this paper is organised as follows: the system model, including the light propagation model, network model, modulation and multiple access schemes is presented in Section II. The statistics of signal-to-interference-plus-noise ratio (SINR) and spectral efficiency for FFR schemes are analysed in Section III. The results are presented in Section IV and the effects of key parameters are discussed. Conclusions are given in Section V.

II. System Model

In this study, a system level analysis is carried out to evaluate the performance of an optical attocell network. Since the transmission data rate is much faster than the channel variation due to user movement, users are considered to be quasi-static. In addition, this study focuses on the downlink performance of the system, so the effects on the system performance and the operation of handover schemes are outside the scope of this study. User equipment is placed at the desktop height where a typical height of 0.85 m is used. A PD receiver with a field of view (FOV) of 90° (full FOV) is mounted on the top of the user equipment. The FOV of the receiver is defined as the angle between the normal of the PD surface and the direction with the maximum incident angle to the receiver, which is illustrated in Fig. 1. The receiver is orientated upwards. All BS are mounted on the ceiling where a typical value for ceiling height of 3 m is used. The direction of the BS optical transmitter is vertically downwards.

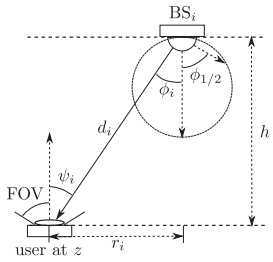

Fig. 1. LOS light propagation geometry.

A. Light Propagation Model

In order to estimate the signal power from a specified BS to a user, a propagation model is necessary to calculate the path loss. The dominant transmitted signal component in this system is the light through the line-of-sight (LOS) path. This channel can be modelled using the direct-current (dc) channel gain. The corresponding two-dimensional (2-D) geometry is shown in Fig. 1. The dc gain from the ith BS to the observed user can be calculated as [18]:

$$G_i = \frac{(m+1)A_{\mathrm{pd}}}{2\pi d_i^2}\cos^m(\phi_i)\cos(\psi_i),$$

where m denotes the Lambertian emission order which is given by $m = -\ln(2)/\ln(\cos(\phi_{1/2}))$ in which $\phi_{1/2}$ is the half-power semi-angle of the LED; A_{pd} is the physical area of the receiver PD; d_i denotes the Euclidean distance between BS_i and the user; ϕ_i denotes the corresponding light radiance angle; and ψ_i is the corresponding light incidence angle. The optical source has a half-power semi-angle $\phi_{1/2}$ of 60°, which is sufficient for a diffused luminary. The variables d_i, ϕ_i and ψ_i can be rewritten as a function of r_i by using $\cos(\phi_i) = \cos(\psi_i) = \frac{h}{d_i}$ and $d_i = \sqrt{r_i^2 + h^2}$. As shown in Fig. 1, r_i refers to the horizontal separation between the user and the i^{th} BS. The LOS transmission model can then be converted to a function of r_i as:

$$G_i(r_i) = \frac{(m+1)A_{\mathrm{pd}}h^{m+1}}{2\pi}\left(r_i^2 + h^2\right)^{-\frac{m+3}{2}}. \qquad (1)$$

Occasionally, the LOS path may be shadowed or completely blocked. In these cases, a user may need an alternative serving BS or rely on a diffused link. Due to the modelling complexity and the limited space in this paper, these issues are treated as special cases for future study. Therefore, we assume that shadowing and non-LOS transmission issues are outside the scope of this work.

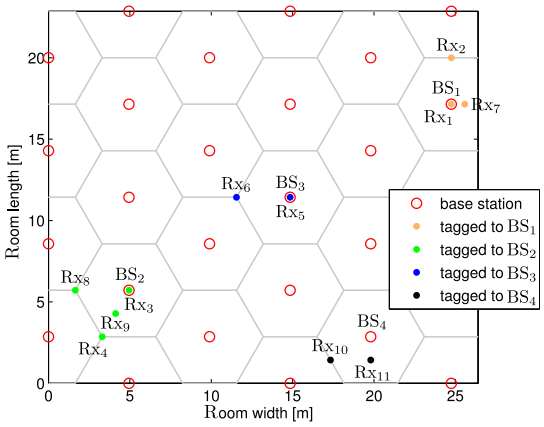

Fig. 2. An optical attocell network embedded in a large room of size 23 m × 26 m × 3 m. The number of cells is 27. The cell radius $R = 3.3$ m and the cell radius definition is shown in Fig. 7.

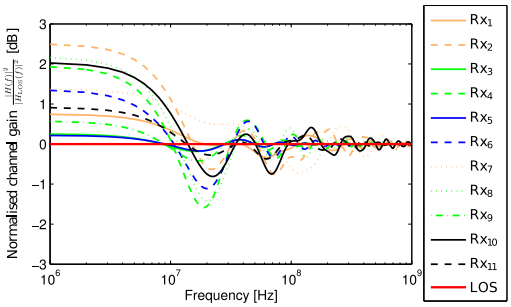

Fig. 3. Normalised channel gain against frequency. The corresponding receiver locations are shown in Fig. 2.

In addition to the LOS transmission, light from reflections (mainly from walls, ceiling and floor) causes multi-path distortion to the optical channel. In order to observe this multi-path distortion effect, information about the channels considering multi-path reflection is required. An effective way to estimate this information is by using the multi-path ray-tracing simulation [19] to generate the channel data. However, it is time-consuming and difficult to show cases for all indoor environments and all user positions. Therefore, a number of examples are demonstrated to reflect the typical and worst cases. In these examples, the simulated environment is a large empty room of size 23 m × 26 m × 3 m. The room size is related to the cell size and the number of cells in the network. The optical source of each BS has a half-power semi-angle $\phi_{1/2}$ of 60°, which is sufficient for a diffused luminary. The reflectivity of walls and the ceiling is 0.7, and the reflectivity of the floor is 0.3. Reflected signal components up to the third order are considered in the simulation. The network deployment and the user receiver positions are shown in Fig. 2. Each user in the room is served by the closest BS. Among all of the tessellating shapes, a hexagon cell shape shows a reasonable approximation to a circle [20]. Therefore, the hexagonal network deployment is preferred in the modelling of the cellular network. In this initial performance evaluation of a VLC based cellular system, it is intuitive to adopt the same network deployment.

Based on the method introduced in [19], the initial generated data are in the form of impulse responses. It is observed from these impulse responses that the overall signal power contribution from wall reflections is not as significant as those shown in [19] due to the large size of the considered room. Furthermore, the contribution from the third and higher order reflections is negligible due to the significant path loss and absorptions. The second order reflection generally corresponds to the reflections between floor and ceilings, and contributes significantly to the reflected signal power. The first order reflection corresponds to the reflections by the walls to the receiver. Its significance strongly depends on whether the transmitter and the receiver is close to one or more walls of the room. When a user is in the edge of the room, the first order reflection contributes significantly to the reflected signal. Therefore, the channel frequency response of the users in the room edge would be the worst case due to wall reflections. The channels corresponding to 'Rx_5' and 'Rx_6' are in the centre of the room as shown in Fig. 2. Their performance would reflect the typical channel characteristics in an optical attocell network. The user positions for the remaining nine channels are in the edge of the room, which would reflect the characteristics of the worst case channel.

It is important to assess whether the channel is flat in a wide frequency range, and therefore the simulated results are shown in the form of channel gain calculated as a function of frequency $|H(f)|^2$. Conventionally, the channel gain is normalised with the channel gain at dc. In this study, two cases are compared: with, and without the reflected signal. In order to highlight the difference, the channel gain is normalised by the channel gain with only a LOS component. The normalised channel gain is calculated by $\frac{|H(f)|^2}{|H_{\mathrm{LOS}}(f)|^2}$. The result is shown in Fig. 3.

With an increase of frequency, all of the normalised channel gains fluctuate around 0 dB (channel gain with LOS only). The variation of the fluctuation is less than 3 dB. In addition, for users that are further away from the room edges, due to the lower significance of the first order reflection, the channel gain variation with frequency is less significant compared with the room edge user case. For example, the channel gain variation for Rx_5 and Rx_6 are less than 1.5 dB as shown in Fig. 3. The maximum achievable signal-to-noise ratios (SNRs) in many VLC experiments are around 30 dB [9], [21], [22]. However, the received SNR decreases when the user is away from the cell centre due to a larger path loss. In order to ensure that the system is not limited by the receiver noise, the considered systems in this study are configured to have a worst case SNR (user at cell edge) of more than 10 dB. In the case of a SNR of 10 dB, uncoded four-quadrature amplitude modulation is used, which requires a minimum SNR of about 10 dB. Therefore, compared with the considered SNR range of 10 to 30 dB, the variation in channel gain is minor. In addition, the effect of adding reflected signals offers extra channel gain at some frequencies while it decreases the channel gain at other frequencies. On average, adaptive bit

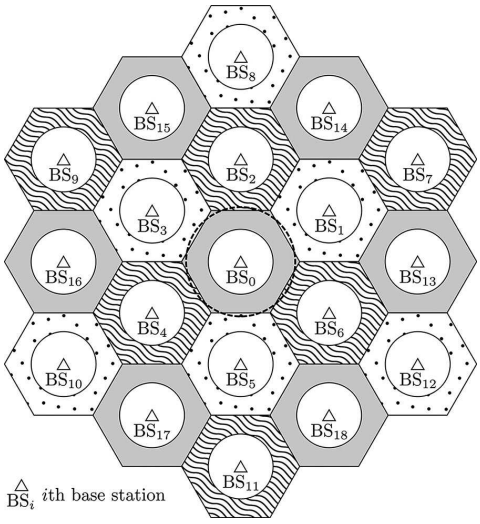

Fig. 4. Two-layer optical attocell network model with 19 cells. The patterns in the edge regions of every cells demonstrate the FR pattern for the FFR schemes, and the corresponding reuse factor is 3.

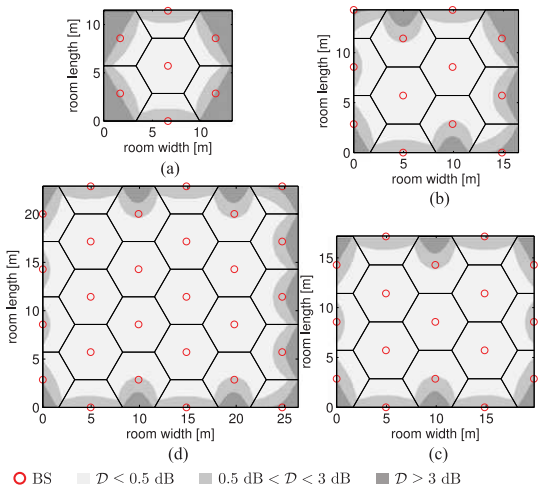

Fig. 5. The 2-D spatial distribution of $\mathcal{D}$ in the deployed networks with different network sizes. (a) 11.4 m × 13.2 m room with seven cells. (b) 14.3 m × 16.5 m room with 12 cells. (c) 17.1 m × 19.8 m room with 17 cells. (d) 22.9 m × 26.4 m room with 27 cells. The used cell radius is $R = 3.3$ m.

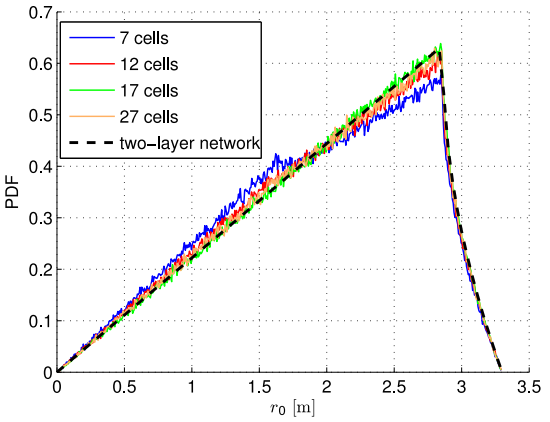

Fig. 6. Statistics of the horizontal separation between the serving BS and the user in different networks. 'two-layer network' refers to the results for the two-layer network model. '7 cells', '12 cells', '17 cells' and '27 cells' refer to the results for the deployed networks with different network sizes. The corresponding network deployments are shown in Fig. 5.

loading in OFDM can compensate for the variation in channel gain. Therefore, approximating the frequency domain channel gain to be flat would not cause significant inaccuracy in the analysis. The reason for this minor multi-path distortion is the dominance of the LOS in the channel. When the Rician factor is high enough, the channel gain can be approximated to be flat in the frequency domain [23]. Therefore, the multi-path effect caused by wall reflections is assumed to be negligible and can be mitigated by OFDM [24] in this study.

B. Cellular Network Model

When evaluating the user performance in the room shown in Fig. 2, the serving BS changes depending on the position of a user. In addition, for users in different cells, the set of interfering BS is different. Furthermore, the coverage area of cells in the edge of the room is part of a hexagon. All of these factors mean that it is complex to analyse the system performance. Therefore, an alternative simplified model is considered to estimate the performance of a realistic system. Here, a network which extends to infinity in the 2-D plane is considered. In this case, the layout of the interfering BS and the cell shape would be identical for the users in any cell. As the interference is generally dominated by the closest interfering BS, the interference from BS further away from the user is not considered for simplicity. Thus, a two-layer hexagonal network model shown in Fig. 4 is used to analyse the user performance. In this two-layer network model, 19 BS with index i are considered, where $i = 0, \ldots, 18$. The performance of the users in the central cell served by the 0th BS is evaluated to estimate the performance of users in the network deployed in a room. For the convenience of description, the network deployed in a room is termed as a 'deployed network' in the remainder of this paper. Some of the neighbouring BSs cause interference to the users in the central cell. Whether the ith BS causes interference depends on the reuse scheme in the system.

Despite the difference in the user performance in the two-layer network model and the deployed networks, the results shown in Figs. 5 and 6 demonstrate that this is minor. Firstly, the closer the considered cell is to the room edge, the less the number of interfering BS to the users. Consequently, it would seem that the two-layer network model only offers a good estimation to the user performance in the cells in the room central area. However, as mentioned above, the interference is dominated by the closest interfering BS. Even if the user is in the cell in the edge

TABLE I
INTERFERENCE LEVEL DIFFERENCE

number of cells	7	12	17	27
$\mathcal{D} < 0.5$ dB	48%	64%	76%	77%
$\mathcal{D} < 3$ dB	75%	89%	95%	94%

of the room, as long as it is close to the cell edge towards the room centre, the received interference should be close to that received in the two-layer network model. To demonstrate the accuracy of the interference estimation by using the two-layer network model, simulations of the 2-D spatial distribution of the interference power in the deployed networks with full frequency reuse (FR) are carried out. In addition, the interference power estimated by using the two-layer network model in all positions in the deployed network is calculated and compared to the simulated interference. The interference calculation is based on (1). The interference in the deployed network is defined as $\tilde{\mathcal{I}}$. The interference estimated for the two-layer network model is defined as $\mathcal{I}$. The difference between $\tilde{\mathcal{I}}$ and $\mathcal{I}$ is defined as $\mathcal{D} = |10\log_{10}(\tilde{\mathcal{I}}/\mathcal{I})|$. A lower value of $\mathcal{D}$ indicates a better approximation of the interference by using the two-layer network model. The spatial distributions of $\mathcal{D}$ in rooms with 7, 12, 17 and 27 cells are shown in Fig. 5. It shows that a significant interference difference occurs only in the room edges. The notable results are summarized in Table I, and it shows that the proportion of the area showing significant deviation in the interference estimation decreases with an increase of the number of cells in a room. In the case of 27 cells, 77% of the area has $\mathcal{D}$ lower than 0.5 dB and 94% of the area has $\mathcal{D}$ lower than 3 dB. In other words, the interference level is poorly estimated by the two-layer network model in only 6% of the room area. Since a large number of deployed cells is the typical case in an optical attocell network, the two-layer network model is considered to offer good approximation in terms of interference.

In addition, due to the limitation of the room edge, the non-hexagon cells in the edge of the room cause a deviation in the statistics of the path loss corresponding to the transmission of the desired signal in the deployed network from the case in the two-layer network model. In order to evaluate this difference, the empirical statistics of r_0 based on random user locations in different cases are simulated and compared. The random location of users follows a Possion point process (PPP). As described in Section II-A, r_0 refers to the horizontal separation between the user and the 0th BS in the two-layer network model. For the deployed network, r_0 refers to the horizontal separation between the user and its serving BS. It can be observed in Fig. 6 that the difference between the probability density function (PDF) of r_0 in a deployed network and that in the two-layer network model diminishes with an increase of the number of cells in the deployed network. Except for the case with 7 cells, the PDFs of r_0 in the deployed network shows a close agreement with that in the two-layer network model. Therefore, the performance in the two-layer network is considered to be a reasonable estimation of the deployed network. The estimation accuracy is also demonstrated in the SINR results in Section IV as shown in Fig. 10.

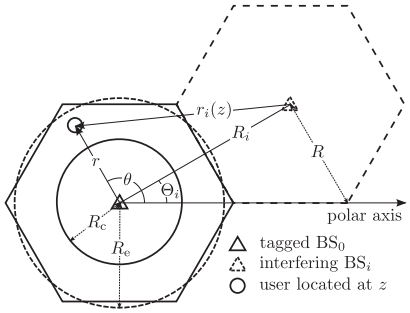

Fig. 7. Geometric model with polar coordinates.

In the two-layer network model, the coverage area of each cell is divided into a cell central area and a cell edge area as shown in Fig. 4. In order to further simplify the analysis, a circular cell approximation is applied to the considered central cell as shown in Fig. 7. The radius of the hexagonal cell is defined as R. The approximated circular cell has the same coverage area as the original hexagonal cell. Therefore, the equivalent radius of the circular cell is defined as $R_e \approx 0.91R$. In the system using FFR, the radius of the central area is defined as R_c. A parameter $\delta = \frac{R_c}{R_e}$ is defined to determine the size of cell central and edge area. For the convenience of the analysis in Section III, the indices of the 18 nearby BS are grouped into three sets based on the reuse pattern shown in Fig. 4. They include $\mathrm{I_A} = \{13, 14, 15, 16, 17, 18\}$, $\mathrm{I_B} = \{2, 4, 6, 7, 9, 11\}$ and $\mathrm{I_C} = \{1, 3, 5, 8, 10, 12\}$. Note that the edge users in the 0th cell reuse the same spectral resources as those in $\mathrm{I_A}$ in the FFR systems.

The location of a user and interfering BS are defined using a 2-D polar coordinate system. The origin of the coordinates is placed at the location of BS_0. The orientation of the polar axis is shown in Fig. 7. The location of a user in the central cell is defined by $z = (r, \theta)$, where r is the horizontal separation between the user and the origin and $r \in [0, R_e]$; and θ is the polar angle of the user and $\theta \in [0, 2\pi)$. The location of the $i\text{th}$ BS is defined in a similar way as (R_i, Θ_i), where R_i is the horizontal separation between BS_i and the origin, and Θ_i is the polar angle of BS_i. Since the network deployment and the cell radius R are given, the values of (R_i, Θ_i) are fixed and can be readily calculated. In order to estimate the signal power from BS_i to the observed user, the horizontal separation between BS_i to the user at z is essential, which is defined as $r_i(z)$. For $i = 0$, $r_0(z) = r$. The observed user, the serving BS, and the interfering BS_i form a triangle in the case of $i \neq 0$, $r_i(z)$ can be calculated using the rule of cosine as:

$$r_i(z) = \sqrt{r^2 + R_i^2 - 2R_i r\cos(\theta - \Theta_i)}.$$

C. DCO-OFDM and Multiple Access

The application of optical-OFDM can be extended to an OFDMA system to realise multiple access in an optical attocell network. Due to the relatively high spectral efficiency of

DCO-OFDM, this modulation scheme is used in this study. In an OFDM frame, the K frequency domain quadrature amplitude modulated data symbols before the inverse discrete Fourier transform (IDFT) are defined as: $X = [X_0\ X_1\ X_2\ \cdots\ X_{K-1}]$. Since an intensity modulated signal is a real-value signal, Hermitian symmetry is required to make the OFDM symbols contain only real samples. This requires $X_k = X^*_{K-k}$, where $[\cdot]^*$ is the complex conjugate operation. In addition, X_0 and $X_{K/2}$ are set to zero [6]. Consequently, only $\tilde{K} = K/2 - 1$ symbols carry information. Also, the intensity modulated signal is unipolar. In order to avoid negative samples, a dc-bias is required. After carrying out the K-point IDFT and the addition of a dc-bias, the time domain OFDM symbol can be calculated as:

$$x(t) = x_{\mathrm{DC}} + \sum_{k=0}^{K-1} x_k(t),\ t = 0, 1, \ldots, K-1,$$

$$x_k(t) = \frac{X(k)}{\sqrt{K}} \exp\left(\frac{2\pi jkt}{K}\right),$$

where x_{DC} is the dc-bias; $x_k(t)$ represents the signal component which accounts for the modulated symbol on subcarrier k at time slot t; and j is the imaginary unit. After the addition of dc-bias, the remaining negative samples are set to zero. According to the results of the simulated channel impulse responses noted in Section II-A, no significant signal is received when the delay exceeds 50 ns. If a sampling frequency of 40 MHz is used, the length of the cyclic-prefix (CP) is only two OFDM symbols. Since the required CP length is short, the effect of adding a CP is omitted in this study. In a multiple access version of DCO-OFDM, the $\tilde{K}$ transmission channels (subcarriers) are shared by a number of users. In the FFR schemes, these subcarriers are divided into multiple sub-bands. Then the subcarriers in each sub-band are distributed to users who are permitted to use that sub-band for data transmission. Assuming perfect sampling and synchronization, the intensity modulated sample received at time slot t on subcarrier k can be expressed as:

$$y_k(t) = x_{0,k}(t) G_0 R_{\mathrm{pd}} + \sum_{i \in \mathit{И}} x_{i,k}(t) G_i R_{\mathrm{pd}} + z_k(t), \quad (2)$$

where $x_{i,k}(t)$ is the transmitted signal sample from BS_i on subcarrier k at time slot t. In the case of $i = 0$, $x_{0,k}(t)$ is the transmitted signal sample for the desired user; R_{pd} denotes the responsivity of the PD and $z_k(t)$ represents the user receiver noise on subcarrier k. The second term of y_k accounts for the received interference signal, where $\mathit{И}$ is the set of all the interfering BS. The receiver noise is modelled as an additive white Gaussian noise with noise power spectral density of N_0. Therefore, z_k is drawn from a Gaussian distribution with zero mean and variance of $\sigma_k^2 = N_0 W/K$, where W is the total IM bandwidth. Clipping noise and non-linearities are crucial when there is a requirement to minimise the output power of the transmitter. However, it is assumed that the high output power of the BS is sufficient for the indoor lighting function in this study. In other words, there is enough margin for the minimisation of both effects by increasing the clipping threshold [25] and applying pre-distortion techniques [26]. Thus, clipping noise and non-linearities are not considered in this study.

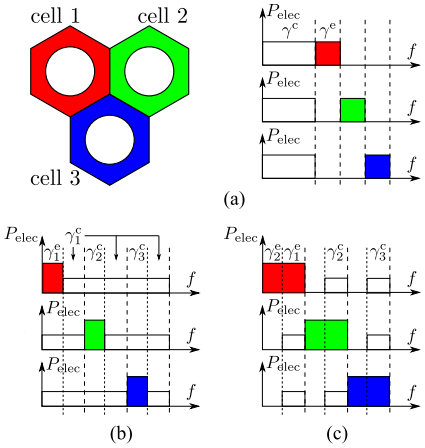

Fig. 8. (a) sFFR. (b) SFR with $\delta^2 > \frac{2}{3}$. (c) SFR with $\delta^2 < \frac{2}{3}$.

D. FFR Schemes

In a FFR system, the serving BS needs to know whether the user is in the cell centre or is in the cell edge. This can be simply realised by determining the average signal strength of the downlink pilot signal. If the pilot signal power is higher than a threshold, this particular user is categorized as a cell centre user. Otherwise, the user is categorized as a cell edge user. It is assumed there is no movement of users within the period between two adjacent pilot signal transmissions. In the following frequency plan, subcarriers in each sub-band are equally distributed to the corresponding users for simplicity and user fairness.

1) Strict FFR: The considered sFFR divides the whole frequency band to three protected sub-bands and an individual common sub-band as shown in Fig. 8(a). The number of subcarriers of each sub-band is set to be proportional to the area of the central or edge regions, which offers good fairness and optimal performance [15]. The common sub-band is reused by the centre users in each cell. As shown in Fig. 8(a), one of the three protected sub-bands is assigned to the edge users of each cell. This assignment also ensures that the same protected sub-band is not reused in adjacent cells. Therefore, the number of subcarriers assigned to the cell centre users K_{c} and the number of subcarriers assigned to the cell edge users K_{e} are given as:

$$K_{\mathrm{c}} = \left\lceil \tilde{K}\delta^2 \right\rceil,$$

$$K_{\mathrm{e}} = \left\lfloor (\tilde{K} - K_{\mathrm{c}})/3 \right\rfloor,$$

respectively.

2) Soft Frequency Reuse: In SFR, the protected sub-bands for cell edge users are also reused in adjacent cells. In order to guarantee the performance of the cell edge users, the transmission power for the cell edge user is increased with a gain of β.

In addition, the different groups of subcarriers are assigned to edge users in adjacent cells. Similar to the sFFR scheme, for fairness, the number of subcarriers assigned to different user groups is proportional to the corresponding area. Therefore, the following frequency plan is used:

$$K_{\mathrm{c}} = \left\lceil \tilde{K}\delta^2 \right\rceil,$$
$$K_{\mathrm{e}} = \min\left(\left\lceil \tilde{K}/3 \right\rceil, \tilde{K} - K_{\mathrm{c}} \right),$$

which is shown in Fig. 8(b) and (c). Note that the maximum available bandwidth for cell edge users is $\tilde{K}/3$ to ensure the orthogonality of the protected sub-bands.

III. Assessment of SINR and Spectral Efficiency

Electrical SINR is an important metric to measure the quality of a wireless connection. Similar to the definition of SNR in an IM/DD optical wireless communication system, SINR is defined as the ratio of the received desired signal electrical power to the summation of noise and interference electrical power. Based on the SINR level, the spectral efficiency can be estimated in order to evaluate the wireless capacity of the system.

A. Full Frequency Reuse

1) Signal-to-Interference-Plus-Noise Ratio: The most straightforward frequency plan is FR, which reuses the whole frequency band in each cell. Here Δ is used to represent the reuse factor. In this case the reuse factor equals one ($\Delta = 1$). In this study, the FR system is used as the benchmark system. According to (2), the SINR of the user at location z on subcarrier k can be written as:

$$\gamma_{\mathrm{FR},k}(z) = \frac{P_{\mathrm{elec},0,k} G_0^2(z) R_{\mathrm{pd}}^2}{\sum_{i \in \mathit{И}} P_{\mathrm{elec},i,k} G_i^2(z) R_{\mathrm{pd}}^2 + \sigma_k^2}, \tag{3}$$

where $P_{\mathrm{elec},i,k}$ denotes the electrical signal power transmitted by BS_i on subcarrier k, which is calculated as:

$$P_{\mathrm{elec},i,k} = \mathbb{E}\left[x_{i,k}^2(t)\right],$$

where $\mathbb{E}[\cdot]$ represents the expectation operation. Since $\Delta = 1$, the set $\mathit{И} = \mathit{И}_{\mathrm{A}} \cup \mathit{И}_{\mathrm{B}} \cup \mathit{И}_{\mathrm{C}}$. To simplify the analysis, an equal electrical power allocation is used. Assuming a total electrical transmission power of $P_{\mathrm{elec,AC}}$, $P_{\mathrm{elec},i,k} = P_{\mathrm{elec,AC}}/(K-2)$. Then, the subscript k can be dropped and (3) can be modified as a function of z as:

$$\gamma_{\mathrm{FR}}(z) = \frac{\left(r^2 + h^2\right)^{-m-3}}{\sum_{i \in \mathit{И}} \left(r_i^2(z) + h^2\right)^{-m-3} + \Omega}, \tag{4}$$

$$\Omega = \frac{4\pi^2 (K-2) N_0 W \kappa^2}{K P_{\mathrm{opt}}^2 (m+1)^2 A_{\mathrm{pd}}^2 R_{\mathrm{pd}}^2 h^{2m+2}}. \tag{5}$$

The derivation of (4) and (5) is shown in Appendix A. Based on (4), the probability $\mathbb{P}[\gamma_{\mathrm{FR}} < T]$ can be calculated, where T is the threshold value.

2) SINR Statistics: In this study, a semi-analytical method is used to calculate the SINR statistics of the optical attocell systems. Assuming a polar angle of θ, the function of the SINR on a subcarrier is monotonically decreasing with respect to r in the region of interest. Therefore, the conditional PDF of SINR can be calculated by using the PDF transformation rule as:

$$f_\gamma(\hat{\gamma}, f(r)|\theta) = \left. \frac{f(r)}{\left|\frac{\partial}{\partial r}\gamma(z)\right|} \right|_{r=\gamma^{-1}(\hat{\gamma}|\theta)},$$

where $f(r)$ is the PDF of r; $f(r)$ is determined by the locations of the considered users (cell edge/centre users); $\gamma^{-1}(\hat{\gamma}|\theta)$ is the inverse function of the SINR function with respect to r for a given θ, in which $\gamma(r_{\max}, \theta) \le \hat{\gamma} \le \gamma(r_{\min}, \theta)$. Here, $r_{\max}$ ($r_{\min}$) is the maximum (minimum) of r in its feasible region. A closed form solution to $\gamma^{-1}(\hat{\gamma}|\theta)$ is unavailable. Numerical methods are used to compute the function. Then the cumulative density function (CDF) of SINR can then be calculated as follows:

$$\mathbb{P}[\gamma < T] = \int_0^{2\pi} \int_{-\infty}^{T} f_\gamma(\hat{\gamma}, f(r)|\theta) \mathrm{d}\hat{\gamma} f_\theta(\theta) \mathrm{d}\theta. \tag{6}$$

Since the spatial location of the users in each cell follows a PPP, the PDF of θ should follow: $f_\theta(\theta) = \frac{1}{2\pi}$. This semi-analytical approach is presented in [27] in detail.

In the case of the FR scheme, the statistics in the whole cell is calculated. Therefore, the PDF $f(r)$ is given as:

$$f(r) = f_r(r) = \frac{2r}{R_{\mathrm{e}}^2}, r \in [0, R_{\mathrm{e}}].$$

In the case of FFR systems, statistics in part of the cell is required. In the calculation of $\mathbb{P}[\gamma < T | r < R_{\mathrm{c}}]$ and $\mathbb{P}[\gamma < T | r \ge R_{\mathrm{c}}]$, the PDF $f(r)$ should be calculated as:

$$f_{r|r<R_{\mathrm{c}}}(r) = \frac{f_r(r)}{\mathbb{P}[r < R_{\mathrm{c}}]}, r \in [0, R_{\mathrm{c}}],$$
$$f_{r|r\ge R_{\mathrm{c}}}(r) = \frac{f_r(r)}{\mathbb{P}[r \ge R_{\mathrm{c}}]}, r \in [R_{\mathrm{c}}, R_{\mathrm{e}}],$$

where $\mathbb{P}[r < R_{\mathrm{c}}]$ ($\mathbb{P}[r \ge R_{\mathrm{c}}]$) is the probability that the user is in the cell central (edge) area. It is shown in [28] that:

$$\mathbb{P}[r < R_{\mathrm{c}}] = \delta^2,$$
$$\mathbb{P}[r \ge R_{\mathrm{c}}] = 1 - \delta^2.$$

3) Spectral Efficiency: In this study, the Shannon-Hartley formula is used to estimate the wireless capacity of the system. In a DCO-OFDM system, the spectral efficiency of a user at z can be calculated as a function of $\gamma(z)$ and Δ:

$$\rho\left(\gamma(z), \Delta\right) = \frac{K-2}{2K\Delta} \log_2\left(1 + \gamma(z)\right).$$

The average spectral efficiency for the users in the whole cell can be calculated as:

$$\bar{\rho} = \mathbb{E}_z[\rho(\gamma(z), \Delta)],$$
$$= \int_0^{2\pi} \int_0^{R_{\mathrm{e}}} \rho(\gamma(r,\theta), \Delta) f_r(r) \mathrm{d}r f_\theta(\theta) \mathrm{d}\theta. \tag{7}$$

In addition, the average spectral efficiency for the users in the cell centre area can be calculated as:

$$\begin{aligned}\bar{\rho}^{\mathrm{c}} &= \mathbb{E}_z[\rho(\gamma(z),\Delta)|r<R_{\mathrm{c}}],\\ &= \int_0^{2\pi}\int_0^{R_{\mathrm{c}}} \rho(\gamma(r,\theta),\Delta) f_{r|r<R_{\mathrm{c}}}(r)\mathrm{d}r f_\theta(\theta)\mathrm{d}\theta. \end{aligned} \quad (8)$$

Similarly, in the case of users in the cell edge area,

$$\begin{aligned}\bar{\rho}^{\mathrm{e}} &= \mathbb{E}_z[\rho(\gamma(z),\Delta)|r\geq R_{\mathrm{c}}],\\ &= \int_0^{2\pi}\int_{R_{\mathrm{c}}}^{R_{\mathrm{e}}} \rho(\gamma(r,\theta),\Delta) f_{r|r\geq R_{\mathrm{c}}}(r)\mathrm{d}r f_\theta(\theta)\mathrm{d}\theta. \end{aligned} \quad (9)$$

In the case of FR scheme, we have $\Delta = 1$. By using (7), the corresponding average spectral efficiency can be calculated as:

$$\bar{\rho}_{\mathrm{FR}} = \mathbb{E}_z[\rho(\gamma_{\mathrm{FR}}(z),1)]. \quad (10)$$

For comparison purpose, the cell edge user spectral efficiency in the case of FR scheme can be calculated as:

$$\bar{\rho}^{\mathrm{e}}_{\mathrm{FR}} = \mathbb{E}_z[\rho(\gamma_{\mathrm{FR}}(z),1)|r\geq R_{\mathrm{c}}]. \quad (11)$$

B. Strict Fractional Frequency Reuse

1) SINR and Its Statistics: In a sFFR system, the SINR at z on a subcarrier in the common sub-band can be written as:

$$\gamma^{\mathrm{c}}(z) = \frac{\left(r^2+h^2\right)^{-m-3}}{\sum_{i\in И}\left(r_i^2(z)+h^2\right)^{-m-3} + \frac{1+2\delta^2}{3}\Omega}. \quad (12)$$

According to the frequency plan defined in II-D1, the SINR at z on a subcarrier in protected sub-bands $\gamma^{\mathrm{e}}(z)$ can also be calculated using (12) except for substituting $И_{\mathrm{A}}$ for $И$. The factor $\frac{1+2\delta^2}{3}$ of Ω is due to the change of the number of used subcarriers in sFFR compared to the case of the FR system. Since a fixed amount of available electrical power and an equal power distribution on each subcarrier are assumed, varying the number of used subcarriers causes change in the available power on each subcarrier.

When determining the distribution of SINR for a sFFR system, both cases of a user in the cell central area and a user in the cell edge area need to be considered. The overall CDF of the SINR can be calculated as follows:

$$\begin{aligned}\mathbb{P}[\gamma_{\mathrm{sFFR}}<T] &= \mathbb{P}[r<R_{\mathrm{c}}]\mathbb{P}[\gamma^{\mathrm{c}}<T|r<R_{\mathrm{c}}]\\ &\quad + \mathbb{P}[r\geq R_{\mathrm{c}}]\mathbb{P}[\gamma^{\mathrm{e}}<T|r\geq R_{\mathrm{c}}], \end{aligned} \quad (13)$$

where $\mathbb{P}[\gamma^{\mathrm{c}}<T|r<R_{\mathrm{c}}]$ and $\mathbb{P}[\gamma^{\mathrm{e}}<T|r\geq R_{\mathrm{c}}]$ are the CDF of the SINR with the conditions that the user is in the cell centre using common sub-band and is in the cell edge using protected sub-band, respectively. They can be calculated using the same method as that described in Section III-A2.

2) Spectral Efficiency: Since the average spectral efficiency varies in different sub-bands, the overall average spectral efficiency should be the average over the whole frequency band. When there are users in both the cell central area and the cell edge area, the overall average spectral efficiency can be calculated as [28]:

$$\bar{\rho}_{\mathrm{sFFR,nor}} = \zeta^{\mathrm{c}}\bar{\rho}^{\mathrm{c}} + \zeta^{\mathrm{e}}\bar{\rho}^{\mathrm{e}},$$

where $\bar{\rho}^{\mathrm{c}}$ ($\bar{\rho}^{\mathrm{e}}$) is the average spectral efficiency for the users taking the common (protected) sub-band for transmission; ζ^{c} and ζ^{e} are the averaging weights for $\bar{\rho}^{\mathrm{c}}$ and $\bar{\rho}^{\mathrm{e}}$, respectively. The averaging weight ζ of an average spectral efficiency $\bar{\rho}$ is calculated as:

$$\zeta = \frac{\Delta K_{\bar{\rho}}}{\tilde{K}}, \quad (14)$$

where $K_{\bar{\rho}}$ refers to the number of subcarriers that achieve an average spectral efficiency of $\bar{\rho}$. All ζ for FFR can be simply derived according to the FFR schemes described in Section II-D. Since all of the averaging weights ζ follow the same rule as (14), and the derivations of each ζ is long but very simple, it would be unnecessary to list all of the derivations of all of the ζs. Only the final results are listed. In the case of sFFR here, ζ^{c} and ζ^{e} can be found as $\zeta^{\mathrm{c}} \cong \delta^2$ and $\zeta^{\mathrm{e}} \cong 1-\delta^2$, respectively [28].

The cell centre users use the common sub-band with $\Delta = 1$, while the cell edge users use the protected sub-band with $\Delta = 3$. Therefore, in conjunction with (8) and (9), $\bar{\rho}^{\mathrm{c}}$ and $\bar{\rho}^{\mathrm{e}}$ in sFFR case can be calculated as:

$$\begin{aligned}\bar{\rho}^{\mathrm{c}} &= \mathbb{E}_z[\rho(\gamma^{\mathrm{c}}(z),1)|r<R_{\mathrm{c}}],\\ \bar{\rho}^{\mathrm{e}} &= \mathbb{E}_z[\rho(\gamma^{\mathrm{e}}(z),3)|r\geq R_{\mathrm{c}}]. \end{aligned} \quad (15)$$

An optical attocell network is a small-cell cellular network in which each BS serves several users and these users are fewer than those in a normal RF cell. Consequently, the problem of an uneven load in different cells is more critical in an optical attocell network. In some extreme cases, there may be no user in a cell when the user density is very low. The use of the FFR technique makes this issue even worse. Since the cell coverage area is divided into centre and edge areas, which are smaller compared with the total cell coverage area, the chance that no active user is present in a specified region (a cell centre or a cell edge area) will be much higher. Consequently, in the case of no user present in a specified area, the corresponding assigned sub-band remains idle, which is a waste of transmission resources. Therefore, the case of no user present in the cell central or edge area needs to be considered. Since the common sub-band is restricted to the cell edge users, for the case that there is no user in the central area, the common sub-band is wasted and $\zeta^{\mathrm{c}} = 0$. Therefore, the corresponding average spectral efficiency is only $\zeta^{\mathrm{e}}\bar{\rho}^{\mathrm{e}}$. For the same reason, when there is no user present in the cell edge area, the average spectral efficiency is only $\zeta^{\mathrm{c}}\bar{\rho}^{\mathrm{c}}$. Thus, the final average spectral efficiency achieved by a sFFR system can be calculated as:

$$\begin{aligned}\bar{\rho}_{\mathrm{sFFR}} &= \mathcal{P}_{\mathrm{c}}\zeta^{\mathrm{c}}\bar{\rho}^{\mathrm{c}} + \mathcal{P}_{\mathrm{e}}\zeta^{\mathrm{e}}\bar{\rho}^{\mathrm{e}}\\ &\quad + (1-\mathcal{P}_{\mathrm{c}}-\mathcal{P}_{\mathrm{e}})\left(\bar{\rho}_{\mathrm{sFFR,nor}}\right), \end{aligned} \quad (16)$$

where $\mathcal{P}_{\mathrm{c}}$ ($\mathcal{P}_{\mathrm{e}}$) denotes the probability that all of the observed users fall into the cell centre (edge) area. It is assumed that the user spatial distribution follows a PPP with a user density of λ. By limiting the users in a specified area of A, the mean number of users within this area is $A\lambda$. According to the probability

mass function of the Possion distribution, the probability that no user in this area is given as:

$$\mathcal{P}_0 = \mathrm{e}^{-A\lambda}.$$

The area of a cell can be found as $A_{\mathrm{cell}} = \pi R_{\mathrm{e}}^2$ according to the geometry shown in Fig. 7. Then, the cell central area and the cell edge area are $A_{\mathrm{cell}}\delta^2$ and $A_{\mathrm{cell}}\left(1-\delta^2\right)$, respectively. Therefore, $\mathcal{P}_{\mathrm{c}}$ and $\mathcal{P}_{\mathrm{e}}$ can be calculated as:

$$\mathcal{P}_{\mathrm{c}} = \mathrm{e}^{-A_{\mathrm{cell}}\left(1-\delta^2\right)\lambda},$$

$$\mathcal{P}_{\mathrm{e}} = \mathrm{e}^{-A_{\mathrm{cell}}\delta^2\lambda}.$$

Since the cell edge users only use the protected sub-band for transmission, the cell edge spectral efficiency for sFFR can be calculated using (15).

C. Soft Frequency Reuse

1) SINR and Its Statistics: In a SFR system, due to the more complex SFR scheme, there are five conditions in the SFR system SINR calculation. In order to efficiently present these SINR expressions, a function is defined as follows:

$$\chi(p_0,p_1,p_2,p_3,z) = \frac{p_0\left(r^2+h^2\right)^{-m-3}}{\Upsilon(p_1,p_2,p_3,z)+\left(\beta\left(1-\max\left(\delta^2,\frac{2}{3}\right)\right)+\delta^2\right)\Omega},$$

where p_0, p_1, p_2, p_2 are the power control factors which equals β or 1 or 0, and

$$\Upsilon(p_1,p_2,p_2,z) = p_1\sum_{i\in\mathit{И}_{\mathrm{A}}}\left(r_i^2(z)+h^2\right)^{-m-3} + p_2\sum_{i\in\mathit{И}_{\mathrm{B}}}\left(r_i^2(z)+h^2\right)^{-m-3} + p_3\sum_{i\in\mathit{И}_{\mathrm{C}}}\left(r_i^2(z)+h^2\right)^{-m-3}.$$

According to the five cases shown in Fig. 8(b) and (c), the corresponding SINR in each cases can be calculated as follows: $\gamma_1^{\mathrm{e}}(z)=\chi(\beta,\beta,1,1,z)$, $\gamma_2^{\mathrm{e}}(z)=\chi(\beta,\beta,0,0,z)$, $\gamma_1^{\mathrm{c}}(z)=\chi(1,1,1,1,z)$, $\gamma_2^{\mathrm{c}}(z)=\chi(1,1,\beta,1,z)$ and $\gamma_3^{\mathrm{c}}(z)=\chi(1,1,1,\beta,z)$. According to the frequency plan described in Section II-D2 and (14), the corresponding averaging weights for average spectral efficiency with each γ are calculated as:

$$\zeta_1^{\mathrm{e}} = \zeta_2^{\mathrm{c}} = \zeta_3^{\mathrm{c}} \cong \frac{2}{3} - \max\left(\delta^2,\frac{2}{3}\right) + \frac{1}{2}\min\left(\delta^2,\frac{2}{3}\right),$$

$$\zeta_2^{\mathrm{e}} \cong 1 - \frac{3}{2}\min\left(\delta^2,\frac{2}{3}\right) \text{ and } \zeta_1^{\mathrm{c}} \cong 3\max\left(\delta^2,\frac{2}{3}\right) - 2.$$

Similar to the case of sFFR, Ω is multiplied by a scaling factor to compensate for the change in transmission power on each subcarrier.

The SINR CDF of a SFR system can be calculated by:

$$\mathbb{P}[\gamma_{\mathrm{SFR}} < T] = \mathbb{P}[r<R_{\mathrm{c}}]\mathbb{P}[\gamma_{\mathrm{SFR}} < T | r < R_{\mathrm{c}}] + \mathbb{P}[r \geq R_{\mathrm{c}}]\mathbb{P}[\gamma_{\mathrm{SFR}} < T | r \geq R_{\mathrm{c}}]. \quad (17)$$

According to the resource plan described in Section II-D2, it is noted that a user in a SFR system receives the signal on multiple subcarriers with different SINR. To simplify the calculation, the SINR experienced by a user in a SFR system is defined as follows: the user randomly selects one of the available subcarriers for transmission, and the SINR experienced on the selected subcarrier is $\tilde{\gamma}$. In (17), the cell edge user SINR distribution $\mathbb{P}[\gamma_{\mathrm{SFR}} < T | r \geq R_{\mathrm{c}}]$ can be calculated as:

$$\mathbb{P}[\gamma_{\mathrm{SFR}} < T | r \geq R_{\mathrm{c}}] = \mathbb{P}[\tilde{\gamma}=\gamma_1^{\mathrm{e}}]\mathbb{P}[\gamma_1^{\mathrm{e}} < T | r \geq R_{\mathrm{c}}] + \mathbb{P}[\tilde{\gamma}=\gamma_2^{\mathrm{e}}]\mathbb{P}[\gamma_2^{\mathrm{e}} < T | r \geq R_{\mathrm{c}}],$$

where $\mathbb{P}[\tilde{\gamma}=\gamma]$ refers to the probability that the subcarrier with a SINR of γ is selected. $\mathbb{P}[\tilde{\gamma}=\gamma_1^{\mathrm{e}}]$ and $\mathbb{P}[\tilde{\gamma}=\gamma_2^{\mathrm{e}}]$ can be calculated as:

$$\mathbb{P}[\tilde{\gamma}=\gamma_1^{\mathrm{e}}] = \frac{\zeta_1^{\mathrm{e}}}{\zeta_1^{\mathrm{e}}+\zeta_2^{\mathrm{e}}/3} = \frac{3}{2}\min\left(\delta^2,\frac{2}{3}\right),$$

$$\mathbb{P}[\tilde{\gamma}=\gamma_2^{\mathrm{e}}] = 1 - \mathbb{P}[\tilde{\gamma}=\gamma_1^{\mathrm{e}}] = 1 - \frac{3}{2}\min\left(\delta^2,\frac{2}{3}\right).$$

Similarly, the centre user SINR CDF $\mathbb{P}[\gamma_{\mathrm{SFR}} < T | r < R_{\mathrm{c}}]$ can be calculated as:

$$\mathbb{P}[\gamma_{\mathrm{SFR}} < T | r < R_{\mathrm{c}}] = \mathbb{P}[\tilde{\gamma}=\gamma_1^{\mathrm{c}}]\mathbb{P}[\gamma_1^{\mathrm{c}} < T | r < R_{\mathrm{c}}] + \mathbb{P}[\tilde{\gamma}=\gamma_2^{\mathrm{c}}]\mathbb{P}[\gamma_2^{\mathrm{c}} < T | r < R_{\mathrm{c}}] + \mathbb{P}[\tilde{\gamma}=\gamma_3^{\mathrm{c}}]\mathbb{P}[\gamma_3^{\mathrm{c}} < T | r < R_{\mathrm{c}}],$$

where

$$\mathbb{P}[\tilde{\gamma}=\gamma_1^{\mathrm{c}}] = \frac{\zeta_1^{\mathrm{c}}}{\zeta_1^{\mathrm{c}}+\zeta_2^{\mathrm{c}}+\zeta_3^{\mathrm{c}}} = 3 - \frac{2}{\max\left(\delta^2,\frac{2}{3}\right)},$$

$$\mathbb{P}[\tilde{\gamma}=\gamma_2^{\mathrm{c}}] = \mathbb{P}[\tilde{\gamma}=\gamma_3^{\mathrm{c}}] = \frac{\zeta_2^{\mathrm{c}}}{\zeta_1^{\mathrm{c}}+\zeta_2^{\mathrm{c}}+\zeta_3^{\mathrm{c}}} = \frac{1}{\max\left(\delta^2,\frac{2}{3}\right)} - 1.$$

All the conditional CDF of the SINR in each case can be calculated using the method described in Section III-A2.

2) Spectral Efficiency: When there are users in both the cell central and the cell edge areas, the overall average spectral efficiency of a SFR system can be determined as follows:

$$\bar{\rho}_{\mathrm{SFR,nor}} = \zeta_1^{\mathrm{e}}\bar{\rho}_1^{\mathrm{e}} + \zeta_2^{\mathrm{e}}\bar{\rho}_2^{\mathrm{e}} + \zeta_1^{\mathrm{c}}\bar{\rho}_1^{\mathrm{c}} + \zeta_2^{\mathrm{c}}\bar{\rho}_2^{\mathrm{c}} + \zeta_3^{\mathrm{c}}\bar{\rho}_3^{\mathrm{c}},$$

where $\bar{\rho}_1^{\mathrm{e}}$, $\bar{\rho}_2^{\mathrm{e}}$, $\bar{\rho}_1^{\mathrm{c}}$, $\bar{\rho}_2^{\mathrm{c}}$ and $\bar{\rho}_3^{\mathrm{c}}$ denote the achievable average spectral efficiency corresponding to γ_1^{e}, γ_2^{e}, γ_1^{c}, γ_2^{c} and γ_3^{c}, respectively. They can be calculated using (8) and (9) as:

$$\bar{\rho}_1^{\mathrm{e}} = \mathbb{E}_z[\rho(\gamma_1^{\mathrm{e}}(z),1) | r \geq R_{\mathrm{c}}],$$

$$\bar{\rho}_2^{\mathrm{e}} = \mathbb{E}_z[\rho(\gamma_2^{\mathrm{e}}(z),3) | r \geq R_{\mathrm{c}}],$$

$$\bar{\rho}_1^{\mathrm{c}} = \mathbb{E}_z[\rho(\gamma_1^{\mathrm{c}}(z),1) | r < R_{\mathrm{c}}],$$

$$\bar{\rho}_2^{\mathrm{c}} = \mathbb{E}_z[\rho(\gamma_2^{\mathrm{c}}(z),1) | r < R_{\mathrm{c}}],$$

$$\bar{\rho}_3^{\mathrm{c}} = \mathbb{E}_z[\rho(\gamma_3^{\mathrm{c}}(z),1) | r < R_{\mathrm{c}}].$$

Similar to the sFFR case, the problem of no user in a specified area needs to be considered. Accounting for no user in the cell edge and also the cell central area, the final average spectral efficiency of a SFR system can be found:

$$\bar{\rho}_{\mathrm{SFR}} = \mathcal{P}_{\mathrm{c}}(\zeta_1^{\mathrm{c}}\bar{\rho}_1^{\mathrm{c}} + \zeta_2^{\mathrm{c}}\bar{\rho}_2^{\mathrm{c}} + \zeta_3^{\mathrm{c}}\bar{\rho}_3^{\mathrm{c}}) + \mathcal{P}_{\mathrm{e}}(\zeta_1^{\mathrm{e}}\bar{\rho}_1^{\mathrm{e}} + \zeta_2^{\mathrm{e}}\bar{\rho}_2^{\mathrm{e}}) + (1-\mathcal{P}_{\mathrm{c}}-\mathcal{P}_{\mathrm{e}})\bar{\rho}_{\mathrm{SFR,nor}}. \quad (18)$$

TABLE II
SYSTEM PARAMETERS

Parameter	Symbol	Value
LED half-power semi-angle	$\phi_{1/2}$	60°
Vertical separation	h	2.15 m
PD area	A_{pd}	1 cm^2
Modulation bandwidth	W	40 MHz
PD responsivity	R_{pd}	0.1 A/W
DC bias factor	κ	3

The cell edge spectral efficiency in a SFR system can be calculated as:

$$\bar{\rho}^{\mathrm{e}}_{\mathrm{SFR}} = \frac{K_{\bar{\rho}^{\mathrm{e}}_1}}{K_{\mathrm{e}}}\bar{\rho}^{\mathrm{e}}_1 + \frac{3K_{\bar{\rho}^{\mathrm{e}}_2}}{K_{\mathrm{e}}}\bar{\rho}^{\mathrm{e}}_2 = \frac{\zeta^{\mathrm{e}}_1\bar{\rho}^{\mathrm{e}}_1 + \zeta^{\mathrm{e}}_2\bar{\rho}^{\mathrm{e}}_2}{1-\delta^2}. \quad (19)$$

IV. RESULTS AND PERFORMANCE ANALYSIS

In this section, the performance of the considered FFR schemes in an optical attocell network in terms of SINR CDF, average spectral efficiency and cell edge spectral efficiency are evaluated. Interference mitigation and improvement in cell edge and average spectral efficiency are expected by using FFR schemes.

A. Parameter Configurations

The system parameters of the evaluated systems are listed in Table II. These values are the default settings in the results presented in this section if the parameters are not otherwise specified. A $\phi_{1/2}$ of 60° is reasonable for lighting performance. A vertical separation between a BS and a user h of 2.15 m is considered due to a user equipment height of 0.85 m and a ceiling height of 3 m. A PD physical area A_{pd} of 1 cm^2 is the generally acceptable in VLC systems [3], [29]. The 40 MHz modulation bandwidth agrees with the 20 MHz flat bandwidth that is provided by a phosphorescent white light LED with equalisation [30]. A PD responsivity R_{pd} of 0.1 is suitable when the receiver only accepts the blue component of light [3]. Since only the negative samples of the OFDM signal after adding the dc-bias is clipped, the dc-bias level κ is equivalent to the bottom clipping level; κ is set to 3, since this value is sufficient to minimise the clipping noise to a level that causes negligible distortion in the transmission [31].

A single LED chip with a typical low rated output optical power cannot provide sufficient optical power to meet the standard lighting requirements. Therefore, multiple LED chips are integrated within an LED luminary, which provide much higher power than a single chip. To simplify the radiation model, each LED light luminary is treated as a point source. In this study, the configuration of the BS output power takes the illumination requirement into account. An average illuminance of at least 500 lx and an illuminance uniformity of at least 0.6 is required in an room used for writing or reading purposes [32]. In this study, the required optical output power that fulfils the illuminance requirement is found to be highly related to the cell radius R. Therefore, the BS output optical power P_{opt} is configured based on the value of R. The considered configuration in this study is listed in Table III. The corresponding illuminance distribution in a room with 27 cells (the cell deployment is shown in Fig. 2) in the form of CDF is presented in Fig. 9. The notable illumination results are summarised in Table III.

TABLE III
BS OUTPUT OPTICAL POWER CONFIGURATION

cell radius R [m]	BS output optical power P_{opt} [W]	average illuminance $\bar{E}_{\mathrm{v}}$ [lx]	illuminance uniformity U_0
2	24	519	0.84
2.25	29	513	0.83
2.5	35	509	0.81
2.75	41	507	0.77
3	48	506	0.73
3.25	56	505	0.69

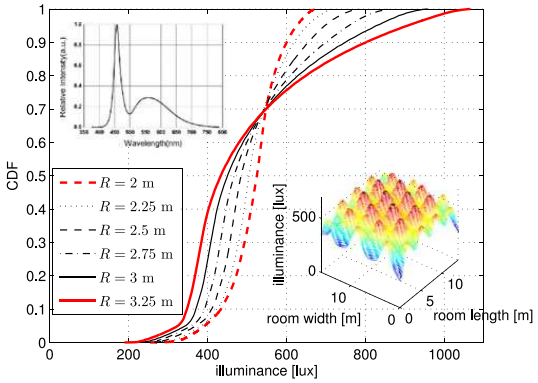

Fig. 9. Illuminance distribution in a room with 27 cells. The network deployment is the same as that shown in Fig. 2, except for the difference in cell radius. The illuminance spatial distribution with $R = 2$ m is shown in the sub-figure on the bottom right. The relative intensity of the LED output against wavelength is shown in the sub-figure on the top left, which is used for the calculation of illuminance.

B. SINR Statistics Results

Fig. 10 shows the results of the SINR statistics based on the two-layer hexagonal network model. Here the noise level is $N_0 = 1 \times 10^{-21}$ A^2/Hz and cell radius is $R = 2.5$ m. In the FFR systems, $\delta = 0.7$ and $\beta = 2$. These results include the calculation using (6), (13) and (17) in the analysis presented in Section III using the numerical method, and the corresponding empirical statistics obtained by Monte Carlo simulation. The agreement between the two results validate the analysis. In addition, the simulation of the deployed networks are presented to validate the accuracy of the estimation by using two-layer network model. As expected, there is an acceptable difference, less than 2 dB, between the results of two-layer network model and those of the deployed network with only 12 cells (room size 10.8 m × 12.5 m) due to the room edge effects. However, with an increase of the number of cells, the difference between the curves of the case with deployed network and that for the

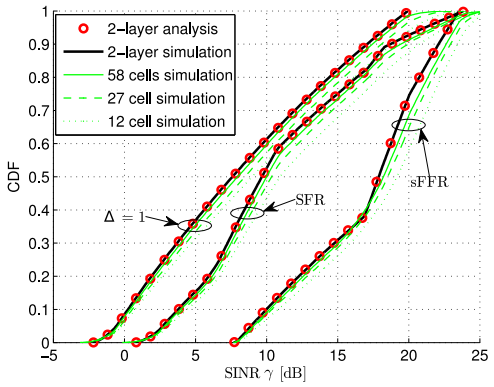

Fig. 10. SINR statistics for different reuse schemes. The network deployment in the room with 12 and 27 cells are the same as those shown in Fig. 5, except for the difference in cell radius. System parameters: $N_0 = 1 \times 10^{-21}$ A^2/Hz, $R = 2.5$ m, $\delta = 0.7$ and $\beta = 2$.

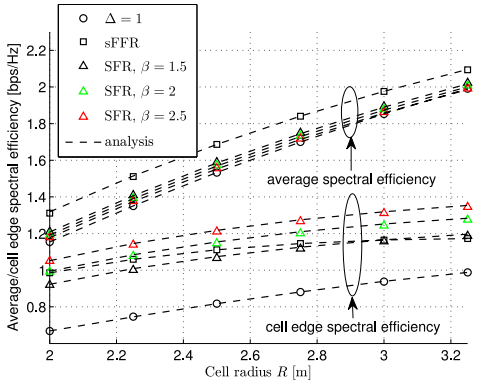

Fig. 11. Average spectral efficiency and cell edge spectral efficiency against cell radius R. System parameters: $\delta = 0.7$, $N_0 = 1 \times 10^{-21}$ A^2/Hz and $\lambda = 1$ user/m^2.

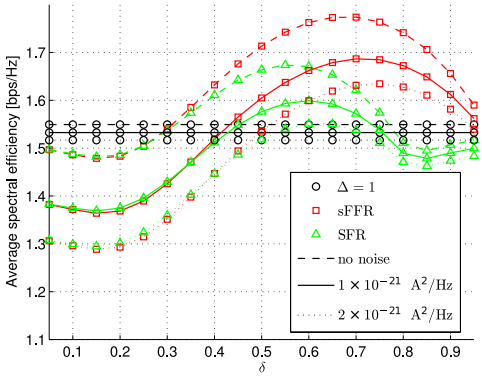

Fig. 12. Average spectral efficiency against δ. System parameters: $R = 2.5$ m, $\lambda = 1$ user/m^2 and $\beta = 2$.

two-layer network diminishes. In the case of 58 cells (room size 26 m $\times$ 30 m), the SINR CDF differences decrease to be in a range between 0.3 to 0.7 dB. Note that another source of mismatch is the circular cell approximation of the 0th cell in the two-layer network model. This mismatch is considered reasonable in many cellular system analysis [28]. Therefore, the performance of the two-layer network model is a reasonable estimation to the practical optical attocell system.

As shown in Fig. 10, the FR system exhibits the worst SINR as expected. In contrast, FFR schemes offer an improved SINR. The sFFR system and the SFR system show improvements of 9.74 and 3.54 dB in terms of minimum SINR (at 10th percentile), respectively. In addition, they also show improvements of 10.3 and 2.07 dB in terms of medium SINR, respectively. Note that the bends in the FFR curves are the results of combining different SINR statistics in multiple regions in a cell and in different sub-bands. These combinations can be observed in the analysis in Sections III-B1 and III-C1.

C. Spectral Efficiency Results

In this section, average spectral efficiency, calculated using (10), (16) and (18), is the metric to demonstrate the improvement in the overall system capacity. In addition, average spectral efficiency in the cell edge area, calculated using (11), (15) and (19), is the metric to show the improvement in cell edge user experience.

1) Effect of Cell Radius: Fig. 11 shows the average spectral efficiency and the cell edge spectral efficiency results with different cell radius R. In these results, $\delta = 0.7$, $N_0 = 1 \times 10^{-21}$ A^2/Hz, and $\lambda = 1$ user/m^2. Both the analytical calculation and the simulation are presented. The close agreement validates the related analysis. With a fixed $\phi_{1/2}$, the increase of cell radius results in a decrease in the interference between users in adjacent cells [27]. In other words, a larger cell provides better overall signal quality. In addition, a smaller cell leads to a higher value of $\mathcal{P}_c$ and $\mathcal{P}_e$, which results in loss in average spectral efficiency in FFR systems. Therefore, both the average spectral efficiency and the cell edge spectral efficiency for any reuse scheme is an increasing function of R.

The improvement of using sFFR is in the range from 5% to 14% in terms of average spectral efficiency and is in the range from 19% to 47% in terms of cell edge spectral efficiency. The improvement of using SFR is in the range from 0% to 5% in terms of average spectral efficiency and is in the range from 21% to 57% in terms of cell edge spectral efficiency. Generally, the sFFR system achieves the highest average spectral efficiency. The SFR system is more flexible, since it can achieve a good balance between cell edge user performance and overall system performance by adjusting parameter β. Both sFFR and SFR schemes improved the cell edge user experience significantly.

2) Effects of δ and Noise Level: Fig. 12 shows the average spectral efficiency against δ. In the results, $R = 2.5$ m, $\lambda = 1$ user/m^2 and $\beta = 2$ in SFR systems. As shown in Section II-D, the channel assignment is proportional to the corresponding coverage area for FFR systems. When δ is too small, the majority of the users are cell edge users who are assigned a reuse factor

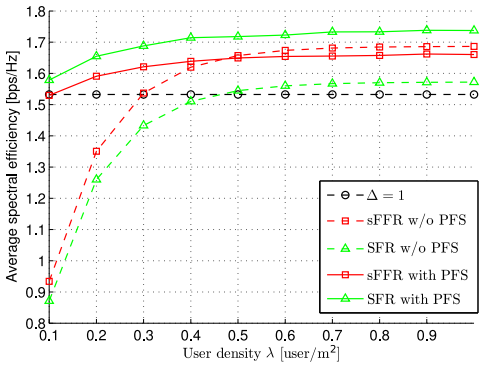

Fig. 13. Average spectral efficiency against user density λ. System parameters: $\delta = 0.7$, $R = 2.5$ m, $N_0 = 1 \times 10^{-21}$ A^2/Hz and $\beta = 2$.

of 3, which considerably decreases the spectral efficiency of the system. When δ is too large, fewer users can be covered by the cell edge area. Consequently, average spectral efficiency decreases significantly due to the increased interference received by the cell centre users who are close to the edge of the cell central area ($r \to R_c$). In addition, when δ is close to 0 or 1, either $\mathcal{P}_c$ or $\mathcal{P}_e$ is significant, which also causes a decrease in spectral efficiency.

Fig. 12 also shows the cases with different noise levels. Intuitively, the higher the noise level, the lower the average spectral efficiency for systems with any reuse schemes. In addition, the higher the noise level, the lower improvement that can be obtained from the FFR schemes. For example, when considering the improvement of the sFFR scheme with optimal δ, the improvement in terms of average spectral efficiency is 15% if there is no receiver noise. However, this improvement decreases to 8% if the noise level is increased to $N_0 = 2 \times 10^{-21}$ A^2/Hz. Furthermore, it is noted that the noise level may affect the optimal configuration of δ. When noise is not considered, the optimal δ for sFFR is around 0.7 and this is in line with [28]. In the case of SFR, the optimal δ is around 0.55. However, with the increase in the noise level, optimal δs for FFR systems increase to a slightly higher level.

3) Effects of Active User Density and Proportional Fairness Scheduling (PFS): As shown in Section III-B2, the user density λ is crucial to the value of $\mathcal{P}_c$ and $\mathcal{P}_e$, which may cause a significant effect on the system spectral efficiency. Fig. 13 shows the effect of user density on the average spectral efficiency of different systems. In the results, $\delta = 0.7$, $R = 2.5$ m, $N_0 = 1 \times 10^{-21}$ A^2/Hz and $\beta = 2$ in SFR systems. Both FFR systems show a similar trend with respect to the variations in the λ. Generally, if λ is too small, the average spectral efficiency of FFR systems decreases significantly. For example, in the case of $\lambda = 0.1$ user/m^2, the FFR system exhibits an average spectral efficiency lower than 1 bps/Hz, which is much lower than the benchmark.

In order to solve the issue caused by low user density, PFS [33] is considered in conjunction with the FFR techniques. With a given FR scheme, there are L different sub-bands for transmission. The sub-band l has K_l subcarriers, where $l = 1, 2, \cdots, L$. $K_{l,n}$ subcarriers in sub-band l are assigned to user n. Thus $\sum_{n=1}^{N} K_{l,n} = K_l$. Therefore, the data rate achieved by user n can be calculated as follows:

$$C_n = \sum_{l=1}^{L} K_{l,n}\, s_{l,n},$$

where $s_{l,n}$ is the achievable data rate by user n on a subcarrier in sub-band l. With a given system realisation, user locations are determined. Therefore, all $s_{l,n}$ are fixed for that realisation. In this study, PFS aims at maximising the following objective function:

$$\Lambda = \sum_{n=1}^{N} \ln\left(C_n\right). \tag{20}$$

Conventional per subcarrier PFS requires channel frequency selectivity to converge to a robust solution. However, the assumptions used in this study make the channel gain flat within each sub-band. This causes problems in the convergence of the scheduling solution by using the per subcarrier based PFS. Therefore, an alternative algorithm is used to achieve the same PFS function. The details of this modified PFS is introduced as follows. A scheduling plan matrix is defined as:

$$\mathbf{K} = \begin{bmatrix} K_{1,1} & \cdots & K_{L,1} \\ \vdots & \ddots & \vdots \\ K_{1,N} & \cdots & K_{L,N} \end{bmatrix},$$

which lists the $K_{l,n}$ for all users in every sub-bands. Based on a specified $\mathbf{K}$, the corresponding set of user data rates can be calculated as follows:

$$\mathbf{C}\{\mathbf{K}\} = \begin{bmatrix} C_1(K_{1,1} & \cdots & K_{L,1}) \\ \vdots & & \\ C_N(K_{1,N} & \cdots & K_{L,N}) \end{bmatrix}.$$

The modified PFS algorithm is listed in Algorithm 1. The α in Algorithm 1 is a forgetting factor for the calculation of average user data rate $\bar{\mathbf{C}}$. The proof of Algorithm 1 maximising (20) is shown in Appendix B.

PFS can achieve a good balance between spectral efficiency and user fairness. More importantly, it can dynamically distribute spectral resources depending on the current load condition. With this benefit of PFS, the sub-band availability constraint can be adjusted as follows: the whole sub-band assigned to a cell is available to any active user in that cell. In the case of no user in the cell edge (centre) area of the cell, PFS will assign the resources preserved for edge (centre) users to centre (edge) users. Note that although cell edge users achieve low SINR by using the sub-band prepared for centre users, through appropriate modulation and coding adjustment, transmission with low spectral efficiency can be established [34], which is better than the sub-band being unused. This is the reason for the PFS

approach improving the FFR system performance when user density is low. Under conditions where users are present in both areas, PFS avoids assigning subcarriers in sub-bands for centre user to edge users, because these resources are extremely inefficient for cell edge users. Consequently, the majority of the transmission resources are assigned to the cell centre users. Since PFS has the ability to keep the fairness between centre and edge user, it will prevent the centre users accessing 'good' resources in the protected sub-band. Therefore, PFS also avoids assigning subcarriers in sub-bands for cell edge users to centre users. This is the reason why the sub-band availability constraint can be lessened when PFS is used in FFR systems. Additionally, due to the small number of users in an optical attocell, the computational complexity of the PFS will be much lower than the PFS in conventional RF cellular systems.

In Fig. 13, the average spectral efficiency of the FFR systems with PFS are also demonstrated. It can be observed that PFS effectively alleviates the spectral efficiency decrease for FFR systems under the condition of low λ. In addition, it is noted that the performance of sFFR with PFS and $\lambda = 1$ user/m^2 is slightly worse compared with that without PFS. This is because the data rate difference between centre users and edge users is significant. Therefore, the PFS trades some spectral efficiency for better fairness. In the case of SFR with $\lambda = 1$ user/m^2, PFS further increases the average spectral efficiency. This is because the data rate gap between centre users and edge users is small. Therefore, the PFS can gain additional spectral efficiency with a low loss of fairness.

V. Conclusion

A DCO-OFDM-based optical attocell network with FFR schemes was considered in this paper. An analytical framework of the FFR application in an optical attocell network was proposed. Both the sFFR and SFR schemes were considered. A method of calculating the statistics of the achievable SINR and the average spectral efficiency in a two-layer network model was presented. The numerical results show a close agreement with the results of the Monte Carlo simulations. By comparing with the networks deployed in a rectangular room, the performance of the two-layer model was demonstrated to be a good estimation of the practical optical attocell network. The performance of the optical attocell network with FFR was evaluated and compared with a benchmark system with full frequency reuse scheme. The results showed that FFR schemes can effectively improve the downlink SINR in an optical attocell network. In addition, FFR schemes offer significant improvements in the cell edge spectral efficiency of an optical attocell system. Furthermore, the average spectral efficiency is slightly improved. Also, the effects of the key parameters were studied, such as cell radius R, cell centre/radius ratio δ and active use density λ. It was identified that the optimal value for δ is 0.7 for sFFR and 0.55 for SFR. With an increase in the noise level, these optimal values become greater and the gain from FFR schemes decreases. In addition, a low user density λ significantly decreases the achievable average spectral efficiency. However, PFS can be used to effectively alleviate this problem.

Algorithm 1 : Proportional fairness scheduling

1: **for** $l = 1, 2, \ldots, L$ **do**
2: $\quad K_{l,1} = K_{l,2} = \cdots = K_{l,N} = K_l/N$
3: **end for**
4: $\bar{\mathbf{C}} = \mathbf{C}\{\mathbf{K}\}$
5: **for** $l = 1, 2, \ldots, L$ **do**
6: $\quad \mathbf{S} = \left[\frac{s_{l,1}}{\bar{C}_1}, \frac{s_{l,2}}{\bar{C}_2}, \ldots, \frac{s_{l,N}}{\bar{C}_N}\right]$ and $\mathbf{S}_n = \frac{s_{l,n}}{\bar{C}_n}$.
7: $\quad n_{\max} = \arg\max_n \mathbf{S}_n$ and $n_{\min} = \arg\min_n \mathbf{S}_n$.
8: $\quad$ **if** $K_{l,n_{\max}} < K_l$ **then**
9: $\quad\quad$ **if** $K_{l,n_{\min}} = 0$ **then**
10: $\quad\quad\quad$ Exclude $\mathbf{S}_{n_{\min}}$ from $\mathbf{S}$ and go back to step 8.
11: $\quad\quad$ **end if**
12: $\quad\quad K_{l,n_{\max}} = K_{l,n_{\max}} + 1$, $K_{l,n_{\min}} = K_{l,n_{\min}} - 1$
13: $\quad$ **end if**
14: **end for**
15: $\bar{\mathbf{C}} = \bar{\mathbf{C}}(1-\alpha) + \mathbf{C}\{\mathbf{K}\}\alpha$
16: Iterate from step 6 to step 16 until $\mathbf{K}$ converge.

Appendix

A. SINR Simplification: $\Delta = 1$

In VLC systems, the limiting factor of the LED transmitter is its average optical power output. Therefore, it is reasonable to calculate the maximum acceptable signal electrical power based on the available optical power output of the LED transmitter. In [35], it is shown in DCO-OFDM that:

$$\frac{P_{\mathrm{opt}}^2}{P_{\mathrm{elec,AC}} + x_{\mathrm{DC}}^2} = \frac{\kappa^2}{1+\kappa^2},$$

where P_{opt} is the average optical output of the LED transmitter and κ is a parameter reflecting the dc-bias level which is given as $\kappa = x_{\mathrm{DC}}/\sqrt{P_{\mathrm{elec,AC}}}$. Then we can find that $P_{\mathrm{elec,AC}} = P_{\mathrm{opt}}^2/\kappa^2$ and

$$P_{\mathrm{elec},i,k} = \frac{P_{\mathrm{opt}}^2}{(K-2)\kappa^2}. \tag{A.1}$$

Insert (A.1) and (1) in (3), it can be found that:

$$\gamma_{\mathrm{FR}}(z) = \frac{\frac{P_{\mathrm{opt}}^2 (m+1)^2 A_{\mathrm{pd}}^2 R_{\mathrm{pd}}^2 h^{2m+2} \left(r_0^2(z)+h^2\right)^{-m-3}}{(2\pi)^2 (K-2)\kappa^2}}{\sum_{i\in И} \frac{P_{\mathrm{opt}}^2 (m+1)^2 A_{\mathrm{pd}}^2 R_{\mathrm{pd}}^2 h^{2m+2} \left(r_i^2(z)+h^2\right)^{-m-3}}{(2\pi)^2 (K-2)\kappa^2} + \sigma_k^2},$$

$$= \frac{\left(r^2+h^2\right)^{-m-3}}{\sum_{i\in И} \left(r_i^2(z)+h^2\right)^{-m-3} + \Omega},$$

where

$$\Omega = \frac{4\pi^2 (K-2) N_0 W \kappa^2}{K P_{\mathrm{opt}}^2 (m+1)^2 A_{\mathrm{pd}}^2 R_{\mathrm{pd}}^2 h^{2m+2}}.$$

B. Proportional Fairness Scheduling

In step 12 of Algorithm 1, $K_{l,n_{\max}}$ and $K_{l,n_{\min}}$ are adjusted while other elements in $\mathbf{K}$ remain the same. In this proof, we

only consider varying one of the L sub-bands $\hat{l}$. The resource allocation plan for other sub-bands remains the same. Since $\sum_n K_{\hat{l},n} = K_{\hat{l}}$, $K_{\hat{l},n_{\min}}$ varies if $K_{\hat{l},n_{\max}}$ changes its value. Their relationship is shown as follows:

$$K_{\hat{l},n_{\min}} = M - K_{\hat{l},n_{\max}},$$
$$M = K_{\hat{l}} - \sum_{n \neq n_{\min}, n_{\max}} K_{\hat{l},n}.$$

A variable $\hat{K}$ is defined to replace $K_{\hat{l},n_{\max}}$. Then Λ can be considered to be the function of $\hat{K}$. Thus, we can write Λ as:

$$\begin{aligned}\Lambda\left(\hat{K}\right) =& \ln\left(C_{n_{\max}}\left(\hat{K}\right)\right) \\ &+ \ln\left(C_{n_{\min}}\left(\hat{K}\right)\right) + \sum_{n \neq n_{\min}, n_{\max}} \ln\left(C_n\right) \\ =& \ln\left(\hat{K} s_{\hat{l},n_{\max}} + \sum_{l \neq \hat{l}} K_{l,n_{\max}} s_{l,n_{\max}}\right) \\ &+ \ln\left(\left(M - \hat{K}\right) s_{\hat{l},n_{\min}} + \sum_{l \neq \hat{l}} K_{l,n_{\min}} s_{l,n_{\min}}\right) \\ &+ \sum_{n \neq n_{\min}, n_{\max}} \ln\left(C_n\right).\end{aligned}$$

Then it can be found that:

$$\frac{\mathrm{d}\Lambda\left(\hat{K}\right)}{\mathrm{d}\hat{K}} = \frac{s_{\hat{l},n_{\max}}}{C_{n_{\max}}\left(\hat{K}\right)} - \frac{s_{\hat{l},n_{\min}}}{C_{n_{\min}}\left(\hat{K}\right)}.$$

If we let $\hat{K} = K_{\hat{l},n_{\max}}$, according to step 7 of Algorithm 1, we have that $\frac{\mathrm{d}\Lambda(\hat{K})}{\mathrm{d}\hat{K}} \geq 0$. This means that $\Lambda(\hat{K})$ is an increasing function at $K_{\hat{l},n_{\max}}$. Therefore, if we slightly increase $\hat{K}$, the probability that $\Lambda(\hat{K})$ will increase is high. To guarantee the convergence of Algorithm 1, the increment of $\hat{K}$ is minimised to one, since the number of subcarriers has to be an integer. With the updating of $\mathbf{K}$ in Algorithm 1, the values of elements in $\mathbf{S}$ in step 6 of Algorithm 1 will converge to a same value. When $\mathbf{S}$ converge for all sub-bands, Λ is maximised.

REFERENCES

[1] Visible light communication (VLC)—A potential solution to the global wireless spectrum shortage. (2011). GBI Research, Tech. Rep. GBISC017MR. [Online]. Available: http://www.gbiresearch.com/

[2] D. O'Brien, "Visible light communications: Challenges and potential," in *Proc. IEEE Photon. Conf.*, Arlington, VA, USA, Oct. 2011, pp. 365–366.

[3] L. Zeng, D. O'Brien, H. Minh, G. Faulkner, K. Lee, D. Jung, Y. Oh, and E. T. Won, "High data rate multiple input multiple output (MIMO) optical wireless communications using white LED lighting," *IEEE J. Sel. Areas Commun.*, vol. 27, no. 9, pp. 1654–1662, Dec. 2009.

[4] R. Mesleh, H. Elgala, and H. Haas, "Optical spatial modulation," *IEEE/OSA J. Opt. Commun. Netw.*, vol. 3, no. 3, pp. 234–244, Mar. 2011.

[5] J. Armstrong, "OFDM for optical communications," *J. Lightw. Technol.*, vol. 27, no. 3, pp. 189–204, Feb. 2009.

[6] D. Tsonev, S. Sinanovic, and H. Haas, "Complete modeling of nonlinear distortion in OFDM-based optical wireless communication," *J. Lightw. Technol.*, vol. 31, no. 18, pp. 3064–3076, Sep. 15, 2013.

[7] M. Alouini and A. Goldsmith, "Area spectral efficiency of cellular mobile radio systems," *IEEE Trans. Veh. Technol.*, vol. 48, no. 4, pp. 1047–1066, Jul. 1999.

[8] H. Haas, "High-speed wireless networking using visible light," *SPIE Newsroom*, Apr. 19, 2013, doi:10.1117/2.1201304.004773.

[9] D. Tsonev, H. Chun, S. Rajbhandari, J. J. D. McKendry, S. Videv, E. Gu, M. Haji, S. Watson, A. E. Kelly, G. Faulkner, M. D. Dawson, H. Haas, and D. O'Brien, "A 3-Gb/s single-LED OFDM-based wireless VLC link using a gallium nitride μLED," *IEEE Photon. Technol. Lett.*, vol. 26, no. 7, pp. 637–640, Apr. 2014.

[10] J. Fakidis, D. Tsonev, and H. Haas, "A comparison between DCO-OFDMA and synchronous one-dimensional OCDMA for optical wireless communications," in *Proc. IEEE 24th Int. Symp. Pers. Indoor Mobile Radio Commun.*, London, U.K., Sep. 8–11, 2013, pp. 3605–3609.

[11] G. W. Marsh and J. M. Kahn, "Channel reuse strategies for indoor infrared wireless communications," *IEEE Trans. Commun.*, vol. 45, no. 10, pp. 1280–1290, Oct. 1997.

[12] K. Cui, J. Quan, and Z. Xu, "Performance of indoor optical femtocell by visible light communication," *Opt. Commun.*, vols. 298/299, pp. 59–66, Jul. 2013.

[13] B. Ghimire and H. Haas, "Self-organising interference coordination in optical wireless networks," *EURASIP J. Wireless Commun. Netw.*, vol. 1, no. 131, Apr. 2012.

[14] T. Novlan, R. Ganti, A. Ghosh, and J. Andrews, "Analytical evaluation of fractional frequency reuse for OFDMA cellular networks," *IEEE Trans. Wireless Commun.*, vol. 10, no. 12, pp. 4294–4305, Dec. 2011.

[15] T. Novlan, J. Andrews, I. Sohn, R. Ganti, and A. Ghosh, "Comparison of fractional frequency reuse approaches in the OFDMA cellular downlink," in *Proc. IEEE Global Telecommun. Conf.*, Miami, FL, USA, Dec. 6–10, 2010, pp. 1–5.

[16] V. V. Huynh, N.-T. Le, N. Saha, M. Chowdhury, and Y. M. Jang, "Inter-cell interference mitigation using soft frequency reuse with two FOVs in visible light communication," in *Proc. Int. Conf. ICT Convergence*, Jeju Island, Korea, Oct. 15–17, 2012, pp. 141–144.

[17] C. Chen, N. Serafimovski, and H. Haas, "Fractional frequency reuse in optical wireless cellular networks," in *Proc. IEEE 24th Int. Symp. Pers. Indoor Mobile Radio Commun.*, London, U.K., Sep. 8–11, 2013, pp. 3594–3598.

[18] J. M. Kahn and J. R. Barry, "Wireless infrared communications," *Proc. IEEE*, vol. 85, no. 2, pp. 265–298, Feb. 1997.

[19] J. Barry, J. Kahn, W. Krause, E. Lee, and D. Messerschmitt, "Simulation of multipath impulse response for indoor wireless optical channels," *J. Sel. Areas Commun.*, vol. 11, no. 3, pp. 367–379, Apr. 1993.

[20] A. Goldsmith, *Wireless Communications*. Cambridge, U.K.: Cambridge Univ. Press, 2005.

[21] G. Cossu, A. M. Khalid, P. Choudhury, R. Corsini, and E. Ciaramella, "3.4 Gbit/s visible optical wireless transmission based on RGB LED," *Opt. Express*, vol. 20, pp. B501–B506, 2012.

[22] A. M. Khalid, G. Cossu, R. Corsini, P. Choudhury, and E. Ciaramella, "1-Gb/s transmission over a phosphorescent white LED by using rate-adaptive discrete multitone modulation," *IEEE Photon. J.*, vol. 4, no. 5, pp. 1465–1473, Oct. 2012.

[23] V. Jungnickel, V. Pohl, S. Nonnig, and C. von Helmolt, "A physical model of the wireless infrared communication channel," *IEEE J. Sel. Areas Commun.*, vol. 20, no. 3, pp. 631–640, Apr. 2002.

[24] H. Rohling, Ed., *OFDM: Concepts for Future Communication Systems*, 1st ed. Berlin, Germany: Springer-Verlag, 2011.

[25] S. Dimitrov, S. Sinanovic, and H. Haas, "Clipping noise in OFDM-based optical wireless communication systems," *IEEE Trans. Commun.*, vol. 60, no. 4, pp. 1072–1081, Apr. 2012.

[26] H. Elgala, R. Mesleh, and H. Haas, "Non-linearity effects and predistortion in optical OFDM wireless transmission using LEDs," *Int. J. Ultra Wideband Commun. Syst.*, vol. 1, no. 2, pp. 143–150, 2009.

[27] C. Chen, I. Muhammad, D. Tsonev, and H. Haas, "Analysis of downlink transmission in DCO-OFDM-based optical attocell networks," presented at the IEEE Global Telecommun. Conf., Austin, TX, USA, Dec. 8–12, 2014.

[28] H. Zhu and J. Wang, "Performance analysis of chunk-based resource allocation in multi-cell OFDMA systems," *IEEE J. Sel. Areas Commun.*, vol. 32, no. 2, pp. 367–375, Feb. 2014.

[29] T. Komine and M. Nakagawa, "Fundamental analysis for visible-light communication system using LED lights," *IEEE Trans. Consum. Electron.*, vol. 50, no. 1, pp. 100–107, Feb. 2004.

[30] J. Grubor, S. C. J. Lee, K.-D. Langer, T. Koonen, and J. W. Walewski, "Wireless high-speed data transmission with phosphorescent white-light

leds," in *Proc. 33rd Eur. Conf. Exhib. Opt. Commun.*, Berlin, Germany, Sep. 16–20, 2007.
[31] S. Dimitrov, H. Haas, M. Cappitelli, and M. Olbert, "On the throughput of an OFDM-based cellular optical wireless system for an aircraft cabin," in *Proc. Eur. Conf. Antennas Propag.*, Rome, Italy, Apr. 11–15, 2011, pp. 3089–3093.
[32] *Light and Lighting—Lighting of Work Places—Part 1: Indoor Work Places*, European Standard EN 12464-1, Jun. 2011.
[33] T.-D. Nguyen and Y. Han, "A proportional fairness algorithm with QoS provision in downlink OFDMA systems," *IEEE Commun. Lett.*, vol. 10, no. 11, pp. 760–762, Nov. 2006.
[34] H. Burchardt, Z. Bharucha, H. Haas, and G. Auer, "Uplink interference protection and fair scheduling for power efficient OFDMA networks," presented at the 8th Int. Workshop Multi-Carrier Systems Solutions, Herrsching, Germany, May 3–4, 2011.
[35] J. Armstrong and B. J. C. Schmidt, "Comparison of asymmetrically clipped optical OFDM and DC-biased optical OFDM in AWGN," *IEEE Commun. Lett.*, vol. 12, no. 5, pp. 343–345, May 2008.

Cheng Chen (S'14) received the B.Eng. degree in electronic and electrical engineering from the University of Strathclyde, Glasgow, U.K., in 2011, and the M.Sc. degree in communications and signal processing from the Imperial College London, London, U.K., in 2012. He is currently working toward the Ph.D. degree in electrical engineering at the University of Edinburgh, Edinburgh, U.K. His research interests include visible light communication networking and interference mitigation.

Stefan Videv received the B.Sc. degree in electrical engineering and computer science and the M.Sc. degree in communications, systems, and electronics from Jacobs University Bremen, Bremen, Germany, in 2007 and 2009, respectively, and the Ph.D. degree thesis titled techniques for green radio cellular communications from the University of Edinburgh, Edinburgh, U.K., in 2013. He is currently an Experimental Officer at the Li-Fi Research and Development Centre, University of Edinburgh, and is working in the field of visible light communications. His research interests include the prototyping of communication systems, smart resource allocation, and energy efficient communications.

Dobroslav Tsonev (S'11–M'14) received the B.Sc. degree in electrical engineering and computer science from Jacobs University Bremen, Bremen, Germany, in 2008, the M.Sc. degree in communication engineering with specialization in electronics from the Munich Institute of Technology, Munich, Germany, in 2010, and the Ph.D. degree in electrical engineering from the University of Edinburgh, Edinburgh, U.K., in 2015. He is currently a Research Associate at the Li-Fi Research and Development Centre, University of Edinburgh. His main research interests include optical wireless communications with an emphasis on visible light communications.

Harald Haas (S'98–AM'00–M'03) received the Ph.D. degree from the University of Edinburgh, Edinburgh, U.K., in 2001. He is currently the Chair of Mobile Communications at the University of Edinburgh. He was an invited speaker at TED Global 2011, and his talk has been watched online more than 1.6 million times. He is the cofounder and the Chief Scientific Officer at pureLiFi Ltd. He holds 31 patents and has more than 30 pending patent applications. He has published 300 conference and journal papers including a paper in Science. His main research interests include optical wireless communications, hybrid optical wireless and RF communications, spatial modulation, and interference coordination in wireless networks. He first introduced and coined spatial modulation and Li-Fi. Li-Fi was listed among the 50 best inventions in TIME Magazine 2011. He is a co-recipient of the best paper award at the *IEEE Vehicular Technology Conference* in Las Vegas in 2013 and in Glasgow in 2015. In 2012, he was the only one who received the prestigious Established Career Fellowship from the Engineering and Physical Sciences Research Council (EPSRC) within Information and Communications Technology in the U.K. He received the Tam Dalyell Prize 2013 awarded by the University of Edinburgh for excellence in engaging the public with science. In 2014, he was selected by EPSRC as one of the ten Recognizing Inspirational Scientists and Engineers Leaders.

IEEE ICC 2016 - Optical Networks and Systems

Non-line-of-sight Channel Impulse Response Characterisation in Visible Light Communications

Cheng Chen, Dushyantha Basnayaka and Harald Haas
Li-Fi R&D Centre, Institute for Digital Communications, The University of Edinburgh, Edinburgh, UK
E-mail:{cheng.chen, d.basnayaka, h.haas}@ed.ac.uk

***Abstract*—One of the important issues in an indoor visible light communication (VLC) system is the multi-path (MP) effect due to reflections. Generally, the MP effect can be characterised by the channel impulse response (CIR). Methods based on ray-tracing/Monte Carlo simulations are primarily used to obtain these impulse responses, but this generally leads to time consuming computer simulations. In this study, an analytical approach is proposed to directly and accurately calculate the non-line-of-sight (NLOS) components of the CIR due to the interior surface reflections in a room. The proposed method could be used in system-level simulations of a networked VLC system (also referred to as a LiFi attocell network), which requires a large number of channels with different transmitter and receiver deployments to be generated in a computationally efficient manner.**

***Index Terms*—visible light communications, channel impulse response, multipath effect.**

I. Introduction

Wireless broadband Internet has become an essential commodity like electricity and water. At least a tenfold increase of mobile data traffic is expected in next five years [1]. The massive increase of the number of wireless access points (APs) in the network, also referred to as network densification, has been identified as a simple yet very effective method to meet this exponentially increasing in wireless data traffic demand. Human behavioural research shows that most of the time people are in an indoor environment [2] when they generate or consume wireless data. Hence, from the human behavioural perspective, transforming the existing illumination sources into wireless APs that provide both illumination and broadband Internet access is a very effective method to densify wireless networks. Visible light communication (VLC) is a technology which enables the transformation of conventional lighting infrastructures into high speed APs [3]. Such network formed by visible light APs is also referred to as a LiFi attocell network.

One of the most critical and limiting issues in an indoor VLC system is the multi-path (MP) effect due to interior surface reflections, which has often been neglected in research studies. Knowledge of the channel information due to non-line-of-sight (NLOS) paths is important in LiFi attocell systems which cover a wide area, and is important to produce more realistic results. In addition, it is also useful when designing specialized modulation schemes for NLOS VLC links. Therefore, many researchers have explored methods to determine the channel impulse response (CIR) due to NLOS paths. A number of simulation methods are widely used to obtain the CIRs. The most commonly used method was proposed in [4], and it splits the reflection surfaces into large number of small elements. The interactions between each pair of elements are calculated. Although an accurate CIR can be obtained with a very small element size, the computational complexity is very high which leads to time consuming computer simulations. In some studies on multiple input multiple output (MIMO) or networked VLC systems, a large number of random channel realisations are required. Therefore, a method to calculate VLC indoor channels with a reasonable balance between accuracy and efficiency is required. Some improved methods have been proposed in [5], [6], which lead to shorter simulation time. However, the gains are still not sufficient for large-scale system level simulations. Some researchers have explored channel models with lower complexity [7], [8]. However, for some link deployment or frequency range, the accuracy of these models is insufficient. VLC channel characterisation using a commercial optical software named Zemax® has also been considered by researchers [9].

In [10], an analytical ceiling bounce model was proposed to characterise the NLOS CIR for diffused wireless infrared links. In a VLC system, the deployment of the transmitter and receiver is typically different from that in a diffused infrared system. Motivated by this approach and the issues mentioned, in this study, the work in [10] is extended and an analytical model to generate the NLOS CIR for VLC links is proposed. Firstly, the complicated NLOS paths are classified into a number of categories. The signals travelling via the paths in the same category are simpler to analyse. Then the overall CIR is approximated as a superposition of these CIRs for each category. In this paper, the CIR due to the paths via a single wall reflection is considered. It is shown that by combining the CIRs due to multiple wall reflections in a room, the dominate characteristics of the overall CIR can be obtained. Due to space limitations here, the calculations of the CIRs due to higher order reflections will be presented in a forthcoming publication.

The remainder of this paper is organised as follows: the analytical results for the first order wall reflection CIR are presented in Section II. In Section III, the NLOS CIR in a cuboid room is considered. Also, the proposed method is compared with a conventional method [6] in this case study. Finally, the conclusions are given in Section IV.

978-1-4799-6664-6/16/$31.00 ©2016 IEEE

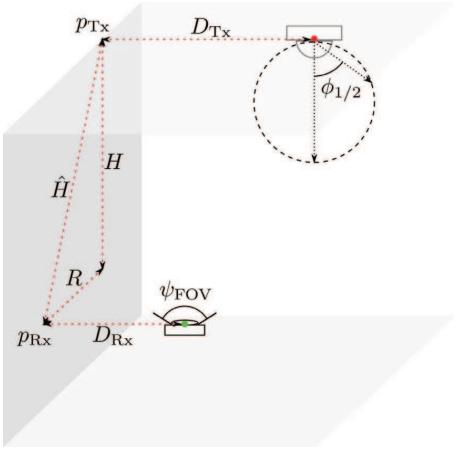

Fig. 1. The geometry of the transmission deployment with a single wall reflection. The key geometric parameters required in the calculation include D_{Tx}, D_{Rx}, R and H.

II. Single Wall Reflection Channel Impulse Response

In a typical indoor VLC system, the transmitters are installed in the ceiling of a room and facing downwards, while the receivers are lower heights depending on the use of the mobile device. The receiver detector is assumed to be facing upwards to the ceiling.

The transmission paths due to first order reflection are an important factor in the NLOS channel, especially when the link is close to the edge of the room. Due to the nature of the transmitter and receiver deployment in VLC, the walls of the room become the main reflectors for the first order reflections. Therefore, the channel due to a single wall reflection is considered. A scenario of a transmitter, a receiver and a wall extending infinitely to the horizontal directions are assumed, as shown in Fig. 1. In this scenario, the transmitter is D_{Tx}, and the receiver is D_{Rx} away from the wall. The projection of the transmitter on the wall is denoted as p_{Tx}, and the projection of the receiver on the wall is denoted as p_{Rx}. The Euclidean distance between p_{Tx} and p_{Rx} is $\hat{H}$. In the considered wall plane, point p_{Tx} is R away from point p_{Rx} in the horizontal direction; and point p_{Tx} is H away from point p_{Rx} in the vertical direction. It can be concluded that:

$$\hat{H}^2 = H^2 + R^2. \tag{1}$$

The considered light source is assumed to follow a Lambertian radiation pattern [11]. The mode number of the light source of the considered transmitter is denoted as m, which is determined by the half-power semiangle $\phi_{1/2}$ as $m = -1/\log 2(\cos\phi_{1/2})$. The physical area of the photodiode (PD) of the receiver is denoted as A_{pd}. The case with full receiver field of view (FOV) of $\psi_{\mathrm{FOV}} = 180°$ is considered. The smaller the receiver FOV, the less the received NLOS signal power, as the range of the incident angle is reduced. The reflectivity of the wall is denoted as ρ.

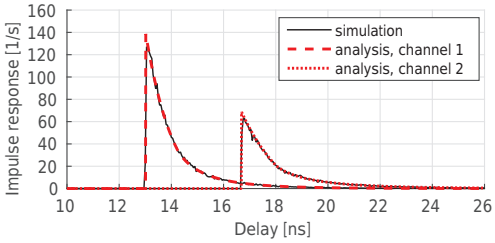

Fig. 2. Single wall reflection channel impulse response results. Channel 1 parameters: $H = 2$ m, $R = 1.5$ m, $D_{\mathrm{Tx}} = 1.5$ m, $D_{\mathrm{Rx}} = 1.5$ m, $\phi_{1/2} = 45°$. Channel 2 parameters: $H = 2.25$ m, $R = 2$ m, $D_{\mathrm{Tx}} = 2$ m, $D_{\mathrm{Rx}} = 2$ m, $\phi_{1/2} = 60°$.

Proposition 1. *Considering a VLC single wall reflection channel with the given parameters of H, R, D_{Tx}, D_{Rx}, ρ, m and A_{pd}, the channel impulse response $h_{\{H,R,D_{\mathrm{Tx}},D_{\mathrm{Rx}},\rho,m,A_{\mathrm{pd}}\}}(t)$ can be calculated as:*

$$h(t) = \int_{\theta_{\min}}^{\theta_{\max}} f(r_{\max},\theta)\frac{r_{\max}\mathrm{d}r_{\max}}{\mathrm{d}t} - f(r_{\min},\theta)\frac{r_{\min}\mathrm{d}r_{\min}}{\mathrm{d}t}\mathrm{d}\theta, \tag{2}$$

where $f(r,\theta)$ is defined as (4)*, where $\mathcal{R}(v)$ is the ramp function which is defined as:*

$$\mathcal{R}(v) = \begin{cases} v & : v \geq 0 \\ 0 & : v < 0 \end{cases}. \tag{3}$$

In (2)*, the terms $r_{\max}$, $r_{\min}$, $\theta_{\max}$ and $\theta_{\min}$ can be calculated as:*

$$r_{\min} = \begin{cases} \frac{\hat{H}\cos\theta\left(D_{\mathrm{Tx}}^2 - D_{\mathrm{Rx}}^2\right) - ct\sqrt{\beta}}{2\left(c^2t^2 - \hat{H}^2\cos^2\theta\right)} & : t_0 < t < t_{\mathrm{T}} \\ 0 & : t \geq t_{\mathrm{T}} \end{cases}, \tag{5}$$

$$r_{\max} = \frac{\hat{H}\cos\theta\left(D_{\mathrm{Tx}}^2 - D_{\mathrm{Rx}}^2\right) + ct\sqrt{\beta}}{2\left(c^2t^2 - \hat{H}^2\cos^2\theta\right)}, \tag{6}$$

$$\beta = \left(c^2t^2 - \hat{H}^2\cos^2\theta\right)\left(c^2t^2 - \hat{H}^2 - 2D_{\mathrm{Tx}}^2 - 2D_{\mathrm{Rx}}^2\right) + \left(D_{\mathrm{Tx}}^2 - D_{\mathrm{Rx}}^2\right)^2. \tag{7}$$

$$\theta_{\min} = \begin{cases} U(D_{\mathrm{Tx}} - D_{\mathrm{Rx}})\pi - \arccos(\gamma) & : t_0 < t < t_{\mathrm{T}} \\ 0 & : t \geq t_{\mathrm{T}} \end{cases}, \tag{8}$$

$$\theta_{\max} = \begin{cases} U(D_{\mathrm{Tx}} - D_{\mathrm{Rx}})\pi + \arccos(\gamma) & : t_0 < t < t_{\mathrm{T}} \\ 2\pi & : t \geq t_{\mathrm{T}} \end{cases}, \tag{9}$$

$$\gamma = \frac{1}{\hat{H}}\sqrt{c^2t^2 + \frac{\left(D_{\mathrm{Tx}}^2 - D_{\mathrm{Rx}}^2\right)^2}{c^2t^2 - \hat{H}^2 - 2D_{\mathrm{Tx}}^2 - 2D_{\mathrm{Rx}}^2}},$$

where c denotes the speed of light; t denotes the time delay; $U(v)$ is the unit step function; and the time threshold t_0 and

$$f(r,\theta)=\frac{\rho(m+1)D_{\mathrm{Tx}}D_{\mathrm{Rx}}A_{\mathrm{pd}}\left[\mathcal{R}\left(\frac{H}{2}-\frac{r(H\cos\theta-R\sin\theta)}{H}\right)\right]^{m}\mathcal{R}\left(\frac{H}{2}+\frac{r(H\cos\theta-R\sin\theta)}{H}\right)}{2\pi^{2}\left(r^{2}-\hat{H}r\cos\theta+\frac{\hat{H}^{2}}{4}+D_{\mathrm{Tx}}^{2}\right)^{\frac{m+3}{2}}\left(r^{2}+\hat{H}r\cos\theta+\frac{\hat{H}^{2}}{4}+D_{\mathrm{Rx}}^{2}\right)^{2}}. \tag{4}$$

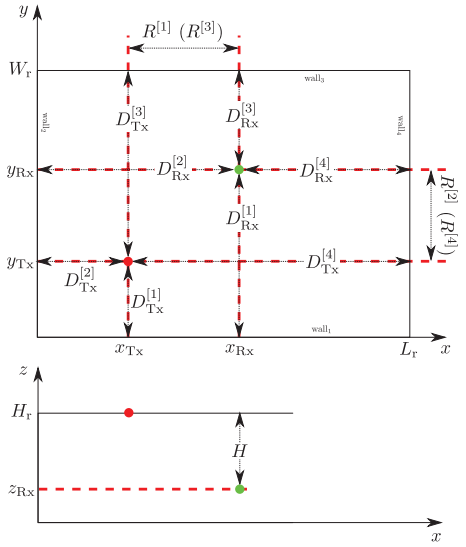

Fig. 3. The top view and the side view of the geometry of the transmission deployment in a cuboid room.

t_{T} can be calculated as:

$$t_0=\frac{\sqrt{\hat{H}^2+\left(D_{\mathrm{Tx}}+D_{\mathrm{Rx}}\right)^2}}{c}, \tag{10}$$

$$t_{\mathrm{T}}=\frac{\sqrt{\hat{H}^2/4+D_{\mathrm{Tx}}^2}+\sqrt{\hat{H}^2/4+D_{\mathrm{Rx}}^2}}{c}. \tag{11}$$

In addition, the terms $\frac{\mathrm{d}r_{\max}}{\mathrm{d}t}$ and $\frac{\mathrm{d}r_{\min}}{\mathrm{d}t}$ are given as (12) *and* (13)*, respectively.*

The proof of this proposition is given in the Appendix. Expression (2) includes a single integration operation, which can be efficiently calculated using a standard numerical method.

Fig. 2 shows the results of the single wall reflection CIR generated by the numerical calculation using (2). In addition, the corresponding simulated results are presented for comparison. In the remainder of this paper, all simulated results are produced using the approach introduced in [6]. In the results, the reflectivity of the walls and the physical area of the PD are $\rho=0.7$ and $A_{\mathrm{pd}}=1\ \mathrm{cm}^2$, respectively. For the first presented channel, $H=2$ m, $R=1.5$ m, $D_{\mathrm{Tx}}=1.5$ m, $D_{\mathrm{Rx}}=1.5$ m, $\phi_{1/2}=45°$. For the second presented channel, $H=2.25$ m, $R=2$ m, $D_{\mathrm{Tx}}=2$ m, $D_{\mathrm{Rx}}=2$ m, $\phi_{1/2}=60°$. In both cases, the analytical results show close agreement to the simulated results, which validates the analytical expressions in this section.

TABLE I

i	$R^{[i]}$	$D^{[i]}_{\mathrm{Tx}}$	$D^{[i]}_{\mathrm{Rx}}$
1	$\lvert x_{\mathrm{Tx}}-x_{\mathrm{Rx}}\rvert$	y_{Tx}	y_{Rx}
2	$\lvert y_{\mathrm{Tx}}-y_{\mathrm{Rx}}\rvert$	x_{Tx}	x_{Rx}
3	$\lvert x_{\mathrm{Tx}}-x_{\mathrm{Rx}}\rvert$	$W_{\mathrm{r}}-y_{\mathrm{Tx}}$	$W_{\mathrm{r}}-y_{\mathrm{Rx}}$
4	$\lvert y_{\mathrm{Tx}}-y_{\mathrm{Rx}}\rvert$	$L_{\mathrm{r}}-x_{\mathrm{Tx}}$	$L_{\mathrm{r}}-x_{\mathrm{Rx}}$

TABLE II

quantities	Symbol	Value
Room size	$L_{\mathrm{r}}\times W_{\mathrm{r}}\times H_{\mathrm{r}}$	5 m × 5 m × 3 m
Transmitter location	$(x_{\mathrm{Tx}},y_{\mathrm{Tx}},H_{\mathrm{r}})$	$(2, 2.5, 3)$ m
Receiver location	$(x_{\mathrm{Rx}},y_{\mathrm{Rx}},z_{\mathrm{Rx}})$	$(2.5, 1, 0.75)$ m
Half-power semiangle	$\phi_{1/2}$	60°
PD physical area	A_{pd}	1 cm^2
Surface reflectivity	$[\rho_{\mathrm{ceil}}\ \rho_{\mathrm{floor}}\ \rho_{\mathrm{wall}}]$	[0.7 0.3 0.7]

III. NLOS Channel Impulse Response in a Room

In this section, the analytical CIR in a cuboid room based on the expressions introduced in Section II is demonstrated and compared with the corresponding simulated NLOS CIR. Since there are four walls in a cuboid room, the analytical NLOS CIR is approximated by the superposition of the single wall reflection CIRs by the four walls of the room as:

$$\hat{h}(t)=\sum_{i=1}^{4}h_{\{H,R^{[i]},D^{[i]}_{\mathrm{Tx}},D^{[i]}_{\mathrm{Rx}},\rho^{[i]},m,A_{\mathrm{pd}}\}}(t). \tag{14}$$

Assume a cuboid room with a size of $L_{\mathrm{r}}\times W_{\mathrm{r}}\times H_{\mathrm{r}}$, a transmitter located at $(x_{\mathrm{Tx}},y_{\mathrm{Tx}},H_{\mathrm{r}})$ and a receiver located at $(x_{\mathrm{Rx}},y_{\mathrm{Rx}},z_{\mathrm{Rx}})$. The origin of the coordinates is placed at one of the corners of the room as shown in Fig. 3. The parameters $R^{[i]}$, $D^{[i]}_{\mathrm{Tx}}$ and $D^{[i]}_{\mathrm{Rx}}$ in (14) are determined based on those given in Table I, and H is calculated as $H=H_{\mathrm{r}}-z_{\mathrm{Rx}}$.

Fig. 4 shows the result of a NLOS CIR in a cuboid room calculated using (14). The corresponding parameters are listed in Table II. Considering the CIR results with delay less than 20 ns, the analytically calculated CIR offers an accurate estimation of the simulated CIR. The four spikes in the curves correspond to the four first order reflections bounced by walls. In the case of a delay greater than 20 ns, the simulated result exhibits a higher received signal power due to higher order reflections. The results further show that the accuracy of the analytical CIR specially after 20 ns can be significantly improved if part of the CIRs of second order paths are included into (14). Because of space limitations, the analysis of the NLOS CIR caused by higher order reflections is not presented in this paper, but will be available in a future publication.

$$\frac{\mathrm{d}r_{\max}}{\mathrm{d}t} = \frac{c}{2}\left(\frac{c^2t^2}{\beta}\left(1+\frac{c^2t^2-\hat{H}^2-2\left(D_{\mathrm{Rx}}^2+D_{\mathrm{Tx}}^2\right)}{c^2t^2-\hat{H}^2\cos^2\theta}\right)-\frac{2ct\left(D_{\mathrm{Rx}}^2-D_{\mathrm{Tx}}^2\right)\hat{H}\cos\theta+\beta\left(c^2t^2+\hat{H}^2\cos^2\theta\right)}{\left(c^2t^2-\hat{H}^2\cos^2\theta\right)^2}\right) \tag{12}$$

$$\frac{\mathrm{d}r_{\min}}{\mathrm{d}t} = \frac{c}{2}\left(-\frac{c^2t^2}{\beta}\left(1+\frac{c^2t^2-\hat{H}^2-2\left(D_{\mathrm{Rx}}^2+D_{\mathrm{Tx}}^2\right)}{c^2t^2-\hat{H}^2\cos^2\theta}\right)-\frac{2ct\left(D_{\mathrm{Rx}}^2-D_{\mathrm{Tx}}^2\right)\hat{H}\cos\theta-\beta\left(c^2t^2+\hat{H}^2\cos^2\theta\right)}{\left(c^2t^2-\hat{H}^2\cos^2\theta\right)^2}\right) \tag{13}$$

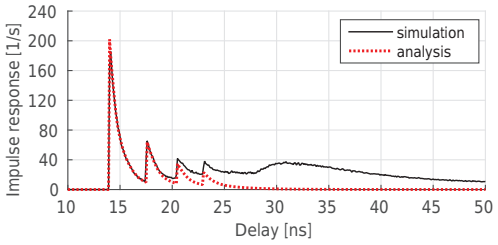

Fig. 4. NLOS channel impulse responses in a cuboid room.

IV. Conclusions

In this paper, an analytical method with low computational complexity for calculating the NLOS channel impulse response was proposed. It has been successfully used to approximate the impulse response of a NLOS VLC channel in a cuboid room as an example. The analytical result is compared with the channel impulse response generated using a conventional ray tracing simulation, and it has been shown that the proposed method offers very high accuracy for the dominated first order multi-path components. The model will be extended to higher order reflections in future studies.

Appendix
Proof of Proposition 1

For a transmission via a single wall reflection path, the optical power is radiated from the source to one of the points on the considered reflector. Then, some of the reflected signal power can be collected by the PD of the receiver. A different point on the reflector gives a different length of the reflection path, which results in different delay of the received optical power. In order to relate the receiver optical power to the time delay, the following problem is considered: which set of points on the reflector offers a received power P collected by the PD with a delay less than time t? Assuming that the reflector plane is defined by a Cartesian coordinate x-y, the received power $P(t)$ can be written as $P(t) = \iint_{W(t)} f(x,y)\mathrm{d}x\mathrm{d}y$, where $W(t)$ is the set of points giving delays less than t; $f(x,y)$ denotes the channel direct-current (DC) gain of the reflection path via point (x,y) on the reflector. Intuitively, the impulse response could be obtained by calculating the derivative of $P(t)$ with respect to the delay t [10]. Therefore, the CIR can

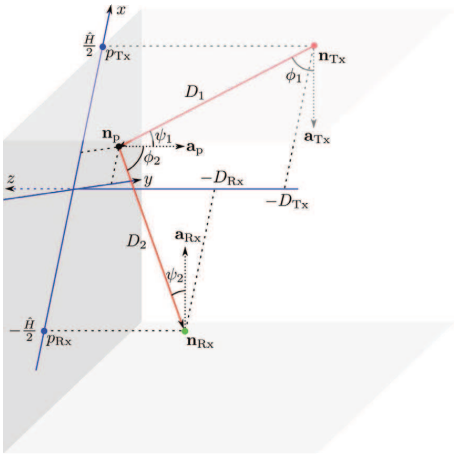

Fig. 5. The geometry of the single wall reflection transmission with 3-D Cartesian Coordinates x-y-z.

be written as:

$$h(t) = \frac{\mathrm{d}}{\mathrm{d}t}\left[\iint_{W(t)} f(x,y)\mathrm{d}x\mathrm{d}y\right]. \tag{A.1}$$

Next, the objective is to calculate the expressions $f(x,y)$ and $W(t)$. The channel DC gain of a single reflection is given as [12]:

$$f = \frac{\rho(m+1)A_{\mathrm{pd}}}{2\pi^2 D_1^2 D_2^2}\cos^m\phi_1\cos\psi_1\cos\phi_2\cos\psi_2,$$

where D_1 denotes the Euclidean distance between the transmitter and the considered point on the reflector; ϕ_1 and ψ_1 denote the radiant angle and the incident angle corresponding to the transmission before the reflection; D_2 denotes the Euclidean distance between the considered point on the reflector and the receiver; ϕ_2 and ψ_2 denote the radiant angle and the incident angle corresponding to the transmission after the reflection. In order to retrieve $f(x,y)$, the location and orientation of all of the important points need to be defined in a 3-dimensional (3-D) Cartesian coordinate system x-y-z. As shown in Fig. 5, the points on the reflector are within the x-y plane, the x-axis is defined on the straight line across the projection points p_{Tx} and p_{Rx}. The direction of the x-axis is from p_{Rx} to p_{Tx}. The origin is defined at the mid-

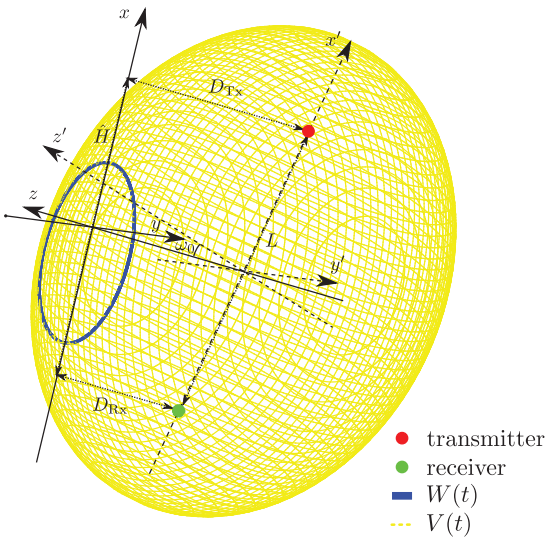

Fig. 6. The geometry of the transmission deployment with $W(t)$ and $V(t)$.

point of the segment between p_{Tx} and p_{Rx}. Therefore, the transmitter has a location of $\boldsymbol{n}_{\mathrm{Tx}} = \left(\frac{\hat{H}}{2}, 0, -D_{\mathrm{Tx}}\right)$ and has an orientation of $\boldsymbol{a}_{\mathrm{Tx}} = \left(-\frac{H}{\hat{H}}, \frac{R}{\hat{H}}, 0\right)$. The receiver has a location of $\boldsymbol{n}_{\mathrm{Rx}} = \left(-\frac{\hat{H}}{2}, 0, -D_{\mathrm{Rx}}\right)$ and has an orientation of $\boldsymbol{a}_{\mathrm{Rx}} = \left(\frac{H}{\hat{H}}, -\frac{R}{\hat{H}}, 0\right)$. The considered point on the reflector is located at $\boldsymbol{n}_{\mathrm{p}} = (x, y, 0)$ and the orientation is $\boldsymbol{a}_{\mathrm{p}} = (0, 0, -1)$. According to [4],

$$D_1^2 = \left(x - \frac{\hat{H}}{2}\right)^2 + y^2 + D_{\mathrm{Tx}}^2,$$

$$D_2^2 = \left(x + \frac{\hat{H}}{2}\right)^2 + y^2 + D_{\mathrm{Rx}}^2,$$

and

$$\cos\phi_1 = \frac{\boldsymbol{a}_{\mathrm{Tx}}\left(\boldsymbol{n}_{\mathrm{p}} - \boldsymbol{n}_{\mathrm{Tx}}\right)^{\mathrm{T}}}{D_1} = \frac{\frac{H}{2} - \frac{Hx - Ry}{\hat{H}}}{D_1},$$

$$\cos\psi_1 = \frac{\boldsymbol{a}_{\mathrm{p}}\left(\boldsymbol{n}_{\mathrm{Tx}} - \boldsymbol{n}_{\mathrm{p}}\right)^{\mathrm{T}}}{D_1} = \frac{D_{\mathrm{Tx}}}{D_1},$$

$$\cos\phi_2 = \frac{\boldsymbol{a}_{\mathrm{p}}\left(\boldsymbol{n}_{\mathrm{Rx}} - \boldsymbol{n}_{\mathrm{p}}\right)^{\mathrm{T}}}{D_2} = \frac{D_{\mathrm{Rx}}}{D_2},$$

$$\cos\psi_2 = \frac{\boldsymbol{a}_{\mathrm{Rx}}\left(\boldsymbol{n}_{\mathrm{p}} - \boldsymbol{n}_{\mathrm{Rx}}\right)^{\mathrm{T}}}{D_2} = \frac{\frac{H}{2} + \frac{Hx - Ry}{\hat{H}}}{D_2}.$$

Therefore, the channel DC gain $f(x, y)$ can be written as (A.2), where the ramp functions are used to avoid the cases of negative channel gain due to the incident angle or radiant angle being greater than $\pi/2$.

Then the expression for $W(t)$ is calculated. Parameter L denotes the Euclidean distance between the transmitter and the receiver, which can be calculated as:

$$L^2 = \hat{H}^2 + \left(D_{\mathrm{Tx}} - D_{\mathrm{Rx}}\right)^2. \tag{A.3}$$

A photon travelling from the transmitter to the receiver via a single reflection using less than time t requires the reflection points to fall in the interior of an ellipsoid [10], as shown in Fig. 6. The foci of this ellipsoid are the locations of the transmitter and the receiver. The function of this ellipsoid is denoted as $V(t)$. Then the integration region $W(t)$ should be the intersection between the wall plane $(z = 0)$ and the interior ellipsoid $V(t)$ as shown in Fig. 6.

In the 3-D Cartesian coordinates x-y-z, the transmitter and the receiver are located at $\left(\frac{\hat{H}}{2}, 0, -D_{\mathrm{Tx}}\right)$ and $\left(-\frac{\hat{H}}{2}, 0, -D_{\mathrm{Rx}}\right)$, respectively. For the convenience of calculating the function of $W(t)$, another 3-D Cartesian coordinates x'-y'-z' system is used. In this coordinate system, the transmitter and the receiver is located at $\left(\frac{L}{2}, 0, 0\right)$ and $\left(-\frac{L}{2}, 0, 0\right)$, respectively. Therefore, the function of $V(t)$ can be written as:

$$\frac{x'^2}{(ct/2)^2} + \frac{y'^2}{(ct/2)^2 - (L/2)^2} + \frac{z'^2}{(ct/2)^2 - (L/2)^2} \leq 1. \tag{A.4}$$

The conversion between the two coordinate systems can be achieved by [10]:

$$\begin{bmatrix} x' \\ y' \\ z' \end{bmatrix} = \begin{bmatrix} \cos\omega_0 & 0 & \sin\omega_0 \\ 0 & 1 & 0 \\ -\sin\omega_0 & 0 & \cos\omega_0 \end{bmatrix} \begin{bmatrix} x \\ y \\ z \end{bmatrix} + \begin{bmatrix} \frac{D_{\mathrm{Tx}} + D_{\mathrm{Rx}}}{2}\sin\omega_0 \\ 0 \\ \frac{D_{\mathrm{Tx}} + D_{\mathrm{Rx}}}{2}\cos\omega_0 \end{bmatrix}, \tag{A.5}$$

where ω_0 is the rotation angle of the coordinates. It can be calculated as:

$$\omega_0 = \arctan\left(\frac{D_{\mathrm{Tx}} - D_{\mathrm{Rx}}}{\hat{H}}\right). \tag{A.6}$$

By inserting (A.3), (A.5) and (A.6) into (A.4), the following inequality can be obtained:

$$x^2 + y^2 - \left(\frac{\hat{H}x}{ct} + \frac{D_{\mathrm{Rx}}^2 - D_{\mathrm{Tx}}^2}{2ct}\right)^2 - \frac{1}{4}\left(c^2t^2 - \hat{H}^2 - 2D_{\mathrm{Tx}}^2 - 2D_{\mathrm{Rx}}^2\right) \leq 0. \tag{A.7}$$

For the convenience of the following calculation, a polar coordinate system r-θ is used to redefine the points on the plane of the reflector, where r denotes the radius and θ denotes the polar angle. The origin of the polar coordinate is located at the origin of the x-y Cartesian coordinate system. The direction of the polar axis is superposed upon the x-axis. Therefore, these two coordinate systems have the following relationship:

$$x = r\cos\theta, \tag{A.8}$$

$$y = r\sin\theta. \tag{A.9}$$

In addition, the 2-dimensional integration in (A.1) is decomposed into two 1-D integrations as:

$$h(t) = \frac{\mathrm{d}}{\mathrm{d}t}\left[\int_{\theta_{\min}}^{\theta_{\max}}\int_{r_{\min}}^{r_{\max}} f(r,\theta) r \mathrm{d}r\mathrm{d}\theta\right], \tag{A.10}$$

$$f(x,y)=\frac{\rho(m+1)A_{\mathrm{pd}}D_{\mathrm{Tx}}D_{\mathrm{Rx}}\left[\mathcal{R}\left(\frac{H}{2}-\frac{Hx-Ry}{\hat{H}}\right)\right]^{m}\mathcal{R}\left(\frac{H}{2}+\frac{Hx-Ry}{\hat{H}}\right)}{2\pi^{2}\left(\left(\frac{\hat{H}}{2}+x\right)^{2}+y^{2}+D_{\mathrm{Rx}}^{2}\right)^{2}\left(\left(\frac{\hat{H}}{2}-x\right)^{2}+y^{2}+D_{\mathrm{Tx}}^{2}\right)^{\frac{m+3}{2}}}. \tag{A.2}$$

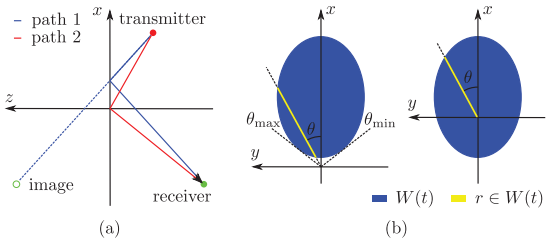

Fig. 7. (a) Path 1 corresponds to the minimum delay t_0. path 2 corresponds to the threshold delay t_{T}. (b) Two cases of $W(t)$ with different ranges of θ and r. left: $t_0 < t < t_{\mathrm{T}}$, right: $t \geq t_{\mathrm{T}}$.

where $f(r,\theta)$ can be calculated by inserting (A.8) and (A.9) into (A.2). The expression of $f(r,\theta)$ is as shown in (4). Eventually, equation (A.10) can be simplified by using the chain rule as shown in (2). Next, the objective is to calculate the values of $\theta_{\min}$, $\theta_{\max}$, $r_{\min}$, $r_{\max}$, $\frac{\mathrm{d}r_{\max}}{\mathrm{d}t}$ and $\frac{\mathrm{d}r_{\min}}{\mathrm{d}t}$. These values are highly related to the value of time delay t. Among all of the first order reflection paths, there is a shortest path, shown as path 1 in Fig. 7 (a). Therefore, any time delay has to be greater than the time that is required for the photon to travel via this path t_0. Intuitively, this minimum time delay can be calculated by (10). In addition, there is another path for the light reflected by the point located at the origin of the coordinates, shown as path 2 in Fig. 7 (a). The time required for the photon to travel via path 2 is defined as t_{T}, which can be calculated by (11). Fig. 7 (b) shows that with a given θ there is a limited range for r. In order to find the two bounds $r_{\min}$ and $r_{\max}$, the inequality (A.7) is converted to an equation with variables x and y replaced by r and θ as:

$$\frac{c^2t^2}{4}\left(\hat{H}^2+2D_{\mathrm{Tx}}^2+2D_{\mathrm{Rx}}^2-c^2t^2-\frac{\left(D_{\mathrm{Rx}}^2-D_{\mathrm{Tx}}^2\right)^2}{c^2t^2}\right)-$$
$$\hat{H}\cos\theta\left(D_{\mathrm{Rx}}^2-D_{\mathrm{Tx}}^2\right)r+\left(c^2t^2-\hat{H}^2\cos^2\theta\right)r^2=0.$$

Then r is treated as the unknown of the equation. Two solutions of r can be calculated by solving the equation. In the case of $t_0 < t < t_{\mathrm{T}}$, the origin is outside the region of $W(t)$ as shown in the plot on the left-hand side of Fig. 7 (b). The range of r is between the two solutions of r. Moreover, to make sure the existence of the solution to r, term (7) should not be less than zero. Therefore, it requires:

$$\cos^2\theta\geq\frac{c^2t^2}{\hat{H}^2}+\frac{\left(D_{\mathrm{Tx}}^2-D_{\mathrm{Rx}}^2\right)^2}{\hat{H}^2\left(c^2t^2-\hat{H}^2-2D_{\mathrm{Tx}}^2-2D_{\mathrm{Rx}}^2\right)}.$$

In the case of $t \geq t_{\mathrm{T}}$, the origin is inside the region of $W(t)$ as shown in the plot on the right-hand side of Fig. 7 (b). The range of r is from 0 to one of the two solutions of r. In this case, term (7) is always greater than zero. Therefore, there is no extra restriction for the range of θ. So the expression of $r_{\min}$, $r_{\max}$, $\frac{\mathrm{d}r_{\max}}{\mathrm{d}t}$, $\frac{\mathrm{d}r_{\min}}{\mathrm{d}t}$, $\theta_{\min}$ and $\theta_{\max}$ can be calculated as expression (5), (6), (12), (13), (8) and (9), respectively.

Acknowledgement

C. Chen acknowledges support received from the NPRP award [NPRP 5-980-2-411] which is from the Qatar National Research Fund (a member of The Qatar Foundation), and D. A. Basnayaka, and H. Haas acknowledge support from the Engineering and Physical Sciences Research Council (EPSRC) under Established Career Fellowship grant EP/K008757/1.

References

[1] Cisco Visual Networking Index, "Global Mobile Data Traffic Forecast Update, 2014-2019," CISCO, White Paper, Feb. 2015.
[2] D. Lopez-Perez, A. Valcarce, G. de la Roche, and J. Zhang, "OFDMA Femtocells: A Roadmap on Interference Avoidance," *IEEE Communications Magazine*, vol. 47, no. 9, pp. 41–48, Jun. 2009.
[3] H. Haas, "High-speed Wireless Networking Using Visible Light," SPIE Newsroom, Apr. 19 2013.
[4] J. Barry, J. Kahn, W. Krause, E. Lee, and D. Messerschmitt, "Simulation of multipath impulse response for indoor wireless optical channels," *IEEE J. Select. Areas Commun.*, vol. 11, no. 3, pp. 367–379, Apr. 1993.
[5] F. Lopez-Hermandez and M. Betancor, "DUSTIN: algorithm for calculation of impulse response on IR wireless indoor channels," *Electronics Letters*, vol. 33, no. 21, pp. 1804–1806, Oct 1997.
[6] F. Lopez-Hernandez, R. Perez-Jimenez, and A. Santamaria, "Ray-tracing Algorithms for Fast Calculation of the Impulse Response on Diffuse IR-wireless Indoor Channels," *Optical Engineering*, vol. 39, no. 10, pp. 2775–2780, Oct. 2000.
[7] V. Jungnickel, V. Pohl, S. Nonnig, and C. von Helmolt, "A Physical Model of the Wireless Infrared Communication Channel," *IEEE Journal on Selected Areas in Communications*, vol. 20, no. 3, pp. 631–640, Apr. 2002.
[8] P. Chvojka, S. Zvanovec, P. A. Haigh, and Z. Ghassemlooy, "Channel characteristics of visible light communications within dynamic indoor environment," *J. Lightw. Technol.*, vol. 33, no. 9, pp. 1719–1725, May 2015.
[9] E. Sarbazi, M. Uysal, M. Abdallah, and K. Qaraqe, "Ray Tracing Based Channel Modeling for Visible Light Communications," in *Signal Processing and Communications Applications Conference*, Trabzon, Apr. 23–25 2014, pp. 702–705.
[10] J. B. Carruthers and J. M. Kahn, "Modeling of Nondirected Wireless Infrared Channels," *IEEE Transactions on Communications*, vol. 45, no. 10, pp. 1260–1268, Oct. 1997.
[11] S. Dimitrov and H. Haas, *Principles of LED Light Communications*. Cambridge University Press, 2015.
[12] T. Komine and M. Nakagawa, "Fundamental analysis for visible-light communication system using LED lights," *IEEE Transactions on Consumer Electronics*, vol. 50, no. 1, pp. 100–107, Feb. 2004.

Globecom 2014 - Optical Networks and Systems Symposium

Analysis of Downlink Transmission in DCO-OFDM-Based Optical Attocell Networks

Cheng Chen, Muhammad Ijaz, Dobroslav Tsonev and Harald Haas
Institute for Digital Communications
Li-Fi R&D Centre
The University of Edinburgh EH9 3JL, Edinburgh, UK
{cheng.chen, m.ijaz, d.tsonev, h.haas}@ed.ac.uk

***Abstract*—In this paper, an indoor visible light communication (VLC) cellular network, referred to as an optical attocell network, is analysed at system level. A line-of-sight (LOS) ray-tracing model is used to characterise the light propagation and its effect on the performance of an intensity modulation (IM) and direct detection (DD) communication system. Orthogonal frequency division multiple access (OFDMA) based on direct-current optical orthogonal frequency division multiplexing (DCO-OFDM) is used as a multi-user access scheme. The signal-to-interference-plus-noise ratio (SINR) for a user with a random location in an optical attocell is studied. An analytical approach to calculate the statistics of the SINR is presented and verified by Monte Carlo simulations. Moreover, average spectral efficiency is also studied in order to estimate the downlink wireless capacity of the optical attocell network. The spectral efficiency of the system has been found to be strongly dependent on the radius of an optical attocell and on the half-power semi-angle of the light transmission profile. Guidelines for the configuration of the relevant attocell parameters are provided. An optical attocell with an average spectral efficiency of 5.9 bits/s/Hz is demonstrated for an appropriate set of attocell parameters.**

***Index Terms*—visible light communications, cellular networks, optical orthogonal frequency division multiplexing and orthogonal frequency division multiple access.**

I. Introduction

The shortage of spectral resources in the radio frequency (RF) region has sparked considerable research interest in the field of optical wireless communications (OWC) for indoor applications [1]. In particular, a lot of interest has been directed towards the visible light spectrum. VLC can offer data transmission and lighting functionality concurrently. A VLC system can be realised with a light emitting diode (LED) as a transmitter and a photodiode (PD) as a detector. Due to the incoherent emission of the LED, coherent modulation/detection techniques are not possible in VLC. Therefore, intensity modulation with direct detection techniques have to be used to encode data. VLC offers several advantages over RF communication systems [2]. For example, a VLC system generates virtually no electromagnetic radiation in the RF spectrum region. Additionally, VLC is inherently robust against eavesdropping. Furthermore, due to the intrinsic properties of light there is no co-channel interference (CCI) between VLC systems in adjacent rooms, which indicates that the optical spectral resources can be reused aggressively in space.

It is widely recognised that an increased spatial reuse of spectral resources offers a considerable gain in wireless capacity [3]. VLC offers a unique opportunity to create a small-scale cellular network that can be embedded into a room with multiple light fixtures, thereby further reducing the reuse distance of the optical spectral resource. In this type of cellular networks, each spatially separated lighting element is used as a base station (BS), which covers multiple users in the small area (typically 1-10 m^2) underneath it. A system of this kind offers full coverage to users in an indoor environment. It is also expected to provide a considerable improvement in wireless system capacity compare to RF communication. Optical orthogonal frequency division multiplexing (O-OFDM) has been researched as one of the prime candidates for signal modulation in VLC [4], [5]. It provides an optimal utilization of the communication resources through adaptive modulation and coding (AMC). Moreover, O-OFDM offers a straightforward multi-user access scheme which is referred to as: OFDMA. Since the DC-bias in DCO-OFDM is harnessed for illumination purposes [6], DCO-OFDM can be used to achieve a high spectral efficiency in the downlink transmission. When illumination is not required such as in the uplink, an power and spectral efficient OFDM variant named enhanced unipolar OFDM [7] can be used.

A number of studies on optical wireless networks have been carried out. The authors of [8] have proposed a cellular scheme to mitigate CCI using a larger spatial reuse distance in an indoor infrared wireless communication system. In [9], the performance of optical wireless hotspots was compared to that achieved by an RF system. That study also investigated the relationship between signal-to-noise ratio (SNR) and the horizontal distance of a user from the cell centre. A VLC system adopting cellular characteristics using a light shaping diffuser was proposed in [10]. A small-cell optical cellular network with full function of an RF cellular system has been proposed in [6]. In an RF cellular system, a personal femtocell is known as an attocell [11]. In [6], the optical small-cell network is referred to as an optical attocell network. However, unlike the personal RF attocell, the light properties and the existing infrastructure readily allow for full wireless indoor networking, but with cell sizes much smaller than that used in heterogeneous RF wireless networks. An optical attocell

978-1-4799-3512-3/14/$31.00 ©2014 IEEE

network is characterised by multiple optical access points (APs) where one AP serves multiple users, and multiple users can communicate to one or more optical APs in the uplink. In addition, it also allows for user mobility and enables handover.

In this paper, a system level analysis of the downlink transmission in an optical attocell network based on DCO-OFDM is proposed. The SINR for a user and system average spectral efficiency are considered and investigated. Analytical method to calculate the cumulative distribution function (CDF) of the SINR and for the average spectral efficiency are provided and validated by Monte Carlo simulation. The impact of important parameters such as the radius of an optical attocell and the half-power semi-angle of the light emission profile is also studied.

The remainder of the paper is organized as follows: Section II presents the system model of the considered optical attocell network. Section III presents the analysis of the SINR. Section IV presents the analysis of the average spectral efficiency. Finally, conclusions are presented in Section V.

II. System Model

The downlink geometric deployment in an optical attocell network is illustrated in Fig. 1. The following assumptions are made in order to simplify the analysis: i) BSs are placed in a regular hexagonal lattice, since this deployment minimises the overlap between coverage areas of adjacent BSs; ii) the ceiling luminaries (BS downlink transmitters) are considered as point sources and are facing downward; iii) each user has a downlink receiver with a PD facing straight up; iv) the concentrator and optical filter are assumed to have unity gain; v) the vertical separation between a BS and a user is fixed with a specified distance h; vi) the receiver field of view (FOV) is wide enough for the users in a given cell to receive the signal from the tagged BS and from the BSs in the six neighbouring cells only. This FOV configuration guarantees a seamless coverage of the system with a minimum number of interference sources.

A. Propagation Model

The reflection paths are omitted in this study for a number of reasons. First of all, the optical OFDM techniques are adopted. One of the motivations for using OFDM is that it is more resilient to inter-symbol interference (ISI) with low complexity equalisation in the frequency domain. Secondly, a deployment in a large indoor environment with sparse reflection objects (e.g. walls, furnitures) is assumed in this study, which has a less dispersive channel power delay profile in the major part of the room. In addition, a commercially available white LED is assumed to be used in the considered system. A typical white LED has a 3 dB bandwidth of about 20 MHz when combined with a blue filter at the receiver side [12]. This means that the sample period is long enough to have the signal power from the LOS path and the short reflected paths (at most 15 m longer than the LOS path) fall into a single symbol time slot. On the other hand, the ISI power caused by the rest of the reflection paths is negligible (more than 30 dB smaller compared to the LOS signal power). Therefore, only the LOS path is considered in the light propagation for the downlink transmission. In other words, the users generally experience a communication channel with a near-flat frequency response. As shown in [13], the LOS optical channel can be well-characterised by its direct-current (DC) gain. The DC gain of the channel from BS_i to an given user is given as:

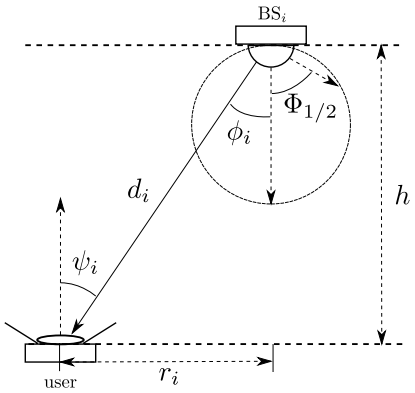

Fig. 1. Downlink system link in an optical attocell network.

$$G_i = \frac{(m+1)A_{\mathrm{pd}}}{2\pi d_i^2}\cos^m(\phi_i)\cos(\psi_i), \tag{1}$$

where m denotes the Lambertian emission order, which is given by $m = -\ln(2)/\ln(\cos(\Phi_{1/2}))$ where $\Phi_{1/2}$ is the half-power semi-angle of the LED; A_{pd} is the physical area of the user receiver PD; d_i represents the Euclidean distance between BS_i and the user; ϕ_i denotes the corresponding light radiance angle; and ψ_i is the light incidence angle, in which $i = 0, 1, 2, \cdots$. BS_0 corresponds to the tagged BS, while the rest of the BSs are interfering BSs.

B. Orthogonal Frequency Division Multiple Access

The application of DCO-OFDM can be extended to an OFDMA system to realise multi-user access in an optical attocell network. The K frequency domain quadrature amplitude modulated data symbols before the inverse discrete Fourier transform (IDFT) are defined as $\boldsymbol{X} = [X_0\ X_1\ X_2\ \cdots\ X_{K-1}]$. Since an intensity modulated signal is a real-valued signal, Hermitian symmetry is required to make the OFDM symbols contain only real samples. This requires that $X_k = X_{K-k}^*$, where $[\cdot]^*$ is the complex conjugate operation. In addition, X_0 and $X_{K/2}$ are set to zero [5]. Consequently, only $K_{\mathrm{t}} = K/2 - 1$ symbols carry information. Through the K-point IDFT and the addition of a DC-bias, the time domain OFDM symbol can be described as follows:

$$\boldsymbol{x}(t) = x_{\mathrm{DC}} + \sum_{k=0}^{K-1}\boldsymbol{x}_k(t),\ t = 0, 1, \cdots, K-1, \tag{2}$$

$$\boldsymbol{x}_k(t) = \frac{\boldsymbol{X}(k)}{\sqrt{K}}\exp\left(\frac{2\pi jkt}{K}\right), \tag{3}$$

where x_{DC} is the DC-bias and $\boldsymbol{x}_k(t)$ represents the signal component at time t which accounts for the modulated symbol on subcarrier k. After the addition of a DC-bias, any remaining negative samples are set to zero. Since the required cyclic-prefix (CP) length is typically short in OWC [14], the effect of adding a CP is omitted in this study. In a multiple access version of DCO-OFDM, the K_{t} transmission channels are shared by a number of users. Each user is allocated one or more subcarriers for transmission. Assuming perfect sampling and synchronization, the sample received at time t of the intensity modulated signal received by an given user on subcarrier k can be expressed as:

$$\boldsymbol{y}_k(t) = \boldsymbol{x}_{0,k}(t)G_0R_{\mathrm{pd}} + \sum_{i\in И} \boldsymbol{x}_{i,k}(t)G_iR_{\mathrm{pd}} + \boldsymbol{n_k}(t), \quad (4)$$

where $\boldsymbol{x}_{i,k}(t)$ is the transmitted signal from BS_i on subcarrier k at time t; In the case of $i = 0$, $\boldsymbol{x}_{0,k}(t)$ is the desired transmitted signal for the given user; R_{pd} denotes the responsivity of the PD; and $\boldsymbol{n_k}(t)$ represents the user receiver noise signal on subcarrier k. The noise is dominated by shot noise and thermal noise with a noise power spectral density (PSD) of N_0. Therefore, $\boldsymbol{n_k}$ has zero mean and a variance of $\sigma_k^2 = N_0W_{\mathrm{sc}}$, where W_{sc} is the bandwidth of each subcarrier. Assuming a total intensity modulation bandwidth of W, W_{sc} can be expressed as $W_{\mathrm{sc}} = W/K$. The second term of $\boldsymbol{y}_k$ accounts for the received interference signal, where И is the set of all of the interfering BSs. Because the channel has a near-flat frequency response, the maganitude response over the whole frequency band is assumed to be unity. Clipping noise and non-linearities of the LED are not considered as these are outside the scope of this study.

III. Signal-to-Interference-Plus-Noise Ratio Assessment

A. SINR model Setup

SINR is an important metric to measure the quality of a wireless connection. Similar to the definition of SNR in an IM/DD OWC system, SINR is defined as the ratio of the received desired signal electrical power to the noise and interference electrical power. Based on (4), the SINR for the given user on subcarrier k is given as:

$$\gamma_k = \frac{P_{\mathrm{elec},0,k}G_0^2R_{\mathrm{pd}}^2}{\sum\limits_{i\in И} P_{\mathrm{elec},i,k}G_i^2R_{\mathrm{pd}}^2 + \sigma_k^2}, \quad (5)$$

where $P_{\mathrm{elec},i,k}$ denotes the electrical signal power transmitted by BS_i on subcarrier k. The conversion between the average electrical power and the average optical power obeys the following relationship in a DCO-OFDM system as [15]:

$$\frac{P_{\mathrm{opt}}^2}{P_{\mathrm{elec,AC}} + x_{\mathrm{DC}}^2} = \frac{\kappa^2}{1+\kappa^2}, \quad (6)$$

$$\kappa = x_{\mathrm{DC}}/\sqrt{P_{\mathrm{elec,AC}}}, \quad (7)$$

where $P_{\mathrm{opt}} = \mathbb{E}[\boldsymbol{x}(t)] = x_{\mathrm{DC}}$ is the average transmitted optical power in which $\mathbb{E}[\cdot]$ is the expectation operator, and $P_{\mathrm{elec,AC}} = \mathbb{E}[\sum_{k=0}^{K-1}\boldsymbol{x}_k^2(t)] = \sum_{k=0}^{K-1}\mathbb{E}[\boldsymbol{x}_k^2(t)]$ denotes the total electrical power for transmission excluding the DC-bias. After rearranging (6), it can be found that:

$$P_{\mathrm{elec,AC}} = P_{\mathrm{opt}}^2/\kappa^2. \quad (8)$$

It is assumed that an equal power allocation is conducted over the $K-2$ subcarriers that carry signals, and all BS transmitters emit the same average optical power. Then:

$$P_{\mathrm{elec},i,k} = \frac{P_{\mathrm{opt}}^2}{(K-2)\kappa^2}. \quad (9)$$

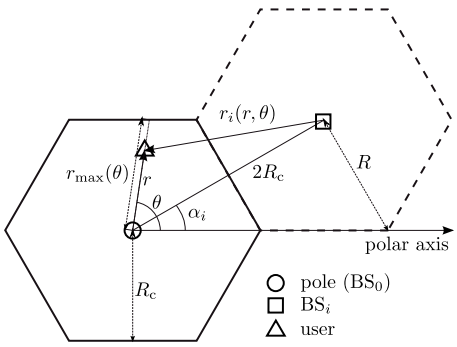

Fig. 2. Optical attocell network geometry model with a polar coordinate system.

B. SINR Statistics Analysis

In this subsection, we conduct an analysis of the statistics of the SINR based on the randomness of the user locations. It is assumed that the user location follows a uniform distribution in an optical attocell. The objective is to find the CDF of the SINR for a user. However, there are a number of variables present in (1) which are related to user location. In order to simplify the analysis, the following modification in (1) is carried out. From Fig. 1, it can be found that:

$$\cos(\phi_i) = \cos(\psi_i) = \frac{h}{d_i}, \quad (10)$$

$$d_i = \sqrt{r_i^2 + h^2}, \quad (11)$$

where r_i is the horizontal separation between BS_i and the user. Inserting (10) and (11) into (1) gives:

$$G_i = \frac{(m+1)A_{\mathrm{pd}}h^{m+1}}{2\pi}(r_i^2+h^2)^{-\frac{m+3}{2}}. \quad (12)$$

With this step, the number of variables in the light propagation model is reduced to one. By inserting (12) into (5) and by rearranging, (5) can be rewritten as:

$$\gamma_k = \frac{(r_0^2+h^2)^{-m-3}}{\sum\limits_{i\in И}(r_i^2+h^2)^{-m-3} + \Omega}, \quad (13)$$

where

$$\Omega = \frac{4\pi^2\kappa^2N_0W(K-2)}{\left((m+1)A_{\mathrm{pd}}h^{m+1}P_{\mathrm{opt}}R_{\mathrm{pd}}\right)^2K}. \quad (14)$$

TABLE I
SYSTEM PARAMETERS

Parameter	Symbol	Value
BS LED optical power	P_{opt}	10 W
vertical separation	h	2.15 m
Noise PSD	N_0	1×10^{-21} A^2/Hz
PD area	A_{pd}	1 cm^2
PD responsivity	R_{pd}	0.6 A/W
DC bias factor	κ	3

Since the observed optical attocell coverage area is rotational symmetric, it is reasonable to determine the user location with a polar coordinate system as shown in Fig. 2. The pole of the coordinate is defined at the centre of the tagged cell. The direction of the polar axis is shown in Fig. 2. The location of a user is defined by two variables r and θ. The variable r denotes the horizontal separation between user and the pole. The variable θ represents the polar angle corresponding to the user location. The location of a user in an optical attocell is confined within a hexagon. Therefore, for a user with a specified θ, the possible r should be within a in a specified region. The smallest r is intuitively zero, while the maximum possible r can be calculated as a function of θ as:

$$r_{\max}(\theta) = R_{\text{c}} / \cos\left(\theta \bmod \frac{\pi}{3} - \frac{\pi}{6}\right), \tag{15}$$

where R_{c} is defined as the distance between the pole and an edge of the optical attocell. The radius of the the cell is denoted by R, which is defined as the distance between the pole and a vertex of the cell boundary. The variables R_{c} and R satisfy the following relationship: $R_{\text{c}} = \sqrt{3}R/2$, see Fig. 2.

Furthermore, r_i in (13) can be calculated from the user location variables r and θ. Since the tagged BS is just located at the pole of the coordinate, r_0 equals r. According to the hexagonal layout of the BSs, we can find that BS_i is located at $(2R_{\text{c}}, \alpha_i)$, where

$$\alpha_i = \frac{\pi i}{3} - \frac{\pi}{6}, i = 1, 2, \ldots, 6. \tag{16}$$

By considering the triangle with vertices at the pole, the given user and the BS_i, it can be shown that r, θ and r_i are related to each other by the law of cosines as demonstrated in Fig. 2. Therefore, r_i can be calculated with the following expression:

$$r_i(r, \theta) = \sqrt{r^2 - 4R_{\text{c}} r \cos(\theta - \alpha_i) + 4R_{\text{c}}^2}. \tag{17}$$

By applying the above variable substitution, (13) can be modified to a function of the user location (r, θ) as:

$$\gamma(r, \theta) = \frac{(r^2 + h^2)^{-m-3}}{\sum_{i=1}^{6} (r_i(r, \theta)^2 + h^2)^{-m-3} + \Omega}. \tag{18}$$

In order to find the distribution of $\gamma(r, \theta)$, the statistics of r and θ should be known. The determination of the distribution of r and θ can be fomulated as a problem in geometric probability. This can be solved by evaluating the volume ratio [16]. For example, a point is uniformly distributed within a given set Ш. Set Д is defined as a subset of Ш. Then the probability that the point falls in Д can be calculated as the ratio of the volume of Д to the volume of Ш. Following this approach, the conditional probability density function (PDF) of r with a specified θ and the PDF of θ can be calculated as follows:

$$f_r(r|\theta) = \frac{2r}{r_{\max}^2(\theta)}, \tag{19}$$

$$f_\theta(\theta) = \frac{r_{\max}^2(\theta)}{4\sqrt{3}R_{\text{c}}^2}. \tag{20}$$

The conditional PDF of the SINR achieved by users located at a position with a polar angle of θ can be derived from (19) with the PDF transformation rule as:

$$f_\gamma(\gamma|\theta) = \left.\frac{f_r(r|\theta)}{\left|\frac{\partial}{\partial r}\gamma(r, \theta)\right|}\right|_{r=\Gamma(\hat{\gamma}|\theta)}, \tag{21}$$

where $\Gamma(\hat{\gamma}|\theta)$ is the inverse function of (18) with respect to the variable r in the interval $\hat{\gamma} \in [\gamma(r_{\max}(\theta), \theta), \gamma(0, \theta)]$. Using (20) and (21), the joint PDF of γ and θ can be calculated by adopting Bayes' theorem as:

$$f_{\gamma,\theta}(\gamma, \theta) = f_\gamma(\gamma|\theta) f_\theta(\theta). \tag{22}$$

Furthermore, by integrating (22) from 0 to 2π, the PDF of γ can be derived as:

$$f_\gamma(\gamma) = \int_0^{2\pi} f_{\gamma,\theta}(\gamma, \theta)\, \mathrm{d}\theta. \tag{23}$$

Finally, the CDF of the SINR for a user can be calculated as:

$$F_\gamma(\hat{\gamma}) = \int_{\hat{\gamma}}^{\infty} f_\gamma(\gamma)\, \mathrm{d}\gamma. \tag{24}$$

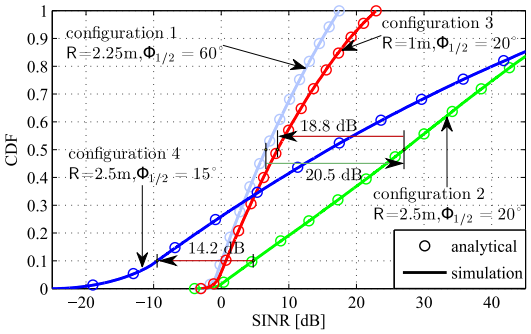

Fig. 3. Cumulative distribution function of the SINR per subcarrier with (R = 2.25 m, $\Phi_{1/2} = 60°$), (R = 2.5 m, $\Phi_{1/2} = 20°$), (R = 1 m, $\Phi_{1/2} = 20°$) and (R = 2.5 m, $\Phi_{1/2} = 15°$).

Fig. 3 shows the SINR CDF numerical results of the analytical approach for optical attocells with different configurations. The system parameters are listed in Table. I. For each optical attocell configuration, a Monte Carlo simulation of the system is also carried out. The good agreement between the Monte Carlo simulation results and the numerical results validates the accuracy of the presented analytical approach. In order to

demonstrate the effects of varying R and $\Phi_{1/2}$, systems with four specified configurations are presented.

A typical R of 2.25 m and a general Lambertian source transmitter ($\Phi_{1/2} = 60°$) are used in the configuration 1 system, which achieves a median SINR of only 6.6 dB. By adjusting R and $\Phi_{1/2}$, the median SINR achieved by a system with the configuration 2 ($R = 2.5$ m, $\Phi_{1/2} = 20°$) increases to 27.1 dB. This shows a 20.5 dB improvement relative to the configuration 1. Using configuration 2 as a baseline, configuration 3 and 4 systems are demonstrated to see the effect of changing the value of R or $\Phi_{1/2}$, respectively. For configuration 3 ($R = 1$ m, $\Phi_{1/2} = 20°$), the decrease of R causes a significant drop of 18.8 dB in median SINR relative to the configuration 2 system. In an RF cellular network, a user in the cell centre always has an overwhelmingly shorter distance to the tagged BS than the distance to any interfering BS regardless of the cell radius. However, in an optical attocell, this feature of proximity to the tagged BS for a cell centre user is not so prominent. This is because the transmission distance in an optical attocell network is determined not only by the horizontal separation between a user and a BS, but also is determined by the vertical separation h. Therefore, in the case of which h is significant relative to the horizontal separations, the users may experience interference power which is as high as the desired signal power. For configuration 4 ($R = 2.5$ m, $\Phi_{1/2} = 15°$), the further dcrease of $\Phi_{1/2}$ causes a significant drop of 14.2 dB in the guaranteed SINR (at the 10th percentile) compared to the configuration 2 system. The variable $\Phi_{1/2}$ determines m, which controls the radiation pattern of the LED, thereby controlling the optical power spatial distribution at the observed horizontal surface. For a specified R, $\Phi_{1/2}$ should be carefully adjusted in order to guarantee enough power to achieve full coverage in the cell and at the same time not to introduce too much interference in adjacent cells. In the system with configuration 4, $\Phi_{1/2} = 15°$ is too small for edge users in the optical attocell to have sufficient signal power to overcome the noise level, which causes the poor system performance.

The parameters A_{pd}, P_{opt}, κ and R_{pd} determine the effect of receiver noise only, since all of these parameters only exist in the denominator of the noise term Ω in (18). As long as practical constraints permit, these parameters should be as large as possible to minimise the effect of the receiver noise. In case the performance is limited by interference, changing these parameters shows a minor impact on the user performance. The configuration of h is complicated and it is typically determined by the indoor environment geometry and the height of the user equipment. Therefore, its impact on the user performance is outside the scope of this work, but it will be considered in future work.

IV. Average Spectral Efficiency Assessment

The wireless downlink capacity of the optical attocell network is also considered and studied in this work. A simple estimation can be conducted using the Shannon-Hartley theorem to calculate the spectral efficiency of the optical attocell network. Since the optical attocell network is based on DCO-OFDM in the downlink, the spectral efficiency can be expressed as [4]:

$$\rho(r,\theta) = \frac{K-2}{2K}\log_2\left(1+\gamma(r,\theta)\right). \tag{25}$$

Accordingly, the average spectral efficiency is calculated as:

$$\mathbb{E}[\rho] = \int_0^{2\pi}\left(\int_0^{r_{\max}(\theta)}\rho(r,\theta)f_r(r|\theta)\mathrm{d}r\right)f_{\boldsymbol{\theta}}(\theta)\mathrm{d}\theta. \tag{26}$$

The results in III-B show that the appropriate configurations of R and $\Phi_{1/2}$ are interdependent. Therefore, instead of controlling $\Phi_{1/2}$, a parameter δ, which characterises the relationship between R and $\Phi_{1/2}$, can be manipulated in order to evaluate its effects on the average spectral efficiency. The general function of δ is to achieve coarse control of the spatial distribution of the received optical power in an optical attocell. It is realised by forcing the received optical power at a specified region of the optical attocell to be half of the power that is received at the cell centre. This concept is illustrated in Fig. 4. The parameter δ is defined as a real number between 0 and 1. At the same time, α_1 and α_2 are defined as two points with $r = 0$ and $r = \delta R$, respectively. The polar angle of the point is independent of the corresponding received optical power. For a specified δ, m needs to be adjusted to fulfil the following criterion:

$$P_{\mathrm{opt}}G_{s,\alpha_1} = 2P_{\mathrm{opt}}G_{s,\alpha_2}. \tag{27}$$

By inserting (12) in (27), m can be determined as a function of δ as follows:

$$m = 2/\log_2\left(\left(\frac{\delta R}{h}\right)^2+1\right)-3. \tag{28}$$

The impact of the configuration of δ and R on the achievable average spectral efficiency is shown in Fig. 5. The relationship between the average spectral efficiency and δ for R=1 m, 1.5 m, 2 m and 2.5 m is demonstrated. The other system parameters used in this study are listed in Table. I. The results show that as δ increases from 0.2, the average spectral

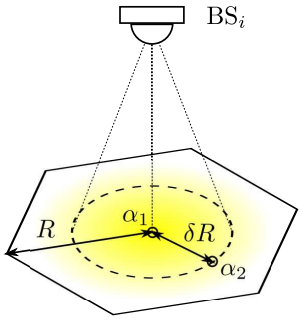

Fig. 4. α_1 is located at the pole, α_2 has a radius of δR. $\Phi_{1/2}$ is configured to make the received optical power at α_1 two times higher than the received optical power at α_2.

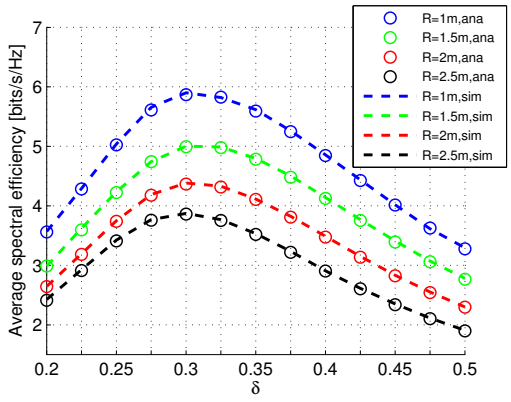

Fig. 5. Average spectral efficiency versus δ for R=1 m, 1.5 m, 2 m, 2.5 m. The notation 'ana' denotes the analytical result, while 'sim' denotes the simulated result.

efficiency also increases initially. However, when δ approaches a value of around 0.3, the average spectral efficiency reaches a peak value. With a further increase in δ, the average spectral efficiency decreases. All of the four cases for different values of R show this same trend. It is interesting to note that with a fixed δ, the average spectral efficiency of the system is higher for smaller values of R, which is a desired outcome as it favours small cell deployment. Among the demonstrated systems, the system for $R = 1$ m offers the highest average spectral efficiency of 5.9 bits/s/Hz at $\delta = 0.3$. These results indicate a general way to configure R and $\Phi_{1/2}$ with a given setting for the other parameters. This can be achieved by initially setting R to be as small as possible. Then, by finding the value of δ for which the optical attocell network achieves the highest average spectral efficiency. Fig. 5 also shows that the optimal value of δ varies little with R. Finally, based on the optimal δ, the corresponding $\Phi_{1/2}$ can be evaluated using (28).

Although the described method for optimising R and $\Phi_{1/2}$ can lead to high average spectral efficiency, there are many practical factors which further limit these parameters. For example, R cannot be too small, since this would lead to excessive handover requirements for moving users and would lead to massive optical hardware installations. Moreover, a LED with small $\Phi_{1/2}$ is undesired for illumination purposes.

V. Conclusion

This paper proposed a framework for the system-level analysis of the downlink transmission in a DCO-OFDM-based optical attocell network. An analysis for a LOS link in terms of SINR and average spectral efficiency was proposed. The impact of an optical attocell radius R and the impact of the LED half-power semi-angle were analysed in terms of achievable SINR and average spectral efficiency for a downlink transmission. The results showed that these parameters play key roles in achieving high SINR and spectral efficiency. Guidelines for the configuration of R and $\Phi_{1/2}$ to achieve high average spectral efficiency were provided. An optical attocell network achieving an average spectral efficiency of 5.9 bits/s/Hz was demonstrated. However, the impact of the variations in the vertical separation between a BS and a user and the impact of the variations in the receiver orientation were not considered in this study. In addition, the effects of shadowing and link blockage were omitted. These issues will be considered in future work.

Acknowledgement

Professor Haas acknowledges support from the Engineering and Physical Sciences Research Council (EPSRC) under Established Career Fellowship grant EP/K008757/1.

References

[1] H. Elgala, R. Mesleh, and H. Haas, "Indoor Optical Wireless Communication: Potential and State-of-the-Art," *IEEE Commun. Mag.*, vol. 49, no. 9, pp. 56–62, Sep. 2011, ISSN: 0163-6804.

[2] A. Jovicic, J. Li, and T. Richardson, "Visible Light Communication: Opportunities, Challenges and the Path to Market," *IEEE Commun. Mag.*, vol. 51, pp. 26–32, Dec. 2013.

[3] M. Alouini and A. Goldsmith, "Area Spectral Efficiency of Cellular Mobile Radio Systems," *IEEE Trans. Veh. Technol.*, vol. 48, no. 4, pp. 1047–1066, Jul. 1999.

[4] S. Dimitrov and H. Haas, "Information Rate of OFDM-Based Optical Wireless Communication Systems with Nonlinear Distortion," *J. Lightw. Technol.*, vol. 31, no. 6, pp. 918–929, Mar. 15 2013.

[5] D. Tsonev, S. Sinanovic, and H. Haas, "Complete Modeling of Nonlinear Distortion in OFDM-based Optical Wireless Communication," *J. Lightw. Technol.*, vol. 31, no. 18, pp. 3064–3076, Sep. 15 2013.

[6] H. Haas, "High-speed wireless networking using visible light," SPIE Newsroom, Apr.19 2013.

[7] D. Tsonev and H. Haas, "Avoiding Spectral Efficiency Loss in Unipolar OFDM for Optical Wireless Communication," in *Proc. of the Int. Conf. on Commun. (ICC)*, Sydney Australia, Jun. 10–14 2014.

[8] G. W. Marsh and J. M. Kahn, "Channel Reuse Strategies for Indoor Infrared Wireless Communications," *IEEE Trans. Commun.*, vol. 45, no. 10, pp. 1280–1290, Oct. 1997.

[9] D. O'Brien and M. Katz, "Optical Wireless Communications within Fourth-Generation Wireless Systems [Invited]," *J. Opt. Netw.*, vol. 4, no. 6, pp. 312–322, Jun. 2005.

[10] D. Wu, Z. Ghassemlooy, H. Le-Minh, S. Rajbhandari, and Y. Kavian, "Power Distribution and Q-factor Analysis of Diffuse Cellular Indoor Visible Light Communication Systems," in *16th Eur. Conf. Netw. and Opt. Commun. (NOC 2011)*, Newcastle upon Tyne, UK, 20–22 Jul. 2011, pp. 28–31.

[11] J. Gozalvez, "Heterogeneous Wireless Networks [Mobile Radio]," *IEEE Veh. Technol. Mag.*, vol. 6, no. 2, pp. 9–13, Jun. 2011.

[12] J. Grubor, S. Randel, K.-D. Langer, and J. Walewski, "Bandwidth-efficient Indoor Optical Wireless Communications with White Light-Emitting Diodes," in *6th International Symposium on Communication Systems, Networks and Digital Signal Processing*, Graz, Jul., 25 2008, pp. 165–169.

[13] J. M. Kahn and J. R. Barry, "Wireless Infrared Communications," *Proc. IEEE*, vol. 85, no. 2, pp. 265–298, Feb. 1997.

[14] H. Elgala, R. Mesleh, and H. Haas, "Practical Considerations for Indoor Wireless Optical System Implementation Using OFDM," in *Proc. IEEE 10th Int. Conf. Telecommun. (ConTel)*, Zagreb, Croatia, Jun. 8–10 2009, pp. 25–29.

[15] J. Armstrong and B. J. C. Schmidt, "Comparison of Asymmetrically Clipped Optical OFDM and DC-Biased Optical OFDM in AWGN," *IEEE Commun. Lett.*, vol. 12, no. 5, pp. 343–345, May 2008.

[16] D. Stoyan, W. S. Kendall, and J. Mecke, *Stochastic Geometry and its Applications*, 2nd ed. John Wiley and Sons, 1995.

Downlink SINR Statistics in OFDM-Based Optical Attocell Networks with a Poisson Point Process Network Model

Cheng Chen, Dushyantha Basnayaka and Harald Haas
Li-Fi Research and Development Centre
Institute for Digital Communications
The University of Edinburgh EH9 3JL, Edinburgh, UK
{cheng.chen, d.basnayaka, h.haas}@ed.ac.uk

***Abstract*—In this paper, the downlink signal-to-interference-plus-noise ratio (SINR) statistics are analysed in a direct current-biased optical orthogonal frequency division multiplexing (DCO-OFDM) based optical attocell network with a Poisson point process (PPP) cell deployment. An optical attocell system utilises existing lighting fixtures in an indoor environment to function as a small-cell cellular network. It uses each luminary as a base station (BS) to serve multiple nearby mobile users. Similar to a conventional radio frequency (RF) cellular system, the grid cell deployment is restricted by many practical issues in an optical attocell network. Therefore the performance of the system with PPP cell deployment is considered in this study in order to identify a lower bound for practical attocell networks with irregular cell deployment. An analytical framework is presented and compared with the computer simulations. Also the SINR statistics with different cell deployments are compared and discussed.**

***Index Terms*—cellular network, optical attocell network, Poisson point process, visible light communication.**

I. Introduction

With the development of wireless communication technology and emergence of advanced mobile devices, there is a significant increase in data traffic in wireless networks. The radio frequency (RF) spectral resources is becoming insufficient to meet the future demand. Researchers aim to solve this 'spectral crisis' in two ways. One of the methods is to explore new spectral resources for wireless transmission. The commonly considered frequency ranges are at the 60 GHz and optical region. In particular, visible light communication (VLC) has been researched because of three main characteristics [1]: i) using visible light for wireless transmission is licence-free; ii) it reuses the energy for lighting to provide an extra data transmission function, which means it is energy-efficient. iii) visible light cannot penetrate opaque objects. This property means that VLC offers security benefits. Also it intuitively avoids co-channel interference (CCI) between VLC systems in adjacent rooms. In this study, light emitting diodes (LEDs) and photodiodes (PDs) are used as the core components of the VLC transceivers, and intensity modulation/direct detection (IM/DD) techniques are used. The other method to deal with the challenge of the limited spectrum is to improve the usage efficiency of the existing spectral resource, such as adaptive resource allocation and cognitive radio. In particular, reducing the reuse distance of the spectrum resource offers significant improvements in terms of area spectral efficiency [2].

The concept of optical attocell network combines the methods mentioned above. It uses the licence-free visible light frequency band as the data transmission medium and an extremely small spatial reuse distance [3]. In a large indoor environment, typically many lighting devices are installed. This gives a unique opportunity to set up a cellular system in a single room, and this is termed an optical attocell network. An optical attocell network uses each luminary as a base station (BS) to serve multiple nearby users. This cellular system achieves bi-directional communication links and supports handover for moving users. The main limiting factors for the performance of an optical attocell network are the modulation bandwidth and the CCI between users in adjacent cells. To solve the bandwidth issue, wide-band LEDs have been researched and manufactured. A gallium nitride micro LED with a much wider bandwidth than typical commercially available white LED was considered in [4]. In addition, bandwidth-efficient modulation schemes were proposed to maximise the achievable throughput. In [5], [6], a data rate of 513 Mbps and 1 Gbps were achieved experimentally by using rate-adaptive discrete multi-tone modulation with white LEDs, respectively. In [4], a data rate of 3 Gbps was achieved by using a similar modulation scheme with a micro LED. Another energy efficient orthogonal frequency-division multiplexing (OFDM) scheme was proposed in [7], termed enhanced unipolar OFDM (eU-OFDM). It can enable energy and spectrum efficient communication in scenarios where lighting is not required. CCI degrades the signal quality received by users, especially for cell edge users. Several interference mitigation techniques were considered in optical attocell networks such as busy-burst signalling [8] and fractional frequency reuse [9].

In a previous study, a semi-analytical approach was carried out to evaluate the downlink transmission performance in an optical attocell network with hexagonal cell deployment [10]. Such a hexagonal grid cell deployment is highly idealised in RF cellular systems, which is considered to be obsoleted in [11]. Instead, uneven cell deployment is more common due to

978-1-4799-5952-5/15/$31.00 ©2015 IEEE

the difference in transmission power, mobile user density and some geometric constraints such as obstacles for placing BS in an ideal position. Therefore, Poisson point process (PPP) cell deployment was introduced to analyse the performance of cellular networks. The results show that the performance of PPP model is a lower bound for a practical cellular system. In addition, by considering the PPP cell deployment allows tools from stochastic geometry to be used, which makes the performance of the cellular network more tractable. The same issue is also true for an optical attocell system. In an optical attocell network, the hexagonal grid cell deployment is possible, but unlikely due to wiring complexity, uneven lighting requirements and aesthetic quality. Therefore, in this study, a worst case random cell deployment with PPP is considered in an optical attocell network. An analytical framework for the downlink signal-to-interference-plus-noise ratio (SINR) statistics with PPP cell deployment is presented. In addition, the results of the systems with different cell deployments are compared to show the significance of the results with PPP cell deployment.

The remainder of this paper is organised as follows: the downlink system model in an optical attocell network is presented in Section II. The PPP cell deployment and the analytical SINR statistical results are introduced in Section III. The performance of the systems with different cell deployments are compared in Section IV. Conclusions are given in Section V.

II. Downlink System Model

A. Propagation Model

In this study, a room with large number of luminaries are considered. Each luminary is treated as a point source. It is assumed that the PD detector installed on the user mobile device is facing upward. A full receiver FOV of 180° is assumed as it can reflect the performance in the worst case CCI. In addition, a wide FOV reduces the chance that the serving BS is outside the FOV of the desired receiver. The existence of line-of-sight (LOS) path is very likely due to the existence of multiple nearby accessible BSs. Therefore, the LOS channel direct current (DC) gain is used as the path loss model [12]. Some experiments show that reliable VLC connection without LOS path is also achievable [13], which implies that the optical attocell cellular system is not just a LOS system. Considering the i^{th} BS and a user of interest, the channel DC gain between them is calculated as:

$$G_i = \frac{(m+1)A_{\text{pd}}}{2\pi d_i^2}\cos^m(\phi_i)\cos(\psi_i), \tag{1}$$

where $i = 0, 1, \cdots$; A_{pd} is the physical area of the PD; d_i represents the Euclidean distance between the i^{th} BS and the user; ϕ_i is the angle of radiance from the i^{th} BS; ψ_i is the angle of incidence to the user; and m denotes the Lambertian emission order, which is related to the LED half-power semi-angle by $m = -\ln(2)/\ln(\cos(\Phi_{1/2}))$. The LED half-power semi-angle $\Phi_{1/2}$ indicates the angle of radiance at which the emitted optical power is half of that emitted with $\phi_i = 0$. In this study, a fixed vertical separation h between BSs and the user mobile device is assumed. The geometry of the above model is illustrated in Fig. 1, which also shows the following relationships: $\cos(\phi) = \cos(\psi) = \frac{h}{d_i}$ and $d_i = \sqrt{r_i^2 + h^2}$, where r_i is the horizontal separation between the i^{th} BS and the user. Therefore, expression (1) can be converted to a function of r_i as follows:

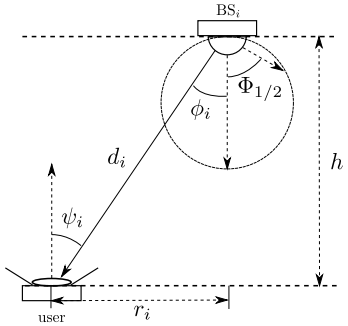

Fig. 1. LOS light propagation geometry.

$$G_i(r_i) = \frac{(m+1)A_{\text{pd}}h^{m+1}}{2\pi\left(r_i^2 + h^2\right)^{\frac{m+3}{2}}}. \tag{2}$$

Since the detector area is much larger than the wavelength, small scale fading does not exist in an IM/DD VLC system. Shadowing and the blockage issues are not considered in the channel model in this study.

B. DCO-OFDM Transmission

In an optical attocell system, a strong LOS connection between a BS and a user is likely to be established as each BS only covers the users close to it. Consequently, the multi-path effect due to wall reflection is minor [14]. In addition, OFDM is used in this system, which can eliminate the inter-symbol interference (ISI) caused by the multi-path effect. This offers a near-flat frequency response of the wireless channel. Therefore, the multi-path effect due to wall reflection is omitted in this study and the magnitude response over the whole frequency band is assumed to be unity. Among several optical OFDM schemes, DC-biased optical (DCO)-OFDM achieves a high spectral efficiency. Therefore, it is used in the optical attocell system to maximise the achievable data rate. Typically, in order to overcome the distortion of the clipping noise, a high optical power is required in a DCO-OFDM system. In this study, it is assumed that both illumination and communication functions are provided by the optical attocell system, which means the optical power for downlink communication is high [3]. It has been shown that a signal-to-noise ratio (SNR) up to 70 dB is achievable in a single cell deployment with such high output optical power [15]. At the transmitter side of an OFDM system, a frequency domain symbol sequence with K quadrature amplitude modulation (QAM) data symbols are defined as: $X = [X_0\ X_1\ X_2\ \cdots\ X_{K-1}]$. An IM/DD

system requires the time-domain OFDM signal to be real and unipolar. In a DCO-OFDM system, $X_k = X^*_{K-k}$ and $X_0 = X_{K/2} = 0$ are required to ensure that the transmitted signal is real [16], which is termed as Hermitian symmetry. Here $[\cdot]^*$ is the complex conjugate operation. Consequently, only $K = K/2 - 1$ symbols carry information bits. On the other hand, an unipolar signal is achieved by adding a DC-bias. After the K-point inverse discrete Fourier transform (IDFT) operation and the addition of the DC-bias, the time domain OFDM symbol at time slot t can be calculated as:

$$x(t) = x_{\mathrm{DC}} + \sum_{k=0}^{K-1} \frac{X_k \mathrm{e}^{\left(\frac{2\pi j k t}{K}\right)}}{\sqrt{K}}, \; t = 0, 1, \cdots, K-1, \quad (3)$$

where x_{DC} denotes the DC-bias component; and j represents the imaginary unit. After the addition of DC-bias, the remaining negative samples are set to zero. Since it is assumed that the ISI caused by reflection is negligible, the required cyclic-prefix (CP) length would in turn be short in an optical attocell network. Therefore, the penalty of adding a CP is also omitted in this study. Assume that the sampling and the synchronization are perfect, the time-domain signal received by the user device at time slot t can be expressed as:

$$y(t) = x_0(t) G_0 R_{\mathrm{pd}} + \sum_{i \in \mathit{И}} x_i(t) G_i R_{\mathrm{pd}} + n(t), \quad (4)$$

where $x_i(t)$ denotes the transmitted signal from the i_{th} BS at time slot t. In the case of $i = 0$, x_0 represents the desired transmitted signal for the user of interest; R_{pd} denotes the responsivity of the PD; and $n(t)$ represents the receiver noise sample at time slot t. The second term of $y(t)$ denotes the received interference signal, where $\mathit{И}$ is the set of all the interfering BSs. The receiver noise is modelled as an Additive White Gaussian Noise (AWGN) with a noise power spectral density (PSD) of N_0. Since the 0^{th} subcarrier and the $K/2^{\mathrm{th}}$ subcarrier are not used, $n(t)$ is drawn from a Gaussian distribution with zero mean and variance of $\sigma^2 = \frac{K-2}{K} N_0 W$, where W is the total available intensity modulation bandwidth. By using appropriate DC-bias level, clipping noise can be minimised to a level that causes negligible distortion in the transmission [17]. Non-linearity effects of the LED can be effectively mitigated by using pre-distortion techniques [18]. Therefore, it is trivial to consider these minor effects in this study.

C. Signal-to-Interference-plus-Noise Ratio

SINR is an important metric to evaluate the connection quality and the transmission capacity in a cellular system. Based on the user received signal (4), the downlink SINR can be calculated by:

$$\gamma = \frac{P_{\mathrm{elec},0} G_0^2 R_{\mathrm{pd}}^2}{\sum\limits_{i \in \mathit{И}} P_{\mathrm{elec},i} G_i^2 R_{\mathrm{pd}}^2 + \sigma^2}, \quad (5)$$

where $P_{\mathrm{elec},i}$ denotes the electrical signal power transmitted by BS_i excluding the DC component, which is calculated by $P_{\mathrm{elec},i} = \mathbb{E}\left[x_i^2(t)\right]$, where $\mathbb{E}[\cdot]$ represents the expectation

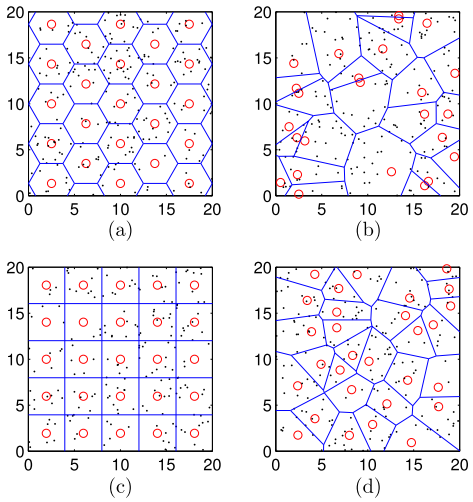

Fig. 2. (a) Hexagonal cell deployment. (b) PPP cell deployment. (c) square cell deployment. (d) HCPP cell deployment. The circles in the figure represent the positions of the BSs, while the dots represent the positions of the users.

operation. In this study, no power control is considered, and a fixed electrical power for each BS is considered, which means $P_{\mathrm{elec},0} = P_{\mathrm{elec},1} = \cdots = P_{\mathrm{elec}}$. The cases with different electrical power for each BS can also be handled by the analysis described in this paper, but it is omitted here for simplicity. The relationship between the average electrical power and the average optical power in a DCO-OFDM system can be given as [16]:

$$\frac{P_{\mathrm{opt}}^2}{P_{\mathrm{elec}} + x_{\mathrm{DC}}^2} = \frac{\eta^2}{1 + \eta^2}, \quad (6)$$

$$\eta = x_{\mathrm{DC}} / \sqrt{P_{\mathrm{elec}}}, \quad (7)$$

where η represents a DC-bias factor, which determines the level of DC-bias depth. Increasing η would decrease the clipping noise, but also decrease the amount of available electrical power for a certain amount of average optical power. After rearranging (6), it can be found that:

$$P_{\mathrm{elec}} = P_{\mathrm{opt}}^2 / \eta^2. \quad (8)$$

By inserting (8) and (2) into (5), the downlink SINR received by the user can be rewritten as:

$$\gamma = \frac{\left(r_0^2 + h^2\right)^{-m-3}}{\sum\limits_{i \in \mathit{И}} \left(r_i^2 + h^2\right)^{-m-3} + \Omega} = \frac{S}{\Upsilon + \Omega}, \quad (9)$$

$$\Omega = \frac{4\pi^2 (K-2) N_0 W \eta^2}{K P_{\mathrm{opt}}^2 (m+1)^2 A_{\mathrm{pd}}^2 R_{\mathrm{pd}}^2 h^{2m+2}}, \quad (10)$$

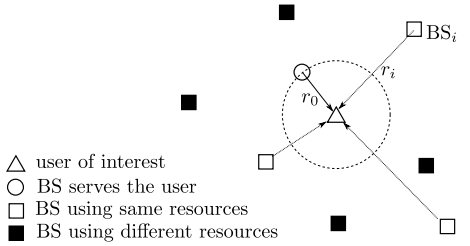

Fig. 3. PPP network deployment. Choose the closest BS as the serving BS. Part of the remaining BSs causes interference to the user according the reuse factor Δ.

where $S = \left(r_0^2 + h^2\right)^{-m-3}$ denotes the effect of desired signal power; $\Upsilon = \sum_{i \in \mathit{И}} \left(r_i^2 + h^2\right)^{-m-3}$ denotes the effect of interfering signal power; and Ω denotes the effect of receiver noise variance.

III. Poisson Point Process Network Model and SINR Statistics

The optical attocell cellular network model considered in this study is similar to that presented in [11]. The two-dimensional (2-D) positions of both the BS and the mobile user are arranged according to a stationary homogeneous Poisson point process with a fixed density. Each user is associated with the closest BS to it. This results in coverage areas of BSs following a Voronoi tessellation on the 2-D plane. The cell deployment is shown in Fig. 2 (b).

Without loss of generality, the network model is simplified as follows. The desired user is assumed to be located at the origin. BSs are randomly distributed around the user based on a PPP of density Λ. The network extends to infinity in all directions. Note that CCI is the main concern of this study. Thus, it is important to consider the users experiencing the worst case CCI. Since interference is higher with an increase of the neighbouring BSs, an infinite network offers this worst case CCI condition. The first closest BS to the user (r_0 away from the user) serves the user. A cellular system with a reuse factor of Δ divides the available transmission resource into Δ equal blocks. In a grid network, these resource blocks are assigned to cells with a reuse pattern that avoids adjacent cells using the same resource, thereby mitigating the CCI. However, such a reuse pattern cannot be used in a PPP network as the BS locations are independent from each other. Therefore, each cell randomly selects one of the the Δ resource blocks for transmission regardless of the location of these cells. This is equivalent to amending the density of the interfering BSs to be $\frac{\Lambda}{\Delta}$. The simplified cellular network model is shown in Fig. 3.

Next, the main results of the SINR statistics achieved by the system with PPP cell deployment is presented. Firstly, the calculation of the probability density function (PDF) of interference Υ conditioning on r_0, $f_\Upsilon(\upsilon|r_0)$, is considered. However, the exact expression of $f_\Upsilon(\upsilon|r_0)$ is difficult to calculate due to the mathematical complexity. Alternatively, an expansion based on the Gram-Charlier series and Laguerre polynomials proposed in [19] is used to approximate the distribution. In this approximation, the PDF is expanded as a sum of gamma densities, which can be calculated if the row moments of the distribution are known. Therefore, the characteristic function $\varphi_{\Upsilon|r_0}(\omega) = \mathbb{E}\left[\mathrm{e}^{j\omega\Upsilon}|r_0\right]$ is evaluated. Based on the relationship between the characteristic function and the cumulant generating function, the expression of the n^{th} cumulant of Υ conditioning on r_0 can be calculated as:

$$\kappa_n(\Upsilon|r_0) = \frac{\Lambda\pi\left(r_0^2 + h^2\right)^{1-n(m+3)}}{\Delta(n(m+3)-1)}. \tag{11}$$

Then the corresponding n^{th} row moment can be calculated recursively by the following relationship as:

$$\mu_n = \begin{cases} 1 & : n = 0 \\ \kappa_1 & : n = 1 \\ \kappa_n + \sum_{l=1}^{n-1} \binom{n-1}{l-1} \kappa_l \mu_{n-l} & : n \geq 2 \end{cases}. \tag{12}$$

Since the row moments are known, the approximated expression for $f_\Upsilon(\upsilon|r_0)$ can be calculated. Then the SINR CDF can be calculated using the following equation:

$$\begin{aligned} \mathbb{P}[\gamma < T] &= \mathbb{P}\left[\Upsilon > S/T - \Omega\right] \\ &= \int_0^\infty \int_{\frac{S}{T}-\Omega}^\infty f_{r_0}(b) f_\Upsilon(\upsilon|r_0) \mathrm{d}\upsilon \mathrm{d}b, \end{aligned} \tag{13}$$

where $f_{r_0}(b) = 2\pi\Lambda b \mathrm{e}^{-\Lambda\pi b^2}$ is the PDF of the distance between the origin and the nearest node [20]. The final result of $\mathbb{P}[\gamma < T]$ is concluded in (14). The detailed derivation will be presented in a future publication.

The accuracy of (14) is evaluated by comparing its results to the corresponding Monte Carlo simulations. The main system parameters are listed in Table I. In the results, three systems with different configurations are considered, as shown in Fig. 4. Although the cell does not have a regular coverage area for the system with the PPP cell deployment, it is important to make sure that systems with different cell deployments have the same BS density in order to achieve a fair comparison. Assuming the system with a hexagonal grid cellular model has a cell radius of R, the corresponding PPP network should have a BS density of $\Lambda = \frac{1}{A_{\text{cell}}} = \frac{2\sqrt{3}}{9R^2}$. It can be found that the numerical results of the analysis calculated using (14) generally matches the corresponding Monte Carlo simulation, except for a minor mismatch at the high SINR region. This

TABLE I
System Parameters

Parameter	Symbol	Value
BS LED optical power	P_{opt}	10 W
vertical separation	h	2.25 m
Noise PSD	N_0	1×10^{-20} A^2/Hz
PD area	A_{pd}	1 cm^2
PD responsivity	R_{pd}	0.6 A/W
DC-bias factor	η	3
number of subcarriers	K	512

$$\mathbb{P}[\gamma < T] = \int_0^{\infty} \frac{2\pi\Lambda b}{\mathrm{e}^{\Lambda\pi b^2}} \sum_{n=0}^{\infty} \left(\frac{\beta^{\alpha} \sum_{l_1=0}^{n} C_{l_1}^{n} \mu_{l_1}(\Upsilon)}{n!\Gamma(\alpha+n)} \right) \left(\sum_{l_2=0}^{n} \frac{C_{l_2}^{n} \Gamma\left(l_2+\alpha, \beta\left(1/T\left(b^2+h^2\right)^{m+3} - \Omega\right)\right)}{\beta^{l_2+\alpha}} \right) \mathrm{d}b, \tag{14}$$

$$\beta = \frac{(2m+5)\left(b^2+h^2\right)^{m+3}}{m+2}, \ \alpha = \frac{\Lambda\pi(2m+5)\left(b^2+h^2\right)}{\Delta(m+2)^2}, C_l^n = \binom{n}{l}(-1)^{n-l}\beta^l S_l^n, \ S_l^n = \begin{cases} 1 & : l > n-1 \\ \prod_{\iota=l}^{n-1}(\alpha+\iota) & : l \le n-1 \end{cases}.$$

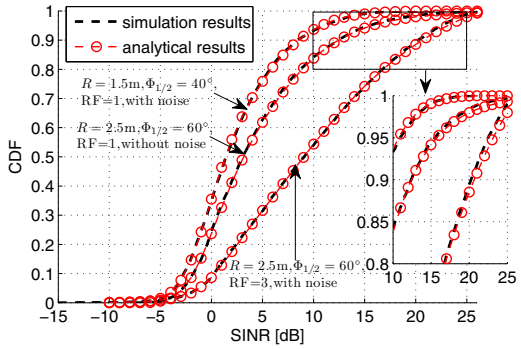

Fig. 4. The analytical and simulated results of the CDF of the downlink transmission SINR achieved by PPP networks.

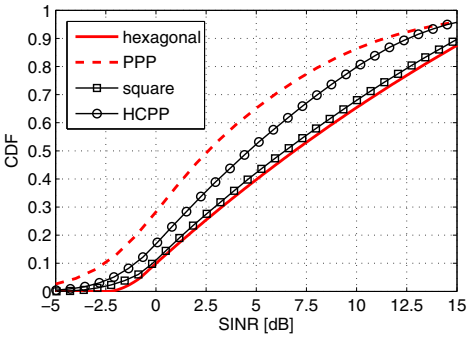

Fig. 5. The SINR statistics of systems with PPP, hexagonal, square and HCPP cell deployments. The half-power semi-angle $\Phi_{1/2} = 60°$ and the reuse factor $\Delta = 1$. The BS station density $\Lambda = 0.062$ BS/m^2 which corresponds to $R = 2.5$ m in the case of hexagonal network. In the case of HCPP, the protection distance $c = 2$ m.

mismatch is caused by the approximation for $f_{\Upsilon}(\upsilon|r_0)$ which uses the expansion introduced in [19]. The mismatch becomes obvious when the overall interference level is very low. Therefore, the best match can be observed for the system with $R = 1.5$ m, $\Phi_{1/2} = 40°$, $\Delta = 1$ and noise distortion. This is because, the noise variance is much higher than the interference in the high SINR region. In another case with $R = 2.5$ m, $\Phi_{1/2} = 60°$, $\Delta = 1$ and without noise distortion, the differences between analysis and simulation in the high SINR region becomes significant due to the absence of noise distortion. In the case with $R = 2.5$ m, $\Phi_{1/2} = 60°$, $\Delta = 3$ and noise distortion, the interference level is lower relative to the cases with $\Delta = 1$. Consequently, the differences become even greater despite the presence of noise. However, generally the distribution at low SINR region is of higher importance. Thus, it is still valid to consider (14) to be an accurate result.

IV. SINR Statistics Comparison

For a system with a hexagonal cell deployment, the locations of BSs are fully correlated, which guarantees a minimum distance between the desired user and the interfering BSs, as shown in Fig. 2 (a). One of the fundamental characteristics of light propagation from an optical source is that the received signal power is constant along a circle centred at the source. The hexagon shape provides the best approximation to this circle compared to square or triangle. Therefore, CCI is minimised in a hexagonal network. In contrast, the locations of BSs are completely uncorrelated in a PPP network as shown in Fig. 2 (b). In the worst case, BSs are extremely close to each other, which causes significant CCI. Thus, similar to [11], we expect to use the performance of the system with the hexagonal (PPP) cell deployment as an upper (lower) bound of the practical system performance. In order to demonstrate this expectation, systems with these two cell deployments are compared to the systems with the cell deployments that are likely to be used in practice.

A. Square Network

The first potential cell deployment in practice considered here is the square lattice cellular model, in which BSs are placed on a square lattice as shown in Fig. 2 (c). This arrangement is common in indoor lighting network deployment due to several advantages, which include design simplicity, providing good illumination uniformity and compliance to the shape of a room.

In the square network, the cell size is controlled by a parameter L which is defined as the distance between the two closest BSs. In order to have a fair comparison, the density of the BSs should be the same as the case with hexagonal network and PPP network. This requires: $L = \sqrt{A_{\text{cell}}} \approx 1.61R$.

B. Hard-Core Point Process Network

In some cases, the room may not need uniform illumination. For example, illumination is enhanced in the task areas[1], while

[1]Area within which the visual task is carried out.

less lighting is required in the remaining areas. This fact would introduce an uneven lighting network deployment. In this case, the position of BSs may be unregulated, but it is unlikely to place two luminaries extremely close to each other. Therefore, the Matérn type I hard-core point process (HCPP) is considered to model the BSs position, as shown in Fig. 2 (d).

The HCPP is based on a PPP with the condition that the shortest distance between any two nodes is greater than a specified threshold c. To generate a set of nodes according to a HCPP, a set of nodes following a PPP with a density of Λ_0 is necessary. Then each point is marked with a random number. A dependent thinning process is carried out for each marked node as follows: retain the marked node if there is no other node within the circle centred at the marked node with a radius of c. After the thinning, the HCPP nodes density would be reduced. Therefore, to generate a HCPP with density of Λ, the initial PPP density Λ_0 has to be [21]: $\Lambda_0 = -\ln(1-\Lambda\pi c^2)/\pi c^2$.

C. Results and Discussions

Fig. 5 shows the SINR CDF results with four different cell deployments, namely hexagonal, PPP, square and HCPP cell deployments. The system parameters follow those listed in Table I. As expected, due to the independence of BS placement, the PPP network shows the worst performance. It exhibits a median SINR of about 2.5 dB. In contrast, the strict control of BS location with hexagonal lattice mitigates the CCI, thereby providing the best SINR performance with a median SINR of about 6.9 dB. Due to the undesired approximation of a square to a circle, the system with a square network offers a slightly worse SINR than the the case of a hexagonal network. The achieved median SINR is 6.5 dB. For the case of the HCPP network, the achieved median SINR is about 4.6 dB, which is better than the case of the PPP network because of the minimum distance constraint. Therefore, it is concluded that the downlink SINR performance in an optical attocell network with a PPP (hexagonal) cell deployment can be considered as a lower (upper) bound for the case of practical systems.

V. Conclusion

This paper presents a new analytical framework for the system performance of an optical attocell network. The downlink SINR statistics in a DCO-OFDM based optical attocell network with PPP cell deployment have been considered. An analytical expression for the statistics of SINR in PPP network has been presented. The result shows the accuracy of the expression. In addition, the SINR statistics of the PPP network are compared to systems with hexagonal, square and HCPP cell deployments. The results have demonstrated that the system with PPP (hexagonal) cell deployment behaves as an lower (upper) bound for the systems with square and HCPP cell deployments. These results can be used to estimate the performance of a practical optical attocell system without using time-consuming computer simulations. Furthermore, they can be used as benchmarks for further research on optical attocell systems, and as a guideline for setting up a practical system.

Acknowledgement

Professor Haas acknowledges support from the Engineering and Physical Sciences Research Council (EPSRC) under Established Career Fellowship grant EP/K008757/1.

References

[1] H. Elgala, R. Mesleh, and H. Haas, "Indoor Optical Wireless Communication: Potential and State-of-the-Art," *IEEE Commun. Mag.*, vol. 49, no. 9, pp. 56–62, Sep. 2011, ISSN: 0163-6804.

[2] M. Alouini and A. Goldsmith, "Area Spectral Efficiency of Cellular Mobile Radio Systems," *IEEE Trans. Veh. Technol.*, vol. 48, no. 4, pp. 1047–1066, Jul. 1999.

[3] H. Haas, "High-speed Wireless Networking Using Visible Light," SPIE Newsroom, Apr. 19 2013.

[4] D. Tsonev, H. Chun, S. Rajbhandari, J. J. D. McKendry, S. Videv, E. Gu, M. Haji, S. Watson, A. E. Kelly, G. Faulkner, M. D. Dawson, H. Haas and D. O'Brien, "A 3-Gb/s Single-LED OFDM-based Wireless VLC Link Using a Gallium Nitride μLED," *IEEE Photon. Technol. Lett.*, vol. 26, no. 7, pp. 637–640, Apr. 2014.

[5] A. M. Khalid, G. Cossu, R. Corsini, P. Choudhury, and E. Ciaramella, "1-Gb/s transmission over a phosphorescent white LED by using rate-adaptive discrete multitone modulation," *IEEE Photon. J.*, vol. 4, no. 5, pp. 1465–1473, Oct. 2012.

[6] J. Vucic, C. Kottke, S. Nerreter, K. D. Langer, and J. W. Walewski, "513 Mbit/s Visible Light Communications Link Based on DMT-Modulation of a White LED," *J. Lightw. Technol.*, vol. 28, no. 24, pp. 3512–3518, Dec. 2010.

[7] D. Tsonev and H. Haas, "Avoiding Spectral Efficiency Loss in Unipolar OFDM for Optical Wireless Communication," in *Proc. of the Int. Conf. on Commun.*, Sydney, Australia, Jun. 10–14 2014.

[8] B. Ghimire and H. Haas, "Self-Organising Interference Coordination in Optical Wireless Networks," *EURASIP J. Wireless Commun. Netw.*, vol. 1, no. 131, Apr. 2012.

[9] C. Chen, N. Serafimovski, and H. Haas, "Fractional Frequency Reuse in Optical Wireless Cellular Networks," in *Proc. IEEE 24th Int. Symp. Pers. Indoor and Mobile Radio Commun. (PIMRC)*, London, UK, Sep. 8–11, 2013, pp. 3594–3598.

[10] C. Chen, I. Muhammad, D. Tsonev, and H. Haas, "Analysis of Downlink Transmission in DCO-OFDM-Based Optical Attocell Networks," in *IEEE Global Telecommun. Conf. 2014*, Austin, Dec., 8–12 2014.

[11] J. Andrews, F. Baccelli, and R. Ganti, "A Tractable Approach to Coverage and Rate in Cellular Networks," *IEEE Trans. Commun.*, vol. 59, no. 11, pp. 3122–3134, Nov. 2011.

[12] J. M. Kahn and J. R. Barry, "Wireless Infrared Communications," *Proc. IEEE*, vol. 85, no. 2, pp. 265–298, Feb. 1997.

[13] N. Serafimovski, "pureVLC Demonstrates Li-Fi Using Reflected Light," Sep. 2013. [Online]. Available: http://purelifi.com/purevlc-demonstrates-li-fi-using-reflected-light/

[14] C. Chen, S. Videv, D. Tsonev, and H. Haas, "Fractional Frequency Reuse in DCO-OFDM-based Optical Attocell Networks," *J. Lightw. Technol.*, vol. PP, no. 99, pp. 1–1, 2015.

[15] L. Wu, Z. Zhang, J. Dang, and H. Liu, "Adaptive Modulation Schemes for Visible Light Communications," *J. Lightw. Technol.*, vol. 33, no. 1, pp. 117–125, Jan 2015.

[16] J. Armstrong and B. J. C. Schmidt, "Comparison of Asymmetrically Clipped Optical OFDM and DC-Biased Optical OFDM in AWGN," *IEEE Commun. Lett.*, vol. 12, no. 5, pp. 343–345, May 2008.

[17] S. Dimitrov, S. Sinanovic, and H. Haas, "Signal Shaping and Modulation for Optical Wireless Communication," *J. Lightw. Technol.*, vol. 30, no. 9, pp. 1319–1328, May 2012.

[18] H. Elgala, R. Mesleh, and H. Haas, "Non-linearity Effects and Predistortion in Optical OFDM Wireless Transmission Using LEDs," *Int. J. of Ultra Wideband Commun. and Syst.*, vol. 1, no. 2, pp. 143–150, 2009.

[19] J. Bowers, Newton L., "Expansion of Probability Density Functions as A Sum of Gamma Densities with Applications in Risk Theory," *Trans. Soc. Actuaries*, vol. 18, no. 52, pp. 125–147, 1966.

[20] M. Haenggi, "On Distances in Uniformly Random Networks," *IEEE Trans. Inf. Theory*, vol. 51, no. 10, pp. 3584–3586, Oct 2005.

[21] D. Stoyan, W. S. Kendall, and J. Mecke, *Stochastic Geometry and its Applications*, 2nd ed. John Wiley and Sons, 1995.

2013 IEEE 24th International Symposium on Personal, Indoor and Mobile Radio Communications: Special Sessions

Fractional Frequency Reuse in Optical Wireless Cellular Networks

Cheng Chen*, Nikola Serafimovski* and Harald Haas*
*Institute for Digital Communications Joint Research Institute for Signal and Image Processing
The University of Edinburgh EH9 3JL, Edinburgh, UK
{cheng.chen, n.serafimovski, h.haas}@ed.ac.uk

***Abstract*—Interference coordination in optical wireless cellular networks using different frequency reuse techniques are discussed and compared in this paper. On the one hand, full frequency reuse maximises the system throughput at the cost of poor cell-edge user performance. On the other hand, cluster-based static resource partitioning offers good cell-edge user performance at the cost of low system throughput. Fractional frequency reuse (FFR) is introduced as a compromise between cell-edge user performance and the system throughput with low system complexity. Simulation results show that a guaranteed user throughput of 5.6 Mbps and an average area spectral efficiency (ASE) of 0.3389 bps/Hz/m^2 are achieved by the FFR optical wireless system with appropriate power control factors. These results show considerable throughput improvement compared to both benchmark systems. It is also shown that by adjusting the LED transmission optical power of a system using visible light spectrum, the illumination requirement for an office room can be satisfied without extra lighting facilities.**

***Index Terms*—optical wireless communications, fractional frequency reuse, co-channel interference and orthogonal frequency division multiple access.**

I. Introduction

Recent work has shown many advantages of optical wireless (OW) technology [1]. These advantages make OW a suitable candidate for improving the performance of heterogeneous networks. OW uses visible light or infrared light which are unregulated. Furthermore, inexpensive incoherent light emitting diodes (LED) and photo diodes (PD) can be applied at the transceiver, which lower the cost of the OW systems. In particular, OW system can be used in safety critical environments where radio frequency (RF) transmissions are restricted. In addition, optical signals cannot penetrate opaque objects, which means that the optical signal is confined to a single room or a specific area. This makes OW particularly suitable for security critical applications. In addition to security, this mitigates the interference to adjacent rooms. In the multi-user OW system, optical orthogonal frequency division multiplexing (O-OFDM) based on optical intensity modulation (IM) and direct detection (DD) can be used to realise an orthogonal frequency division multiple access (OFDMA) cellular network [2].

The limited bandwidth of the IM/DD systems makes it essential to reuse the finite available bandwidth to meet the high throughput requirements. However, full frequency reuse and ubiquitous system coverage result in co-channel interference (CCI) between users in adjacent cells. Therefore, cellular interference coordination must be considered. Several interference coordination techniques have been investigated in the literature. On the one hand, the simplest method is to apply traditional cluster-based resource partitioning [3]. This technique assigns different sub-bands to neighbouring cells to avoid CCI. However, this technique significantly reduces the available bandwidth in each cell and restricts the achievable peak data rates in the cell [4]. On the other hand, a self-organising interference mitigation technique is proposed in [5]. It uses busy burst (BB) signalling and channel reciprocity of the time division duplex (TDD) technique to define a dynamic interference aware resource allocation solution for interference coordination. However, its dynamic decision relies on channel information feedback, which increases the overhead of the transmission. A method that strikes a reasonable trade-off between the overall spectral efficiency and the cell-edge user throughput is fractional frequency reuse (FFR) [6]. It partitions the available bandwidth for the cell-edge users to avoid CCI and uses the full system bandwidth for the cell centre users in an attempt to maximise the system throughput. Once the system is established, users can simply choose their transmission modes by comparing the received signal to interference plus noise ratio (SINR) with a pre-determined threshold. The system employing the BB protocol requires extra mini time slots to feedback the channel information. In contrast, FFR system exploits regular feedback to transmit the mode decision. Therefore, FFR has the potential to achieve effective interference coordination with low complexity and better quality of service for the cell-edge users, thereby making it a fairer system than full frequency reuse system.

To the best of our knowledge, this paper introduces FFR as an interference coordination technique in an optical cellular network for the first time. The corresponding simulations demonstrate that FFR effectively improves the cell-edge user throughput and the overall system throughput, relative to the systems applying full frequency reuse and standard cluster-based resource partitioning schemes.

The remainder of the paper is organised as follows. Section II introduces the system model including LED array deployment, transmission model and metrics. Section III introduces the FFR applied to the OW system. Simulation results and discussions are presented in Section IV. Finally, we conclude the paper in Section V.

978-1-4577-1348-4/13/$31.00 ©2013 IEEE

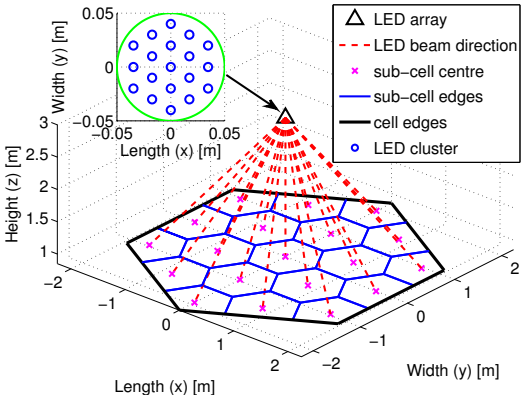

Fig. 1. The inlay figure at the left top corner illustrates the arrangement of the LED array. The main figure illustrates the coverage arrangement in a cell. Each LED cluster in the LED array covers a different region of a cell.

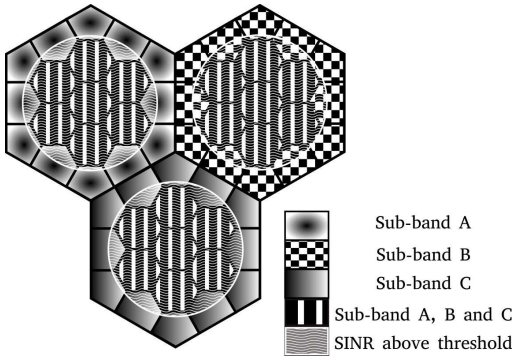

Fig. 2. Deployment of fractional frequency reuse in an optical wireless system.

II. System Model

A. LED array deployment

Multiple LED arrays are used as APs serving the users underneath them. They are distributed on the ceiling using the hexagonal grid model to form a cellular network. An LED array is composed of multiple LEDs with different beam directions. Accordingly, the coverage area in the room is divided into multiple cells. Each cell is divided into multiple sub-cells to enable the discrete cell region division that will be discussed in Section III. In addition, several low power LEDs are integrated with the same beam direction to form a higher power LED cluster to guarantee enough signal strength. An LED cluster provides coverage for a single sub-cell. The spatial alignment of all the beams of the LED clusters establishes the cell coverage. Furthermore, the half-power angle should be small (typically 10°) to confine most of the signal power within each sub-cell [7]. An example LED array deployment and the sub-cell coverage arrangement are illustrated in Fig. 1.

There are several advantages that result from using this LED array deployment: 1) a small half-power angle results in less CCI, 2) the received optical power distribution in the cell is relatively uniform compared to an AP composed of a single LED with wide half-power angle, 3) the deployment of multiple sub-cells leads to a more accurate approximation of the hexagonal cell shape.

B. Optical channel DC gain

The free space channel model between a transmitter at the AP side and a receiver at the user side is introduced. Since the signal at the receiver is dominated by the line-of-sight (LOS) component, only the LOS path is considered while any multi-path effects are disregarded. The optical channel DC gain from the transmitter to the receiver is given by [7]

$$G = \frac{(m+1)A}{2\pi d^2}\cos^m(\phi)T_{\rm s}(\psi)g_{\rm c}(\psi)\cos(\psi), \qquad (1)$$

where m denotes the Lambertian emission order which is given by $m = -\ln(2)/\ln(\cos(\Phi_{1/2}))$, where $\Phi_{1/2}$ is the half-power angle of the LED; A is the area of the PD; d is the distance between the transmitter and receiver; ϕ is the radiant angle; ψ is the incident angle; $T_{\rm s}(\psi)$ is the optical filter gain and $g_{\rm c}(\psi)$ is the concentrator gain which is given by

$$g_{\rm c}(\psi) = \begin{cases} \frac{n^2}{\sin^2\Psi_{\rm c}} & 0 \le \psi \le \Psi_{\rm c}, \\ 0 & \psi > \Psi_{\rm c}, \end{cases} \qquad (2)$$

where $\Psi_{\rm c}$ is the concentrator FOV and n denotes the internal refractive index.

C. Metrics

The OFDMA system is assumed to experience a flat-fading channel. This is valid for intensity modulated OW systems which do not suffer from fading effects as the information carrying signal is encoded in the intensity of the signal as opposed to the in-phase and quadrature electric fields in RF systems. The received SINR on each sub-carrier can be expressed as [5]

$$\gamma_u = \frac{\left(\sum_{i\in L(n)} R_{\rm pd}G_{n,i,u}P_{n,i,u}\right)^2 F_{\rm oe}}{\sum_{\hat{n}\neq n}\left(\sum_{i\in I(\hat{n})} R_{\rm pd}G_{\hat{n},i,u}P_{\hat{n},i,u}\right)^2 F_{\rm oe} + \sigma^2}, \qquad (3)$$

where $R_{\rm pd}$ is the PD responsitivity; $P_{n,i,u}$ is the LED optical transmission power per sub-carrier from LED cluster i of LED array n to the user u; $G_{n,i,u}$ is the channel DC gain from LED cluster i of LED array n to the user u; $F_{\rm oe}$ denotes the optical to electrical conversion factor; $L(n)$ is the set containing the LED clusters contributing to the desired signal of LED array n; $I(n)$ is the set of the LED clusters contributing to the interfering signal in LED array n and σ^2 denotes the power of the noise which is dominated by ambient light shot noise. Modulation schemes are not considered in this paper. Instead, we use the Shannon capacity formula to establish an upper

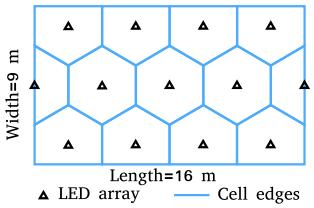

Fig. 3. The cellular network arrangement in the simulated room.

bound on the downlink capacity. The achievable data rate per sub-carrier is given by

$$R_{\mathrm{sc}} = B_{\mathrm{sc}} \log_2(1+\gamma), \tag{4}$$

where B_{sc} denotes the bandwidth of a sub-carrier. The considered data rate metrics are the user throughput and the system throughput that refers to the aggregate throughput of all users in a cell. To account for the average spectral efficiency in the whole network and to highlight the short reuse distance in the room, area spectral efficiency (ASE) is also considered as one of the data rate metrics which is calculated by using [8] as follows:

$$\eta = \frac{\sum_{u \in S} R_{\mathrm{user}}(u)}{B_{\mathrm{sys}} A_{\mathrm{room}}}, \tag{5}$$

where $R_{\mathrm{user}}(u)$ is the data rate achieved by user u, S is the set of all the users within the room, B_{sys} denotes the total system bandwidth and A_{room} is the area of the room.

III. Fractional Frequency Reuse in Optical Wireless

The considered FFR technique is similar to the soft frequency reuse (SFR) applied in an RF system. The entire bandwidth is partitioned into several sub-bands, depending on the reuse factor. In this case, the deployment with a reuse factor of 3 for the cell-edge users is illustrated in Fig. 2. One practical and simple method to partition a cell region is to compare the received SINR of the user using full frequency reuse with a pre-determined threshold [6]. The same approach is applied in an OW system to achieve frequency reuse. However, in an OW system the allocation of the sub-bands is performed in a discrete manner rather than a continuous one. In particular, the transmission of users in each sub-cell is dominated by a single LED cluster. If any section of the sub-cell experiences an SINR that is less than the threshold, then the sub-cell is included in the exterior region and the dominating LED cluster transmits on one of the available sub-bands. Otherwise, the sub-cell is included in the interior region and the corresponding LED cluster is permitted to use the entire bandwidth for transmission. In this manner, each cell is partitioned into an interior region and an exterior region. Indeed, the interior/exterior user partitioning is a discrete approximation of the continuous process when compared to the FFR technique in RF systems. Since the centre users in one cell share sub-band with edge users in adjacent cells, the transmission power for edge users should be higher than that for the centre users. Therefore, a coarse power control is needed. The power control factor β is defined as

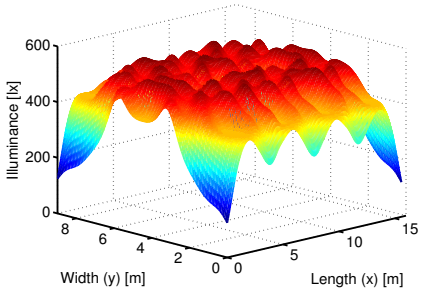

Fig. 4. The spatial distribution of the received horizontal illuminance on the measurement plane in the room.

$$\beta = \frac{P_{n,i,u}}{P_{n,j,u}}, \tag{6}$$

where the LED cluster i belongs to the set that dominates the coverage of the exterior sub-cells while the LED cluster j belongs to the set that dominates the coverage of the interior sub-cells.

IV. Results and Discussions

A cellular network is assumed in a 15.6 m $\times$ 9.0 m $\times$ 3 m large office. The coverage area in the room is divided into 13 hexagonal cells and served by 13 LED arrays, as shown in Fig. 3. The optical receivers are placed at a height of 0.85 m. This is a typical desk height and defines the measurement plane. The PD receiver is facing upward toward the ceiling. The system uses OFDMA based on DC-biased optical OFDM (DCO-OFDM) [2]. To achieve the lighting function concurrently, visible light is used. The system bandwidth is divided into 512 sub-carriers. However, only 255 sub-carriers are used for information data transmission due to the Hermitian symmetry constraint. The performance of the system applying FFR with a reuse factor of 3 for edge users is compared to the benchmark systems which use full frequency reuse and traditional resource partitioning with a static reuse factor of 3. For simplicity, the downlink transmission power of each LED is equally distributed among the sub-carriers that are used. For the benchmark systems, this transmission power is fixed. For the FFR system, the transmission power of the LEDs serving the interior and exterior users are adjusted to maintain the value of β. The SINR threshold for FFR is set to 10 dB which, after some initial investigations, was found to achieve a good compromise between the edge user throughput and the overall system throughput. To guarantee a fair comparison, the total downlink transmission power of all systems is normalised. The system parameters are listed in Table I.

TABLE I
SIMULATION PARAMETERS

Parameters	Values
Optical transmitter radiant power for transmission	63 mW
Transmitter semi-angle	10°
PD responsitivity	0.28 A/W
PD area	1.5 cm^2
Optical filter gain	1.0
Concentrator refractive index	1.5
System bandwidth	20 MHz
Number of sub-carriers	512
Number of users	40
Noise power spectral density	$1 \times 10^{-21} A^2/Hz$

A. Illuminance requirement

Aside from data transmission, the system should also guarantee the required illumination levels, which are 400 lx for reading purposes [9]. The spatial distribution of the horizontal illuminance on the measurement plane is depicted in Fig. 4. Above 90% of the area in the room receives illuminance of above 400 lx, which indicates that the illumination requirement is mostly satisfied.

B. SINR performance

The SINR distributions in the room with full frequency reuse and FFR are illustrated in Fig. 5 and Fig. 6, respectively. As previously mentioned, the bandwidth is equally partitioned into sub-band A, B and C for interference coordination in the exterior region of the cell in the FFR technique. The first three SINR spatial distributions depicted in Fig. 6 correspond to the distributions of SINR on the sub-carriers in sub-bands A, B and C, respectively. The last distribution D shown in Fig. 6 is the average SINR distribution over all three sub-bands. In the full frequency reuse system, the cell-edge user SINR falls in the range of -2.6 dB to 9 dB. In contrast, in the FFR system, since interference is mitigated for the exterior sub-cells by applying traditional resource partitioning, there is an increase in the SINR. Consequently, the SINR for the exterior region of the cell is within the range of 26 dB to 36 dB. On the one hand, in the full frequency reuse system, the cell-centre SINR is within the range of 10 dB to 29 dB. On the other hand, in the FFR system, the interference mitigation also improves the cell-centre average SINR to the range of 24 dB to 32 dB, as shown in Fig. 6.D. Therefore, significant improvement in terms of overall SINR is achieved by using FFR relative to the full frequency reuse system.

C. Throughput performance

It is assumed that 40 users are uniformly distributed in the network. A proportional fair scheduler is used to allocate the sub-carriers to multiple users in each cell. This achieves a good trade-off between fairness and system throughput performance [10]. Table II shows the average ASE of the entire network and the guaranteed user throughput (measured at the first percentile of the user throughput) achieved by the systems with different techniques and parameters. Fig. 7 shows the cumulative distribution function (CDF) of the downlink user throughput. Fig. 8 shows the CDF of the downlink system throughput.

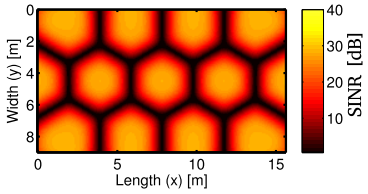

Fig. 5. The spatial distributions of the received SINR on the whole frequency band in the room for the system applying full frequency reuse with a receiver FOV of 70°.

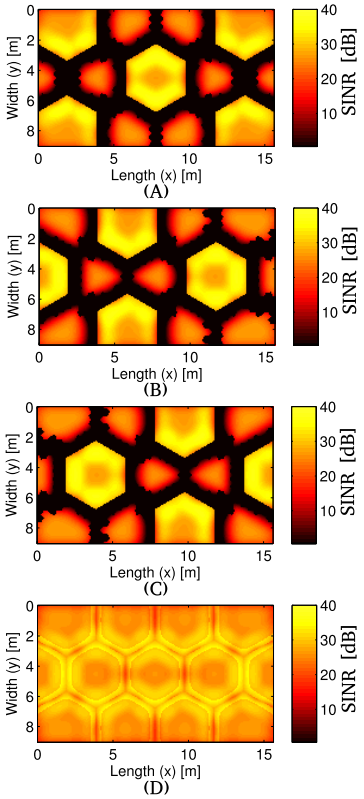

Fig. 6. Plot A, B and C correspond to the spatial distributions of the received SINR on the sub-band A, B and C for the system using FFR, respectively. The receiver FOV is 70° and the value of β is 4, which provides a balanced performance in terms of overall system throughput and cell-edge user throughput. The black region indicates the sub-band is unavailable to the users in that region. Plot D correspond to the average SINR distribution over all three sub-bands

In each figure, "FR" denotes the full frequency reuse system, "RP" denotes the traditional resource partitioning system and "FFR" denotes fractional frequency reuse system. In particular, the curves corresponding to the FFR systems with β values

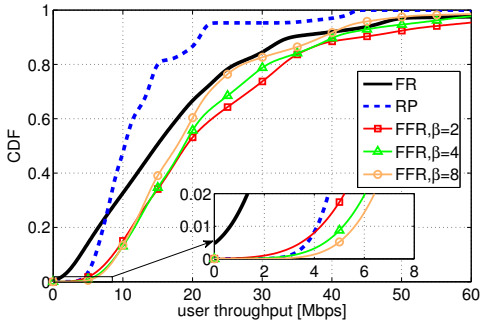

Fig. 7. The CDF curves of the user throughput. "FR" denotes the full frequency reuse system, "RP" denotes the traditional resource partitioning system and "FFR" denotes the fractional frequency reuse system.

TABLE II
AREA SPECTRAL EFFICIENCY AND GUARANTEED USER THROUGHPUT

Frequency partitioning technique	ASE [bps/Hz/m^2]	Guaranteed user throughput [Mbps]
FR	0.2607	0.6
RP	0.1776	4.1
FFR, $\beta = 2$	0.3389	4.3
FFR, $\beta = 4$	0.3211	5.2
FFR, $\beta = 8$	0.2937	5.6

of 2, 4 and 8 are presented in each figure. For the exterior users in the system applying FFR, a power gain of β increases the signal quality further. This results in a better performance for the exterior sub-cells in the FFR system relative to a system applying only traditional resource partitioning. The improvement in terms of guaranteed user throughput is in the range of 5% to 37%. All three sub-bands are available for transmission for the interior users in the system applying FFR. In addition, due to the interference mitigation, the average SINR in the FFR scenario is higher than the SINR in the full frequency reuse scenario as discussed in Section IV-B. This improves the performance of the FFR system relative to the two benchmark systems in terms of both the user throughput and system throughput, as shown in Fig. 7 and Fig. 8. The improvement relative to the full frequency reuse system in terms of average ASE is in the range of 13% to 30%. On the one hand, when $\beta = 8$, the cell-edge user throughput is enhanced at the cost of cell-centre user throughput. In this case, a guaranteed user throughput of 5.6 Mbps is achieved. However, the average ASE is only 0.2937 bps/Hz/m^2. On the other hand, when β is decreased to 2, the SINR of the cell-centre users is improved. This results in a higher average ASE of 0.3389 bps/Hz/m^2 and a lower guaranteed user throughput of 4.3 Mbps. In Fig. 8, it is shown that there is a small proportion of the cells which have a relatively lower system throughput of about 35 Mbps. This occurs when all users in these cells are in the exterior sub-cells, which is reasonable due to the low user density in each cell. In this case, the interior sub-bands are idle which wastes bandwidth and results in a lower system throughput. In future work, we will address this issue.

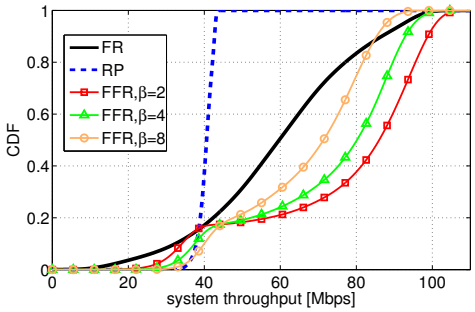

Fig. 8. The CDF curves of the system throughput.

V. CONCLUSIONS

This paper addressed the issue of interference coordination in an optical wireless OFDMA cellular network deployed in an office environment by using FFR. The performance of the system applying FFR was compared to systems that used full frequency reuse and cluster-based resource partitioning with a reuse factor of 3. The results showed that FFR improves the system in terms of cell-edge users throughput and overall system throughput relative to the two benchmark systems. In addition, by adjusting the power control factor β, the performances of cell-centre and cell-edge users can be balanced to meet the design requirements.

ACKNOWLEDGEMENT

Prof. Haas acknowledges the Engineering and Physical Sciences Research Council (EPSRC) for the support of this work under Established Career Fellowship grant EP/K008757/1.

REFERENCES

[1] H. Elgala, R. Mesleh, and H. Haas, "Indoor Optical Wireless Communication: Potential and State-of-the-Art," *IEEE Commun. Mag.*, vol. 49, no. 9, pp. 56–62, Sep. 2011, ISSN: 0163-6804.

[2] J. Armstrong, "OFDM for Optical Communications," *Journal of Lightwave Technology*, vol. 27, no. 3, pp. 189–204, Feb. 2009.

[3] V. H. MacDonald, "The Cellular Concept," *The Bell Systems Technical Journal*, vol. 58, no. 1, pp. 15–43, Jan. 1979.

[4] Z. Xie and B. Walke, "Enhanced Fractional Frequency Reuse to Increase Capacity of OFDMA Systems," in *International Conference on New Technologies, Mobility and Security (NTMS)*, Dec. 2009, pp. 1–5.

[5] B. Ghimire and H. Haas, "Resource Allocation in Optical Wireless Networks," in *Proc. of the 22nd Annual IEEE International Symposium on Personal, Indoor and Mobile Radio Communications (PIMRC '11)*. Toronto, Canada: IEEE, 11–14 Sep. 2011.

[6] T. Novlan, J. Andrews, I. Sohn, R. Ganti, and A. Ghosh, "Comparison of Fractional Frequency Reuse Approaches in the OFDMA Cellular Downlink," in *Global Telecommunications Conference*, Dec. 2010, pp. 1–5.

[7] J. M. Kahn and J. R. Barry, "Wireless Infrared Communications," *Proceedings of the IEEE*, vol. 85, no. 2, pp. 265–298, Feb. 1997.

[8] M. Alouini and A. Goldsmith, "Area Spectral Efficiency of Cellular Mobile Radio Systems," *IEEE Transactions on Vehicular Technology*, vol. 48, no. 4, pp. 1047–1066, 1999.

[9] T. Komine and M. Nakagawa, "Fundamental analysis for visible-light communication system using LED lights," *IEEE Transactions on Consumer Electronics*, vol. 50, no. 1, pp. 100–107, Feb. 2004.

[10] M. Pischella and J. C. Belfiore, "Power control in distributed cooperative OFDMA cellular networks," *IEEE Transactions on Wireless Communications*, vol. 7, no. 5, pp. 1900–1906, May 2008.

Globecom 2013 Workshop - Optical Wireless Communications

Joint Transmission in Indoor Visible Light Communication Downlink Cellular Networks

Cheng Chen*, Dobroslav Tsonev* and Harald Haas*
*Institute for Digital Communications
The University of Edinburgh EH9 3JL, Edinburgh, UK
{cheng.chen, d.tsonev, h.haas}@ed.ac.uk

***Abstract*—In future visible light communication (VLC) systems, networked multi-cell operation is required to achieve seamless coverage and high data rate in typical indoor environments. We refer to this type of cellular network as optical atto-cell network. In such network, co-channel interference (CCI) between adjacent optical atto-cells limits the performance of the network. In order to maximise system throughput and improve signal quality in the whole coverage area, it is necessary to mitigate CCI. In this paper, the concept of multi-point joint transmission (JT) is adapted to a VLC cellular network. It can generally be described as concurrent data transmission from multiple cooperating base stations (BSs) to a mobile station (MS). In a VLC JT system, strong CCI is avoided by co-ordinated transmission and, in addition, we exploit a particular characteristic of intensity modulation (IM) systems. This is that signals always superimpose constructively which is in stark contrast to radio frequency (RF)-based systems. Therefore, the cell-edge user signal to interference plus noise ratios (SINRs) can be improved. The results show that the JT scheme improves the median SINR by 16.4 dB compared to a full frequency reuse system. Additionally, a JT system exhibits a 67.6% improvement in terms of median system throughput compared to a static resource partitioning system with a reuse factor of 3.**

***Index Terms*—visible light communications, joint transmission, co-channel interference and orthogonal frequency division multiple access.**

I. Introduction

Recent work has shown that optical wireless (OW) technology has significant potential to provide high speed wireless transmission in an indoor environment [1]. In addition, an OW system uses unregulated bandwidth and can be applied where radio frequency (RF) transmission is restricted. Therefore, OW is a suitable candidate for a complementary technology to RF communications. Inexpensive light emitting diodes (LEDs) and photo diodes (PDs) can serve as front-end elements. Visible light communication (VLC) technology has the potential to realise the functions of illumination and data transmission at the same time. This could lead to lower installation costs and improved power efficiency. In order to achieve communication to multiple roaming mobile stations (MSs) in an office or home indoor environment, a cellular network composed of small optical atto-cells is proposed. The goal is to achieve seamless coverage and high spectral efficiency. An optical atto-cell network can be realised by installing multiple LED access points (APs) in the ceiling of a room with careful alignment. Each AP acts as a base station (BS) and covers the users within its illumination region. If a MS moves out of the coverage region of an AP, handover techniques will guarantee seamless wireless service provision by ensuring that the MS is always served by the most suitable AP.

In an optical atto-cell network, using the same frequency resources in adjacent cells causes co-channel interference (CCI). This significantly degrades the signal to interference plus noise ratio (SINR) available to a cell-edge user, thereby resulting in high outage probability and low data rate. Therefore, interference coordination techniques are required to mitigate CCI. Several approaches are considered in the literature. The simplest approach is applying traditional static resource partitioning [2] by splitting cells into clusters. Within a cluster, frequency resources are allocated in an orthogonal fashion. In this manner, interfering users are separated in space to mitigate CCI. Decreased available bandwidth in each cell is the main drawback of this approach, which significantly limits the user data rate. A busy-burst-based self-organised interference coordination technique is proposed in [3]. It uses the uplink signal to acquire channel information and applies a dynamic interference-aware resource allocation scheme. The busy-burst signalling approach shows significant improvements in terms of fairness and spectral efficiency relative to the static resource partitioning approach. Another technique to mitigate CCI is to adapt the concept of joint transmission (JT) [4] to optical atto-cell networks. In a JT system, a MS can be served by multiple nearby BSs, thereby improving the acquired signal quality. Since this approach substitutes interference signals with desired signals, the received SINR can be significantly improved, especially for the cell-edge MSs. However, many challenges such as backhaul constraints, accurate

978-1-4799-2851-4/13/$31.00 ©2013IEEE

synchronisation and multi-path fading effects limit the performance of JT systems. In a VLC system, due to the special features of intensity modulation and direct detection (IM/DD) [5], it is possible to overcome these difficulties in an optical atto-cell network. The authors in [6] demonstrate that it is possible to achieve a multi-point cooperative transmission scheme in a single user VLC system in a small indoor environment with improved optical power gain and reduced bit error rate (BER). The contribution of this work is to adapt JT to the downlink transmission in an optical atto-cell network in order to mitigate CCI and improve the cell-edge user performance in terms of received SINR and system throughput.

The remainder of the paper is organised as follows. Section II describes the system models. Section III describes the proposed JT scheme. This includes the system characteristics, JT framework and frequency resource planning. Section IV presents the simulation results and discussions. Finally, we conclude the paper in section V.

II. System Model

The system of interest is deployed in a large indoor environment. The entire coverage area is divided into N_{ap} cells with hexagonal shape. N_{ap} BSs each equipped with an LED array are located at the centres of their corresponding cells providing two-way communication to MSs. Each LED array is composed of 7 LED clusters. Since a single LED cannot provide sufficient optical power for communication or illumination, multiple low power LEDs with the same beam direction form a high power LED cluster, which works as a large LED to reach the required power level. Despite the small half-power semiangle of a single LED (20° LED semiangle at half power), each cluster has a slightly different beam direction to cover a different small region of the total coverage area. Each LED cluster is denoted by a tuple $v = (i, n)$ showing that it is the i_{th} LED cluster within the n_{th} LED array, where $i \in [1, 2, \cdots, 7]$ and $n \in [1, 2, \cdots, N_{\mathrm{ap}}]$. Direct-current-biased optical orthogonal frequency division multiplexing (DCO-OFDM) [7] is used in order to realise orthogonal frequency division multiple access (OFDMA) which provides the means to achieve multiple access and combat inter-symbol interference (ISI).

A. Channel

Due to the employment of highly directional LEDs, the signal power from reflected paths is low. Besides, a cyclic prefix is considered in the OFDM frame which mitigates the impact of inter-symbol interference (ISI) and a single tap equaliser can be used. Therefore, the optical channel can be accurately approximated by the line-of-sight (LOS) path. It is valid to consider the channel DC gain only. The channel DC gain G from an LED to a PD detector is given by [5],

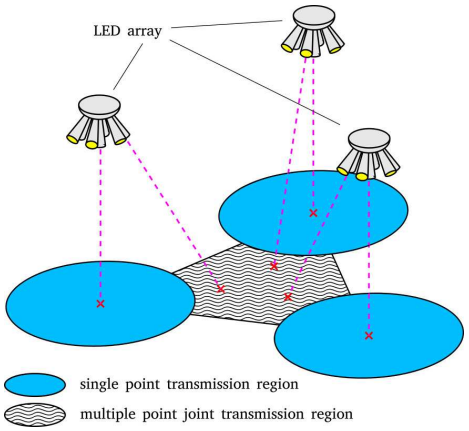

Fig. 1. Multi-point joint transmission.

$$G = \frac{(m+1)A}{2\pi d^2} \cos^m(\phi) T_{\mathrm{s}}(\psi) g_{\mathrm{c}}(\psi) \cos(\psi), \quad (1)$$

where A denotes the physical area of the PD detector; d is the distance between the LED and the PD detector; ϕ represents the radiation angle at the transmitter side; ψ represents the incidence angle at the receiver side; $T_{\mathrm{s}}(\psi)$ models the optical filter gain which is assumed to be 1 in this work; $g_{\mathrm{c}}(\psi)$ denotes the concentrator gain and m is the Lambertian emission order. The ideal concentrator has a gain of:

$$g_{\mathrm{c}}(\psi) = \begin{cases} \frac{n^2}{\sin^2 \Psi_{\mathrm{c}}} & 0 \le \psi \le \Psi_{\mathrm{c}}, \\ 0 & \psi > \Psi_{\mathrm{c}}, \end{cases} \quad (2)$$

where Ψ_{c} models the receiver FOV and n denotes the internal refractive index. The Lambertian emission order is related to the transmitter semiangle at half-power $\Phi_{1/2}$ by $m = -\ln(2)/\ln(\cos(\Phi_{1/2}))$.

B. OFDMA

In an OFDM system, the modulation symbols are converted to OFDM symbols by using the inverse discrete Fourier transform (IDFT) of size K as follows:

$$x_t = \frac{1}{\sqrt{K}} \sum_{k=0}^{K-1} x_k \exp\left(j \frac{2\pi}{K} tk\right), \quad (3)$$

where x_k denotes each of the K data symbols that are used to compose the OFDM symbol, x_t. Due to the requirement for real-valued OFDM symbols, a Hermitian symmetry constraint must be imposed in the frequency domain. Therefore, only half of the total subcarriers

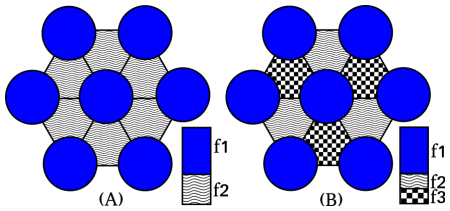

Fig. 2. Plot A and B are the joint transmission frequency plan 1 and 2, respectively.

carry information. Multiple access is realised by allocating different subcarriers to different users. Additionally, a DC-bias and signal clipping are introduced to ensure that the OFDM symbols are positive. The DC-bias and signal clipping are set in a manner that the additional noise is negligible [8]. Although the DC bias carries no information, this portion of power is not wasted since the luminous power must be high enough to meet the illumination requirement. The illuminance should be at least 400 lx for reading purposes [9].

C. SINR

SINR is used as the metric to evaluate the received signal quality at a specified user on each of the allocated subcarriers. The received SINR $\gamma_k(u)$ of MS u on subcarrier k is defined as [10]

$$\gamma_k(u) = \frac{\left(\sum_{v\in V(u)} N_{\mathrm{l}} P_{\mathrm{opt},k} R_{\mathrm{pd}} G_{v,u}\right)^2 F_{\mathrm{OE}}}{\sum_{\hat{u}\neq u}\left(\sum_{\hat{v}\in V(\hat{u})} N_{\mathrm{l}} P_{\mathrm{opt},k} R_{\mathrm{pd}} G_{\hat{v},u}\right)^2 F_{\mathrm{OE}} + \sigma^2}, \tag{4}$$

where N_{l} denotes the number of LEDs per cluster; $P_{\mathrm{opt},k}$ is the optical power of an LED used on subcarrier k; $V(u)$ is the set which contains all the tuples of LED clusters serving user u, and the number of the serving LED clusters for a user varies from 1 to 3; R_{pd} models the PD responsitivity; $G_{v,u}$ is the channel DC gain from LED cluster v to MS u; $\hat{u}$ denotes the users that reuses the same subcarrier k in the system, F_{OE} is the optical to electrical conversion factor and σ^2 represents the electrical additive white Gaussian noise (AWGN) power on each subcarrier. The noise power is dominated by ambient light shot noise and receiver thermal noise. The effects of other noise sources such as clipping noise are omitted since their contribution is negligible. Therefore, the noise power is defined by [3],

$$\sigma^2 = 2qI_{\mathrm{bg}}B_{\mathrm{sc}} + \frac{4K_{\mathrm{b}}TB_{\mathrm{sc}}}{R_{\mathrm{f}}}, \tag{5}$$

where q is the charge of an electron; I_{bg} denotes the current due to background light; B_{sc} denotes the bandwidth of a subcarrier; K_{b} is the Boltzmann constant; T models the absolute temperature and R_{f} is the feedback resistance of the transimpedance amplifier (TIA).

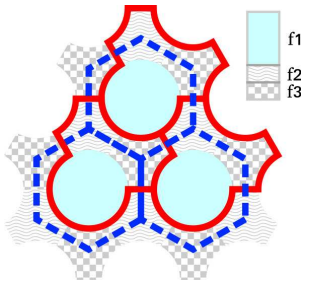

Fig. 3. The area of the region specified by the blue dashed lines (cell coverage area) equals the area of the region specified by the red solid curves. This implies that the JT2 system has the same reuse factor as that of a full frequency reuse system.

In this paper, the downlink user capacity is computed using the Shannon-Hartley theorem:

$$C(u) = \sum_{k\in M(u)} B_{\mathrm{sc}} \log_2(1+\gamma_k(u)), \tag{6}$$

where $M(u)$ represents the set of subcarriers allocated to user u. Lowpass frequency response and non-linear current to optical power transfer function of the LED are not considered here in order to simplify the system model. It is assumed that the detrimental impact of these imperfections are reduced by a proper system design [8].

III. Joint Transmission in VLC

A. Characteristics

In an optical atto-cell network, many system specific properties support the implementation of JT: 1) a very high-speed low-latency connection between BSs is easy to realise due to the short physical distance between BSs; 2) there is no fading effect in IM/DD systems due to constructive combination of intensity modulated signals; Therefore, extra coding and strict synchronisation requirement are unnecessary; 3) since only the LOS path is significant, the time differences between the arrival of signal components from different BSs are small relative to a symbol period; 4) an OFDM-based system has an inherent ability to combat ISI. Applying JT not only improves the communication quality at cell-edges, but also makes the connection more reliable. Since three LOS channels exist simultaneously as a result of the proposed cellular structure, data connection can still be guaranteed for the case that one or two LOS paths are blocked.

B. Framework

Fig. 1 shows the JT system model assumed in this paper. Among the 7 LED clusters in an LED array, the central one works in the single point transmission mode

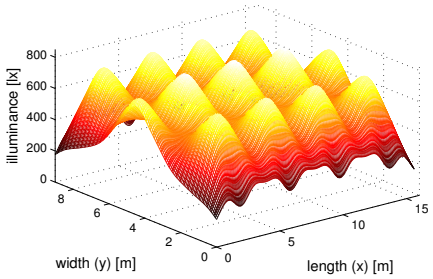

Fig. 4. Illuminance distribution.

TABLE I

Parameters	Symbol	Values
Equivalent LED optical power	P_{opt}	63 [mW]
LED semiangle at half-power	$\Phi_{1/2}$	20°
LED centre luminous intensity	$I(0)$	57.7 [cd]
Number of LEDs per cluster	N_{l}	40
PD responsitivity	R_{pd}	0.28 [A/W]
PD physical area	A	1.5 [cm^2]
Receiver field of view	Ψ_c	70°
LED modulation bandwidth	W	20 [MHz]
JT SINR threshold	γ_{th}	10 dB
Current due to background light	I_{bg}	5100 [μA]
Feedback resistance of TIA	R_{f}	6 [kΩ]
LED cluster beam direction angle	α	38.13°
E/O conversion factor	F_{OE}	1/9

covering the users in the cell-centre. Each of the other 6 exterior LED clusters in an array faces one of the 6 vertices of the hexagonal cell. Since every three adjacent cells have a common vertex, three exterior LED clusters from different adjacent arrays cover a cell corner region. This region is defined as a JT region which is centred at a vertex of a cell. Since there are 6 corners in each cell, there are six JT regions around an LED array. We assume that the system has an uplink system in order to allow MSs to communicate with BSs, and each MS is able to determine the downlink signal strength.

The working mechanisms of the system are described as follows: 1) the central LED cluster of each array transmits a pilot signal to all MSs with a unique sequence to identify the corresponding LED array; 2) each MS selects the BS providing the strongest signal as a primary BS and selects the BSs providing the second and the third strongest signals as the secondary BSs; 3) a MS estimates the received SINR by considering the signal from the primary BS as a desired signal and the other signals as interference; 4) if the SINR is above a predetermined threshold which determines the maximum BER for reliable data transmission, the user replies to the BSs through uplink channel requesting single point transmission from the primary BS; 5) otherwise, the user replies to the BSs requesting JT from the primary and the secondary BSs. Then, the BSs use a predetermined look up table to select the appropriate LED clusters for transmission. With a given BS cooperation set, the look up table provides the tuples of LED clusters that are used to serve the MS using JT. For example, if the cooperation set includes BSs A, B and C, the LED clusters which cover the region closest to the common vertex shared by cell A, B and C are selected to provide JT.

C. Frequency Planning

Since the magnitude response of the channel is flat, scheduling is simplified. We assume that the subcarriers are evenly distributed among the user population in the coverage area. Fig. 2 illustrates the frequency reuse pattern. For the first plan shown in Fig. 2 (A), the frequency band is divided into two subbands. The first subband is reused in each single point transmission region, while the second subband is reused in each multi-point JT region. The number of subcarriers in single point transmission subband N_{st} is set as follows:

$$N_{\text{st}} = \left\lceil \frac{A_{\text{st}} N_{\text{band}}}{A_{\text{total}}} \right\rceil, \tag{7}$$

where A_{st} denotes the total combined area of single point transmission regions, A_{total} denotes the total coverage area and N_{band} denotes the number of all subcarriers. The number of subcarriers in the JT subband, N_{jt}, is calculated by (8) as

$$N_{\text{jt}} = N_{\text{band}} - N_{\text{st}}. \tag{8}$$

This frequency allocation plan ensures spatially uniform availability of frequency resources. This is to support the assumptions of a uniform user distribution as well as equal target data rate of all users in the network. However, there is no interference mitigation between adjacent JT regions. Therefore, low SINRs are achieved at the boundaries of two adjacent JT regions. For the second plan shown in Fig. 2 (B), the subband for JT regions is divided into two partitions as follows:

$$N_{\text{jt1}} = N_{\text{jt2}} = \lfloor (N_{\text{band}} - N_{\text{st}})/2 \rfloor. \tag{9}$$

The two JT subbands are reused in a pattern such that adjacent JT regions always use different subbands in order to mitigate CCI. The subband for single point transmission remains the same. This frequency plan offers improved receiver SINR performance, but fewer number of subcarriers are available in the JT regions. For convenience, the JT systems with frequency plan 1 and 2 are defined as JT1 system and JT2 system, respectively.

In a full frequency reuse system, the whole frequency band is permitted to be used in each cell. Within a cell coverage area (hexagon indicated by blue dashed line boundaries in Fig. 3), subcarriers are not reused. In a JT2 system, the entire set of subcarriers are prevented

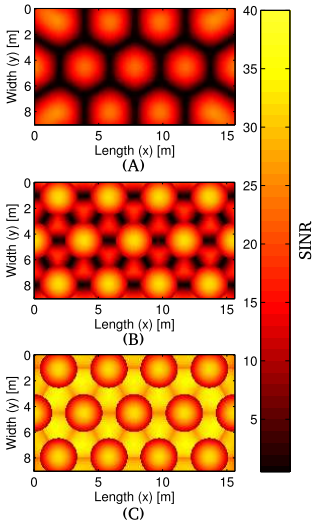

Fig. 5. SINR distribution of the system using (A) full frequency reuse (B) joint transmission 1 (C) joint transmission 2.

from being reused within the region bounded by red solid curves in Fig. 3. The area of this region is exactly equal to the coverage area of a cell. Therefore, the reuse factor of a JT2 system is equivalent to the one in a full frequency reuse system.

IV. Results and Discussions

A. Simulation setup

The investigated downlink cellular network scenario is deployed in a 15.6 m $\times$ 9 m $\times$ 3 m office room with a total of 13 LED arrays. It is assumed that mobile devices with a PD receiver are located 0.85 m above the floor, which is the typical height of a desk top. All PD receivers are facing upward towards the ceiling. The IFFT/FFT size of the applied OFDMA system is 512. For simplicity, no power control is applied and all LEDs have the same average optical transmit power. The phosphor-based white LED described in [9] is used in the system model. Since only the optical power of blue light is used for communication purposes, the effective optical power is 50% of the total power. 40 users are uniformly distributed in the room. Key simulation parameters are listed in Table I. Because the main contribution of this paper is to demonstrate the potential gain in terms of SINR and throughput achieved by JT systems, some of the system parameters including $\Phi_{1/2}$, α, γ_{th} and Ψ_c are determined empirically in order to guarantee reasonable system performance while it is recognised that an optimisation of these parameters would potentially further enhance the system performance.

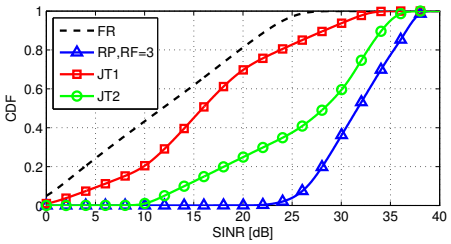

Fig. 6. Cumulative distribution function of received SINR. FR refers to full frequency reuse system, RP, RF=3 refers to static resource partitioning system with a reuse factor of three, JT1 refers to joint transmission system 1 and JT2 refers to joint transmission system 2.

B. Benchmark systems

The JT systems are compared against two benchmark systems. One of the benchmark systems uses full frequency reuse (FR) with a reuse factor of one. The other system uses traditional static resource partitioning (RP) with a reuse factor of three [2]. The simulation parameters for them are the same as for the JT systems in order to guarantee a fair comparison.

C. Illumination function

For a VLC system, it is important to fulfil the lighting requirements. Fig. 4 illustrates that the majority of the area (more than 90%) in the room benefits from illuminance within the required range. For better lighting performance, extra lighting fixtures without communication function can be installed to complement the low illuminance at room edges.

D. Receiver SINR

Fig. 5 shows the SINR distribution for the different systems. The benchmark FR system achieves the worst SINRs. For the JT1 system, the cell-edge SINRs are improved compared to the FR system, especially for the users near the centre of JT regions. However, due to the lack of interference mitigation between adjacent JT regions, the users at the boundaries between adjacent JT regions achieve poor SINR. In contrast, in the JT2 system, the same frequency band is not reused in adjacent JT regions. Therefore, the cell-edge user SINR is further improved (above 30 dB) compared to the JT1 system at the cost of spectrum reuse. Fig. 6 presents the cumulative distribution function (CDF) of the SINRs in different systems. It demonstrates that JT1 and JT2 systems exhibit a 4.1 dB and a 16.4 dB improvement, respectively, in terms of median SINR relative to an FR system.

E. Downlink throughput

Fig. 7 and Fig. 8 show the CDF of the downlink system throughput and the user throughput in the dif-

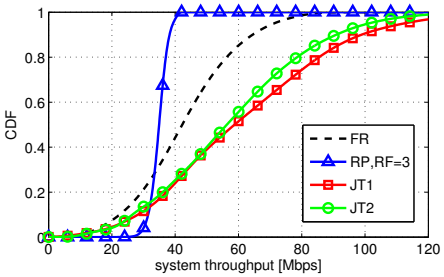

Fig. 7. Cumulative distribution function of the system throughput.

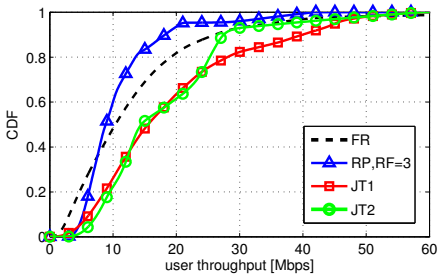

Fig. 8. Cumulative distribution function of the user throughput.

ferent systems. The system throughput is defined as the aggregate data rate in the given optical cell, while the user throughput is defined as the transmission data rate achieved by a single MS. With the largest reuse factor, the RP system achieves the lowest median system throughput of 34.9 Mbps. In contrast, an FR system with a reuse factor of one achieves a higher median system throughput of 42.3 Mbps. As discussed in section III-C, the JT2 system has the same reuse factor as the FR system. In addition, the JT2 system exhibits strong robustness to CCI. Therefore, the JT2 technique achieves a median system throughput of 56.3 Mbps, which is significantly higher than both the FR and the RP systems. However, the maximum number of subcarriers a user could use is determined by his location and is limited by the size of the respective subband. Therefore, the peak user throughput for the JT2 system is lower than the JT1 system. Since the JT1 system enforces a more aggressive frequency reuse, it achieves the highest median system throughput of 58.5 Mbps. The JT1 and the JT2 systems show a 67.6% and a 61.3% improvement compared to the RP system, respectively. The JT scheme also shows improvement in terms of the guaranteed user throughput (defined as the minimum data rate with 90% confidence) compared to the benchmarks. The JT1 and the JT2 systems achieve a 6.3 Mbps and a 7.5 Mbps guaranteed user throughput, respectively. These numbers are 100% to 140% higher than the guaranteed user throughput achieved by an FR system.

V. Conclusions

This paper addressed multi-point joint transmission in indoor optical atto-cell networks in order to achieve seamless coverage, high data rate and multiple access. The performance of a cellular system that applies joint transmission was compared to the performance of a full frequency reuse system and a static resource partitioning system with a reuse factor of three. The results showed that the joint transmission systems achieved higher cell-edge SINRs compared to a full frequency reuse system. In addition, a joint transmission system also achieved 67.6% improvement in terms of median system throughput compared to a static resource partitioning system. However, the downside of joint transmission systems is that they need extra signalling overhead.

Acknowledgement

Prof. Haas acknowledges support from the Engineering and Physical Sciences Research Council (EPSRC) under Established Career Fellowship grant EP/K008757/1.

References

[1] H. Elgala, R. Mesleh, and H. Haas, "Indoor Optical Wireless Communication: Potential and State-of-the-Art," *IEEE Commun. Mag.*, vol. 49, no. 9, pp. 56–62, Sep. 2011, ISSN: 0163-6804.

[2] G. W. Marsh and J. M. Kahn, "Channel Reuse Strategies for Indoor Infrared Wireless Communications," *IEEE Transactions on Communications*, vol. 45, no. 10, pp. 1280–1290, Oct. 1997.

[3] B. Ghimire and H. Haas, "Self Organising Interference Coordination in Optical Wireless Networks," *EURASIP Journal on Wireless Communications and Networking*, 2012, to appear.

[4] P. Baier, M. Meurer, T. Weber, and H. Tröger, H.ger, "Joint transmission (jt), an alternative rationale for the downlink of time division cdma using multi-element transmit antennas," in *IEEE Sixth International Symposium on Spread Spectrum Techniques and Applications*, vol. 1, 2000, pp. 1–5 vol.1.

[5] J. M. Kahn and J. R. Barry, "Wireless Infrared Communications," *Proceedings of the IEEE*, vol. 85, no. 2, pp. 265–298, Feb. 1997.

[6] G. Prince and T. Little, "On the performance gains of cooperative transmission concepts in intensity modulated direct detection visible light communication networks," in *2010 6th International Conference on Wireless and Mobile Communications (ICWMC)*, 2010, pp. 297–302.

[7] J. Armstrong, "OFDM for Optical Communications," *Journal of Lightwave Technology*, vol. 27, no. 3, pp. 189–204, Feb. 2009.

[8] S. Dimitrov and H. Haas, "Information rate of ofdm-based optical wireless communication systems with nonlinear distortion," *Journal of Lightwave Technology*, vol. 31, no. 6, pp. 918–929, 2013.

[9] J. Grubor, S. Randel, K.-D. Langer, and J. Walewski, "Bandwidth-efficient indoor optical wireless communications with white light-emitting diodes," in *6th International Symposium on Communication Systems, Networks and Digital Signal Processing*, 2008, pp. 165–169.

[10] S. Dimitrov, H. Haas, M. Cappitelli, and M. Olbert, "On the Throughput of an OFDM-based Cellular Optical Wireless System for an Aircraft Cabin," in *Proc. of European Conference on Antennas and Propagation (EuCAP 2011)*, Rome, Italy, 11–15 Apr. 2011, invited Paper.

Bibliography

[1] Cisco Visual Networking Index, "Global Mobile Data Traffic Forecast Update, 20152020," White Paper, CISCO, Feb. 2016. [Online]. Available: http://www.cisco.com/c/en/us/solutions/collateral/service-provider/visual-networking-index-vni/mobile-white-paper-c11-520862.pdf.

[2] L. Hanzo and H. Haas and S. Imre and D. O'Brien and M. Rupp and L. Gyongyosi, "Wireless Myths, Realities, and Futures: From 3G/4G to Optical and Quantum Wireless," *Proc. IEEE*, vol. 100, pp. 1853–1888, May 2012.

[3] M. Elkashlan and T. Q. Duong and H. H. Chen, "Millimeter-Wave Communications for 5G: Fundamentals: Part I ," *IEEE Commun. Mag.*, vol. 52, pp. 52–54, Sept. 2014.

[4] S. Dimitrov and H. Haas, *Principles of LED Light Communications: Towards Networked Li-Fi*. Cambridge University Press, 2015.

[5] "DIN Standard 5031: Optical Radiation Physics and Illuminating Engineering," 1982.

[6] H. Haas, "High-speed Wireless Networking Using Visible Light." SPIE Newsroom, 2013. [Online]. Available: http://spie.org/newsroom/4773-high–speed-wireless-networking-using-visible-light.

[7] A. Goldsmith, *Wireless Communications*. Cambridge University Press, 2005.

[8] Q. C. Li, H. Niu, A. T. Papathanassiou, and G. Wu, "5G Network Capacity: Key Elements and Technologies," *IEEE Veh. Technol. Mag.*, vol. 9, pp. 71–78, Mar. 2014.

[9] A. Ghosh, T. A. Thomas, M. C. Cudak, R. Ratasuk, P. Moorut, F. W. Vook, T. S. Rappaport, G. R. MacCartney, S. Sun, and S. Nie, "Millimeter-Wave Enhanced Local Area Systems: A High-Data-Rate Approach for Future Wireless Networks," *IEEE J. Sel. Areas Commun.*, vol. 32, pp. 1152–1163, June 2014.

[10] J. Andrews, H. Claussen, M. Dohler, S. Rangan, and M. Reed, "Femtocells: Past, Present, and Future," *IEEE J. Sel. Areas Commun.*, vol. 30, pp. 497–508, Apr. 2012.

[11] "High-capacity indoor wireless solutions: Picocell or femtocell?." Fujitsu network communications inc. [Online]. Available: https://www.fujitsu.com/us/Images/High-Capacity-Indoor-Wireless.pdf.

[12] H. Haas, L. Yin, Y. Wang, and C. Chen, "What is LiFi?," *J. Lightw. Technol.*, vol. 34, pp. 1533–1544, Mar. 2016.

[13] J. M. Kahn and J. R. Barry, "Wireless Infrared Communications," *Proc. IEEE*, vol. 85, pp. 265–298, Feb. 1997.

[14] C. Chen, D. Basnayaka, and H. Haas, "Non-line-of-sight Channel Impulse Response Characterisation in Visible Light Communications," in *IEEE Int. Conf. on Commun.*, (Kuala Lumpur, Malaysia), pp. 1–6, May 2016.

[15] C. Chen, D. Basnayaka, X. Wu, and H. Haas, "Efficient Analytical Calculation of Non-line-of-sight Channel Impulse Response in Visible Light Communications." Unpublished, submitted to J. Lightw. Technol.

[16] C. Chen, I. Muhammad, D. Tsonev, and H. Haas, "Analysis of Downlink Transmission in DCO-OFDM-Based Optical Attocell Networks," in *Proc. of IEEE Global Commun. Conf.*, (Austin, TX), Dec., 8–12 2014.

[17] C. Chen, D. Basnayaka, and H. Haas, "Downlink SINR Statistics in OFDM-Based Optical Attocell Networks with a Poisson Point Process Network Model," in *Proc. of IEEE Global Commun. Conf.*, (San Diego, CA), pp. 1–6, Dec., 6–10 2015.

[18] C. Chen, D. A. Basnayaka, and H. Haas, "Downlink Performance of Optical Attocell Networks," *J. Lightw. Technol.*, vol. 34, pp. 137–156, Jan. 2016.

[19] G. W. Marsh and J. M. Kahn, "Channel Reuse Strategies for Indoor Infrared Wireless Communications," *IEEE Trans. Commun.*, vol. 45, pp. 1280–1290, Oct. 1997.

[20] C. Chen, N. Serafimovski, and H. Haas, "Fractional Frequency Reuse in Optical Wireless Cellular Networks," in *Proc. of the Int. Symp. on Personal, Indoor and Mobile Radio Commun.*, (London, United Kingdom), pp. 3594–3598, Sept., 8–11 2013.

[21] C. Chen, S. Videv, D. Tsonev, and H. Haas, "Fractional Frequency Reuse in DCO-OFDM-Based Optical Attocell Networks," *J. Lightw. Technol.*, vol. 33, pp. 3986–4000, Oct 2015.

[22] C. Chen, D. Tsonev, and H. Haas, "Joint Transmission in Indoor Visible Light Communication Downlink Cellular Networks," in *IEEE Globecom Workshops*, (Atlanta, GA), pp. 1127–1132, Dec., 9–13 2013.

[23] J. B. Carruthers and J. M. Kahn, "Modeling of Nondirected Wireless Infrared Channels," *IEEE Trans. Commun.*, vol. 45, pp. 1260–1268, Oct. 1997.

[24] Z. Ghassemlooy, W. Popoola, and S. Rajbhandari, *Optical Wireless Communications: System and Channel Modelling with MATLAB®*. Taylor & Francis, 2012.

[25] A. G. Bell, "Selenium and the Photophone," *Nature*, vol. 22, no. 569, pp. 500–503, 1880.

[26] F. R. Gfeller and U. Bapst, "Wireless In-House Data Communication Via Diffuse Infrared Radiation," *Proc. IEEE*, vol. 67, pp. 1474–1486, Nov. 1979.

[27] P. Barker and A. C. Boucouvalas, "Performance modeling of the IrDA protocol for infrared wireless communications," *IEEE Commun. Mag.*, vol. 36, no. 12, pp. 113–117, 1998.

[28] European Commission, "Technical briefing: Phasing out Incandescent Bulbs in the EU," Sept. 2008. [Online]. Available: http://ec.europa.eu.

[29] P. H. Pathak, X. Feng, P. Hu, and P. Mohapatra, "Visible light communication, networking, and sensing: A survey, potential and challenges," *IEEE Commun. Surveys Tutorials*, vol. 17, pp. 2047–2077, Fourthquarter 2015.

[30] D. Tsonev, H. Chun, S. Rajbhandari, J. J. D. McKendry, S. Videv, E. Gu, M. Haji, S. Watson, A. E. Kelly, G. Faulkner, M. D. Dawson, H. Haas and D. O'Brien, "A 3-Gb/s Single-LED OFDM-based Wireless VLC Link Using a Gallium Nitride μLED," *IEEE Photon. Technol. Lett.*, vol. 26, pp. 637–640, Apr. 2014.

[31] G. Cossu, A. M. Khalid, P. Choudhury, R. Corsini, and E. Ciaramella, "3.4 Gbit/s visible optical wireless transmission based on RGB LED," *Optics Express*, vol. 20, pp. B501–B506, 2012.

[32] IEEE Std. 802.15.7-2011, "IEEE Standard for Local and Metropolitan Area Networks, Part 15.7: Short-Range Wireless Optical Communication Using Visible Light," 2011.

[33] G. Miao, J. Zander, K. W. Sung, and S. B. Slimane, *Fundamentals of Mobile Data Networks*. Cambridge University Press, 2016.

[34] M. Alouini and A. Goldsmith, "Area Spectral Efficiency of Cellular Mobile Radio Systems," *IEEE Trans. Veh. Technol.*, vol. 48, pp. 1047–1066, July 1999.

[35] D. Lpez-Prez, M. Ding, H. Claussen, and A. H. Jafari, "Towards 1 Gbps/UE in Cellular Systems: Understanding Ultra-Dense Small Cell Deployments," *IEEE Commun. Surveys Tutorials*, vol. 17, pp. 2078–2101, Fourthquarter 2015.

[36] H. Elgala, R. Mesleh, and H. Haas, "Practical Considerations for Indoor Wireless Optical System Implementation Using OFDM," in *Proc. IEEE 10th Int. Conf. Telecommun. (ConTel)*, (Zagreb, Croatia), pp. 25–29, June 8–10 2009.

[37] D. Tsonev, S. Sinanovic, and H. Haas, "Complete Modeling of Nonlinear Distortion in OFDM-based Optical Wireless Communication," *J. Lightw. Technol.*, vol. 31, pp. 3064–3076, Sept. 15 2013.

[38] D. Tsonev, S. Videv, and H. Haas, "Unlocking Spectral Efficiency in Intensity Modulation and Direct Detection Systems," *IEEE J. Sel. Areas Commun.*, vol. PP, no. 99, pp. 1–1, 2015.

[39] "Purelifi product: Li-flame," 2015. [Online]. Available: http://purelifi.com/lifi-products/li-flame/.

[40] M. B. Rahaim, A. M. Vegni, and T. D. C. Little, "A Hybrid Radio Frequency and Broadcast Visible Light Communication System," in *IEEE GLOBECOM Workshops*, pp. 792–796, Dec., 5–9 2011.

[41] B. Ghimire and H. Haas, "Self-Organising Interference Coordination in Optical Wireless Networks," *EURASIP J. Wireless Commun. Netw.*, vol. 1, Apr. 2012.

[42] Z. Chen, N. Serafimovski, and H. Haas, "Angle Diversity for an Indoor Cellular Visible Light Communication System," in *Proc. of IEEE Veh. Technol. Conf.*, (Seoul, South Korea), pp. 1–5, May 18–21, 2014.

[43] M. Pischella and J. C. Belfiore, "Power Control in Distributed Cooperative OFDMA Cellular Networks," *IEEE Trans. Wireless Commun.*, vol. 7, pp. 1900–1906, May 2008.

[44] J. Fakidis, D. Tsonev, and H. Haas, "A Comparison between DCO-OFDMA and Synchronous One-Dimensional OCDMA for Optical Wireless Communications," in *Proc. IEEE 24th Int. Symp. Pers. Indoor and Mobile Radio Commun.*, (London, UK), pp. 3605–3609, Sept. 8–11 2013.

[45] A. Ahmed, L. M. Boulahia, and D. Gaiti, "Enabling Vertical Handover Decisions in Heterogeneous Wireless Networks: A State-of-the-Art and A Classification," *IEEE Commun. Surveys Tutorials*, vol. 16, pp. 776–811, Second 2014.

[46] Y. Wang and H. Haas, "Dynamic Load Balancing With Handover in Hybrid Li-Fi and Wi-Fi Networks," *J. Lightw. Technol.*, vol. 33, pp. 4671–4682, Nov. 2015.

[47] O. Tipmongkolsilp, S. Zaghloul, and A. Jukan, "The Evolution of Cellular Backhaul Technologies: Current Issues and Future Trends," *IEEE Commun. Surveys Tutorials*, vol. 13, pp. 97–113, First 2011.

[48] X. Ge, H. Cheng, M. Guizani, and T. Han, "5G Wireless Backhaul Networks: Challenges and Research Advances," *IEEE Network*, vol. 28, pp. 6–11, Nov. 2014.

[49] W. Ni, R. P. Liu, I. B. Collings, and X. Wang, "Indoor Cooperative Small Cells over Ethernet," *IEEE Commun. Mag.*, vol. 51, pp. 100–107, Sept. 2013.

[50] A. Papaioannou and F. N. Pavlidou, "Evaluation of Power Line Communication Equipment in Home Networks," *IEEE Syst. J.*, vol. 3, pp. 288–294, Sept. 2009.

[51] H. Kazemi, M. Safari, and H. Haas, "A Wireless Backhaul Solution Using Visible Light Communication for Optical Attocell Networks." submitted to IEEE Global Commun. Conf., 2016.

[52] BS EN 62471:2008, "Photobiological Safety of Lamps and Lamp Systems," Sept. 2008.

[53] A. Neumann, J. J. Wierer, W. Davis, Y. Ohno, S. R. J. Brueck, and J. Tsao, "Four-color Laser White Illuminant Demonstrating High Color-rendering Quality," *Opt. Express*, vol. 19, pp. A982–A990, July 2011.

[54] D. Tsonev, S. Videv, and H. Haas, "Towards a 100 Gb/s Visible Light Wireless Access Network," *Opt. Express*, vol. 23, pp. 1627–1637, Jan. 2015.

[55] T. Komine and M. Nakagawa, "Fundamental Analysis for Visible-light Communication System Using LED Lights," *IEEE Trans. Consum. Electron.*, vol. 50, pp. 100–107, Feb. 2004.

[56] H. L. Minh, D. O'Brien, G. Faulkner, L. Zeng, K. Lee, D. Jung, Y. Oh, and E. T. Won, "100-Mb/s NRZ visible light communications using a postequalized white LED," *IEEE Photonics Technol. Lett.*, vol. 21, pp. 1063–1065, Aug. 2009.

[57] European Standard EN 12464-1, "Lighting of Indoor Work Places," Jan. 2009.

[58] J. R. Meyer-Arendt, "Radiometry and Photometry: Units and Conversion Factors," *Appl. Opt.*, vol. 7, pp. 2081–2084, Oct. 1968.

[59] "VESTA 165mm Recessed LED Downlighter." [Online]. Available: http://www.istl.com/vesta.php.

[60] "64 W LED panel," Aug. 2014. [Online]. Available: http://wellmaxled.com/portfolio/64-w-led-panel-light.

[61] H. Elgala, R. Mesleh, and H. Haas, "Non-linearity Effects and Predistortion in Optical OFDM Wireless Transmission Using LEDs," *Inderscience Int. J. of Ultra Wideband Commun. and Systems*, vol. 1, no. 2, pp. 143–150, 2009.

[62] E. F. Schubert, *Light-Emitting Diodes*. Cambridge University Press, Sept. 2012.

[63] J. J. D. McKendry, D. Massoubre, S. Zhang, B. R. Rae, R. P. Green, E. Gu, R. K. Henderson, A. E. Kelly and M. D. Dawson, "Visible-light communications using a CMOS-controlled micro-light-emitting-diode array," *J. Lightw. Technol.*, vol. 30, no. 1, pp. 61–67, 2012.

[64] R. Baets, D. Delbeke, R. Bockstaele, and P. Bienstman, "Resonant-cavity Light-emitting Diodes: a Review," in *Proc. SPIE*, vol. 4996, pp. 42–49, July 3 2003.

[65] J. Vucic, C. Kottke, S. Nerreter, K. D. Langer, and J. W. Walewski, "513 Mbit/s Visible Light Communications Link Based on DMT-Modulation of a White LED," *J. Lightw. Technol.*, vol. 28, pp. 3512–3518, Dec. 2010.

[66] A. M. Khalid, G. Cossu, R. Corsini, P. Choudhury, and E. Ciaramella, "1-Gb/s Transmission Over a Phosphorescent White LED by Using Rate-adaptive Discrete Multitone Modulation," *IEEE Photon. J.*, vol. 4, pp. 1465–1473, Oct. 2012.

[67] J. Barry, J. Kahn, W. Krause, E. Lee, and D. Messerschmitt, "Simulation of Multipath Impulse Response for Indoor Wireless Optical Channels," *IEEE J. Select. Areas Commun.*, vol. 11, pp. 367–379, Apr. 1993.

[68] F. J. Lopez-Hernandez, R. Perez-Jimenez, and A. Santamara, "Ray-tracing algorithms for fast calculation of the channel impulse response on diffuse IR wireless indoor channels," *Optical Eng.*, vol. 39, no. 10, pp. 2775–2780, 2000.

[69] F. J. Lopez-Hermandez and M. J. Betancor, "DUSTIN: Algorithm for Calculation of Impulse Response on IR Wireless Indoor Channels," *Electronics Lett.*, vol. 33, pp. 1804–1806, Oct. 1997.

[70] V. Jungnickel, V. Pohl, S. Nonnig, and C. von Helmolt, "A Physical Model of the Wireless Infrared Communication Channel," *IEEE J. Sel. Areas Commun.*, vol. 20, pp. 631–640, Apr. 2002.

[71] J. Grubor, S. C. J. Lee, K. D. Langer, T. Koonen, and J. W. Walewski, "Wireless High-Speed Data Transmission with Phosphorescent White-Light LEDs," in *33rd European Conf. and Exhibition of Optical Commun. - Post-Deadline Papers*, (Berlin, Germany), pp. 1–2, Sept., 16–20 2007.

[72] K. Lee, H. Park, and J. Barry, "Indoor Channel Characteristics for Visible Light Communications," *IEEE Commun. Lett.*, vol. 15, pp. 217–219, Feb. 2011.

[73] J. Armstrong, "OFDM for Optical Communications," *J. Lightw. Technol.*, vol. 27, pp. 189–204, Feb. 2009.

[74] S. Dimitrov, S. Sinanovic, and H. Haas, "Clipping Noise in OFDM-Based Optical Wireless Communication Systems," *IEEE Trans. Commun.*, vol. 60, pp. 1072–1081, Apr. 2012.

[75] J. Xu, J. Zhang, and J. G. Andrews, "On the Accuracy of the Wyner Model in Cellular Networks," *IEEE Trans. Wireless Commun.*, vol. 10, pp. 3098–3109, Sept. 2011.

[76] J. Andrews, F. Baccelli, and R. Ganti, "A tractable approach to coverage and rate in cellular networks," *IEEE Trans. Commun.*, vol. 59, pp. 3122–3134, Nov. 2011.

[77] J. G. Andrews, F. Baccelli, and R. K. Ganti, "A new tractable model for cellular coverage," in *48th Annual Allerton Conf. on Commun., Control, and Computing*, pp. 1204–1211, Sept. 2010.

[78] A. Guo and M. Haenggi, "Spatial Stochastic Models and Metrics for the Structure of Base Stations in Cellular Networks," *IEEE Trans. Wireless Commun.*, vol. 12, pp. 5800–5812, Nov. 2013.

[79] J. Grubor, S. Randel, K. D. Langer, and J. W. Walewski, "Bandwidth-efficient Indoor Optical Wireless Communications with White Light-emitting Diodes," in *6th Int. Symp. on Commun. Systems, Networks and Digital Signal Process.*, (Graz), pp. 165–169, July 2008.

[80] H. Schulze, "Frequency-Domain Simulation of the Indoor Wireless Optical Communication Channel," *IEEE Trans. Commun.*, vol. 64, pp. 2551–2562, June 2016.

[81] P. Chvojka, S. Zvanovec, P. A. Haigh, and Z. Ghassemlooy, "Channel Characteristics of Visible Light Communications Within Dynamic Indoor Environment," *J. Lightw. Technol.*, vol. 33, pp. 1719–1725, May 2015.

[82] F. Miramirkhani and M. Uysal, "Channel Modeling and Characterization for Visible Light Communications," *IEEE J. Photonics*, vol. 7, pp. 1–16, Dec. 2015.

[83] P. F. Mmbaga, J. Thompson, and H. Haas, "Performance Analysis of Indoor Diffuse VLC MIMO Channels Using Angular Diversity Detectors," *J. Lightw. Technol.*, vol. 34, pp. 1254–1266, Feb 2016.

[84] D. O'Brien and M. Katz, "Optical wireless communications within fourth-generation wireless systems [invited]," *J. of Optical Networking*, vol. 4, pp. 312–322, 2005.

[85] D. Wu, Z. Ghassemlooy, H. Le-Minh, S. Rajbhandari, and Y. Kavian, "Power Distribution and Q-factor Analysis of Diffuse Cellular Indoor Visible Light Communication Systems," in *16th European Conference on Networks and Optical Communications (NOC 2011)*, (Newcastle upon Tyne, UK), pp. 28–31, 20–22 July 2011.

[86] F. Xiong, *Digital Modulation Techniques*. Artech House Publishers, 2nd edition ed., 2006.

[87] H. Burchardt, S. Sinanović, Z. Bharucha, and H. Haas, "Distributed and Autonomous Resource and Power Allocation for Wireless Networks," *IEEE Trans. Commun.*, Aug. 2013.

[88] D. Stoyan, W. S. Kendall, and J. Mecke, *Stochastic Geometry and its Applications*. John Wiley and Sons, 2nd ed., 1995.

[89] B. Almeroth, A. Fehske, G. Fettweis, and E. Zimmermann, "Analytical Interference Models for the Downlink of a Cellular Mobile Network," in *IEEE Globcom Workshops*, (Houston, Texas), pp. 739–743, Dec. 5–9 2011.

[90] E. Sousa and J. Silvester, "Optimum Transmission Ranges in a Direct-Sequence Spread-Spectrum Multihop Packet Radio Network," *IEEE J. Sel. Areas Commun.*, vol. 8, pp. 762–771, June 1990.

[91] J. Bowers, Newton L., "Expansion of Probability Density Functions as A Sum of Gamma Densities with Applications in Risk Theory," *Trans. Soc. Actuaries*, vol. 18, no. 52, pp. 125–147, 1966.

[92] M. Haenggi, "On Distances in Uniformly Random Networks," *IEEE Trans. Inf. Theory*, vol. 51, pp. 3584–3586, Oct. 2005.

[93] V. Chandrasekhar, J. Andrews, and A. Gatherer, "Femtocell Networks: A Survey," *IEEE Commun. Mag.*, vol. 46, no. 9, pp. 59–67, 2008.

[94] C. Hansen, "WiGiG: Multi-Gigabit Wireless Communications in the 60 GHz Band," *IEEE Wireless Commun.*, vol. 18, pp. 6–7, Dec. 2011.

[95] P. Chandhar and S. Das, "Area Spectral Efficiency of Co-Channel Deployed OFDMA Femtocell Networks," *IEEE Trans. Wireless Commun.*, vol. 13, pp. 3524–3538, July 2014.

[96] H.-S. Jo, P. Xia, and J. Andrews, "Downlink Femtocell Networks: Open or Closed?," in *Proc. of IEEE Int. Conf. on Commun.*, (Kyoto, Japan), pp. 1–5, June, 5–9 2011.

[97] W. C. Cheung, T. Quek, and M. Kountouris, "Throughput Optimization, Spectrum Allocation, and Access Control in Two-Tier Femtocell Networks," *IEEE J. Sel. Areas Commun.*, vol. 30, pp. 561–574, Apr. 2012.

[98] D. Muirhead, M. Imran, and K. Arshad, "Insights and Approaches for Low-Complexity 5G Small-Cell Base-Station Design for Indoor Dense Networks," *IEEE Access*, vol. 3, pp. 1562–1572, 2015.

[99] C. Yiu and S. Singh, "Empirical capacity of mmWave WLANS," *IEEE J. Sel. Areas Commun.*, vol. 27, pp. 1479–1487, Oct. 2009.

[100] K. Cui, J. Quan, and Z. Xu, "Performance of Indoor Optical Femtocell by Visible Light Communication," *Opt. Commun.*, vol. 298–299, pp. 59 – 66, July 2013.

[101] Z. Xie and B. Walke, "Enhanced Fractional Frequency Reuse to Increase Capacity of OFDMA Systems," in *International Conference on New Technologies, Mobility and Security (NTMS)*, pp. 1–5, Dec. 2009.

[102] T. Novlan, R. Ganti, A. Ghosh, and J. Andrews, "Analytical Evaluation of Fractional Frequency Reuse for OFDMA Cellular Networks," *IEEE Trans. Wireless Commun.*, vol. 10, pp. 4294–4305, Dec. 2011.

[103] T. Novlan, J. Andrews, I. Sohn, R. Ganti, and A. Ghosh, "Comparison of Fractional Frequency Reuse Approaches in the OFDMA Cellular Downlink," in *Proc. IEEE Global Telecommun. Conf.*, (Miami, FL), pp. 1–5, Dec. 6–10 2010.

[104] V. V. Huynh, N.-T. Le, N. Saha, M. Chowdhury, and Y. M. Jang, "Inter-Cell Interference Mitigation Using Soft Frequency Reuse with Two FOVs in Visible Light Communication," in *Int. Conf. ICT Convergence*, (Jeju Island), pp. 141–144, Oct. 15–17 2012.

[105] P. W. Baier, M. Meurer, T. Weber, and H. Troger, "Joint transmission (JT), an alternative rationale for the downlink of time division CDMA using multi-element transmit antennas," in *Spread Spectrum Techniques and Applications, 2000 IEEE Sixth International Symposium on*, vol. 1, (Parsippany, NJ), pp. 1–5, Sept. 6–8, 2000.

[106] G. B. Prince and T. D. C. Little, "On the Performance Gains of Cooperative Transmission Concepts in Intensity Modulated Direct Detection Visible Light Communication Networks," in *6th Int. Conf. on Wireless and Mobile Commun.*, pp. 297–302, Sept. 2010.

[107] H. Zhu and J. Wang, "Performance Analysis of Chunk-Based Resource Allocation in Multi-Cell OFDMA Systems," *IEEE J. Sel. Areas in Commun.*, vol. 32, pp. 367–375, Feb. 2014.

[108] L. Zeng, D. O'Brien, H. Minh, G. Faulkner, K. Lee, D. Jung, Y. Oh, and E. T. Won, "High Data Rate Multiple Input Multiple Output (MIMO) Optical Wireless Communications Using White LED Lighting," *IEEE J. Sel. Areas Commun.*, vol. 27, pp. 1654–1662, Dec. 2009.

[109] T.-D. Nguyen and Y. Han, "A Proportional Fairness Algorithm with QoS Provision in Downlink OFDMA Systems," *IEEE Commun. Lett.*, vol. 10, pp. 760–762, Nov. 2006.

[110] T. Komine, S. Haruyama, and M. Nakagawa, "A Study of Shadowing on Indoor Visible-Light Wireless Communication Utilizing Plural White LED Lightings," *Wireless Personal Commun.*, vol. 34, no. 1, pp. 211–225, 2005.